DEVELOPMENT AND VALIDATION OF A BIOMECHANICAL MODEL OF THE HUMAN UPPER ARM

SERDAR ARITAN

A THESIS SUBMITTED IN PARTIAL FULFILMENT OF THE REQUIREMENTS OF THE MANCHESTER METROPOLITAN UNIVERSITY FOR THE DEGREE OF

DOCTOR OF PHILOSOPHY

Biomechanics Research Group

the Manchester Metropolitan University

September 1998

Contents

Abstract 9

Declaration 10

Copyright 11

Dedication 12

Acknowledgements 13

1. General Introduction and Literature Review

1.1. Introduction and Characterisation and modelling of Soft Biological Tissue 14

1.1.1. Skin fat and Muscle Structure 15

1.1.2. Contraction of Muscle 17

1.1.3. Mechanical Properties of Soft Biological Tissue 18

1.1.3.1. Ultrasound Experiments and Results 20

1.1.3.2. Indentor Test Results 22

1.1.4. Models of Multiple Body Segments and The Whole Body 27

1.2. Finite Element Modelling 30

1.3. Aims of the Study 33

1.4. Summary by Chapter 35

2. Program for Generation of Three-dimensional Finite Element Mesh from MRI Scans of Human Limbs.

2.1. Introduction 37

2.2. Methods 38

2.2.1. Data Preparation and Processing 43

2.2.1.1. Data Preparation 43

2.2.1.1.1. Cleaning 43

2.2.1.1.2. Calibration and Data Conversion 45

2.2.1.2. Data Processing Algorithms and Data Structures 48

2.2.1.2.1. Smoothing Procedure 48

2.2.1.2.2. Differentiation Procedure 49

2.2.1.2.3. Sorting Procedure 50

2.2.1.2.4. Cutting-off Procedure 51

2.2.1.2.5. External Edge Correction (manual correction) 52

2.2.1.2.6. Automated Procedure for Layer Separation (optional) 52

2.2.1.2.7. Cleaning The Marked Edges and Creating Final ASCII Files 52

2.2.2. FE Mesh Generation and Three-dimensional Image Construction 54

2.2.3. Additional Features 56

2.3. Results and Discussions 56

2.4. Summary 59

3. Experiment Design I

Mechanical Test Design and Pneumatic System

3.1. General Description of the Testing System 60

3.1.1. Main Frame 60

3.1.2. Squeezing Chamber 62

3.1.3. Load Cell 64

3.2. Creep Test Design 65

3.3. Stress-Relaxation Test Design 70

3.3.1. Load Cell Carrier 72

3.3.2. Pneumatic Design of Stress-Relaxation Test 73

3.3.2.1. Pneumatic Cylinders 74

3.3.2.2. Filter/Regulator and Lubricator 76

3.3.2.3. Emergency Stop 76

3.3.2.4. Pneumatic Poppet Relays 76

3.4. Stress-Strain Test Design 76

3.4.1. Stepping Linear Actuator 79

3.4.2. Pneumatic Design of Stress Strain Test 80

3.4.2.1. Voltage-to-Pressure Converter 81

3.5. Health and Safety Aspects of the Instrumentation 82

3.6. Summary 83

4. Experiment Design II

Electronic Circuit design and Software

4.1. General Description of the Electronic Design and Software 84

4.2. Computer Input / Output 85

4.3. Load Cell Readings 86

4.3.1. Load Cell Amplification 86

4.3.2. Analog-to-Digital Converter 88

4.4. Programmable Interval Timer 89

4.5. Creep Test 91

4.5.1. Opto-Encoder 92

4.5.2. Data Collection and Control Software for Creep Test 92

4.6. Stress-Relaxation Test 95

4.6.1. Control of Pneumatic Valves 95

4.6.2. Data Collection and Control Software for Stress-Relaxation Test 95

4.7. Stress-Strain Test 98

4.7.1. Stepper Motor and Control 98

4.7.2. Stepper Motor Driving Circuit 99

4.7.3. Feedback Circuit for Voltage-to Pressure Converter 100

4.7.4. Data Collection and Control Software for Stress-Strain Test 100

4.8. Summary 104

5. Mechanical Tests and Results

5.1. Mechanical Testing of Soft Biological Tissue 105

5.2. Creep Tests 105

5.2.1. Creep Test Data Collection 106

5.2.2. Mathematical Description of Creep Test Data 110

5.3. Stress-Relaxation Tests 113

5.3.1. Stress-Relaxation Test Data Collection 114

5.3.2. Mathematical Description of Stress-Relaxation Test Data 118

5.4. Stress-Strain Tests 122

5.4.1. Stress-Strain Test Data Collection 122

5.4.2. Mathematical Description of Stress-Strain Test Data 125

5.6. Seat Belt Testing 127

5.7. Summary 130

6. Mechanical Models of Viscoelastic Behaviour

6.1. Viscoelastic Models 131

6.1.1. Maxwell Model 132

6.1.2. Kelvin-Voigt Model 134

6.2. Standard Linear Solid 137

6.2.1. Stress-Relaxation Behaviour of Standard Linear Solid 138

6.2.2. Creep Behaviour of Standard Linear Solid 139

6.3. Mechanical Modelling of Bulk Tissue 139

6.3.1. Creep Behaviour of Bulk Tissue 140

6.3.2. Stress-Relaxation Behaviour of Bulk Tissue 143

6.3.3. Stress-Strain Behaviour of Bulk Tissue 146

6.4. Summary 164

7. Finite Element Simulation of Bulk Tissue

7.1. An Introduction to Finite Element Method 165

7.2. Solutions of Equations 166

7.3. Finite Element Meshing 167

7.3.1. Volume Meshing 167

7.4. Finite Element Analysis 171

7.4.1. Time Domain Analysis of Viscoelastic Material 172

7.4.2. Incremental Variables 176

7.4.3. Results of Finite Element Analysis 176

7.5. Summary 179

8. Discussion and Conclusions

8.1. Discussion 180

8.1.1. Introduction 180

8.1.2. New Equipment and Development 181

8.1.2.1. Overview 181

8.1.2.2. Hardware 183

8.1.2.3. Software 185

8.1.3. Determination of Soft Tissue Properties 188

8.1.3.1. Image Processing and Geometrical Modelling 188

8.1.3.2. Experimental Factors 189

8.1.3.2.1. Creep Test 190

8.1.3.2.2. Stress-Relaxation Test 193

8.1.3.2.3. Stress-Strain Test 196

8.1.4. Model Development 198

8.1.4.1. Mechanical Model development 199

8.1.4.2. Finite Element Model Development 201

8.2. Further directions 202

8.3. Conclusions 203

8.4. Limitations of the Study 204

8.5. Recommendations for Further Research 205

References 207

Appendices

A. Technical Drawings 218

B. Creep Test 232

B.1. Curve Fitting 233

B.2. Comparison of protocols 239

B.3. Model Fitting 242

C. Stress-Relaxation Test 248

C.1. Curve Fitting 249

C.2. Comparison of Protocols 255

C.3. Model Fitting 258

D. Stress-Strain Test 264

D.1. Curve Fitting 265

D.2. Comparison of Protocols 269

E. Experiment Pictures 271

F. Publications 277

Abstract

A methodology was developed to study in vivo muscular bulk tissue behaviour. Muscular bulk tissue can be regarded as composite, non-isotropic, incompressible, non-linear viscoelastic material from the biomechanical point of view. The human upper arm was chosen to investigate the bulk properties. To determine the mechanical properties of the bulk tissue in vivo, required accurate geometry of the tissue, which was obtained by using Magnetic Resonance Imaging. A new algorithm, consequently, new software was developed for creating a realistic finite element mesh.

A new testing machine and control software were designed to investigate the response of the muscle bulk tissue under compression. The testing machine is capable of running three different type of tests which are creep, stress-relaxation and stress-strain tests. Contracted and relaxed test conditions were applied.

Specific mechanical models – the Voigt model for creep behaviour or the Maxell model for stress-relaxation behaviour - were developed for different type of experiments. Both the creep and stress-relaxation and the stress-strain behaviour of the muscular bulk tissue was represented by using a standard linear solid model. The elastic modulus of bulk tissue was estimated from these models for both test conditions. Finally, a three-dimensional finite element model was created by using mechanical modelling parameters with a realistic internal geometry of the human upper arm. A new computational framework was developed to apply the finite element method to anisotropic, viscoelastic soft tissue. Results showed that the formulation could represent anisotropy and time dependent behaviour of soft biological tissue

Declaration

No portion of the work referred to in this thesis has been submitted in support of an application for another degree or qualification of this or any other university or other institution of learning.

Copyright

- Copyright in text of this thesis rests with the Author. Copies (by any process) either in full, or of extracts, may be made only in accordance with instructions given by the Author and lodged in the Manchester Metropolitan University Library. Details may be obtained from the Librarian. This page must form part of any such copies made. Further copies (by any process) of copies made in accordance with such instructions may not be made without the permission (in writing) of the Author.

- The ownership of any intellectual property rights which may be described in this thesis is vested in the Manchester Metropolitan University, subject to any prior agreement to the contrary, and may not be made available for use by third parties without the written permission of the University, which will prescribe the terms and conditions of any such agreement.

Further information on the conditions under which disclosures and exploitation may take place is available from the Head of Department.

Dedication

To My Father.

"Sevgili Babama"

Acknowledgements

The Author is particularly indebted to his research director Prof. Roger Bartlett and supervisor Dr. Olutunde Oyadiji at University of Manchester for their inspiration, supervision and invaluable comments during the course of this research. Sincere appreciation to Dr. Peter Dabnichki for introducing the Author to the subject and his early supervision. Special thanks to Prof. Anthony Sargeant for his advice on muscle physiology.

Many thanks to Mr. Thomas McKee for his technical advice support for the design and implementation of the electronic circuits for the test rig. To all technicians, Barry, Gerry, Gary and Robert for their help in the design of the test rig.

I would like to express my special thanks to Hacettepe University in Ankara Turkey for the financial support.

My special gratitude to all my friends in the biomechanics research group at MMU, especially, Dr. Diane Taktak, Mr. Costantinos Maganaris, and in the engineering department at Istanbul Technical University, Dr. Erdem Imrak, at University of Manchester Dr. Feroz Kottamal and to all those not already mentioned for their help and encouragement. Finally I would like to thank my girl friend Julie for her patience and her encouragement to finish this research.

Chapter 1

General Introduction and Literature Review

1.1. Introduction and Characterisation and Modelling of Soft Biological Tissue

Understanding and characterising the mechanical response of soft biological tissues is a fundamental problem in biomechanics. Adequate models are needed to allow the study of both normal tissue function and the effects of disease and injury on these tissues. These models may help to understand the nature of some diseases such as pressure sores etc.

The mechanical behaviour of biological materials is determined by their structure. The factors which control mechanical response include the gross (bulk) and microscopic tissue morphology, the chemical composition of the tissue, fluid flow in the tissue, directionality of tissue fibre structures, and the interfaces between various structures.

Soft tissues generally exhibit nonlinearity, nonhomogeneity, anisotropy and viscoelasticity. Viscoelastic materials present some difficulties for characterising their mechanical response. Energy storage and dissipation within the complex molecular structure produce hysteresis and allows creep and stress relaxation to occur. Soft tissues are relatively compliant at low strains and become dramatically stiffer at high strains. There is a continuing need to develop methods that reveal the complete set of anisotropic material properties. These properties are important in case and control studies and in numerical implementations of constitutive equations in biological tissue. This study was developed to demonstrate these properties and to provide experience in analysis of this type of data.

1.1.1. Skin Fat and Muscle Structure

Skin is a passive soft tissue, it follows the deformation of the underlying soft tissues, the mechanical properties of which have a significant influence on the appearance and behaviour of skin. Figure 1.1. shows a cross-section of skin. The first two layers, the epidermis and the dermis are connected. The dermis is also connected by collagen fibres to a subcutaneous fatty tissue, called the hypodermis. This structure serves as a fat container for the body [42].

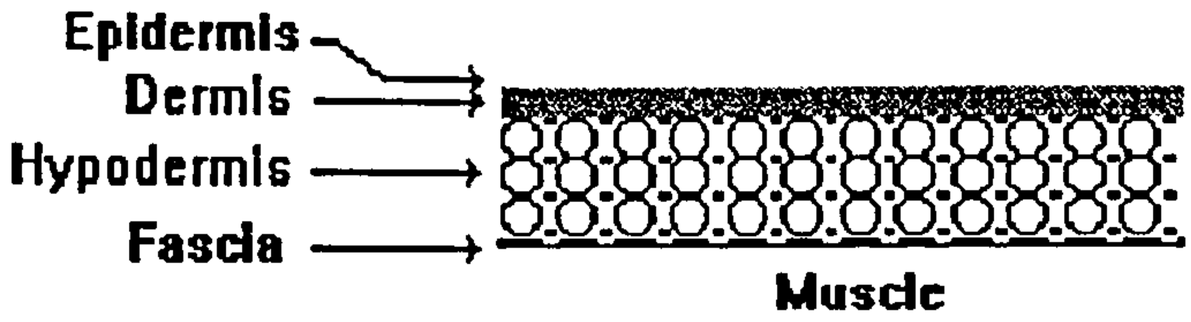

Figure 1.1. Layered skin structure

Muscles are found in all more-advanced animals, both invertebrate and vertebrate. All muscles are transducers converting chemical into electrical energy, heat energy and some useful mechanical energy. Anatomically, muscles can be classified in many ways: in terms of function, innervation, body location and histology. The histologic classification is most widely used. Histologically, two types of muscles can be distinguished in vertebrates: striated and smooth. Striated muscle has alternating dark and light bands distributed in a regular pattern across long fibres. Smooth muscle consists of shorter fibres with no striations [3].

The entire muscle is surrounded by a sheath of connective tissue. Each large bundle is divided into smaller bundles, and each of these is finally subdivided into muscle fibres. A large portion of striated muscle is made of these fibres, 10-100 μm in diameter, and of

lengths that reach 0.3 m or more in long muscles. The ends of the fibres of many strained muscles are attached to tendons [3, 6, 48].

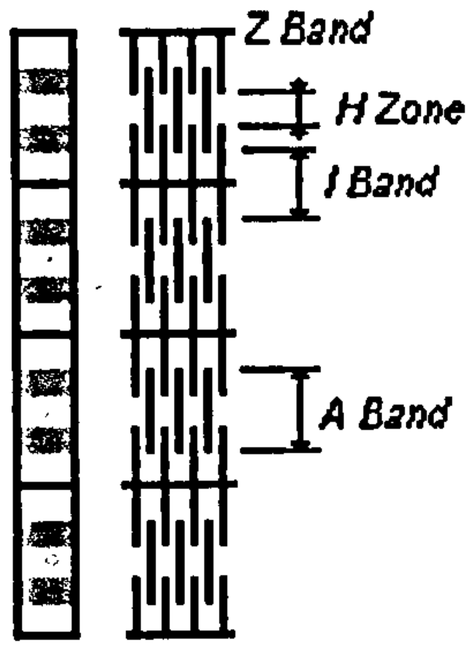

Figure 1.2. Basic contractile unit of the muscle.

Briefly, the systematic arrangement of the myofibrils gives the striated appearance to skeletal muscle. The repeat unit in this pattern is called the sarcomere, and this is the basic contractile unit of muscle (Fig. 1.2). Sarcomeres are bordered by the Z bands (Zwischenscheibe) and consist of myosin and actin, which are also called thick and thin filaments. Thick filaments are located in the centre of the sarcomere. Dark areas made of the thick filaments are called A bands (Anisotropic) [3, 6, 48].

The thin filaments are each attached at one end to Z bands within the sarcomeres. It is seen that the I bands (Isotropic) are the parts of the actin filaments that do not overlap with the myosin filaments. The H bands are the middle region of the A band into which the action filaments have not penetrated [3, 6, 48].

To explain how actin and myosin filaments move has been a great theme of muscle mechanics research since 1950s. There is little doubt that, during muscle contraction, two kinds of filaments slide against each other with relatively small changes in their own

lengths. Chemical and electron microscopic studies have revealed the fine structure of the myosin filaments, each of which consists of about 180 myosin molecules. Each molecule has a molecular weight of about 500 000 and consists of a long tail piece and a head. The heads project laterally from the filament in pairs, at 180° to each other and at 14.3 nm intervals. These heads seem to be able to 'nod', they lie close to their parent filament in relaxation, but attach to actin filaments when excited. They are called cross-bridges [3, 6, 48].

1.1.2. Contraction of Muscle

Skeletal muscle responds to stimulation by nerve, electric or chemical impulses. When a muscle is stimulated, it twitches. If the muscle is held at constant length, it develops a force. Each simulation elicits a single twitch lasting for a small fraction of a second. If the stimuli are spaced a long time apart, the muscle relaxes to its original length between twitches. Successive twitches may add up to produce a stronger action. The steady contraction is called tetanus. All muscles will eventually fatigue and fail to contract, even though stimulated [43, 6].

The maximum isometric tension depends strongly on length. If the length is too small or too large, the tension drops towards zero. There is an optimum length at which tension is a maximum. When the sarcomere length is in the range 2.0-2.2 μm, the maximum developed tension does not depend on the muscle length (Fig. 1.3). When the muscle fibre is maintained at a length outside this range, the maximum tension developed is smaller. This is often explained in terms of the variations of the number of cross-bridges between myosin and actin fibres. If the muscle is too long, the actin and myosin filaments are pulled too far apart, the cross-bridge number decreases, and the tension drops. If the

muscle is too short, the actin filaments interfere with each other; they may shield each other and hinder the function of cross-bridges [3, 6].

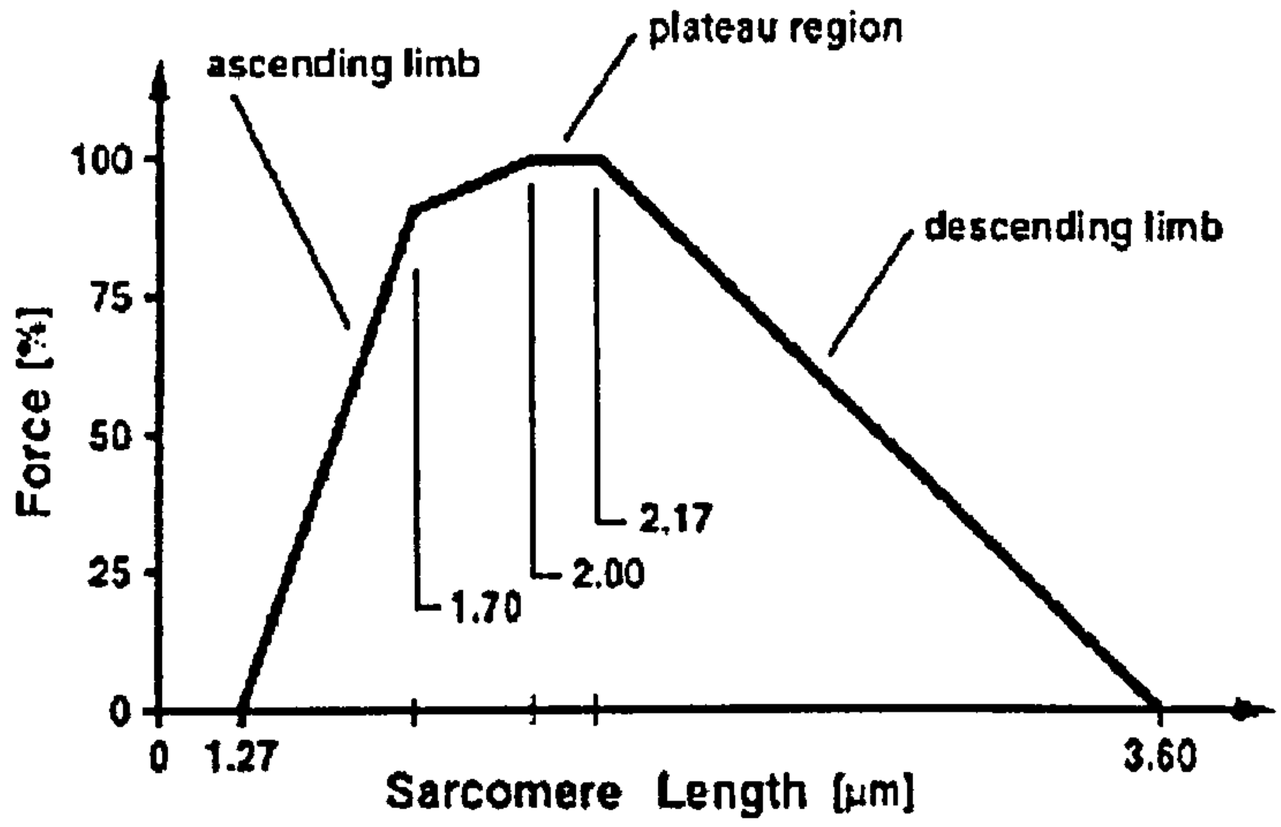

Figure 1.3. Force-length relation of isolated fibres of frog skeletal muscle.

1.1.3. Mechanical Properties of Soft Biological Tissue

The mechanical design and function of an organism occurs at two independent levels: materials and structures. In fact, there is a considerable relationship between structure and mechanical properties. All soft tissues are composite materials. Among the common components of soft tissues, collagen and elastin fibres mostly affect the overall mechanical behaviour of the tissues [53].

The result of the force acting on biomaterials is deformation, which can be measured. The adequacy of the structure to resist these forces depends on its material properties, as well as on the shape of the structure. In solid mechanics, force and displacement are normalised as stress and strain. Stress (σ) is defined as,

$$\sigma = F / A \tag{1.1}$$

where;

F : Force

A : The cross-section area to which the force is applied.

Similarly, deformation or displacement of the material (ΔL) can be expresses as a strain by dividing by the resting length of the material ($\varepsilon = \Delta L / L$). As shown in figure 1.4, the slope of the linear part of the stress-strain curve defines the elastic modulus ($E = \sigma / \varepsilon$). The elastic modulus is an indicator of the material's stiffness in terms of stress and strain [53, 3].

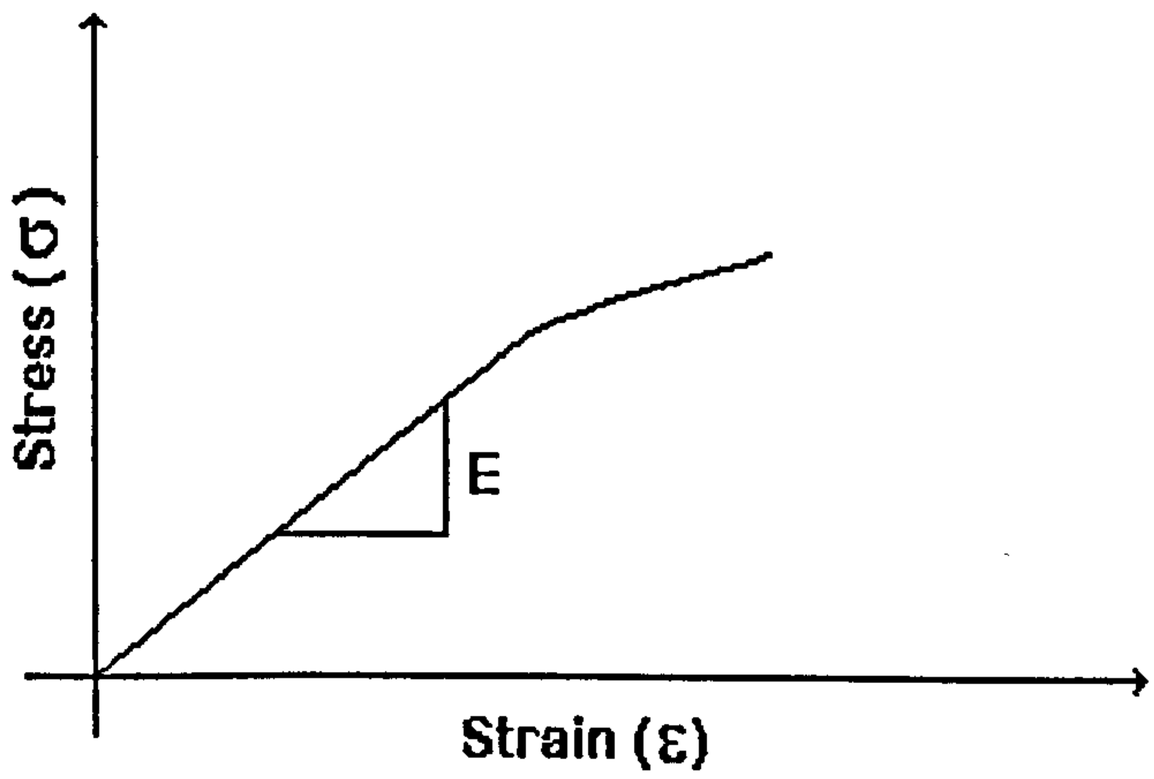

Figure 1.4. Graphical representation of Elastic modulus (E).

The relative magnitude of strain in two planes (lateral strain to the longitudinal strain) perpendicular to the plane of applied stress is defined by the Poisson's ratio (ν) of the material in those planes.

$$\nu_{xy} = -\varepsilon_y / \varepsilon_x, \qquad \nu_{xz} = -\varepsilon_z / \varepsilon_x \tag{1.2}$$

In isotropic materials, ν_{xy} and ν_{xz} are equal. Anisotrophic materials such as bone, muscle and other biomaterials show differing amounts of strain and stiffness along the materials [3, 53].

A muscle is ordinarily thought of as an active system; its prime function is to generate force. Muscles are composite materials, composed of stiff strong fibres, plates or particles in a relatively complaint matrix. The properties of composite materials depend very much upon their structure. Many soft composites change their mechanical properties as part of their normal functioning. Muscle is stiffened by contraction and softened by relaxation.

1.1.3.1. Ultrasound Experiments and Results

Ultrasound testing is used to detect flaws where an ultrasonic source is pressed against the part to be tested, using a gel to act as a sonic coupling to the surface, and sound is passed into the material. Reflections or echoes occur from the back face of the material and any internal discontinuity will reflect the sound wave and generate a signal in the receiver. The time lags of the echoes are measured to determine the thickness of the material and the distance to the discontinuity. The propagation of sound waves through a material is governed by the mechanical properties of that material. Therefore, ultrasound could be a useful aid in studies of the elastic properties of biological tissues. If distortion is produced at a point in an elastic material, it is transmitted as a sound wave or side wave. The sound wave velocity V can be shown as a function of bulk modulus K, and as the density ρ of isotropic material. The equation is written as;

$$V = \sqrt{K/\rho} \tag{1.3}$$

Therefore, the bulk modulus can be calculated if V and ρ are known. However, the elastic constant (such as Elastic modulus, Poisson's ratio) of human tissue cannot be theoritically estimated because of its complex structure and composition, but the constant may be function of elasticity explained above.

Levinson [39] used ultrasound and assumed linear elastic theory to obtain mechanical properties of seven frog sartorius specimens. Linear elastic theory is often applied as a means of defining the mechanical properties of biological materials. Levinson obtained four observable elastic constants associated with a transversely isotropic model. The average values of these constants were;

for resting,

$c_{11} = 2.64$ Pa

$c_{13} = 3.39$ Pa

$c_{33} = 4.40$ Pa

undergoing tetanic contraction,

$c_{11} = 2.65$ Pa

$c_{13} = 3.43$ Pa

$c_{33} = 4.57$ Pa

where index $_1$ and $_3$ represent the transverse and longitudinal axes. In all cases c_{44} was 0 indicating a minimal contribution from longitudinal shear. For all seven specimens, the model of transverse isotropy provided a better fit of the data than that of isotropy [39]. In terms of the characterisation of ultrasonic wave propagation, this approach has been most extensively applied to bone.

Levinson *et al.* [40] also used sonoelastography (which uses ultrasound) to measure the propagation of shear waves induced by externally applied vibrations. Because shear waves predominate in incompressible viscoelastic media at low frequencies, sonoelastic data should be comparable to those obtained using conventional means. They demonstrated the practicality of using sonoelastography to measure the viscoelastic properties of human muscles *in situ*. They recorded vibration propagation speeds as a function of applied load in the quadriceps muscle of ten volunteers, as shown in table 1.1.

Propagation (Hz)	Applied Loads (kgf)	Elastic Modulus (E, kPa)
30	0	7 ± 3
30	7.5	29 ± 12
30	15	57 ± 37
60	0	25 ± 6
60	7.5	75 ± 11
60	15	127 ± 65

Table 1.1. Calculated values of elastic modulus

1.1.3.2. Indentor Test Results

In an indentor test, a steady load is applied to soft tissue under constant environment conditions, the amount of indentation being measured after a fixed time. Indentor tests have been used widely to determine mechanical properties of soft biological tissues, such as cartilage, skin and subcutaneous tissues. In general, biological tissues are multi-phasic and show time-dependent behaviour.

Indentor test is widely used in characterising the mechanical response of biological tissue. Advantages of using an indentor test are to have the ability to analyse samples *in situ* and perform multiple tests at several different sites. When tissue is modelled using the linear biphasic theory, the equilibrium deformation is that of a compressible elastic solid and Poisson ratio ν ($0 \leq \nu \leq 0.5$). In indentation creep or stress-relaxation tests, compressible elastic models can then predict the three-dimensional deformation of a tissue layer at equilibrium. However, determining the material properties of tissue from such a test is a difficult computational task.

Historically, viscoelastic behaviour has also been reported in soft tissues [23, 24, 18, 41, 51]; most of these analyses have used a static linear elastic material model. Hayes *et al.* [24] obtained a theoretical solution to the problem associated with axisymmetric indentation, where the articular cartilage bounded to subchondral bone was modelled as an elastic layer fixed to a rigid boundary. The elastic modulus E can be calculated using the formula;

$$E = P (1 - \nu^2) / 2awk(\nu, a / h) \qquad (1.4)$$

where;

P is the indentation force,

ν the Poisson's ratio,

w the indentation depth,

a the radius of the indentor,

h the thickness of the test tissue,

k a geometry and material-dependent factor.

Sakamoto *et al.* reported similar results using a new mathematical model [62]. The solution of Hayes [24] has been widely used to calculate the elastic modulus of cartilage [19-21] and skin together with subcutaneous tissues.

Sacks *et al.* [61] used weighted indentors to measure, *in vivo*, static stiffness of the soft tissue of the proximal thigh of four male subjects; two paraplegics and two without disabilities. Schock *et al.* [65] reported *in vitro* indentor tests of static stiffness of porcine skin, fat and muscle and compared these with a finite difference analytical model. Assuming linear elasticity, they gave three sets of material properties as in table 1.2.

Tissue	Shear Modulus (kPa)	Bulk Modulus (kPa)
Skin	28.2	53.1
Fat	18.3	12.2
Muscle	48.3	39
Skin	175	178
Fat	61.5	99.2
Muscle	147	169
Skin	1260	1280
Fat	65.2	105
Muscle	43.8	39

Table 1.2. Material properties given by Schock *et al.*(1982)

Their conclusions stated that no single set of data led to adequate agreement between experimental and analytical results; they suggested that more accurate constitutive

equations were needed. They also noted that their model was more accurate at low strains.

Krouskop *et al.* [38] used a Doppler ultrasound motion sensing system to make non-invasive measurement of the elastic modulus of soft tissue *in vivo*. The traditional drawback of ultrasound in measuring tissue properties is that the strain rate is very much higher than the physiological one, making the results useful for detecting anisotropy but not for measurement of stiffness. They used a 10 Hz mechanical oscillator to drive the tissue; using ultrasound only to measure the resulting tissue motion. This method is used to measure dynamic viscoelastic stiffness; results can be seen in table 1.3.

Contraction State	Elastic modulus (kPa) at 10 % Strain
Relaxed	6.204
Mild	35.848
Maximum	108.925

Table 1.3. Tissue properties repeated by Krouskop *et al.* (1987) given as an Elastic Modulus (E).

Chow and Odell [13] analysed wheelchair seating stress using a static, geometrically non-linear model. They studied the deformations and stresses in the buttocks of a seated person using pressure measurement on human subjects, bench tests of the deformations of various seating materials and a non-linear finite element model. Nakamura *et al.* [46] used a static, materially and geometrically non-linear model for cadaver heel tissue, calculating moduli from 500 to 7000 kPa . They created a two-dimensional plane-stress finite element model of the foot to study the effect of various shoe sole materials.

Steege *et al.* [66] used indentor tests of below-knee residua and a static, linearly elastic model to derive an elastic modulus of 60 kPa. Steege and Childress [67] later used a geometrically and materially non-linear model with some improvement noted in the correlation between observed and calculated interface pressures. Reynolds [57] used intendor tests of non-amputated legs and a static, linear elastic model to derive elastic moduli in the range 50 to 145 kPa. Mak *et al.* [41] used indentor tests of residual and non-amputated limbs and a static, linearly elastic model and calculating moduli from 21 to 195 kPa. It is clear that the results presented, even using similar test procedures, gave a very wide range of elastic moduli.

Recently, Vannah *et al.* [76] used indentor tests of non-amputated lower limbs and modelled geometrically and materially non-linear behaviour using large-strain finite element formulation. The resulting composite material stiffness was non-linear and could be approximated using the Jamus-Green-Simpson strain energy function. Typical values for the coefficients were $c_{10} = 2.6$ kPa, $c_{01} = 0.64$ kPa and $c_{11} = 5.57$ kPa.

Oomens *at al.* [49, 50] investigated the time-dependent compression characteristics of *in vitro* skin and subcutaneous fat by using a confined compression test. They modelled the skin as a mixture of a solid and a fluid. A numerical procedure was presented to solve non-linear field equations describing such a mixture. The confined compression test, however, gives quite repeatable results, but it does not represent living tissue behaviour.

Zhang *et al.* [80] investigated the reaction of skin and soft tissue to shear force applied externally to the skin surface. They also measured skin blood flow by using laser Doppler flowmetry while variable shear forces and normal force were applied to the skin surface. They analysed the internal stress using simplified models incorporating elastic theory.

Ursino and Cristalli [75] presented a mathematical model of the mechanical behaviour of arm tissue under the effect of external pressure loads. The model was used to study stress and strain distribution across the tissue and pressure transmission to the brachial artery. They compressed the arm by inflating two independent adjacent cuffs. They calculated elastic modulus and Poisson ratio from 10 subjects. Their results were Elastic modulus E in the range 90 to 115 kPa and Poisson ratio ν in the range 0.44 to 0.38. Their arm model included soft tissue, bone and vessels based on cylindrical geometrical shapes. It is obvious that geometrical simplifications in the modelling might have affected the accuracy of this study.

All investigations show that there is not a single value which defines the mechanical properties of soft tissue. Results usually depend on the research approach (*in vivo* or *in vitro*), tissue type (which part of the human body) and the numerical method applied to extract mechanical properties.

1.1.4. Models of Multiple Body Segments and The Whole Body

Biomechanical modelling of the musculoskeletal system of the human being has been the most challenging task in bioengineering. Many muscle models have been proposed. The range can be from cellular level to whole body. These models can be roughly divided into two classes. The first one is molecular models, which range in complexity from the simple molecular model of Huxley [32] to the considerably more complex models, such as that of Hill [26]. The second group (phenomenological models) also range in complexity from simple models such as the linear viscoelastic models [14] to the extremely complex models such as that of Hatze [22].

The behaviour of *in vivo* and *in vitro* skeletal muscle has been studied extensively [43]. These studies generally have used one-dimensional line models with spring and damper elements; viscoelasticty and non-linear stiffness have been included in the material model. Multidimensional continuum models have been developed for *in vivo* and *in vitro* cardiac muscle. Material models used in this area of research commonly have included non-linear stiffness and geometric effects, but have assumed negligible viscoelasticity [8, 28, 30, 31].

Bogen [8] has created a serious of three-dimensional constitutive relationships by modelling soft tissue as various biphasic cellular networks [8]. Horowitz *et al.* [28] also modelled passive cardiac muscle as fibres in a fluid matrix, gave a formulation for an incompressible (Anisotropic) finite element model and compared results with tensile test data. Humprey and Yin [30] described a constitutive relationship, modelling passive cardiac muscle as noninteracting elastic fibres in a homogeneous matrix and comparing calculated results with biaxial tensile test data of passive cardiac muscle.

Hill's equation refers to the ability of a tetanized skeletal muscle to contract. It is an empirical equation based on experimental data from frog sartorius muscle. A muscle bundle was held at a fixed length L_0 (isometric) by having its ends clamped. It was stimulated electrically at a sufficiently high voltage and frequency so that the maximum tension F_{max} (a function of muscle Length L_0) was developed in the muscle. At this tetanized condition, the muscle was released suddenly (by releasing the end clamp) to a tensile force F smaller than F_{max}. The muscle began to contract immediately, and the velocity of contraction, v, was measured. A typical relationship between F and v is shown in figure 1.5. An empirical equation was then derived to fit the experimental data. Hill's equation shows a hyperbolic relation between F and v. The higher the load, the

slower is the contraction velocity. The higher the velocity, the lower the tension. Thus, active contraction of a muscle is in direct contrast to the viscoelastic behaviour of a passive material [25, 48].

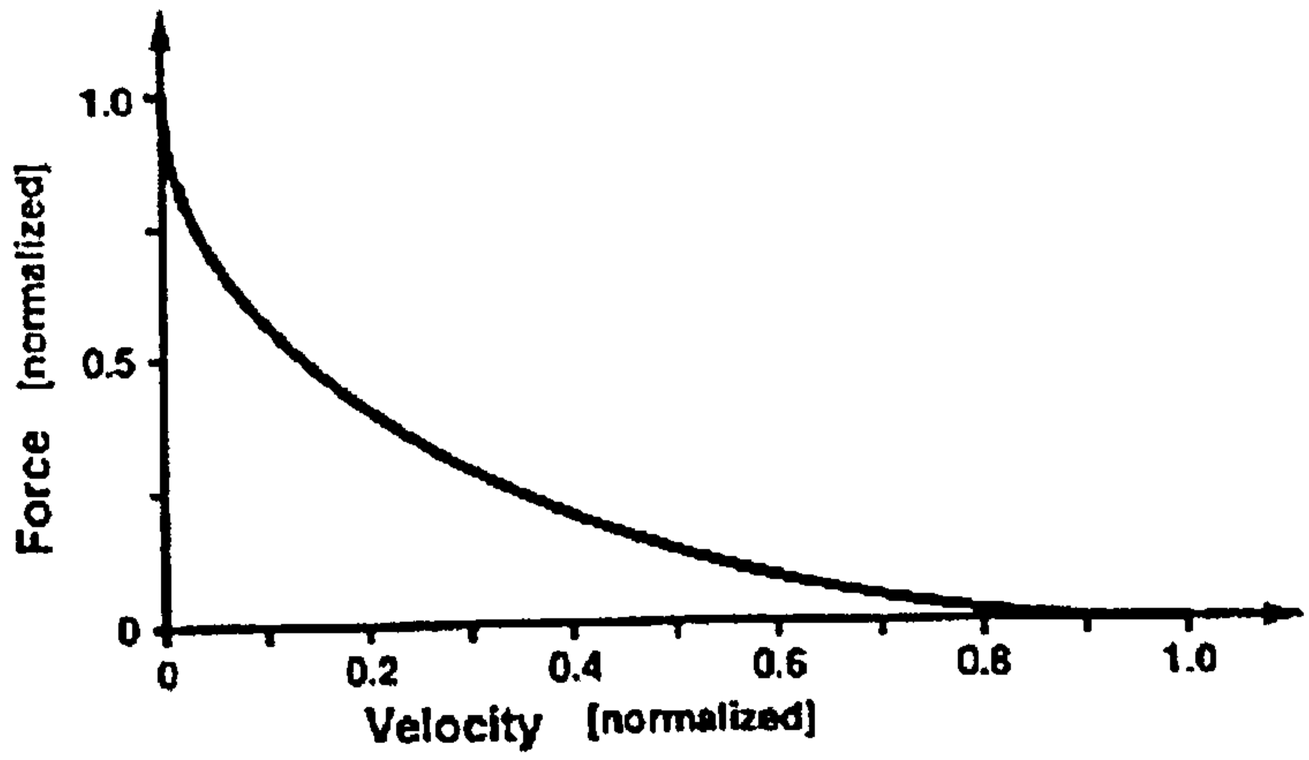

Figure 1.5. Normalised force-velocity relationship of contracting skeletal muscle.

Nowadays, Hill's equation is one of the most widely used in muscle mechanics. This equation is:

$$(F + a)(v + b) = b(F_{max} + a) \tag{1.5}$$

where;

F Muscle tensile force,

F_{max} Maximum isometric force,

v The velocity of contraction,

a, b Constants.

It can be said that Hatze's [22] approaches to muscle and whole body modelling are among the most complex in this area. His muscle model consisted of springs and dashpots to represent the elasticity between actin and myosin and a contractile element

for muscle contraction. Additionally, the muscle model received stimulation to exert force, which simulates the motor neurone system in muscle [22]. In the simple form, the model only consists of a single muscle fibre which contracts isometrically in response to the nerve activation. In the general case, the whole muscle and nervous system can be represented. To apply all these parameters correctly is the main difficulty in this model, which makes the model too complex for real life applications. A schematic representation of Hatze's muscle model (human triceps muscle) can be seen in figure 1.6. Symbols were used to represents the elements in the model which are; CE represents the contractile element, PE represents the parallel elastic element, SE represents the series elastic element, λ designates the length of an element and θ is the pennation angle.

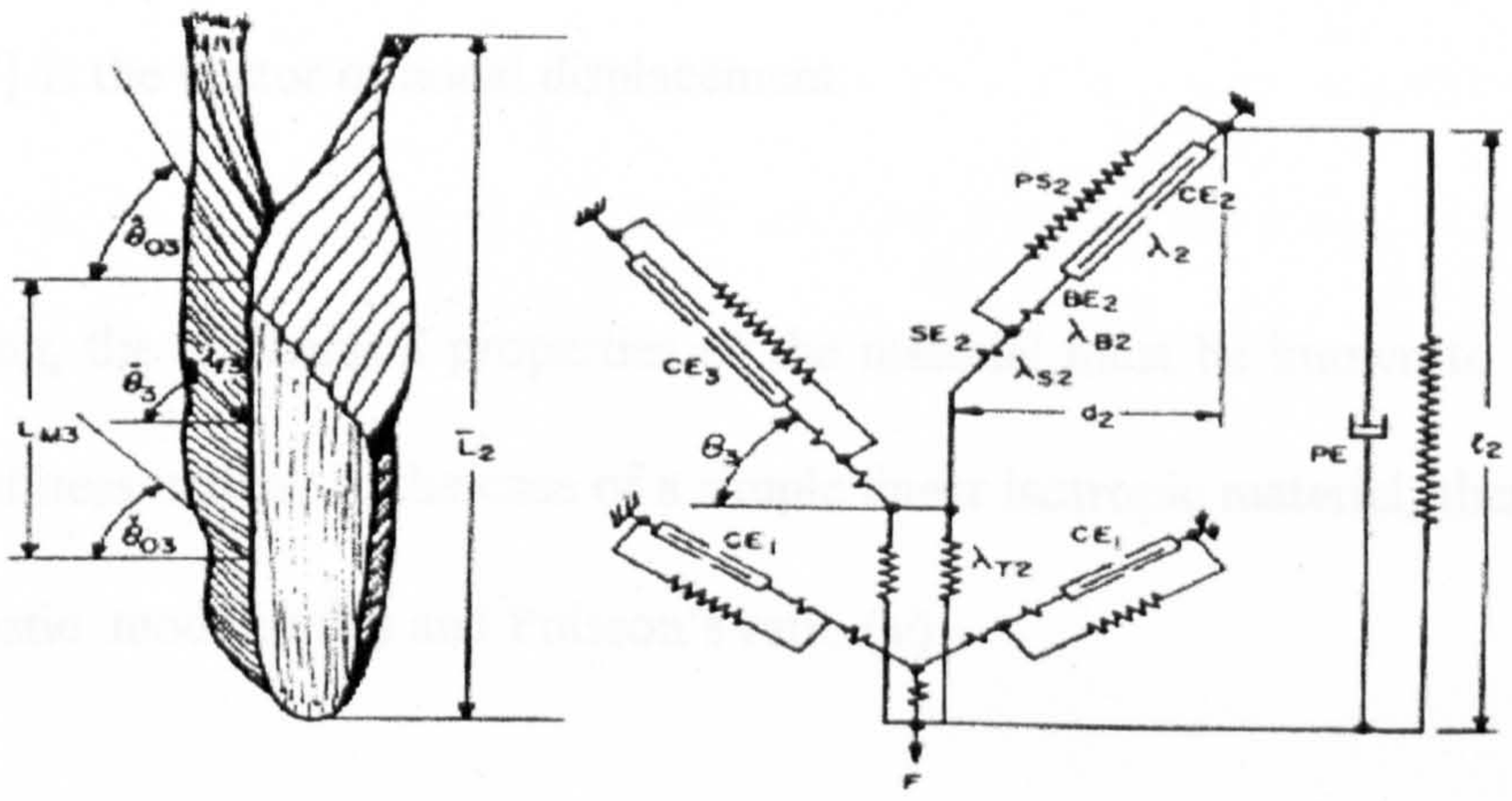

Figure 1.6. Biomechanically equivalent representation of human triceps muscles in Hatze's muscle model.

1.2. Finite Element Modelling

To extract the mechanical properties of bulk tissue, it is usually necessary to formulate and solve difficult non-linear viscoelastic problems involving large deformations. This is why analytical methods are not applicable and numerical methods (in this case finite element) are more suitable for solving this type of problem. Most bioengineers would

accept that finite element analysis (FEA) is the most appropriate method to analyse complex biological systems. FEA is being used in various areas such as the skeletal system (joint loads, bone stress analyses, artificial joints), modelling blood flow, soft tissue mechanics and heat transfer in biological tissues [55].

FEA is simply explained by algebraic equations which are given as follows:

$$\{F\}=[K]\{U\} \tag{1.6}$$

where;

{F} is the vector of nodal forces,

[K] is the element stiffness matrix,

{U} is the vector of nodal displacement.

In modelling, the mechanical properties of the materiel must be known to establish the element stiffness matrix. In the case of a simple linear isotropic materiel, these properties are the Elastic modulus (E) and Poisson's ratio (ν).

FEA can be divided into three sections, which can be described as model creation, solution, result validation and interpretation. The aim of the model creation phase is the mathematical formulation of the finite element model in term of nodes and elements, materiel properties, boundary and interface conditions and applied loads. The solution phase consists of executing a finite element computer program using the previously generated model as the input data. Finally, a crucial part of FEA is the validation and interpretation of the results. Model validation and accuracy must be checked. In other words, does the finite element model (FEM) represent the geometry, loads, material properties, boundary and interface condition of the real structure [40]?

Chapter 1

Finite element modelling in biomechanics has been dominated by bone and cartilage-based research. FEM of bone enables researchers to use standard engineering testing machines to obtain the mechanical properties of bone, and bone has a comparatively simple geometrical shape [55]. Soft tissue finite element modelling has been less researched. The time-dependent behaviour of soft tissues has made it very difficult to obtain mechanical properties. In addition, soft tissue has a more complex structure then bone or cartilage.

The material properties used in finite element models have usually been simplified. Many analyses in FEM proceed without accurate determination of the material properties of tissues. The balance between the complexity required for a good representation of reality and the simplicity required for ease of analysis is the key to good finite element research. Some researchers have focused on more accurate models (such as the geometry and boundary conditions), others have developed better representations of the material properties. Finite element modelling has often been criticised because of the lack of validation in the models [55].

Methods of determining material properties based on FEA have been used by many researchers. Often these method were called "inverse methods", which use measured load- displacement information to calculate the coefficients in an assumed constitutive equation. Using numerical methods, these coefficients are systematically adjusted until the error between the measured and predicted variables (such as nodal coordinates) is within a set tolerance.

Iding *et al.* [33] presented one of the earliest comprehensive descriptions of the inverse method. They applied the inverse method for identifying biological tissues under the

assumption of nonlinear elastic solids. Wineman *et al.* [77] proposed a material identification method using membrane inflation to determine the strain energy function of an incompressible isotropic tissue.

Prior inverse approaches have been mostly done for planar soft tissue *in vitro*. These studies can give satisfactory results in control experiments in two dimensions. For an *in vivo* three-dimensional study, the tissue model demands three-dimensional data collection and analysis. To determine the mechanical properties of three-dimensional bulk tissue *in vivo* has required accurate geometry of the tissue, acquired by using Magnetic Resonance Imaging in this study. Also in the present study, material properties of bulk tissue have been obtained by using a test machine which was designed for running a series of tests. Using the test machine, it was possible to collect creep, stress-relaxation and stress-strain time-dependent (viscoelastic) data from the bulk tissue of the human upper arm.

1.3. Aims of the Study

The overall aim of the study was to establish and validate biomechanically the human upper arm. With this in mind, specific objectives were:

1. To develop a method and equipment to determine the mechanical properties of the human upper arm.
2. To develop a new algorithm to process MRI scans for creating a geometrically accurate finite element mesh.
3. To develop a mechanical model which represents the behaviour of the human upper arm.
4. To develop a finite element model which simulates the human upper arm.

In this study, the determination of the mechanical properties of soft tissue, mechanical and finite element modelling of the human upper arm were proposed in three stages as presented in figure 1.7.

The first was the experiment design, which included a new test machine design (chapter 3 and 4) and a new image analysis programme (chapter 2), to obtain accurate representation of the human upper arm, and finally data collection (chapter 5). In the second stage, one-dimensional mechanical models (chapter 6) were proposed to simulate the behaviour of soft tissue. As an output from the mechanical modelling, initial mechanical properties of soft tissue were established for an input to the finite element modelling (chapter 7).

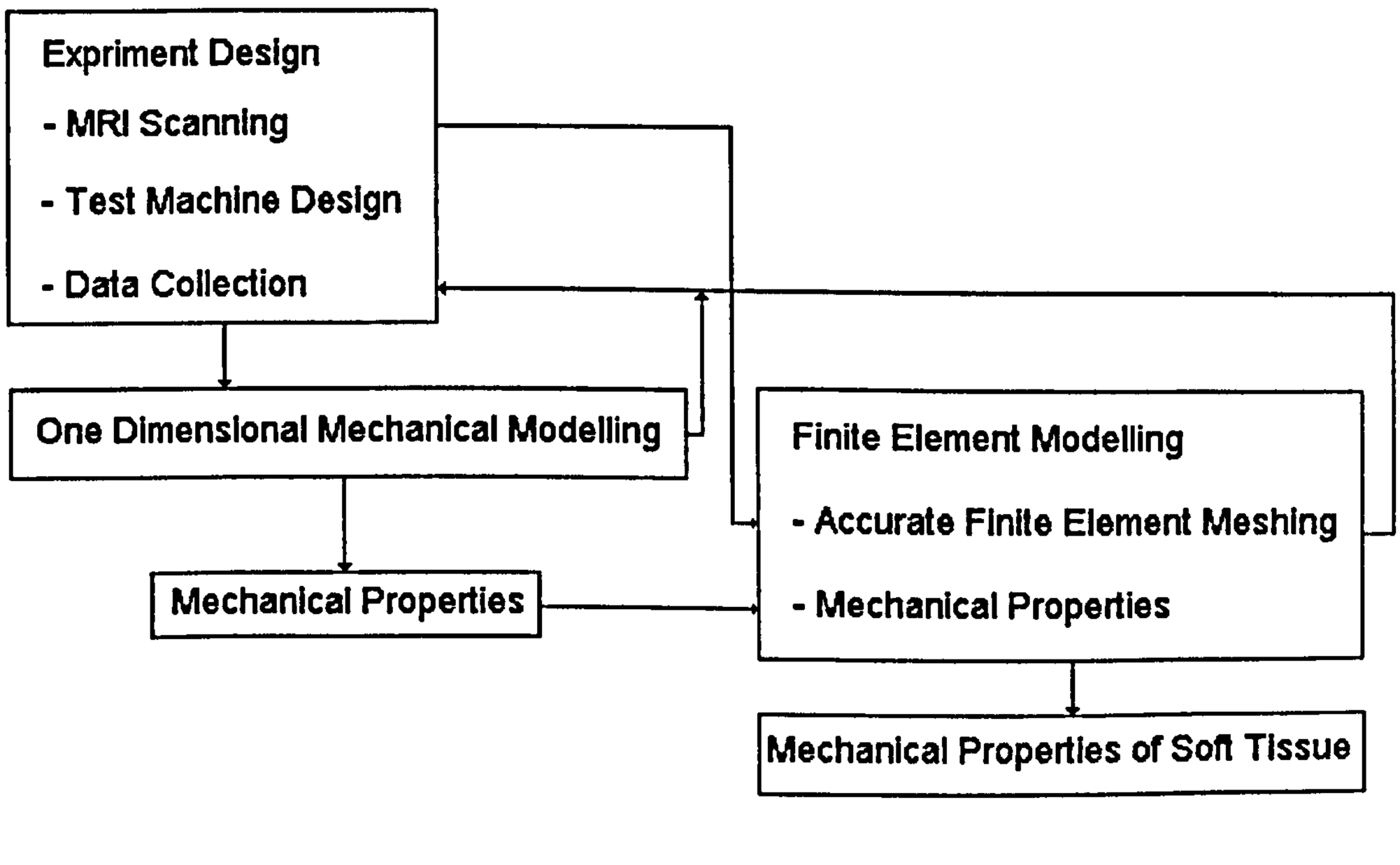

Figure 1.7. The methodology of determining the mechanical properties of soft tissue.

The final stage was finite element modelling; the finite element mesh was generated from MRI scans and the mechanical properties were estimated from the mechanical

modelling. The mechanical properties were refined until the finite element simulation and the experiment results converged.

1.4. Summary by Chapters

The contents of the subsequent chapters are summarised below.

Chapter 2 describes a new method and algorithm to create an automatic finite element mesh which is the first phase of finite element modelling. This relates to objective 2 in the previous section. A new computer program was written to generate an automatic finite element mesh from magnetic resonance imaging (MRI) scans of human upper arm. The program is written in the C programming language. The accurate mesh generation was crucial as input for the finite element stage of the modelling (Chapter 7).

Chapter 3 is based on the mechanical design of the test machine which was used to collect data for the experiment. This relates to objective 1 in the previous section. The machine was designed to apply uniform pressure to the arm. The test machine was capable of running three different tests, creep, stress-relaxation and stress-strain tests. Load cells were used to measure the pressure on the arm and the force exerted by muscle contraction.

Chapter 4 explains the electronic design and the computer programs which work with the electronic circuits. This relates to objective 1 in the previous section. Data collection and control of the system were achieved by using an analog-to-digital converter and a programmable input-output controller. A strain gauge amplifier was also designed to convert the signal from the load cell.

Chapter 5 presents the data collected from the creep tests, stress-relaxation tests and stress-strain tests. In addition to data collection, data collection procedures are explained in this chapter. Polynomial equations were also fitted to these results to create a mathematical representation of the raw data.

Chapter 6 focuses on the mechanical modelling that was developed to simulate soft tissue behaviour, which accounts for their non-linear time dependent behaviour. This relates to objective 3 in the previous section. Three different types of mechanical model were used to simulate the soft tissue behaviour. The Kelvin-Voigt model for the creep behaviour, the Maxell model for stress relaxation behaviour and the Standard Linear Solid model for both behaviours were used to simulate the soft tissue. The results of these models were a starting point for finite element modelling which is explained in the next chapter.

Chapter 7 is based on finite element modelling of the upper arm. This relates to objective 4 in the previous section. Using the mesh generation program (explained in chapter 2), a three-dimensional finite element mesh was created. To simulate the behaviour of bulk tissue, the same test procedure in the experiment were applied to the geometrically identical finite element mesh of subjects arm.

Chapter 8 is based on the discussion section of the design of the test machine, mechanical modelling and finite element simulation of experiment data. Finally this chapter concludes the findings in this thesis and presents suggestions for future work.

Chapter 2

Program for Generation of Three-dimensional Finite Element Mesh from Magnetic Resonance Imaging Scans of Human Limbs

2.1. Introduction

Finite Element Analysis (FEA) provides a technique to quantitatively analyse complex biological systems for which other solution strategies are either impractical or completely intractable. The application of the Finite Element Model (FEM) to any problem in structural analysis typically involves three basic phases [7].

- Model creation
- Solution
- Result validation and interpretation

The goal of the model creation phase is the mathematical description of the finite element model in terms of nodes and elements, material properties, boundary and interface conditions, and applied loads. The model creation phase can often be the most labour-intensive phase of FEA. Therefore, basic geometrical shapes have been chosen to lessen the labour for creating the model.

Finite element modelling in bioengineering is basically dominated by bone and cartilage research for many reasons; the first is that bone and cartilage can be reconstructed by using relatively simple geometrical shapes. The second reason is that the mechanical properties of bone and cartilage have been studied extensively and produced reliable

results. Unfortunately not all these conditions are valid for bulk soft tissue research; simple geometrical shapes are too far from reality to reconstruct the cross-sectional morphology of bulk soft tissue.

The aim of this study was to obtain accurate three-dimensional coordinate input for a finite element mesh. The program converts MRI scans to pixel coordinates and allocates the boundaries of the different tissue layers. The purpose of the program is to use magnetic resonance imaging (MRI) and computerized tomography (CT) scans, converting them into input data for FE models or other engineering applications such as custom-made prosthesis manufacturing.

There are many commercially available computer programs for edge recognition and contour tracing. These programs have mainly been developed for image enhancement or artistic work with image processing [15]. Medical image display software is also available but was designed to visualize cross-sections of the human body for anatomical purposes [58]. Image processing usually involves techniques for filtering, storing, retrieving and enhancing images [12, 19, 63]. However construction of a finite element model demands more than image processing; it basically involves definition of the boundaries, for which image processing techniques are used, along with a model-specific development strategy.

2.2. Methods

Magnetic Resonance Imaging is the use of nuclear magnetic resonance of protons to produce proton density map or images of the human body. MRI is presently the most accurate and informative technique for obtaining cross-sectional images. However,

transforming the scans into appropriate coordinates demands image processing. If an image contains a single uniformly grey object on a contrasting background, the contour line can be defined by the grey level [12, 19, 63].

Eighteen cross-sectional images of the right upper arm were obtained by using a Siemens Magnetom Impact 1 Tesla MRI scanner. MRI scans were obtained with configuration of T1 Spin Echo and 8 mm slice thickness and 180° field of view. The subject was supine with his arm fully abducted. The images were photographed on Ilford FP4 Plus negative film and printed onto matt photographic printing paper (Fig. 2.1).

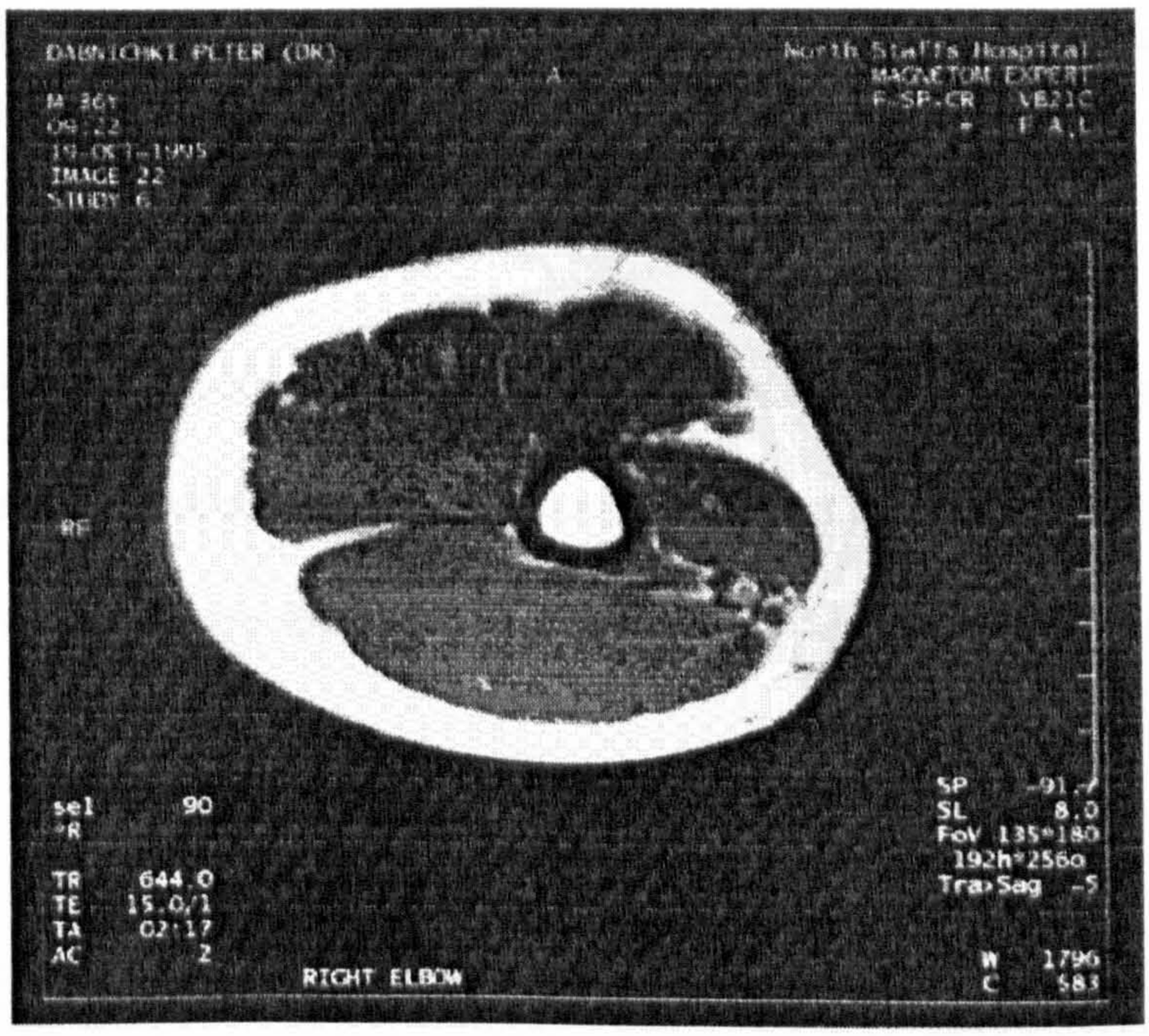

Figure 2.1: Photographed and scanned MRI scan.

All MRI pictures were scanned with a Hewlett Packard Scanjet IIcx with a 256 grey scale and saved as Bitmap (Windows -BMP - RGB coded) formatted files [35]. Any unnecessary information (patient and hospital names, information about MRI scans, etc.) was erased by using a commercial graphics program. The images were re-sized according to VGA high resolution (640x480, 16 colours) standards and saved as a 16

grey scale palette. The aspect ratio was 1.0003, which was considered in the subsequent calculations to be a unity.

The program was written in the C programming language and compiled by the Borland C++ compiler version of 3.1 in the DOS environment [54]. The program uses multiple source files, which, in Borland C++, can be handled by defining a project file. The project file in this program consists of four source files. The main source file is named as mri.c, which has the main( ) function and the others are lst.c, bitmap.c and mouse.c. These files are compiled in a large memory model; in this, in DOS, the data and code are limited to 1 Megabyte, and far pointers are used for both code and data segments. Far pointers can point almost anywhere in memory. These files are explained below:

File mri.c has the functions that handle the menu facilities. The program is menu driven. Therefore, all menu control and access functions are described in this source code. In this source code 13 functions are declared. The complete source code of the mri.c can be seen on Diskette I.

File lst.c is the computational part of the program. Data processing of the images is done in this module. In this source code 22 computational functions are declared. These functions are sequential and run consecutively. The complete source code of lst.c is printed on Diskette I.

File bitmap.c consist of functions that handle the windows device independent bitmap graphics files (short name is BMP file). These functions deal with showing, saving BMP

files and changing palette values. To handle BMP files 8 functions are declared. The complete source code of bitmap.c can be seen on Diskette I.

File mouse.c has mouse control functions. Unfortunately DOS itself does not support the mouse. Using a mouse (external pointer - mouse or trackball) in DOS needs a mouse device driver which sets the software interrupt 33h in the interrupt vector table [54]. Trapping this interrupt allows mouse functions to be used. For using the mouse, 17 functions are declared. The complete source code is given on Diskette I. The program's main screen that includes menu options can be seen from figure 2.2.

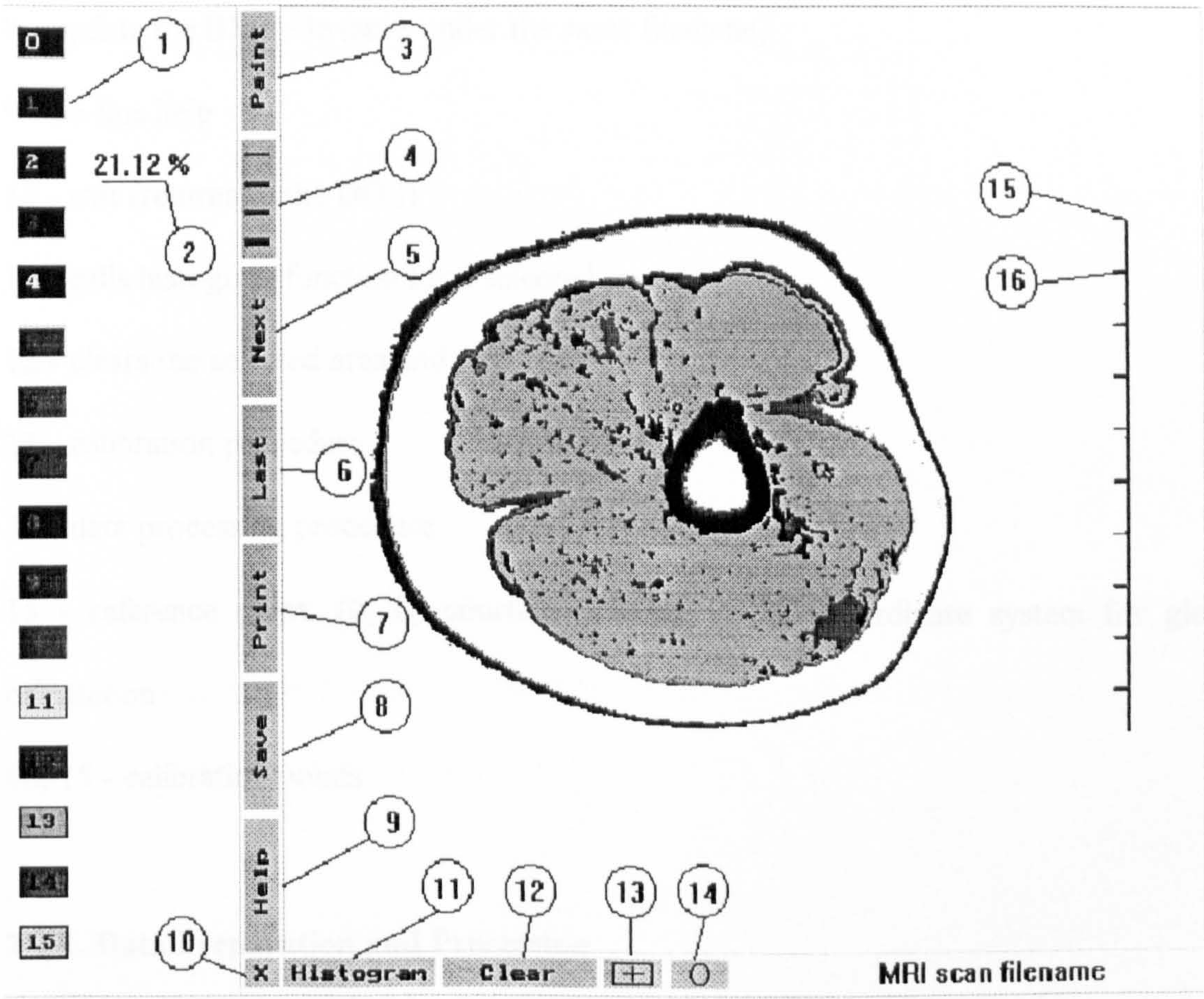

Figure 2.2. The program's main screen and menu options

In figure 2.2 the encircled numbers are described below;

1 - colour value legend

2 - histogram: the percentage of respective colour in a selected area

3 - manual painting

4 - selection of line thickness for the manual painting

5 - call the next scan from the sequence

6 - call the previous scan from the sequence

7 - print active MRI scan

8 - update the BMP file (save under the same filename)

9 - on-line help

10 - exit (returns to the DOS)

11 - calls histogram function for a selected area

12 - clears the selected area and relevant histogram values

13 - calibration procedure

14 - data processing procedure

15 - reference point: (0, 0) coordinate in the global coordinate system for global orientation

16, 15 - calibration points

2.2.1. Data Preparation and Processing

The program can be separated into two major stages, data preparation and data processing. The block diagram can be seen in figure 2.3.

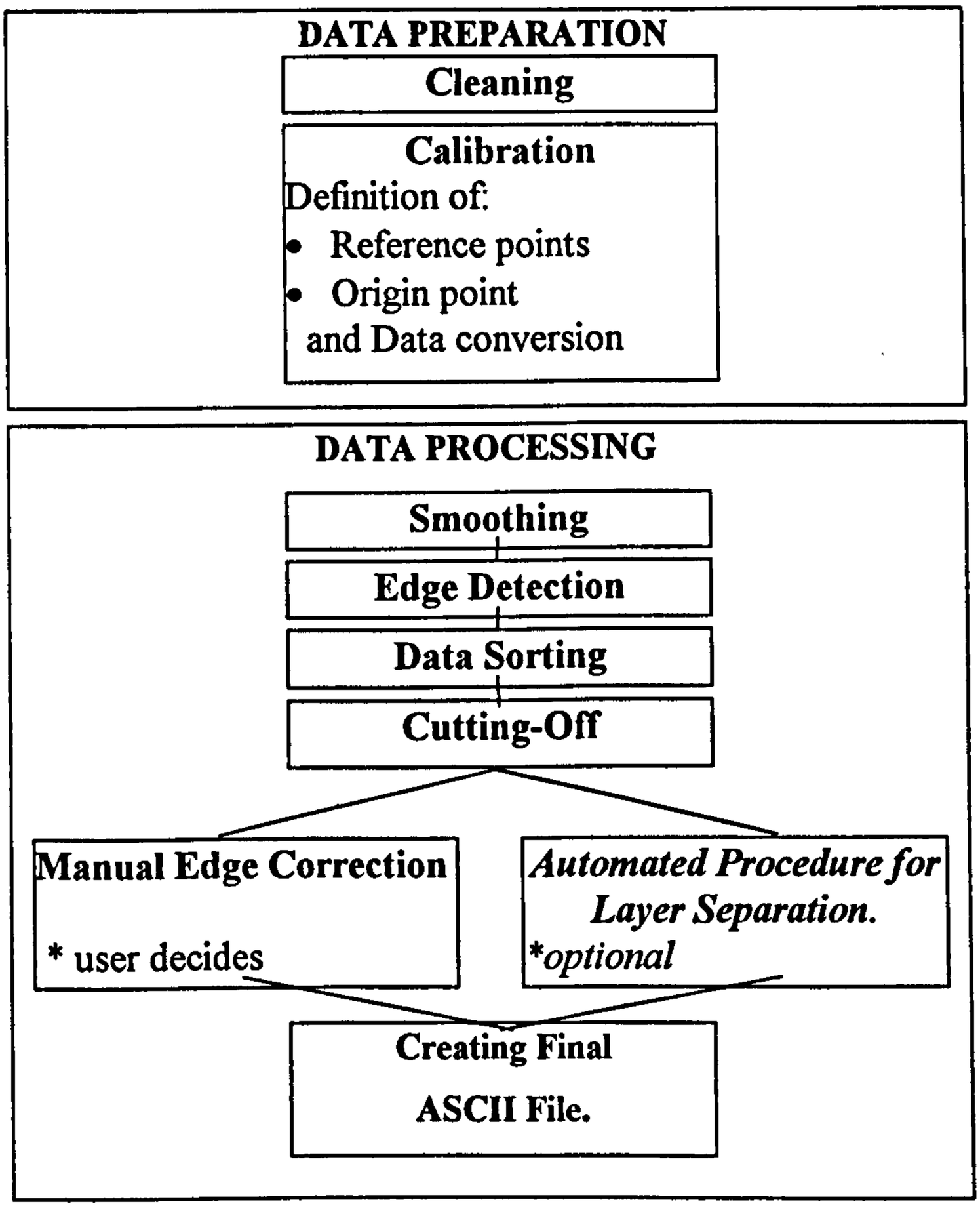

Figure 2.3. Two main stages in the program.

2.2.1.1. Data Preparation

In the first stage, data preparation consists of cleaning, calibration and subsequently data conversion procedures.

2.2.1.1.1. Cleaning

The cleaning procedure can be used to paint neglected spots (defects) which occur during the period of conversion of the MRI scans into bit-mapped pictures. These spots are usually caught by the data processing algorithm as an edge. The difference can be

seen from a comparison of figures 2.4 and 2.5. Figure 2.4 is a scanned picture and the figure 2.5 is a cleaned picture before data processing. Cleaning, or preparation of the MRI scans, can also save crucial data processing time. Comparing the original MRI films (photographed pictures) and scans can avoid erasing or altering useful information.

Figure 2.4. Scanned MRI picture.

The cleaning procedure can also be called at any time in the program. To clean the defects, the user has to click on the paint button (Button 3, Fig. 2.2) and the cursor will change its shape from a cross to an arrow which is an indicator of which mode has been selected. The role of the paint function is to eliminate any defects that are introduced during the scanning procedure, and this is done by selecting the appropriate background colour and arrow thickness. The user can adjust the paint block thickness by simply

indicating the required thickness shown in button 4 (Fig. 2.2) and can also change the paint colour by pressing the mouse button over the colour legend (Box 1, Fig. 2.2). To paint the selected areas, the left mouse button is pressed while moving the cursor over the defect. Once painting is complete, the user presses both mouse buttons simultaneously, and will then be returned to the main screen.

Figure 2.5. Cleaned MRI scan.

2.2.1.1.2. Calibration and Data Conversion

In the calibration procedure, pixel-domain data is basically transformed into real world coordinates. Converting the pixels into standard measurement units demands at least two points; the distance between these should be known. To start the calibration procedure,

Button 13 (Fig. 2.2) is first selected, and this procedure now expects three points to be selected by the user. The first two points are calibration points (Fig. 2.2. Boxes 15 and 16), selected using the mouse cursor, and the third point is the central origin of the radial scan lines (Fig. 2.6).

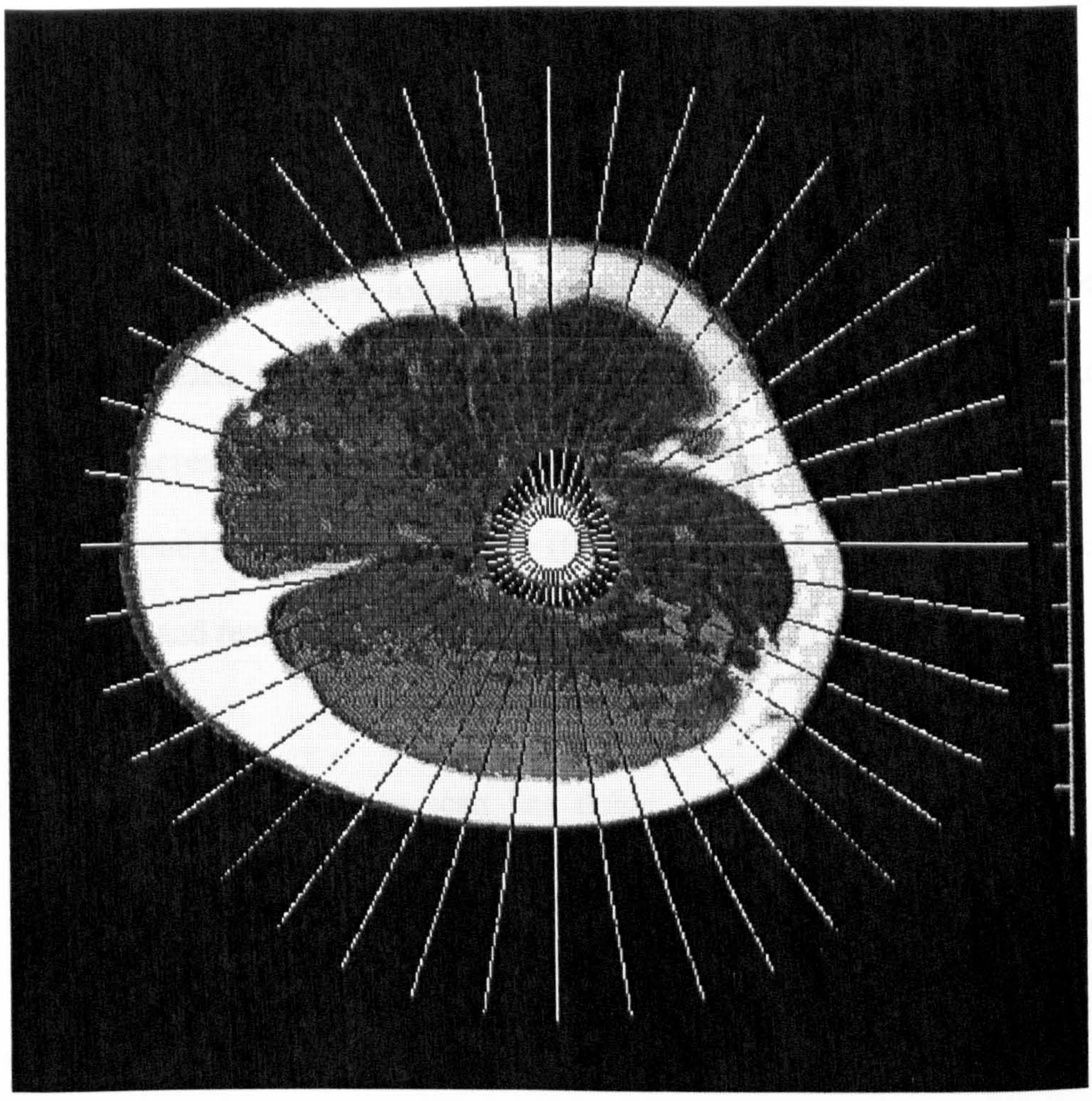

Figure 2.6. Two calibration points (top right of the picture) and 9° separated scan lines.

In addition, the first calibration point is accepted as a fixed point (Fig. 2.2, box 15), which is located in the same place in all MRI scans, and recorded into the calibration file. The frequency of the scan lines can be adjusted by the user. In figure 2.6 the MRI scan is divided into 40 equal slices giving a 9° scan interval. The length of the scan lines can also be adjusted by the user, using keyboard keys [+] and [-] to adjust the length of the outer

scan line limit, and [a] or [z] to adjust the inner scan line length. This approach is similar to centre-based detection [74]. This gives the user flexibility for scanning particular parts of the MRI scans. If the user is not happy with the position of the calibration points or origin of the radial scan lines, the user can re-run this procedure and re-enter the origin and calibration points.

Data conversion runs after the calibration procedure ends. In this procedure, the colour values where the previously defined scan lines intersect with the scanned image are recorded into the file in binary format. To read the colour values, the procedure is accessed into the video buffer and proceeds in a clock-wise direction where the radius of the scan line decreases one pixel. Finally, these values are recorded into the file (filename.all) as one (integer) colour value + (float) Cartesian coordinate of the pixel. Basically reading and recording the colour values involves two nested loops.

```
for( int J = scan_line_up_limit; J >= scan_line_down_limit; J--){
        for( int I = 0; I< number_of_scan_line; I++)  {
                x2 = (float) j * sin( (float) I * PI / (number_of_scan_line / 2));
                y2 = (float) j * cos( (float) I * PI / (number_of_scan_line / 2));
                col = getpixel( org_x + x2, org_y + y2);
                enter( col, (x2 * ratio), (y2 * ratio);
        }
}
w
```

here variables and functions;

scan_line_up_limit : user defined upper limit of the scan line.

scan_line_down_limit : user defined lower limit of the scan line.

number_of_scan_line : the number of desired scan lines.

x2: x component of the pixel.

y2: y component of the pixel.

org_x : x component of origin points of scan lines.

org_y : y component of origin points of scan lines.

ratio : number of pixels between reference points / actual size of reference points.

getpixel(int x, int y) : it is a function that returns the colour value of the given coordinates (Borland BGI library function) [54].

enter(int colour_value, float x_cor, float y_cor, FILE *stream) : it is a function that records the given values into file that stream file pointer points.

2.2.1.2. Data Processing Algorithms and Data Structures

The algorithms used in the data processing unit are sequential and are initiated by pressing button 14 (Fig. 2.2).

2.2.1.2.1. Smoothing Procedure

Smoothing is applied to the colour values in the binary file (filename.all) that was recorded in the data conversion. The colour value of the individual pixels in every scan line is smoothed by using the moving average method.

In this procedure, sharp colour changes are smoothed and transitions between layers are softened. The new colour value is assigned according to the result of the smoothing.

Finally, the calculated colour value and Cartesian coordinates are recorded into the new file (filename.smt) in binary format and the previous file (filename.all) is deleted.

$f(x, y) = Colour_{value}$

$f(x, y) = (float)\ ((\ f(x_{n+h}, y_{n+h}) + f(x_n, y_n)\ ) / 2)$ $\qquad (h = 0, 1, 2, \ldots, n-1)$

Data structure: (float) Colour + (float) Cartesian co-ordinates

2.2.1.2.2. Differentiation Procedure

This procedure uses finite difference calculus [21, 56]. If the colour difference between two consecutive values is greater than 1.0 a possible edge is indicated and recorded into a binary file.

$$\Delta f(x, y) = |\ f(x_{n+h}, y_{n+h}) - f(x_n, y_n)\ |$$

If $\Delta f(x, y) > k \Rightarrow$ mark as an possible edge

$0 < k < 15$

Checking this condition along the defined radial lines allows the detection and recording of all possible edges into a binary file. In addition to this procedure, cylindrical coordinates are derived from the Cartesian coordinates, as follows:

Data structure : (float) Colour + (float) Cartesian coordinates

+ (float) Cylindrical Coordinates;

2.2.1.2.3. Sorting Procedure

The Quicksort Algorithm that was developed by C.A. Hoare in 1962 [36, 37, 64] was used for ordering within the file in cylindrical coordinates: firstly in ascending value of the angles, as the main key, and then by descending length, as the subkey in cylindrical coordinates in the file. The data were sorted and recorded within the pre-existing binary file as the data structure remains unchanged.

Quicksort is a good example of a recursive function. It is based on the exchange sort. Given an array, one element is chosen and the others partitioned into two subsets - those less than the partition element and those greater than or equal to it. The same process is then applied recursively to the two subsets. When a subset has fewer than two elements, it does not need any sorting; this stops the recursion [36, 37]. Generally, quicksort is the optimum sort because it is so fast. However, when only very small lists of data are to be sorted (less than 100), the overhead created by quicksort's recursive calls may offset the benefits of a better algorithm. In rare cases like this, one of the simpler sorts (such as the bubble sort) may be quicker [64].

The unknown length of the scan line length forced the use of external storage (such as Floppy Disk or Hard Disk) for sorting. Using Random Access Memory (RAM) without knowing the size of the array (the maximum value must be defined) is wasteful in terms of memory. Therefore, instead of allocating memory, the use of a disk file is more suitable for sorting. There are two types of disk files: sequential and random access. Many disk files are too large to be sorted easily in memory and required special techniques. Random access disk files have two major advantages over sequential disk files. First, they are easy to maintain: information can be copied without having to copy

the entire list. Secondly, they can be treated as a very large array on disk, which simplifies sorting.

As a result of performing the sorting procedure, the possible edges are grouped along the radial lines and ordered by decreasing distance (length of the radius-vector of the point) from the origin of the cylindrical coordinate system. This procedure was based on the assumption that the recorded edge with the longest length in the scan line is accepted as the outer edge.

2.2.1.2.4. Cutting-off Procedure

The initial cut-off value is a default real number that can be adjusted by the user in the beginning of the program run but cannot be changed from scan to scan to preserve a uniform criteria within the structure. Until desired edge numbers are reached, the cut-off value is adjusted automatically. This condition effectively merges the skin, fat and muscle defining them as a homogeneous layer.

The longest length is accepted as the outer $edge_0$ and the procedure is applied to the rest of the data.

$edge_0 = length_0$

$\Delta l(i) = length_i - length_{i-1}$

$If\ \Delta l(i) > cut\text{-}off_{value} \quad \Rightarrow \quad true : edge_i = f(x_i, y_i)$

$false : \phi\ (nil)$

$if\ i > number_of_edges \quad \Rightarrow \quad cut\text{-}off_{value} = cut\text{-}off_{value} + increment$

2.2.1.2.5. External Edge Correction (manual correction)

This procedure is evoked if more than the desired number of edges is detected in one radial scan line. Excessive edges can be seen exposed on the MRI scan, which helps the user to determine unwanted edges. These unwanted edges are usually caused by the existence of non-homogeneous inclusions in the tissue. Naturally, the program does not know which edge is unwanted and therefore shows all the edges, letting the user mark unwanted edges among them. To mark the unwanted edge, the keyboard is used. With arrow keys, the user can forward and reverse between the edges and can mark the edge by pressing the delete key.

2.2.1.2.6. Automated Procedure for Layer Separation (optional)

This part of the programme is optional; it allows the user to obtain automatically the correct number of edges and, therefore, to avoid user intervention. The inconvenience of this option is that it requires the user to have a very good pre-estimation for thickness tolerances and a very clear idea of what must be discarded from and be left in the created model. This affects the choice of parameters and weight factors. The difficulties of these definitions come from the mutually contradictory requirements - a high level of accuracy for edge detection and neglecting relatively large inclusions as "non-significant". These pre-estimated values can be entered into the configuration file.

2.2.1.2.7. Cleaning The Marked Edges and Creating Final ASCII Files

In this procedure, marked edges are deleted from the binary file and a final ASCII file is created. As a feedback to the user (how close the edges approximate to the real boundaries), all consecutive edges are linked to one another to construct two-dimensional representations of the layers; these are superimposed on the MRI scan (Fig.

2.7) as white boundaries. Linking these nodes allows viewing of the boundary of the finite element model. These points can be seen better in figure 2.8, in which every point represents the node information (in the Cartesian coordinate system) for the finite element mesh. To create the finite element mesh, these nodes can be linked by the mesh generator program (see section 2.2.2.). if the user is satisfied with the result, then the next MRI scan can be processed by pressing the button 5 (Fig. 2.2) which switches the active screen and the MRI scan in the sequence. Otherwise, the user can process the current MRI scan until reaching a satisfactory result.

Figure 2.7. Two-dimensional represent of the layers on the MRI scans.

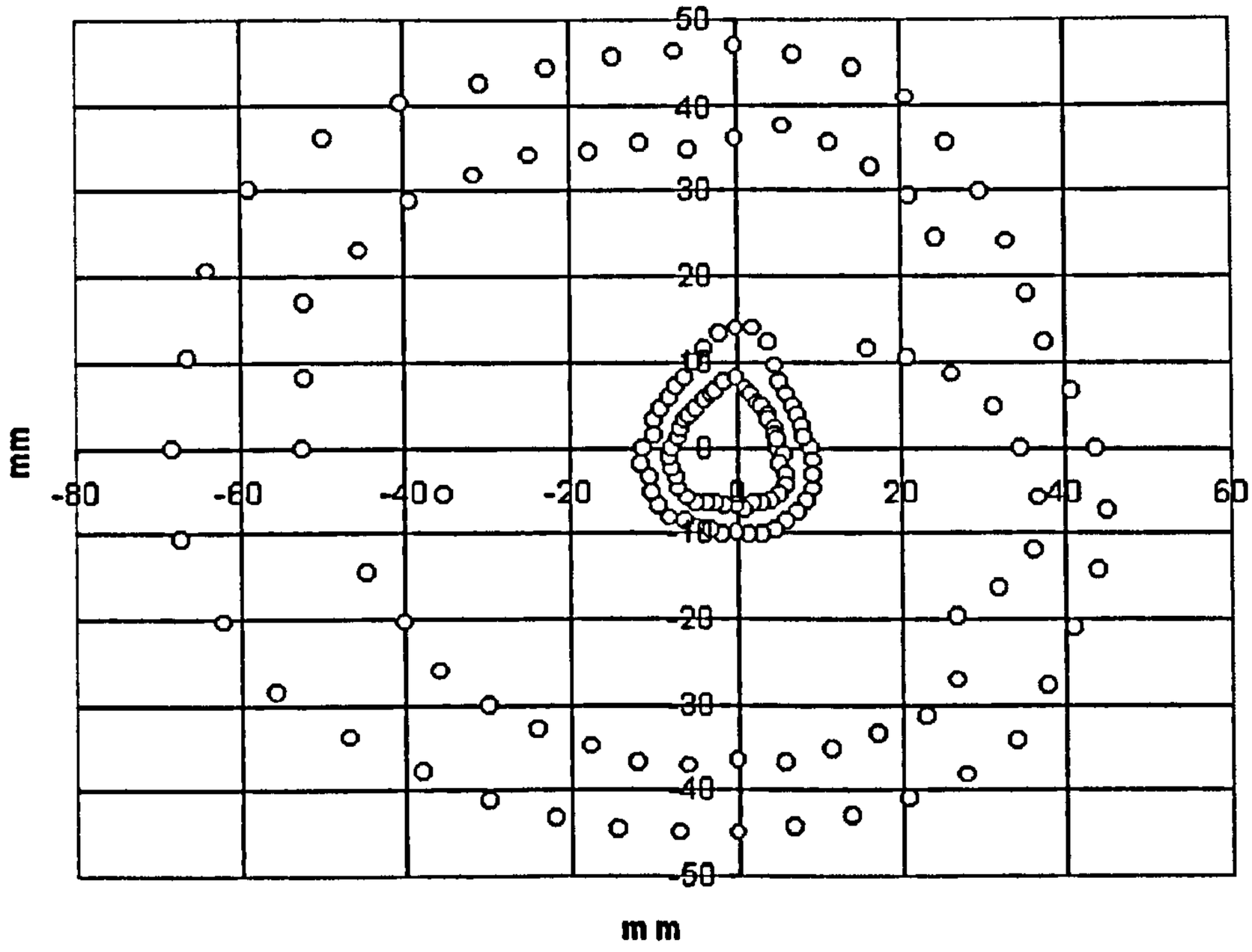

Figure 2.8. Cartesian coordinates of the edges of the MRI scan.

2.2.2. Finite Element Mesh Generation and Three-dimensional Image Construction

Finite element mesh generation and the three-dimensional representation of the images is a stand-alone program that uses the final binary output file created (Fig. 2.9a). It has limited capabilities and is intended to be used solely for mesh generation and visualisation purposes. The visualisation is created as the nodes are ordered layer-by-layer and the corresponding nodes are linked by straight lines. For mesh generation, the user can set the desired divide (Fig 2.9b. dashed line) between the boundaries (Fig. 2.9b. solid line) and the program generates the mesh coordinates as an ASCII file. The routine has some helpful features such as zoom-in, zoom-out, rotations and auto-scaling, as can be seen from figure 2.9a. These features help the user to assess visually the results and to obtain a reasonably good approximation for the finite element model.

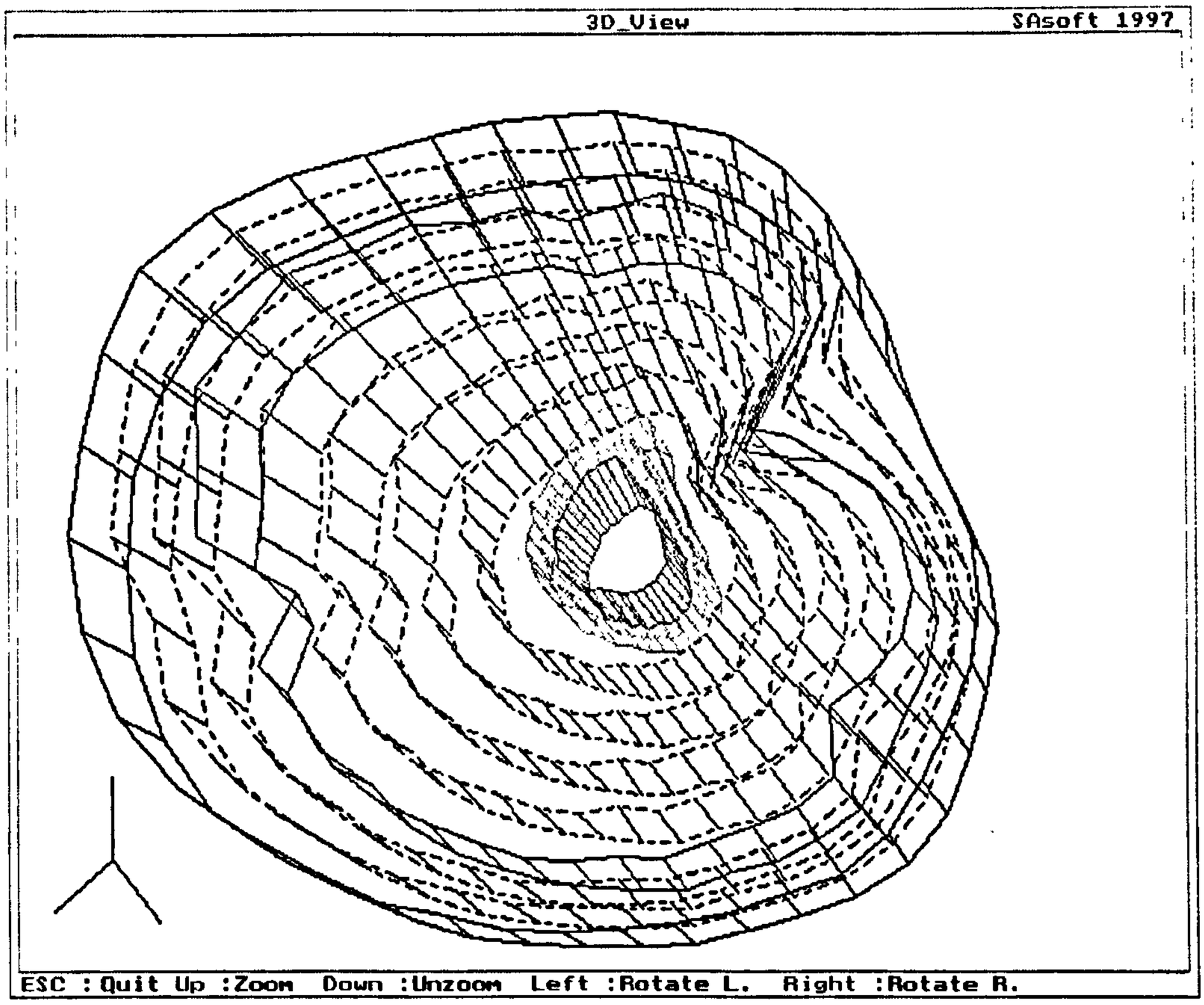

Figure 2.9a. Three-dimensional representation of the MRI scans and generated FE mesh

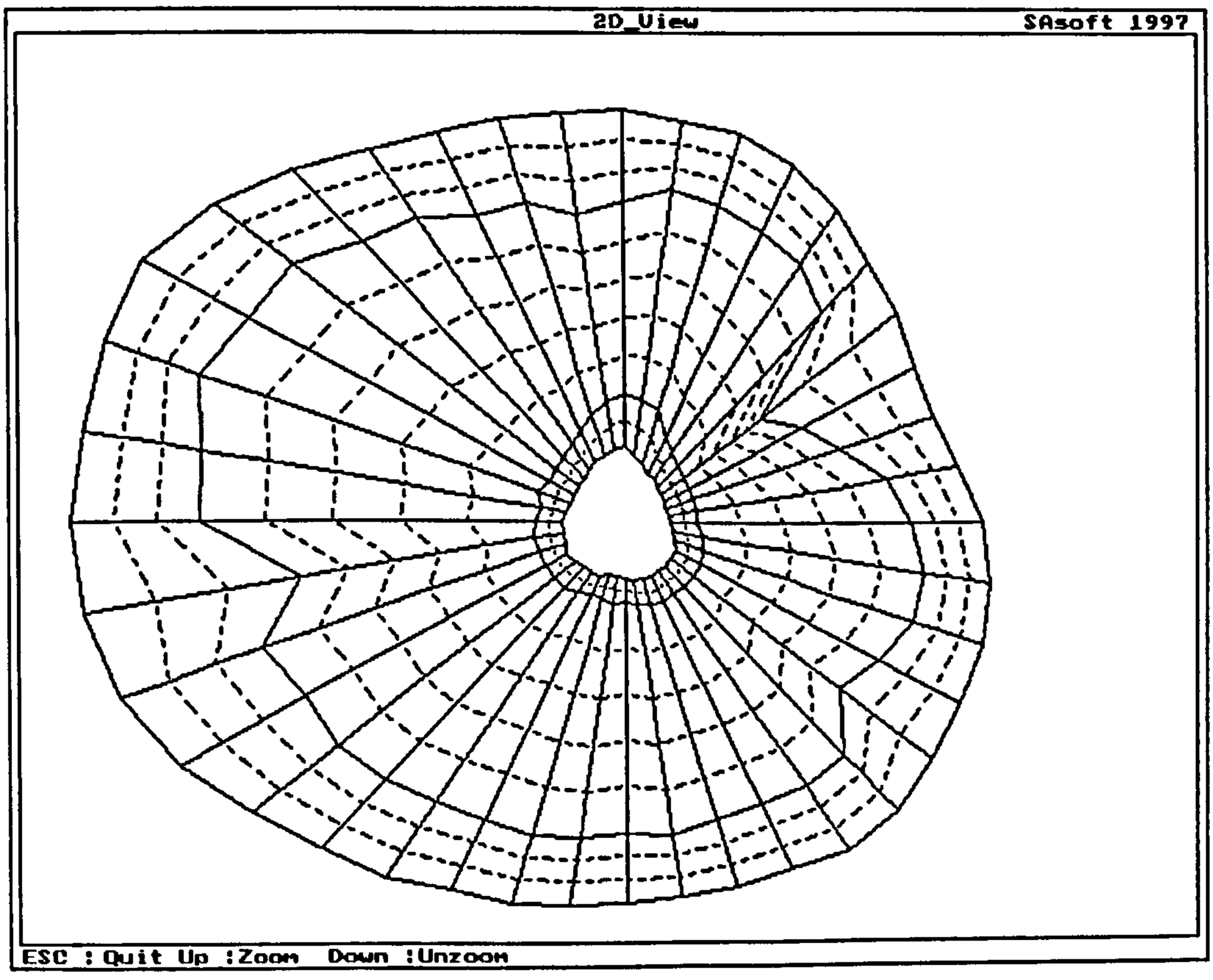

Figure 2.9b. Two-dimensional representation of the MRI scan and generated FE mesh

2.2.3. Additional Features

The program has some additional features that are explained below.

Saving the active MRI scan can be run by pressing menu button 8 (Fig 2.2). This facility can be helpful for updating when the MRI scan was cleaned. It saves the MRI scan with the same filename.

Printing the MRI scan allows the user to print an active MRI scan by pressing menu button 7 (Fig. 2.2). Printing images on the gray scale needs half-toning for which the "blue noise distribution" method is used in the program. The user can also switch between the MRI scans by pressing menu button 5 (Fig. 2.2) for the next MRI scan and pressing menu button 6 (Fig. 2.2) for the previous MRI scan. Colour (16 grey level) distribution of the MRI scan also can be seen by pressing menu button 11 (Fig. 2.2). Before pressing the histogram menu button (button 11, Fig. 2.2) the area must be determined by pointing with the mouse. This can then show the colour distribution of the selected area; for each colour there is a legend (Box 1, Fig. 2.2) and the percentage of this colour can be seen opposite the related legend (Box 2, Fig. 2.2). The user can activate on-line help by pressing menu button 9 (Fig. 2.2); brief explanation of the program and menu buttons then appears on the screen.

2.3. Results and Discussion

The capabilities of the program were illustrated on a sequence of scans of the upper arm. A three dimensional discrete representation of a cylindrical section of the upper arm was created with an angular step increment of 9° and a 0.4 mm accuracy of node positions (Fig. 2.9a).

The formatted images were processed to define the contours of skin and fat (these two layers could be split if required), muscle, bone and marrow (Fig. 2.9b). The developed algorithm, similar to the moving average method, proved its ability to detect inter-layer boundaries when applied to unidirectional reading of pixels. The determination of the edges was based on a comparison of the finite difference value with a threshold value. A circular mask was drawn and overlaid on the cross-sectional scans of the upper arm allowing for uniform discretization of its contours (Fig. 2.6). This circular mask was used to define the coordinates of the upper arm cross-sections in a natural local cylindrical coordinate system. Finally the coordinates from the two-dimensional images were linked to create a three-dimensional wire frame representation of the layers.

The program developed provides a numerical tool for transforming MRI scans into nodal coordinates for input into FEA. It will also be used to study the relative deformation of the limbs in different positions. The averaging method adopted in the numerical realisation is very close to the continuum mechanics approach for homogenisation and allows clear separation of the skin, fat and muscle layers. The precision can be set by the user and parametric interpolation of the discrete contours is available. The output from the program could be used as digital input for manufacturing prosthetics or limb models or as input for graphics software packages.

Furthermore the localised fat content will be estimated with an accuracy which is better than the skinfold calliper. This application suggests that there is scope for some physiological applications, such as finding muscle cross-sections or volumes. The accuracy can be improved significantly by increasing the density of the radial scan lines and using higher resolution graphics cards. The accuracy of reconstruction is directly

related to the ratio between one pixel and the real world length. For multi-connected areas, such as the forearm or the lower part of the leg, it is expected that the user will define the scan lines manually using an external pointing device; the algorithm used in the presented example can then be implemented.

The cumbersome procedure used for transformation of the MRI scans into bit-map files could be avoided completely if the MRI manufacturer provided the format of the graphics file. Then the image could be either directly transformed into a bit-map file or the program could be modified to process different graphics files.

It should be noted that, in several studies, the bone shape was manually digitised [69]. This manual method usually adds an error that is largely stochastic and subjective. The current program can obtain the shape fully automatically and with a greater accuracy.

The program was tested by using 11 different MRI scans and a successful result was obtained for each MRI scan. As long as there is a colour difference between the layers (even if it is not distinguishable by the naked eye) the algorithm can detect the edges.

Some further developments are deemed appropriate:

- To add facilities for conversion of different format graphics files into bit-mapped files.
- To develop an algorithm for more than one bone - e.g. for the forearm or calf.

2.4. Summary

A program was developed to convert MRI images to nodal coordinate input for FEA. The program is written in the C programming language and uses assembly language to access the system resources directly, thereby increasing the computational speed. The total running time for creating the full model with 18 cross-sectional scans was less than 10 minutes including user-intervention and three-dimensional graphics representation. This time can vary depending on the computer specifications and the quality of the MRI scans. The software was designed to be used specifically on limbs, but users could find it applicable to other parts of the human body.

Chapter 3

Experiment Design I

Mechanical Test Design and Pneumatic System

3.1. General Description of the Testing System

New equipment was designed to generate uniform pressure on the upper arm surface and to measure the gross muscle belly response under load. This device is effectively a cuff (a standard car seat belt) that applies controllable uniform pressure around a 45 mm wide band of the upper arm. The seat belt had needed flexibility and strength to cover and apply high load to the upper arm. The deflection of the upper arm was measured from the cuff movement with the increased pressure. This design was used to undertake three different types of mechanical tests: creep, stress-relaxation and stress-strain tests. In these three tests, the same basic parts, which are explained in detail later, were used. Pneumatic actuators were used to activate the moving parts of the stress-relaxation and stress-strain tests. Pneumatics was considered as a safe energy source for the releasing mechanism of the design, compared to electrical and hydraulic actuators. In this chapter, mechanical parts of the design were explained for each test. In the next chapter, electronic parts and data collection procedures were explained.

3.1.1. Main Frame

The main frame, which is shown in figure 3.1. (1), is the carrier of the system. Every single part (mechanical, pneumatic and electronic) in the design was fixed to it. The main frame was made of an aluminium box section (76 mm x 25 mm x 3 mm). Every corner of the frame was fixed by an aluminium angle section (4) bolted with a M5 steel bolt.

The stabiliser (3) is a part of the main frame, which keeps the frame still and prevents any vibrations occurring in the frame that may effect load cell readings. The stabiliser (3) was attached to the main frame by using 2 x M8 bolts. Three square section bars (2) were used, two of which were used for attaching the squeezing chamber. The other one was used for transferring the pneumatic pipeline. The main reasons for choosing aluminium box section were lightness, strength, easy of machining and the hollow shape, which helped the wiring of the electronic instrumentation. A perspective view of the main frame, stabiliser and square section bars can be seen in figure 3.1. The dimensions of the main frame can be found in appendix A.

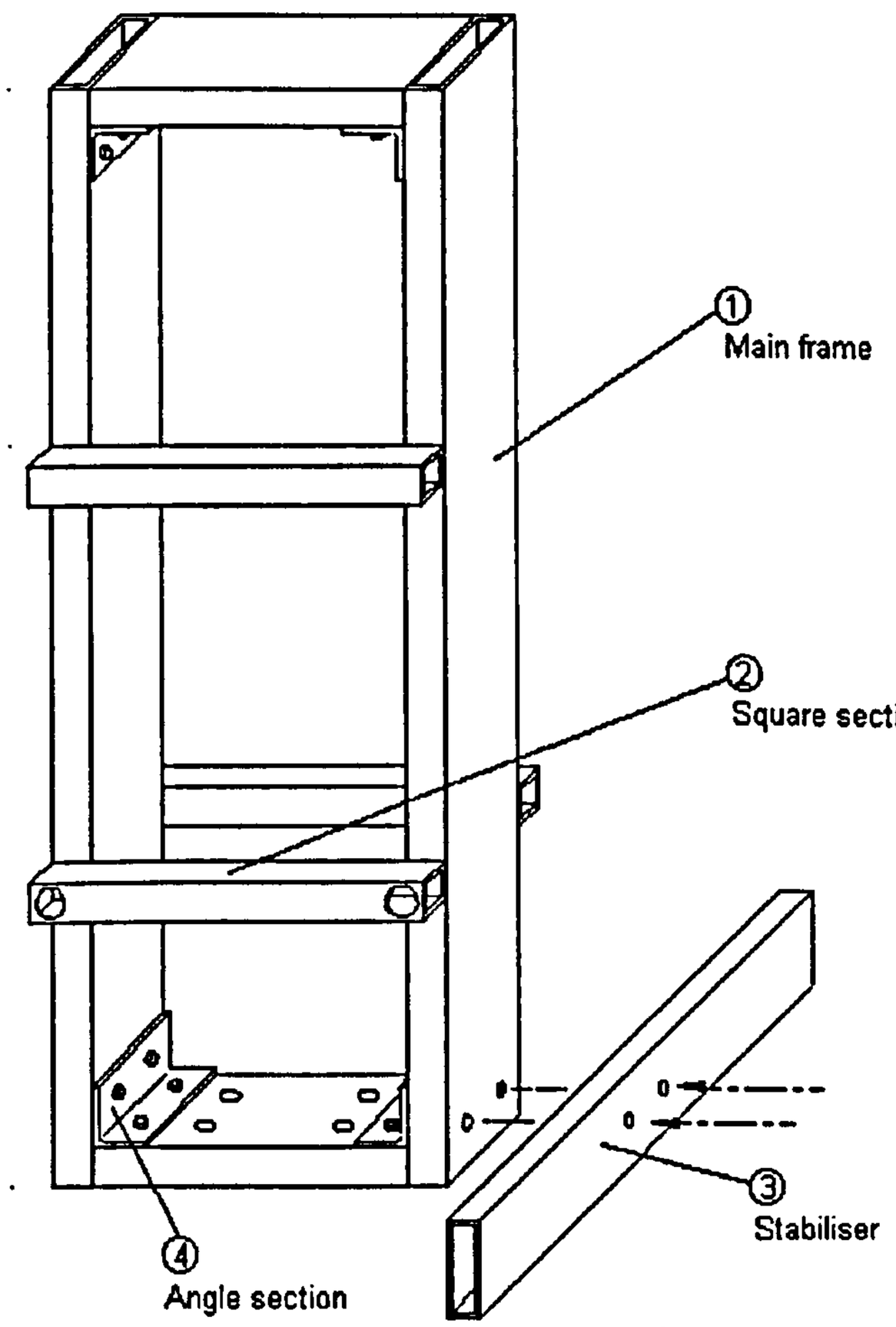

Figure 3.1. Main frame and stabiliser

The main frame was also fixed to the table (Fig. 3.2.) by using 4 x M10 bolts and nuts. To avoid tilting of the table, its legs were connected to each other by using two pieces of rectangular wood. Using a table also created a comfortable space for the subject. An adjustable elbow-resting corner was fixed to the top of the table which stabilised the subject's arm during the test (See appendix E).

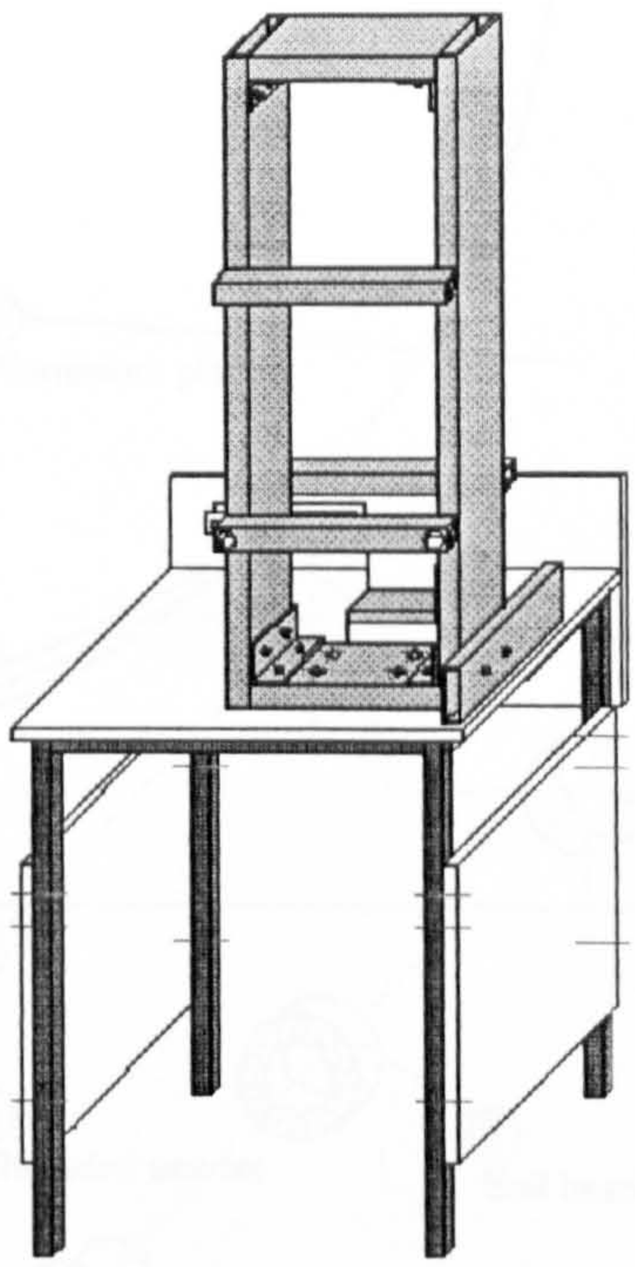

Figure 3.2. Fixation of the main frame to the table.

3.1.2. Squeezing Chamber

The squeezing chamber applied an almost uniform pressure to the upper arm, by pulling up the car seat belt. The car seat belt showed desired flexibility and strength to cover the human upper arm. The chamber consisted of four identical aluminium plates (Fig. 3.3 (6)) and connecting threaded spacers (5). Each pair of plates was joined together to enforce the strength of the plate and create a foundation for ball bearings. These two plates were joined to each other by using the threaded spacers (5) which were tightened

with washers (2) and M5 nuts (1). The spacers' (4) with ball bearings (3) were mounted without any fasteners. A detailed technical drawing can be seen in figure 3.3. The spacers were used for guiding the seat belt and each one had a connection with the seat belt (as shown in figure 3.4.).

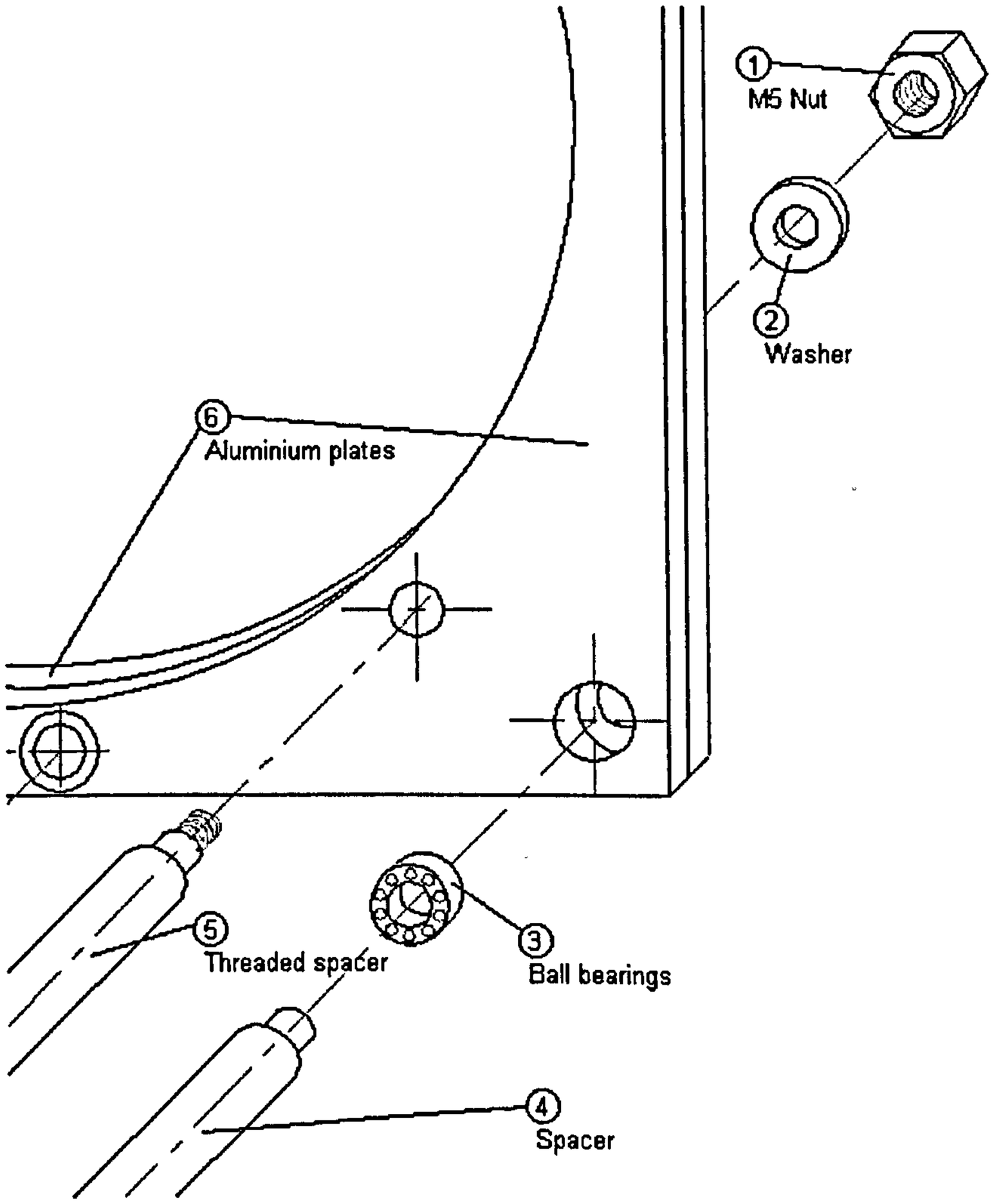

Figure 3.3. Detailed view of ball bearing and fastener.

Using a ball bearing (3) at both ends also reduced the rotational friction of the spacers' (4). A schematic diagram of the squeezing chamber and the topology of the seat belt can be seen in figure 3.4. The closed loop (2) was a standard car seat belt, which had suitable mechanical stretching properties.

The squeezing mechanism had two directions of movement. Movement of the cylinders was transmitted to the squeezing belt through the connecting ring (1): squeezing occurred simultaneously in the squeezing chamber in both directions (Fig. 3.4 - arrows). The drawback of the squeezing chamber was friction between seat belt and spacers but the friction was reduced by using silicone grease. Dimensions and production drawings of the squeezing chamber can be seen in appendix A.

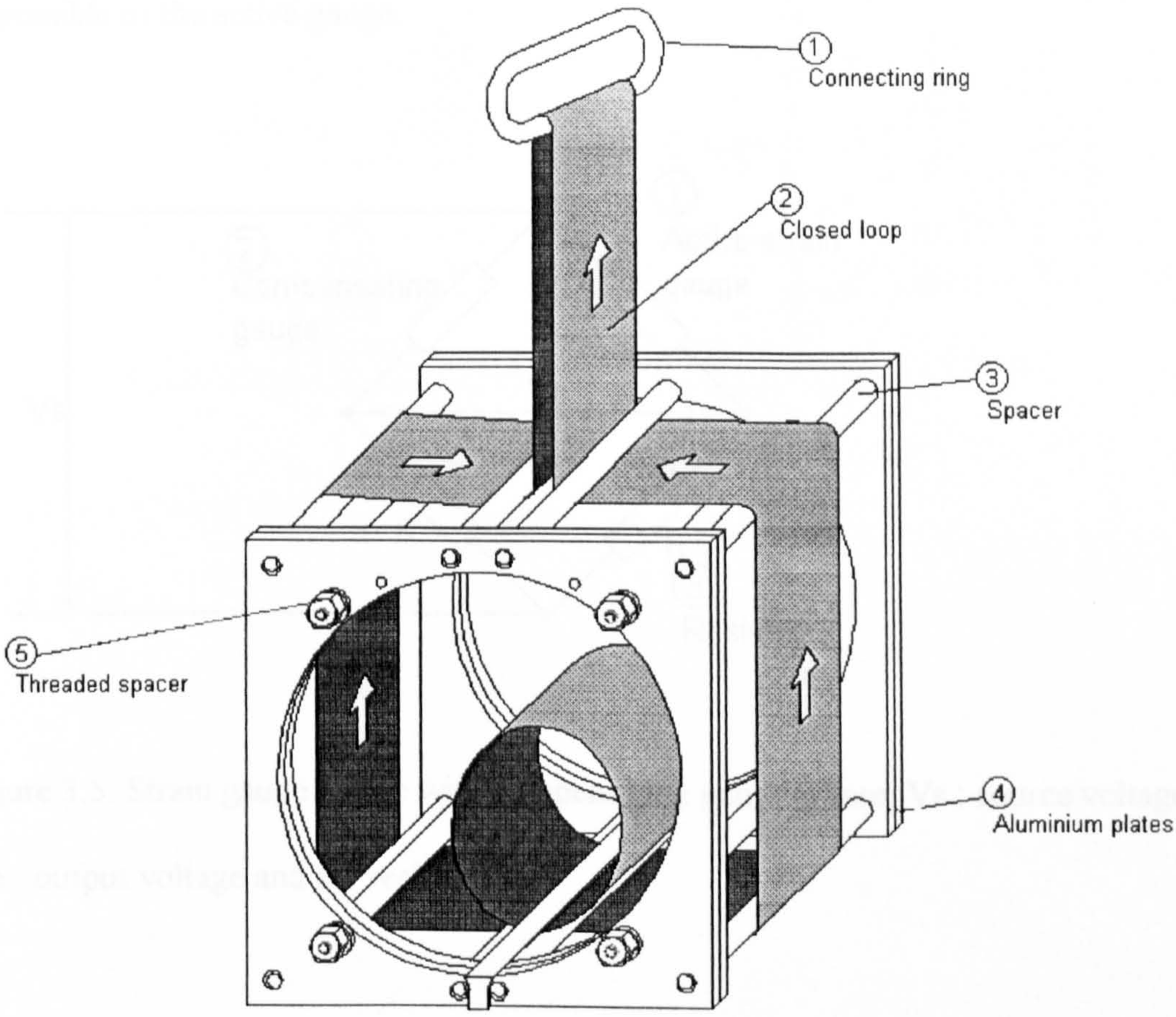

Figure 3.4. Squeezing chamber and topology of seat belt.

3.1.3. Load Cell

Load cells are basically a beam or spring shaped member arranged so that an applied load will cause a proportional strain at certain fixed points on the device. The strain can be detected in several ways, the most common being an arrangement of strain gauges [9, 10, 73]. These gauges convert the strain into an electrical signal, which can be stored or

used as a control signal. Four identical gauges were used, each of them forming one arm of a Wheatstone bridge (Fig. 3.5.) [9, 10, 29, 73]. Changes in temperature cause variations in the resistance of a strain gauge and are a possible source of error. For this reason, an unstrained compensating gauge (2) having the same temperature characteristic as the active gauge (1) was used in the bridge circuit, as in figure 3.5, to correct for temperature effects. To be effective, the compensating gauge must be mounted as close as possible to the active gauge.

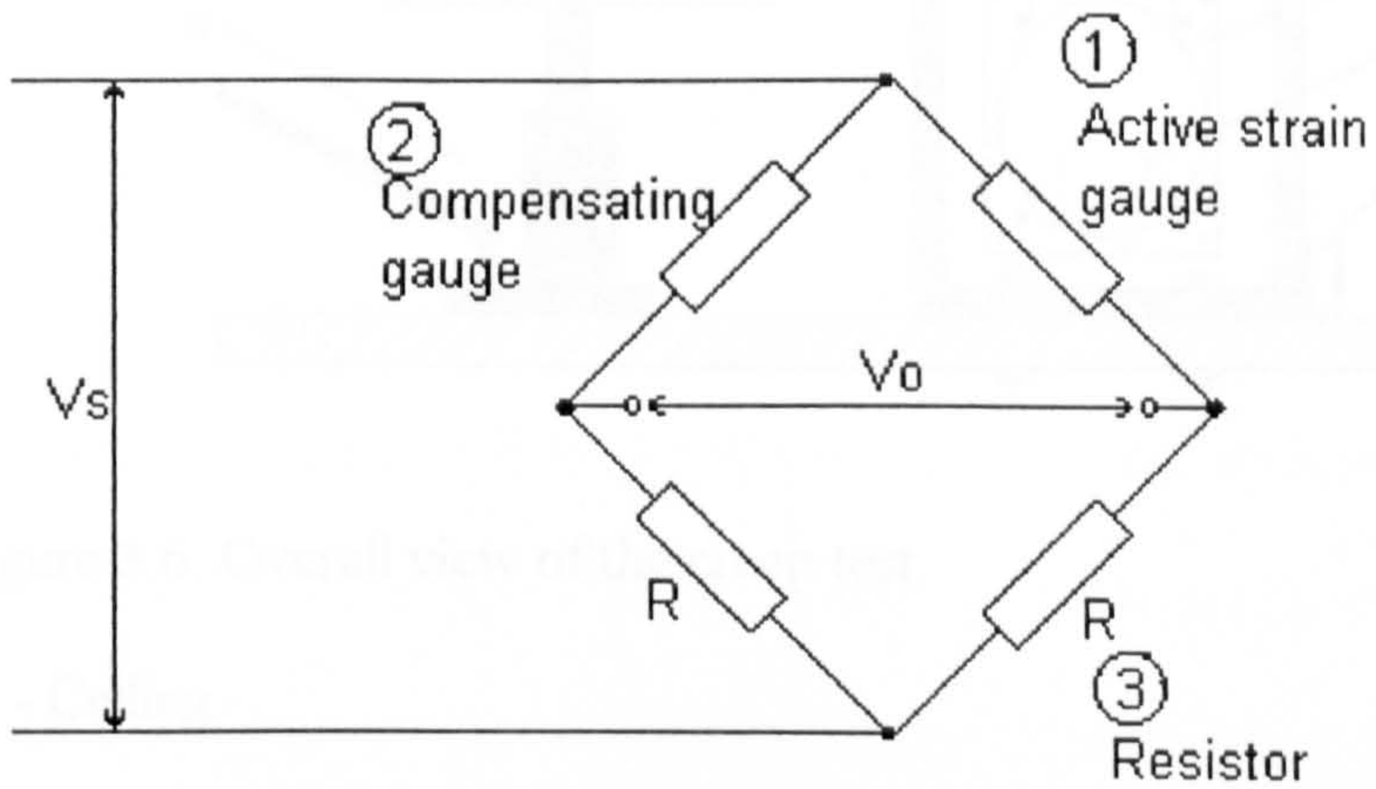

Figure 3.5. Strain gauge bridge with compensating gauge where: Vs : source voltage, Vo : output voltage and R : resistor

To measure the load on the upper arm, a spring like (S-shape) load cell was used to measure the tension on the closed loop belt.

3.2. Creep Test Design

The creep test was designed to apply a constant load to the subject's upper arm and measure (or record) the deformation of the arm. The load and change of the deformation were synchronised and data were stored in the computer. A schematic diagram of the creep test can be seen in figure 3.6, where :

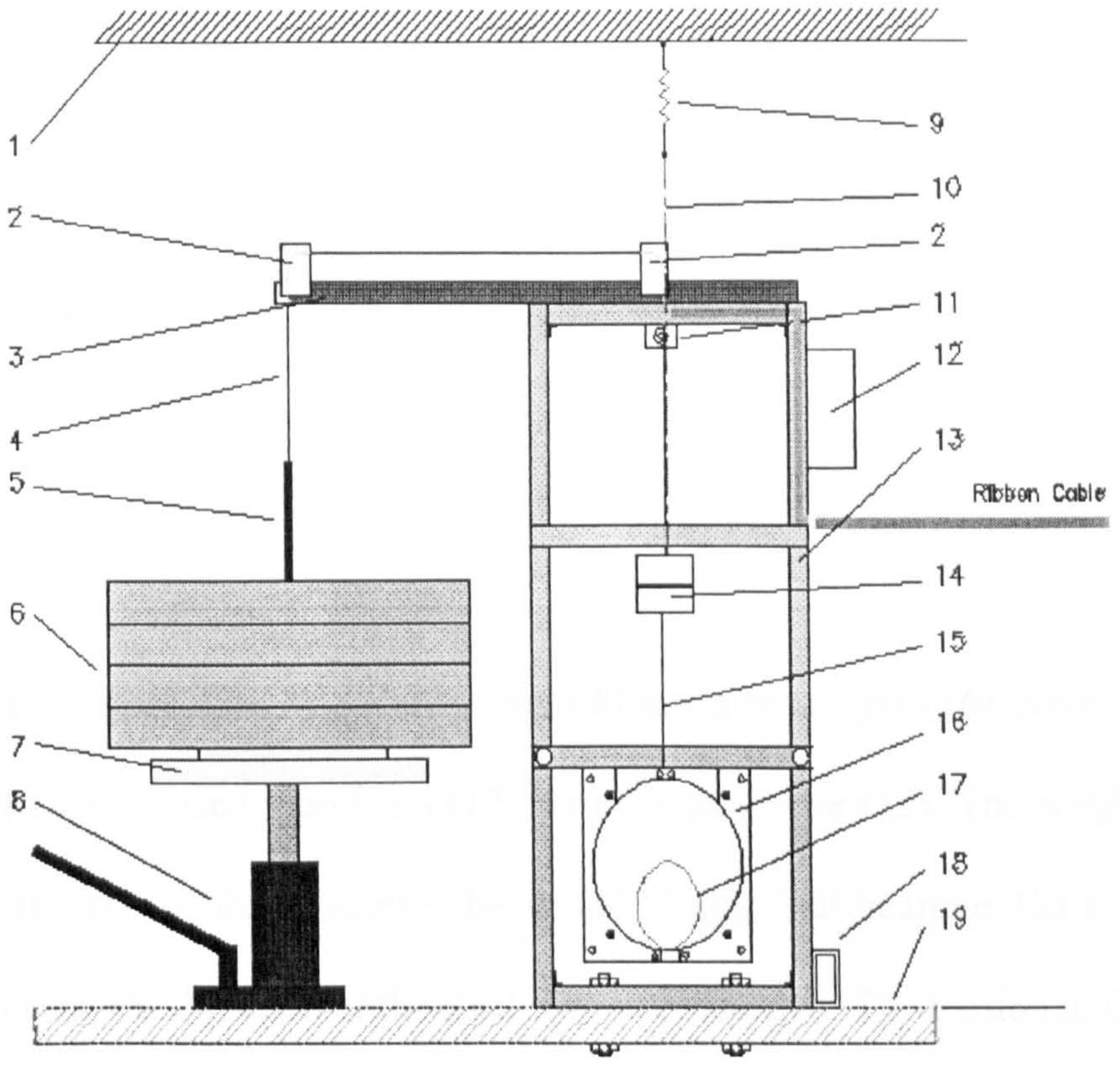

Figure 3.6. Overall view of the creep test.

1 - Ceiling

2 - Ball bearings

3 - Cantilever beam

4 - Steel wire

5 - weight carrier

6 - Weight

7 - Bottle jack weight

8 - Bottle jack

9 - Spring

10 - Cotton tread

11 - Rotary opto-couple

12 - Strain gauge amplifier

13 - Main frame

14 - Load cell

15 - Steel wire

16 - Squeezing chamber

17 - Close loop belt

18 - Stabiliser

19 – Table

To apply a constant load, standard weight-lifting free weights (6) were used, which transmitted to the closed loop band (17) through steel wire (15). The weights (6) were hanged at the end of the cantilever beam (3). Fixing ball bearings (2) on top of the cantilever beam, the direction of the steel wire was changed. The tension in the steel wire (15) was measured by a load cell (14), as this tension represents the global pressure applied to the upper arm. Using a bottle jack (8) the load was lifted. To avoid any dumping effect of the bottle jack, a 15 kg cast iron weight (7) was fixed to the top of the bottle jack (See appendix E). This arrangement gave the bottle jack a continuous release movement. The load was suddenly released by simply rotating the release bolt using a special purpose lever.

Because of the deformation in the arm, the movement of the steel wire was detected and measured by using an opto-couple device (11) (see section 4.5.1). Details of the setting can be seen in figure 3.7. To detect the movement of the steel wire (2), a cotton thread (1) was attached to the load cell (Fig. 3.6 (14)), which was parallel to the steel wire. The tension in the cotton thread was regulated with the spring (Fig. 3.6 (9)) which was connected to the ceiling (Fig. 3.6 (1)), therefore there was always enough tension to rotate the opto-couple. The movement of the cotton thread caused a rotation in the opto-couple device (3), which was recorded in the computer.

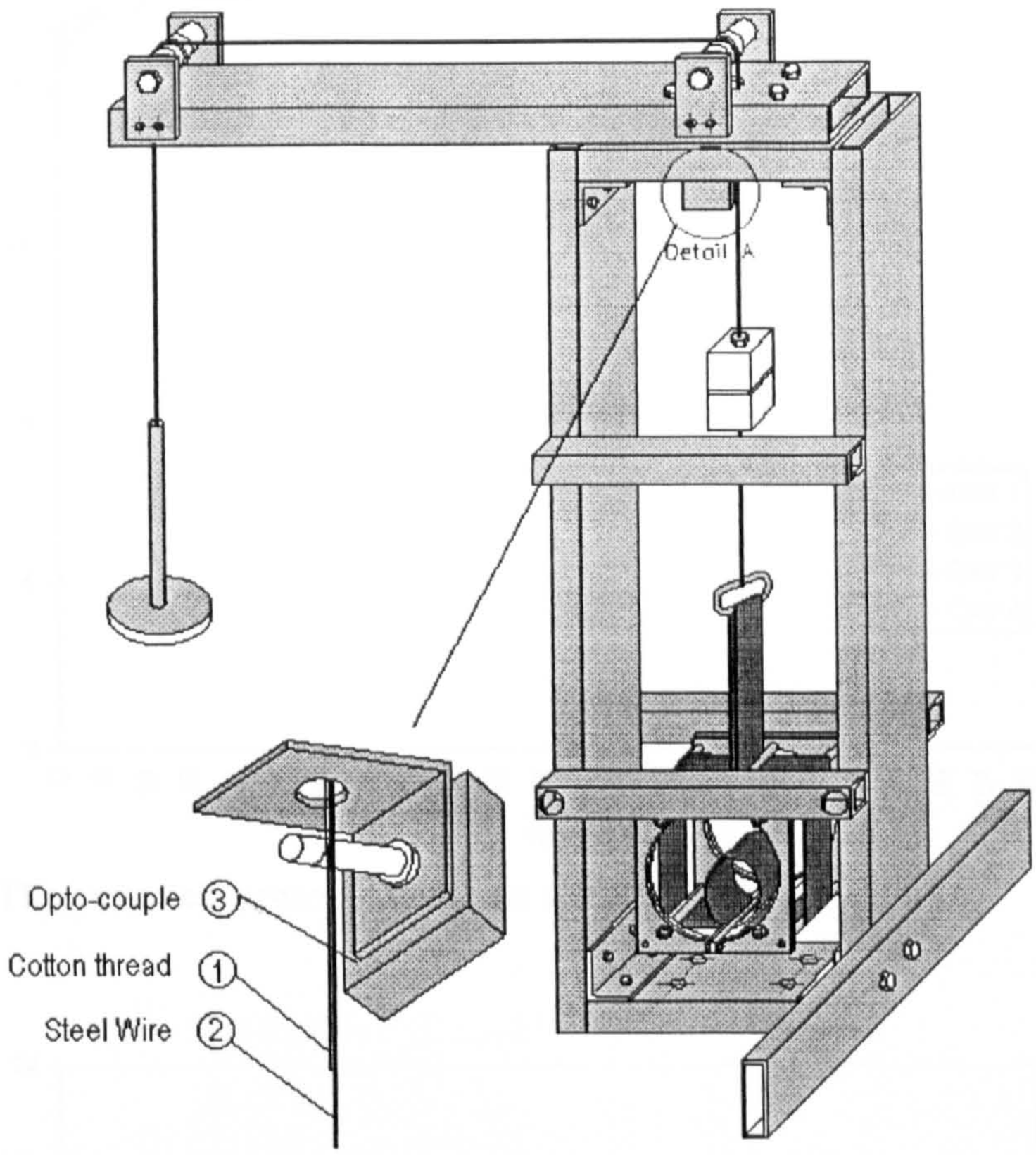

Figure 3.7. Detail view of opto-couple device and its placement.

Applying the same test protocol to the same subject with the exact test condition, the repeatability of the creep test was also tested. The results of the test are shown in figure 3.8 and 3.9. A 60 kgf load was applied to the subject's upper arm on different days. The same subject was tested on four following days. The test results are presented in figure 3.8 and the same results were zoomed to show more details. The difference from the average creep test is ± 0.05 mm. That is why the difference was negligible.

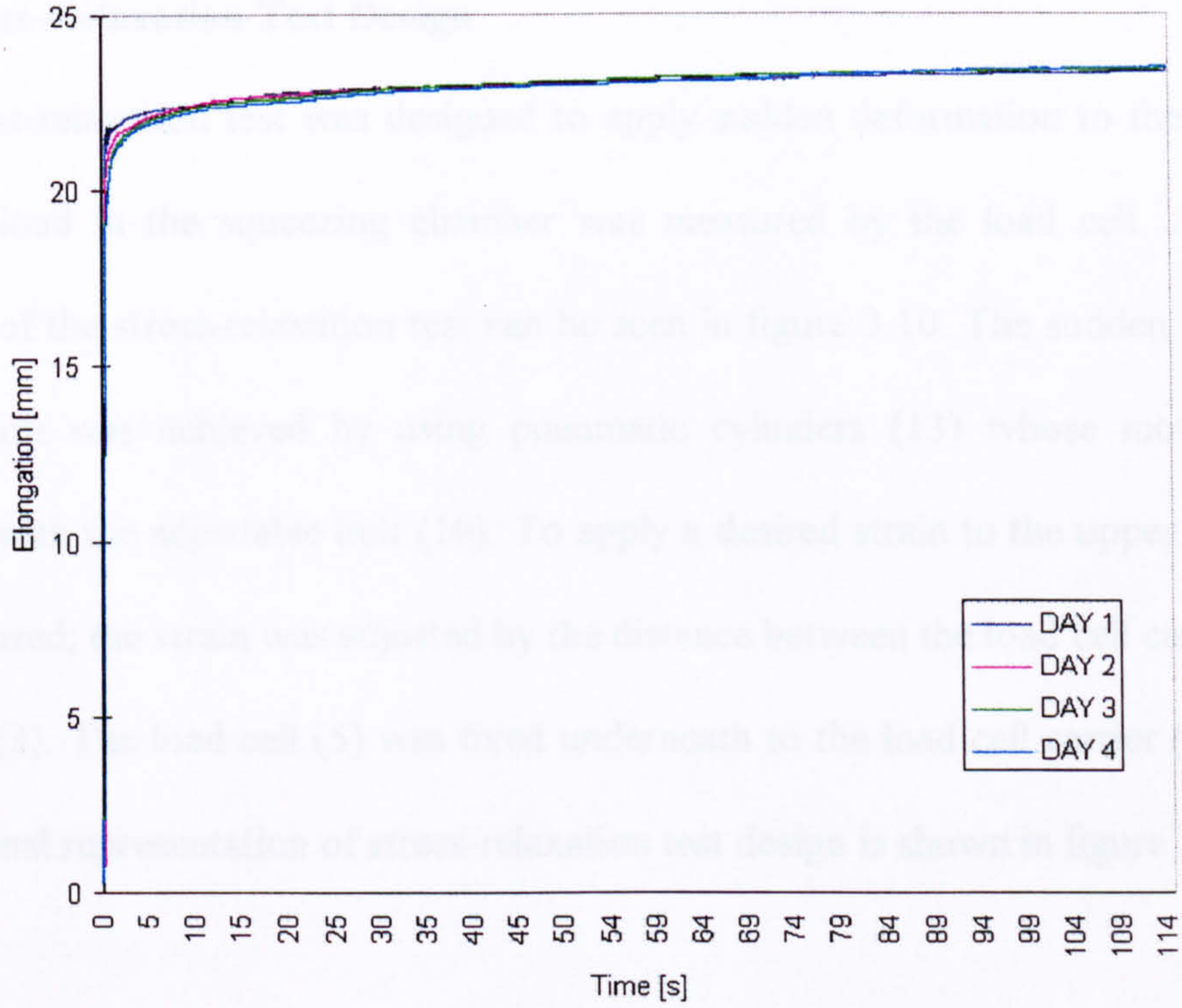

Figure 3.8. The same test protocol with one subject on different days.

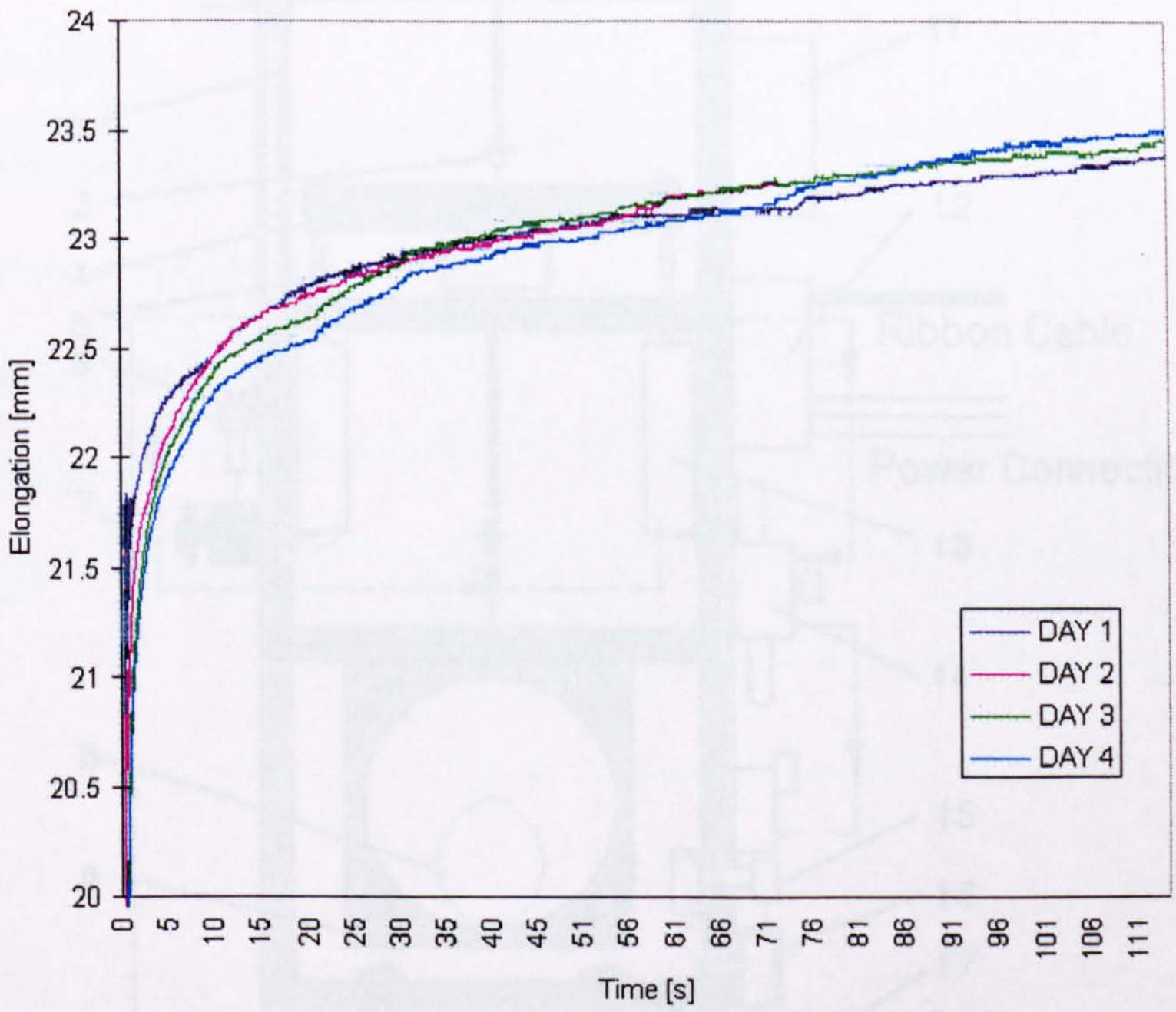

Figure 3.9. The same test on different days (zoomed presentation of Fig. 3.8.)

3.3. Stress-Relaxation Test Design

The stress-relaxation test was designed to apply sudden deformation to the upper arm; and the load in the squeezing chamber was measured by the load cell. A schematic diagram of the stress-relaxation test can be seen in figure 3.10. The sudden deformation of the arm was achieved by using pneumatic cylinders (13) whose movement was stopped with the adjustable bolt (10). To apply a desired strain to the upper arm, a ruler (2) was used; the strain was adjusted by the distance between the load cell carrier (4) and the bolt (3). The load cell (5) was fixed underneath to the load cell carrier (4). A three-dimensional representation of stress-relaxation test design is shown in figure 3.11.

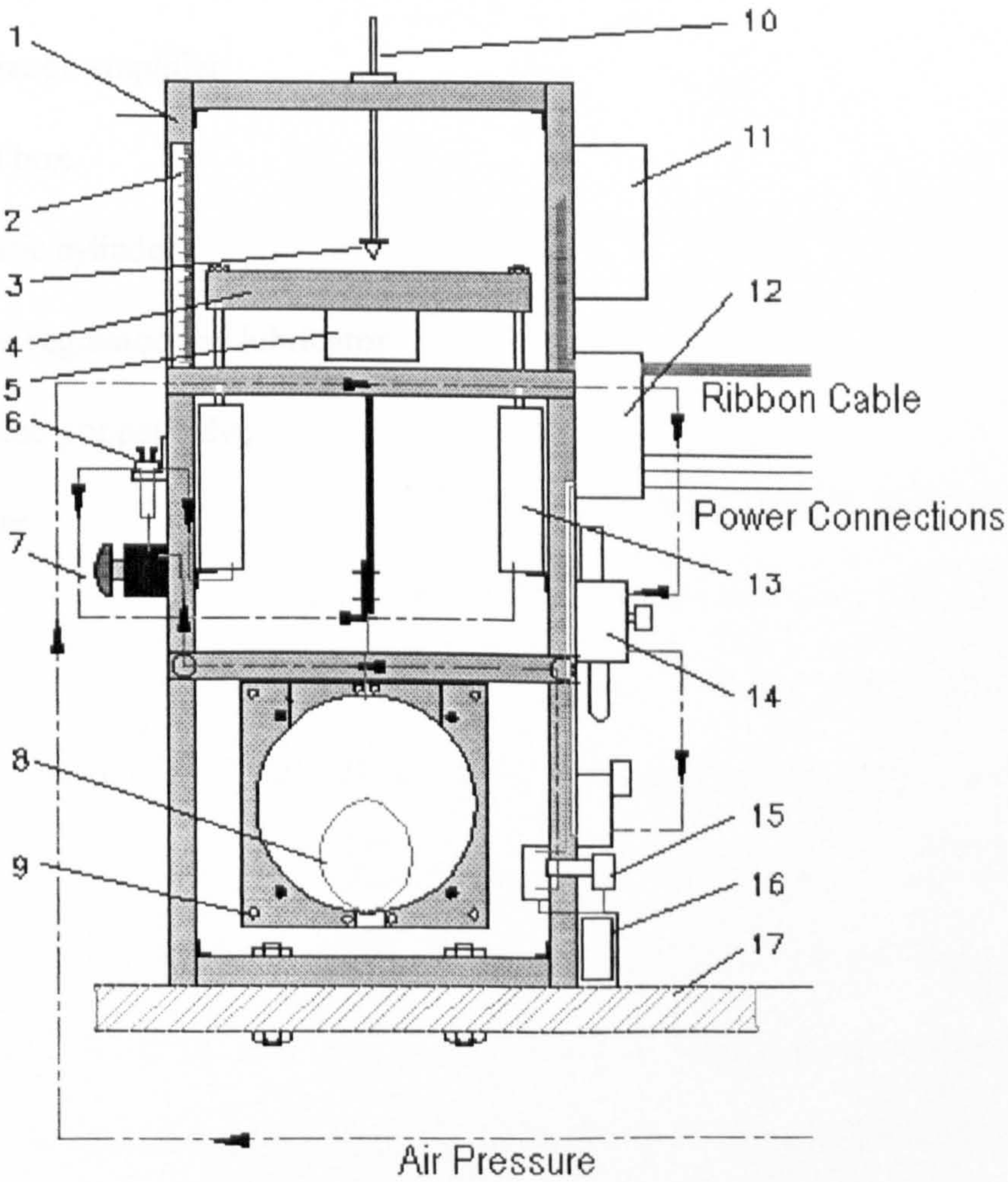

Figure 3.10. Overall view of the stress-relaxation test, where:

1 - Main frame

2 - Ruler

3 - Tip

4 - Load cell carrier

5 - Load cell

6 - Valves

7 - Emergency stop button

8 - Closed loop belt

9 - Squeezing chamber

10 – Adjusting bolt

11 - Strain gauge amplifier

12 - Control box

13 - Pneumatic cylinder

14 - Pressure regulator and lubricator

15 - Pneumatic poppet valve

16 - Stabiliser

17 – Table

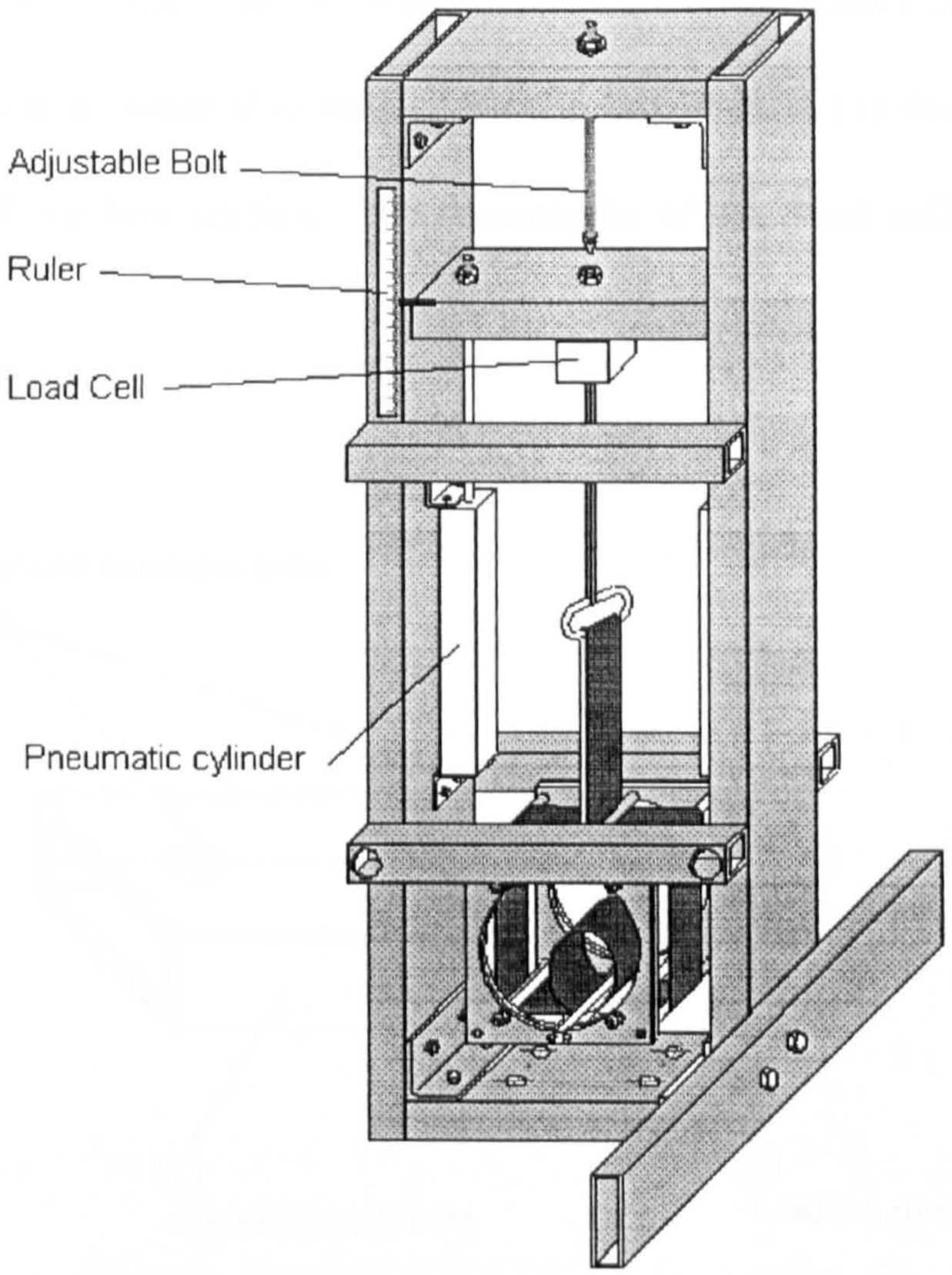

Figure 3.11. Three-dimensional representation of stress-relaxation test.

3.3.1. Load Cell Carrier

The load cell carrier (shown in Fig. 3.10) had three major roles in the system. The first was to transmit the movement of the cylinders (13) to the squeezing belt; the second was to compensate for the misalignment of the cylinders; the last was to provide a fixing point for the load cell against (5) the adjustable stopping bolt (10), which stops the cylinder's movement.

An aluminium box section (Fig. 3.12 (1)) (76 mm x 25 mm x 3 mm) was used as the base for the load cell. Because of the shape of the load cell, it was possible to fix the load cell to the middle of the load cell carrier. To fix the load cell, a 13 mm radius hole (3) was opened in the middle of the load cell carrier. The load cell was attached to the carrier by

using a M12 bolt. The load cell was attached under the load cell carrier. Two holes (2) (diameter 14 mm) were also opened on the box section (1) for fixing cylinder rods in both ends of the box section. The dimensions of the load cell carrier can be seen in appendix A.

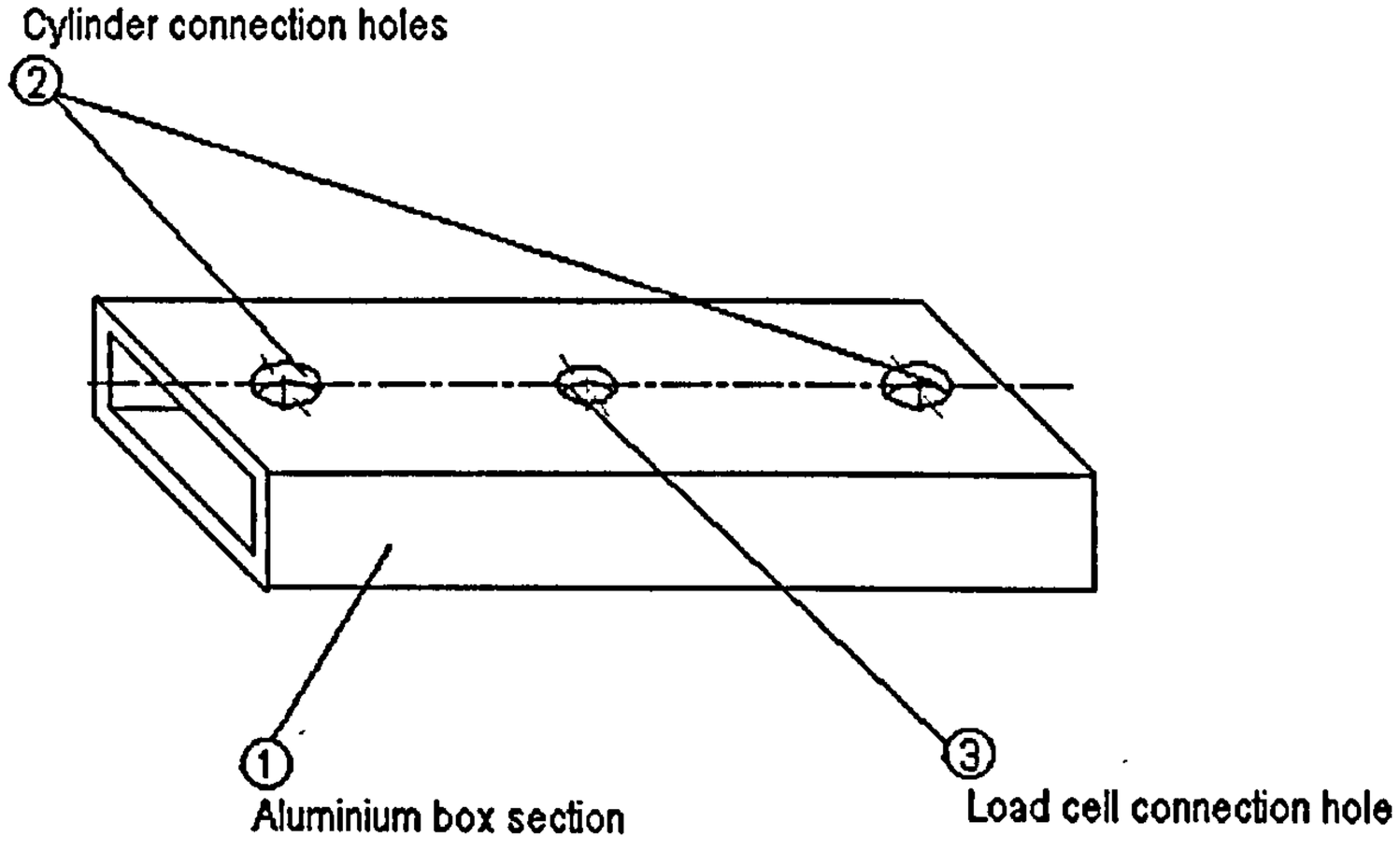

Figure 3.12. Load cell carrier.

3.3.2. Pneumatic Design of Stress-Relaxation Test

During 1964, the European Oil Hydraulic and Pneumatic Committee (CETOP) published a proposal for a range of standardised symbols for hydraulic and pneumatic equipment. These symbols were later recognised by the International Organisation for Standardisation (ISO). In figure 3.13, the pneumatic component layout is represented in terms of these symbols.

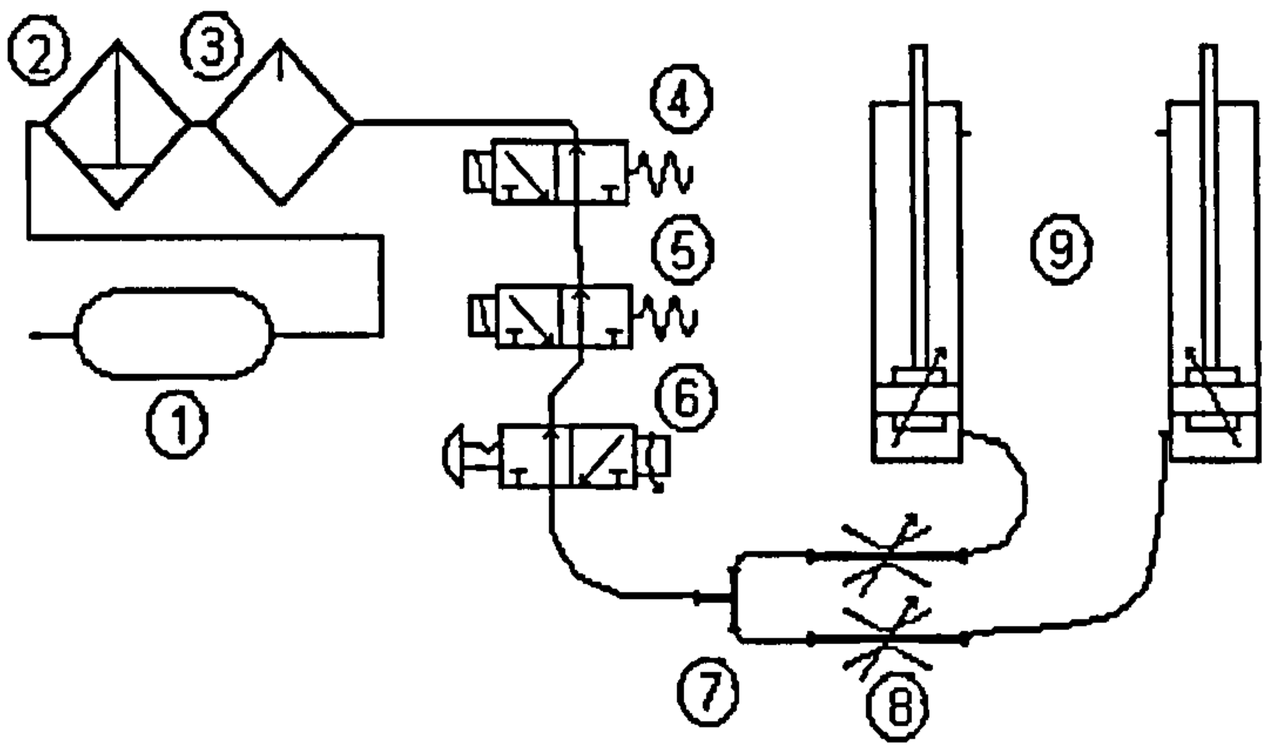

Figure 3.13. Pneumatic component layout of stress-relaxation test

The pneumatic layout can be described fundamentally as follows: first of all, compressed air from the reservoir tank (1), entered the filter/regulator (2) and lubricator (3); the compressed air then reached two relays (4, 5). After the emergency stop (6) the compressed air divided into two directions (7). Finally, the compressed air passed through calibrating valves (8) before entering the cylinders (9).

3.3.2.1. Pneumatic Cylinders

Single acting push (extension) or pull cylinders (Fig. 3.10 (13)) were used to move the load cell carrier that transmitted the force into the squeezing chamber, which subsequently caused deformation in the upper arm. Rod-type pneumatic rams are most commonly used in two-position applications working between end stops; for hold on load, it is necessary that the air supply is connected to the appropriate end of cylinder. To avoid shock loads at the end of the travel, these cylinders incorporated a cushioning device (Fig. 3.14 (3)).

The favourable attributes of rod pneumatic rams are as follows:

- Inexpensive

- Light alloy construction

- Safe, clean working medium

- Range of mounting configurations

- Shock resistant

- Rapid acting

- Ideal for two-position sequence control

- System protected by inherent force limitation [1].

The other difficulty, which was caused by the different friction coefficients of the cylinders, was to synchronise the movement of the cylinders. The cylinders were set at the same cushioning factor (3), to avoid different starting forces. This problem was overcome by using two identical valves (2). To calibrate the cylinders that were exposed to the same pressure in the same period and until the movement of the cylinders were equalised, valve setting (2) was altered. A schematic representation of the calibration can be seen in figure 3.14.

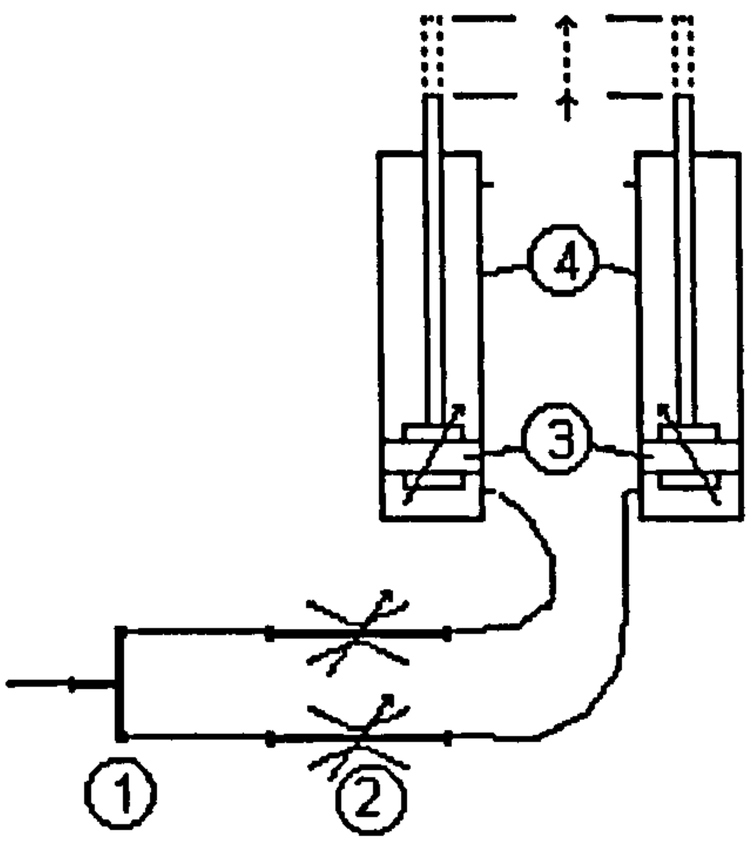

Figure 3.14. Calibration of the cylinders

3.3.2.2. Filter/Regulator and Lubricator

Before entering the cylinders, air passed through the filter/regulator (Fig. 3.13 (2)) and the lubricator (3). The filter/regulator (2) cleansed the air of unwanted material. The regulator was also set to the highest pressure needed, which did not allow a higher pressure in case of malfunction of the system. The lubricator's main task was to oil the air by the desired amount to reduce the friction in the pneumatic cylinders.

3.3.2.3. Emergency Stop

The emergency stop (Fig. 3.13 (6)) was a vital part of the design and safety aspect of the instrumentation. It was placed on the main frame (Fig. 3.10 (7)) in a position which the subject could reach effortlessly. When the subject pressed the emergency stop, the compressed air in the pneumatic cylinders was released into the atmosphere. To operate the emergency stop, only 18 N force was needed from the subject.

3.3.2.4. Pneumatic Poppet Relays

Two relays (Fig. 3.13 (4, 5)) were used to lock the pneumatic cylinders in position and allow them to move in the forward and reverse directions. Both relays, which were normally closed, was controlled by the computer. During the forward movement, they were opened to pass compressed air to the pneumatic cylinders. In the reverse direction, one relay (4) was closed to cut the compressed air flow and the other one (5) was opened to let the air in the pneumatic cylinders pass to the atmosphere.

3.4. Stress-Strain Test Design

The stress-strain test was designed similarly to the stress-relaxation test with a few exceptions. A constant speed of the cylinders was achieved by using a linear stepper motor. The measurement and the control of the pneumatic relays and the linear stepper

motor were synchronised and data were stored in the computer. There was also a new pneumatic component; a voltage-to-pressure converter was added to control the air pressure with respect to the load. A schematic diagram of the system can be seen in figure 3.15.

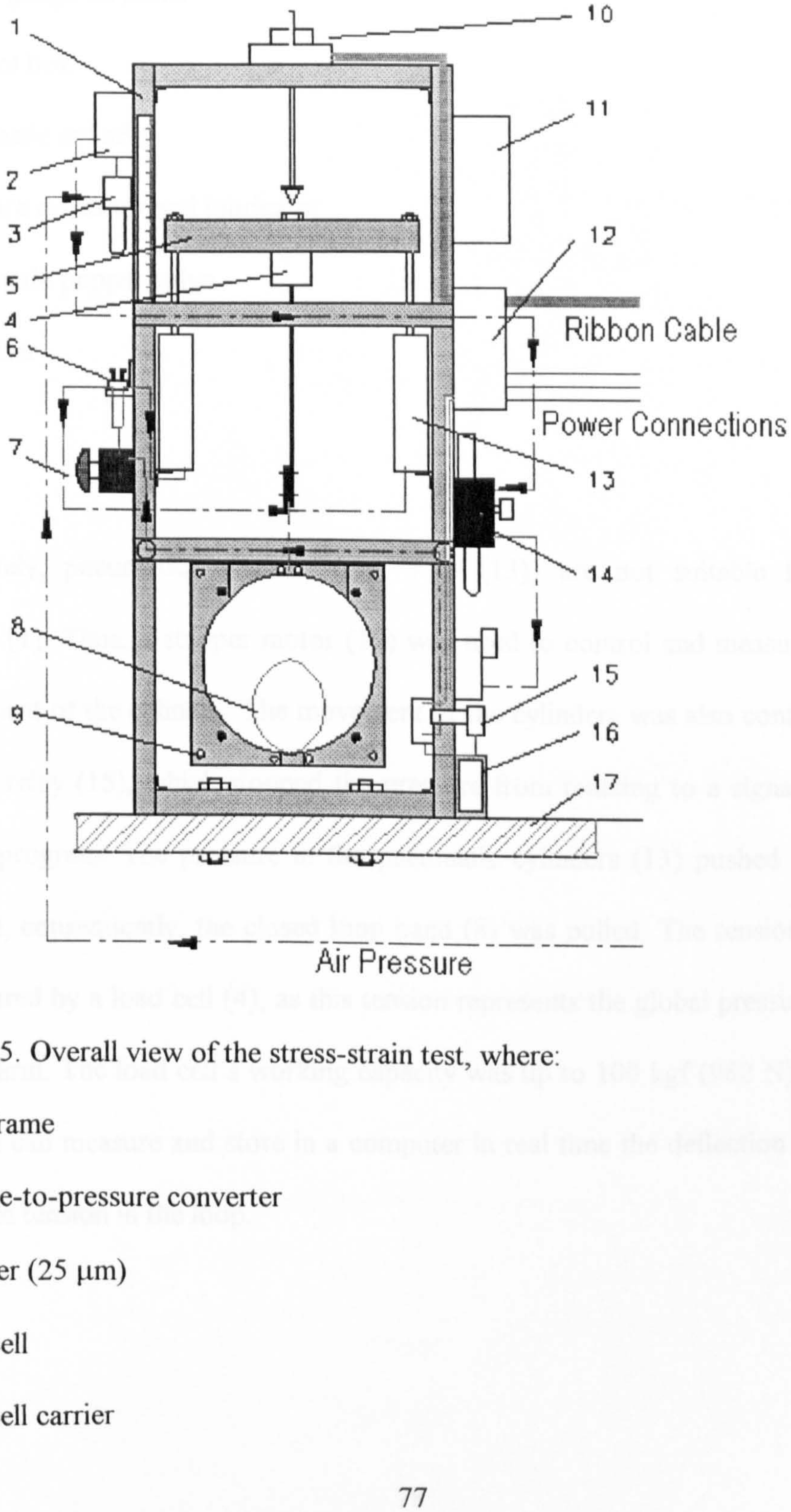

Figure 3.15. Overall view of the stress-strain test, where:

1 - Main frame

2 - Voltage-to-pressure converter

3 - Air filter (25 μm)

4 - Load cell

5 - Load cell carrier

6 - Valves

7 - Emergency stop valve

8 - Closed loop belt

9 - Squeezing chamber

10 - Linear stepping motor

11 - Strain gauge amplifier

12 - Control box

13 - Pneumatic cylinder

14 - Pressure regulator and lubricator

15 - Pneumatic poppet valve

16 - Stabiliser

17 - Table

Unfortunately, pneumatic cylinders (Fig. 3.15 (13)) are not suitable for precision movement [1]. Thus, a stepper motor (10) was used to control and measure accurately the movement of the cylinder. The movement of the cylinders was also controlled by the pneumatic relay (15), which stopped the pressure from reacting to a signal sent by the computer program. The pressure in the pneumatic cylinders (13) pushed the load cell carrier and, consequently, the closed loop band (8) was pulled. The tension of the loop was measured by a load cell (4), as this tension represents the global pressure applied to the upper arm. The load cell's working capacity was up to 100 kgf (982 N). The rest of this design can measure and store in a computer in real time the deflection of the upper arm and the tension in the loop.

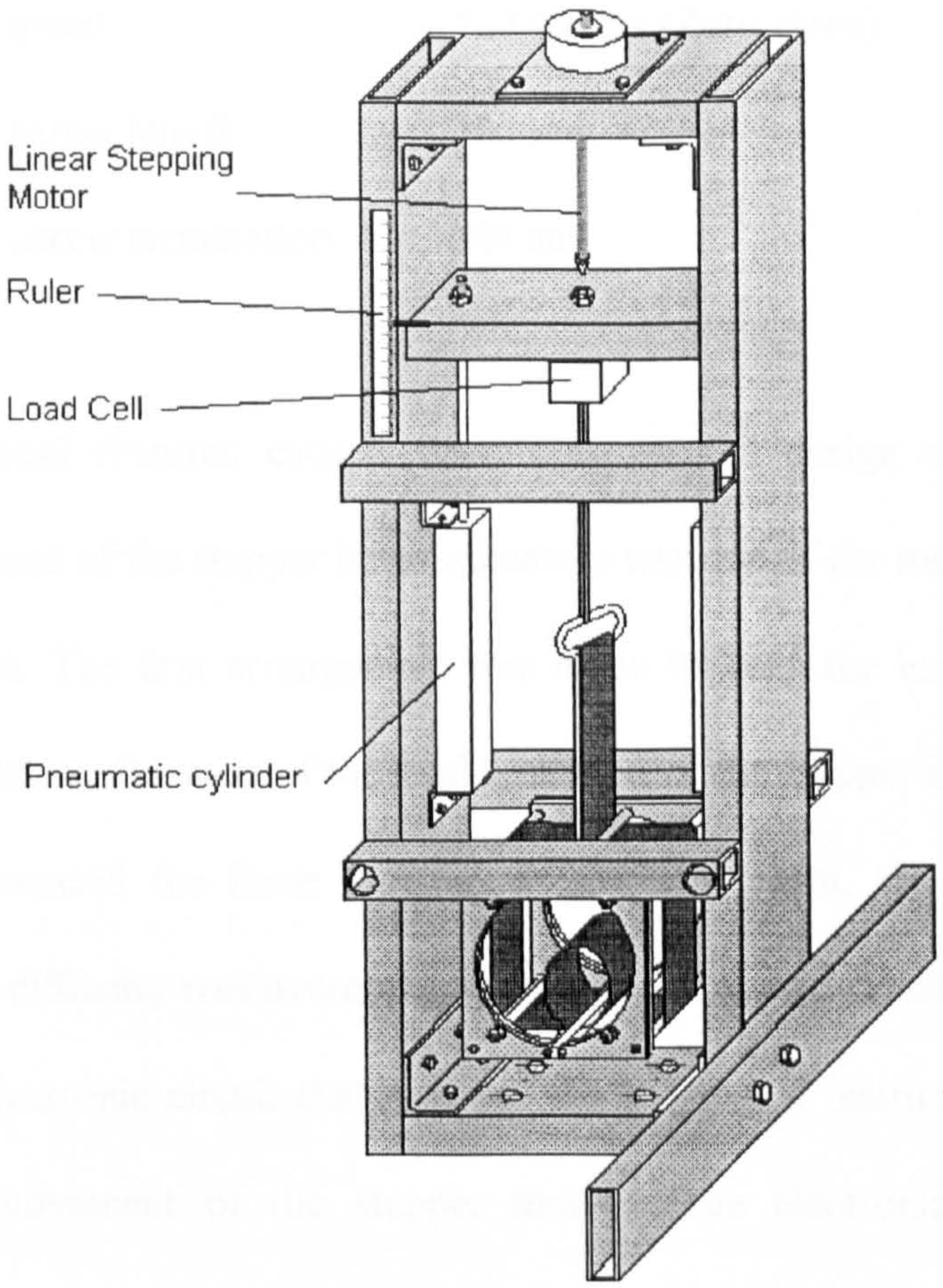

Figure 3.16. Three-dimensional representation of stress-strain test.

3.4.1. Stepping Linear Actuator

The stepping linear actuator converted electrical pulses into accurately defined linear steps using a stepper motor and precision lead screw combination. The actuator body contained the 4-phase unipolar motor arrangement through which the lead screw travelled [8, 25]. To achieve linear travel, the lead screw was prevented from rotation by the load arrangement on the end of the lead screw.

The stepping linear actuator had technical features such as:

Starting force	125 N
Step	0.025 mm
Step accuracy	0.005 mm

Max speed	380 steps/s (Zero force)
Lead screw length	225 mm
Lead screw termination	M4 nut

These technical features caused limitations on the design of the instrument. The maximum speed of the stepper linear actuators was one of the most important drawbacks of the design. The first arrangement was made to keep the load on the stepper linear actuator constant. Because of the load limitation of the stepper linear actuator, when the cylinders increased the force to squeeze the upper arm, the stepper linear actuator stalled. This difficulty was overcome by using a voltage-to-pressure converter (explained later). An electronic circuit that received the movement instruction from the computer controlled movement of the stepper motor. (The electronic circuit and computer program will be explained in chapter 4 section 4.7.)

3.4.2. Pneumatic Design of Stress-Strain Test

The pneumatic layout of the stress-strain test can be described as follows: first of all, compressed air from the reservoir tank (Fig. 3.17 (1)) entered the 25 μm filter (2) and voltage-to-pressure converter (3). After passing through the filter/regulator (4) and lubricator (5) the compressed air reached two relays (6, 7). After the emergency stop (8) the compressed air divided into two directions (9). Finally, the compressed air passed through calibrating valves (10) before entering the cylinders (11).

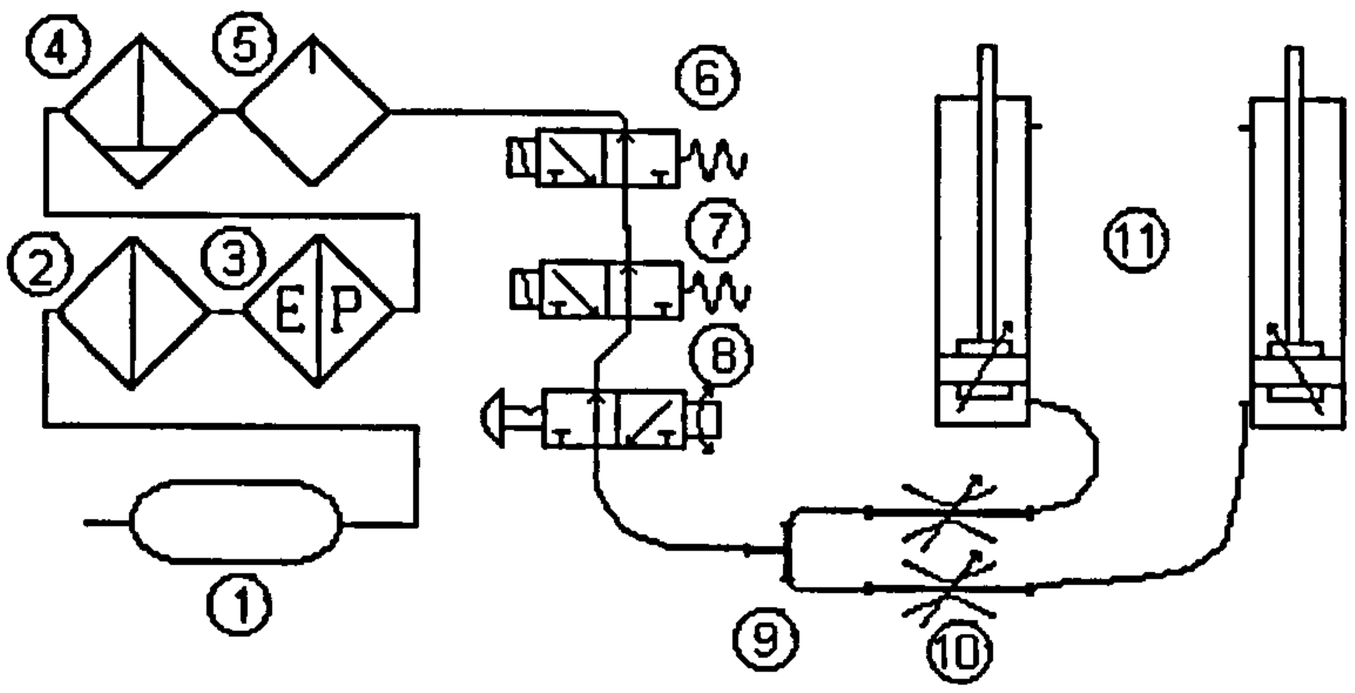

Figure 3.17. Pneumatic component layout of stress-strain test

3.4.2.1. Voltage-to-Pressure Converter

The main reason for using a voltage-to-pressure converter was to keep the load on the stepper linear actuator constant. When the pressure in the cylinders was increased to squeeze the upper arm, the stepper linear actuator stalled because of the load limitation. The voltage-to-pressure converter is a force-balance instrument having a coil suspended in a magnetic field on a flexible mount.

The voltage-to-pressure converter was placed on to the main frame (Fig. 3.15 (2)) which was as close as possible to the actuators to avoid problems with the compliance of the air in the pipeline. First of all, the elementary working pressure was decided by finding the threshold pressure for the stepper motor; this was 200 kPa. When the pressure reached between 200 and 240 kPa, the stepper motor (10) started struggling to move; above 240 kPa, the stepper motor jammed. Using an electronic circuit and the voltage-to-pressure converter, the load on the stepper motor was kept within the elementary working pressure of 180 kPa. The electronic circuit provided a linear feedback (12) from the load cell to the voltage-to-pressure converter. Any increase on the load cell caused an increase in the voltage in the electronic circuit. The voltage-to-pressure converter works

only with oil-free clean dry air filtered to 25 μm. That is why the air filter (3) was also fixed on the main frame and air passed from the filter before entering the voltage-to-pressure converter.

3.5. Health and Safety Aspects of the Instrumentation

Compressed air, although generally considered a safe source of energy, was treated with caution and under no circumstances used for any other purposes than those for which it was intended.

The Health and Safety at Work Act (1974) makes specific requirements on suppliers and users. All equipment was used within the published operating limits for pressure and temperature. During installation of the pneumatic components, the following points were borne in mind.

- All cylinder tie-rods and mountings were firmly fixed.
- All air connections were kept tight.
- All equipment was of the correct size to withstand the maximum anticipated working pressure.
- Special caution was taken not to block off or impede the passage of air from unused ports with any part of the body.
- Extreme caution was taken to ensure that no hands, fingers or other part of the body can become trapped when the cylinders were moving.
- A flex-glass was fixed to the main frame to avoid touching any moving part of the instrument to the subject's face.

3.6. Summary

In this chapter, the mechanical design of the instrument was discussed. First, the common parts for each test (creep, stress-relaxation and stress-strain), which are main frame and squeezing chamber, were explained in detail. Pneumatic design of the stress-relaxation and the stress-strain tests were also discussed. Using of the stepper motor and role of the voltage-to-pressure converter in the stress-strain test were explained. Every component in the design of the instrument was examined.

Chapter 4

Experiment Design II

Electronic Circuit Design and Software

4.1. General Description of the Electronic Design and Software

The design of the mechanical part of the instrumentation was explained in chapter 3. In this chapter, the control of the mechanical parts and data collection will be explained. The control of the pneumatic system and stepper motor were achieved by using electronic circuits and computer input and output (I/O) control. Data collection from the load cell was completed by using analog-to-digital converter (ADC) cards. Electronic circuits were designed to work with the PC data acquisition cards (I/O and ADC cards) and relevant software was written for data collection and storing. The benefits of using PC data acquisition cards are summarised below [73]:

- The PC is the best understood hardware interface in the world.

- Because the PC is a complete subsystem, design effort is minimised.

- Resources can be focused on the application-specific features of the target product.

- Development resource is reduced, saving time and money.

- Access to PC application software enhances the product functionality.

- User familiarity with DOS and Windows interfaces enhances product attractiveness.

Control and data collection software were written in the C programming language. The C programming language is well-suited to development of effective real-time operations and is ideally suited to control and instrumentation applications. The language promotes the use of structure, is highly portable and it yields code which is relatively compact. The software was written in the DOS environment and run on a 486 DX 33 MHz clock speed IBM compatible computer.

4.2. Computer Input/Output

A 24 - line digital input/output (I/O) card was used for reading the opto-couple (encoder) device in the creep test, controlling pneumatic valves for stress-relaxation test and controlling the stepper motor for the stress-strain test. The card is based around the industry standard 8255 Programmable Peripheral Interface (PPI) IC. Power, control, address and data signals were obtained from the computer's expansion bus. A 37-pin male D-type connector was integral to the card and protruded through the expansion card slot to facilitate connection with the outside. The 8255 PPI IC provides the necessary control, latching, buffering and handshaking of data to and from the card. In the card, both CMOS and TTL logic can be read but only TTL +5V can be written. This card is also not able to handle large current devices directly [16, 29, 44, 68, 72, 73, 79]. Therefore, the output of the I/O card was amplified before reaching the stepper motor driver (Fig. 4.9 (5)).

The 8255 PPI has 24 I/O lines divided into three ports -Port A, Port B and Port C - each of 8-lines each (Fig. 4.1 (6)). The three ports are configured in two groups of 12-lines, these are referred to as Group A and Group B. Group A consists of all 8-lines of Port A (PA7-0) and the upper 4-lines of Port C (PC7-4). Group B comprises all 8-lines of Port B(PB7-0) and the lower 4-lines of Port C (PC3-0) [25, 39, 61, 70, 13, 63]. There are three possible operating modes; these can be summarised as follows:

Mode 0: Each group of 12-lines can be configured in a set of 8-lines and a set of 4-lines, to be either inputs or outputs.

Mode 1: Each group of 12-lines can be configured to have 8-lines of I/O. Three of the remaining lines in each group are used for handshaking and a further two-lines are available for inputs or outputs.

Mode 2: Group A is configured to operate in bi-directional bus mode using 8-lines from Port A and 4-lines from Port C and 1-line in Group B Port C for hand shaking. The remaining lines from Group B can be configured to operate in either Mode 0 or Mode 1.

An appropriate I/O base address was selected. In this selection, it is important to avoid choosing addresses that are already used by existing cards otherwise a bus contention would occur and the computer would crash. The operating mode and definition of each port was defined by writing information to the Control register which is located at three bytes above the base address in the I/O map. Addresses already in use were determined by consulting the installation instructions for the existing cards. It was decided that address 0300 hex would be used. This address is designed for prototyping cards.

4.3. Load Cell Readings

The analog value from the load cell was digitised by using one channel of an 8 channel 12-bit single ended ADC. The output of the load cell was amplified by a strain gauge amplifier, up to a suitable level for the ADC. Timing of the data collection was arranged by the timing software (see section 4.4). The A/D conversion time was negligibly small (3 μs), which is why it is considered as real time in the software.

4.3.1. Load Cell Amplification

Unfortunately, the output of the load cell was too small to be read by the ADC and required amplification. A strain gauge amplifier was designed to increase the output voltage. A differential amplifier was chosen for full bridge strain gauge amplification. Lead wires from each strain-gauge element were connected to a Wheatstone bridge amplifier circuit.

The condition required for zero output (Vo in Fig. 4.1) from a Wheatstone bridge is that two pairs of adjacent legs have equal resistances (for example R1= R2 and R3 = R4). The total strain experienced by the gauges of each leg is proportional to the chance in resistance divided by the total leg resistance. The bridge circuits converts resistance changes of the gauge into an amplified voltage output. As variable resistive elements, each strain-gauge forms an 'active' arm of a Wheatstone bridge (R1, R2, R3, R4, in figure 4.1) [9, 29].

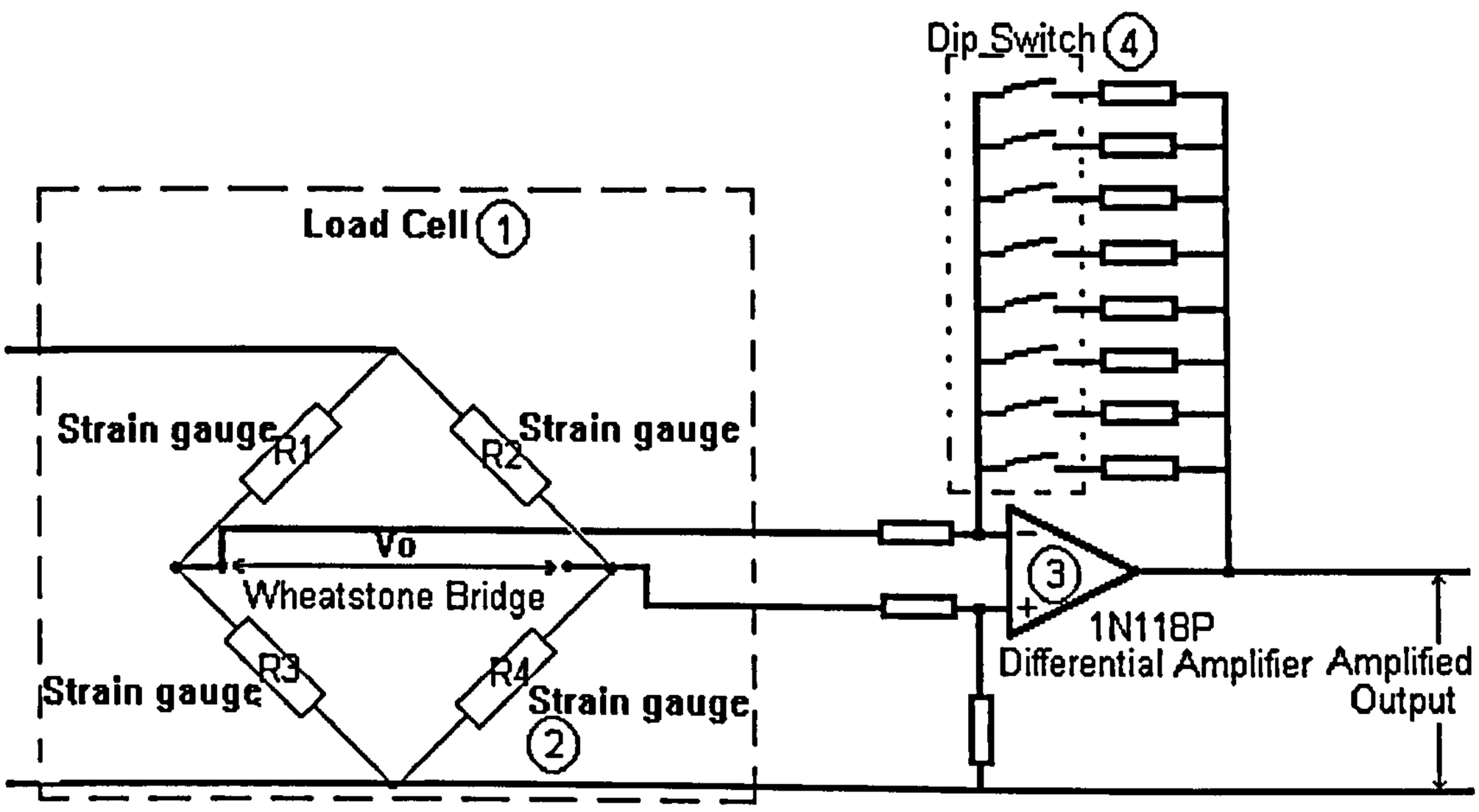

Figure 4.1. Schematic diagram of load cell (Wheatstone bridge) and simple differential amplification (one channel).

A two-channel strain gauge amplifier was designed to read load cell values (Fig. 4.1 (1)). The core of the design was an 1N118P (3) instrumentation amplifier IC. Two 1NA118P instrumentation amplifiers IC were used for amplification. The gain of the amplifier was determined by setting the dip switch (4) in the range of 50, 100, 200, 500, 1000, 2000, 5000 and 10000. The gain was calculated by the equation of $G = 1 + (50k\Omega / Rg)$; where: G was the desired gain; Rg was a suitable resistor for the desired gain.

4.3.2. Analog-to-Digital Converter

The purpose of an analog-to-digital converter (ADC) is to provide an interface between devices which produce analog signals and digital systems such as the microprocessor. The ADC contained a data register from which the converted value was read by the Central Processing Unit (CPU), and a control-status register which contained a control bit to start a conversion and a status bit indicating that a conversion was complete and that the data register could be read by the CPU. Alternatively, some analog-to-digital converters have a hardware input which may be used to start the conversion process. Where the conversion time of an ADC is similar to the execution time of a CPU instruction, it may not be necessary for the converter to generate an interrupt on completion of a conversion, as the CPU will not have to wait for any significant period for the result to be ready [73, 29].

To read the load cell data, an AIP-8d analog data acquisition card was used. The card provides the user with 8 channels of 12-bit analogue inputs. The input range from ± 50 mV to ± 5 volts, or 0 to +10 volts full scale. The card features a user-selectable base address, interrupt source, interrupt level and an on-board timer. The measurement range was set at +5V which had an accuracy of 0.1% full scale.

For correct communication between the card and the host computer, the range of addresses that the card occupied was set up. The base address represented the first address that card will use. The AIP-8d required a total of 8 addresses for correct operation. To avoid occupying the same address with an I/O card, 0306 hex was used as the base address for the ADC.

4.4. Programmable Interval Timer

One of the most common problems in any microcomputer system is the generation of accurate time delays under software control. Instead of setting up timing loops in the system software, the programmer can configure the 8253 IC to match his requirements and initialise one of the counters of the 8253 IC with the desired quantity. Then, upon command, the 8253 IC will count out the delay and interrupt the CPU when it has completed its tasks [16, 44, 68, 72, 79].

The 8253 IC is a programmable interval timer (PIT) device which has three independent 16-bit counters, which can be preset, each offering a count rate of up to 2.6 MHz. Its function is that of a general purpose, multi-timing element that can be treated as an array of I/O ports in the system software. All of the modes (6 modes) for each counter are programmed by the system software by simple I/O operations. Each counter of the 8253 IC is individually programmed by writing a control word into the control word register.

Mode 0: Interrupt on terminal count.

Mode 1: Programmable one-shot

Mode 2: Rate generator. Divide by N counter.

Mode 3: Square wave rate generator.

Mode 4: Software triggered pulse.

Mode 5: Hardware triggered pulse.

In the original PC, a 14 317 180 Hz crystal provided the base clock which was divided by three to generate the 4.77 MHz for the processor. Further division by four leads to a signal with about 1.193 180 MHz, which is applied to the three inputs CLK0-CLK2 of the 8253 IC as the clock signal (Fig. 4.2). Each channel has an associated divisor that

indicates how often the channel generates an interrupt. This divisor may range from 1 to 65536. A divisor of 0 is equivalent to 65536. The PC used these three channels for its purposes as described below:

Channel 0, which is used for the system timer, uses a divisor of 0. The resulting interrupt (INT 8. Interrupt ReQuest - IRQ 0) frequency of 1 193 180 / 65 536 is approximately 18.2065 times per second or once every 54.9 milliseconds. This channel operates in Mode 3 which signifies that the timer generates a square wave.

Channel 1 is used for direct memory access (DMA) memory - refresh operation. It uses a divisor of 18 approximately 66 287. 7778 times per second. This is equivalent to a DMA interrupt being generated once every 15.086 microseconds. Operation of this channel is in Mode 2, which signifies that a pulse is generated once every period.

Channel 2, which is used most often with the speaker port. Ports 40h, 41h, 42h are used as timer channels 0, 1 and 2 respectively. Port 43h is used for mode control.

Interrupt lines INT2 through INT7 appear on the PC bus, INT0 and INT1 appear only on the motherboard. INT0 is used by counter 0 of the 8253 PIT chip. The 8259 (Fig. 4.2) peripheral interrupt controller (PIC) chip maps the INTx line to interrupt number x+8. Hence, the timer interrupt is number 8. Up to eight I/O controller chips can be directly connected to the eight IRQ x (Interrupt ReQuest) inputs to the 8259 PIC IC (Fig. 4.2). When one or more inputs are asserted, the 8259 IC asserts INT (INTerrupt), which directly drives the interrupt pin on the CPU. When the CPU is able to handle the interrupt, it sends a pulse back to the 8259 IC on INTA (INTerrupt Acknowledge).

The 8259 IC is expected to specify which input caused the interrupt by outputting that input's number on the data bus. The CPU hardware then uses that number to index into a table of pointers, called interrupt vectors, to find the address of the procedure to run to service the interrupt.

Unfortunately the PC timer was used to control the time and the date; therefore, the accuracy of the timer was not enough (54.9 ms elapsed for each interrupt to occur) to control to millisecond accuracy. Consequently, the PC interrupt 8 was re-programmed for counting one tenth of millisecond and the new interrupt vector was set for INT8. In the new interrupt routine, three counters and one delay counter were used for counting. The complete program listing of the timer function can be seen on diskette I.

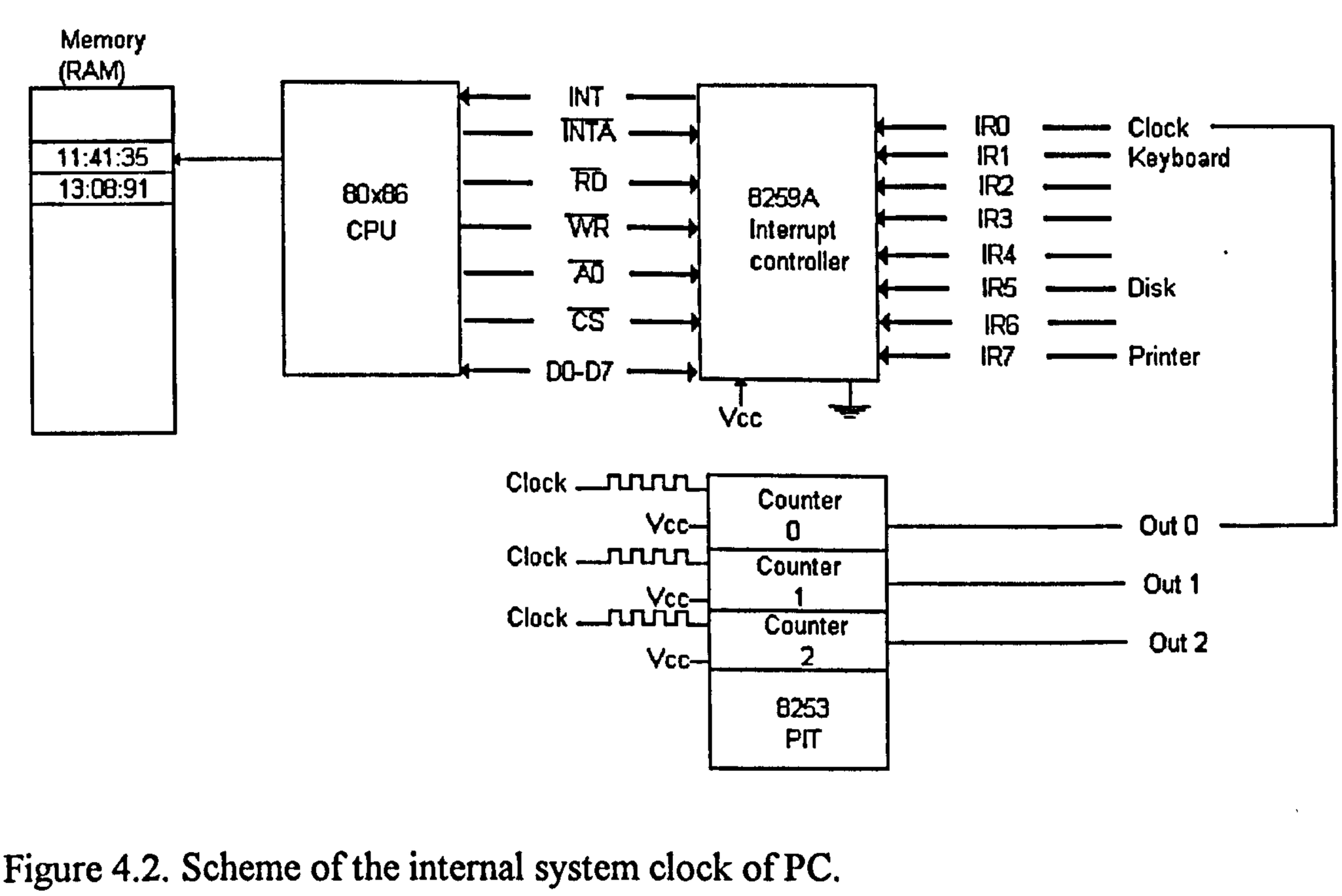

Figure 4.2. Scheme of the internal system clock of PC.

4.5 Creep Test

The constant load in the creep test was achieved by using standard weight-lifting weights and its movement was recorded with electronic circuits and compatible software.

4.5.1. Opto-Encoder

In the creep test, to measure the movement on the seat belt (see section 3.2 figure 3.7) a Hewlett-Packard opto-encoder (Fig. 4.3 (1)) was used. The opto-encoder was capable of reading 0.007 mm accuracy per bit. Two channels of binary output from the encoder (1) was sent to the special purpose chip (2) for the encoder to convert the output to 8-bit binary format which was received by the digital I/O card (3).

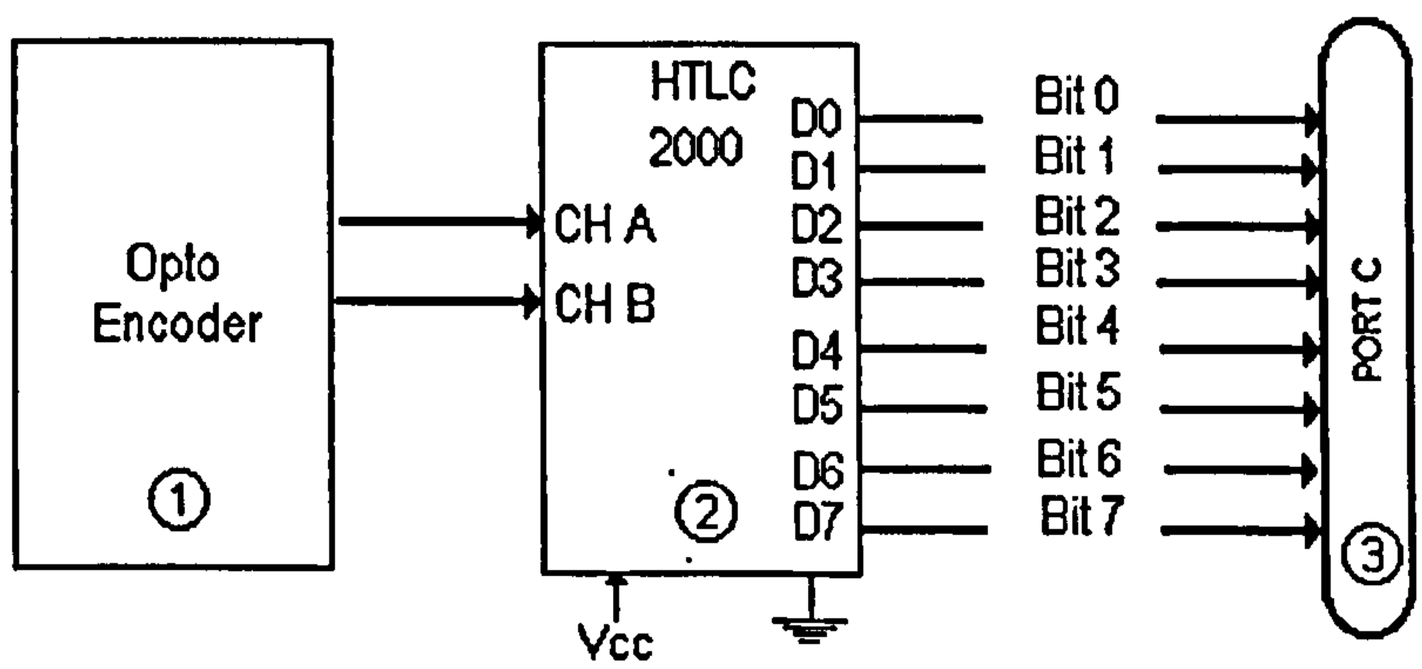

Figure 4.3. Block diagram of measuring the elongation by using an opto-couple device

4.5.2. Data Collection and Control Software for Creep Test

Data collection and system control of the creep test were completed by a computer program. The program was written in the C programming language in the DOS environment. Three-dimensional button graphics and mouse selection were used for entering information and for visualisation of data. The complete source code of the program can be seen on diskette I. To run the program, first of all configuration values must be entered. These are the filename for data collection (writing onto hard disk), which must be related to subject name, test and the constant load for information. The configuration box and menu layout of the program can be seen in figure 4.4.

To set the configuration values, it is enough to click with the mouse to the 'Configuration' button (Fig. 4.4) or press the 'C' key on the keyboard. After selection of the configuration button (either way), a configuration box appears on the screen and waits for the user to enter the necessary values. In case of mis-entering of the value, the 'ESC' key can be pressed to cancel the work.

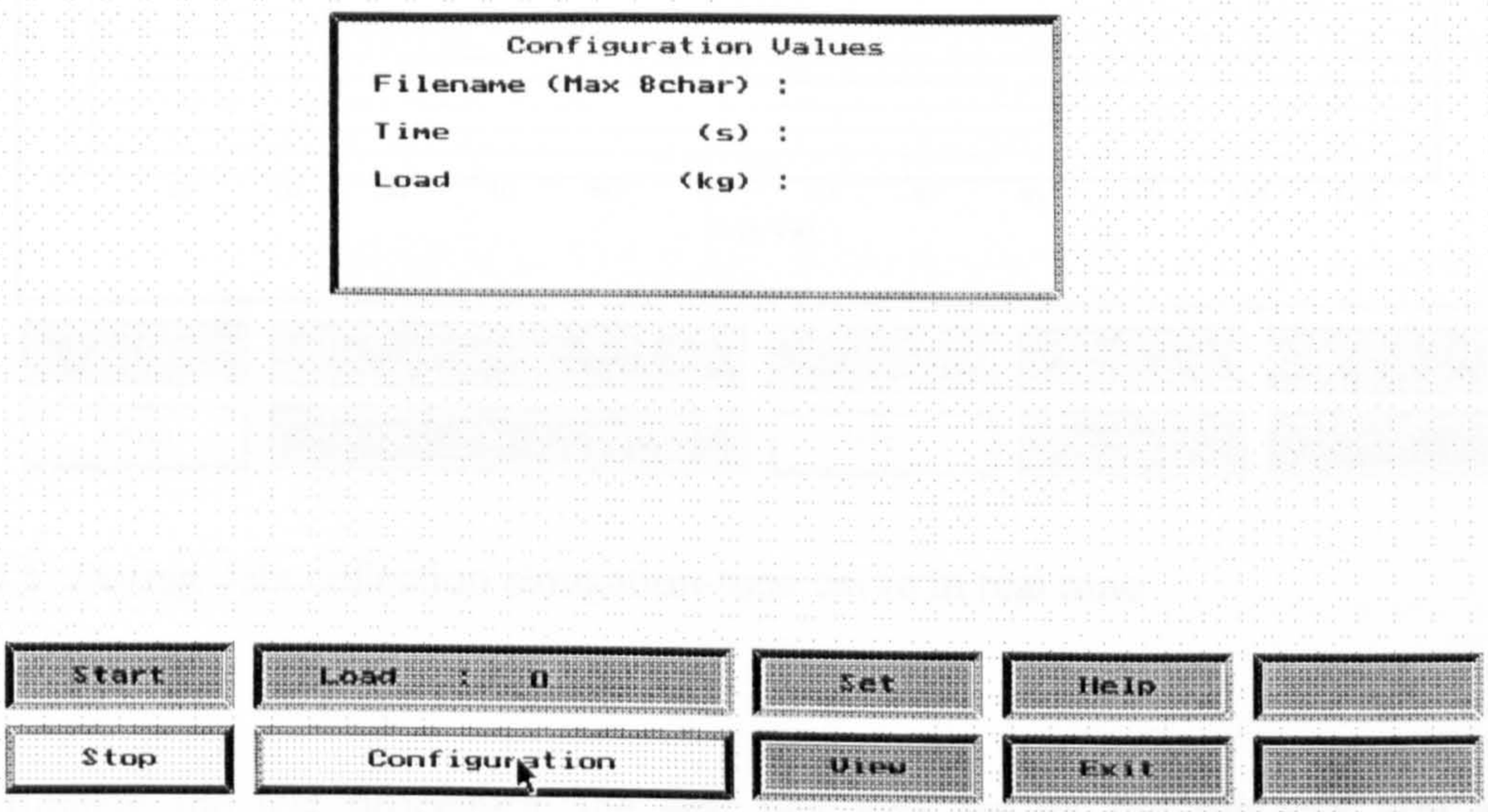

Figure 4.4. Configuration box and menu layout in the creep test software.

To start the test, the user can click the 'Start' button (Fig. 4.4) or press the 'S' key on the keyboard. If configuration values are not entered, the user will be warned to enter the values and that the test is not going to start. When the test was started, the elongation-time curve could be seen in the computer screen by pressing the view button (Fig. 4.5). The curve was plotted in real time as feedback to the researcher. At the same time the test result was recorded onto the computer hard disk in 2.5 kHz. The test could be finished by clicking the 'Stop' button (Fig. 4.5) or pressing any key in the keyboard.

During the data collection, the load cell reading could be seen in the menu (Fig. 4.5), which was very useful for the researcher to find the starting load before running the test.

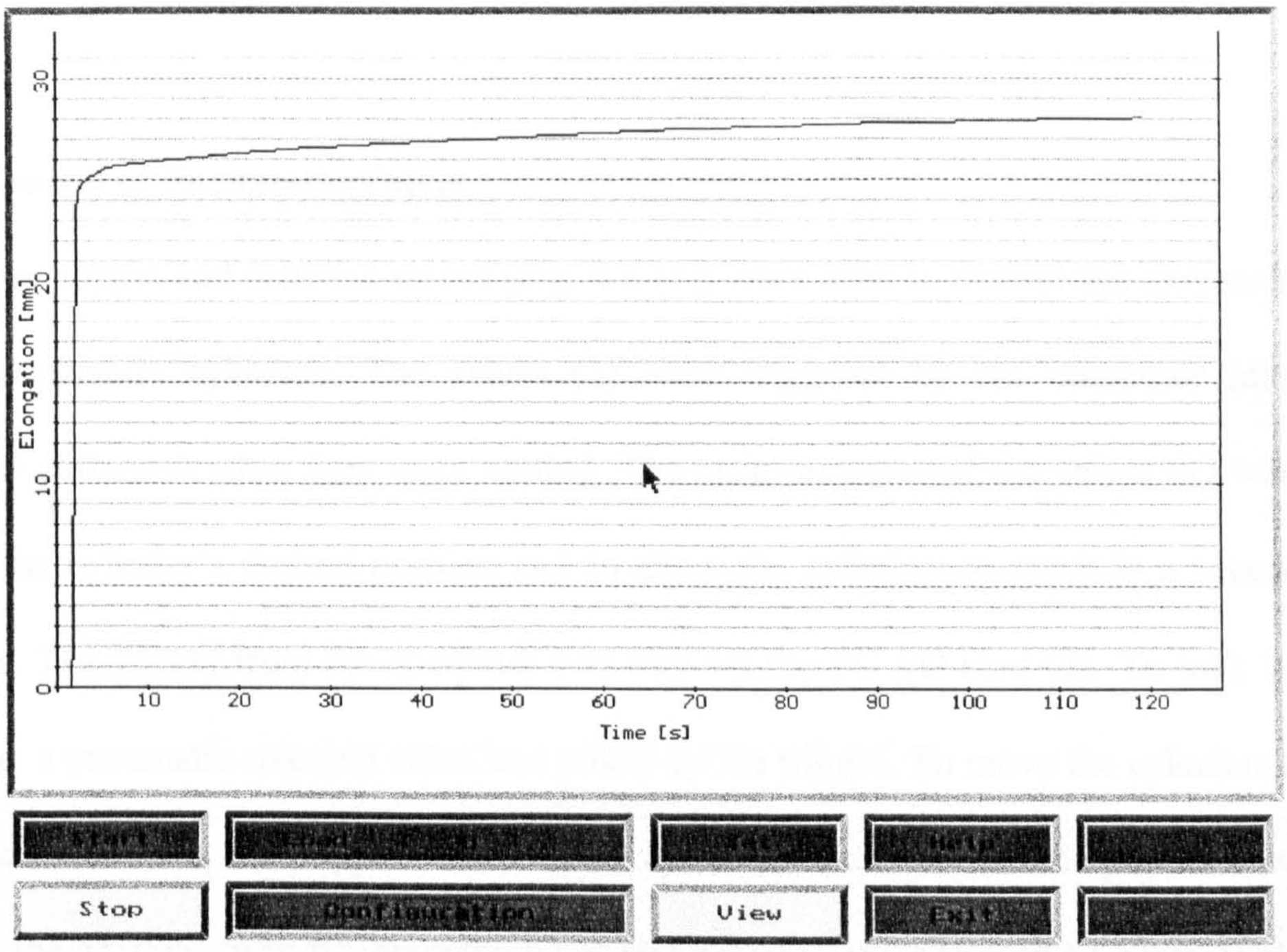

Figure 4.5. During data collection elongation-time curve in real time.

Before running the test procedure, the seat belt was set on the subject's arm and tightened initially by setting the initial load. If the user wants to run the same test (same configuration value) to refresh the computer screen and reset the timer, the 'Set' button (Fig. 4.5) should be clicked by the mouse. The information about the menu buttons could be seen by clicking the 'Help' button (Fig. 4.5) which gave brief information about each button in the menu layout. The user could end the program by simply clicking the 'Exit' button (Fig. 4.5) with the mouse or pressing the 'ESC' key on the keyboard. To prevent accidental pressing of the 'ESC' button on the keyboard or clicking the 'Exit' button by the mouse, the program asked from the user confirmation of the decision.

4.6. Stress-Relaxation Test

The desired sudden movement of the stress-relaxation test was accomplished by using pneumatic cylinders and their control was achieved with electronic design and compatible software.

4.6.1. Control of Pneumatic Valves

Pneumatic poppet and solenoid valves (Fig. 4.6 (1)) were used to control the movement of the pneumatic cylinders. The valves (1) were triggered by the computer (data collection software) when they were needed. The main purposes of the valves (1) were to lock the cylinder's desired position and to allow the cylinders to move in a reverse direction. The trigger from the computer was sent via the PC I/O card (2). To lock the cylinders, a pneumatic solenoid valve was pulled by the trigger. To move the cylinders in the reverse direction, the poppet valve was set by the computer. When the poppet valve stopped the air flow from the compressor, it also released the compressed air from the cylinders to the atmosphere. A schematic diagram of the valves can be seen in figure 4.6.

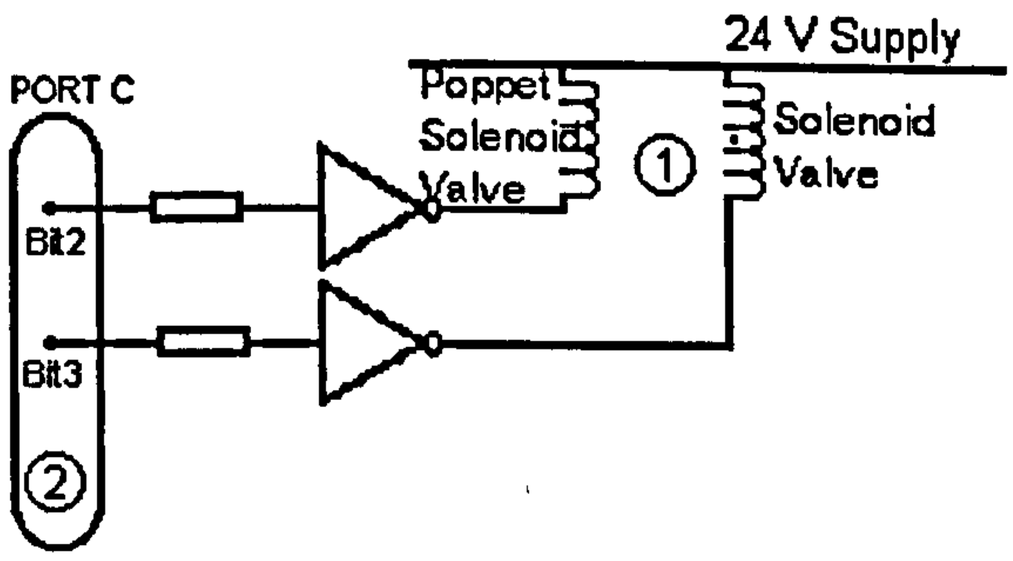

Figure 4.6. Schematic diagrams of circuit used for controlling pneumatic poppet valves.

4.6.2. Data Collection and Control Software for Stress-Relaxation Test

Data collection and system control of the stress-relaxation test were accomplished by a computer program. The program was written in the C programming language in the

DOS environment. Three-dimensional button graphics and mouse selection were used for entering information and for visualisation of data. The complete source code of the program can be seen on diskette I. To run the program, first of all configuration values must be entered. These are the filename for data collection (writing onto hard disk), which must be related to subject name, test and the constant strain in millimetres for information. The configuration box and menu layout of the program can be seen in figure 4.7.

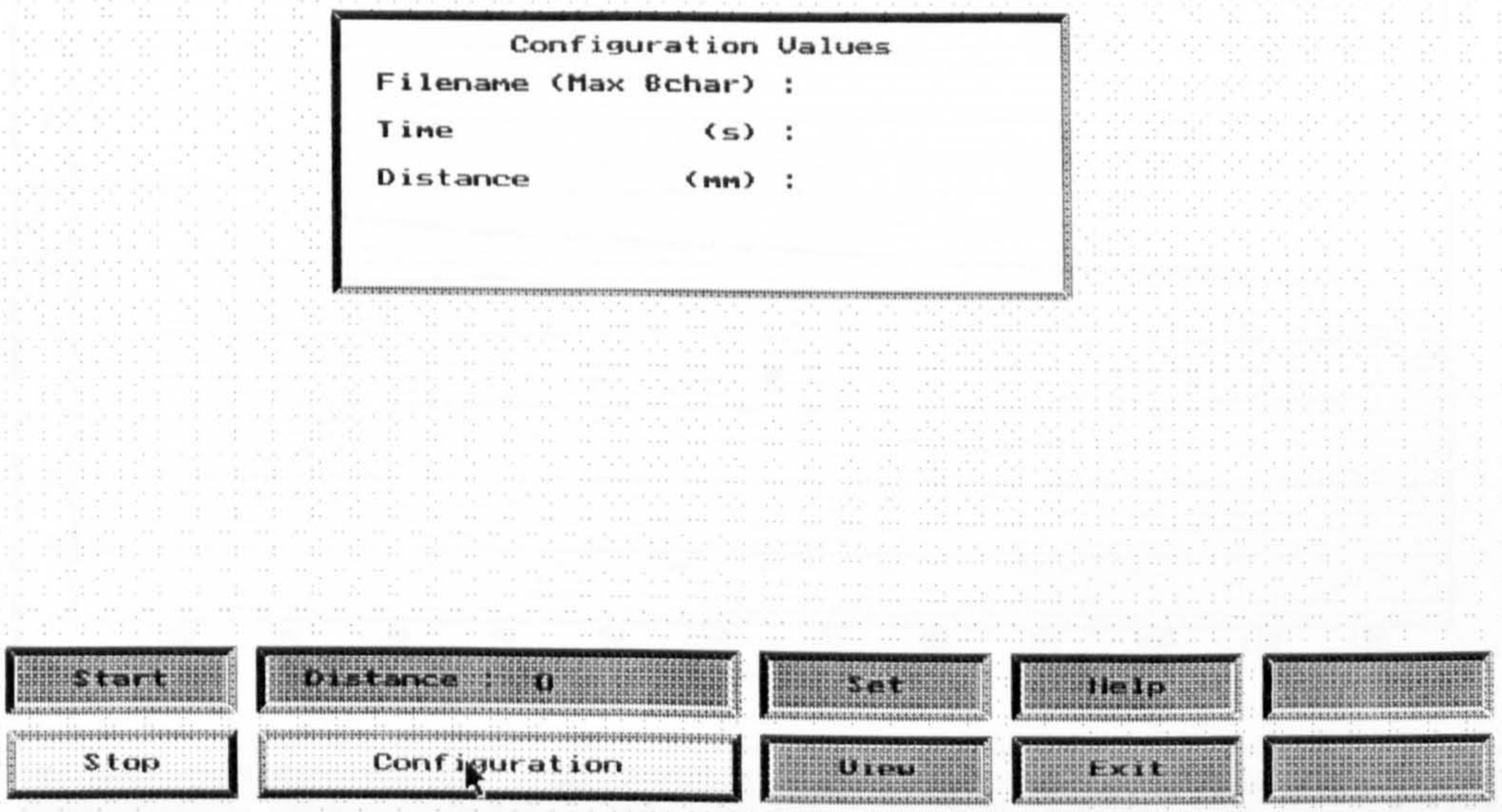

Figure 4.7. Configuration box and menu layout in the stress-relaxation test software.

To set the configuration values, it is enough to click with the mouse to the 'Configuration' button (Fig. 4.7) or press the 'C' key on the keyboard. After selection of the configuration button (either way), a configuration box appears on the screen and waits for the user to enter the necessary values. In case of mis-entering of the value, the 'ESC' key can be pressed to cancel the work.

To start the test, the user can click the 'Start' button (Fig. 4.8) or press the 'S' key on the keyboard. If configuration values are not entered, the user will be warned to enter the values and that the test is not going to start. When the test was started, the load-time curve could be seen in the computer screen by pressing the view button (Fig. 4.8). The curve was plotted in real time as feedback to the researcher. At the same time the test result was recorded onto the computer hard disk in 2.5 kHz. The test could be finished by clicking the 'Stop' button (Fig. 4.8) or pressing any key on the keyboard.

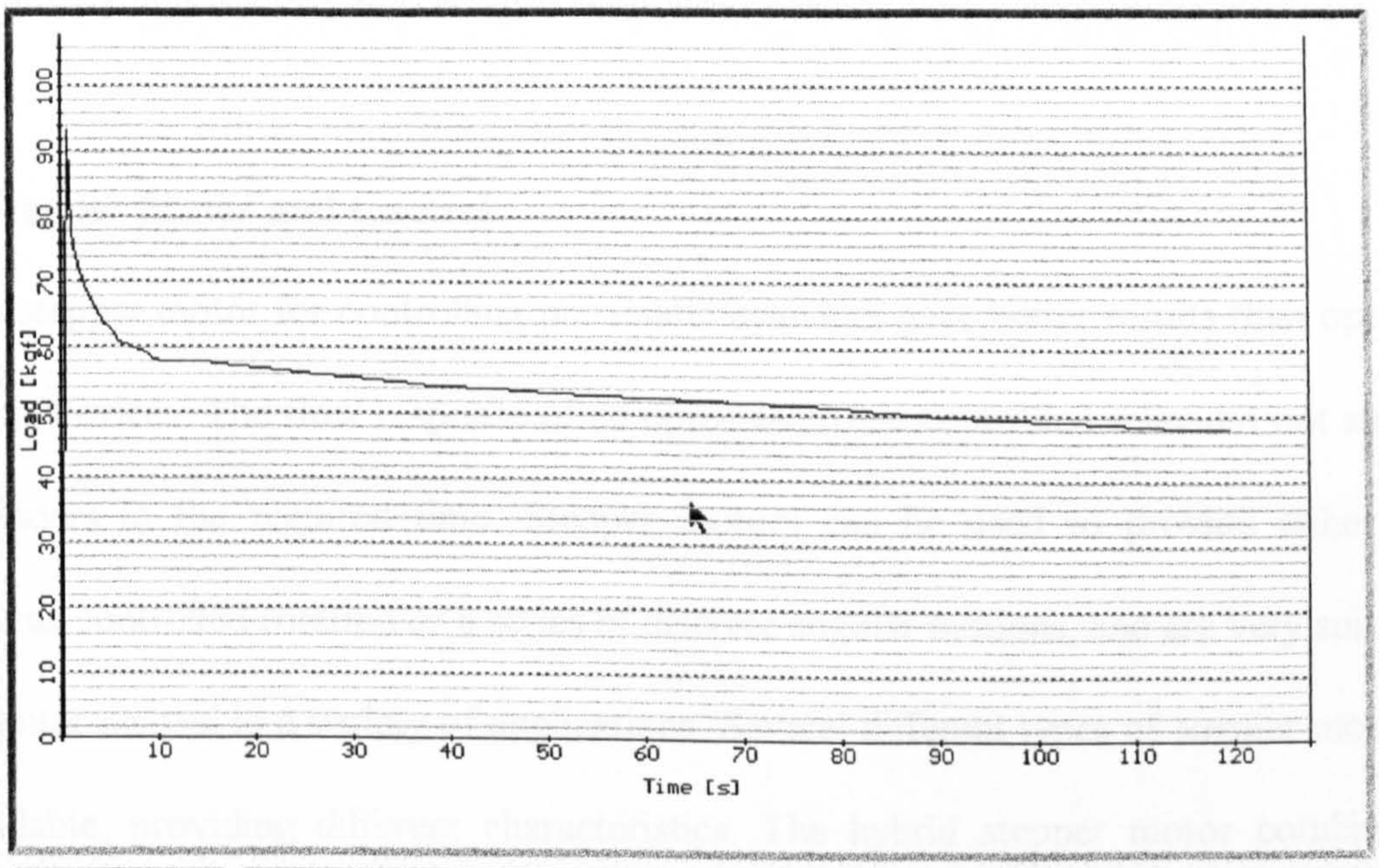

Figure 4.8. During data collection load-time curve in real time.

Before running the test procedure, the seat belt was set on the subject's arm and tightened initially by setting the initial load. If the user wants to run the same test (same configuration value) to refresh the computer screen and reset the timer, the 'Set' button (Fig. 4.8) should be clicked by the mouse. The information about the menu buttons could

be seen by clicking the 'Help' button (Fig. 4.8) which gave brief information about each button in the menu layout. The user could end the program by simply clicking the 'Exit' button (Fig. 4.8) with the mouse or pressing the 'ESC' key on the keyboard. To prevent accidental pressing of the 'ESC' button on the keyboard or clicking the 'Exit' button by the mouse, the program asked from the user confirmation of the decision.

4.7. Stress-Strain Test

The desired constant strain-rate of the stress-strain test was accomplished by using a linear stepping motor; its control was achieved with electronic design and compatible software.

4.7.1. Stepper Motor and Control

Using a stepper motor for controlling pneumatic cylinders gave better results than opto-electronic devices. The slow response of an opto-electronic controlled relay did not stop the cylinders in the required time. Stepper motors can be used to provide either a continuous controlled rotation or a series of discrete angular motions, and are very suited to computer control in a variety of applications. Several different types of stepper motor are available, providing different characteristics. The hybrid stepper motor combines features of the variable reluctance and permanent magnet stepper motors, incorporating a permanent magnet core with a toothed rotor. Hybrid stepper motors generally operate with smaller step angles than the other types of stepper motor [10, 29]. A linear stepper motor was used for controlling the pneumatic cylinders (see section 4.7.2). The linear stepper motor contains a 4-phase unipolar motor arrangement. The direction, velocity and acceleration were controlled by the stepper motor driver board and the computer.

4.7.2. Stepper Motor Driving Circuit

The core of the stepper motor control was the SAA 1027 stepper motor driver integrated circuit (IC) (Fig. 4.9 (1)). The current output of the IC (1) was not enough to drive the linear stepper motor (5), so an octal Darlington IC (2) was used to boost the current. But increasing the current could damage the circuit, so a relay (3) was added to the circuit to reduce the current when the linear stepper motor (5) was idle. The relay (3) was controlled by the computer (via I/O card). To drive the linear stepper motor (5), the IC (1) needed two different pieces of information - direction and step. All the necessary information was sent from the computer via a programmable PC Input / Output card (6). The schematic diagram of the circuit and electronic circuit design can be seen in figure 4.9.

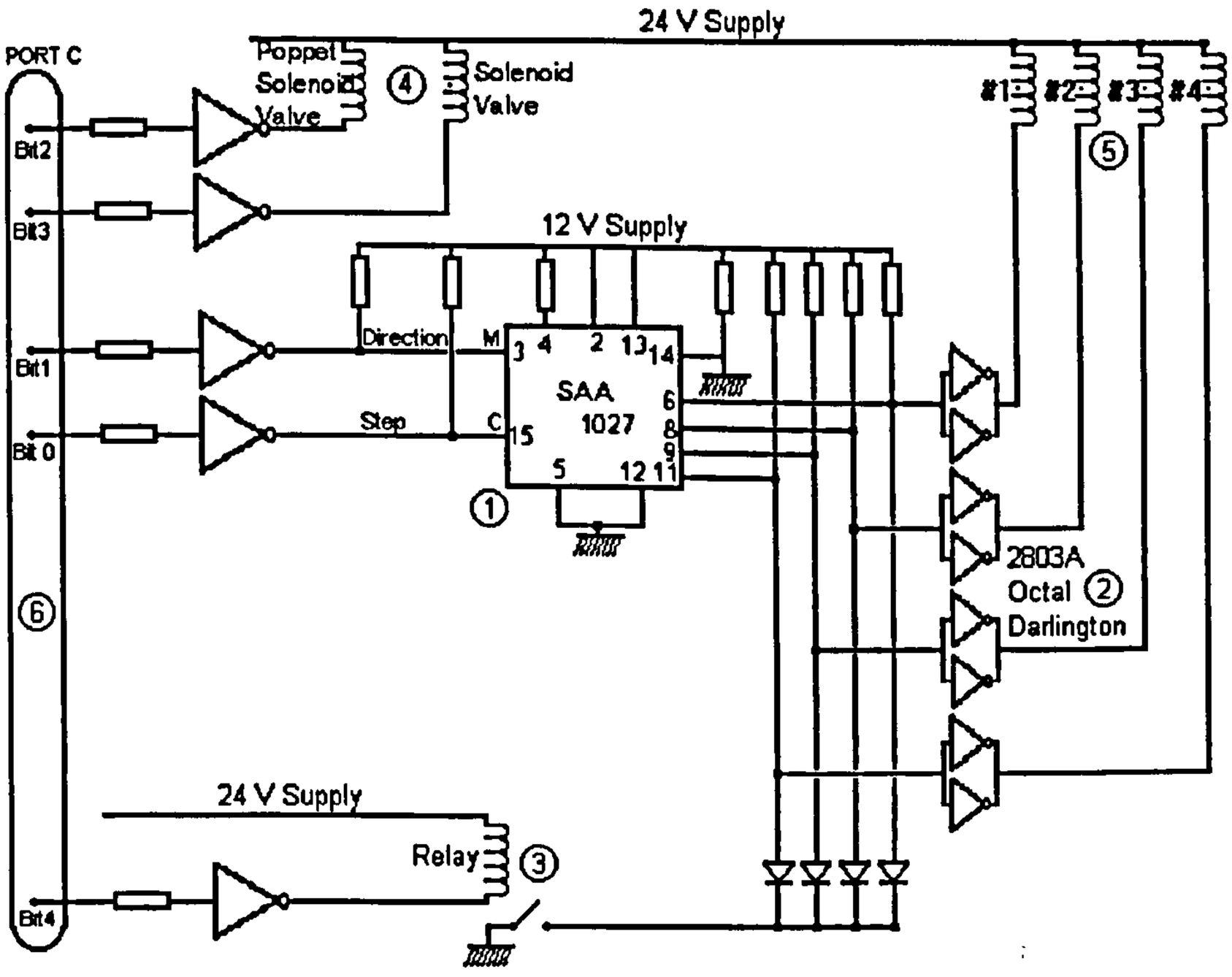

Figure 4.9. Schematic diagrams of circuit used for controlling of stepper motor and pneumatic poppet valves.

4.7.3. Feedback Circuit for Voltage-to-Pressure Converter

To keep the load on the linear stepper motor constant, a voltage-to-pressure converter (Fig. 4.10 (6)) was used. To control the voltage-to-pressure converter, an electronic circuit was designed. The voltage in the converter was adjusted by the electronic circuit which had an offset voltage. The voltage increased proportional to the increase in load cell reading (gain). Offset (2) and gain (1) were set by changing the trimpot value. Amplification of the load cell output was completed by designing a simple operational amplifier (3). Using a transistor (4) and resistor (5), the current was limited to prevent damage to the converter. A schematic diagram of the electronic circuit can be seen in figure 4.10.

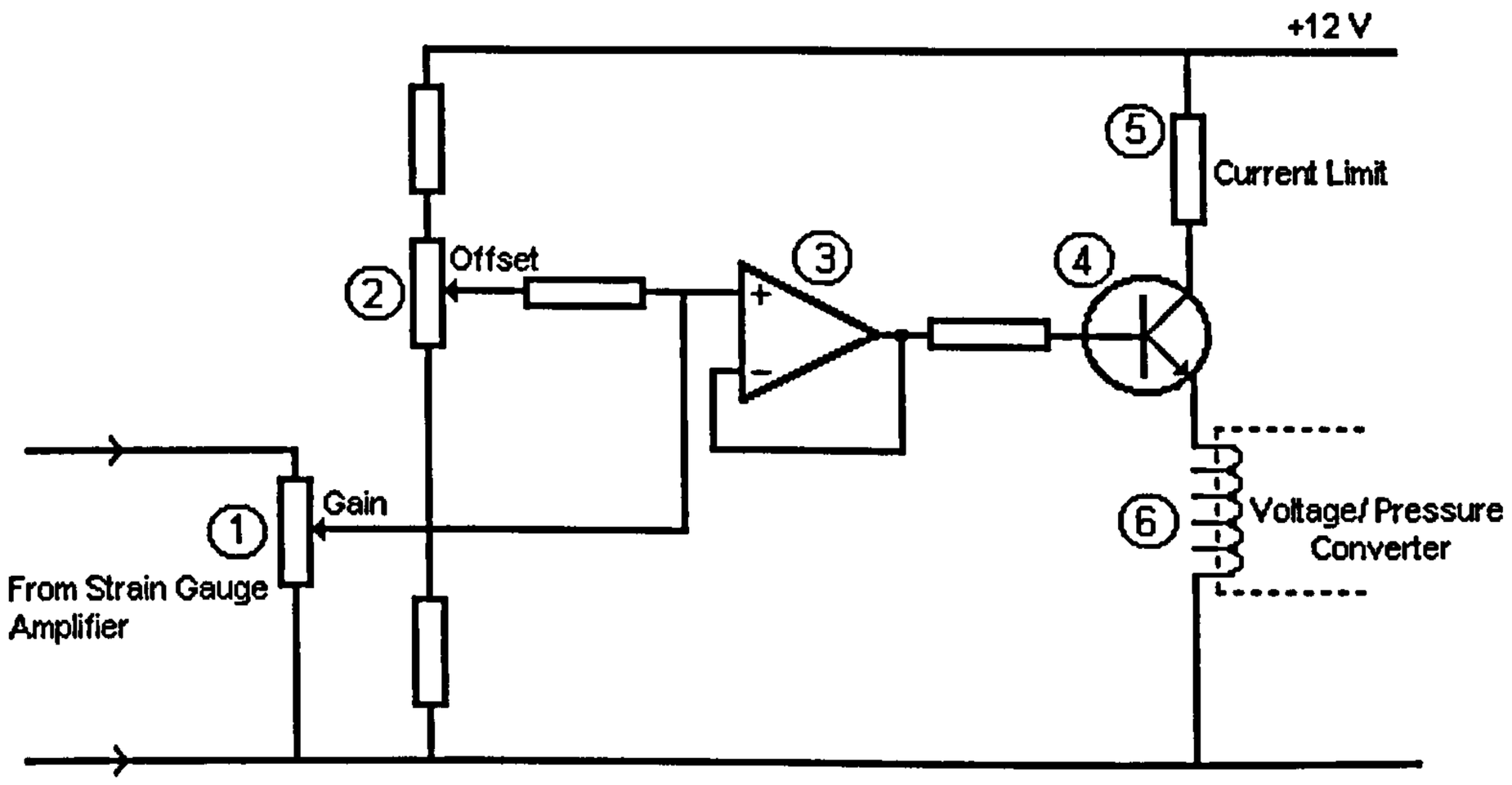

Figure 4.10. Schematic diagrams of circuit used for giving feedback to the voltage to pressure converter.

4.7.4. Data Collection and Control Software for Stress-Strain Test

Data collection and system control of the stress-strain test were accomplished by a computer program. The program was written in the C programming language in the DOS environment. Three-dimensional button graphics and mouse selection were used for entering information and for visualisation of data. The complete source code of the

program can be seen on diskette I. To run the program, first of all configuration values must be entered. These are the filename for data collection (writing onto hard disk), which must be related to subject name and test plus the squeeze time in milliseconds for the desired time for squeezing and speed of stepper motor in millimetres per second. The configuration box and menu layout of the program can be seen in figure 4.11.

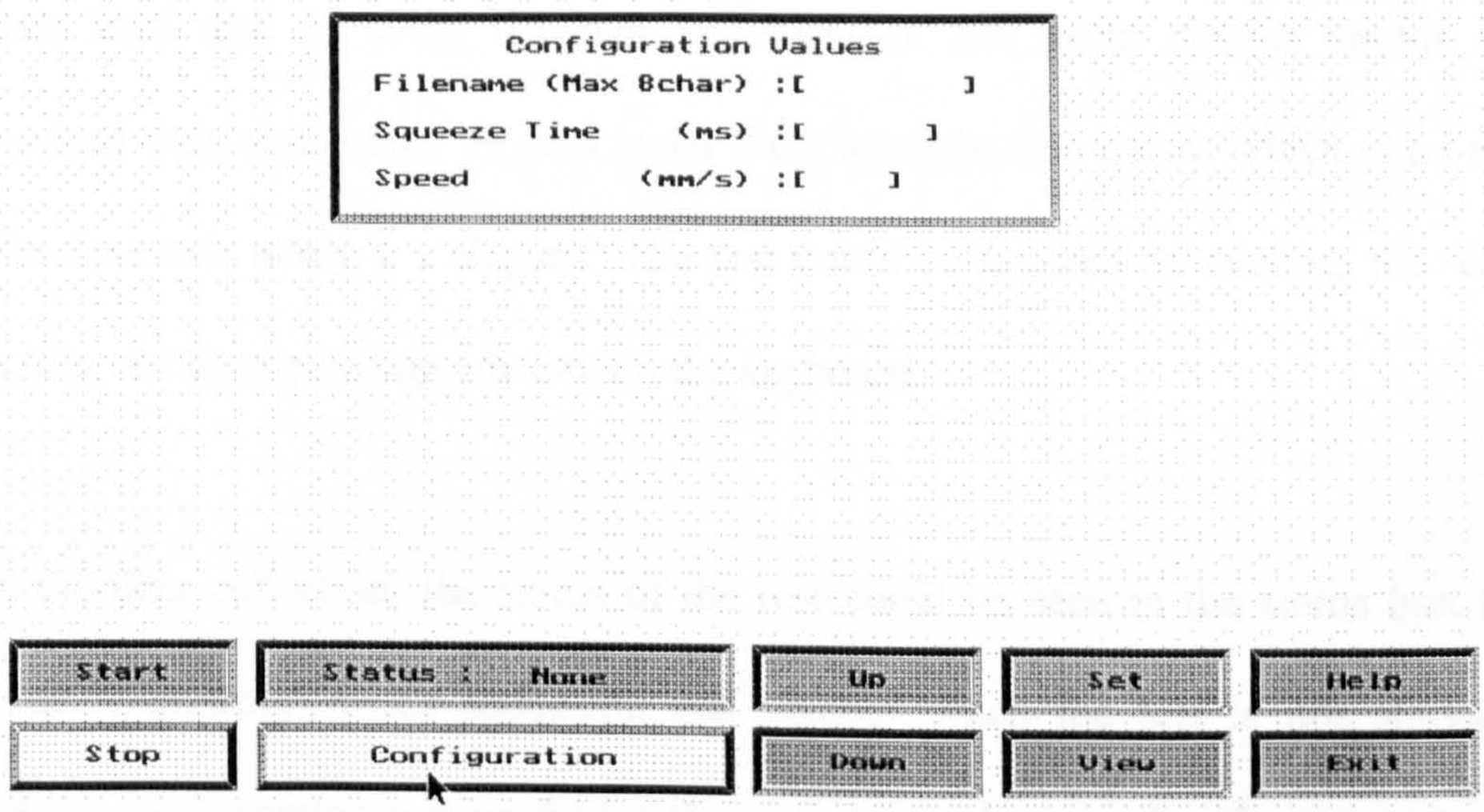

Figure 4.11. Configuration box and menu layout in the test software.

To set the configuration values, it is enough to click with the mouse to the 'Configuration' button (Fig. 4.11) or press the 'C' key on the keyboard. After selection of the the configuration button (either way), a configuration box appears on the screen and waits for the user to enter the necessary values. In case of mis-entering of the value, the 'ESC' key can be pressed to cancel the work.

To start the test, the user can click the 'Start' button (Fig. 4.12) or press the 'S' key on the keyboard. If configuration values are not entered, the user will be warned to enter the values and the test is not going to start. There are also upper and lower limits for the squeezing time and speed. If the user's input is out of the range, the user will be warned for entering an invalid value.

When the test was started, the load-deflection curve could be seen on the computer screen by pressing the view button (Fig. 4.12). The curve was plotted in real time as feedback to the researcher. At the same time the test result was recorded onto the computer hard disk in every 0.1 mm increment of the linear stepper motor. The synchronised time scale could be seen under the load-deflection curve, which put a mark onto the time axis every 1 s elapsed. The test could be finished by clicking the 'Stop' button (Fig. 4.12) or pressing any key on the keyboard.

During the data collection, the status of the test could be seen in the status box (Fig. 4.12), as "Compress" when squeezing and "None" when the test is not started or finished. This information was useful for the researcher when running the test to control the software reliability and accuracy.

Before running the test procedure, the seat belt was set on the subject's arm and tightened initially by clicking the up and down buttons on the menu screen. When the user clicked the 'Up' or 'Down' button (Fig. 4.12) with the left button of the mouse or pressed the 'U' or 'D' on the keyboard, the stepper motor moved 0.1 mm up or down respectively. For quick movement of the linear stepper motor, however, the right button of the mouse or the 'Up arrow' or 'Down arrow' on the keyboard could move the linear stepper motor a 1 mm step.

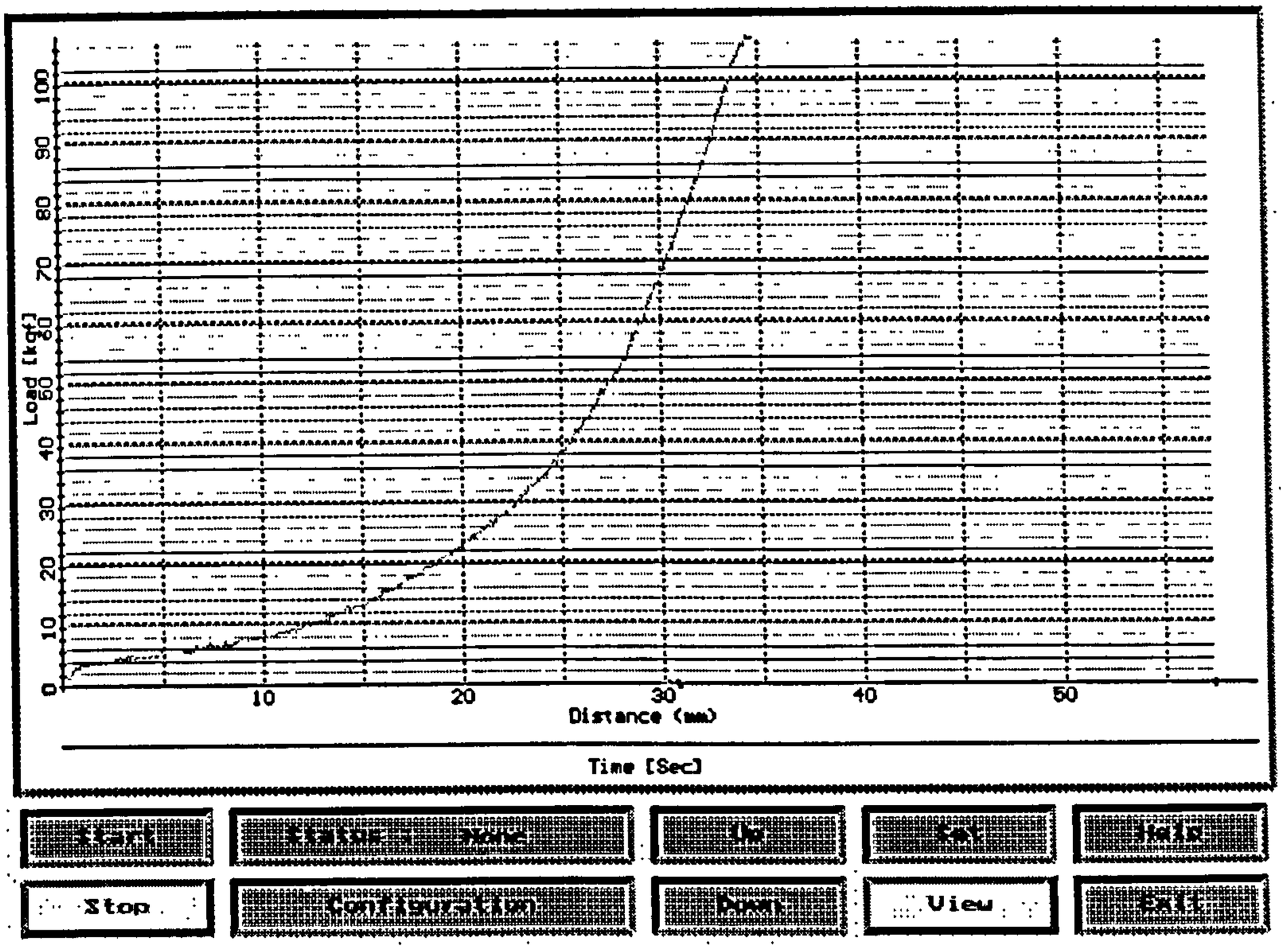

Figure 4.12. During data collection load-deflection curve and time scale in real time.

If the user wants to run the same test (same configuration value) to refresh the computer screen and reset the timer, the 'Set' button (Fig. 4.12) should be clicked by the mouse. The information about the menu buttons could be seen by clicking the 'Help' button (Fig. 4.12) which gave brief information about each button in the menu layout. The user could end the program by simply clicking the 'Exit' button (Fig. 4.11) with the mouse or pressing the 'ESC' key on the keyboard. To prevent accidental pressing of the 'ESC' button on the keyboard or clicking the 'Exit' button by the mouse, the program asked from the user confirmation of the decision.

4.8. Summary

In this chapter, electronic circuits of the moving parts and control cards (ADC and I/O) used in the instruments were explained. A load cell was used for force measurement, amplification of the load cell was also explained in details. An ADC card was used to collect the amplified load cell data. The working principles of the ADC were mentioned and reading data from the card was shown. The timing accuracy was set to one tenth of 1 ms, which was accomplished by defining a new software interrupt. The control of pneumatic valves and stepper motor was achieved by using I/O card, which was accessed from the data collection computer. New programs were written for the data collection for the creep, stress-relaxation and stress-strain tests. The data collection software for each test was explained in detail.

Chapter 5

Mechanical Tests and Results

5.1. Mechanical Testing of Soft Biological Tissue

There are several mechanical tests and testing instruments in mechanical engineering for testing materials. By contrast, there is not a certain type of testing machine and procedure in the area of soft tissue biomechanics. Usually adaptation of mechanical engineering tests has been used for soft tissue research. Most of these tests are very specialised but have not been standardised. Creep and stress-relaxation tests measure the dimensional stability of a material, which is very important in the theory of viscoelasticity. The stress-strain test is less importance in this respect, but is used a great deal to assess the usability of the mechanical models.

5.2. Creep Tests

Creep tests give important practical information and, at the same time, give useful data to understand the theory of mechanical properties of material. In a creep test, the deformation is measured over a period of time by applying a constant load or force. In a creep test, the deformation increases with time. If the strain (ε) is divided by the applied stress (σ), the quantity known as the creep compliance (D):

$$D(t) = \frac{\varepsilon(t)}{\sigma_{t_0}} \qquad (5.1)$$

where;

D(t) : creep compliance

$\varepsilon(t)$: strain as function of time

σ_{to} : constant tensile stress

5.2.1. Creep Test Data Collection

A creep test was applied to two healthy male (ages 29 and 32) subjects by using 10, 20, 30, 40, 50 and 60 kgf static loads. Owing to the long recovery time of the bulk tissue, a 60 minute rest period was given between the tests. Some of the tests were done on different days to avoid tissue damage and biological adaptation to the test. The squeezing area on the subjects' upper arm was marked and all the tests were carried out on this surface. Additionally, MRI scanning of the upper arm was accomplished on the same surface. The subject's upper arm was greased with silicone based grease to reduce friction between the squeezing chamber and the arm. A picture from a creep test can be seen in figure 5.1.

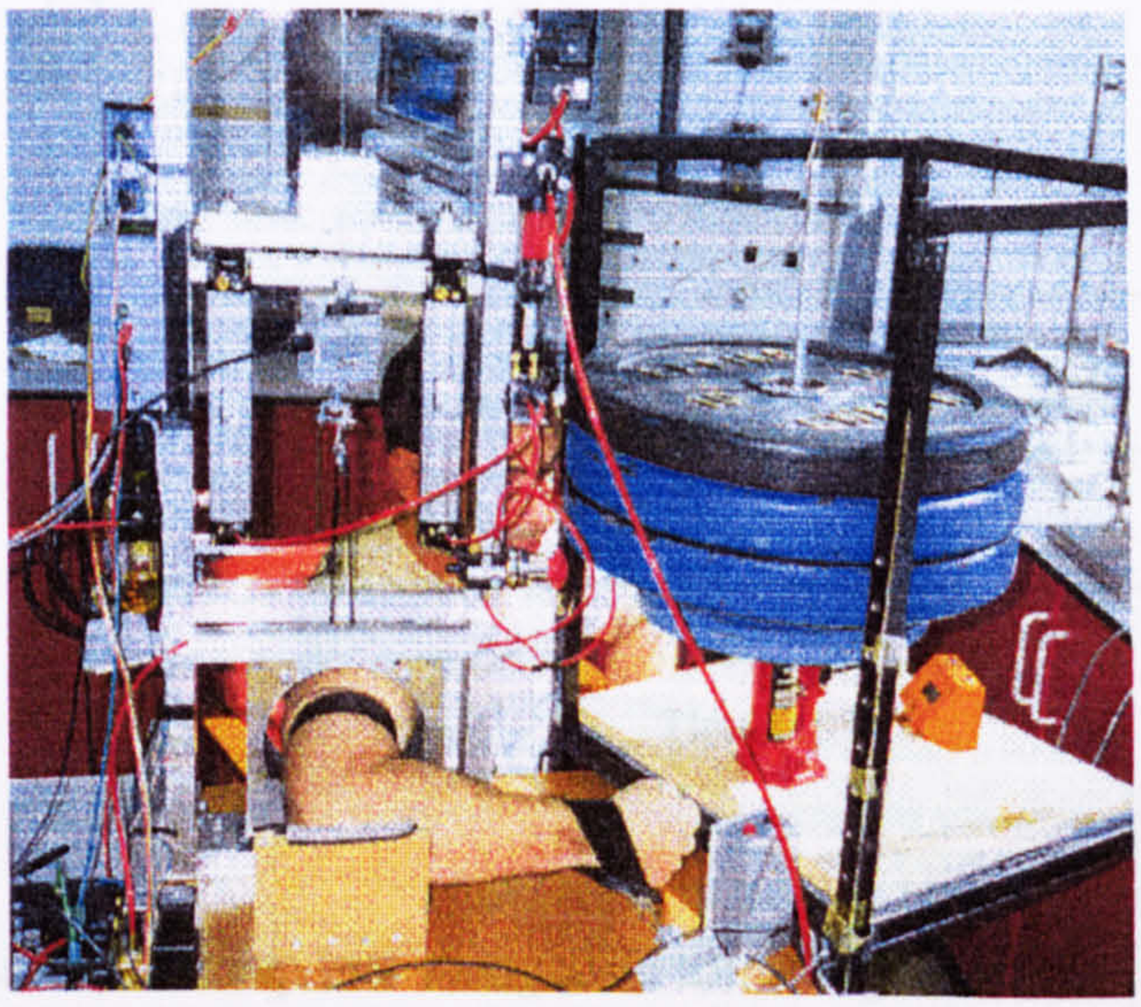

Figure 5.1. A view from creep test with 50 kgf static load.

Because of the increasing moment on the lever (Fig. 3.6 (3)) on the top of the main frame (Fig 3.6 (13)), it was not possible to use more than 60 kg weight. The load was lifted by using a bottle jack. To avoid the damping effect of the bottle jack, a 15 kg cast iron weight was fixed to the top of the bottle jack. This arrangement gave the bottle jack a continuous release movement. The load was suddenly released by simply rotating the release bolt using a special purpose lever.

The creep test data collection, in the computer, was started before the release (See chapter 3 and 4). Time elongation of the seat belt and the tension on the cable between the load and the closed loop belt were recorded with the time mark duration of 120 seconds as a binary file. Two different test procedures were followed. In the first one, the subject did not contract his muscle (relaxed condition) during the data collection. All the calculations, which are represented in this chapter, were done for one of the subjects.

Typical creep test output for the relax procedure of 60 kgf load can be seen in figure 5.2.

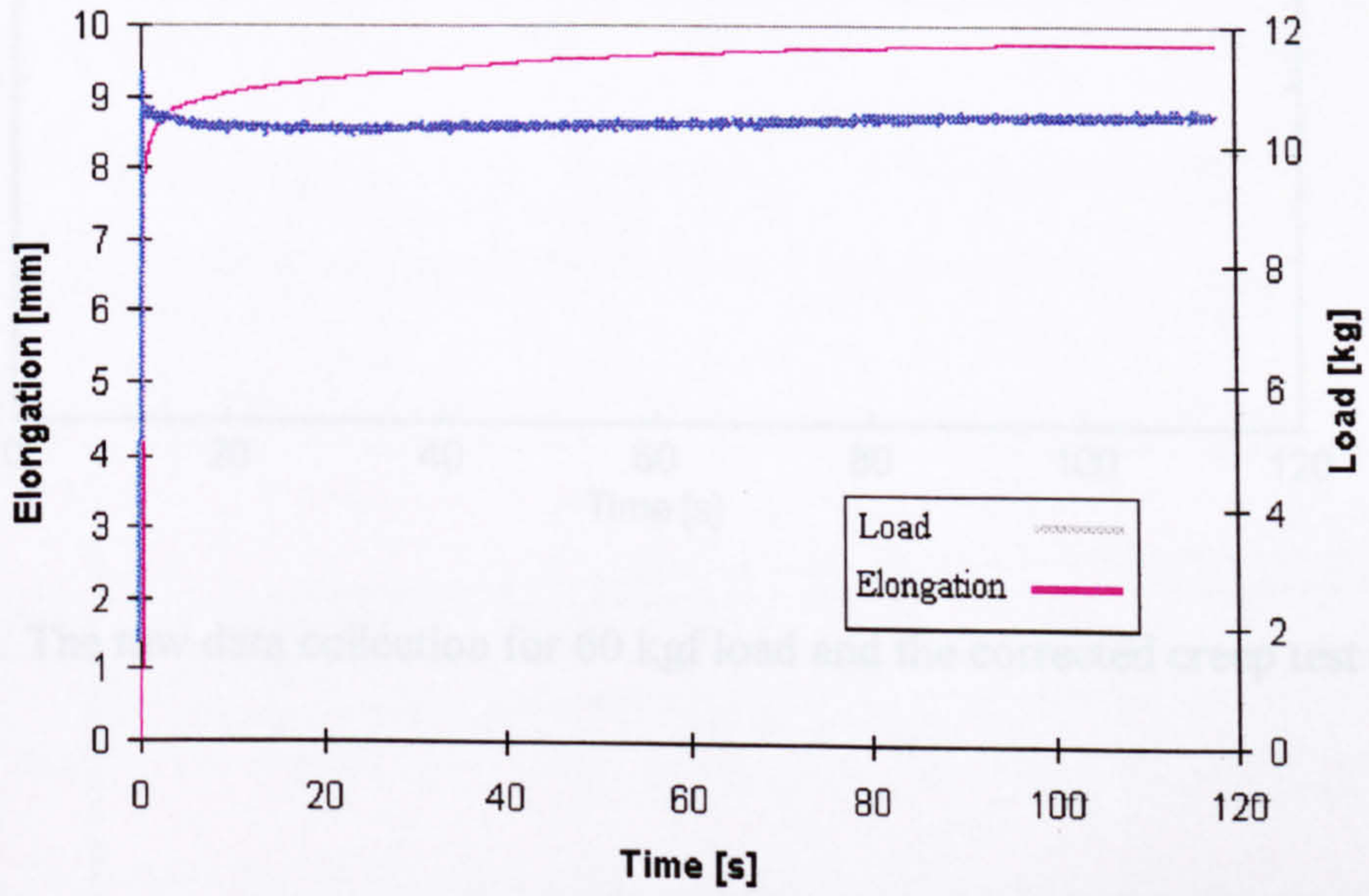

Figure 5.2. A sample creep test elongation for 60 kgf load.

The applied weight was plotted according to the second y-axis. The main reason why a load higher than the applied weight was recorded in figure 6.1 was the addition of the load carrier weight to the load.

Before curve fitting, the effect of the seat belt was removed from the raw data and recorded as a new file. The elongation of the seat belt was calculated by the equation 5.7

in section 5.6. In the creep test, the calculated seat belt elongation was subtracted from the total elongation for each load record. The difference can be seen in the figure 5.3.

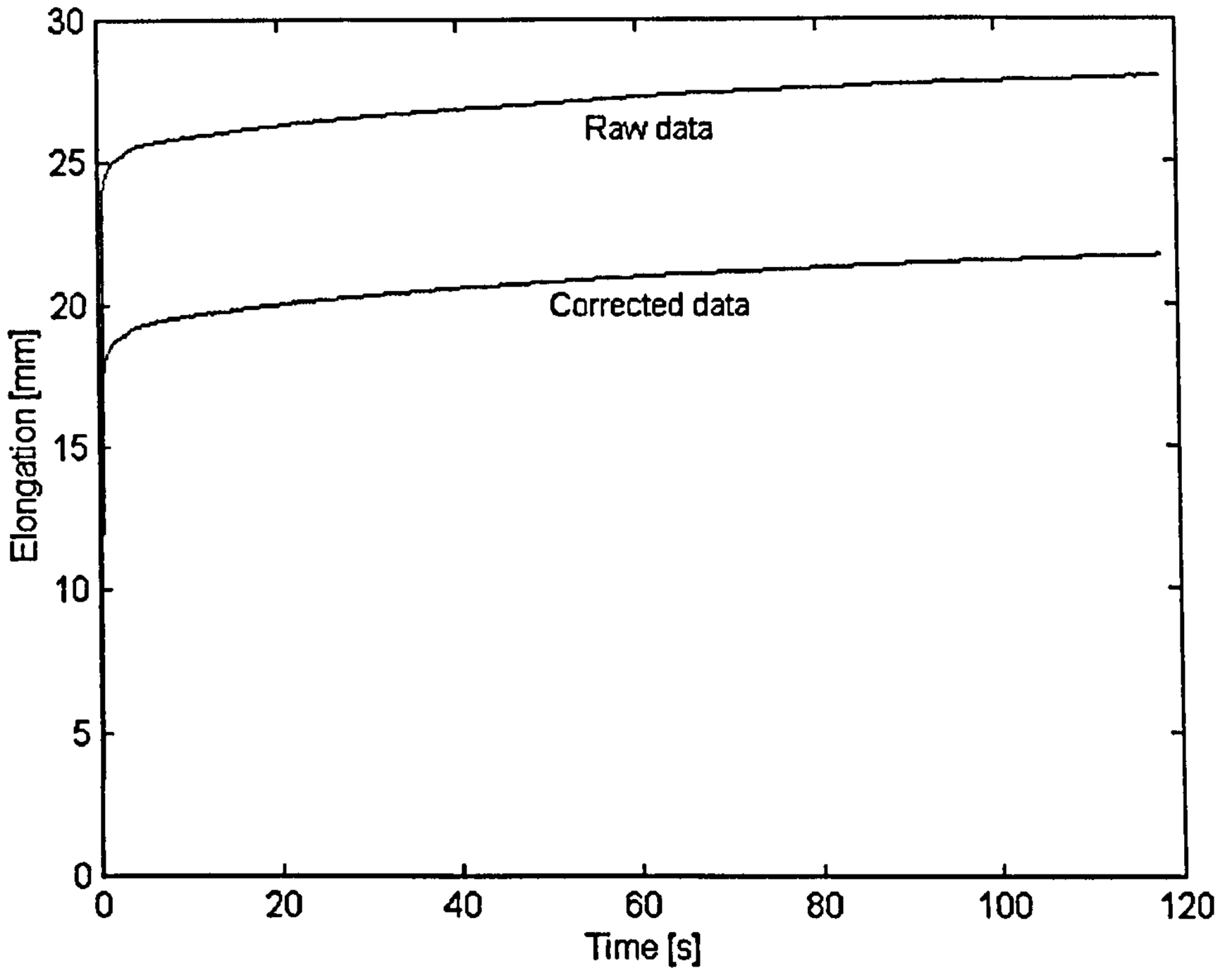

Figure 5.3. The raw data collection for 60 kgf load and the corrected creep test data.

One set of raw creep test experiment results can be seen in figure 5.4. It is clear that a linear increase in the load does not correspond to a linear increase in the elongation. As there is an increase of the load, the creep elongation reaches a limiting load. This means that the subject's arm reaches a state of incompressibility.

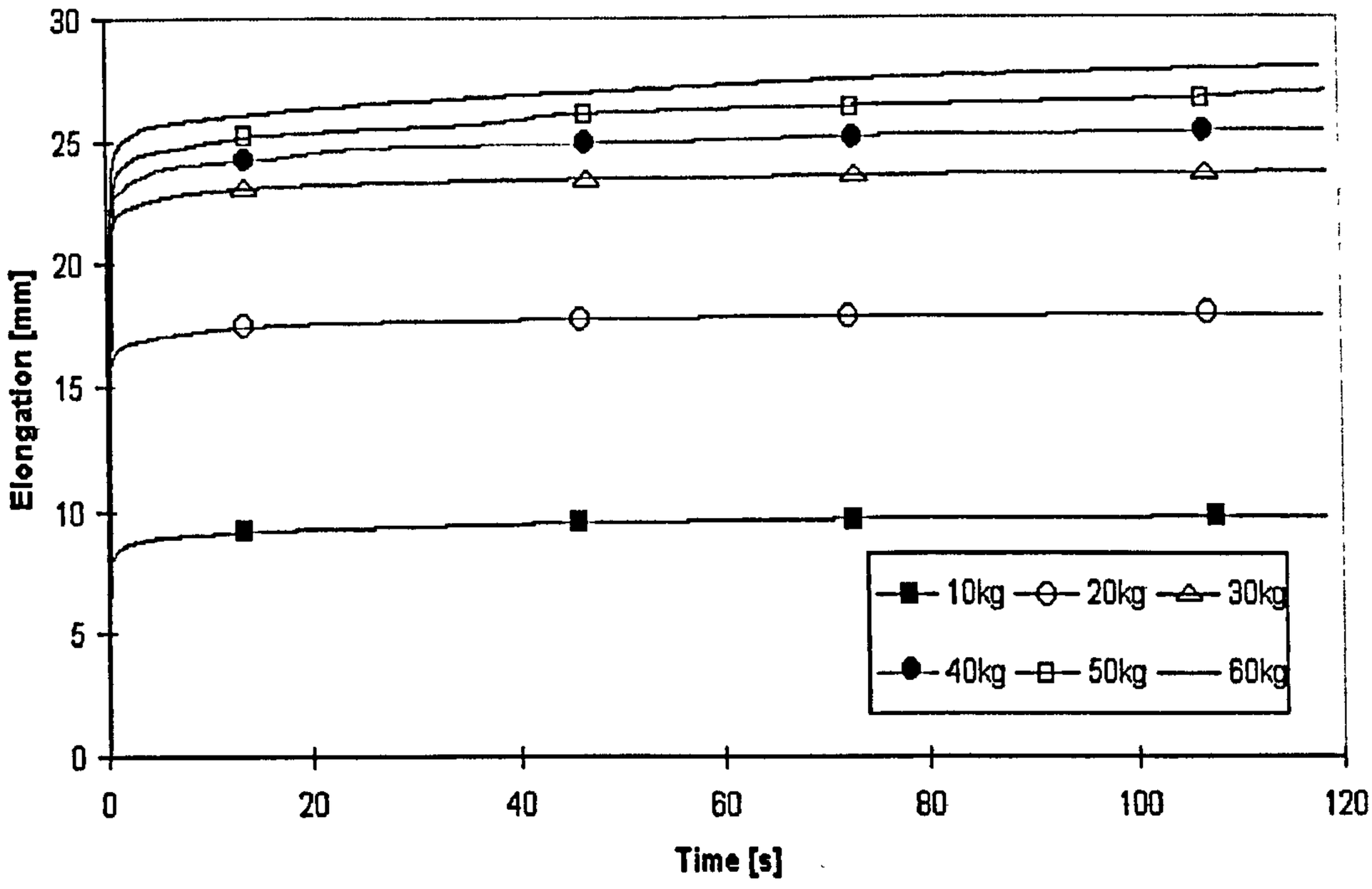

Figure 5.4. A set of creep test data from the relaxed test procedure.

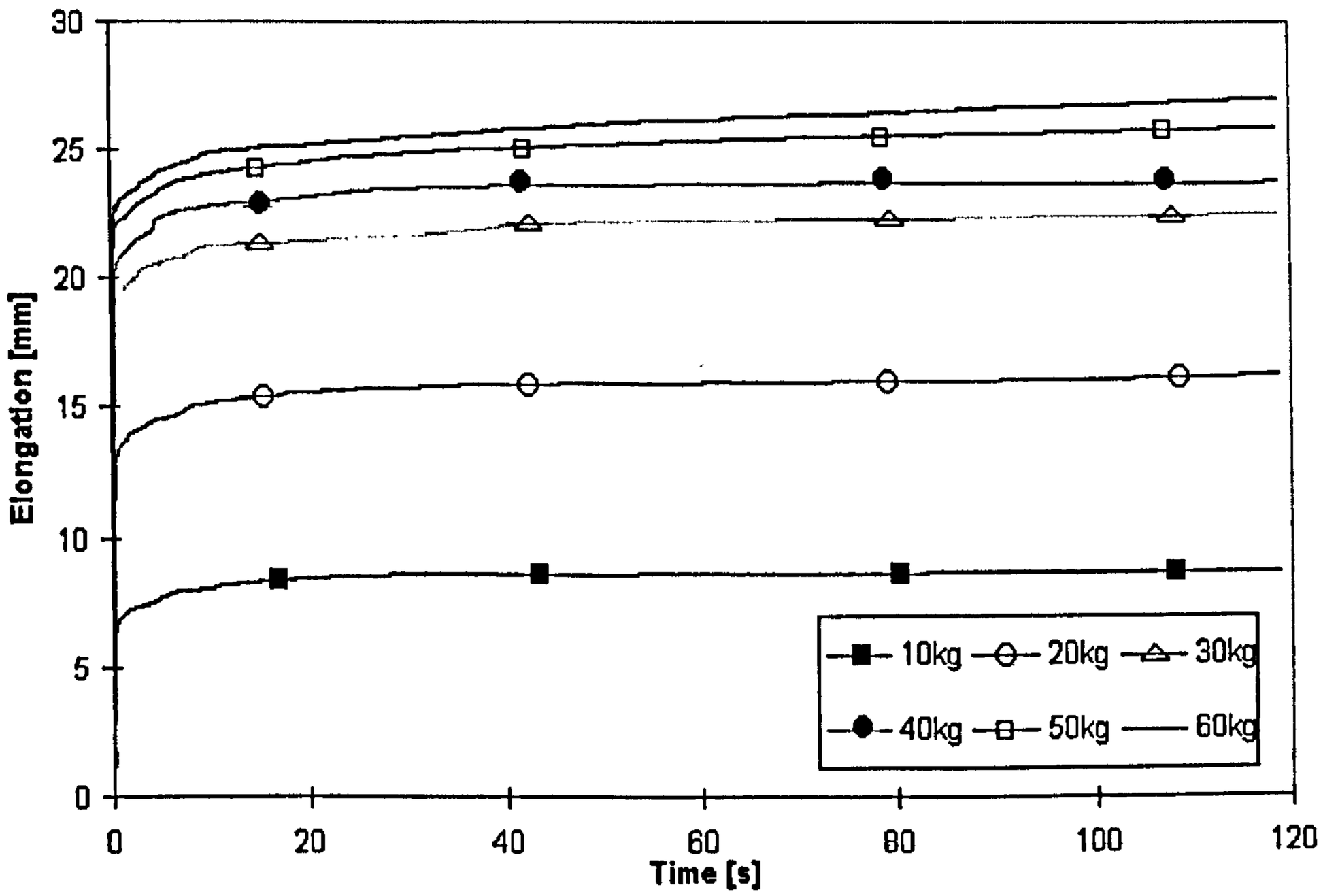

Figure 5.5. A set of creep test data from the contracted muscle test procedure.

In the second test, the subject sustained his muscle contraction at 25% of his maximum voluntary contraction (MVC) during the test. The load cell was connected to the

subject's right wrist so that the force exerted by the muscle could be recorded. During the contraction, the subject's elbow was fixed by the elbow resting corner. Owing to the contraction of the muscle, the experiment naturally gave less elongation than the first test. The difference can be seen by comparing figures 5.4 and 5.5.

5.2.2. Mathematical Description of Creep Test Data

For comparison with the creep test data, a mathematical representation was necessary. The most appropriate way was polynomial curve fitting to the creep data. During the data collection, raw data was recorded as a binary file at 2.5 kHz. The curve fitting was completed by using Matlab 5 commercial software. First, the corrected raw data were averaged every 50 ms interval to fit the maximum matrix size 16384 elements in Matlab software. The averaging of the raw data helped to smooth sudden increases and drops.

The curve fitting was achieved both in linear scales and by converting the linear time and elongation scales into natural logarithmic scales. The fifth and ninth order polynomials did follow the beginning of the raw data. The closest fit was achieved by using the a thirteenth order polynomial. Different order polynomial curve fittings are shown in figure 5.6. Examples of the curve fitting in linear and natural logarithmic scales are shown in figure 5.7. The main reason for using logarithmic conversions was to visualise better the start of the raw data. The rest of the curve fittings and the individual comparisons for every constant load are plotted in appendix B.1. and B.2.

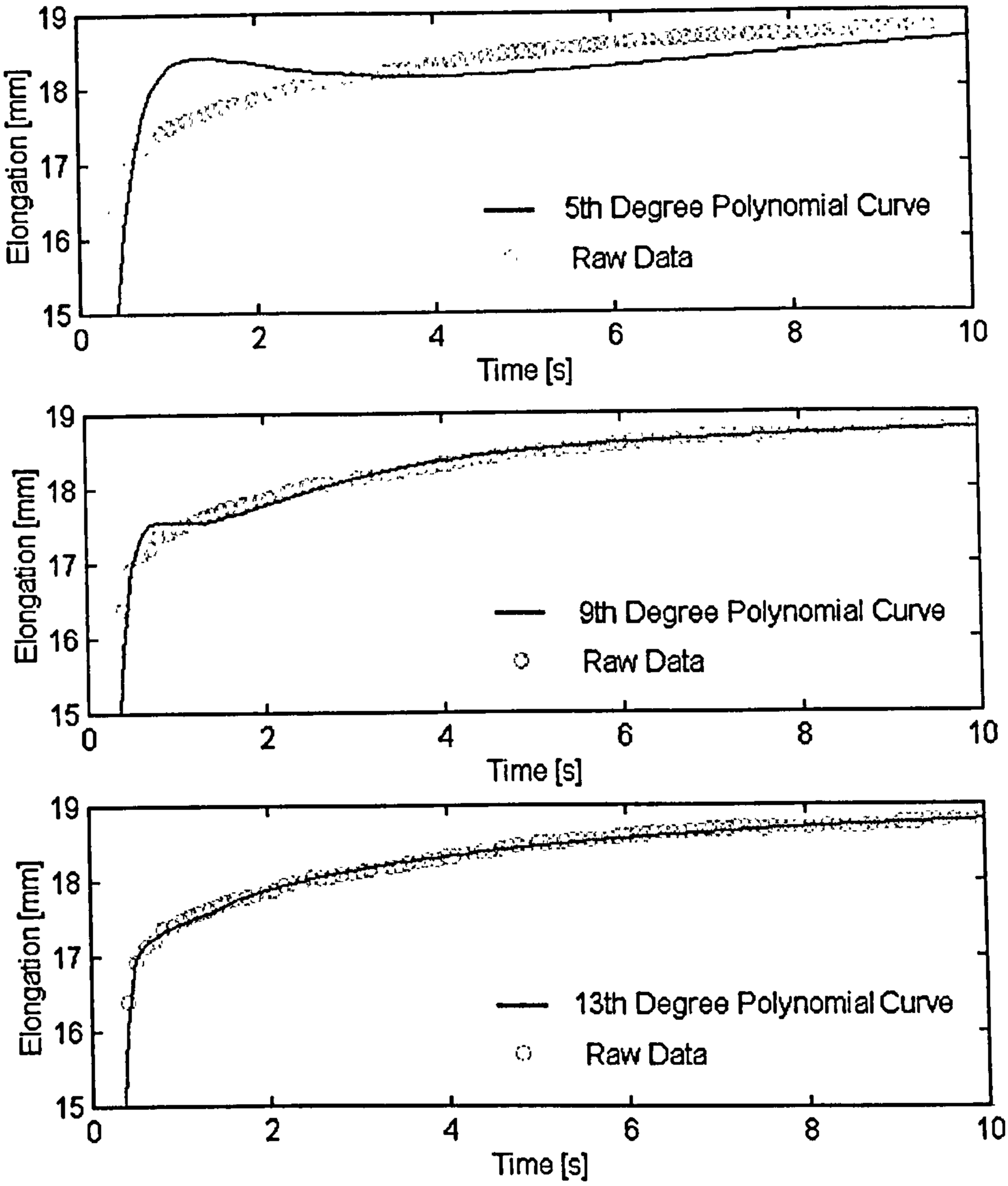

Figure 5.6. Behaviour of different order of polynomials in the raw creep data.

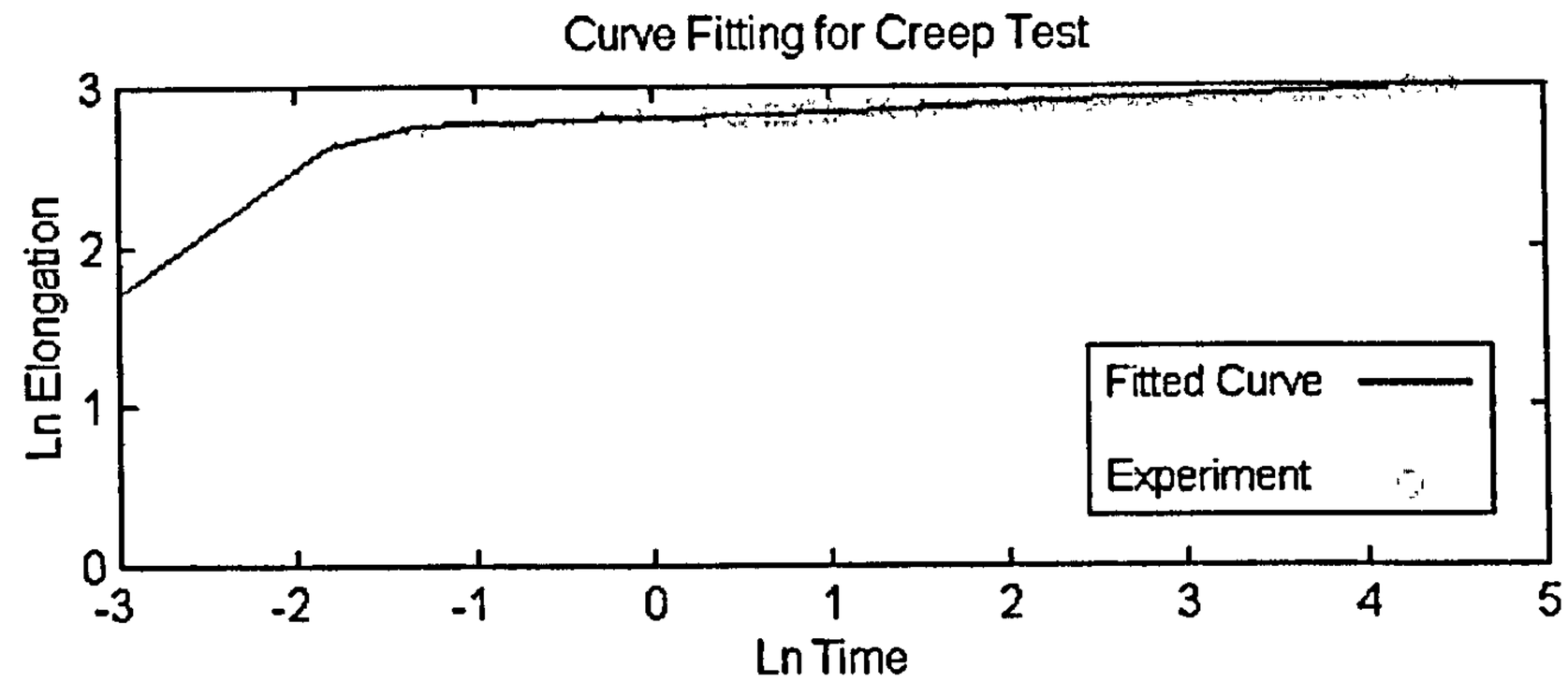

Figure 5.7. Curve fitting for creep test of 25% MVC for 60 kgf constant load.

The coefficients of the curve fitting of subject A were summarised in the table 5.1. The equation can be written as follows;

$$e^{\varepsilon(t)} = e^{ax^{13}} + e^{bx^{12}} + e^{cx^{11}} + e^{dx^{10}} + e^{ex^{9}} + e^{fx^{8}} + e^{gx^{7}} + e^{hx^{6}} + e^{ix^{5}} + e^{jx^{4}} + e^{kx^{3}} + e^{lx^{2}} + e^{mx} + e^{n} \quad (5.2)$$

Load (kgf)	Test Type	a	b	c	d	e	f	g	h	I	j	k	l	m	n
10	Relax	-1.25 10^{-6}	2.89 10^{-5}	-2.68 10^{-4}	1.19 10^{-3}	-1.95 10^{-3}	-3.97 10^{-3}	2.24 10^{-2}	-3.10 10^{-2}	-4.64 10^{-3}	4.54 10^{-2}	-2.47 10^{-2}	-1.93 10^{-2}	6.96 10^{-2}	1.85
10	25 % MVC	3.24 10^{-7}	-4.41 10^{-6}	5.41 10^{-6}	1.87 10^{-4}	-1.02 10^{-3}	3.79 10^{-4}	9.92 10^{-3}	-2.28 10^{-2}	-6.54 10^{-3}	5.79 10^{-2}	-8.85 10^{-3}	-5.60 10^{-2}	8.94 10^{-2}	1.62
20	Relax	1.09 10^{-6}	-2.35 10^{-5}	1.89 10^{-4}	-5.82 10^{-4}	-6.68 10^{-4}	8.91 10^{-3}	-1.62 10^{-2}	-2.23 10^{-2}	1.10 10^{-1}	-1.09 10^{-1}	-1.88 10^{-2}	5.91 10^{-2}	2.49 10^{-2}	2.56
20	25 % MVC	1.97 10^{-8}	-9.29 10^{-7}	-2.95 10^{-5}	3.05 10^{-4}	-1.43 10^{-3}	2.17 10^{-3}	6.73 10^{-3}	-3.17 10^{-2}	3.43 10^{-2}	2.26 10^{-2}	-4.56 10^{-2}	-7.18 10^{-3}	6.79 10^{-2}	2.32
30	Relax	-2.02 10^{-7}	5.66 10^{-6}	-6.34 10^{-5}	3.47 10^{-4}	-7.85 10^{-4}	-9.21 10^{-4}	8.76 10^{-3}	-1.43 10^{-2}	-6.87 10^{-3}	3.79 10^{-2}	-1.66 10^{-2}	-2.79 10^{-2}	4.83 10^{-2}	2.85
30	25 % MVC	-7.90 10^{-7}	1.32 10^{-5}	-7.44 10^{-5}	1.15 10^{-4}	2.28 10^{-4}	8.66 10^{-5}	-3.48 10^{-3}	-3.01 10^{-3}	4.14 10^{-2}	-6.32 10^{-2}	3.85 10^{-3}	4.44 10^{-2}	3.19 10^{-2}	2.69
40	Relax	1.32 10^{-6}	-2.67 10^{-5}	2.01 10^{-4}	-5.78 10^{-4}	-5.58 10^{-4}	7.33 10^{-3}	-1.28 10^{-2}	-1.34 10^{-2}	7.07 10^{-2}	-7.72 10^{-2}	4.55 10^{-3}	3.77 10^{-2}	2.16 10^{-2}	2.85
40	25 % MVC	1.78 10^{-6}	-3.34 10^{-5}	2.16 10^{-4}	-3.34 10^{-4}	-2.22 10^{-3}	9.81 10^{-3}	-4.86 10^{-3}	-3.88 10^{-2}	6.65 10^{-2}	-5.99 10^{-3}	4.25 10^{-2}	2.67 10^{-2}	3.61 10^{-2}	2.73
50	Relax	8.56 10^{-8}	-9.94 10^{-6}	1.92 10^{-4}	-1.55 10^{-3}	5.83 10^{-3}	-5.97 10^{-3}	-2.61 10^{-2}	8.02 10^{-2}	-1.58 10^{-2}	-2.15 10^{-1}	3.02 10^{-1}	-1.25 10^{-1}	3.53 10^{-2}	2.87
50	25 % MVC	2.68 10^{-7}	-4.64 10^{-6}	2.35 10^{-5}	2.37 10^{-5}	-5.52 10^{-4}	1.15 10^{-3}	2.60 10^{-3}	-1.11 10^{-2}	6.04 10^{-3}	1.05 10^{-2}	-1.60 10^{-3}	1.40 10^{-3}	2.56 10^{-2}	2.79
60	Relax	9.94 10^{-7}	-2.11 10^{-5}	1.67 10^{-4}	-5.14 10^{-4}	-5.25 10^{-4}	7.83 10^{-3}	-1.75 10^{-2}	-4.09 10^{-3}	7.35 10^{-2}	-1.07 10^{-1}	4.03 10^{-2}	1.64 10^{-2}	2.96 10^{-2}	2.90
60	25 % MVC	-4.11 10^{-7}	7.46 10^{-6}	-4.81 10^{-5}	9.84 10^{-5}	2.80 10^{-4}	-1.77 10^{-3}	2.88 10^{-3}	1.06 10^{-3}	-1.04 10^{-2}	9.79 10^{-3}	1.19 10^{-2}	-1.15 10^{-2}	2.93 10^{-2}	2.81

Table 5.1. The coefficients table of curve fittings for the creep test.

5.3. Stress-Relaxation Tests

In stress-relaxation tests, the specimen is quickly deformed a given amount, and the stress required to hold this deformation constant is measured as a function of time. If the stress (σ) is divided by the constant strain (ε), a modulus which decreases with time is obtained. Stress-relaxation experiments are very important for the theoretical

understanding of viscoelastic materials. The stress-relaxation modulus (E(t)) can be expressed as follows;

$$E(t) = \frac{\sigma(t)}{\varepsilon_{t0}} \tag{5.3}$$

where:

E(t) : stress-relaxation modulus

$\sigma(t)$: Stress as function of time

ε_{to} : constant strain

5.3.1. Stress-Relaxation Test Data Collection

The stress-relaxation test was also applied to the same two male subjects. A set of six different constant strains was used to test the stress-relaxation response of the arm bulk tissue. The stress-relaxation test consisted of 5, 10, 15, 20, 25 and 30 mm constant strains. Owing to the long recovery time of the bulk tissue, a 60 minute rest period was allowed between the tests. A picture from the stress-relaxation test in contracted procedure can be seen in figure 5.8.

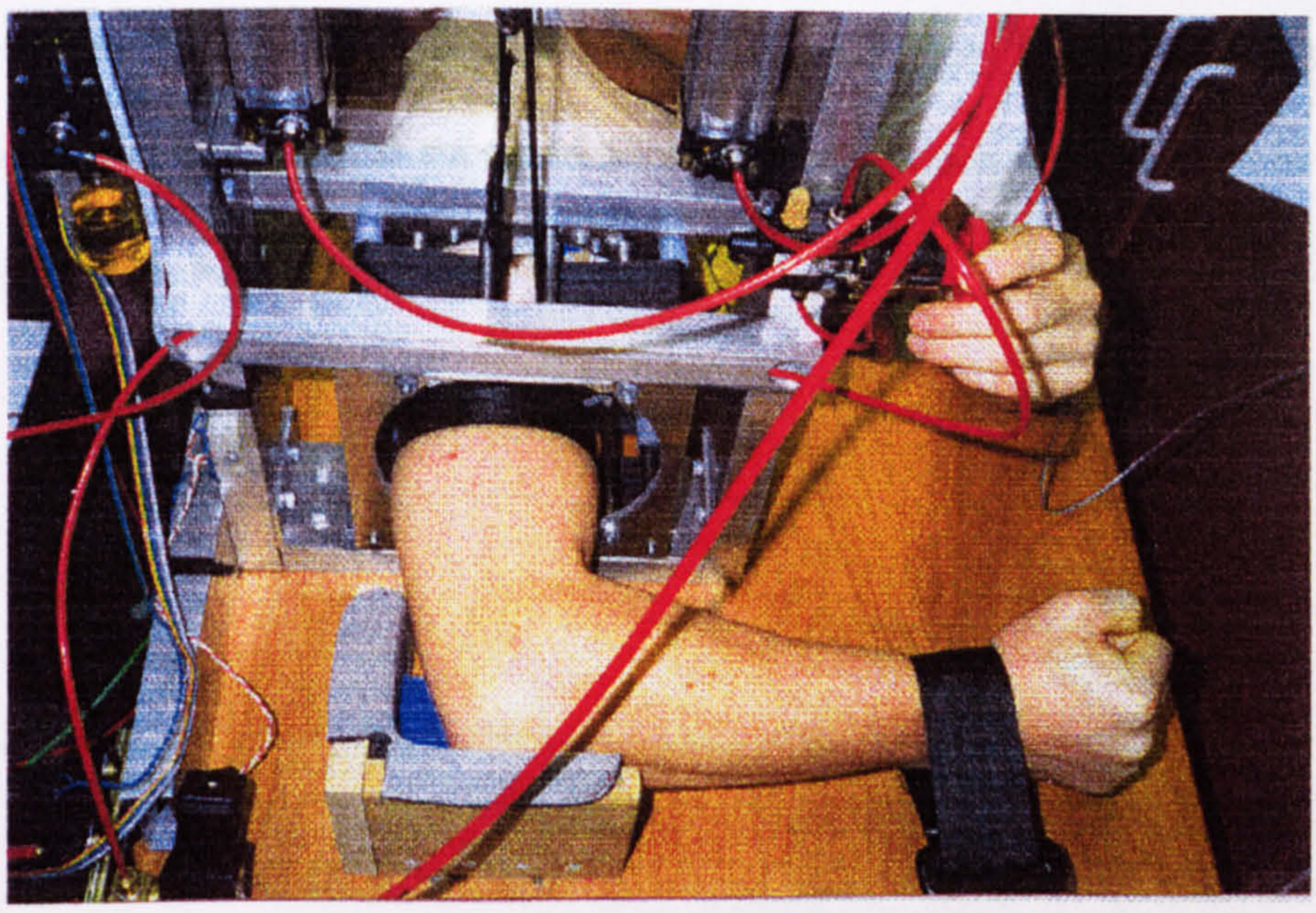

Figure 5.8. A view from the stress-relaxation test with contracted test procedure.

The sudden deformation of the arm was achieved by using pneumatic cylinders (explained in chapter 3 and chapter 4) and its movement was stopped with the end point (see Fig. 3.8 (3)). Unfortunately, this stopping mechanism caused a very high impact for the 5 and 10 mm strains between the load cell carrier and the bolt. The reason the other constant strains did not show this high impact response, was the increasing effect of the damping of the bulk tissue as the increased strain. This impact and its response can be seen in figure 5.9, which shows the first 2 s of data collection. It can be seen in figure 5.9 that the impact response decays over a period of 0.8 s. The data collection period was 120 s, which was the same as the creep test. The complete record of a stress-relaxation test can be seen in figure 5.10.

Unfortunately, the effect of the seat belt could not be removed from the raw data for each load record. It was possible to calculate the elongation of the seat belt, but subtraction of this amount would change the nature of the stress-relaxation test. This is why the averaged elongation of the seat belt was calculated and then subtracted from the constant strain value. An example of the calculation of the real elongation value from the stress-relaxation test can be seen in figure 5.11. The seat belt effect for the 20 mm constant strain test, and the averaged constant strain which was 16 mm (20 – 3.98) in this experiment, are plotted in figure 5.11.

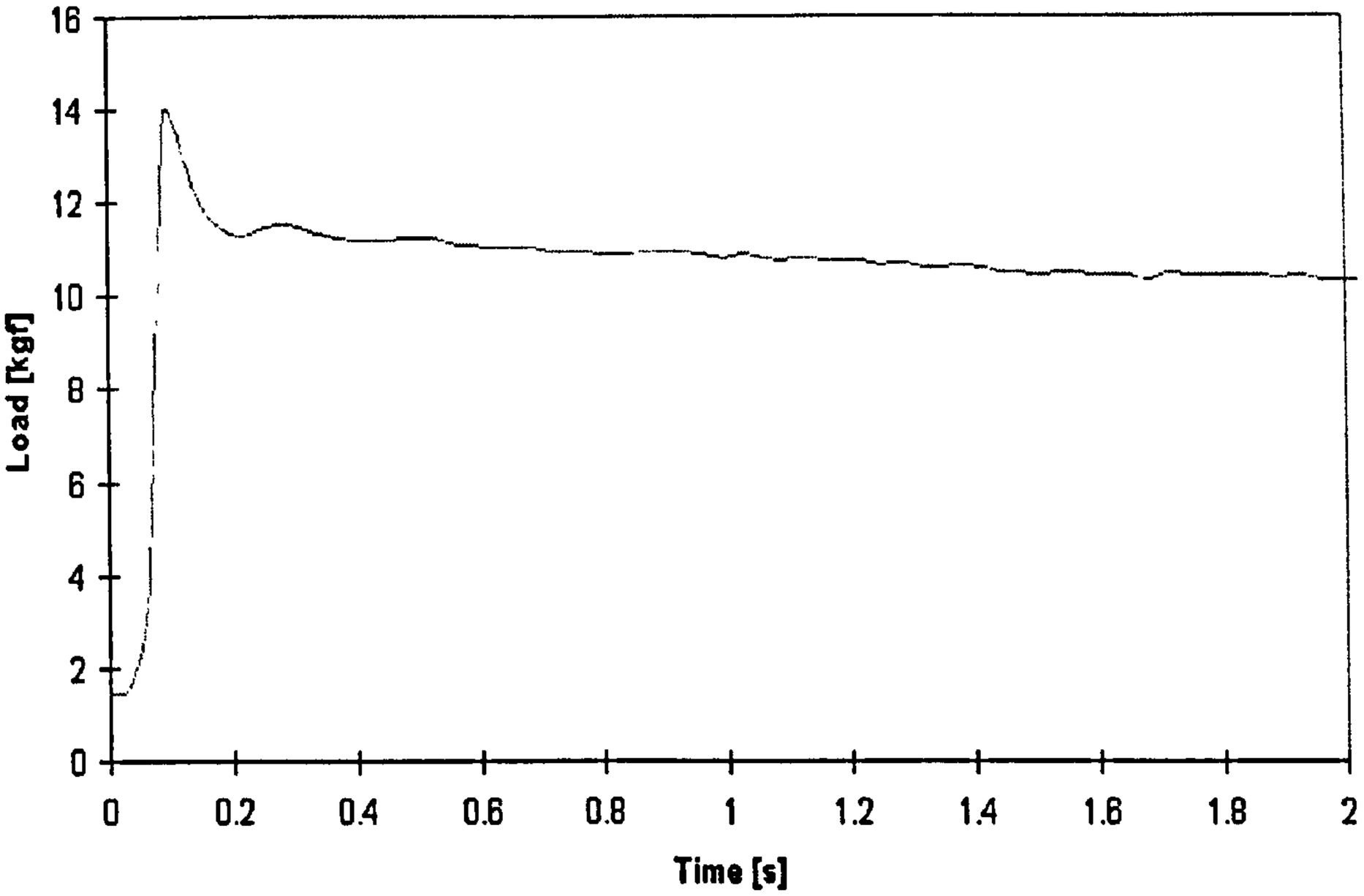

Figure 5.9. Stress-relaxation test, the first 2 seconds of data collection for 10 mm constant strain.

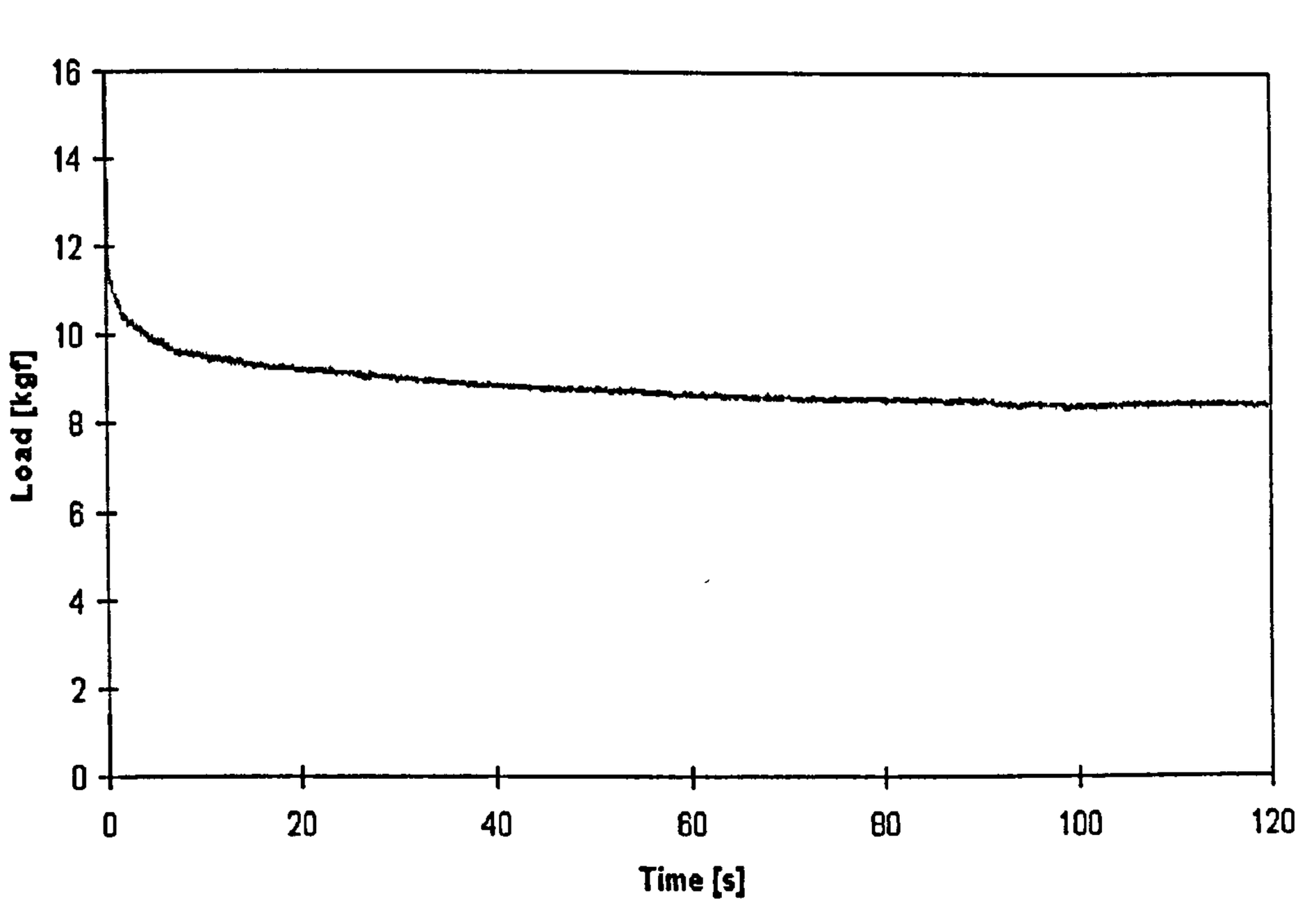

Figure 5.10. Data collection of stress-relaxation test for a period of 120 s.

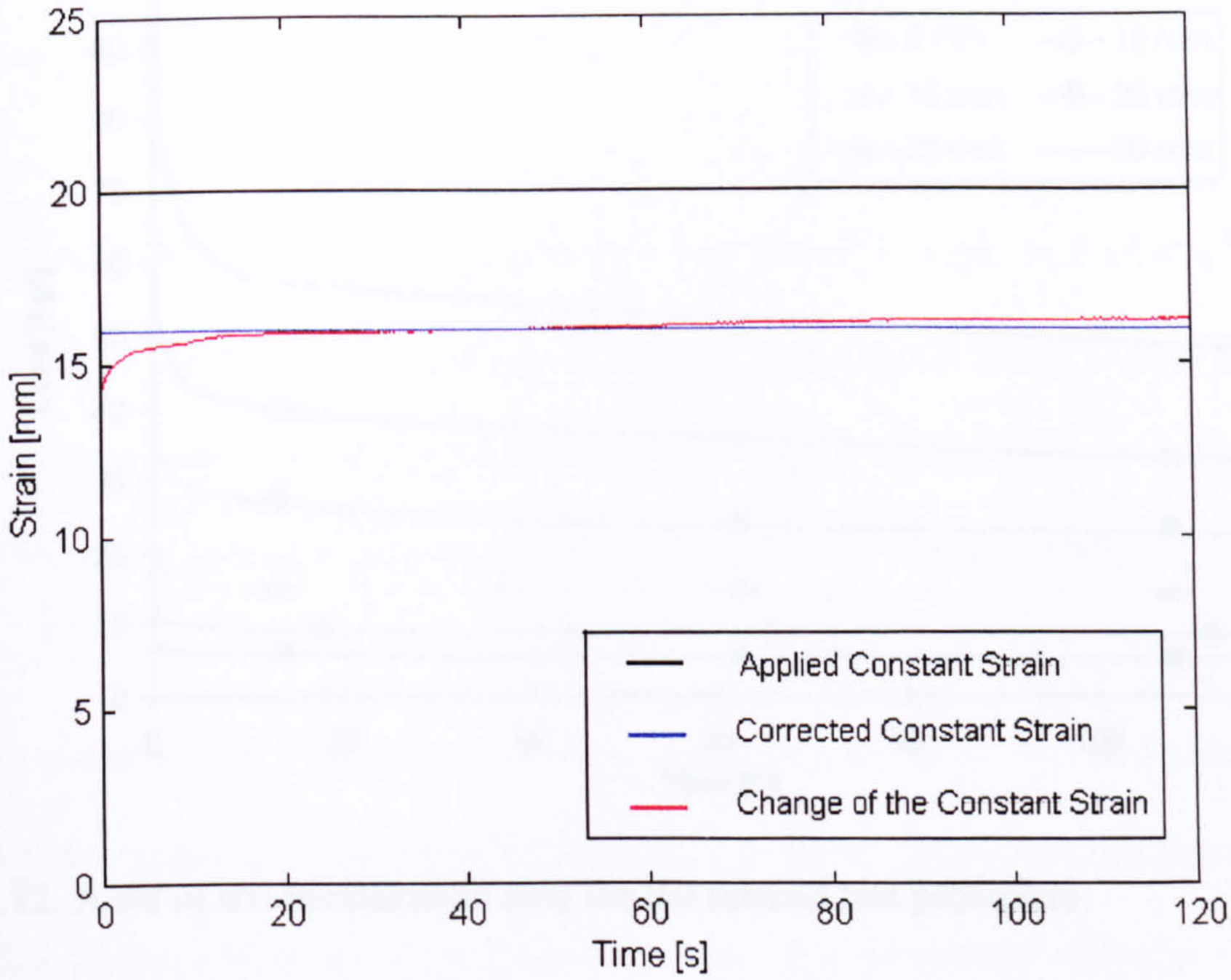

Figure 5.11. The seat belt effect for 20 mm constant strain stress-relaxation test.

Two sets of stress-relaxation data can be seen in figures 5.12 and 5.13. The non-contraction test (relaxed condition) procedure was plotted in figure 5.12. In the second test, the subject contracted his muscle 25% of MVC, exactly according to the procedure used in the creep tests. The experiment was plotted in figure 5.13.

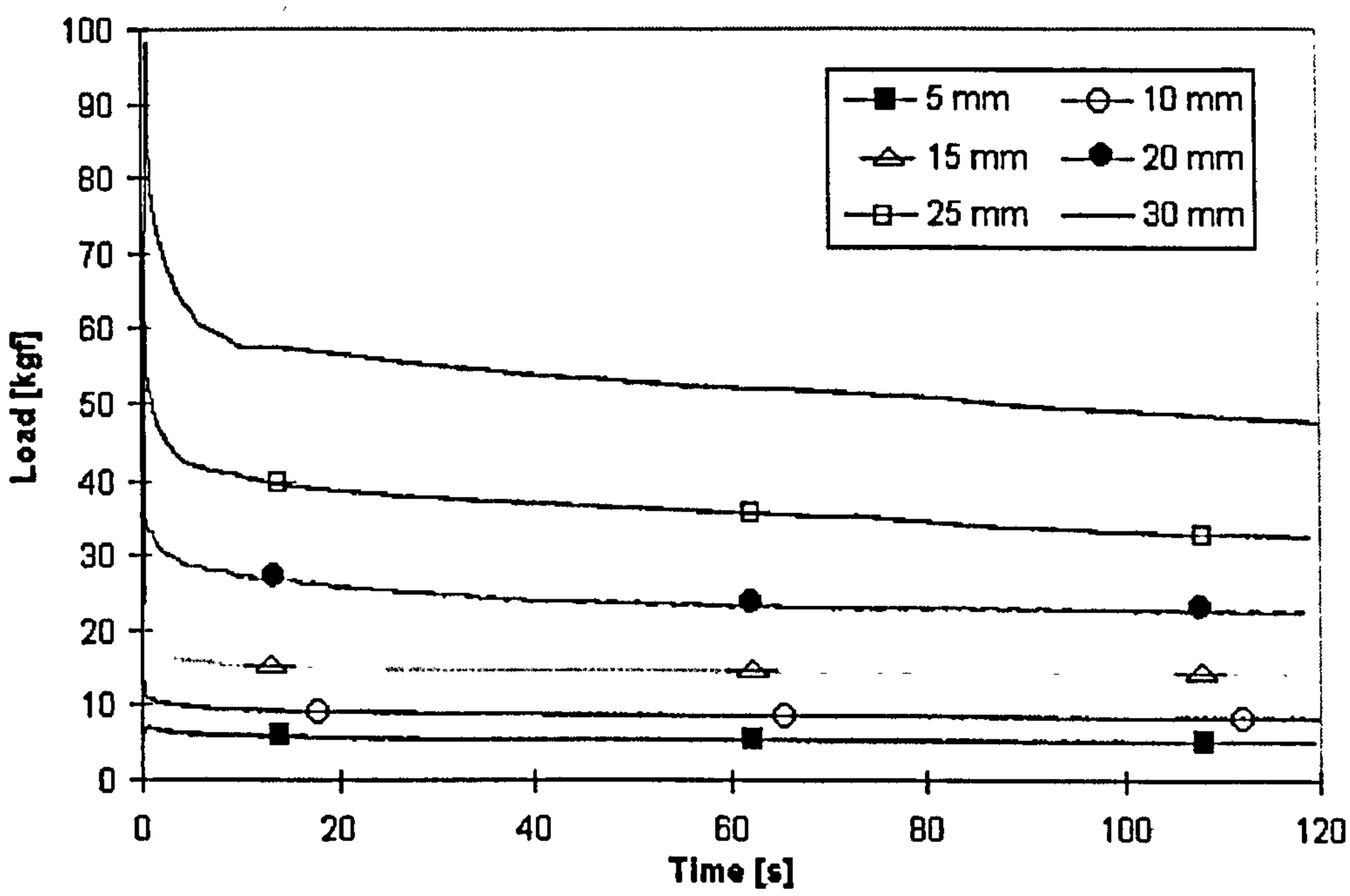

Figure 5.12. A set of stress-relaxation data for the relaxed test procedure.

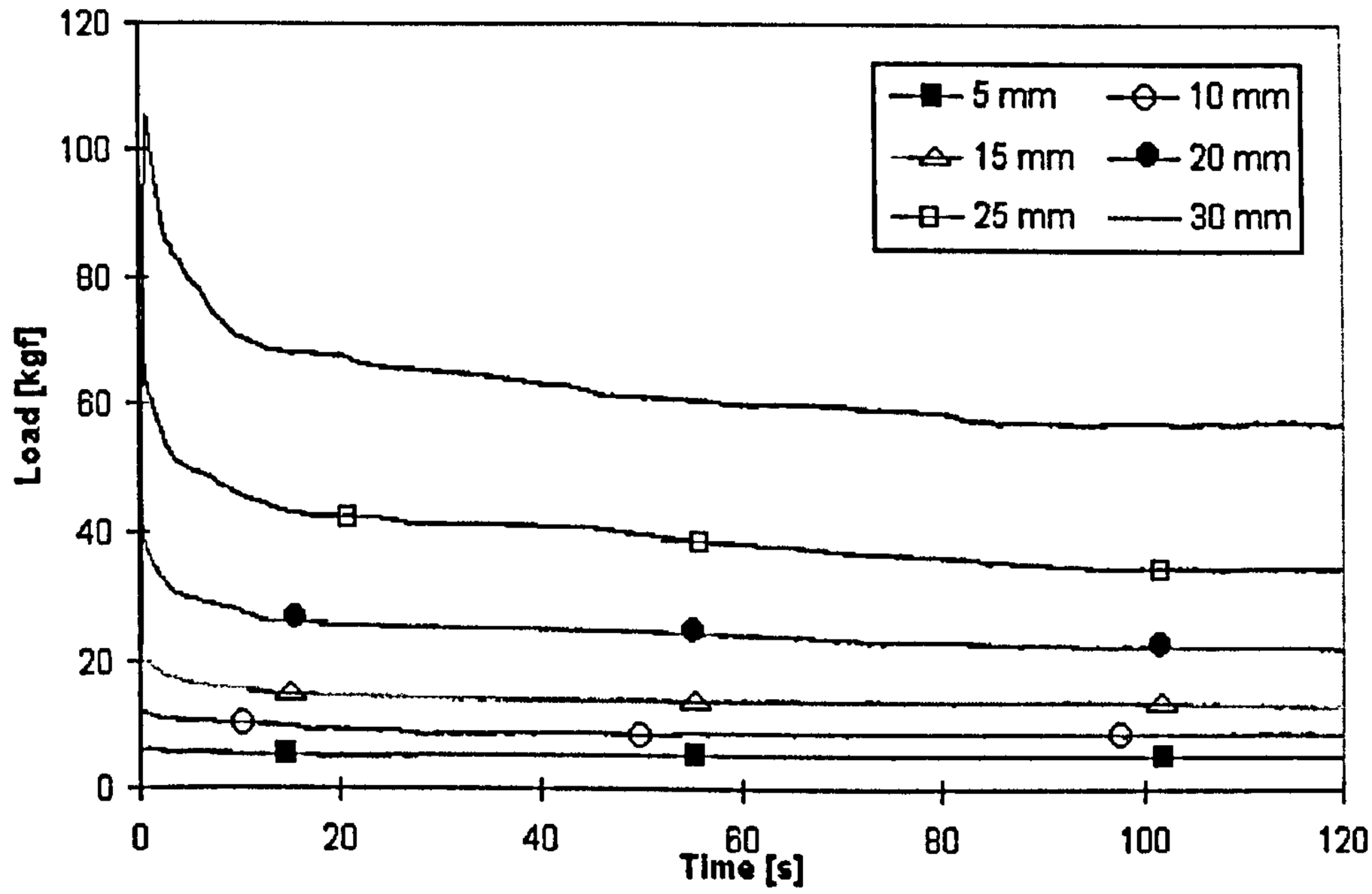

Figure 5.13. A set of stress-relaxation data for the contracted muscle test procedure.

5.3.2. Mathematical Description of Stress-Relaxation Test Data

To be able to analyse and compare the stress-relaxation test data, a mathematical description was necessary. The most appropriate way of doing this was polynomial curve

fitting of the stress-relaxation data. During the data collection, raw data were recorded at the sampling frequency of 2.5 kHz.

First, the peak (highest) point of the raw data was found, and the data after this point were processed. To avoid the impact of the experiment for the curve fitting, the data process starting point was shifted towards to the impact decay point in the effected records. The point shifting can be seen by comparing figures 5.14 and 5.15.

Secondly, the raw data were averaged every 50 ms interval to fit the maximum matrix size of 16384 elements in the Matlab software. The curve fitting was performed both using linear scales and by converting the linear time and elongation scales into natural logarithmic scales. The main reason for using logarithmic conversion was to visualise better the beginning of the raw data. The fifth order polynomial gave the closest fit to the raw data. The curve fitting was performed by using Matlab 5 commercial software.

An example of the sequence of the curve fitting procedure is shown in figures 5.14 and 5.15. The raw data with the linear and natural logarithmic time scales are plotted in figure 5.14. In figure 5.15, the same raw data were plotted with the closest polynomial curve to the raw data. The rest of the curve fittings are presented in appendix C.1. The coefficients of the curve fittings for the subject are summarised in table 5.2. The equation can be written as follows:

$$e^{\varepsilon(t)} = e^{ax^5} + e^{bx^4} + e^{cx^3} + e^{dx^2} + e^{ex} + e^{f} \qquad (5.4)$$

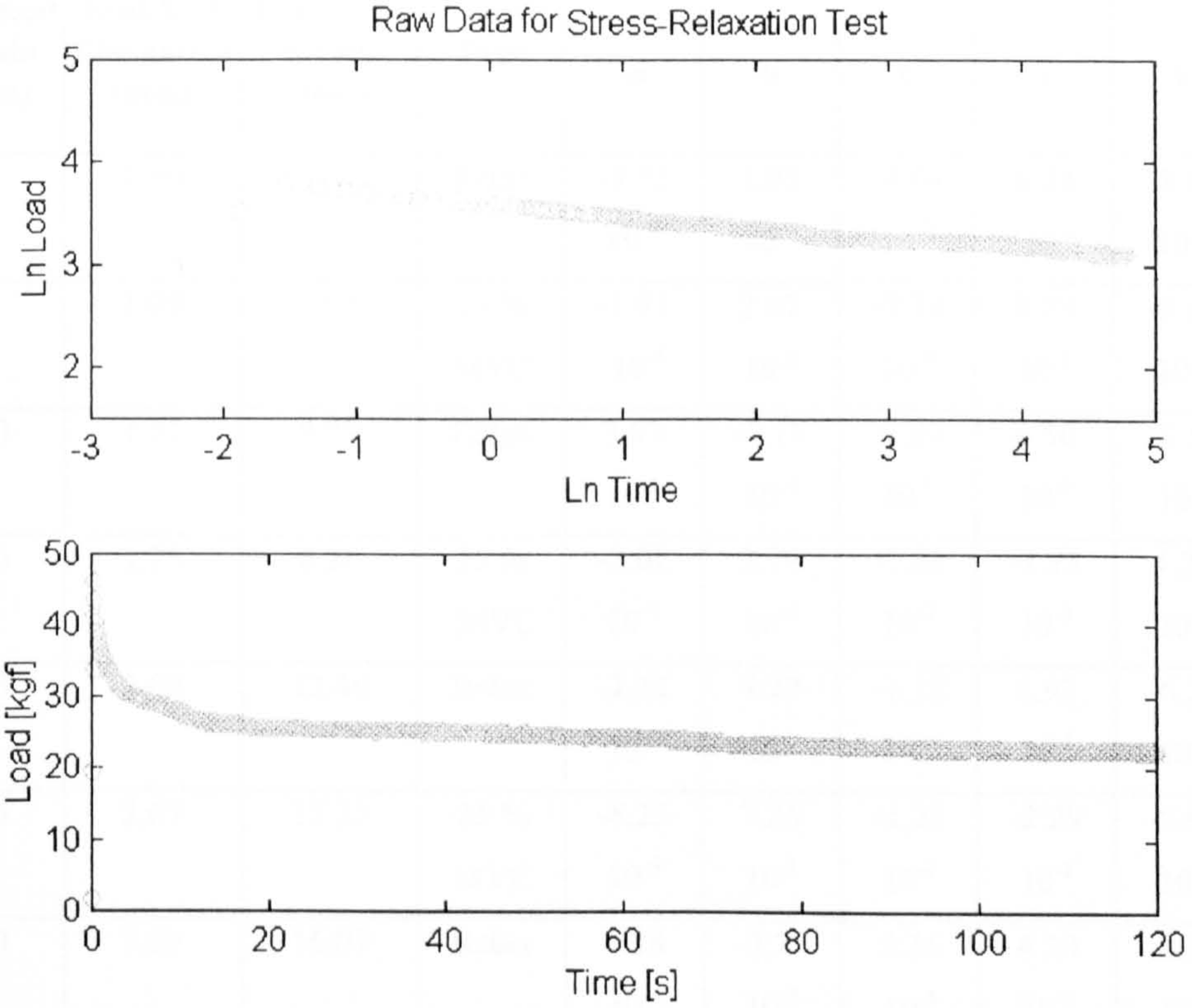

Figure 5.14. Raw stress-relaxation data of 25% MVC with linear and logarithmic time scale for 20 mm constant strain.

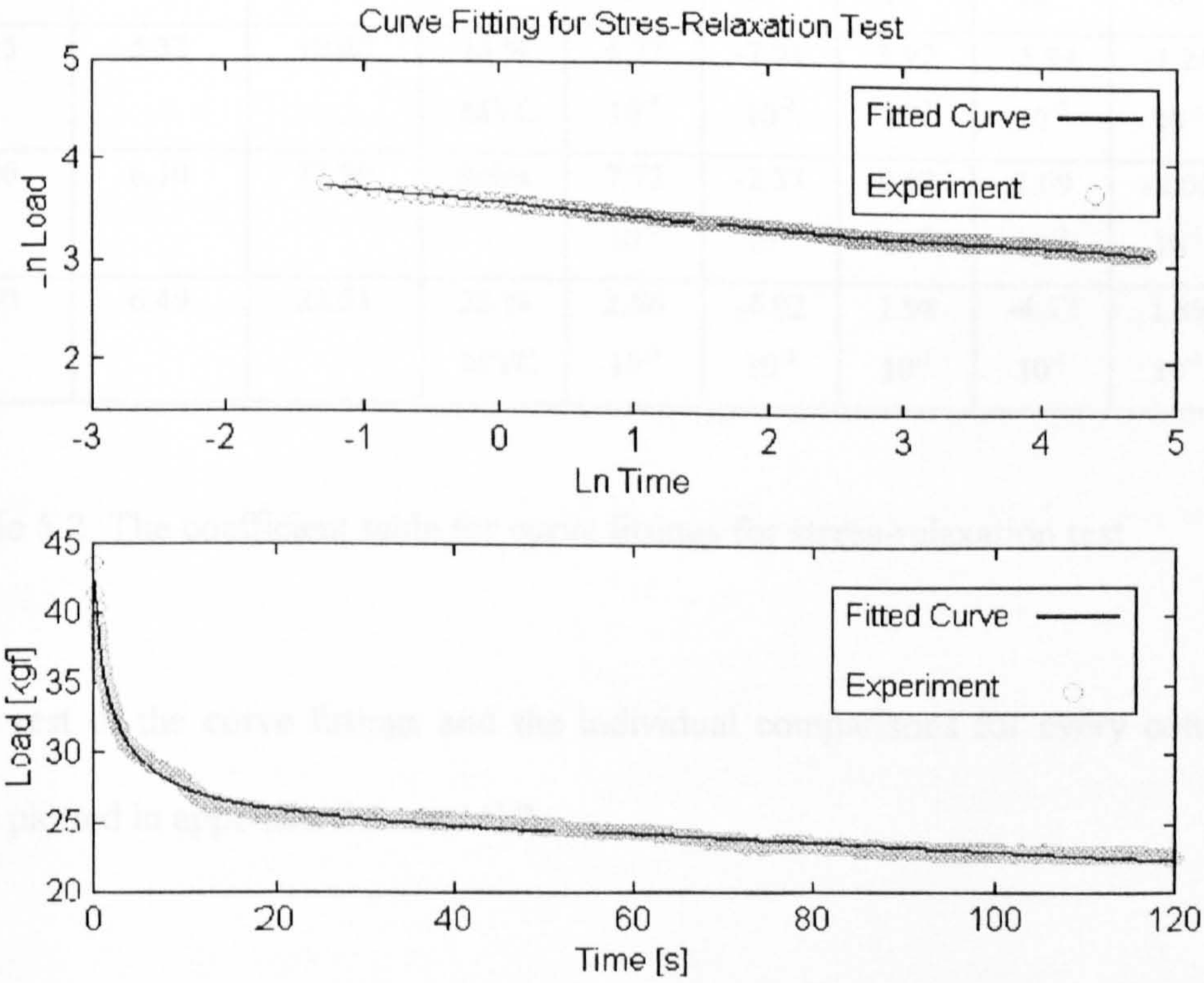

Figure 5.15. Curve fitting for stress-relaxation test of 25% MVC for 20 mm (16 mm corrected) constant strain.

Constant Strain (mm)	Seat Belt Elongation (mm)	Corrected Strain (mm)	Test Type	a	b	c	d	e	f
5	1.06	3.94	Relax	-8.31 10^{-4}	1.05 10^{-2}	-4.64 10^{-2}	8.38 10^{-2}	-1.15 10^{-1}	1.94
5	1.09	3.91	25 % MVC	-1.91 10^{-3}	2.07 10^{-2}	-7.34 10^{-2}	9.89 10^{-2}	-9.43 10^{-2}	1.81
10	1.71	8.29	Relax	3.93 10^{-5}	-1.17 10^{-4}	-1.07 10^{-3}	4.56 10^{-3}	-5.51 10^{-2}	2.37
10	1.75	8.25	25 % MVC	-2.02 10^{-4}	3.74 10^{-3}	-1.20 10^{-2}	-1.73 10^{-2}	4.24 10^{-3}	2.44
15	2.60	12.40	Relax	-1.21 10^{-4}	9.27 10^{-4}	-1.18 10^{-3}	1.92 10^{-3}	-6.24 10^{-2}	2.86
15	2.67	12.33	25 % MVC	-8.23 10^{-4}	7.26 10^{-3}	-1.25 10^{-2}	-2.29 10^{-2}	-3.97 10^{-2}	2.95
20	3.93	16.07	Relax	4.28 10^{-4}	-3.27 10^{-3}	5.36 10^{-3}	4.20 10^{-3}	-8.36 10^{-2}	3.48
20	3.99	16.01	25 % MVC	-3.65 10^{-4}	2.15 10^{-3}	8.28 10^{-4}	-9.54 10^{-3}	-1.21 10^{-1}	3.60
25	5.08	19.92	Relax	-2.49 10^{-4}	1.79 10^{-3}	-6.48 10^{-3}	2.60 10^{-2}	-1.33 10^{-1}	3.92
25	5.32	19.68	25 % MVC	4.77 10^{-4}	-7.91 10^{-3}	3.92 10^{-2}	-5.94 10^{-2}	-1.24 10^{-1}	4.14
30	6.10	23.90	Relax	7.72 10^{-5}	-2.33 10^{-3}	9.92 10^{-3}	1.69 10^{-2}	-2.01 10^{-1}	4.38
30	6.49	23.51	25 % MVC	2.96 10^{-3}	-4.02 10^{-2}	1.98 10^{-1}	-4.12 10^{-1}	1.89 10^{-1}	4.54

Table 5.2. The coefficient table for curve fittings for stress-relaxation test

The rest of the curve fittings and the individual comparisons for every constant strain was plotted in appendix C.1. and C.2.

5.4. Stress-Strain Tests

In the stress-strain test, the build up of force (or stress) was measured as the specimen was being deformed of a constant rate. Occasionally stress-strain tests are modified to measure the deformation of a specimen as the force is applied at a constant rate. Unfortunately, these tests are more difficult to interpret than many other tests.

5.4.1. Stress-Strain Test Data Collection

Stress-strain tests were applied to the same two male subjects. A set of four different constant strain rates was used to test the stiffness of the arm bulk tissue. The stress-strain test consisted of 0.5, 1, 2, and 4 $mm.s^{-1}$ constant strain rates. The main reason for choosing such increases of the strain rate was to show a clear difference between the increments.

The deformation of the arm with a constant strain rate was achieved by using a stepper motor (explained in chapter 4 and chapter 5). The data collection period depended on the constant strain rate. The complete record of a stress-strain test for constant speed of 2 $mm.s^{-1}$ can be seen in figure 5.16, which was plotted with a time scale instead of strain. The increase of the strain was also plotted as a linear increase associated with the secondary axis. In figure 5.17, the same results were plotted as a stress-elongation diagram.

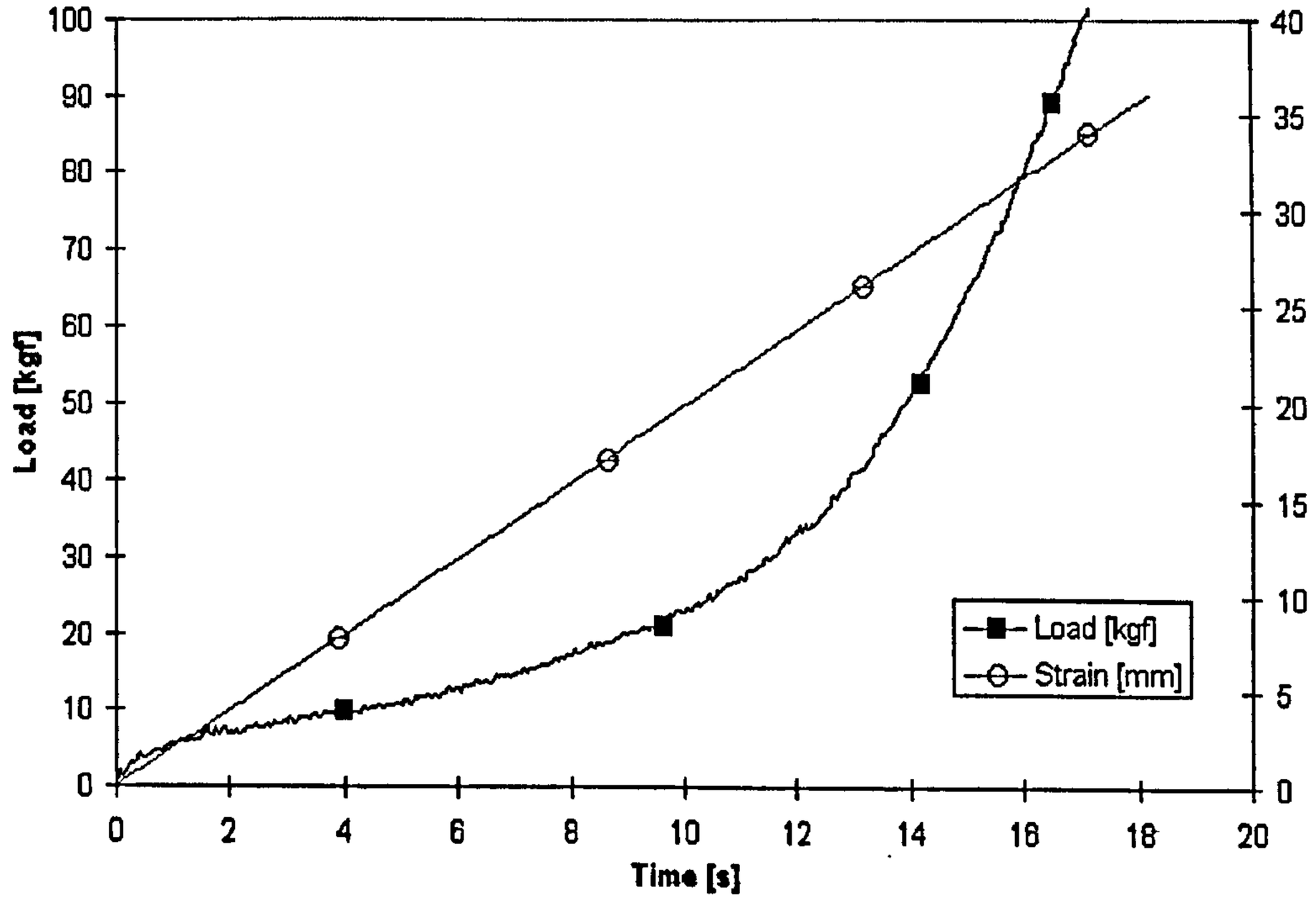

Figure 5.16 Stress-strain test with 2 mm.s^{-1} constant strain rate plotted with a time scale.

Before the curve fitting procedure, the effect of the seat belt was removed from the raw data. The elongation of the seat belt was calculated from equation 5.7 in section 5.6. In the stress-strain test, the seat belt elongation was calculated and subtracted from the total elongation for the load record. The difference can be seen in the figure 5.17. After subtraction of the seat belt effect from the raw data, the strain was reduced.

Two sets of stress-strain tests were applied to the subjects; a non-contraction test (relaxed test) and one at 25% of MVC. The two sets of experiment data can be seen in figures 5.18 and 5.19. The non-contraction test (relaxed condition) procedure was plotted in figure 5.17 and 25% of MVC in figure 5.18. It is also clear from the figures that the increase of the strain rate resulted in less strain in the bulk tissue. There is also less strain for the contracted muscle procedure (Fig. 5.19).

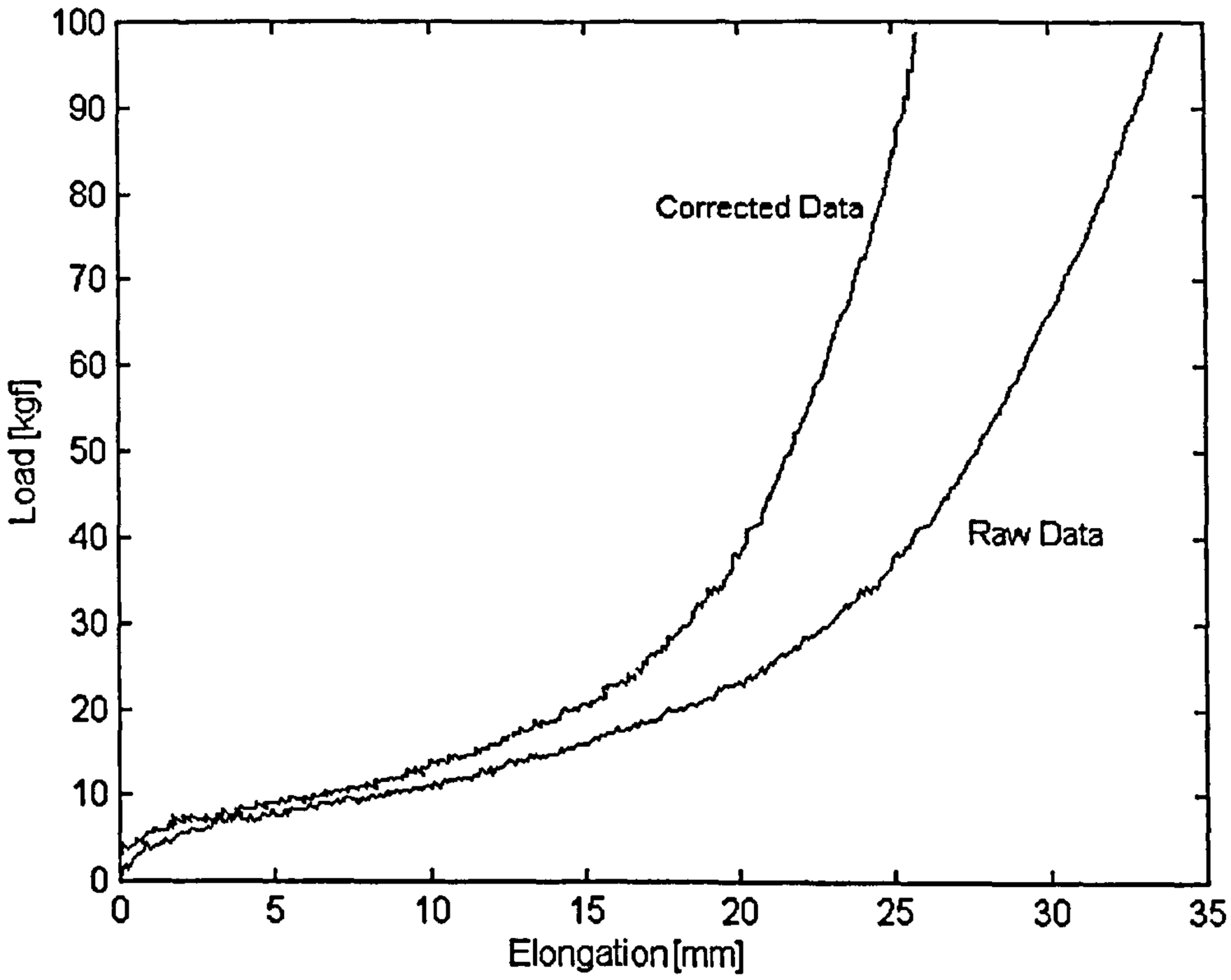

Figure 5.17 A typical stress-strain diagram of human bulk tissue with 2 mm/s constant speed of deformation.

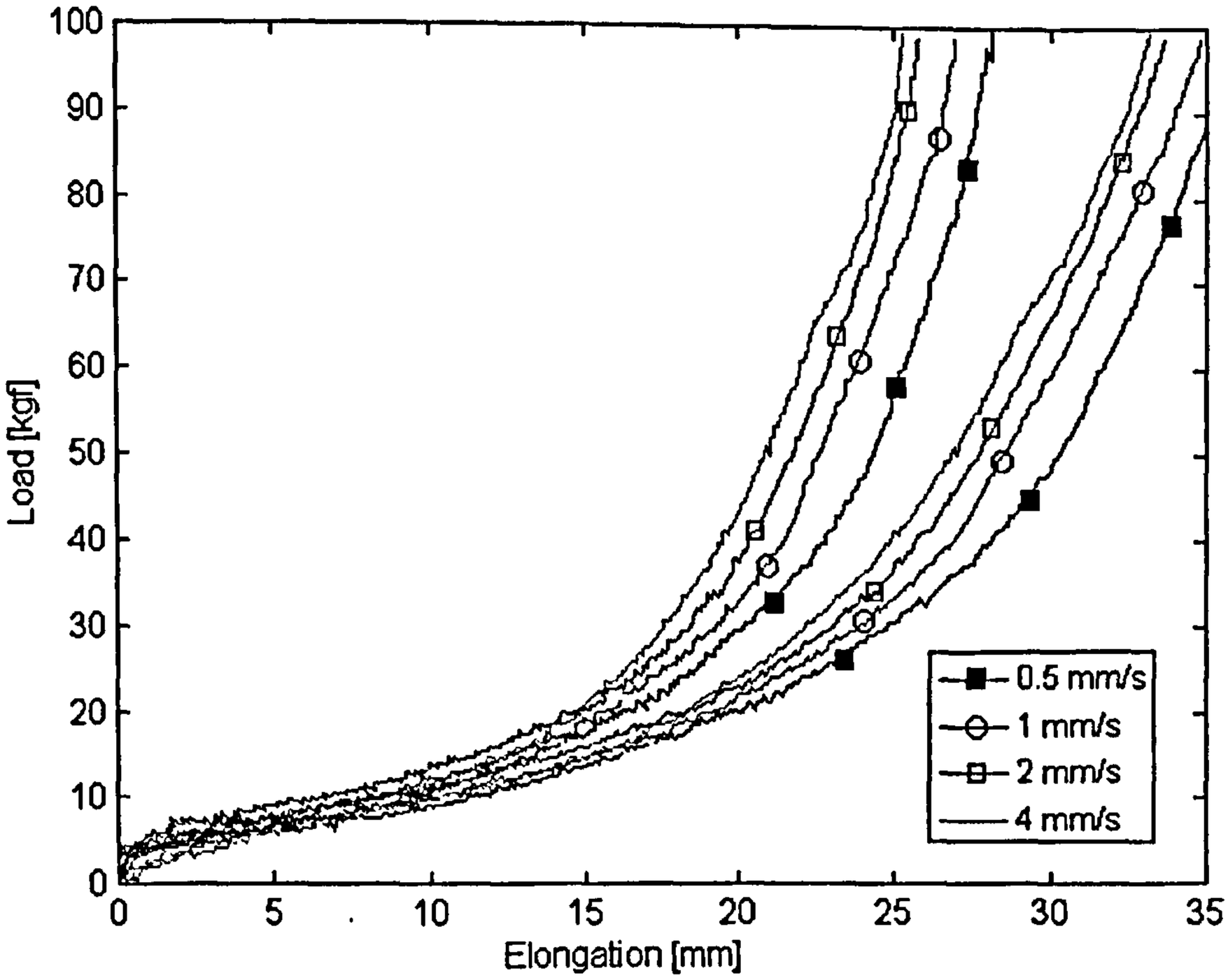

Figure 5.18. A set of stress-strain tests using the relaxed procedure.

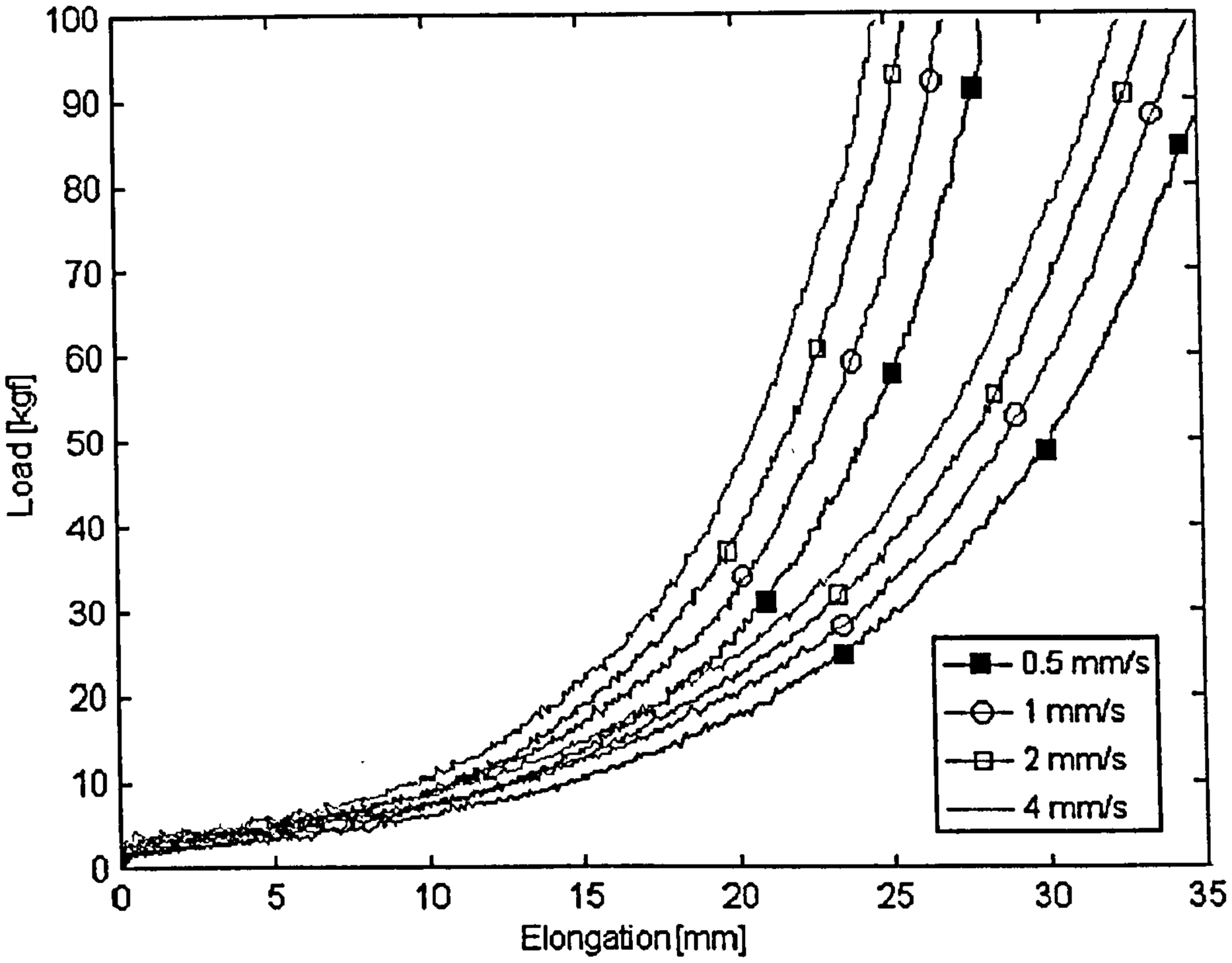

Figure 5.19. A set of stress-strain tests at 25% of MVC.

5.4.2. Mathematical Description of Stress-Strain Test Data

Curve fitting for the stress-strain data was easier then for the stress-relaxation and creep tests. The curve fitting was achieved in linear load and strain scales. A six degree polynomial curve (see equation 5.5) was nicely fitted to all the stress-strain data. An example of six degree polynomial curve fitting to the stress-strain data can be seen in figure 5.20. The curve fittings coefficients (a, b, c, d, e, f and g), for each test, are presented in table 5.3. The rest of the curve fittings and the individual comparisons for every constant strain rate are plotted in appendix D.1 and D.2.

$$f(x) = ax^6 + bx^5 + cx^4 + dx^3 + ex^2 + fx + g \tag{5.5}$$

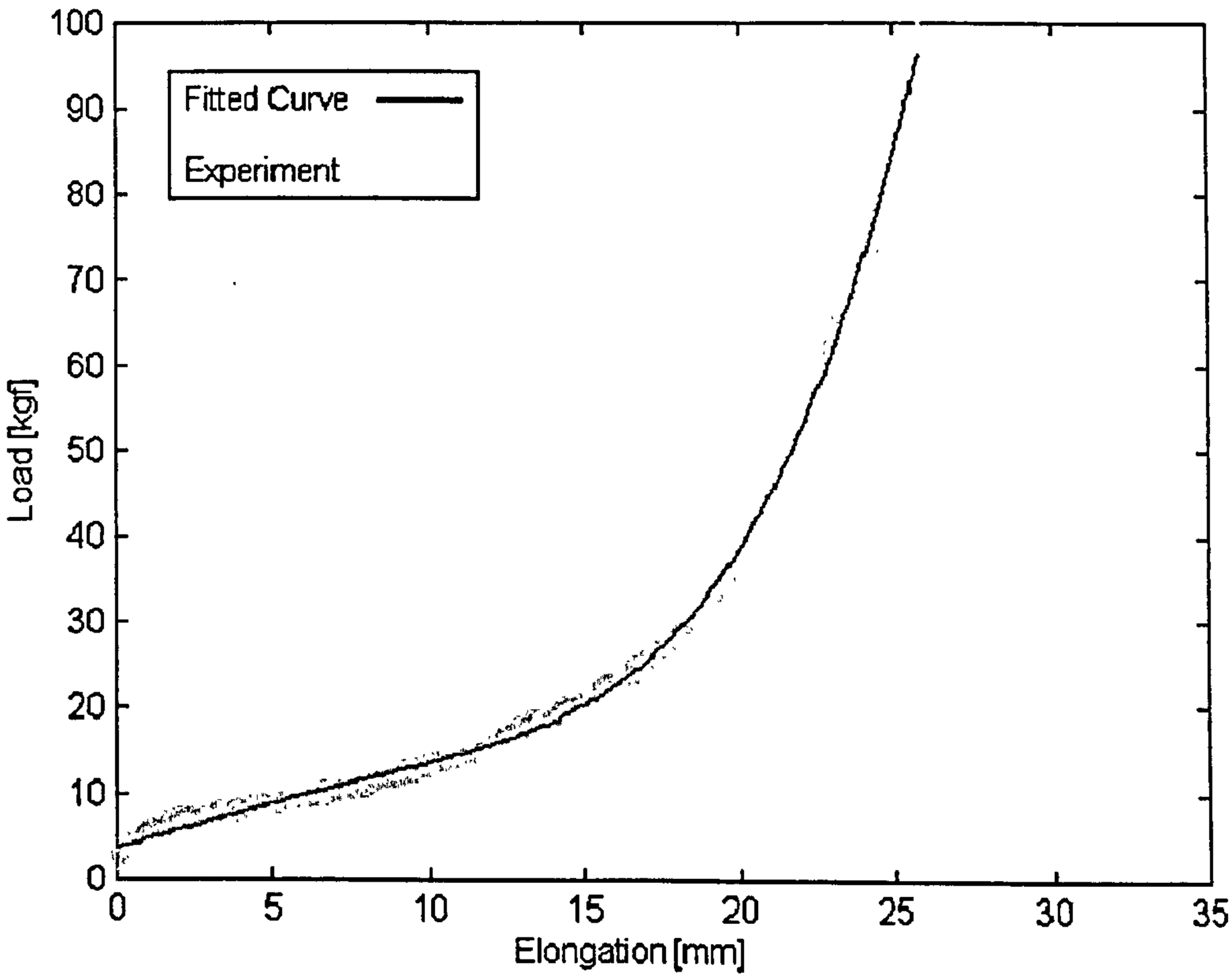

Figure 5.20. Six degree polynomial curve fitting to stress-strain data with 2 $mm.s^{-1}$ constant strain rate in relaxed test condition.

Strain Rate ($mm.s^{-1}$)	Test	a	b	c	d	e	f	g
0.5	Relax	5.42 10^{-7}	-6.58 10^{-6}	-6.86 10^{-4}	2.26 10^{-2}	-2.12 10^{-1}	1.31	2.96
0.5	25 % MVC	1.12 10^{-6}	-7.01 10^{-5}	1.72 10^{-3}	-1.67 10^{-2}	7.19 10^{-2}	3.91 10^{-1}	1.34
1	Relax	-2.89 10^{-6}	2.35 10^{-4}	-6.86 10^{-3}	9.41 10^{-2}	-5.92 10^{-1}	2.18	3.22
1	25 % MVC	6.88 10^{-8}	1.93 10^{-5}	-1.01 10^{-3}	2.19 10^{-2}	-1.85 10^{-1}	1.23	1.31
2	Relax	-3.02 10^{-6}	2.55 10^{-4}	-7.73 10^{-3}	1.13 10^{-1}	-7.99 10^{-1}	3.23	2.69
2	25 % MVC	1.01 10^{-7}	2.64 10^{-5}	-1.49 10^{-3}	3.41 10^{-2}	-2.94 10^{-1}	1.48	1.71
4	Relax	7.52 10^{-7}	-5.56 10^{-5}	1.66 10^{-3}	-1.36 10^{-2}	-4.34 10^{-2}	1.71	5.63 10^{-1}
4	25 % MVC	-1.36 10^{-6}	1.23 10^{-4}	-3.74 10^{-3}	5.64 10^{-2}	-3.64 10^{-1}	1.47	2.47

Table 5.3. The coefficients table for curve fitting of the stress-strain test.

5.6. Seat Belt Testing

The seat belt (Fig. 3.4) had an effect on the measurements, which made it very important to find its mechanical properties. The seat belt did not show a time dependent behaviour. The seat belt was tested by simply using an undeformable material, which was a glass bottle in this study. The glass bottle was covered with silicon grease to lessen the friction between it and the seat belt. A constant load was applied to the glass bottle and the elongation of the seat belt was recorded. The full duration of 120 s creep test data collection for the seat belt can be seen in figure 5.21. It is clear that seat belt elongation did not change by time. The seat belt was also tested with 10, 20, 30, 40, 50 and 60 kgf loads for a duration of 9 s. The result of these tests can be seen in figure 5.22.

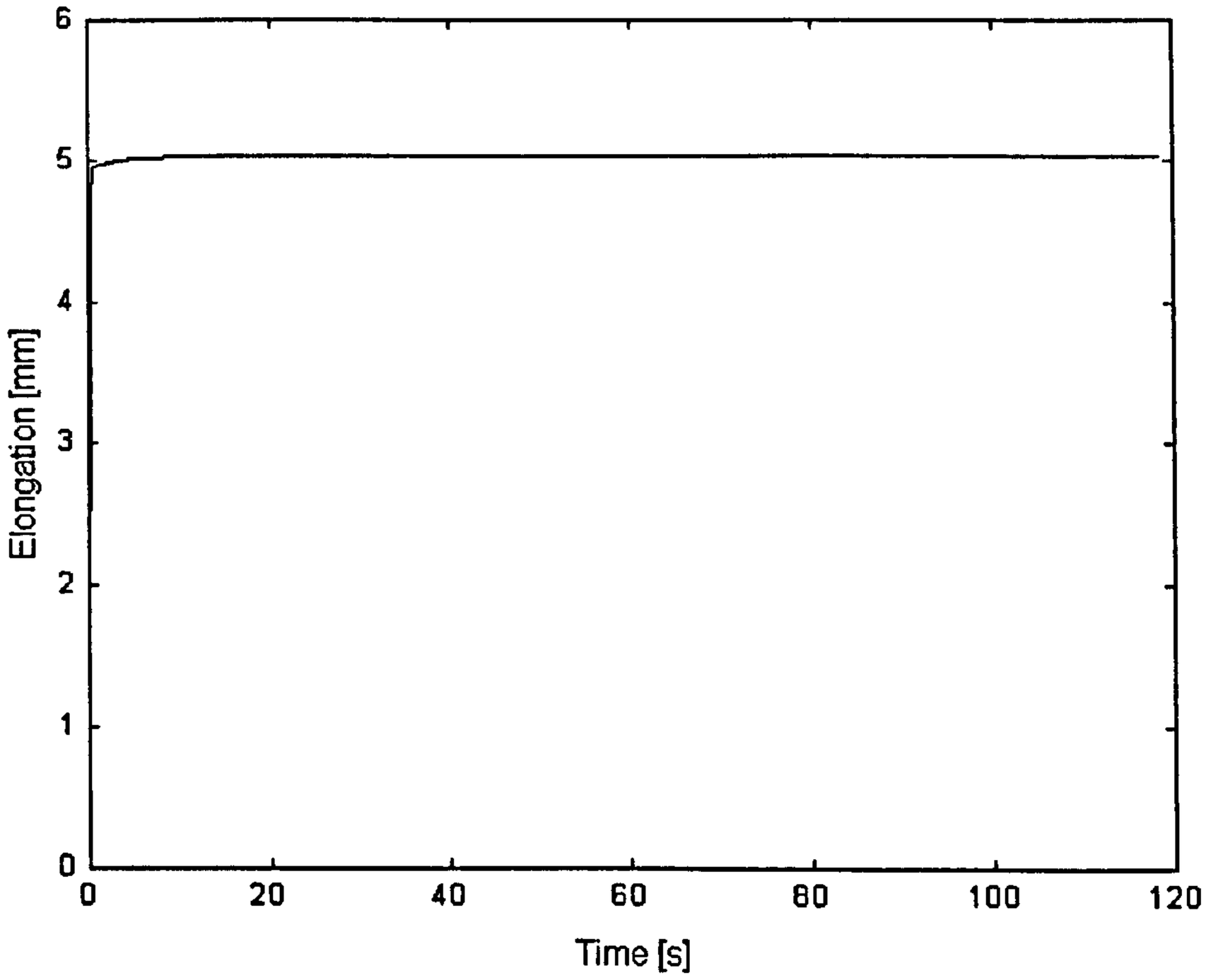

Figure 5.21. Creep test of seat belt duration of 120 s.

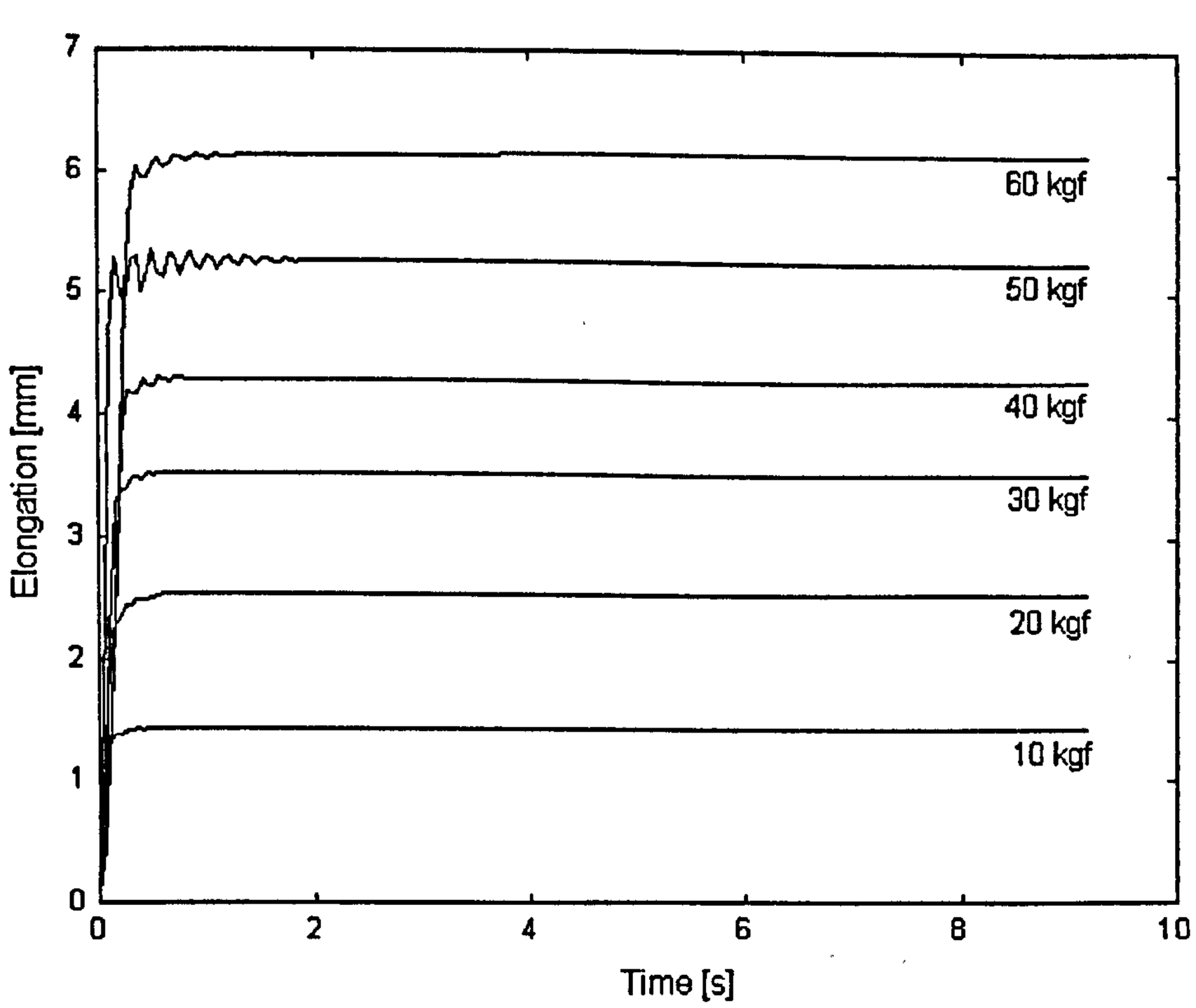

Figure 5.22. Creep test of seat belt with different loads in short duration time.

The elastic modulus of the seat belt was calculated from the constant speed stress-strain test. A set of constant speeds (0.25, 0.30, 0.40, 1 and 2 $mm.s^{-1}$) was applied to the glass bottle and the tension of the seat belt was recorded. As for the creep test, different strain rates did not show time-dependent changes. The result of the stress-strain tests can be seen in figure 5.23.

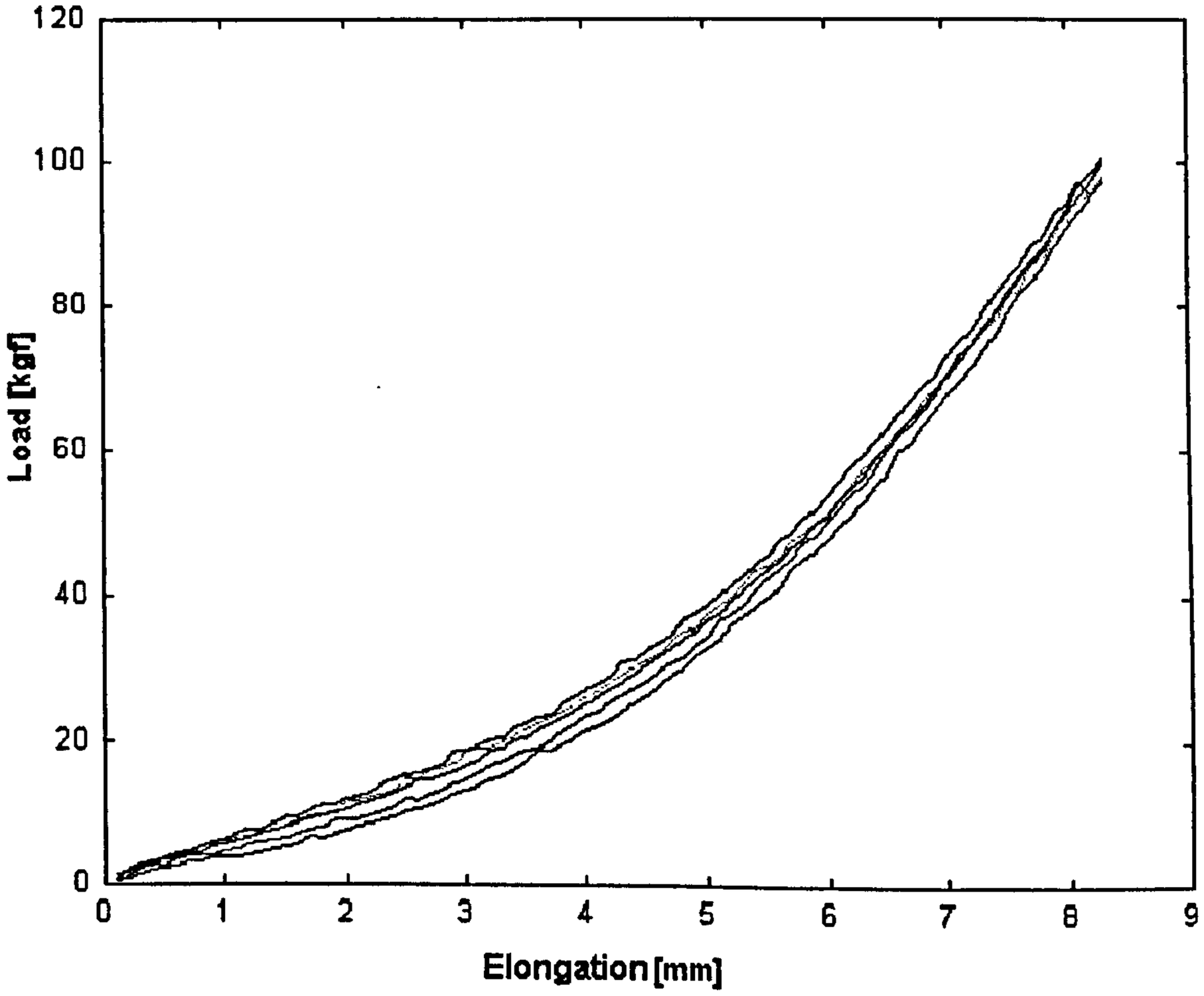

Figure 5.23. Stress-strain test of seat belt with 5 different constant strain rates.

These 5 different constant speed test results were averaged and one representative curve was used for the rest of the calculations. Curve fitting was achieved using linear load and strain scales. A third degree polynomial curve (see equation 5.6 and 5.7) was nicely fitted to the stress-strain data of the seat belt. The third degree polynomial curve fitting to the averaged stress-strain data can be seen in figure 5.24.

The mathematical relation between the stress and strain is shown in equations 5.6 and 5.7:

Stress as a function of strain;

$$\sigma(\varepsilon) = 0.0828\varepsilon^3 + 0.3954\varepsilon^2 + 2.9178\varepsilon + 1.6694 \tag{5.6}$$

Strain as a function of stress;

$$\varepsilon(\sigma) = 0.000012\sigma^3 - 0.0026\sigma^2 + 0.2201\sigma - 0.0408 \tag{5.7}$$

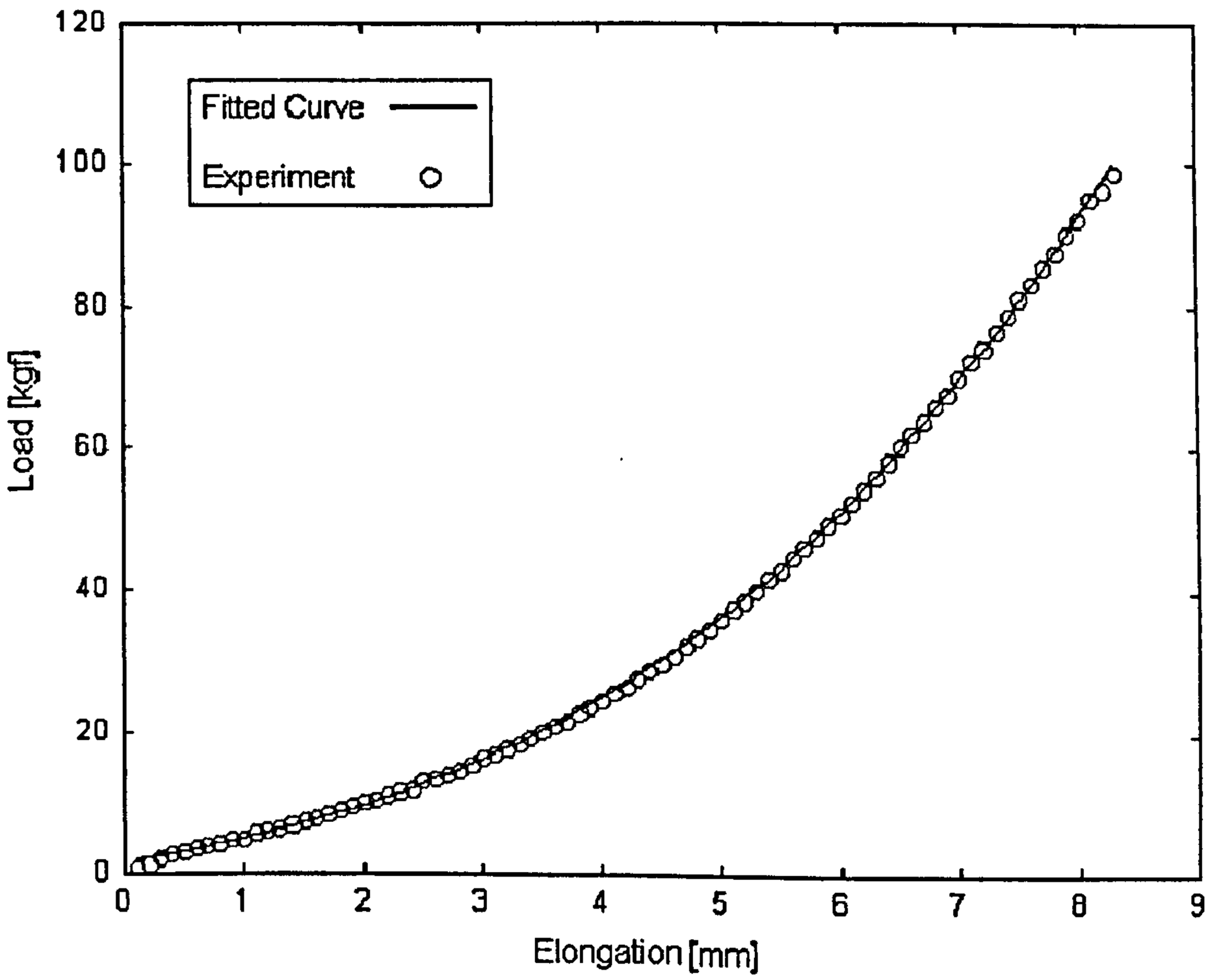

Figure 5.24. Third degree polynomial curve fitting to stress-strain data of seat belt for averaged constant strain rates.

5.7. Summary

To unify the test results, curves were fitted to the creep, the stress-relaxation and the stress-strain results, in keeping with the work of other researchers. In this chapter, the raw data were expressed as polynomial approximations.

Chapter 6

Mechanical Models of Viscoelastic Behaviour

6.1. Viscoleastic Models

Using mechanical modelling techniques, the viscoelastic behaviour of soft tissue was examined. The examination helped to represent the raw data as a mechanical model. Defining parameters in the mechanical model generalised the soft tissue behaviour and increased the predictability.

Very simple models can represents the general creep and stress-relaxation behaviour of soft tissues. The simplest mechanical model that has some of the gross physical behaviour exhibited by bodies subject to uniaxial elongation is a pure Hookean spring (Fig. 6.1). This element is purely elastic and all internal effects are neglected. If the Hookean spring is subjected to an instantaneous stress (σ_0), it will respond instantaneously with a strain ε_0, σ_0 and ε_0 being related by equation 6.1.

$$\sigma_0 = E\varepsilon_0 \tag{6.1}$$

The proportionality constant, E, is the Elastic modulus, which has already been discussed (chapter 1). The instantaneous stress application is assumed to produce no oscillations, only a constant strain [4, 47, 20].

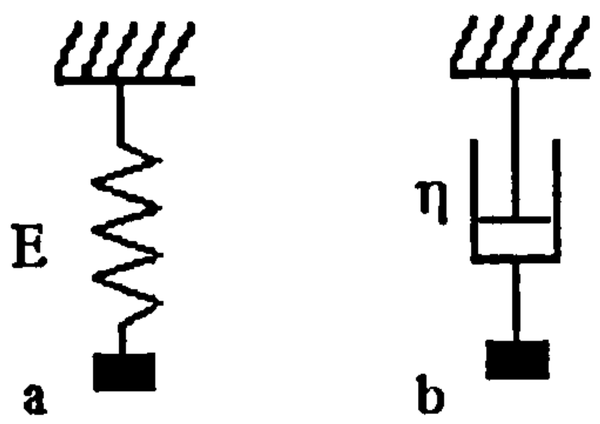

Figure 6.1. Schematic representation of spring and dashpot.

The dominant characteristic of fluids is not their elasticity, but rather their viscosity.

$$\sigma = \eta \frac{d\varepsilon}{dt} \tag{6.2}$$

Newton's law of viscosity (Eq. 6.2) is the equation of motion for a model with a simple linear viscous behaviour. The mechanical analogue of equation (Eq. 6.2) is the dashpot element (Fig. 6.1(b)). This is like a piston in a cylinder filled with a liquid of viscosity η. Integration of the equation 6.2 for constant stress σ_0, yields [4, 20, 47]

$$E(t) = \frac{\sigma_0}{\eta} t \tag{6.3}$$

6.1.1. Maxwell Model

The mechanical response of viscoelastic bodies is poorly represented by either the spring or the dashpot. J.C.Maxwell suggested that a better approximation would result from a series combination of the spring and dashpot element. Such a model, called a Maxell element, is as shown in figure 6.2. The modulus or stiffness of the spring is E and the viscosity of the dashpot is η [4, 20, 47].

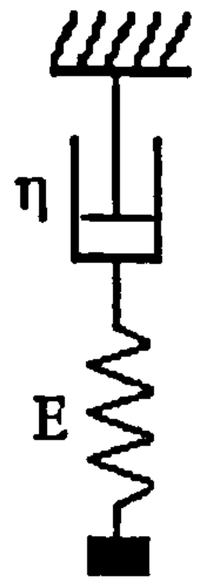

Figure 6.2. Maxwell model

In a stress-relaxation experiment, the model is given a definite strain ε while the stress σ is measured as function of a time.

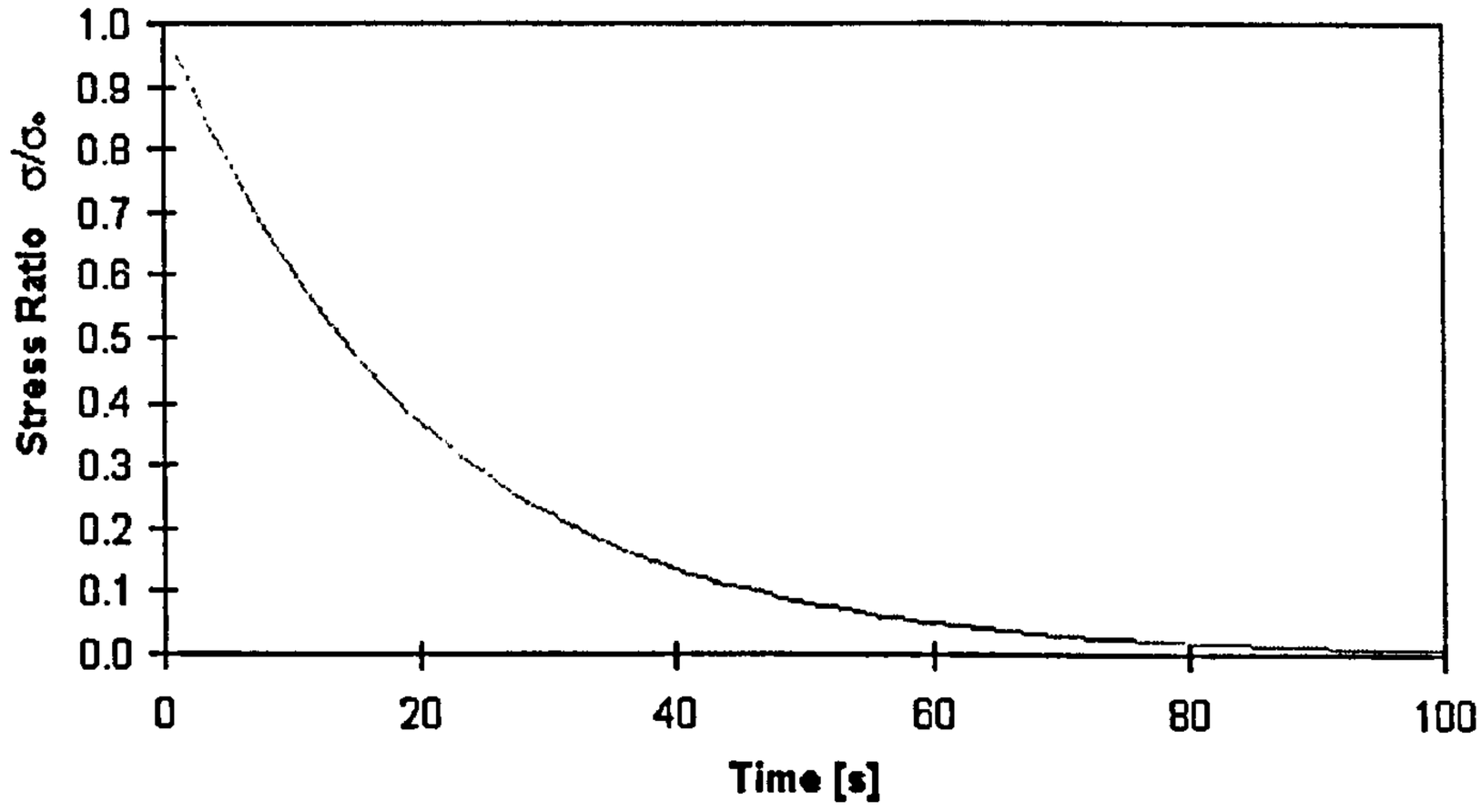

Figure 6.3. Typical stress-relaxation curve on linear time scales.

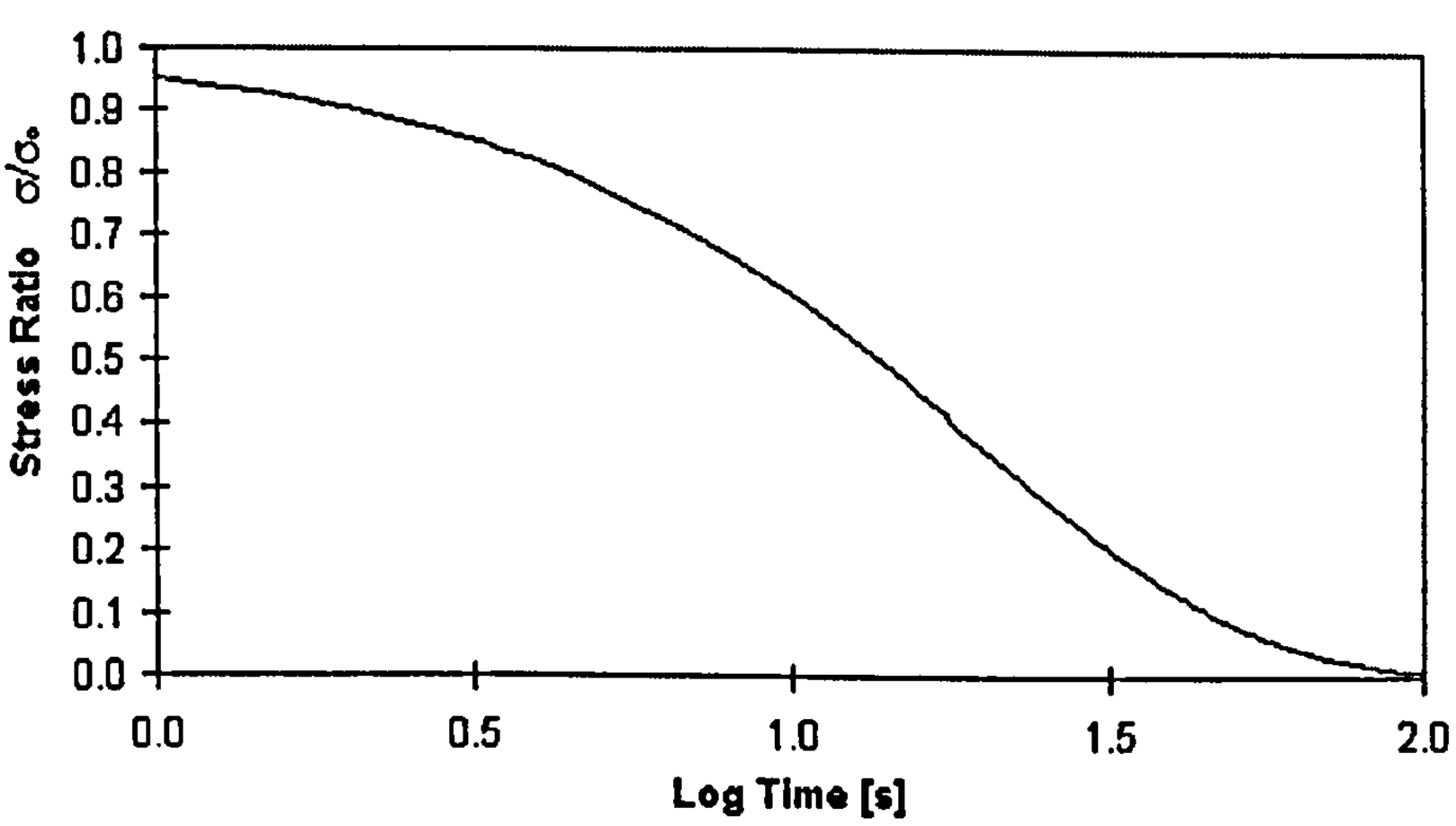

Figure 6.4. Stress-relaxation of a Maxwell model on logarithmic time scale [4, 20].

In the strained model, the change of the elongation of the spring is compensated by an equal change in the dashpot so that the net rate of change is zero. The equation of motion of the Maxwell model [4, 47, 20] is:

$$\frac{d\varepsilon}{dt} = \frac{1}{\mathrm{E}}\frac{d\sigma}{dt} + \frac{\sigma}{\eta} = 0 \tag{6.4}$$

since $\varepsilon = \sigma / \mathrm{E}$ for the spring and $\sigma / \eta = d\varepsilon / dt$ for the dashpot. The solution of the above equation of motion is

$$\frac{\sigma}{\sigma_0} = \mathrm{e}^{-\left(\frac{\mathrm{E}t}{\eta}\right)} = \mathrm{e}^{-t/\tau} \tag{6.5}$$

where;

$$\tau = \eta/\mathrm{E} \tag{6.6}$$

The quantity τ is called the relaxation time of the element.

Equation 6.5 is plotted with two different time scales in figures 6.3 and 6.4 for values that are typical of a viscoelastic material. All the initial deformation takes place in the spring element, while at a later time the dashpot starts to relax so that the stress decreases as a function of time. Most of the relaxation takes place within one decade of time on both sides of the relaxation time [4].

6.1.2. Kelvin-Voigt Model

Another simple element that has been used frequently in connection with viscoelastic behaviour is called the Kelvin-Voigt model. It was first proposed by Kelvin and later, independently, by Voigt [47]. It is more generally known as the Voigt model. The Kelvin-Voigt model has the same fundamental elements as the Maxwell model, except here the spring and the dashpot are in parallel instead of being in series (Fig. 6.5).

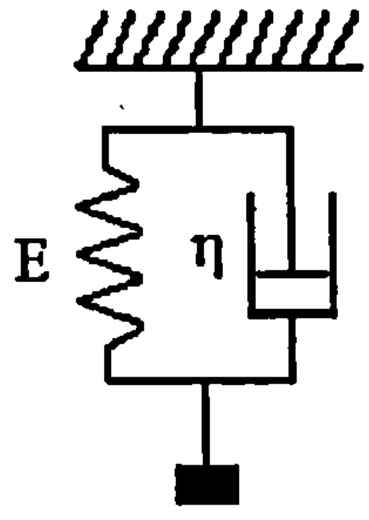

Figure 6.5. Kelvin-Voigt model.

The constraint on the model is that the strain must be the same in both elements. The stress then must be the sum of the stresses in the two individual elements. Thus the fundamental equation of motion for the Kelvin-Voigt model is explained in equation 6.7 [4, 47, 20].

$$\sigma(t) = \varepsilon(t)E + \eta\frac{d\varepsilon(t)}{dt} \tag{6.7}$$

This model is usually used in considering creep experiments. It is not easy to apply to a stress-relaxation experiment. Since the stress is a constant in a creep experiment:

$$\frac{d\varepsilon(t)}{dt} + \frac{\varepsilon(t)}{\tau} = \frac{\sigma_0}{\eta} \tag{6.8}$$

Equation 6.8 is a linear differential equation which can be made exact and then integrated, using the integrating factor $e^{t/\tau}$. The result of the integration is:

$$\varepsilon(t) = \frac{\sigma_0}{E}\left(1 - e^{-t/\tau}\right) \tag{6.9}$$

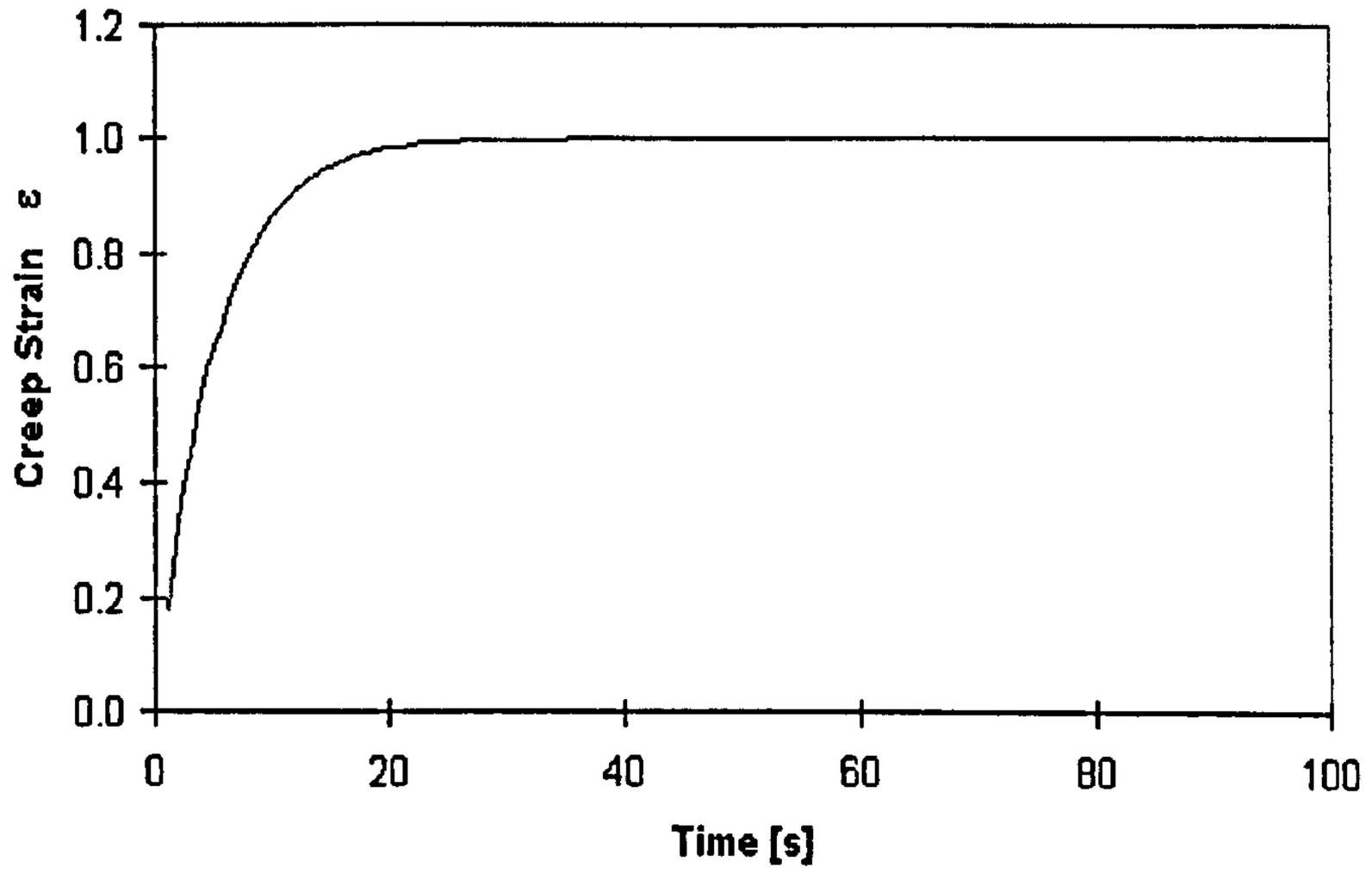

Figure 6.6. Creep behaviour of Kelvin-Voigt model on linear time scale.

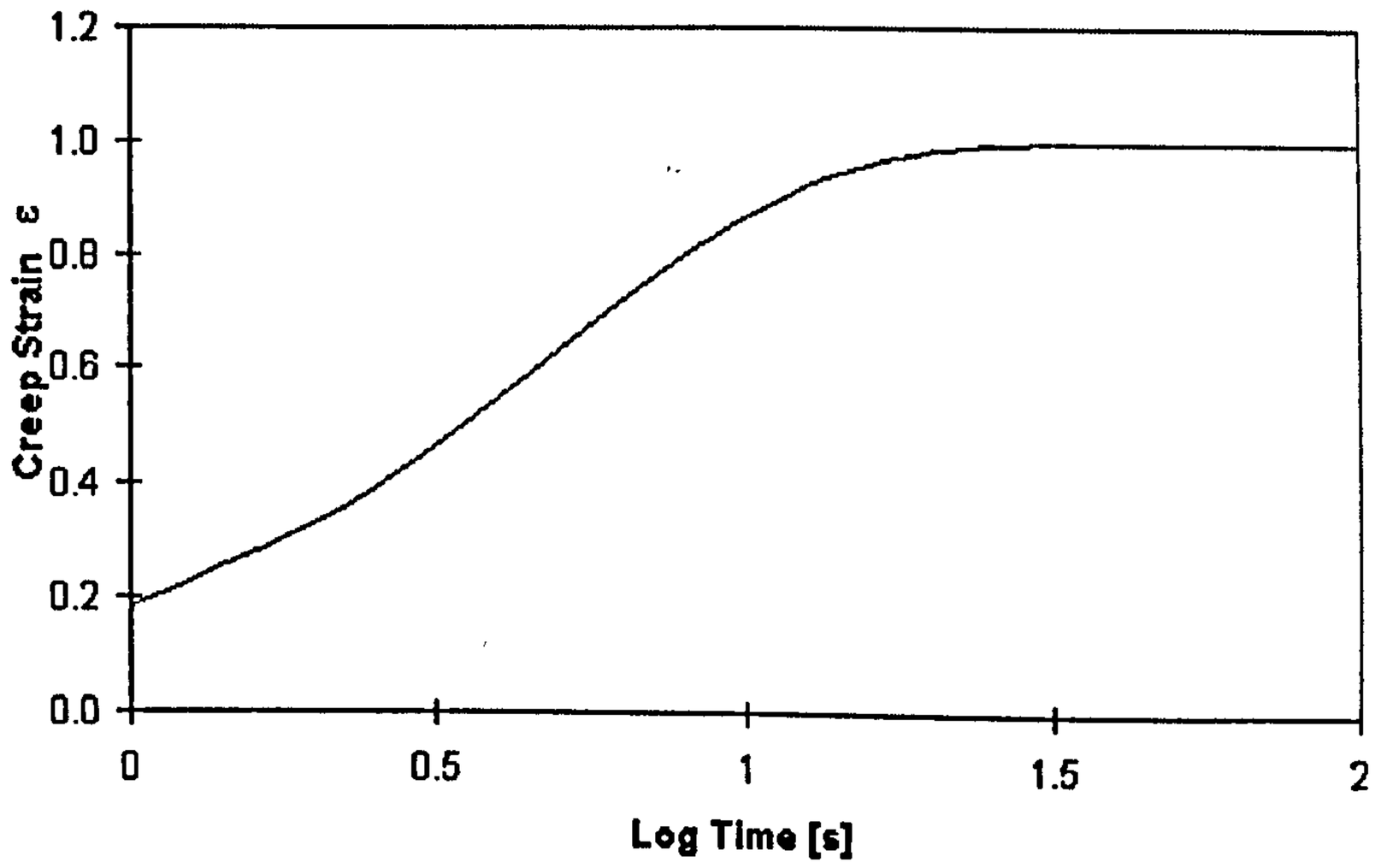

Figure 6.7. Creep behaviour of Kelvin-Voigt model on logarithmic time scale.

Equation 6.9 is plotted with two different time scales in figures 6.6 and 6.7 for typical responses of the Kelvin-Voigt model. When a constant load or force is applied to the model, all the deformation takes place at the same time in the spring and dashpot elements. Elongation continues until the model reaches the equilibrium state. It is clear that stress-relaxation cannot be simulated on a Kelvin-Voigt model, since it would take an infinite force to strain the viscous element instantaneously.

6.2. Standard Linear Solid

The standard linear solid (SLS) is a mechanical model of viscoelastic behaviour consisting of a spring which is in parallel with a series connection of a spring and dashpot as shown in figure 6.8. [47, 20].

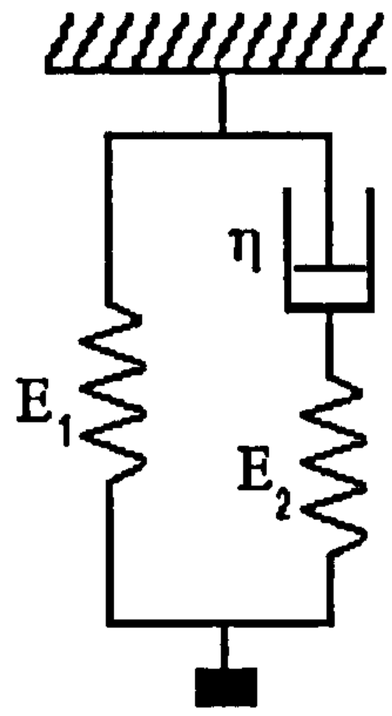

Figure 6.8. Standard linear solid

Proceeding in a similar manner as for the Kelvin-Voigt model, it can be written;

$$\sigma_1 = E_1 \varepsilon_1 \tag{6.10}$$

$$\sigma_2 = E_2 \varepsilon_2 \tag{6.11}$$

for the springs, and

$$\sigma_3 = \eta \frac{d\varepsilon_d}{dt} \tag{6.12}$$

for the dashpot. The applied stress (σ) is equal to $(\sigma_1 + \sigma_2)$ and also $(\sigma_2 = \sigma_3)$. As for the total strain ($\varepsilon = \varepsilon_1 = \varepsilon_2 + \varepsilon_d$). By differentiating the strain with respect to time:

$$\frac{d\varepsilon}{dt} = \frac{d\varepsilon_2}{dt} + \frac{d\varepsilon_d}{dt} = \frac{1}{\mathrm{E}_2}\frac{d\sigma_2}{dt} + \frac{\sigma_2}{\eta} \tag{6.13}$$

after substituting from equation 6.10 and 6.12. Rearranging and putting:

$$\tau = \frac{\eta}{\mathrm{E}_2} \tag{6.14}$$

which gives the constitutive equation of the standard linear solid [20, 47]:

$$\sigma + \tau\frac{d\sigma}{dt} = \mathrm{E}_1\varepsilon + (\mathrm{E}_1 + \mathrm{E}_2)\tau\frac{d\varepsilon}{dt} \tag{6.15}$$

6.2.1. Stress-Relaxation Behaviour of Standard Linear Solid

In the stress-relaxation test, the strain is constant at $\varepsilon = \varepsilon_0$. Thus, the change of the strain by time $\frac{d\varepsilon}{dt} = 0$.

$$\sigma + \tau\frac{d\sigma}{dt} = \mathrm{E}_1\varepsilon_0 \tag{6.16}$$

Noting that, at t = 0, total stress is $\sigma = (\mathrm{E}_1 + \mathrm{E}_2)\varepsilon_0$. Finally, equation 6.17 gives the stress response as:

$$\sigma = (\mathrm{E}_1 + \mathrm{E}_2 e^{-t/\tau})\varepsilon_0 \tag{6.17}$$

6.2.2. Creep Behaviour of Standard Linear Solid

In a creep test, stress is constant at $\sigma = \sigma_0$. Thus $\frac{d\sigma}{dt} = 0$ and

$$\varepsilon + \alpha\tau \frac{d\varepsilon}{dt} = \frac{\sigma_0}{E_1} \tag{6.18}$$

where:

$$\alpha = \frac{E_1 + E_2}{E_1} \tag{6.19}$$

At $t = 0$, $\varepsilon = \frac{\sigma_0}{E_1 + E_2}$. Thus, the creep response is obtained from equation 6.18 as:

$$\varepsilon = (1 - \beta e^{-t/\alpha\tau}) \frac{\sigma_0}{E_1} \tag{6.20}$$

where:

$$\beta = \frac{E_2}{E_1 + E_2} \qquad [20] \tag{6.21}$$

6.3. Mechanical Modelling of Bulk Tissue

To overcome deficiencies, models have been proposed that consist of combinations of the Voigt model for creep behaviour and the Maxell model for stress-relaxation. It is clear that an infinite number of such combinations are possible. Basically in this study, four mechanical models were used to represent the upper arm. Each one represented one main part of the upper arm. Three obvious materials of the arm - skin, fat and muscle - were modelled logically (Fig. 6.9). There were also effect of blood vessels and connective tissue, which were modelled in series to the previous ones. In figure 6.9, a sample cross-section of the upper arm and the model representation are shown.

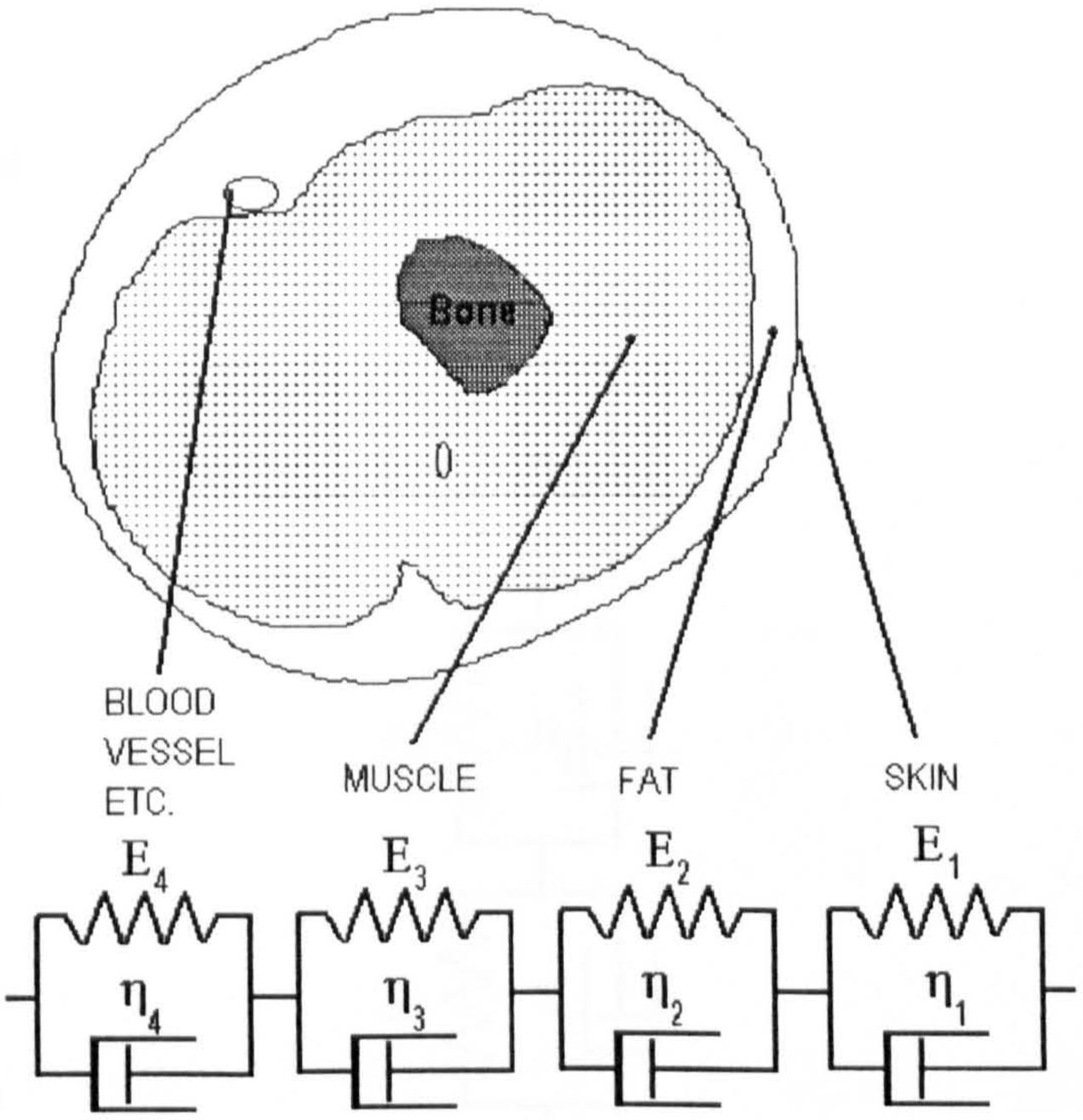

Figure 6.9. Simulation of creep behaviour with four Voigt models in series.

6.3.1. Creep Behaviour of Bulk Tissue

Creep behaviour can be simulated by the four Voigt models in series which are shown in figure 6.10. When a constant load is applied, the initial elongation comes from the springs with moduli E_1, E_2, E_3 and E_4. Later elongation comes from the movement of dashpots with viscosities of η_1, η_2, η_3 and η_4. The total elongation of the model is the sum of the individual elongation of the four parts. The change of the elongation by time is explained by equation 6.22.

$$\varepsilon(t) = \frac{\sigma_0}{E}\left(4 - e^{-t/\tau_1} - e^{-t/\tau_2} - e^{-t/\tau_3} - e^{-t/\tau_4}\right) \tag{6.22}$$

where σ_0 is the applied stress, and the retardation time is defined by:

$$\tau = \frac{\eta_n}{E_n} \tag{6.23}$$

for every model.

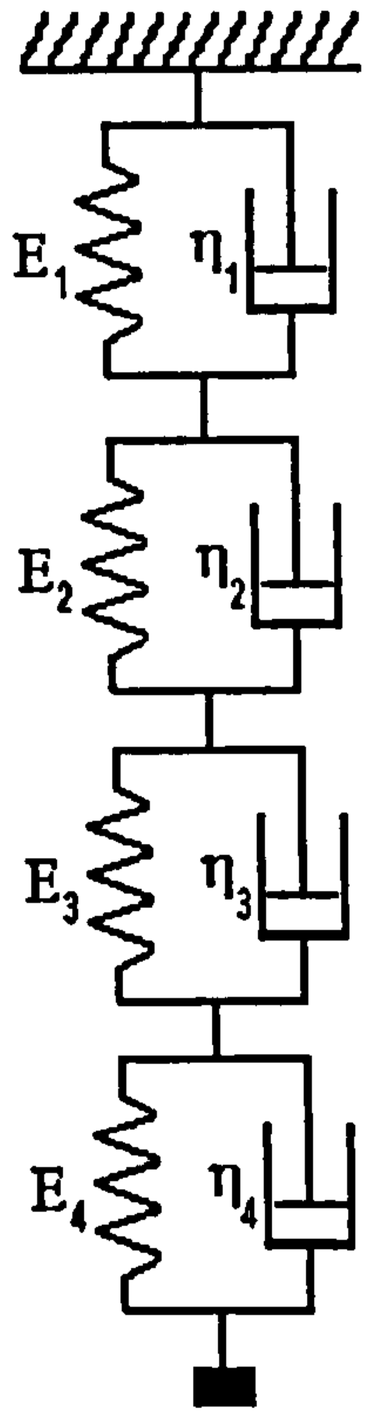

Figure 6.10. Simulation of creep behaviour with four Voigt model in series.

Model fitting was completed by using Matlab commercial software. A new Matlab script was written to find the closest model parameters for each test mentioned in chapter 5. Model fitting was achieved in the linear scale and the natural logarithmic scale. The main reason to use logarithmic scale was to visualise better the start of model fitting. A single Elastic Modulus (E) was defined to represent the bulk modulus of the upper arm. Examples of the model fitting in linear and natural logarithmic scales are shown in figure 6.11. The parameters of the model fitting of the creep results are summarised in table 6.1. The rest of the model fitting figures are represented in appendix B.3.

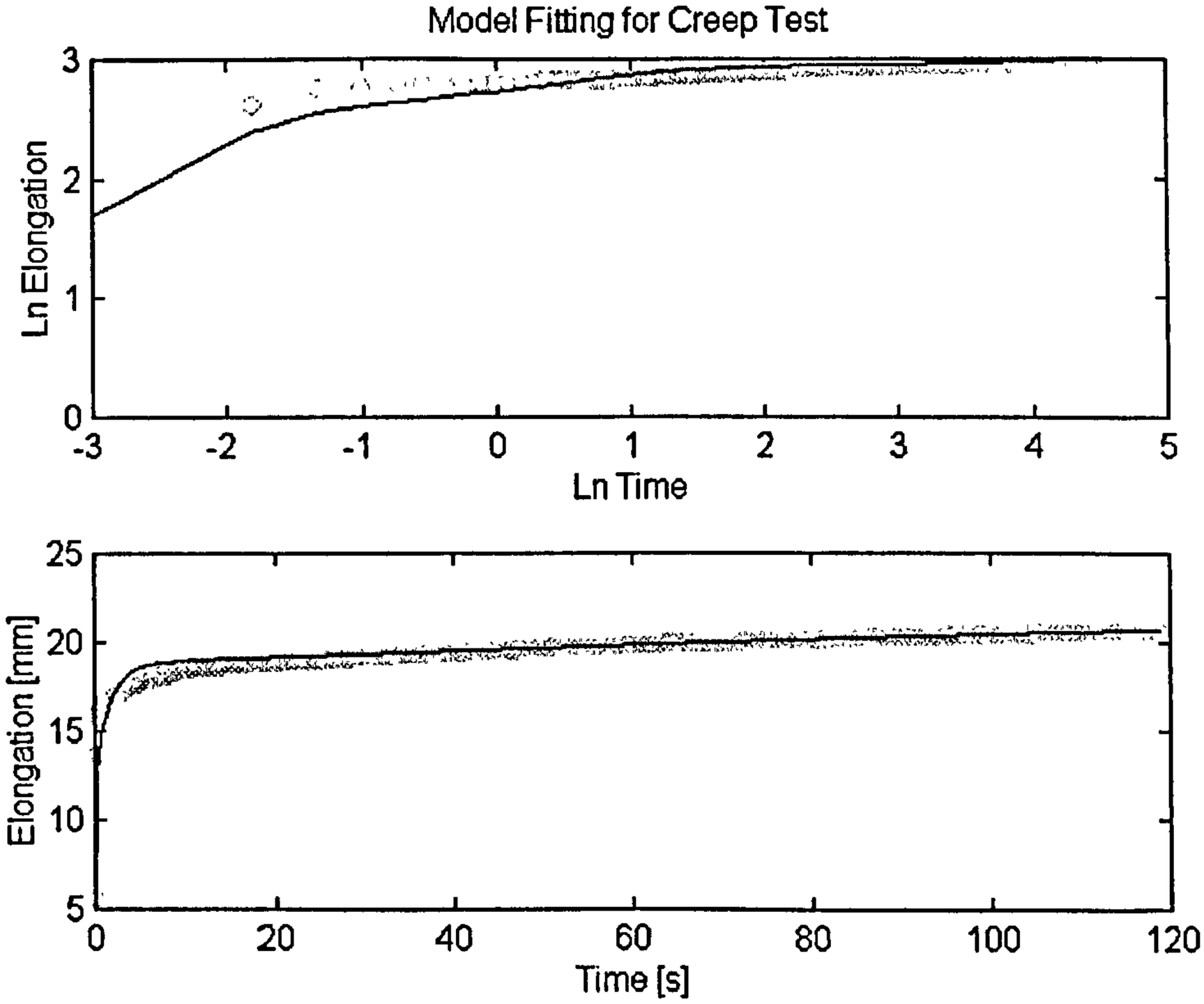

Figure 6.11. Model fitting for creep test of 25 % MVC with 60 kgf constant load.

Load (kgf)	Type	E (kPa)	τ_1 (s)	τ_2 (s)	τ_3 (s)	τ_4 (s)
10	Relaxed	42.5	0.416	0.833	1.666	312.5
10	25 % MVC	48.5	0.083	0.1	1.666	312.5
20	Relaxed	45	0.416	0.833	1.666	312.5
20	25 % MVC	51.5	0.083	0.1	1.666	312.5
30	Relaxed	50.5	0.416	0.833	1.666	312.5
30	25 % MVC	54	0.083	0.1	1.666	312.5
40	Relaxed	65.5	0.416	0.833	1.666	312.5
40	25 % MVC	71	0.083	0.1	1.666	312.5
50	Relaxed	80	0.416	0.833	1.666	312.5
50	25 % MVC	83	0.083	0.1	1.666	312.5
60	Relaxed	92	0.416	0.833	1.666	312.5
60	25 % MVC	96	0.083	0.1	1.666	312.5

Table 6.1. Model parameters of the creep behaviour.

6.3.2. Stress-Relaxation Behaviour of Bulk Tissue

The stress-relaxation behaviour can be simulated by the four Maxell models in series which are shown in figure 6.12. When a constant strain is applied, the sudden movement comes from the springs with the moduli E_1, E_2, E_3 and E_4. Later the relaxation of the springs comes from the movement of dashpots with viscosities of η_1, η_2, η_3 and η_4. The total change of the stress of the model is the sum of the stresses of the individual models in series. Thus the change of the stress with time is explained by equation 6.24.

$$\sigma(t) = \sigma_0\left(e^{-t/\tau_1} + e^{-t/\tau_2} + e^{-t/\tau_3} + e^{-t/\tau_4}\right) \tag{6.24}$$

where σ_0 is the initial stress, and the relaxation time is defined by;

$$\tau = \frac{\eta_n}{E_n}$$

for every model.

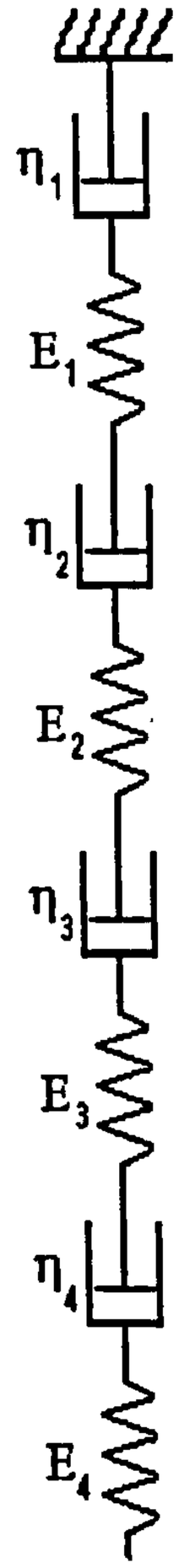

Figure 6.12. Simulation of stress-relaxation behaviour with four Maxell models in series.

As above model fitting was accomplished by using Matlab commercial software. A new Matlab script was written to find the closest model parameters for each test mentioned in chapter 5. Model fitting was achieved in the linear scale and the natural logarithmic scale. Examples of model fitting in linear and natural logarithmic scales are shown in figure 6.13. The parameters of the model fitting of the creep results are summarised in table 6.2. The rest of the model fitting figures are represented in appendix C.3.

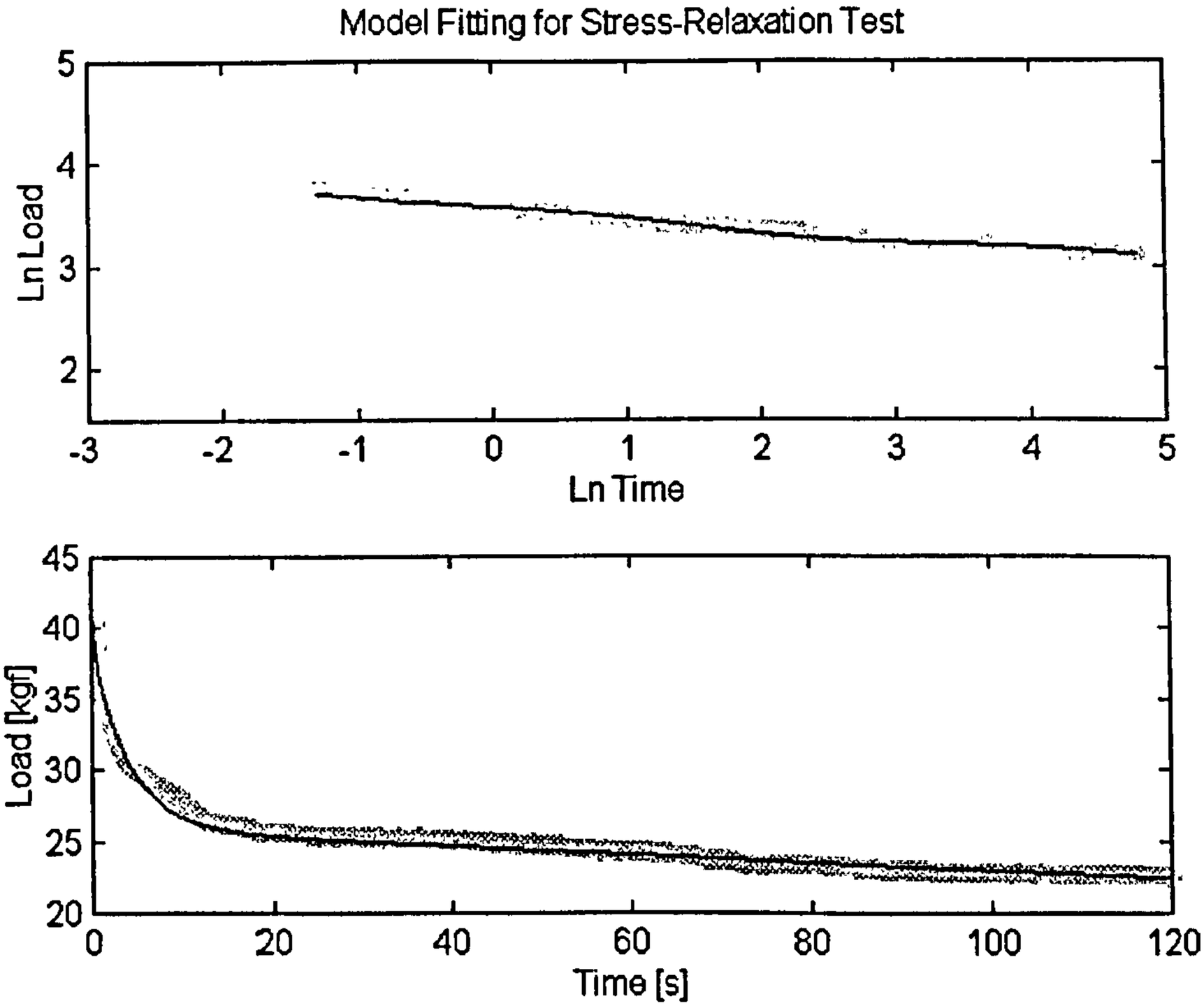

Figure 6.13. Model fitting for stress-relaxation test of 25 % MVC with 20 mm (16 mm corrected) constant strain.

Strain (mm)	Corrected Strain (mm)	Type	σ_0 (kgf)	τ_1 (s)	τ_2 (s)	τ_3 (s)	τ_4 (s)
5	3.94	Relaxed	11.4	0.146	1.818	400	10000
5	3.91	25 % MVC	10.64	0.317	2.222	400	10000
10	8.29	Relaxed	18.08	0.092	0.8	400	10000
10	8.25	25 % MVC	18.08	0.146	2.222	400	10000
15	12.40	Relaxed	30.08	0.113	1.538	400	10000
15	12.33	25 % MVC	27.92	0.162	4	400	10000
20	16.07	Relaxed	50.4	0.206	1.538	400	10000
20	16.01	25 % MVC	51.92	0.162	4	400	10000
25	19.92	Relaxed	79.68	0.689	1.538	400	10000
25	19.68	25 % MVC	79.92	0.869	6.666	400	10000
30	23.90	Relaxed	112.8	0.869	2.857	400	10000
30	23.51	25 % MVC	131.92	0.869	6.666	400	10000

Table 6.2. Parameters of stress-relaxation model.

6.3.3. Stress-Strain Behaviour of Bulk Tissue

Stress-strain behaviour can be simulated by the four Standard Linear Solid (SLS) models in series, which are shown in figure 6.14. When a constant strain-rate is applied, the initial elongation comes from the springs with moduli E_1, E_2, E_3, E_4, E_5, E_6, E_7 and E_8. Later elongation comes from the movement of dashpots, with viscosities η_2, η_4, η_6, and η_8, which depend on the applied strain-rate.

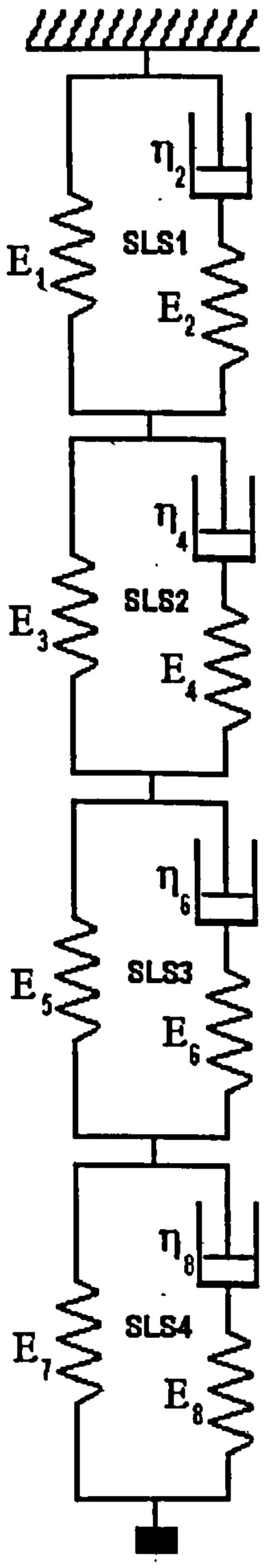

Figure 6.14. Simulation of stress-strain behaviour with four SLS models.

The change of the elongation in the standard linear solid model is explained by equation 6.25. The ratios α and β were defined in equation 6.19 and 6.21 respectively.

$$\varepsilon = (1-\beta_1 e^{-t/\alpha_1 \tau})\frac{\sigma_0}{E_1} + (1-\beta_2 e^{-t/\alpha_2 \tau})\frac{\sigma_0}{E_3} + (1-\beta_3 e^{-t/\alpha_3 \tau})\frac{\sigma_0}{E_5} + (1-\beta_4 e^{-t/\alpha_4 \tau})\frac{\sigma_0}{E_7} \qquad (6.25)$$

Modelling of the stress-strain behaviour was not straightforward; creep and stress-relaxation behaviours of bulk tissue gave very important clues to modelling. First, stress-strain behaviour was modelled by using the same coefficients from creep behaviour modelling. In figure 6.15, the same test shown in figure 6.11 was modelled by using four SLS elements. The same time coefficients (τ_1 τ_2 τ_3 and τ_4) and bulk modulus (E) from creep test modelling were used in the SLS model.

The main difference between the Kelvin-Voigt model and the SLS model is a second spring attached to the dashpot. Therefore, the elastic modulus for each element should be divided between these two springs. Therefore, the distribution of the elastic modulus came from an assumption that 70 % of the material in the upper arm has a viscous part. Accordingly, the best fit of the SLS model was found by changing these distributions. The distribution of the elastic modulus between two springs was as follows: for SLS1 64.5 %, SLS2 69.5 %, SLS3 73 % and SLS4 76.8 %. Another partition of the elastic modulus was to separate the elastic modulus between the SLS elements. This distribution was kept almost equal, which were for SLS1 22 %, SLS2 24 %, SLS3 26 % and SLS4 28 %. The results of the modelling can be seen in figure 6.15.

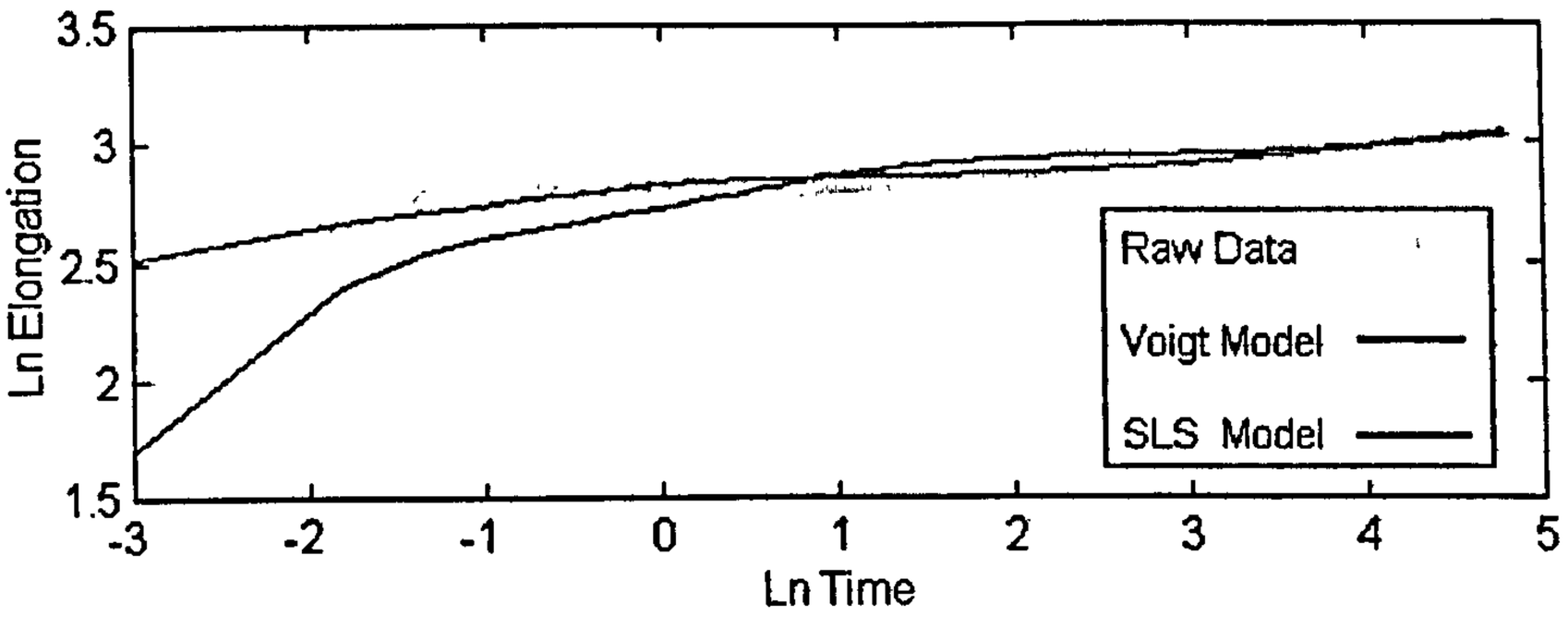

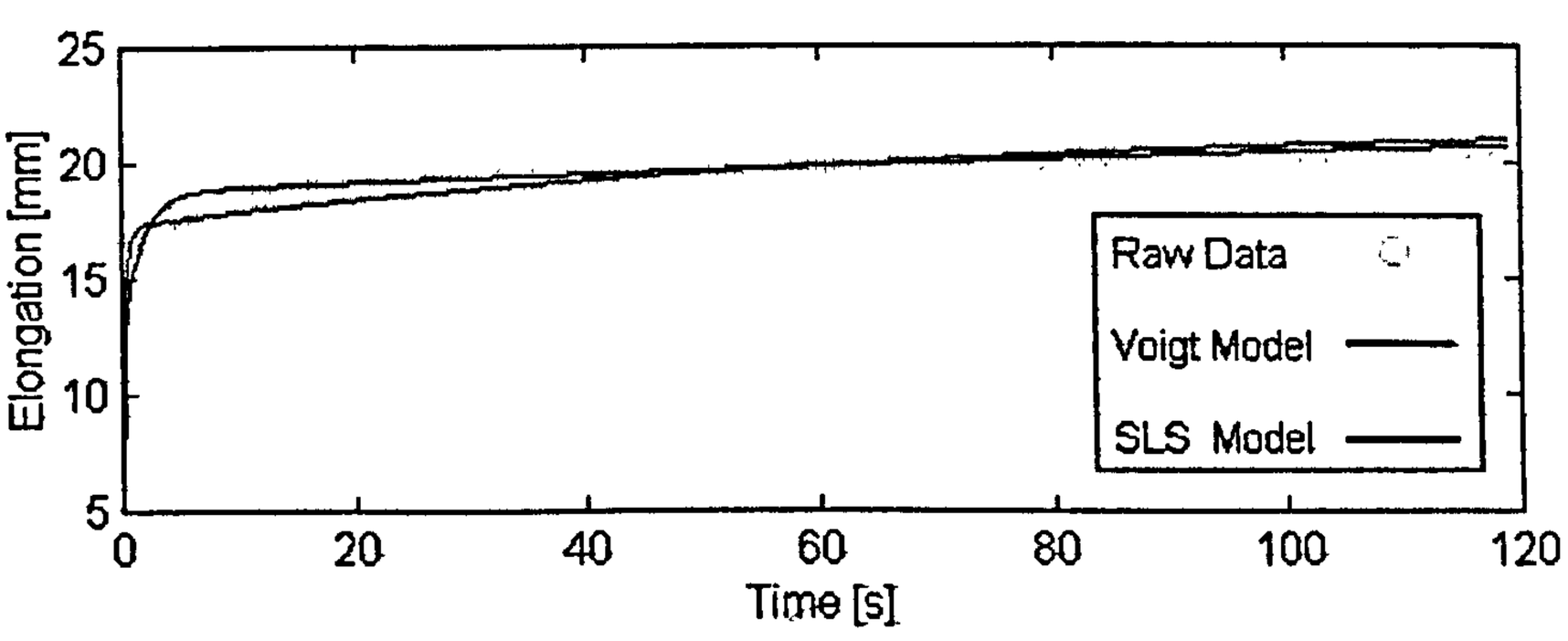

Figure 6.15. Standard linear solid model of creep experiment with 25% MVC.

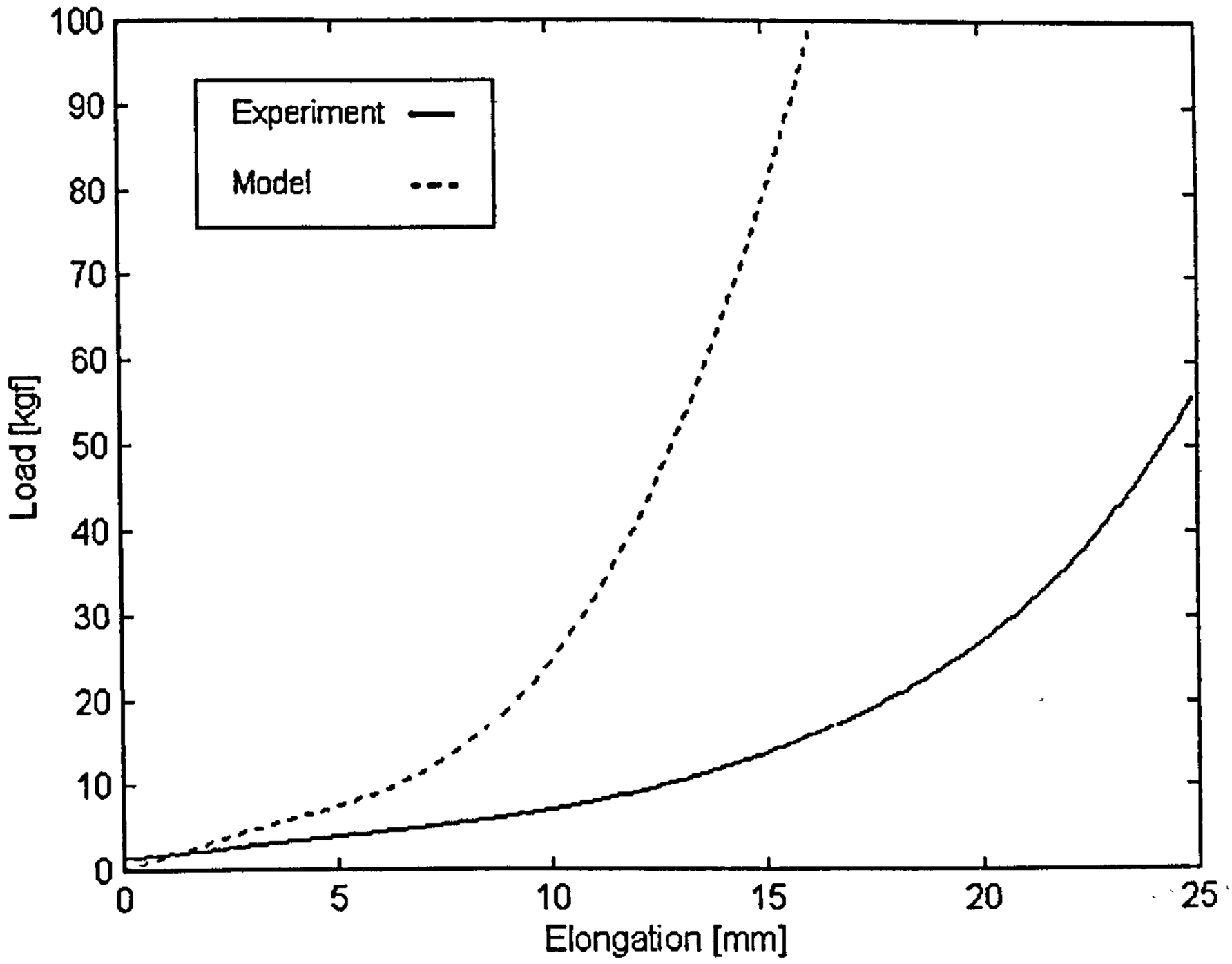

Figure 6.16. The response of the stress-strain simulation of SLS model with the creep model parameters in the contracted procedure.

The same SLS creep model was applied to simulate the stress-strain test with 0.5 $mm.s^{-1}$ constant strain-rate. The response of the SLS model was not satisfactory (Fig. 6.16). The creep model parameters showed a stiffer response than the experiment. The result of the simulation can be seen in figure 6.16, in which the solid line represents the experiment and the dashed line represents the SLS model.

The elastic modulus of the SLS model was calculated from the first derivative of the stress-strain curve fitting equation. In the simulation, the change of the elastic modulus was associated with the strain. Therefore, a new elastic modulus was assigned for each strain increment. Accordingly, the time was also calculated from the speed of the constant strain. The model fitting was corrected by changing the distribution of the elastic modulus between the SLS elements. The distribution of the elastic modulus between the SLS elements was changed to find the closest model to fit the experimental data. The change of the distribution and its effect on the model can be seen in figure 6.17.

The closest model fitting for 0.5 $mm.s^{-1}$ constant strain rate test was plotted in figure 6.18. The distribution of the elastic modulus between the SLS elements was as follows: for SLS1 1.75 %, SLS2 24.25 %, SLS3 33.5 % and SLS4 40.5 %. The same model fitting parameters were used to check the response of the SLS model for different strain-rates. Four different strain-rates, which were 0.5, 1, 2 and 4 $mm.s^{-1}$, were used in the stress-strain test. In the experiment, the faster the strain-rate the stiffer the elastic modulus. Accordingly, a similar response was taken from the SLS model. The response of the SLS model for 1 $mm.s^{-1}$ constant strain-rate was plotted in figure 6.19. In figure 6.20, the response of 2 $mm.s^{-1}$ constant strain test was plotted. Finally, the response of 4 $mm.s^{-1}$ constant strain test is shown in figure 6.21.

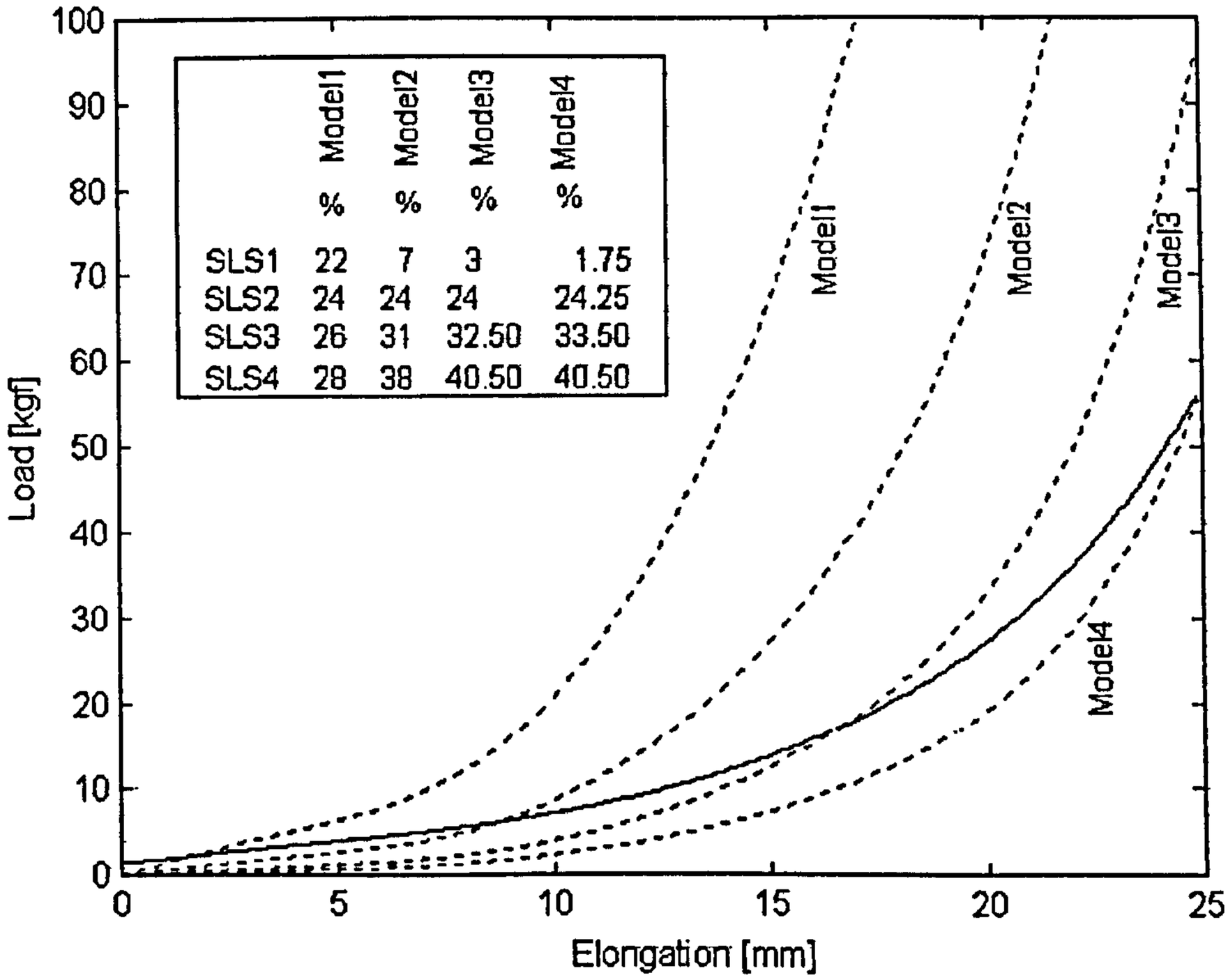

Figure 6.17. The change of the distribution and its effect on the stress-strain model.

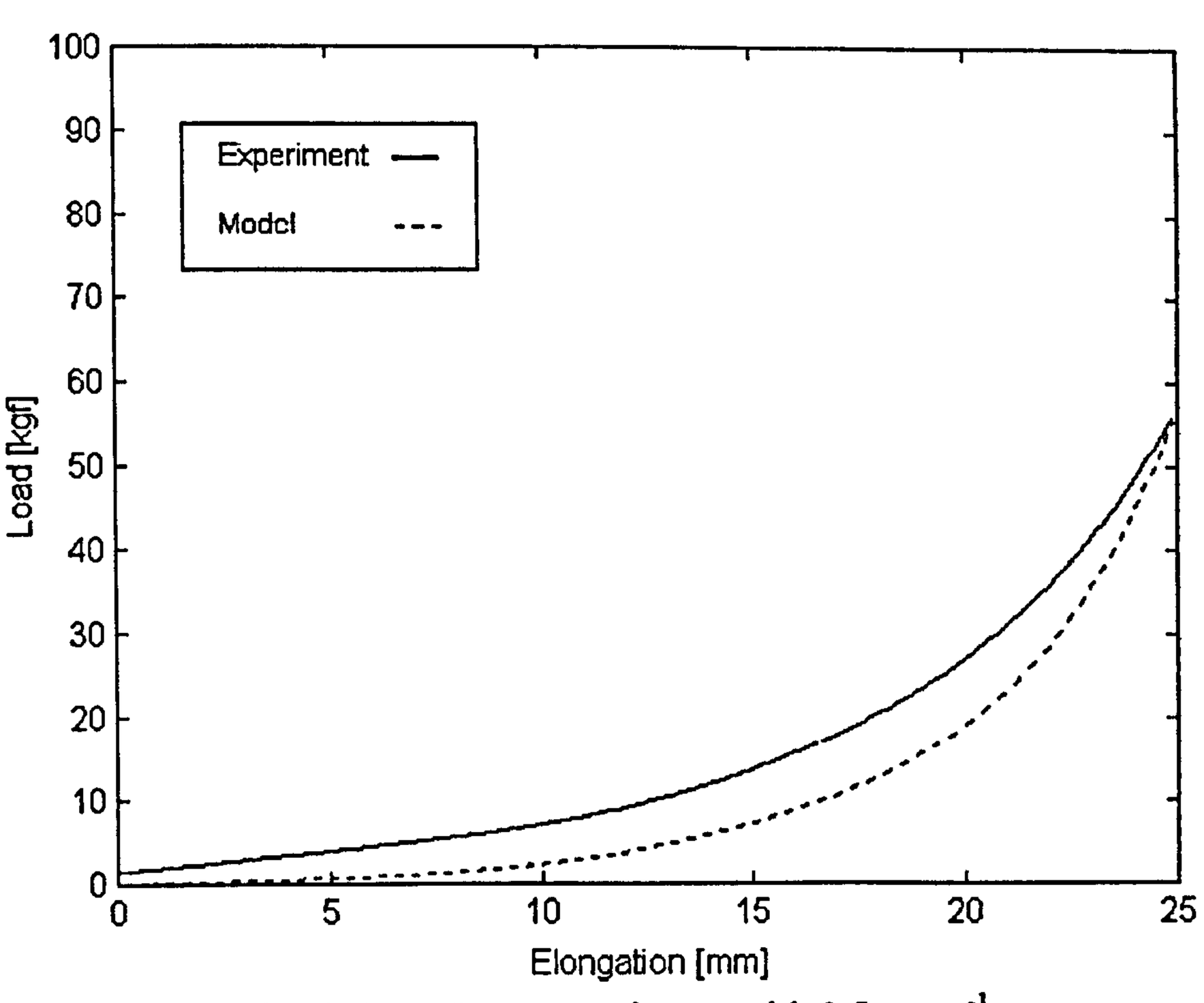

Figure 6.18. SLS simulation of stress-strain test with 0.5 $mm.s^{-1}$ constant strain-rate.

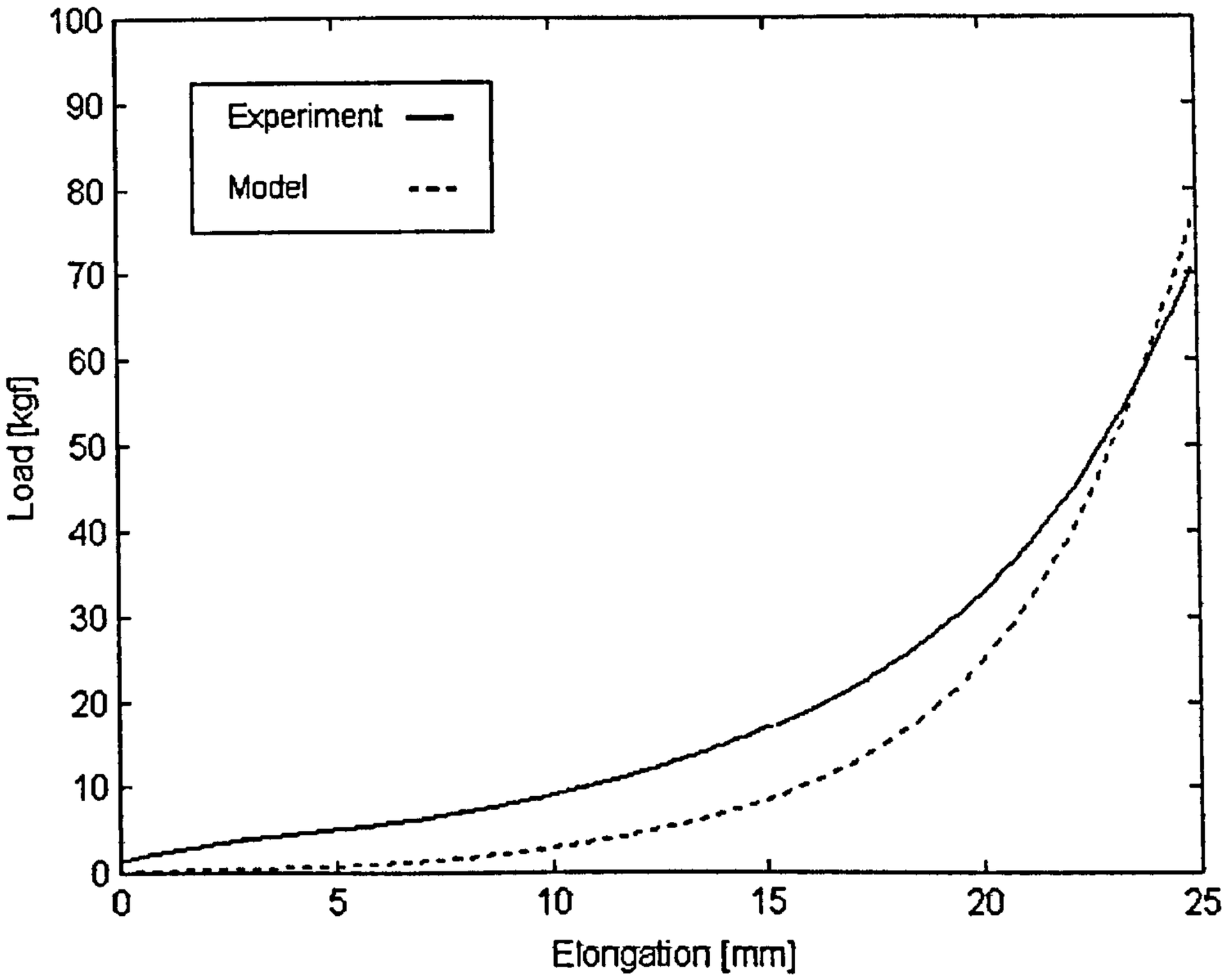

Figure 6.19. SLS simulation of stress-strain test with 1 $mm.s^{-1}$ constant strain-rate.

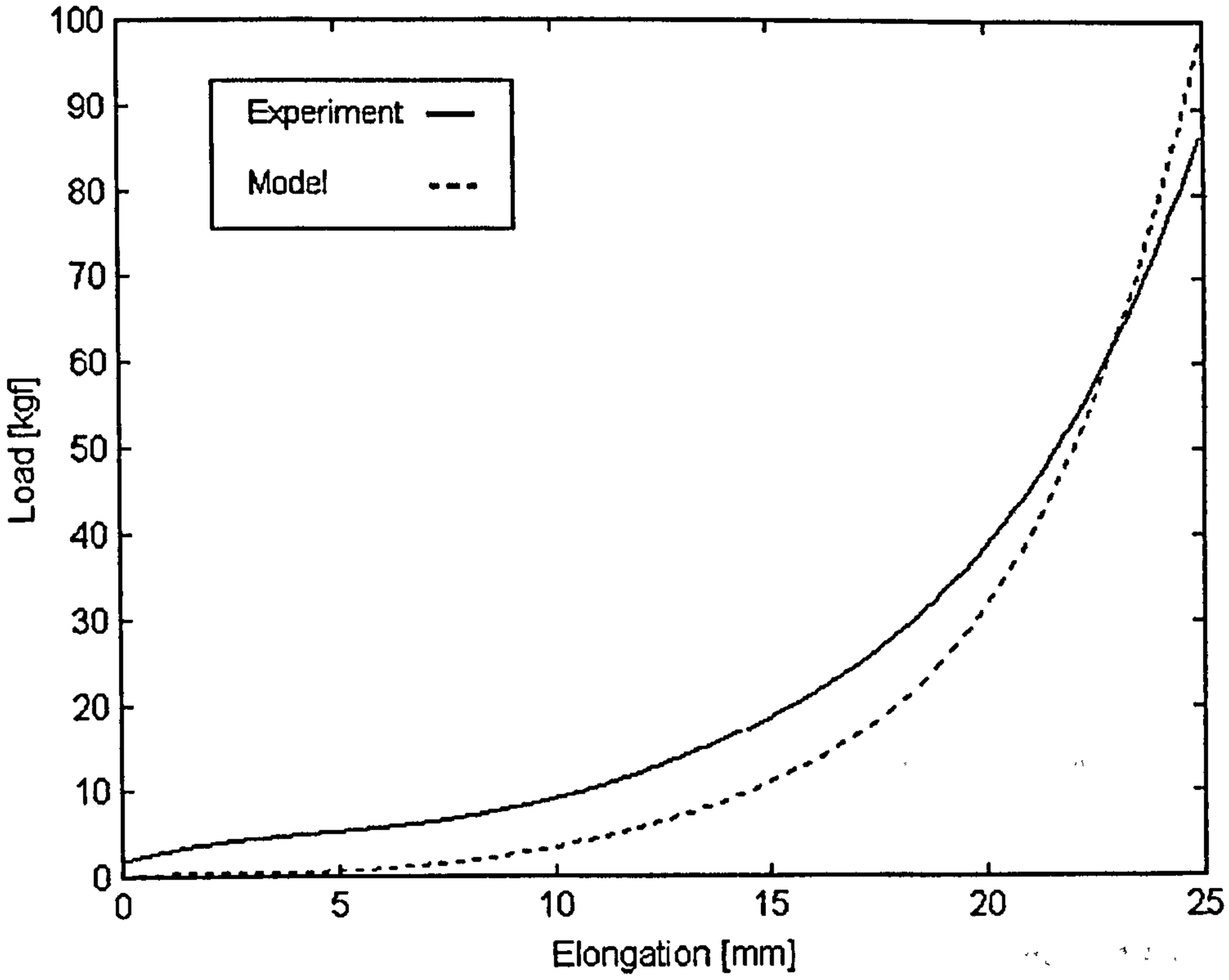

Figure 6.20. SLS simulation of stress-strain test with 2 $mm.s^{-1}$ constant strain-rate.

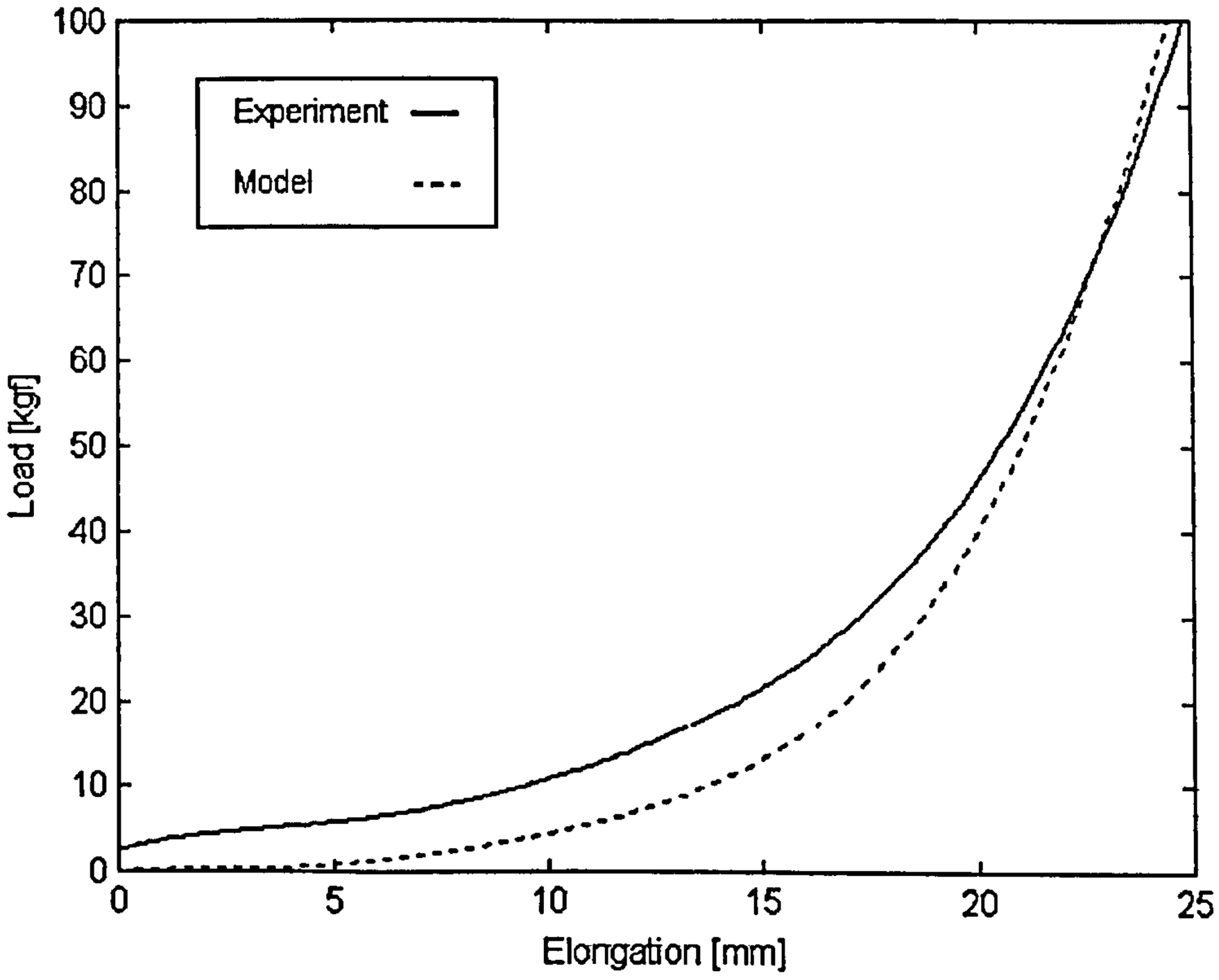

Figure 6.21. SLS simulation of stress-strain test with 4 $mm.s^{-1}$ constant strain-rate.

The same SLS creep model was applied to the relaxed condition of the creep test and the response of the model is plotted in figure 6.22. Then, the creep SLS model was configured to simulate the stress-strain test with 0.5 $mm.s^{-1}$ constant strain-rate. The response of the SLS model was very similar to the response of the contracted test (Fig. 6.16). The creep model parameters showed a stiffer response than the experiment. The result of the simulation can be seen in figure 6.23 in which the solid line represents the experiment and the dashed line represents the SLS model.

The model fitting was corrected by changing the distribution of elastic modulus between the SLS elements. The same distribution ratios as in the contracted test were used to partition the elastic modulus between SLS elements. The response of the SLS model for 0.5 $mm.s^{-1}$, 1 $mm.s^{-1}$, 2 $mm.s^{-1}$ and 4 $mm.s^{-1}$ constant strain-rates are plotted in figures 6.24, 6.25, 6.26 and 6.27 respectively.

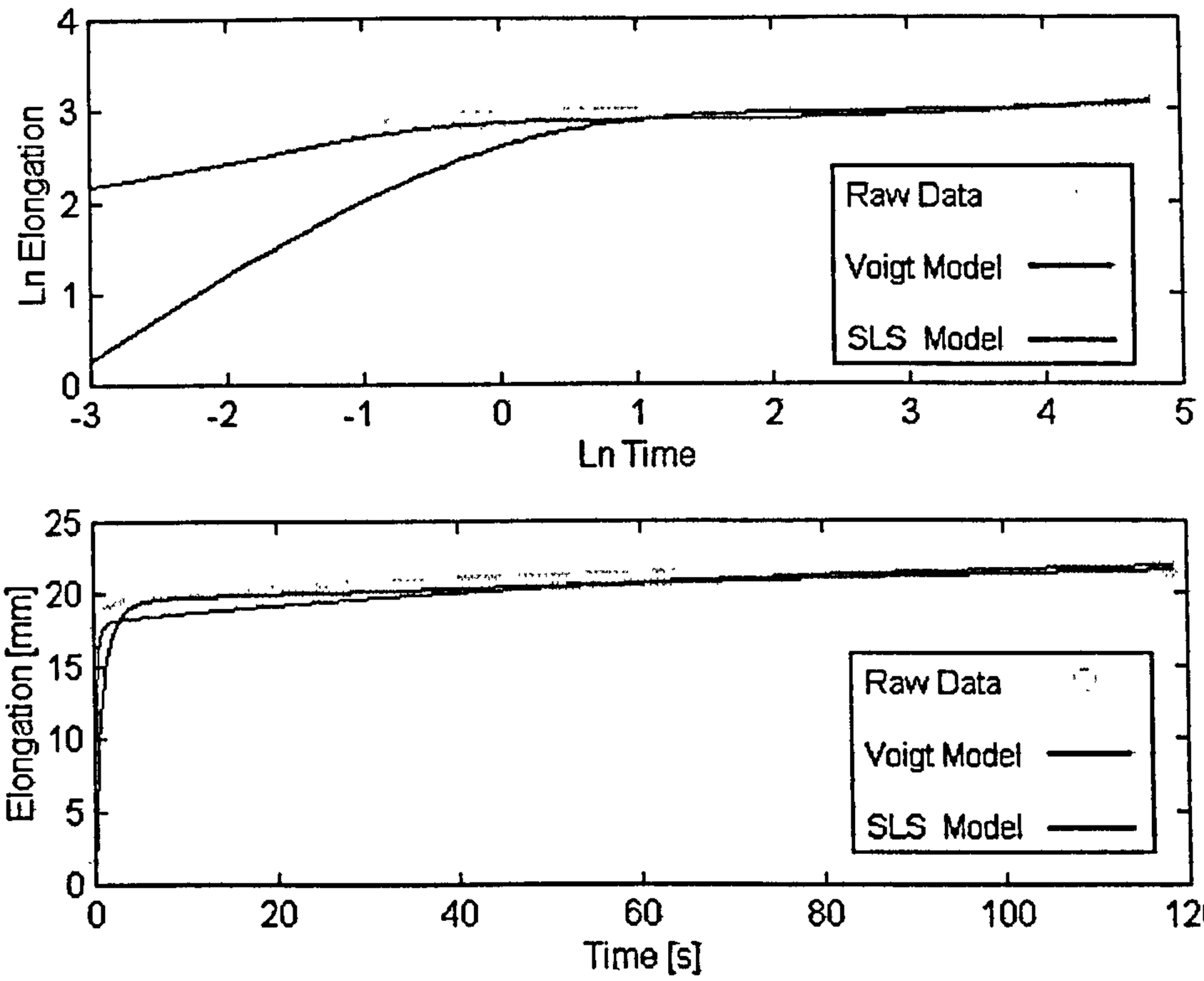

Figure 6.22. Standard linear solid model of creep experiment with relaxed condition.

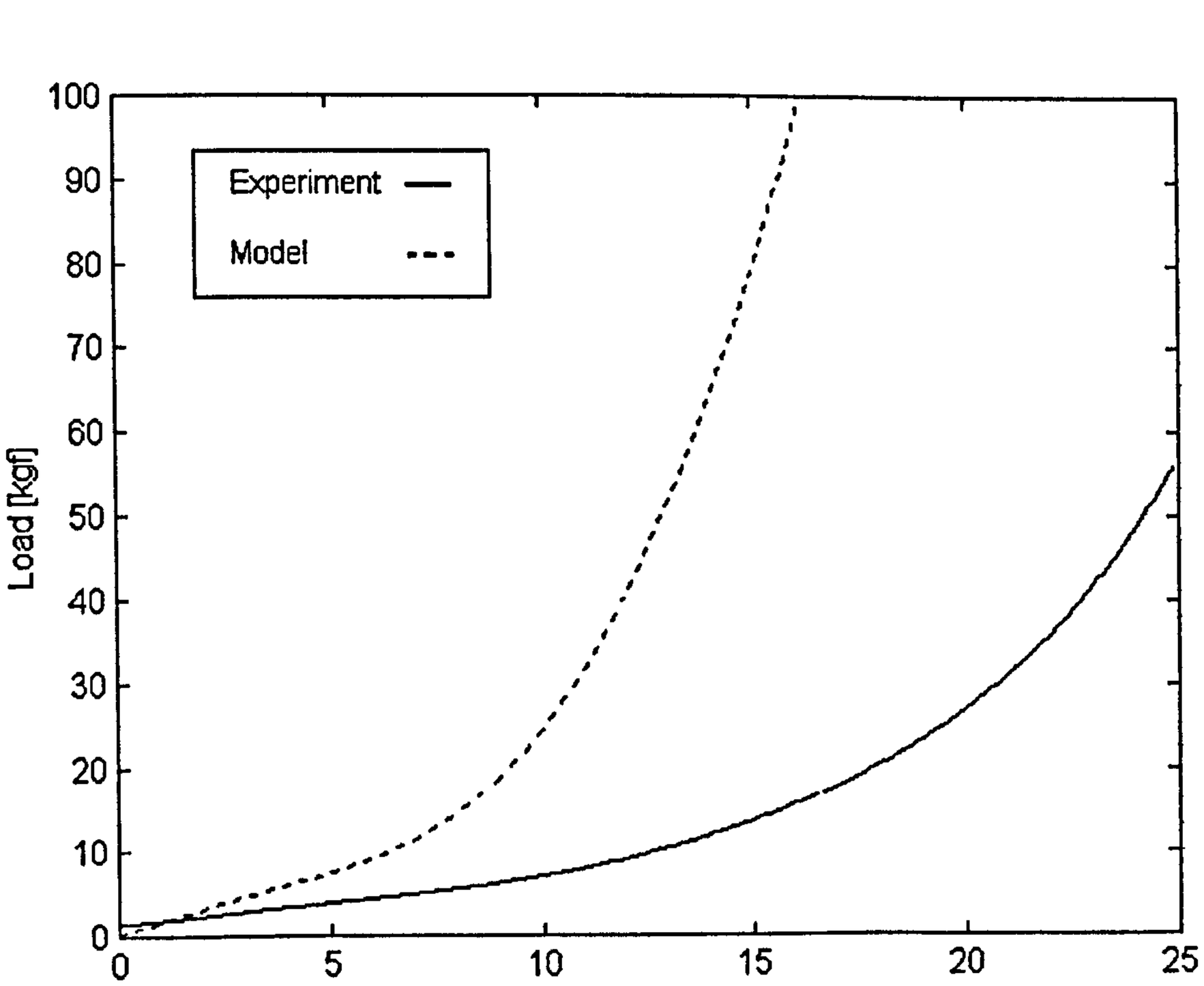

Figure 6.23. The response of the stress-strain simulation of the SLS model with the creep model parameters (relaxed test condition).

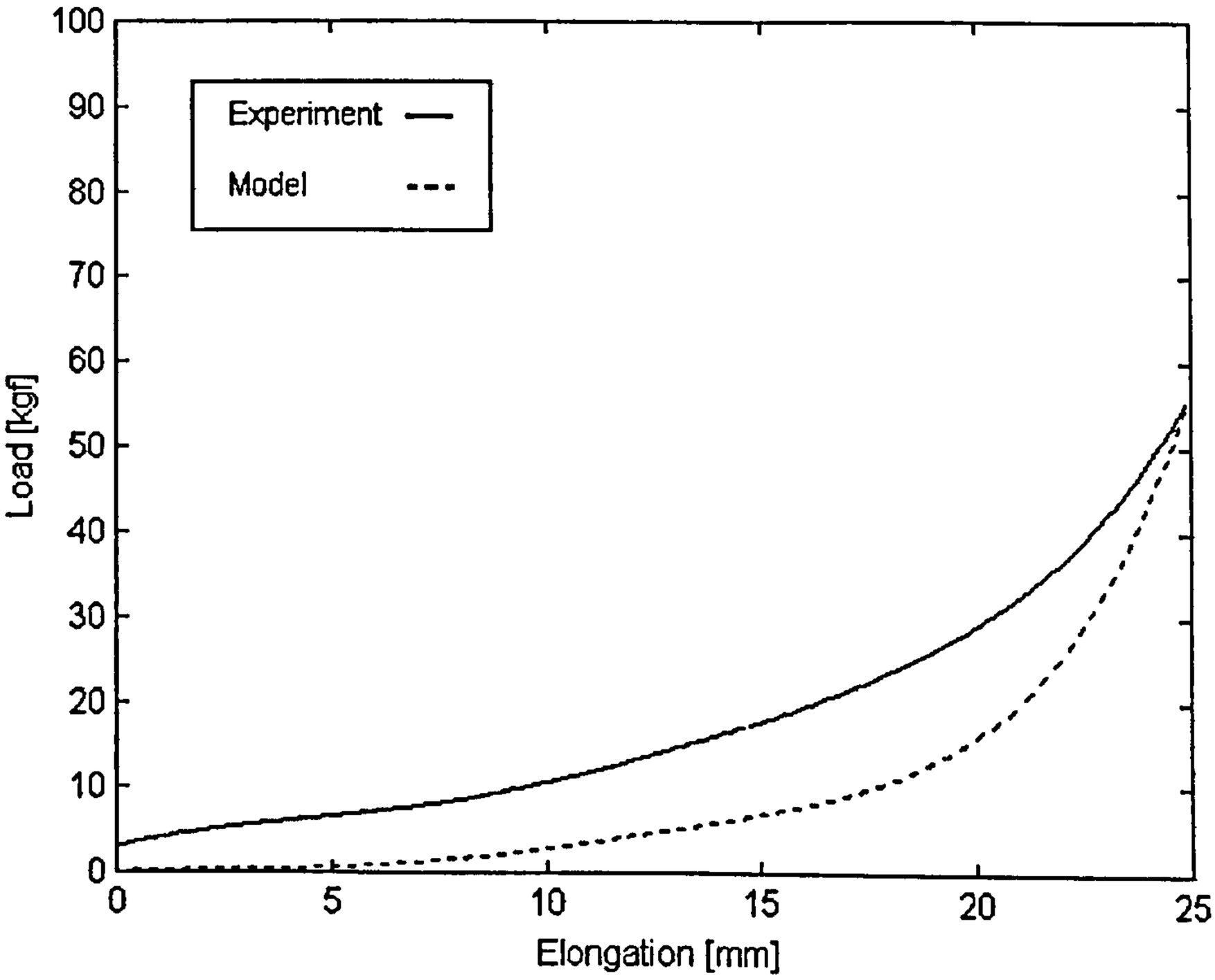

Figure 6.24. SLS simulation of stress-strain test with 0.5 $mm.s^{-1}$ constant strain-rate in the relaxed test condition.

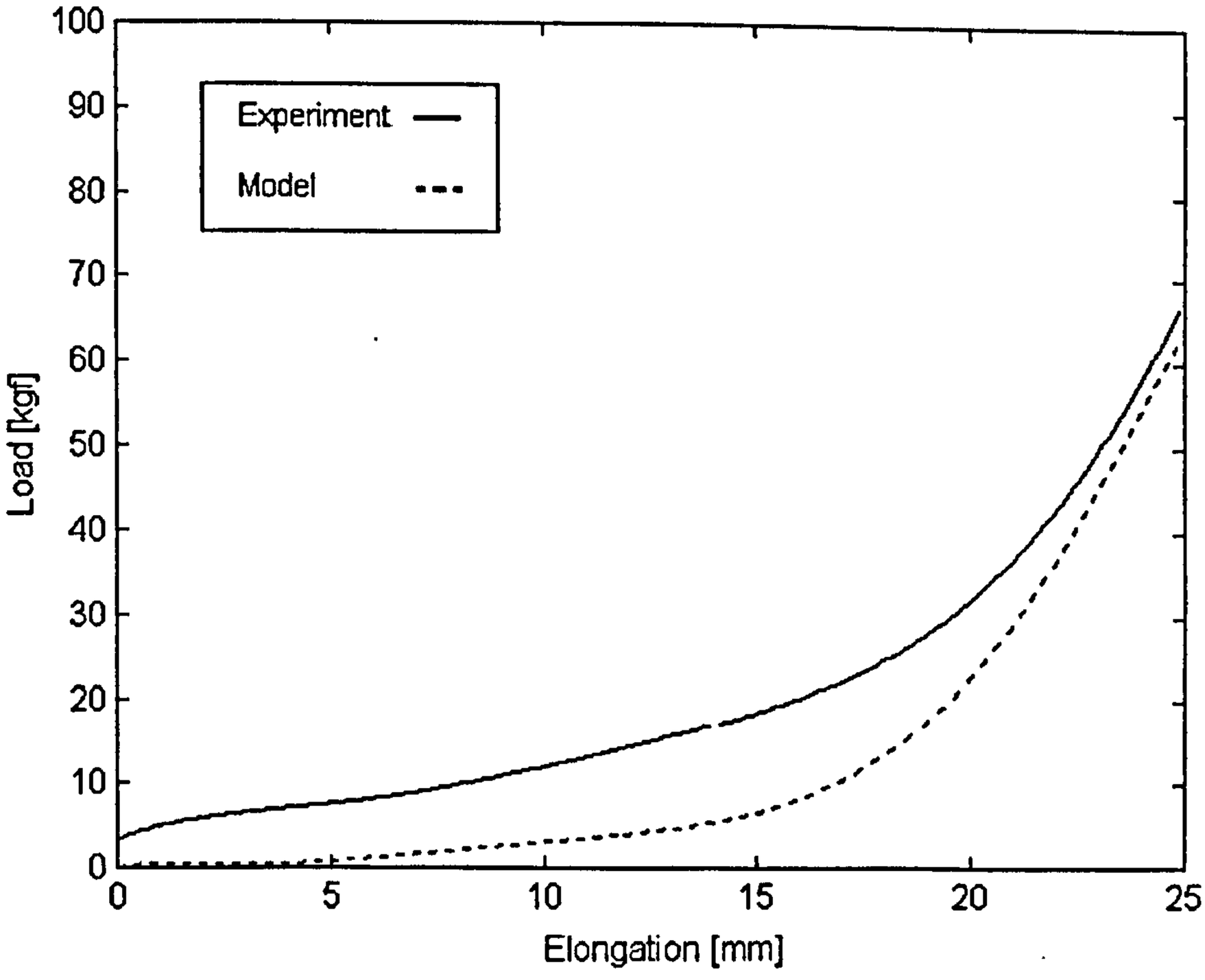

Figure 6.25. SLS simulation of stress-strain test with 1 $mm.s^{-1}$ constant strain-rate in the relaxed test condition.

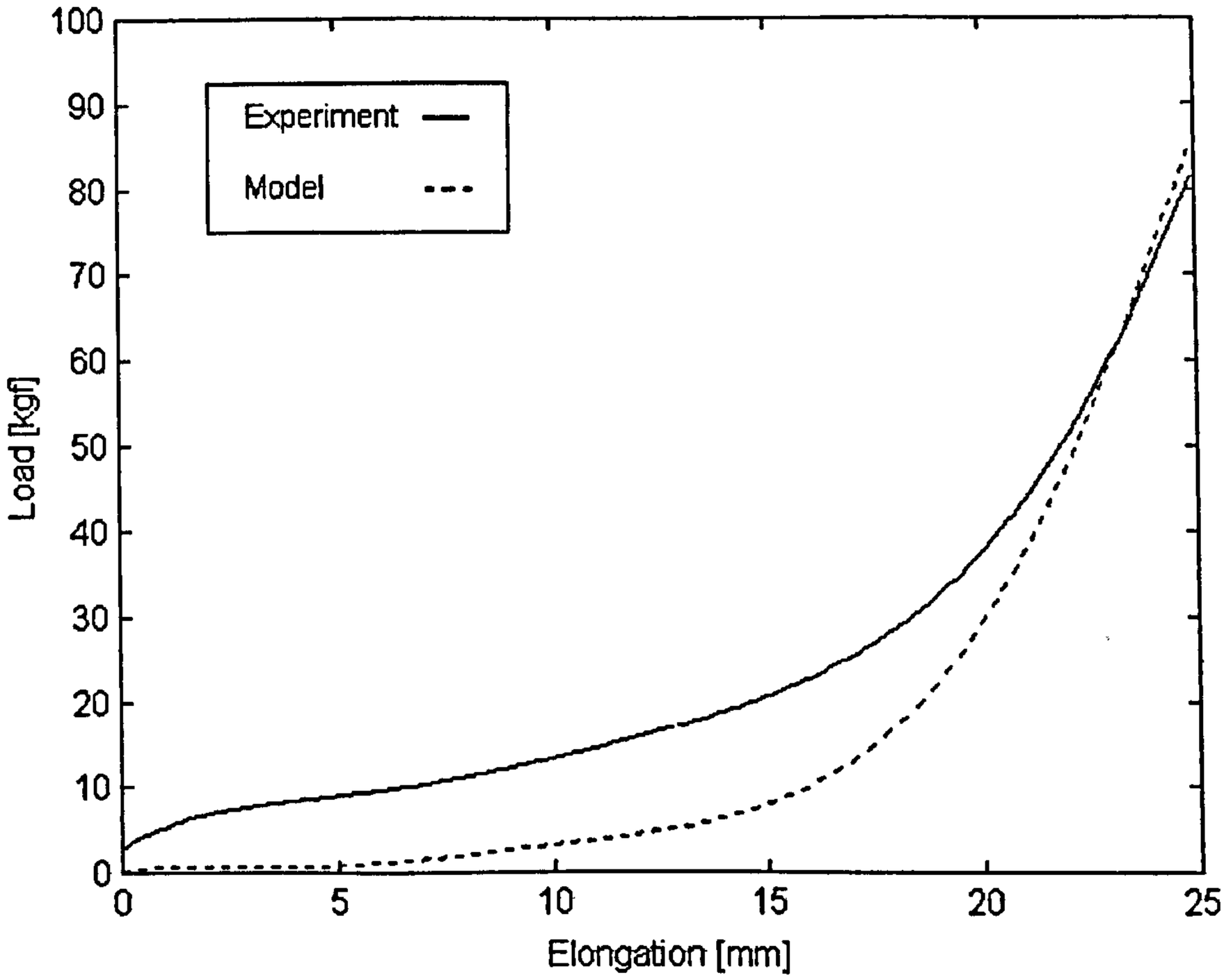

Figure 6.26. SLS simulation of stress-strain test with 2 $mm.s^{-1}$ constant strain-rate in the relaxed test condition.

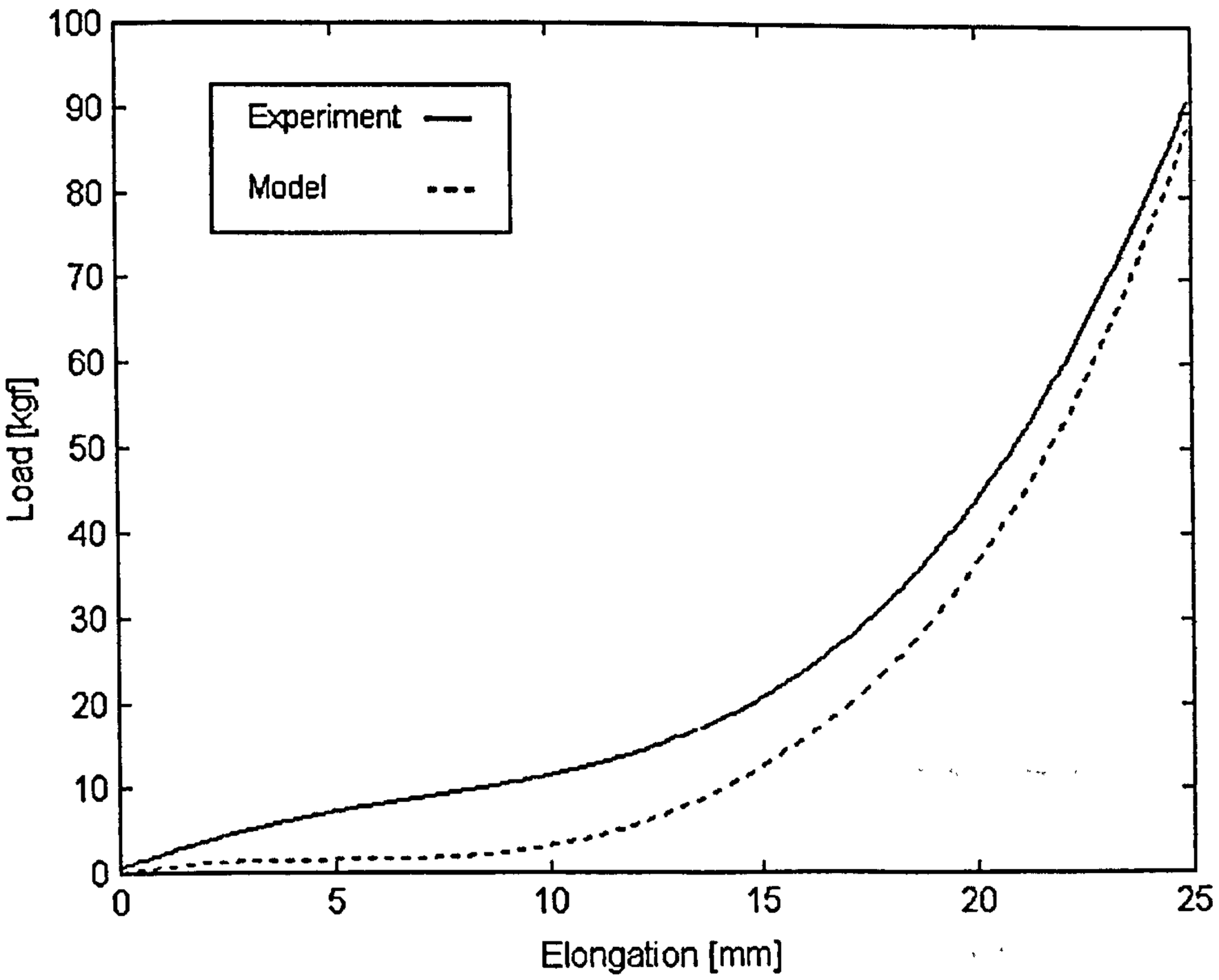

Figure 6.27. SLS simulation of stress-strain test with 4 $mm.s^{-1}$ constant strain-rate in the relaxed test condition.

A similar modelling approach was also applied to the four Maxell element stress-relaxation models. The main difference between the Maxell model and SLS model is the parallel attachment of the second spring to the Maxell element. Therefore, the elastic modulus for each element should be divided between these two springs.

$$\sigma(t) = \sigma_0\left(E_1 + E_2 e^{-t/\tau_1} + E_3 + E_4 e^{-t/\tau_2} + E_5 + E_6 e^{-t/\tau_3} + E_7 + E_8 e^{-t/\tau_4}\right) \qquad (6.17)$$

Consequently, the distribution of the elastic modulus came from an assumption which was considered in the SLS modelling of creep behaviour. Accordingly, the distribution of the SLS model of creep behaviour percentages was kept exactly the same as the SLS model of stress-relaxation behaviour. The distribution of the elastic modulus between the two springs was as follows: for SLS1 64.5 %, SLS2 69.5 %, SLS3 73 % and SLS4 76.8 %. Another partition of the elastic modulus was to separate the elastic modulus between the SLS elements. These distributions were kept almost equal, which were: for SLS1 26 %, SLS2 18 %, SLS3 22 % and SLS4 34 %. The results of the modelling can be seen in figure 6.28.

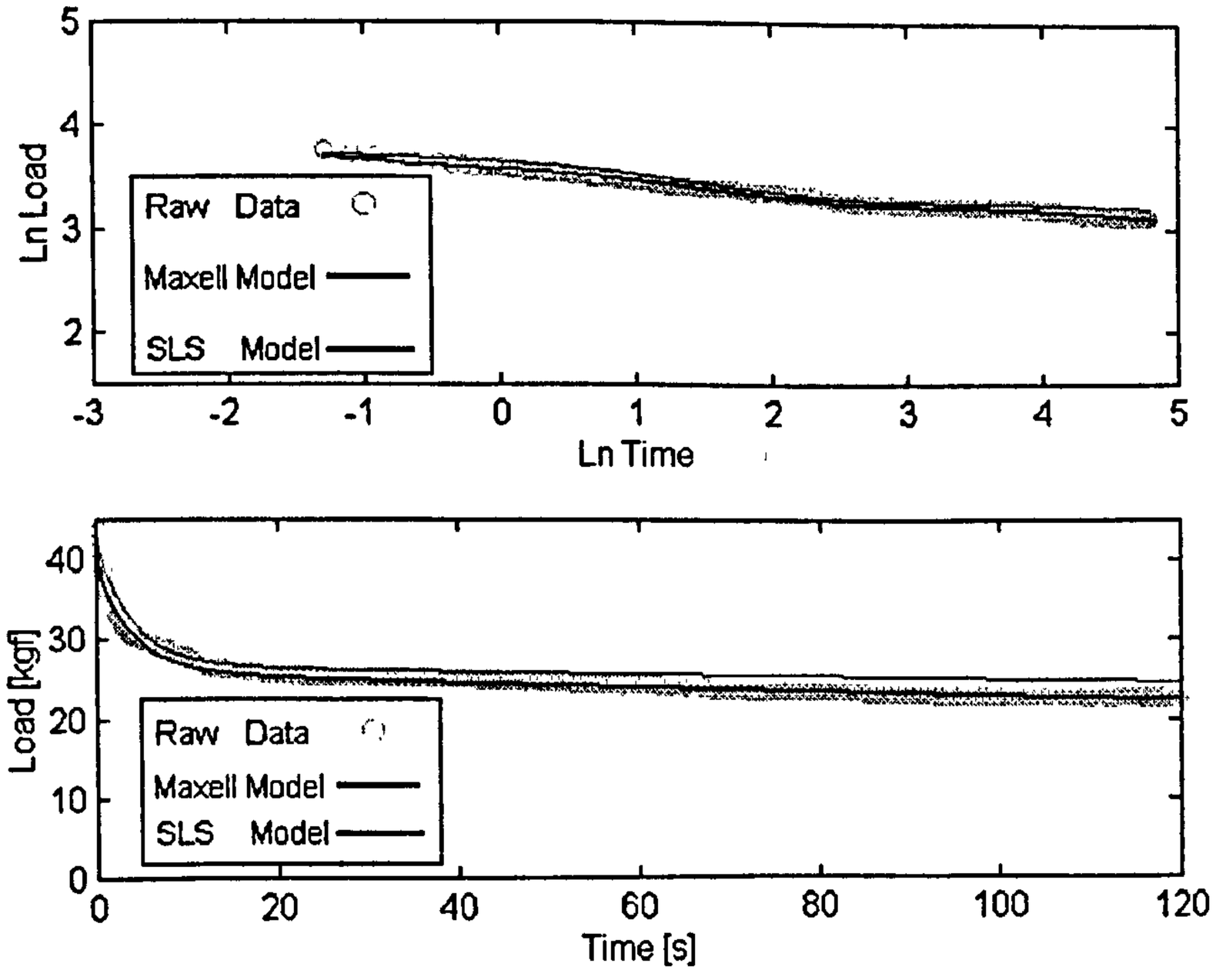

Figure 6.28. Standard linear solid model of stress-relaxation experiment of contracted test condition.

The same SLS model of stress-relaxation was applied to simulate the stress-strain test with 0.5 $mm.s^{-1}$ constant strain-rate. The response of the SLS model was stiffer than the experiment. The result of the simulation can be seen in figure 6.29 in which the solid line represents the experiment and the dashed line represents the SLS model.

The elastic modulus of the SLS model was calculated from the first derivative of the stress-strain curve fitting equation 5.5. In the simulation, the change of the elastic modulus was associated with the strain. Therefore, a new elastic modulus was assigned for each strain increment. Accordingly, the time was also calculated from the speed of the constant strain. The model fitting was corrected by changing the distribution of the elastic modulus between the SLS elements. The closest model fitting is plotted in figure 6.30.

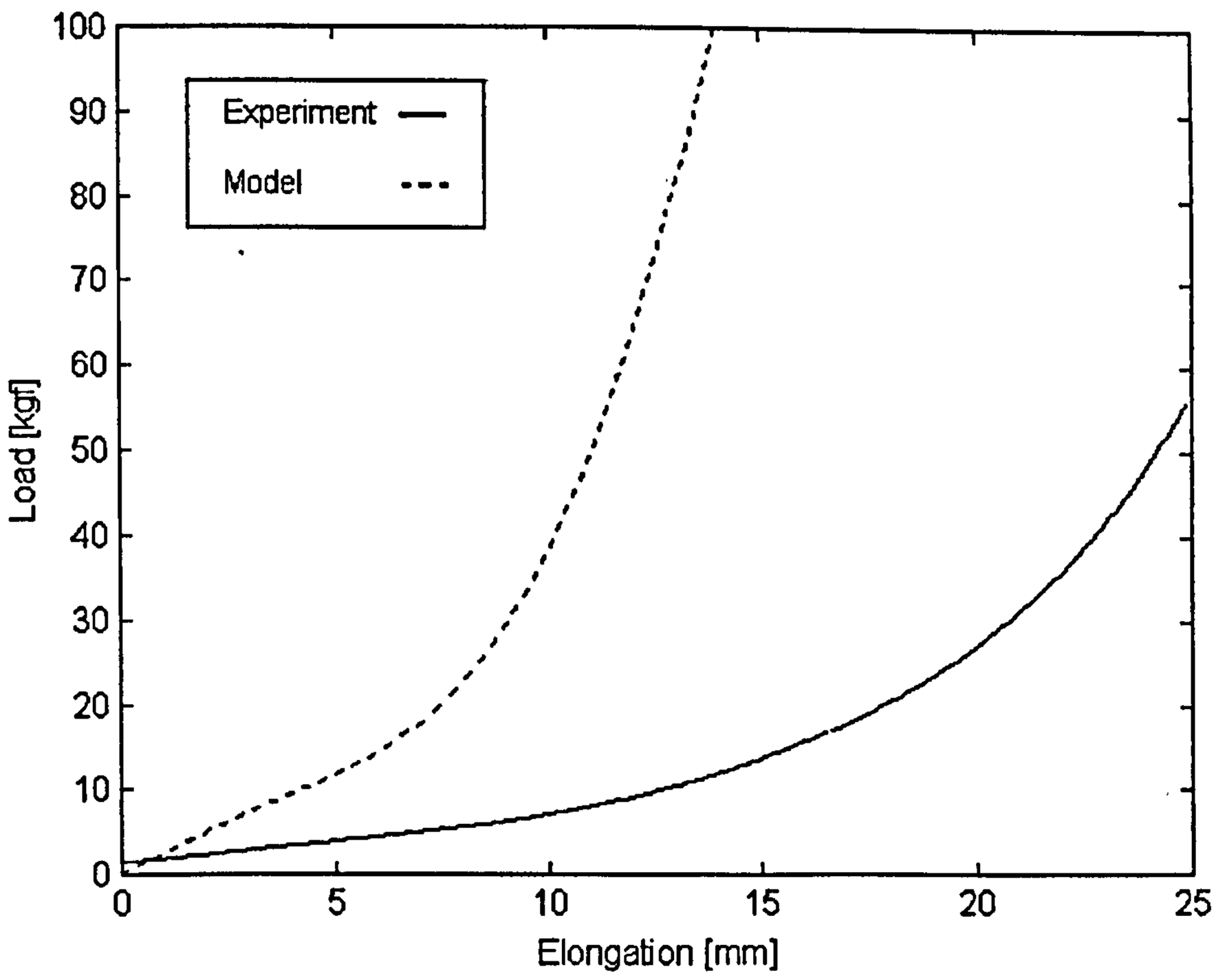

Figure 6.29. The response of the stress-strain simulation of SLS model with the stress-relaxation model parameters (contracted test condition).

The distribution of the elastic modulus between SLS elements was as follows: for SLS1 1.125 %, SLS2 24.125 %, SLS3 34.25 % and SLS4 40.5 %. The same model fitting parameters were used to check the response of the SLS model for different strain-rates. Four different strain-rates, which were 0.5, 1, 2 and 4 $mm.s^{-1}$, were used in the stress-strain test. In the experiment, the faster the strain-rate, the stiffer the elastic modulus. Accordingly, a similar response was taken from the SLS model. The response of the SLS model for 1 $mm.s^{-1}$ constant strain-rate is plotted in figure 6.31. In figure 6.32, the response of 2 $mm.s^{-1}$ constant strain test is plotted. Finally, the response of 4 $mm.s^{-1}$ constant strain test is shown in figure 6.33.

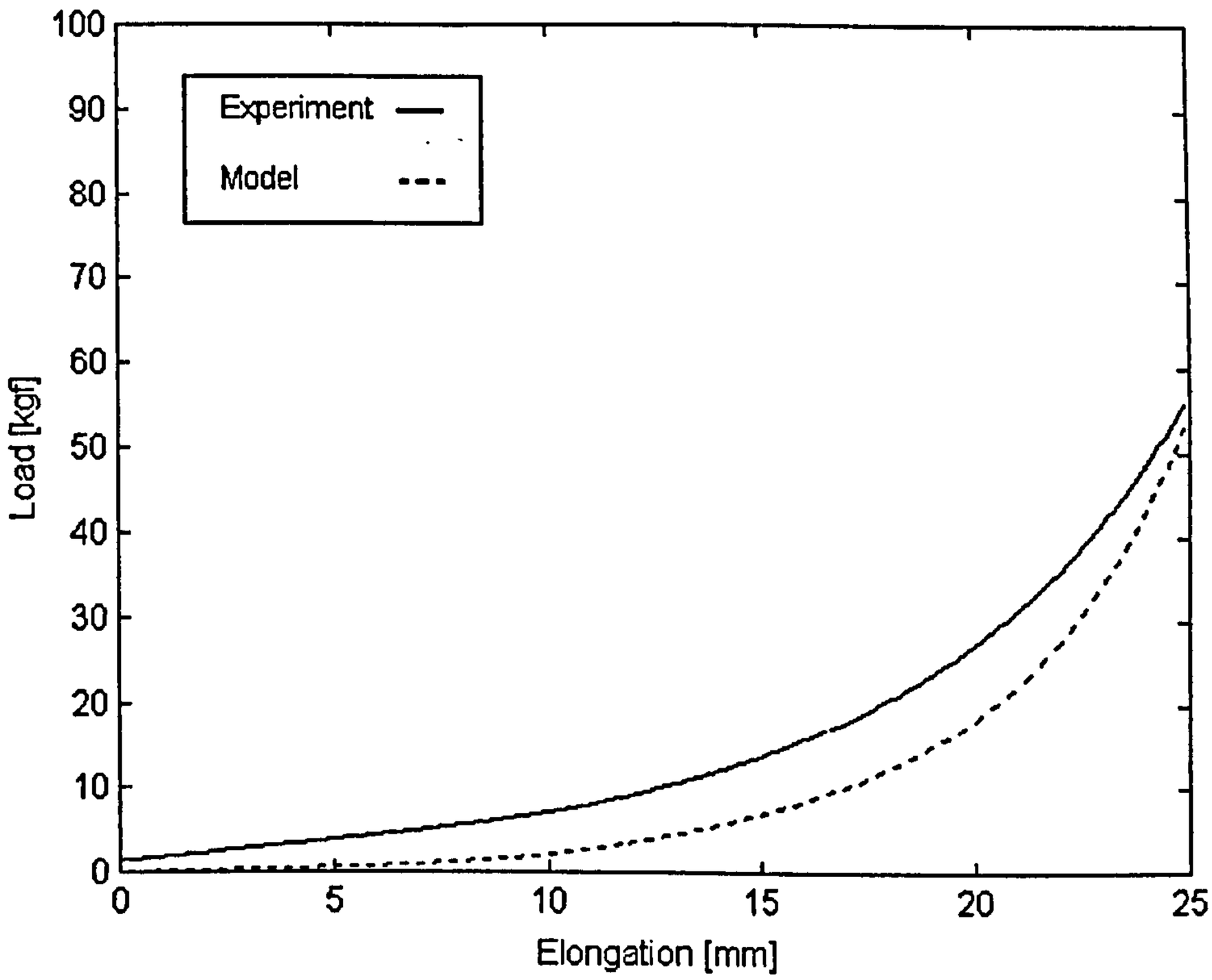

Figure 6.30. SLS simulation of stress-strain test with 0.5 $mm.s^{-1}$ constant strain-rate (contracted test condition).

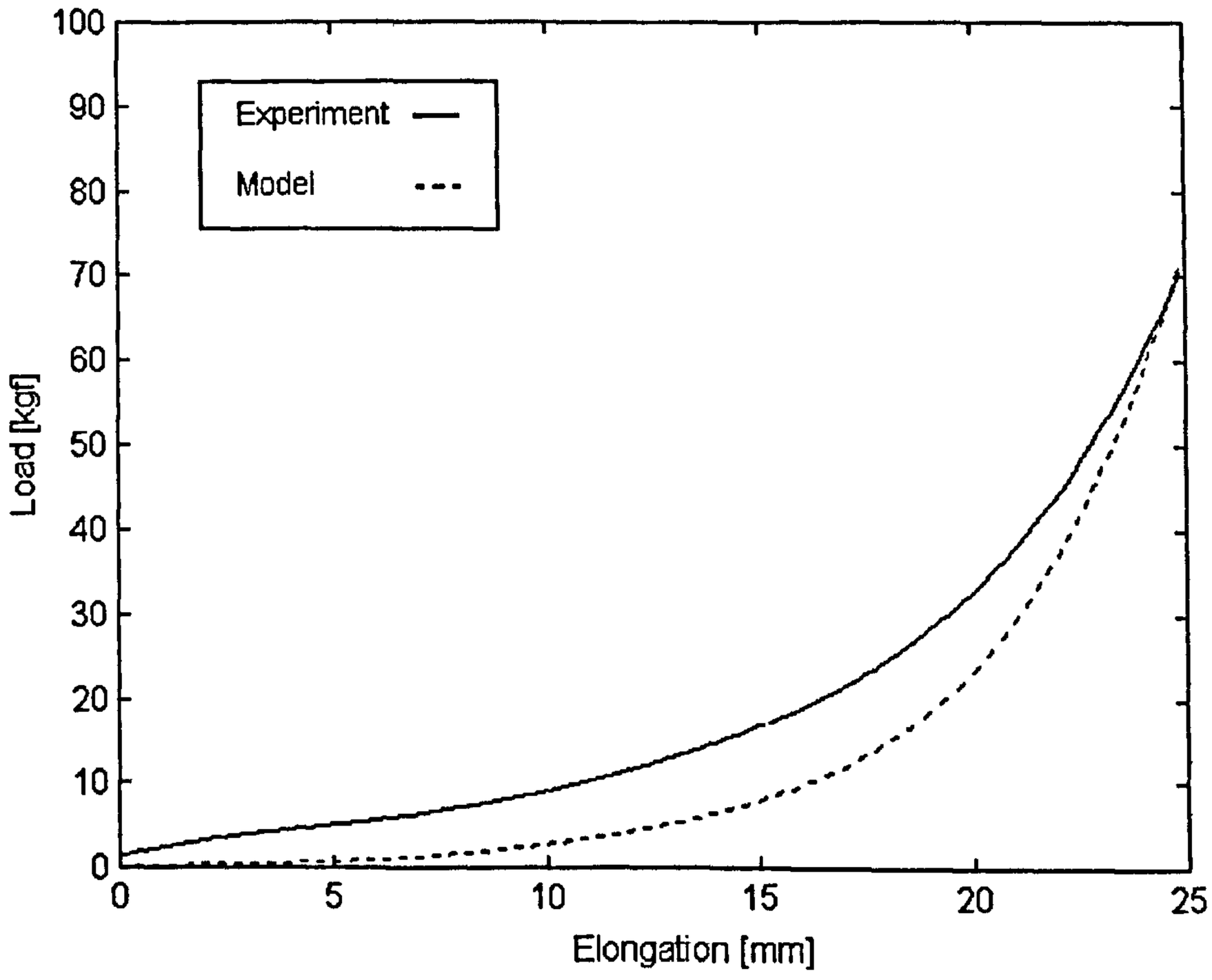

Figure 6.31. SLS simulation of stress-strain test with 1 $mm.s^{-1}$ constant strain-rate (contracted test condition).

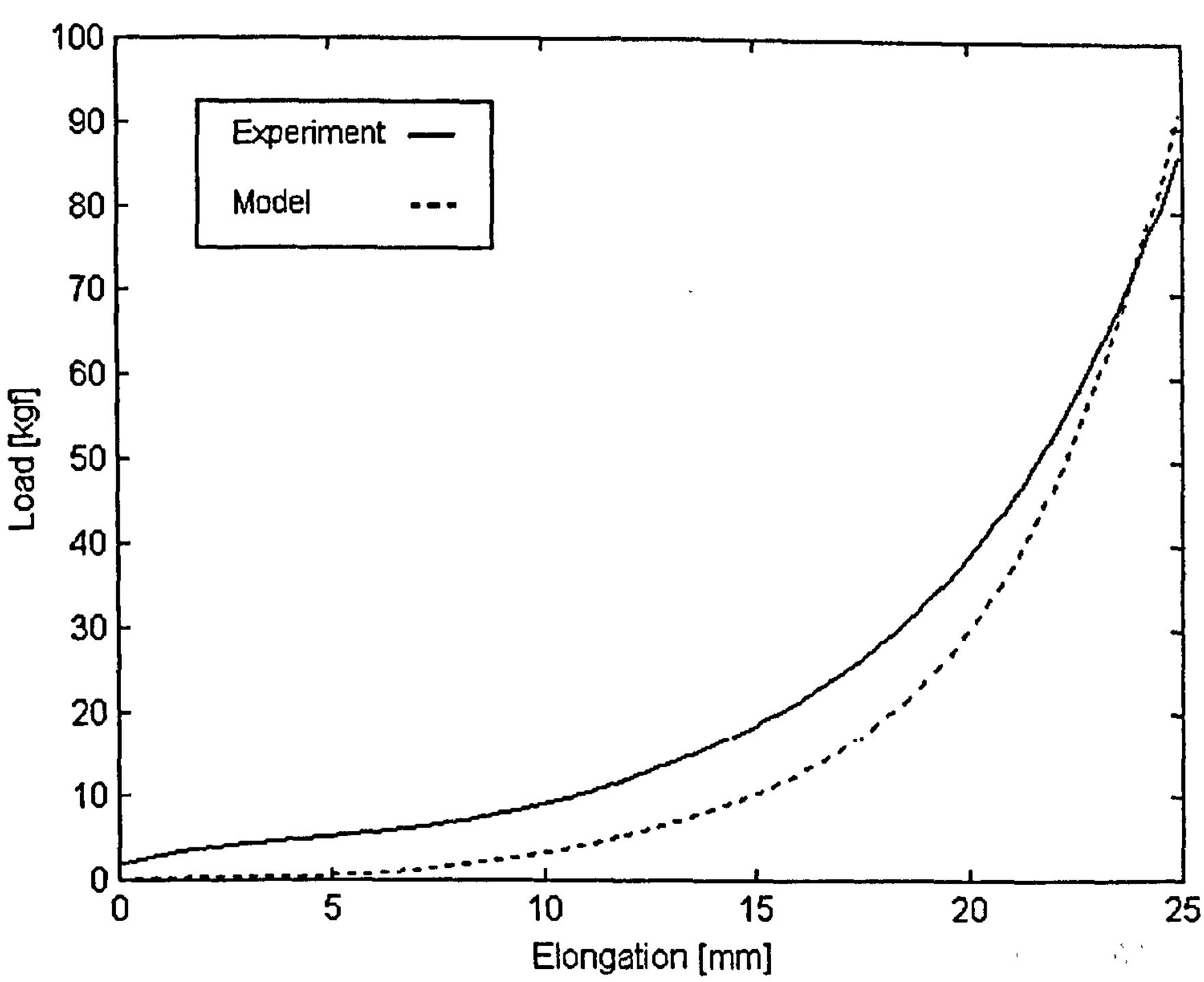

Figure 6.32. SLS simulation of stress-strain test with 2 $mm.s^{-1}$ constant strain-rate (contracted test condition).

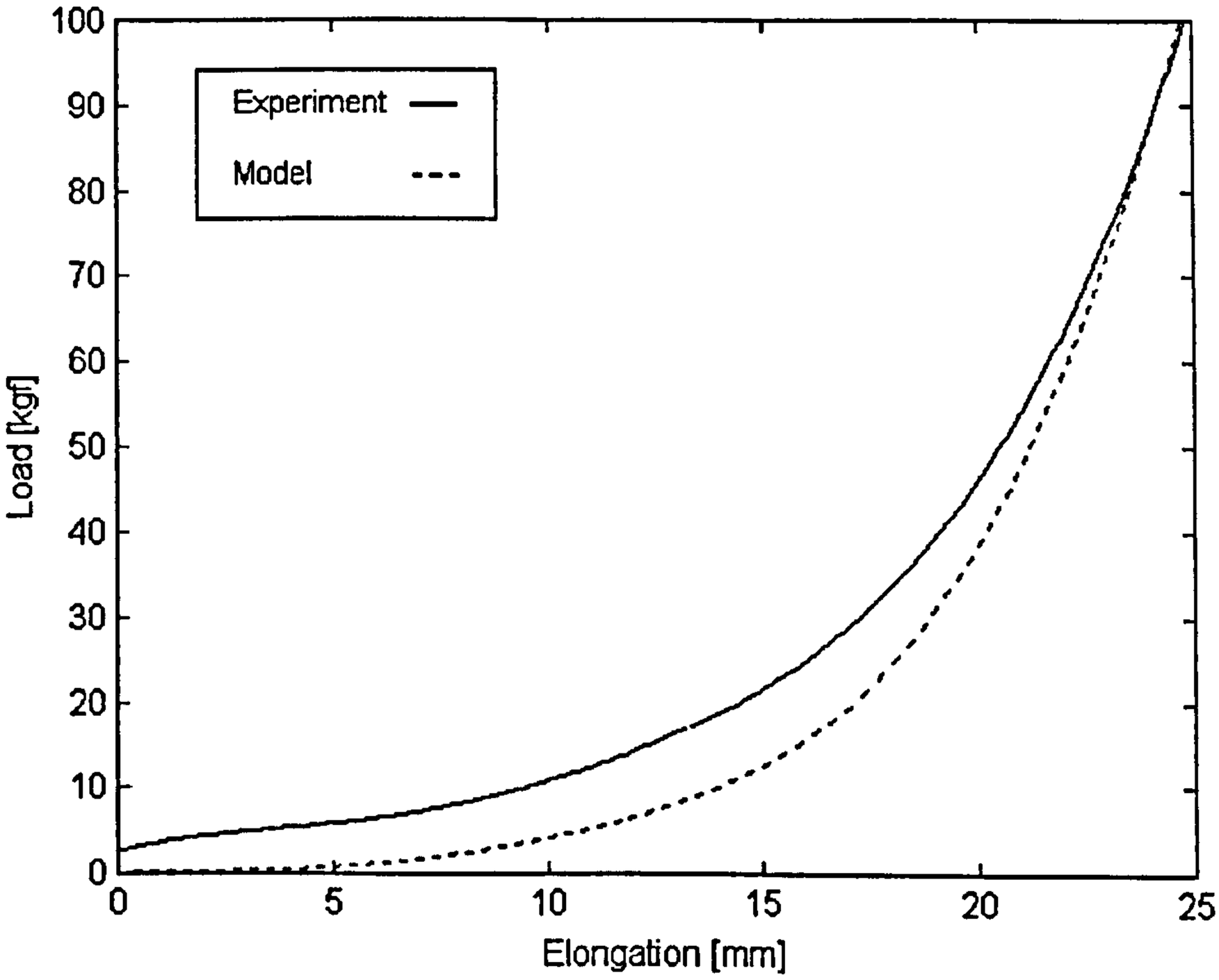

Figure 6.33. SLS simulation of stress-strain test with 4 $mm.s^{-1}$ constant strain-rate (contracted test condition).

The same SLS creep modelling was applied to the relaxed condition of the stress-relaxation test; the response of the model is plotted in figure 6.34. Then, the stress-relaxation SLS model was configured to simulate the stress-strain test with a 0.5 $mm.s^{-1}$ constant strain-rate. The response of the SLS model was very similar to the response of the contracted test (Fig. 6.29). The stress-relaxation model parameters showed a stiffer response than the experiment. The result of the simulation can be seen in figure 6.35, in which the solid line represents the experiment and the dashed line represents the SLS model. The model fitting was corrected by changing the distribution of the elastic modulus between the SLS elements. The same distribution ratios in the contracted test were used to partition the elastic modulus between SLS elements. The response of the SLS model for 0.5 $mm.s^{-1}$, 1 $mm.s^{-1}$, 2 $mm.s^{-1}$ and 4 $mm.s^{-1}$ constant strain-rates is plotted in figures 6.36, 6.37, 6.38 and 6.39 respectively.

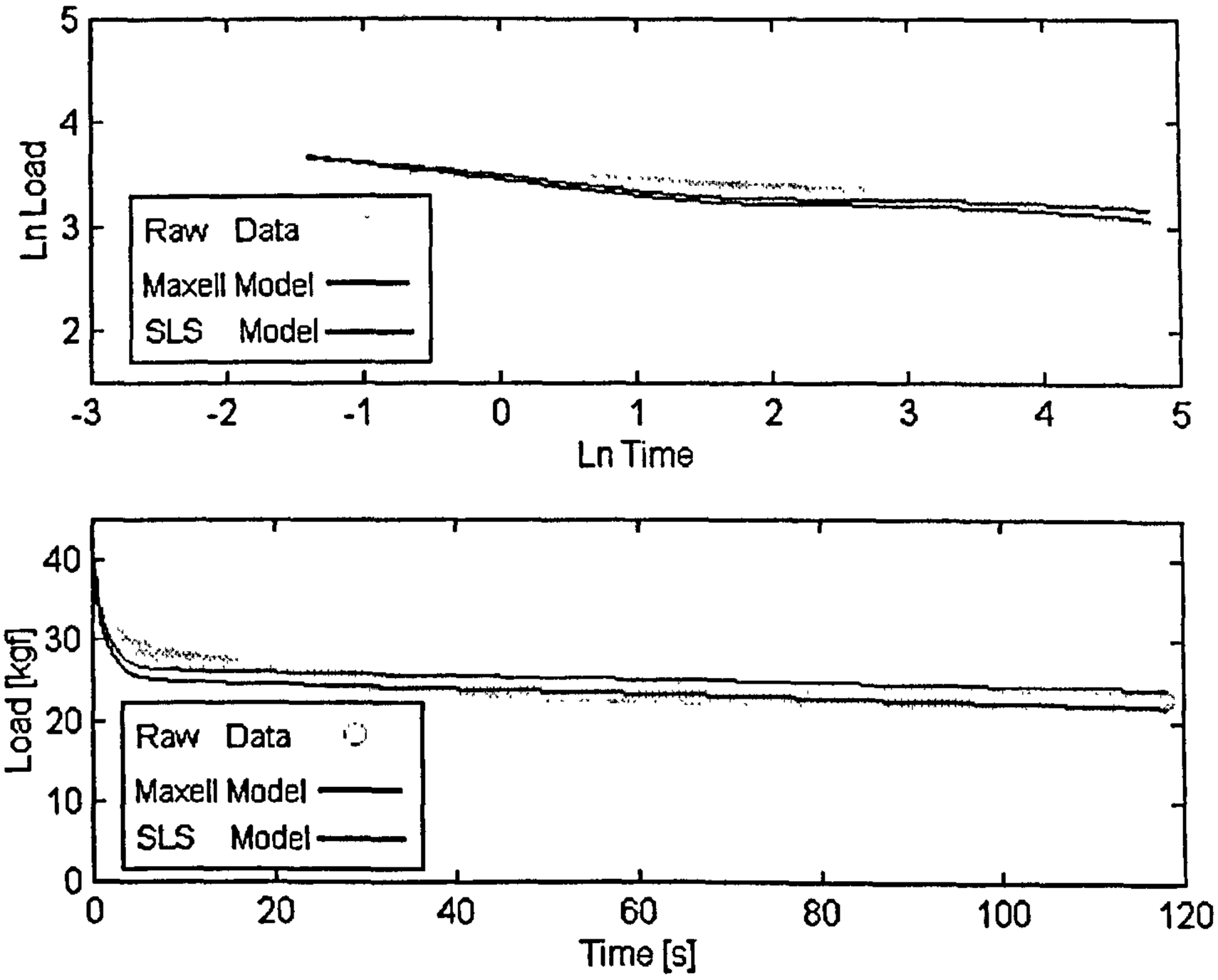

Figure 6.34. Standard linear solid model of stress-relaxation experiment with relaxed test condition.

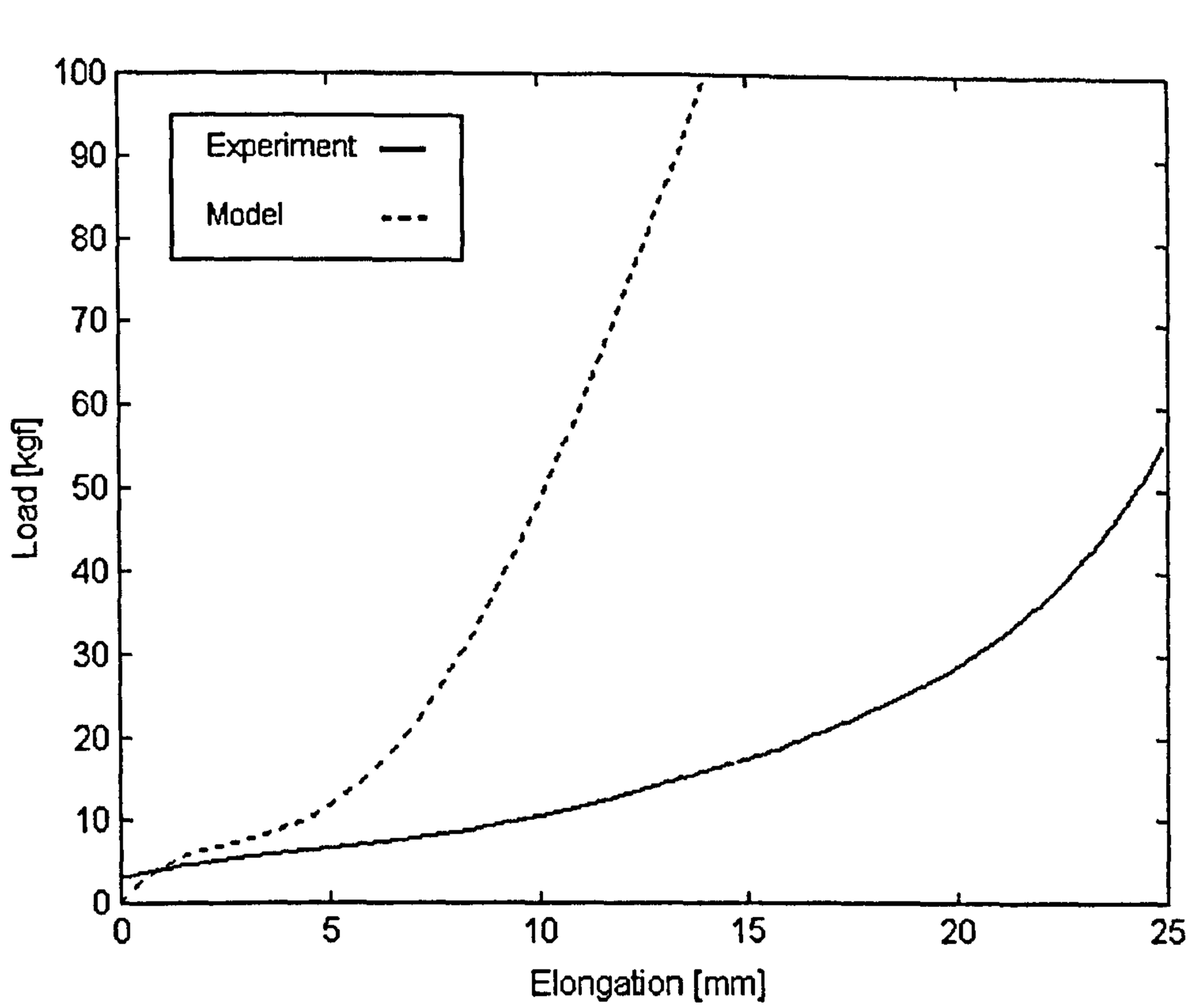

Figure 6.35. The response of the stress-strain simulation of SLS model with the stress-relaxation model parameters (relaxed test condition).

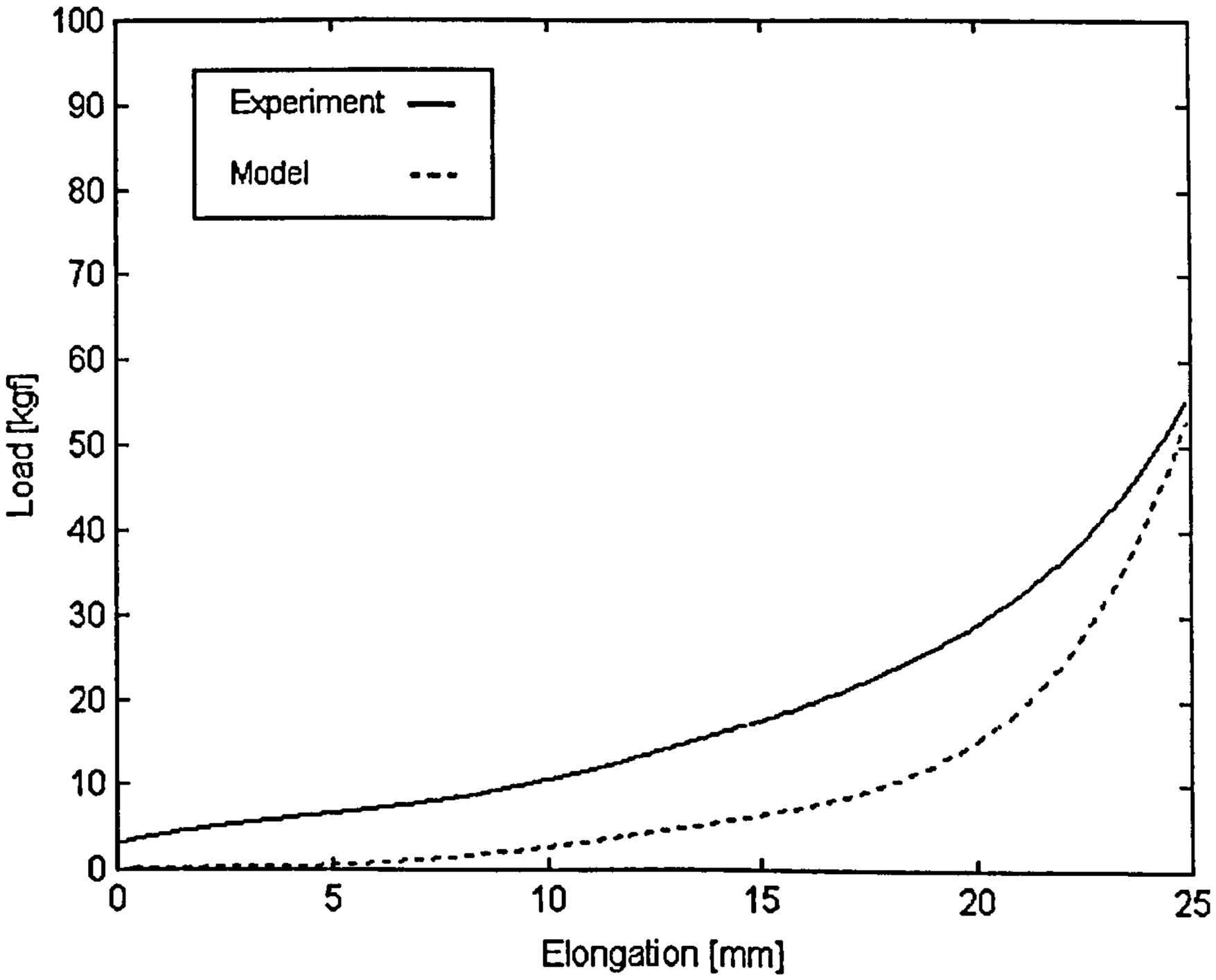

Figure 6.36. SLS simulation of stress-strain test with 0.5 $mm.s^{-1}$ constant strain-rate (relaxed test condition).

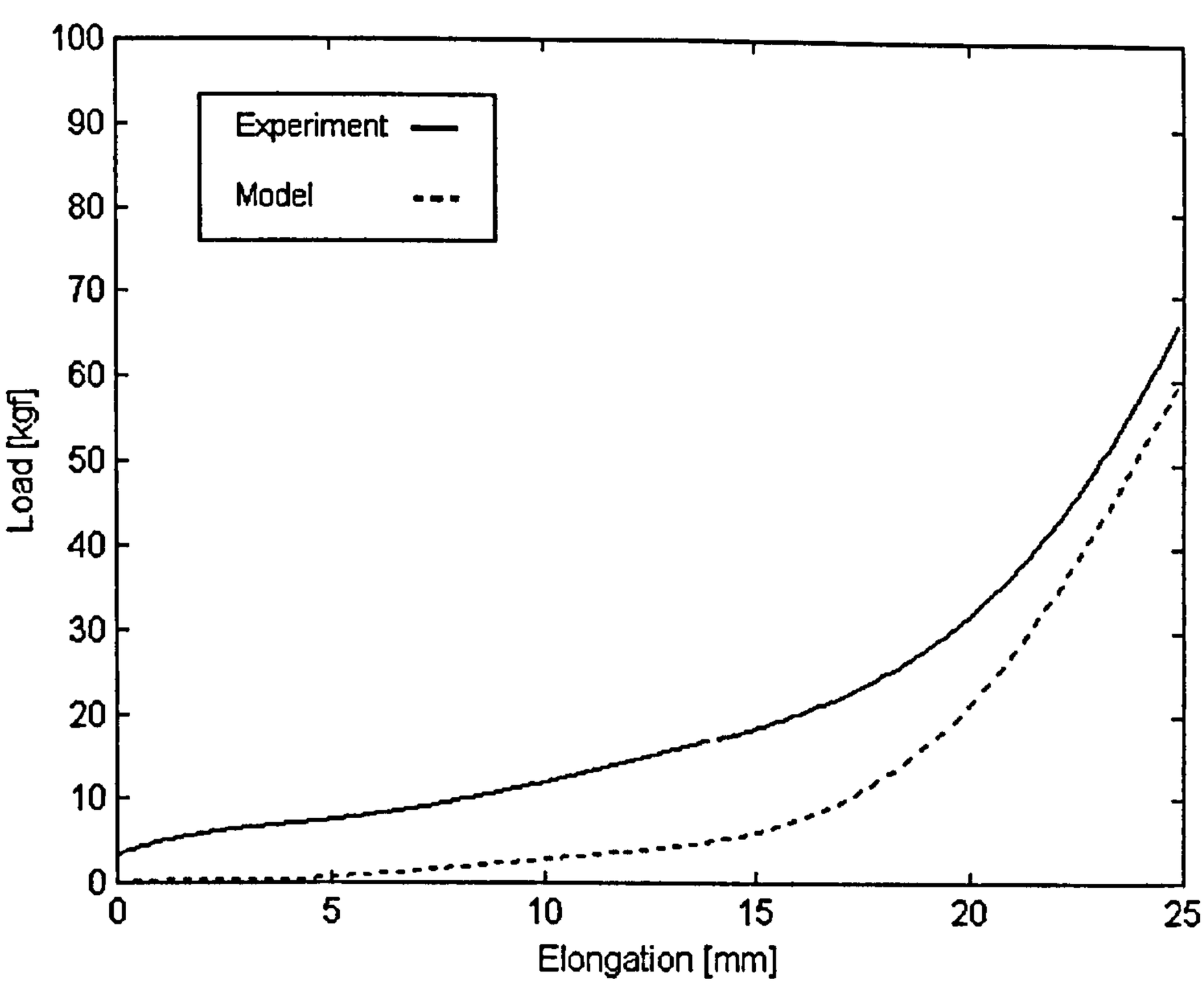

Figure 6.37. SLS simulation of stress-strain test with 1 $mm.s^{-1}$ constant strain-rate (relaxed test condition).

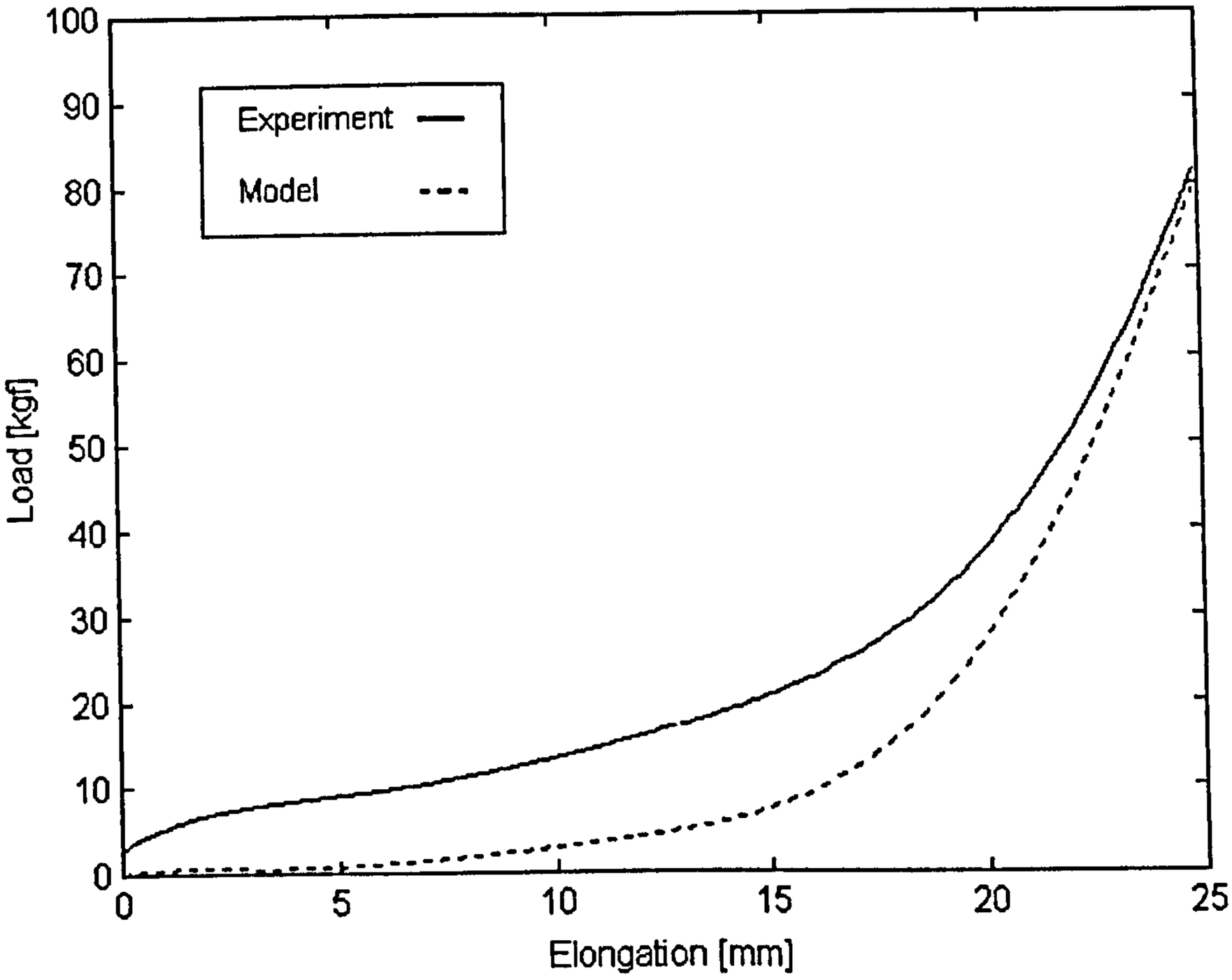

Figure 6.38. SLS simulation of stress-strain test with 2 $mm.s^{-1}$ constant strain-rate (relaxed test condition).

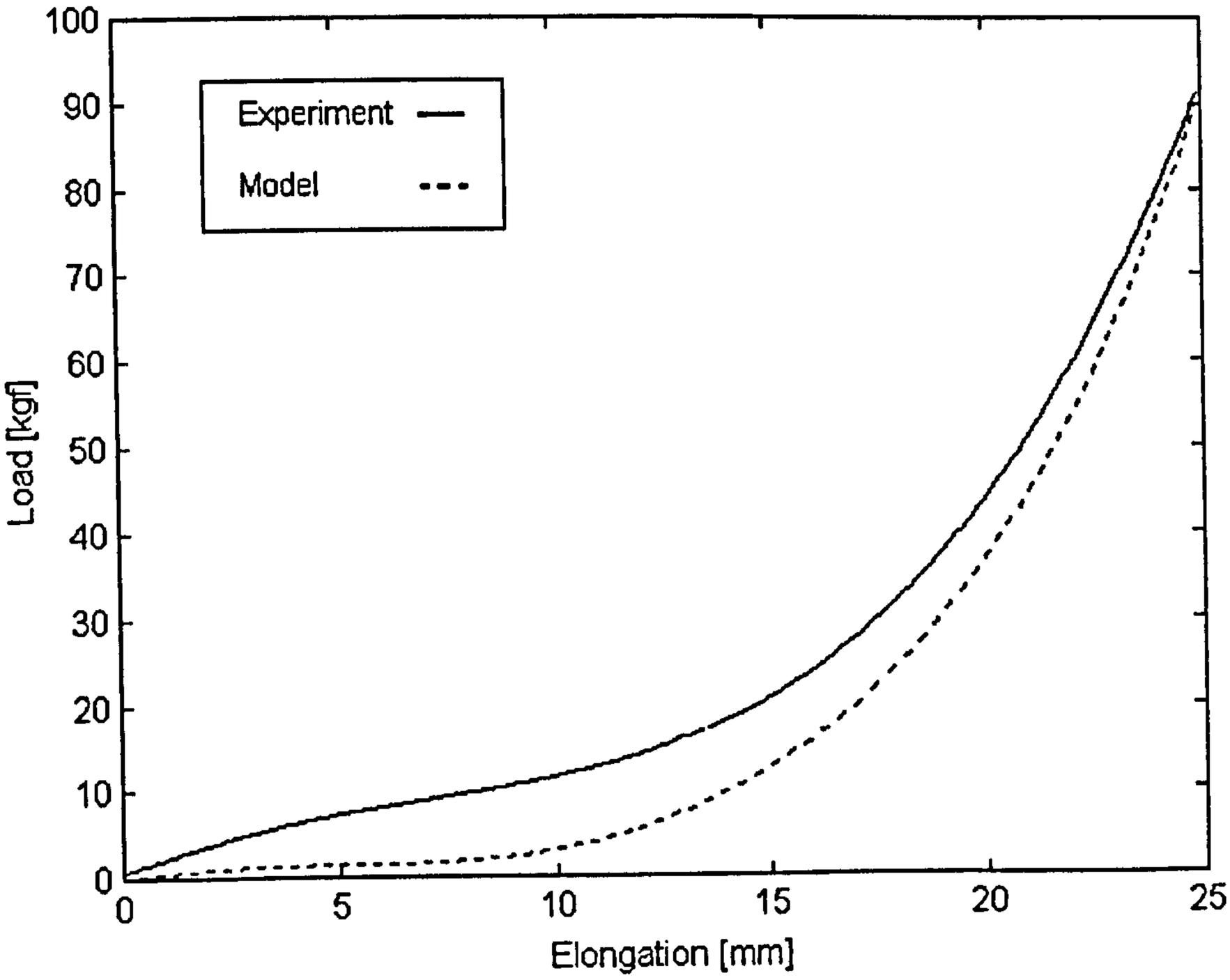

Figure 6.39. SLS simulation of stress-strain test with 4 $mm.s^{-1}$ constant strain-rate (relaxed test condition).

6.4. Summary

In this chapter, mechanical models for the collected raw data were introduced. First, the Kelvin-Voigt model was used to simulate the creep behaviour. The Maxell model simulated the stress-relaxation behaviour of soft tissue. Both behaviours (creep and stress-relaxation) of the soft tissue were tested by using the Standard Linear Solid (SLS) model. Later the same model was used to simulate the stress-strain test. Using modelling techniques, the changes of elastic modulus and coefficient of viscosity were determined and tabulated. Mechanical modelling helped to deduce the elastic modulus and coefficient of viscosity from the mechanical model fitted the experimental results.

Finite Element Simulation of Bulk Tissue

7.1. An Introduction to the Finite Element Method

The finite element method is essentially an extension of the matrix stiffness method. The structure is represented by an assemblage of subdivisions called finite elements. Connection between elements only occurs at the nodes. Simple functions (usually simple polynomials) are taken to represent the displacement in each element when the load is applied. The assumed functions are called displacement or shape functions. They must satisfy certain requirements, which ensure the convergence of the numerical solution process. The choice of function forms an important part of finite element analysis. The magnitudes of the functions are the actual displacement at the nodal points in the element. The solution process is aimed at finding these magnitudes. For example, the solution consists of a series of displacement values at discrete points in the structure when the load is applied [59, 81].

The steps in the solutions are:

- Break the structure in the elements (Discretization of the continuum)
- Determine the stiffness of each element
- Assemble element stiffness into a matrix which defines the stiffness of the whole assembly (structural or global matrix)
- Apply the boundary constraints of the problem
- For the given applied loads use the structural stiffness matrix to determine the displacements at the nodes
- Use the nodal displacement to calculate the stresses in the elements [59, 81].

7.2. Solutions of Equations

The element stiffness matrix [k] relates the element nodal displacements $\{\delta\}$ to the applied forces at the nodes as

$$\{f\}=[k]\{\delta\} \tag{7.1}$$

[k] is determined by using the virtual work principle. This can often be a complicated process because of the integration involved. By assembling the element stiffness matrix, a global structural stiffness matrix {K} is formed.

The structural loading vector {F} is related to the structural nodal displacement {U} via the structural stiffness matrix [K] as;

$$\{F\}=[K]\{U\} \tag{7.2}$$

{F} can be found from the externally applied loads. The size of [K], which is typically very large, depends on the structural degrees of freedom, which, in turn, depends on the problem being tackled. The solution for displacement is usually done by the Gaussian elimination technique. From the known vector {U} the nodal displacements $\{\delta\}$ for each element can be found. From these, the strains for each element can be determined and finally the constitutive relationships (Eq. 7.3) allow the stress to be found in each element [59, 81].

For a linear elastic homogenous isotropic material, the stress vector $\{\sigma\}$ is related to the strain vector $\{\varepsilon\}$ via the constitutive equation given by:

$$\{\sigma\}=[D]\{\varepsilon\} \tag{7.3}$$

In general [D] is a 6x6 symmetrical matrix; only two independent material properties, namely the elastic modulus (E) and Poisson's ratio (ν) are required to form the elements of [D] [59, 81].

7.3. Finite Element Meshing

The choice of the element type for the finite element meshing procedure depends on the type of analysis to be performed and the expected level of precision. The common finite element software provides extended libraries of element types, depending on the number of geometrical and integration nodes, as well as on their disposition and associated properties. The meshing procedure is therefore closely related to the intrinsic properties of the material and constitutes an entire step in the modelling approach. However, some general features can be outlined here to give some indication of how soft tissue simulation may be achieved [7].

7.3.1. Volume meshing

The goal is three-dimensional modelling of the muscular soft tissues; therefore, volume element meshing seems appropriate. Mainly two shapes are available for volume elements: tetrahedrons and hexahedrons [1, 2].

In general, finite element meshes are composed of elements with simple geometric shapes such as segments for curves, triangles or quadrilaterals for surfaces and tetrahedrons and hexahedrons for volumes. However, any other shape may be considered for creating the mesh, as long as it is compatible with the dimension of the

shape to be discretized. In practice, finite element software provides huge libraries of elements, not only distinct in shape or interpolation but also in the properties and functions assigned to them, depending on the kind of analysis to be performed [1, 2].

There is a major interest in using simple geometric shapes because of their symmetric properties, which allow the use of reduced variables in the expression of shape functions. Given the complex shape of the human upper arm bulk tissue, use of 3D brick element seemed more appropriate. A sample of 3D brick element and node topology can be seen in figure 7.1 [2].

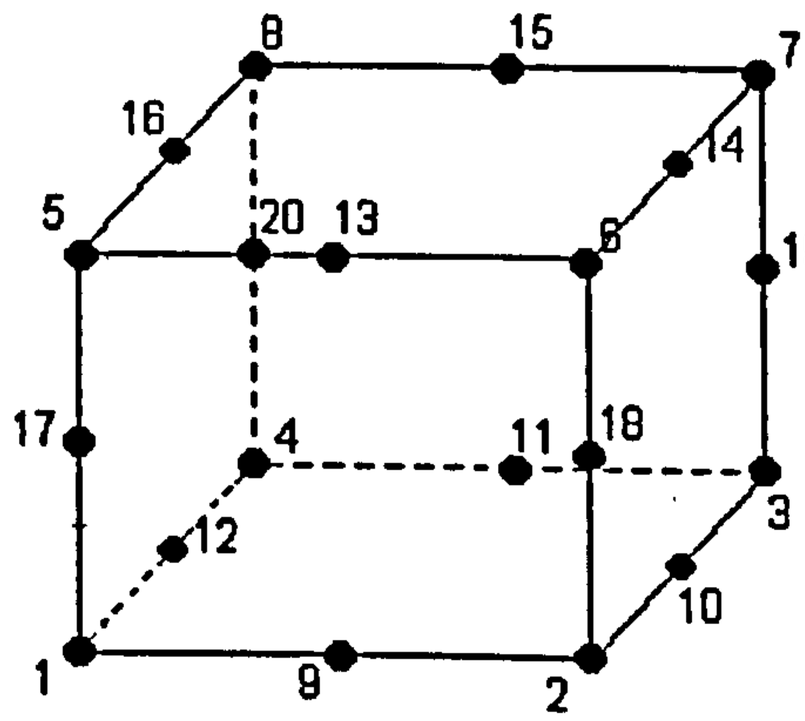

Figure 7.1. 3D brick finite element and node topology.

For the FE analysis, the human upper arm was modelled with the mesh generation program, which was explained in chapter 2. The first output of the program was to determine the boundaries of the human arm in three dimensions. The output of the program can be seen in figure 7.2. To increase the computational speed, the number of elements was kept to a minimum for the prototype finite element model. That is why every slice in figure 7.2 was not consequentially used to create the finite element mesh. For nodal representation of the finite element mesh, skin, muscle and bone coordinates

were connected with the representations for every other slice. Using this simplification, 400 elements were created.

In practice, the PATRAN commercial pre-processor was used for defining the geometry [5]. First, a series of computer programs was written to convert the geometry of the upper arm (Fig. 7.2) to be embedded into a PATRAN session file. The program used PATRAN script to create grids, lines and patches for discretization of the model. The skin-fat couple was modelled as one element, as was muscle. The discretization of the model is shown in figure 7.3 for the fat layer and figure 7.4 for the muscle layer.

The load was applied to the outer element, which is skin-fat, all around the upper arm model. The load was divided into 200 points, which were placed in the middle of every outer element. A schematic representation of loading can be seen in figure 7.5.

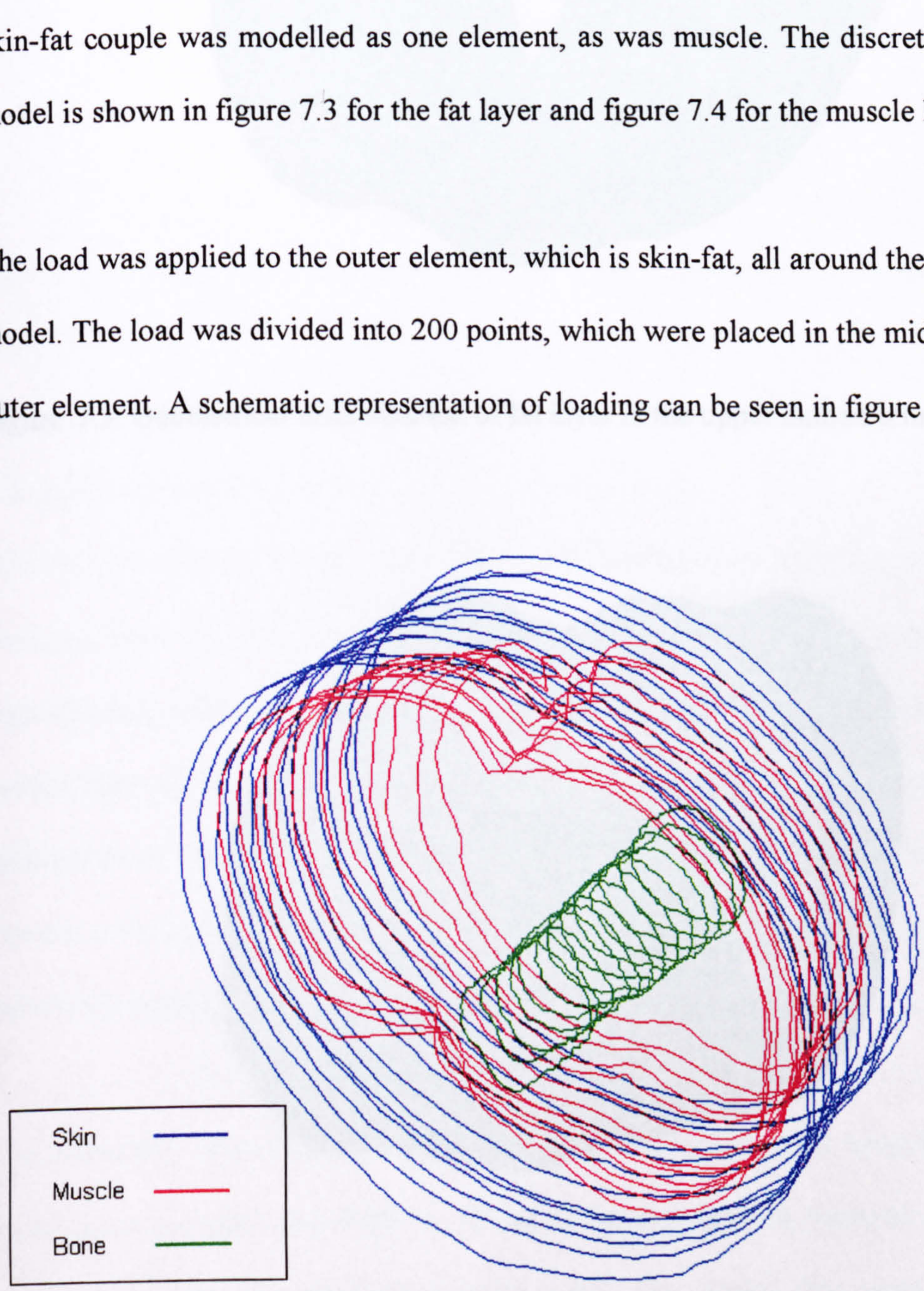

Figure 7.2. The boundaries of the human upper arm.

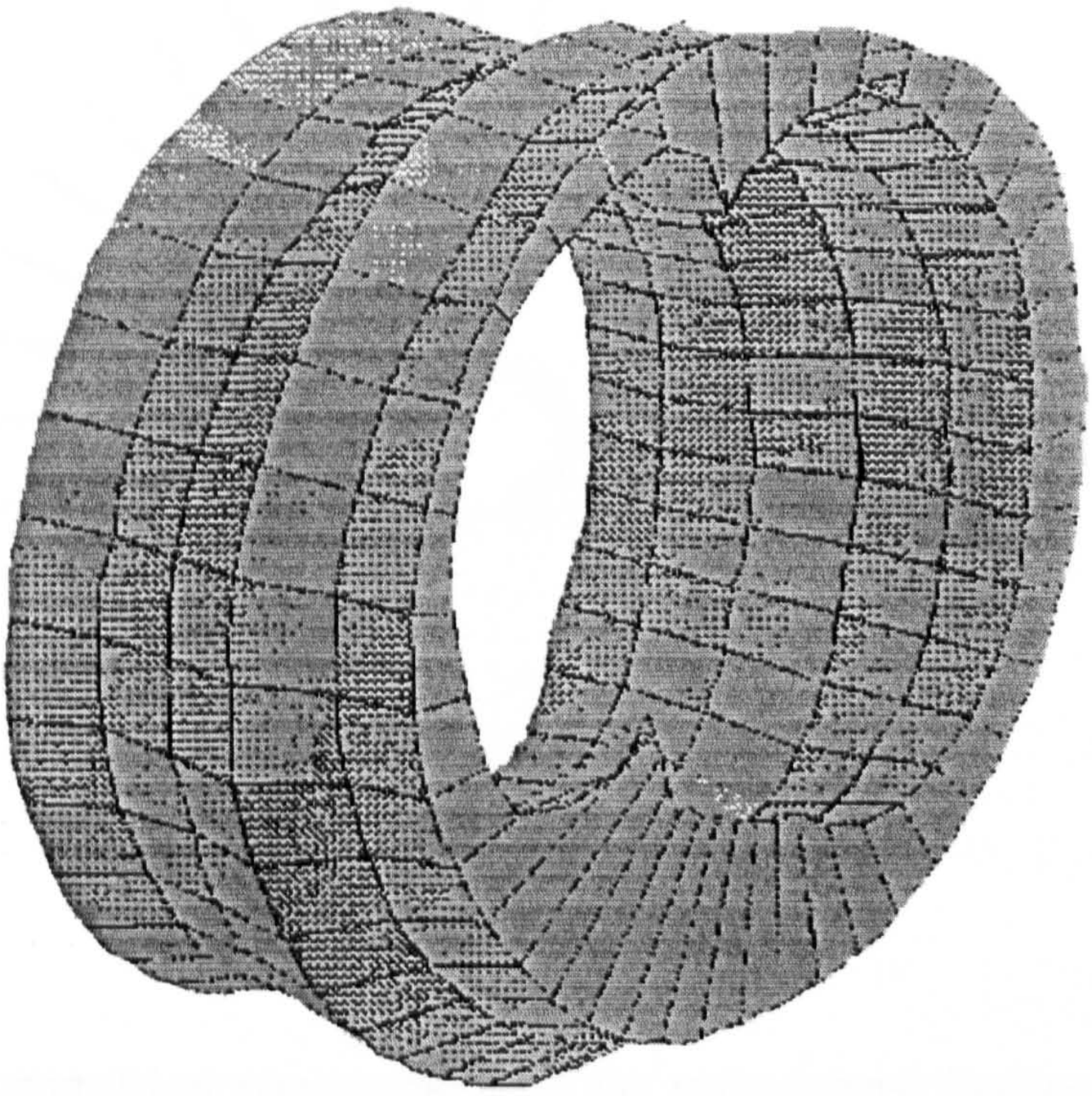

Figure 7.3. Geometrical discretization of fat layer in the upper human arm.

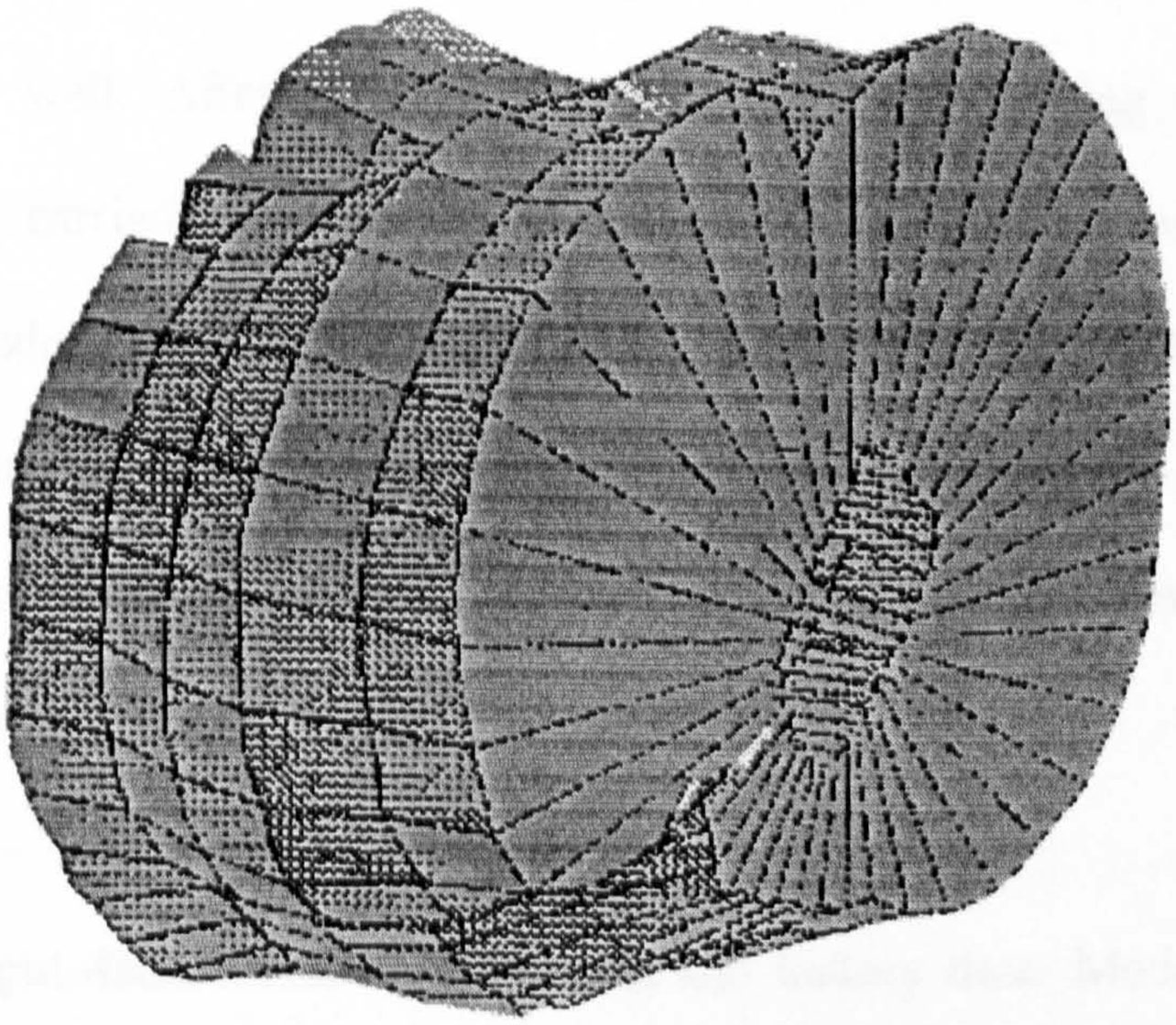

Figure 7.4. Geometrical discretization of muscle layer in the upper human arm.

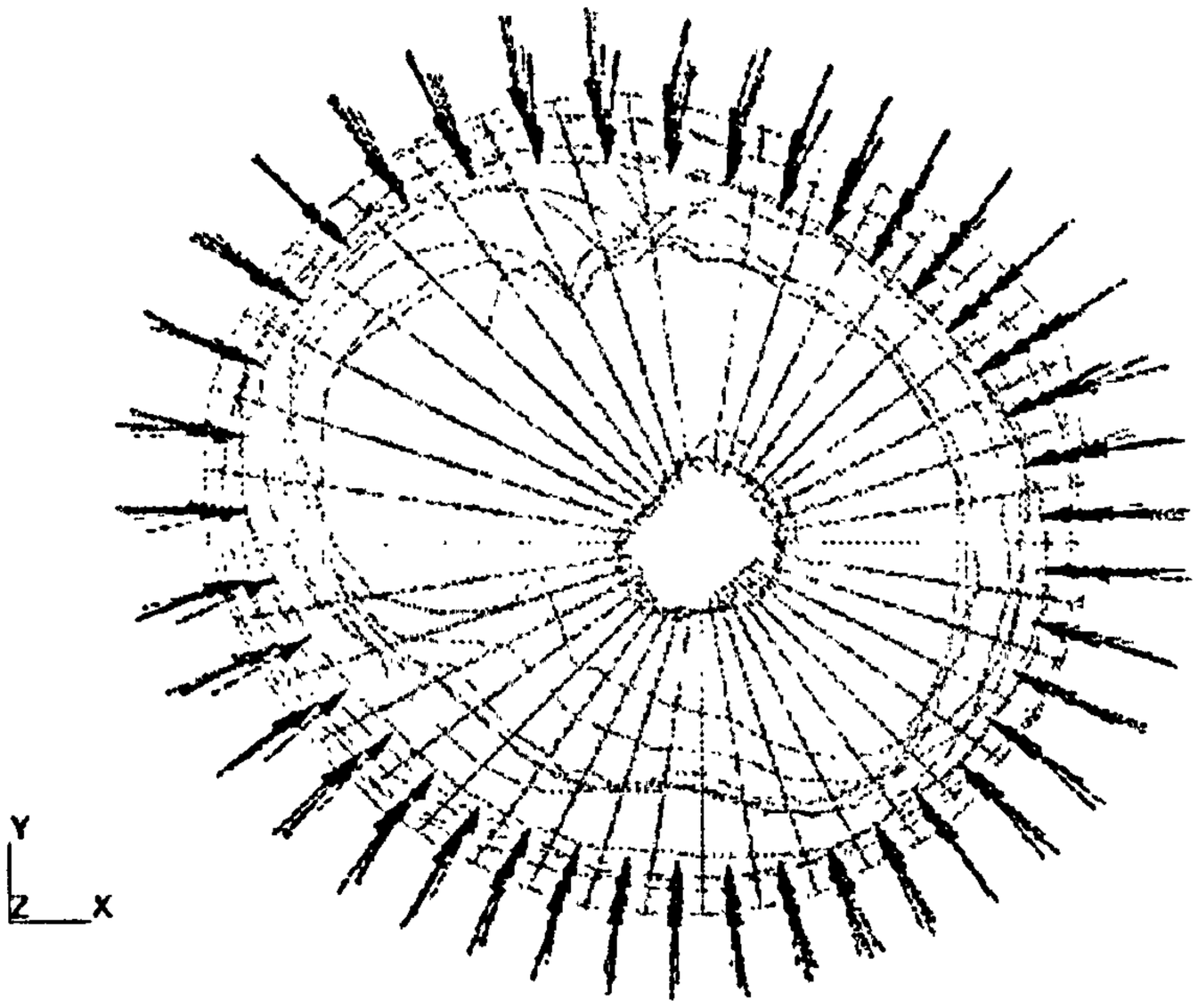

Figure 7.5. The geometrical representation of the experimental loading of the upper arm.

7.4. Finite Element Analysis

The FE tool ABAQUS was used for executing the analysis. PATRAN was used as a post-processor as well. After meshing the geometry and defining elements, node equvalencing was carried out to delete the unwanted nodes. This was followed by optimisation of nodes and elements so that the bandwidth of the stiffness matrix was reduced to a minimum. The bandwidth must be as small as possible to optimise the amount of computer storage required. The discretized model was transferred into an ABAQUS input deck using the interface option [1, 2].

The ABAQUS input deck contains model data and history data. Model data define a finite element model: the elements, nodes, element properties, material definition, and so on - any data that specify the model itself. This model data were created using PATRAN as outlined above. History data define what happens to the model under the

sequence of events or loading for which the response is sought. In ABAQUS, this history was divided into a sequence of steps. Each step was a period of response of a particular type - a static loading, a dynamic response etc. The definition of a step includes the procedure type (static or dynamic analysis). The output required such as stress, strain, deflection, etc, were also defined in these history data. The results file obtained was transferred to PATRAN where the data were displayed and plotted [1, 2].

The creep test for 60 kgf constant load in the relaxed test condition was chosen for finite element simulation. A constant load was used to simplify the analyses. However, the fat-skin and the muscle tissues were defined with a separate geometry, the same mechanical properties were used for finite element analysis. Dynamic analysis was used to investigate the viscoelastic behaviour of the bulk tissue.

7.4.1. Time Domain Analysis of Viscoelastic Material

The time domain dynamic properties of viscoelastic material were represented in the ABAQUS finite element software by means of a "Prony series". This series, which is stated below, requires the values of two constants: the relative moduli g_k and the time constants τ_k. Given a set of experimental dynamic property data or a relaxation function, the major task in representing the data by means of a Prony series is the determination of the constants g_k and τ_k. One method which has been used successfully for determining these constants in the collocation method. One of the advantages of the collocation method over other methods is that it is general and applicable to all response functions. To demonstrate the method the equation for the relaxation modulus of the Wiechert model is chosen. In terms of the long term modulus [1]:

$$G_j = Gt_j = G_\infty + \sum_k G_k * \exp(-t/\tau_k) \qquad (7.4)$$

By rewriting the equation to include the instantaneous modulus (which is the modulus at time zero or when k = 0),

$$G_j = G_g - \sum_k G_k + \sum_k G_k * \exp(-t/\tau_k) \tag{7.5}$$

$$G_j = G_g - \sum_k G_k [1 - \exp(-t/\tau_k)] \tag{7.6}$$

$$G_j = G_g \left(1 - \sum_k G_k / G_g [1 - \exp(-t/\tau_k)]\right) \tag{7.7}$$

let $$g_k = G_k / G_g \tag{7.8}$$

$$G_j = G_g \left(1 - \sum_k g_k [1 - \exp(-t/\tau_k)]\right) \tag{7.9}$$

Where:

$k = 0,2...n$

$j = 1,...k$

G_j = Relaxation modulus

G_e = Equilibrium modulus or long term modulus

G_k = Relative moduli

G_g = Instantaneous modulus or Glassy modulus

g_k = Modulus ratio

τ_k = time constant

t = time

Equation (7.9) is known as a Prony series [1].

For implementation in the ABAQUS finite element code, the modulus G_k is non-dimensionalised by the glassy modulus Gg to give,

$$g_k = G_k / G_g$$

A successful set of g_k and τ_k can only be derived by collocation if the collocation points are neither too widely nor too closely spaced. For this reason, the time intervals are chosen on an equally spaced logarithmic scale, preferably unity for the simplicity of calculation [1].

Calculation of the coefficients started by calculating time constants in the logarithmic scale with a linear increase. Eight time constants were determined with a linear increase in the logarithmic time scale. Then, the relaxation ratio was calculated from the experimental data using Matlab software. The change of the elastic modulus with respect to the instantaneous modulus was calculated for the defined time constants. The coefficients are presented in table 7.1 and accordingly the relaxation of elastic modulus is plotted in figure 7.6.

The instantaneous modulus or glassy modulus of the bulk tissue was determined from the mechanical modelling in chapter 6; this was 92 kPa (see Table 6.1). Another essential viscoelastic parameter for the simulation was the Poisson ratio (ν) which was found from the literature as 0.42 [75].

k	$g_k = G_k / G_g$	τ_k (s)
0	0.28	0.101
1	0.17	0.277
2	0.101	0.760
3	0.096	2.086
4	0.093	5.726
5	0.091	15.713
6	0.087	43.12
7	0.082	118.39

Table 7.1. Constants for Prony series.

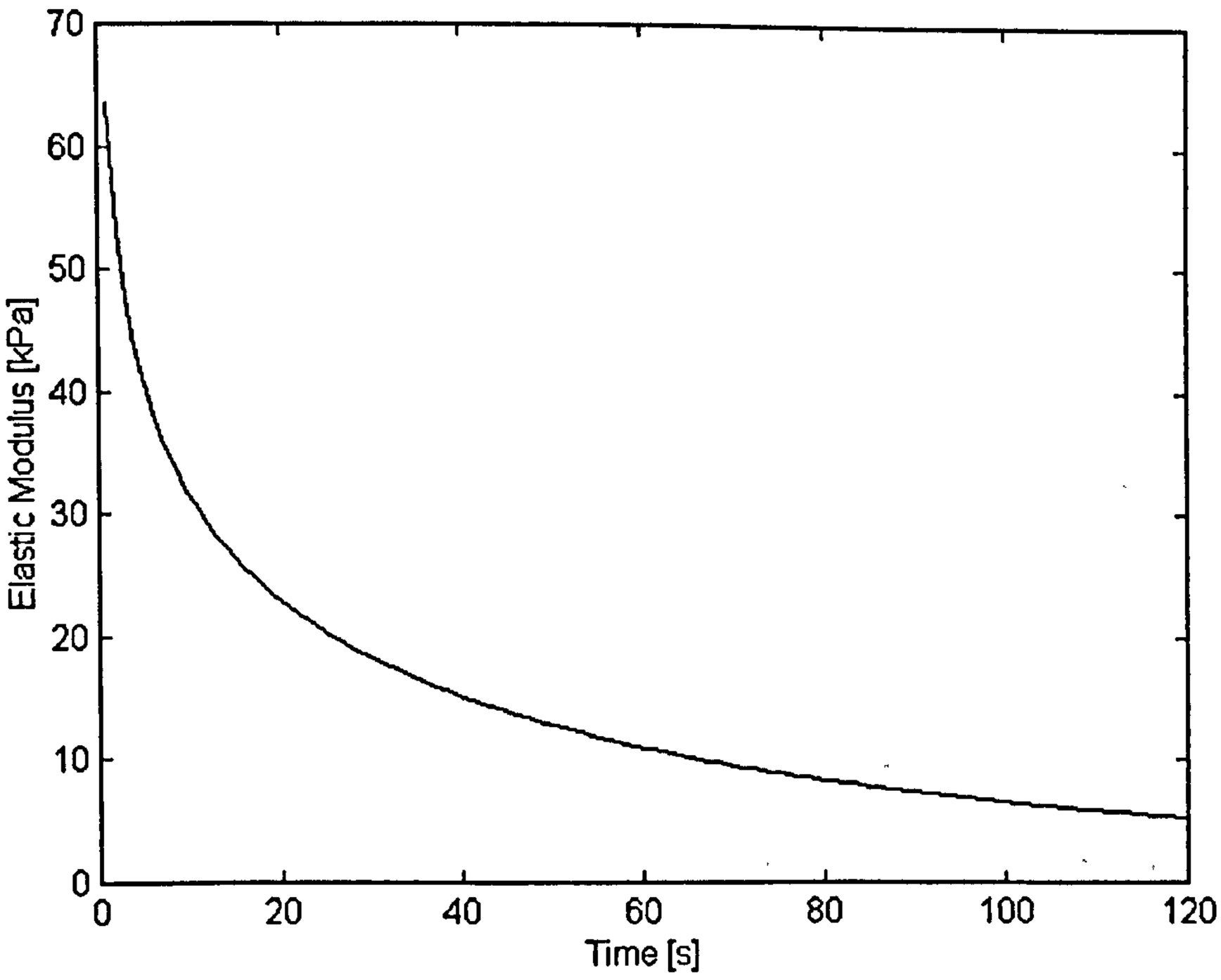

Figure 7.6. Relaxation of the elastic modulus in the creep experiment.

7.4.2. Incremental Variables

Dealing with non-linearity, a solution can only be approximated step-by-step by means of incremental or interactive methods. For this purpose, all relations must be converted into their incremental or interactive forms. As a result of the formulation, the non-linear equations are replaced by linear incremental or interactive relations in which the tensorial terms must be updated at each increment or iteration step. Considering finite deformations, two approaches may be applied: the Lagrangian approach and the Eulerian approach. The Eulerian approach refers all the kinematic and state variables to the current configurations of the continuum [42]. In the finite element simulation of the bulk tissue, the increment was restricted between 1 10^{-4} s and 1 s. The ABAQUS finite element software found out the best time increment for each iteration step [1, 2].

7.4.3. Results of Finite Element Analysis

The ABAQUS finite element software was run on a Silicon Graphics Origin 2000 which is one of the most powerful computers in the U.K. SGI 2000 has just been installed at the Manchester Computing Centre for heavy numerical calculations such as ABAQUS. The present configuration of the system has 40 x R10000 MIPS parallel processors. However, using the smallest number of elements possible from the geometry of the upper arm, the computing time in the SGI 2000 was approximately 8 hours. The non-linearity of the mechanical properties and non-symmetric three-dimensional geometry caused the long calculation time. The geometrical deformation of the human upper arm can be seen in figure 7.7. The deformation of one of the outer nodes was plotted in figure 7.8. It can be noticed that there is a vibration on the node at the beginning of the simulation. This occurred because of a sudden application of the constant load.

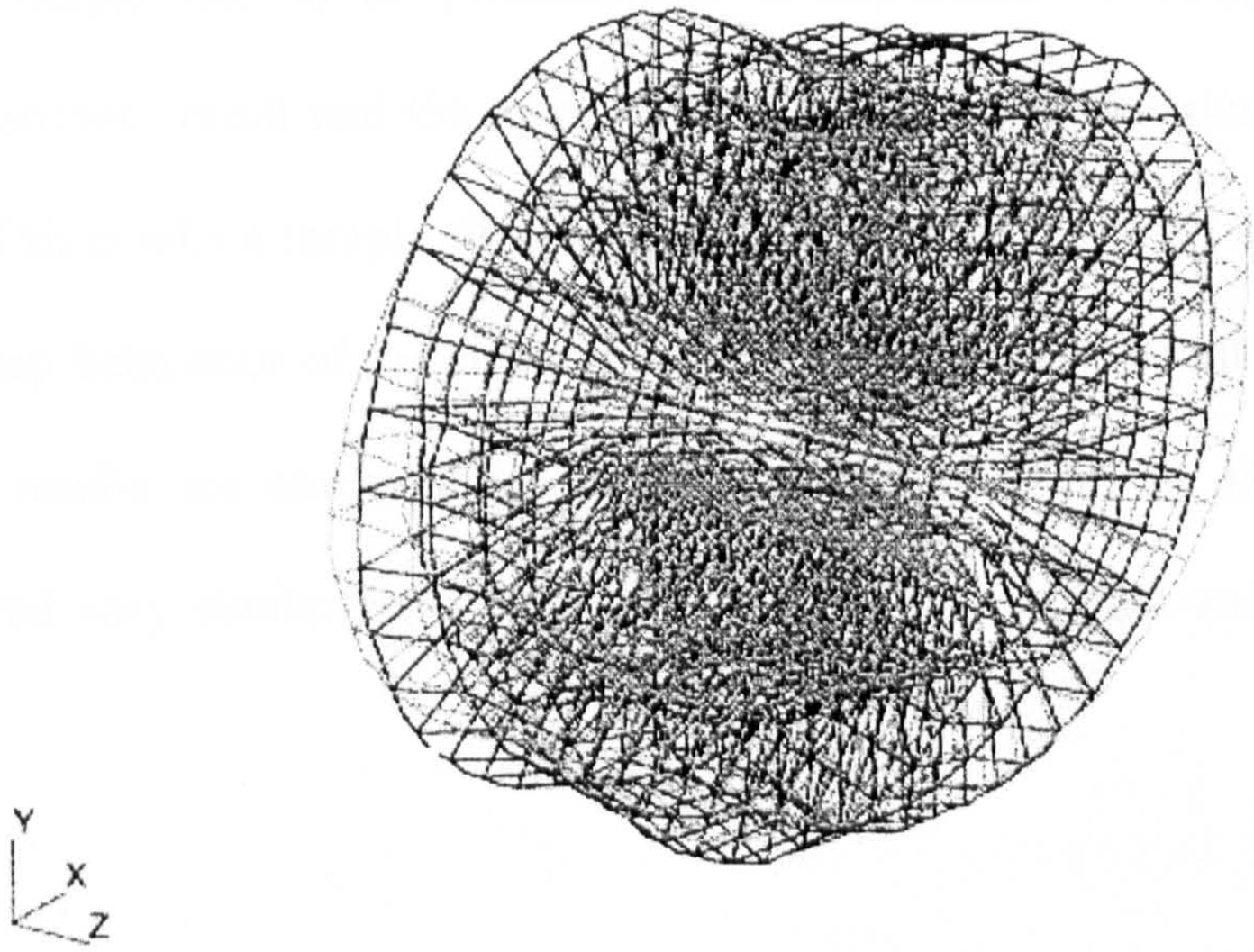

Figure 7.7 shows the deformed shape of the upper human arm under the constant load of 60 kgf.

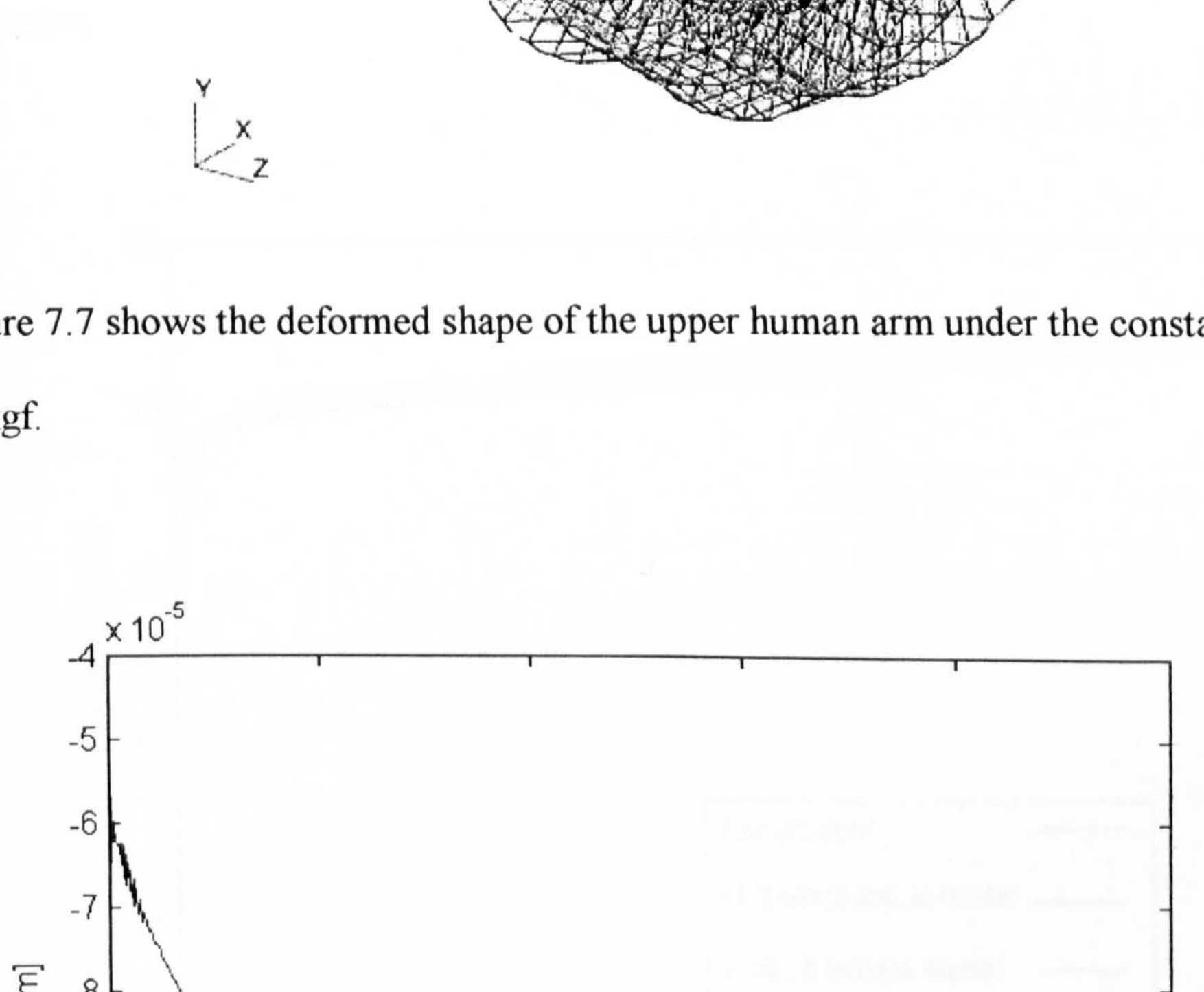

Figure 7.8. The deformation of the outer node in the X direction for 2.5 s.

To compare the finite element simulation to the SLS mechanical model and the experiment, the output had to be processed. It is impossible to compare a one-dimensional experiment result and the mechanical model to a three-dimensional finite element model. This is why a sample slice among the finite element mesh was chosen to represent the creep behaviour of the finite element simulation. The result is plotted in figure 7.9. The results are encouraging, in that the one slice of the finite element simulation showed very similar trends both to the experimental data and mechanical simulation.

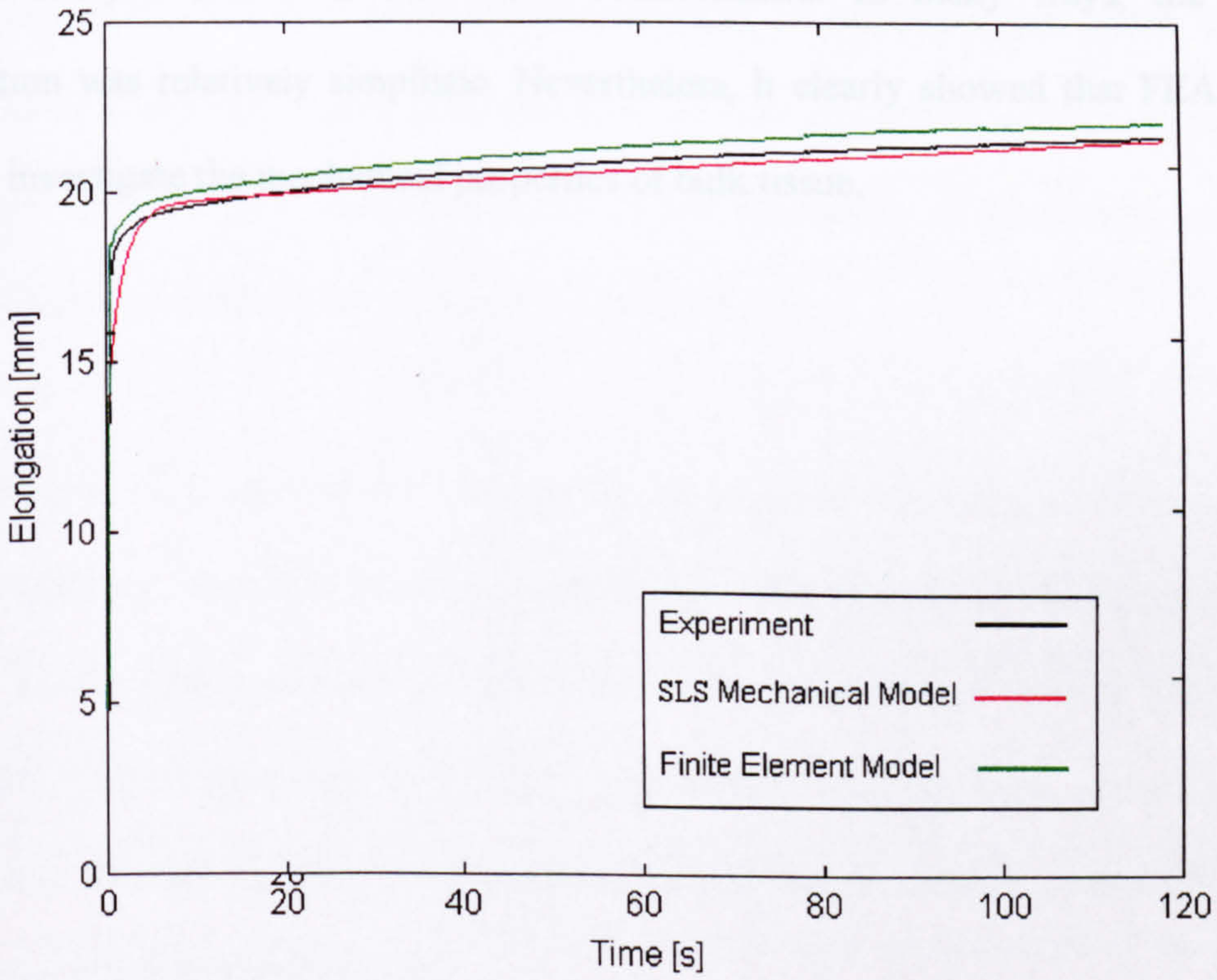

Fig. 7.9. The comparison of the finite element model simulation of experimental data and the mechanical model.

7.5. Summary

In this chapter, the finite element method (FEM) was applied to simulate the creep behaviour of the human upper arm. Using FEM, one-dimensional mechanical modelling of the soft tissue was converted into a three-dimensional FE model. The instantaneous modulus or glassy modulus of the bulk tissue was determined from the mechanical modelling in chapter 6. The time domain dynamic properties of viscoelastic materials were represented in the ABAQUS finite element software by means of a "Prony series".

The simulation presented in this chapter was chosen to illustrate the use of the finite element analysis (FEA) in soft tissue biomechanics. In many ways, the chosen application was relatively simplistic. Nevertheless, it clearly showed that FEA can be used to investigate the mechanical properties of bulk tissue.

Chapter 8

Discussion and Conclusions

8.1. Discussion

8.1.1. Introduction

From a mechanical point of view, all soft tissues are composite materials. These materials are composed of two or more material components which interact to give the composite material its overall properties. Most often these materials can be classified as 'fibre composites', having a certain volume fraction of relatively stiff fibres that are embedded in a less stiff matrix [18]. Much of the time-dependent properties and non-linear behaviour of these materials is due to the interaction of fibres and matrix in transmitting stress through the whole of the material [18].

Soft biological materials are not perfectly elastic because some degree of viscosity is always associated with their mechanical behaviour. This means that the response to an external load is time-dependent and that some of the strain energy input is lost as heat by internal viscous processes. Soft tissues, like muscle, are non-linear, anisotropic and viscoelastic. Because of these complications, finding the mechanical properties of soft tissue is not a straightforward task.

Accordingly, soft tissue biomechanical properties have been neglected by researchers. However, there have been numerous experiments on the mechanical properties of bone and cartilage. Soft tissue research has been limited to *in vitro* studies with exceptions.

8.1.2. New Equipment Design and Development

8.1.2.1. Overview

Another reason why *in vivo* soft tissue research has been neglected by researchers, is the availability of appropriate testing machines to run a series of experiments. Most researchers have used indentor tests to obtain mechanical properties of soft tissue *in vivo*. The drawback of the indentor test is that the load applied to the soft tissue is limited; depending on the cross-section of the indentor tip and the tissue under the indentor, the deformation in three-dimensional. Therefore, some of the response of the soft tissue is not observable. A schematic diagram of an indentor test can be seen in figure 8.1a.

Consequently, a new instrument was designed to apply controllable uniform pressure around the human upper arm *in vivo*. The main difference between the new test machine and the indentor test is that the new design applies the load almost uniformly around the upper arm; therefore, the deformation of the soft tissue was largely in the radial direction. Figure 8.1b shows a schematic representation of the new design, which was capable of running three different type of mechanical test with minor changes to the instrument. These three tests, which were creep, stress-relaxation and stress-strain tests, are very important to understand the viscoelastic behaviour of *in vivo* bulk tissue. The first two are transient methods, usually applied to studies of time-dependent mechanical properties, while the latter method employs a constant strain-rate. Combining these methods allowed the broadening of the experimental time-scale. Results from these tests could than be inter-related qualitatively or by exact mathematical functions.

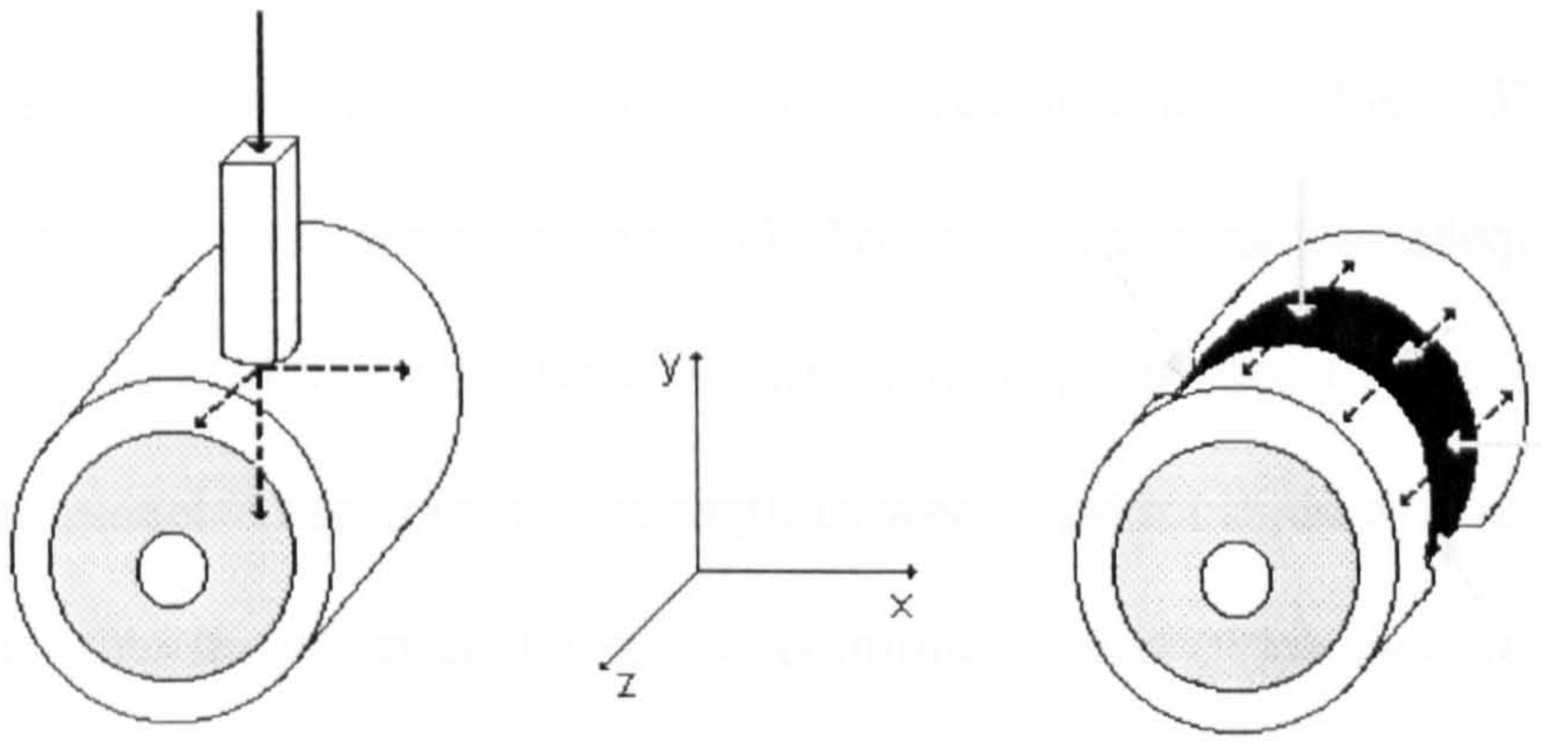

Figure 8.1. Comparison of the indentor test and uniform pressure test.

The realization of the system from concept to hardware and software required competence in the development of a 'mechatronics' approach [10]. In engineering design, a 'mechatronics' approach represents and requires the integration of a wide range of material and information. In this study, this required, particularly:

- The mathematical modelling of mass, spring and damper system with multiple degrees of freedom.
- The selection and application of sensors.
- Instrumentation generally, including the use of portable data collection and test equipment.
- The design and application of electrohydraulic and electropneumatic control systems.
- The use of microprocessor-based development systems.
- The establishing of control algorithms for system development.
- The general knowledge of analog circuit design and electrical installations, signal conditioning and other circuits.

8.1.2.2. Hardware

Taken altogether, this was a complex and challenging engineering problem. The design was started by choosing the structure material. To design the structure adequately for the requirements, the loading on the structure was carefully analysed by applying loads to the prototype model. Therefore, the strength-to-weight ratio played a crucial role in the stage of choosing the material. Therefore aluminium based extrusions were chosen in the construction of the design.

It was also very important to choose a suitable material and to design the mechanism to apply the external load onto the human upper arm. The material needed to be flexible enough to cover the upper arm and strong enough to transmit the external load to the upper arm. A standard car seat belt was suitable to provide these requirements. The squeezing chamber design was explained in detail in chapter 3 section 3.1.2. The seat belt has shown a non-linear elastic behaviour. The mechanical properties of the seat belt were extracted experimentally and modelled.

To accomplish the creep test, the deformation of the upper arm, which occurred due to the applied constant load, had to be measured. The deformation basically took place from the movement of the seat belt. Thus, the movement of the seat belt had to be recorded with time. The linear variable differential transformer (LVDT) has been widely used in this type of precise measurement of displacement. The main objection to using the LVDT was the difficulty of fixing the LVDT on the test rig and the unknown amount of deformation. Hence, an alternative way of measuring was taught. The solution was to use an opto-encoder (Fig. 8.2 (3)) and a cotton thread (1) in parallel with the steel wire (2), which transmitted the load onto the human upper arm. The cotton thread transformed the movement of the seat belt into the opto-encoder as a rotation.

This distinct approach to the measurement performed very efficiently and accurately. The measurement of the load on the seat belt was achieved by using a load cell, which is a popular method of measuring the force. Because of the design of the loading mechanism, the creep test was limited to 60 kgf maximum applicable load.

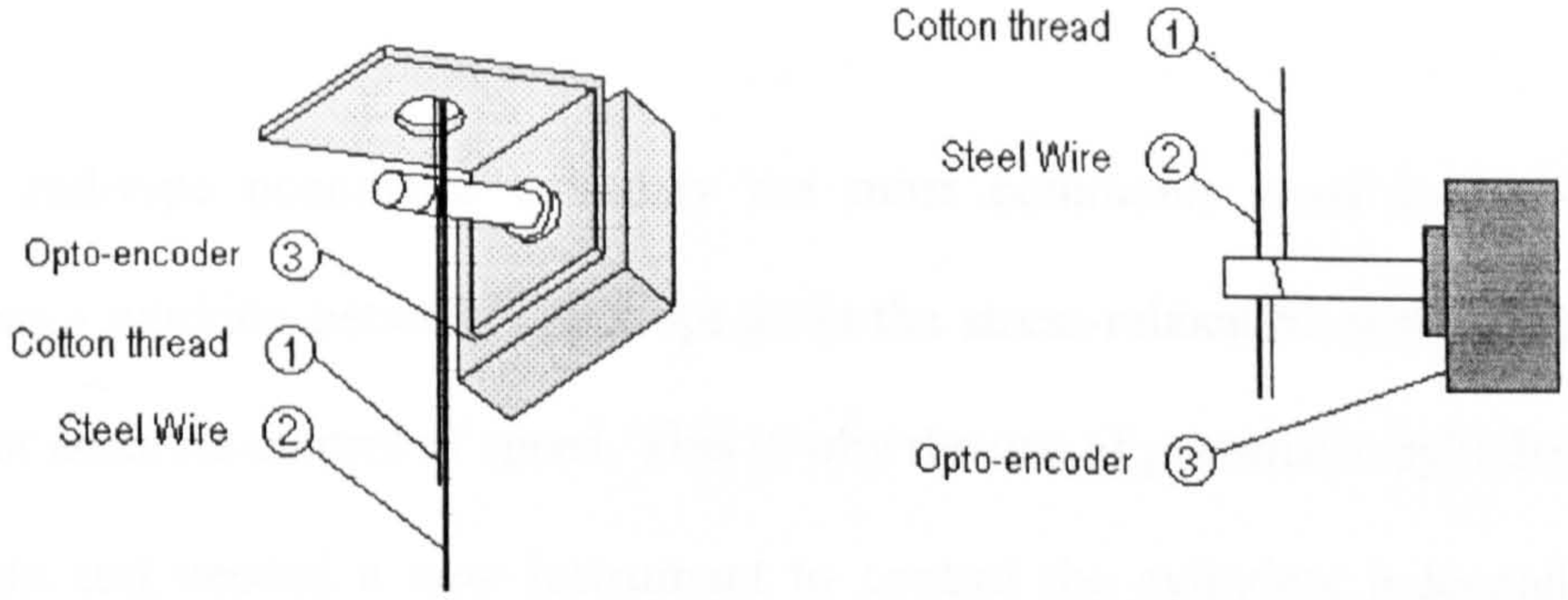

Figure 8.2. The measurement of the seat belt movement.

Choosing the type of the actuator was the next important topic for designing the stress-relaxation and stress-strain test mechanism. The output of the actuator could be related to the measurement made by the sensor, according to the algorithms and calculation processes within the controller, but subject to limitations imposed by the processing rate of the controller. Therefore, the actuator had to be compatible with the chosen sensors and the controllers.

The second decision to be made on choosing the use of linear or rotational actuators. The principal division lies between rotational and linear devices, with motion converters such as gearboxes or rack and pinion systems being added where appropriate. Selection criteria are based first on the magnitude and the range of the primary parameters to be controlled secondary, but significant, considerations such as bulk, weight, cost, accuracy, resolution and rate of response [10].

Considering all parameters mentioned above, a rod-type pneumatic cylinder was the best solution for the required sudden movement of the stress-relaxation test. There was also another reason for choosing the pneumatic cylinder. This was the safety aspect of the design; the applied load had to be released quickly when necessary. Because of the easy release of the compressed air, pneumatic systems were considered a safe energy source.

Although rod-type pneumatic cylinders are most commonly used in two-position applications - working between end stops as in the stress-relaxation test - they are not suitable for accurate control of speed. This is why the use of pneumatic cylinders for the stress-strain test needed a new instrument to control the cylinders independently. A linear stepper motor gave the best solution for controllable movement of the stress-strain test. The linear stepper motor was fixed on top of the main frame to behave as a controllable end stop. The linear stepper motor has 0.025 mm step accuracy, which was more than the resolution needed for the stress-strain test. The drawback of the high resolution step was the maximum speed of the linear stepper motor which was 4.8 $mm.s^{-1}$. The maximum speed was a limitation of the stress-strain test design.

In addition to the mechanism and actuator weight, there was also the weight of the structure and the enclosure to be considered. That is why the fixing points of these components were given careful consideration in the design.

8.1.2.3. Software

It is self-evident that the effectiveness of any PC-based instrumentation or control system will be dependent not only on the hardware used but also on the software which controls the system. Software has a vital role to play, in that it provides an interface

between the user and the physical components of the system. Furthermore, the degree of control, flexibility and ease of use are largely dependent on this software interface. New topdown software was designed to control the moving part of the testing machine and store the output data from the test. The schematic diagram of the software design is shown in figure 8.3.

In the software design, four important concepts were considered carefully: ease of use, flexibility, performance and functionality [60]. To improve the interface between the user and the software, a graphical user interface (GUI) was designed. The GUI allows the user to control the testing machine simply by clicking buttons, which represent the procedure, on the computer screen with the pointing device. Examples of the GUI can be seen in chapter 4 figures 4.4, 4.5, 4.7, 4.8, 4.11 and 4.12.

The importance of the flexibility of the software is that of interfacing with other software packages, so that data can be exported and imported, in a way which is largely transparent to the user. This is why the testing software can export the data to commercial software, such as Matlab and Microsoft Excel, which were used to analyse the data.

Determining the performance of the software design can be very difficult [60], because every application has its determining factors. Generally processing speed is the most important factor for instrumentation software. All software was written in the C programming language.

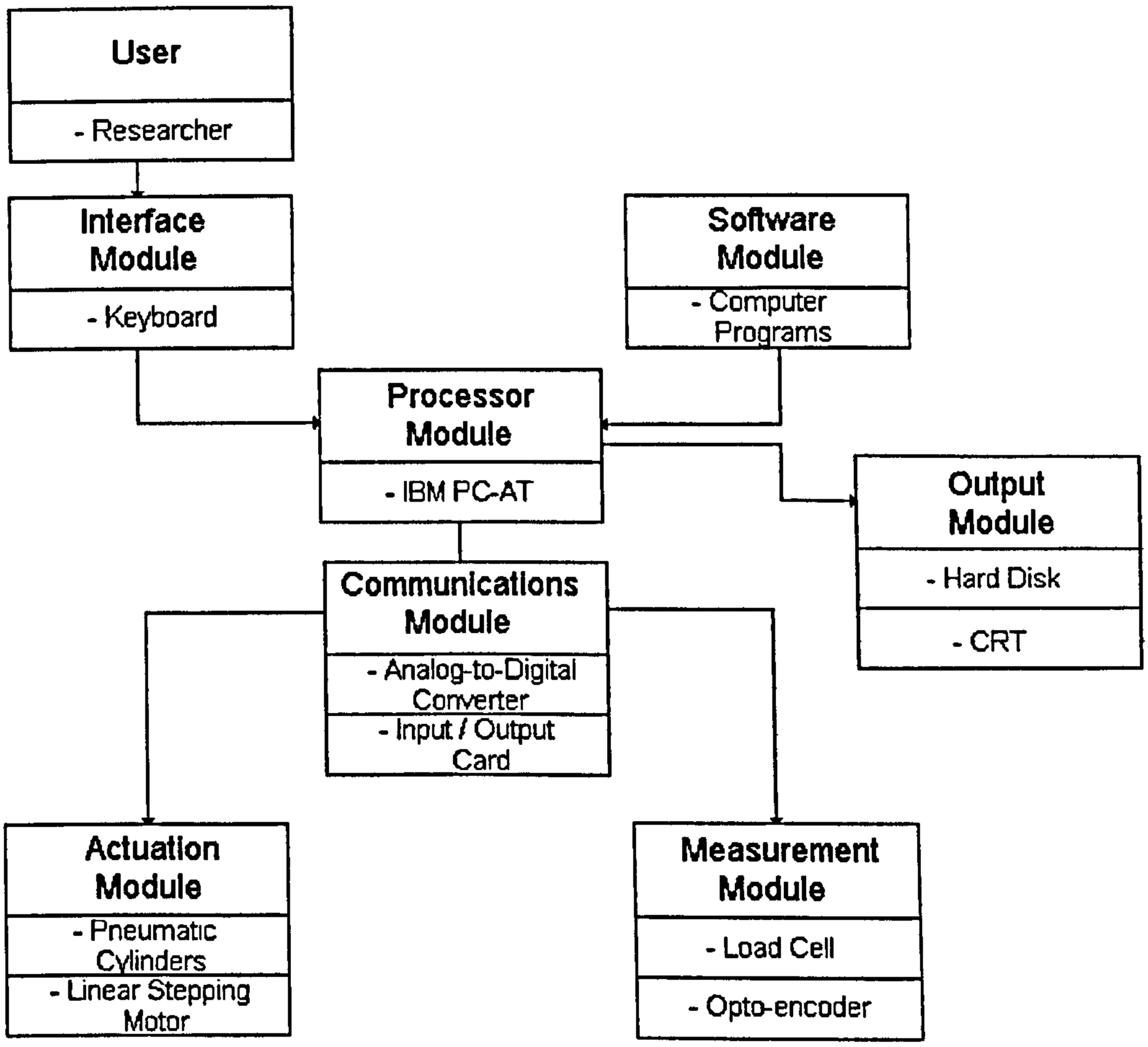

Figure 8.3. The design of the control software.

The C programming language offers some significant advantageous in the development of software for real-time applications. The language promotes use of structure and is highly portable. Furthermore, when compiled, it offers non-comparable execution speeds among the high level languages [54]. The data collection rate was 2.5 kHz during the test and graphical representation of data was plotted in real-time. Collection of data and graphical presentation of the data in real time required the use of assembly language.

Functionality of the software usually helps to add new features to the design. The software was designed to perform many functions in the same hardware. Modules,

which are shown in figure 8.4, used the same data structure. Consequently, the data was transferred or was shared smoothly between the modules.

8.1.3. Determination of Soft Tissue properties

8.1.3.1. Image Processing and Geometrical Modelling

In the development of an *in vivo* method for determining the stiffness of soft tissues, the geometry of the tissues had an important effect on the calculations and modelling stages. Cross-sectional geometry can be best measured from transverse sections of the structure of interest. Working with photographs of sections, digitized coordinates from a given structure's cross-sectional shape data can be obtained from a graphical tablet or a computer screen image acquired via an image scanner. The user determines the coordinates by using a graphical tablet or computer screen. Unfortunately, this method has two main drawbacks: the first is that manual digitising can add user errors to the results. Secondly, it is almost impossible to digitise three dimensions keeping the same global coordinate system.

Computerised tomography (CT) and magnetic resonance imaging (MRI) can be used for the non-invasive determination of cross-sectional contours of various anatomical structures in multiple planes and locations. Several considerations are critical to obtain accurate, precise CT or MRI scans of skeletal structures. CT and MRI scanners code the skeletal structures as black, grey or white, according to user preferences. The optimum settings for imaging a particular issue, such as the human upper arm, vary from scanner to scanner [11, 34].

Commercially available software for shape analysis frequently provides algorithms to determine cross-sectional area, but these algorithms do not work for creating a three-

dimensional mesh. Therefore, a new algorithm, consequently new software, was created to process the MRI or CT scans. There is only one similar approach found in the literature by Tu *et al.* [74], which was used to determine the left ventricular boundary from spatio-temporal volumetric computed tomography images.

The same principles as mentioned in the design of testing software were followed during the design of mesh generation software. The GUI allows the user to manipulate the MRI or CT scans. Mesh generation software can export the data to commercial finite element software, such as ABAQUS, ANSYS or a finite element preprocessor like PATRAN. All software consisted of 5000 lines of code written in the C and assembly programming languages. The detailed explanations of the algorithm and software can be seen in chapter 2.

8.1.3.2. Experimental Factors

Bulk tissue is a complex structural material and it is subject to the same engineering laws that govern the behaviour of engineering materials such as metals, concrete and polymers. The mechanical response of bulk tissue can be observed by subjecting it to tension or compression. Testing of the human upper arm was carried out using three different test procedures to try to determine the bulk properties of the arm. The important factors to be considered when designing such an experiment were:

- Soft biomaterials are usually composites and will almost certainly exhibit non-linear elasticity, i.e. the mechanical response will depend on the amount of strain imposed.

- These materials will probably be anisotropic, i.e. the mechanical properties will depend on the direction of loading.

- Large deformations are likely and must be accommodated by the test instruments and the methods used to calculate stress and strain. In fact, anything above 1% or so is beyond the strict limits of linear elastic theory [18].

8.1.3.2.1. Creep Test

The creep test was applied to the subject with two different protocols. In the first protocol, the subject did not contract his muscle during the test. In the second test, the subject sustained his muscle contraction at 25% of his maximum voluntary contraction (MVC) during the test. The same test protocols were also applied to the stress-relaxation and stress-strain tests. Because of the contraction of the muscle, there was an increase to the upper arm circumference. The difference between the relaxed and the contracted muscle states was 5 mm which caused an expansion of 1.6 mm across the upper arm radius. Consequently, the increase of the arm circumference changed the load surface by an additional 2.25 10^{-4} m^2 which is very small, therefore the effect was ignored.

In the creep test results, the relaxed test procedure showed higher elongation results than the contracted test procedure. It is obvious that this response is caused by the increased stiffness of the contracted muscle tissue. The comparisons can be seen in appendix B.2. Another typical soft biological tissue response can also be seen from figure 8.6, for the relaxed test procedure, and figure 8.7 for the contracted test procedure. The linear increase of the applied load showed a non-linear increase in the elongation. This can be explained, in terms of engineering, by the applied load reaching the limiting load and can also be explained, in terms of soft tissue, by the human upper arm reaching a state of the incompressibility.

An interesting result from the experiment can also be observed - the creeping of the contracted muscle is higher than the relaxed muscle. This response can be interpreted in the following way: To produce force, muscle tends to shorten. Considering the muscle has a constant volume, any decrease in one dimension must therefore result in an increase in another. Deep fascia does not expand in the same way, consequently, the internal pressure of the muscle increases with the contraction. The contracted muscle structure therefore causes a higher creeping response than the relaxed muscle.

The schematic response can be seen in figures 8.4 and 8.5. After this level, the contracted muscle tissue response was higher than the relaxed test condition. The relaxed contracted test conditions are illustrated in figures 8.4 and 8.5.

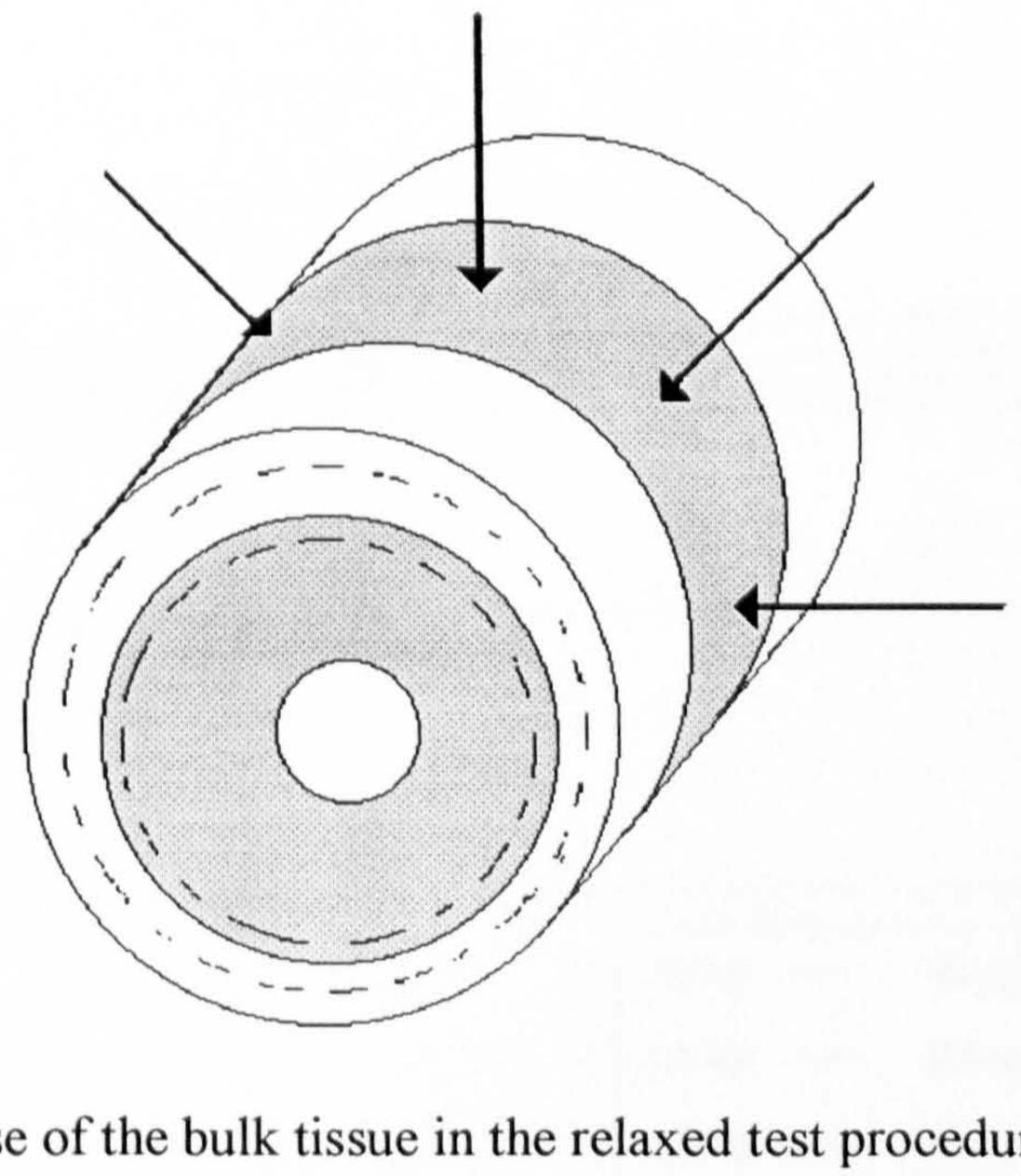

Figure 8.4. The response of the bulk tissue in the relaxed test procedure.

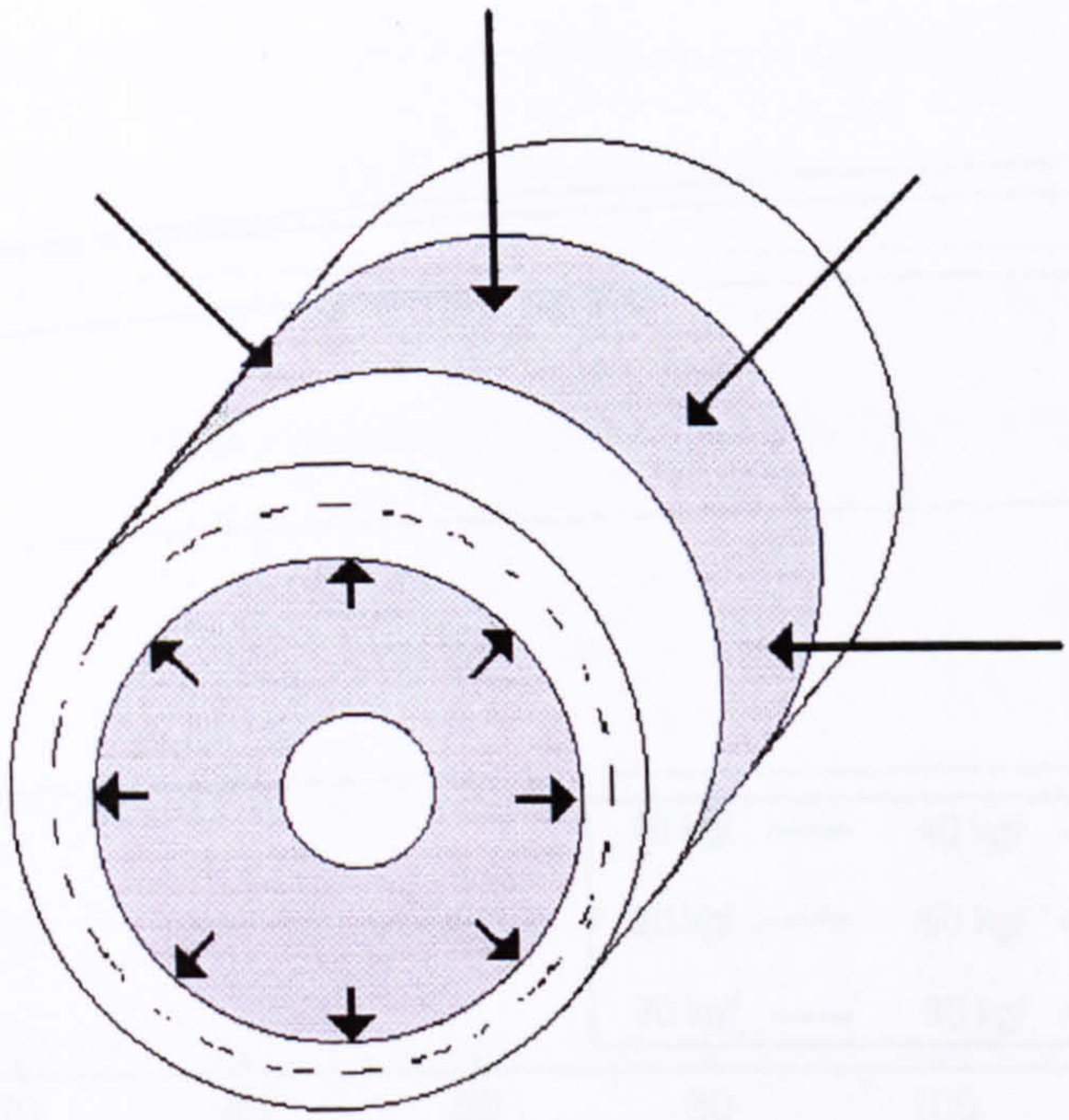

Figure 8.5. The response of the bulk tissue in the contracted test procedure.

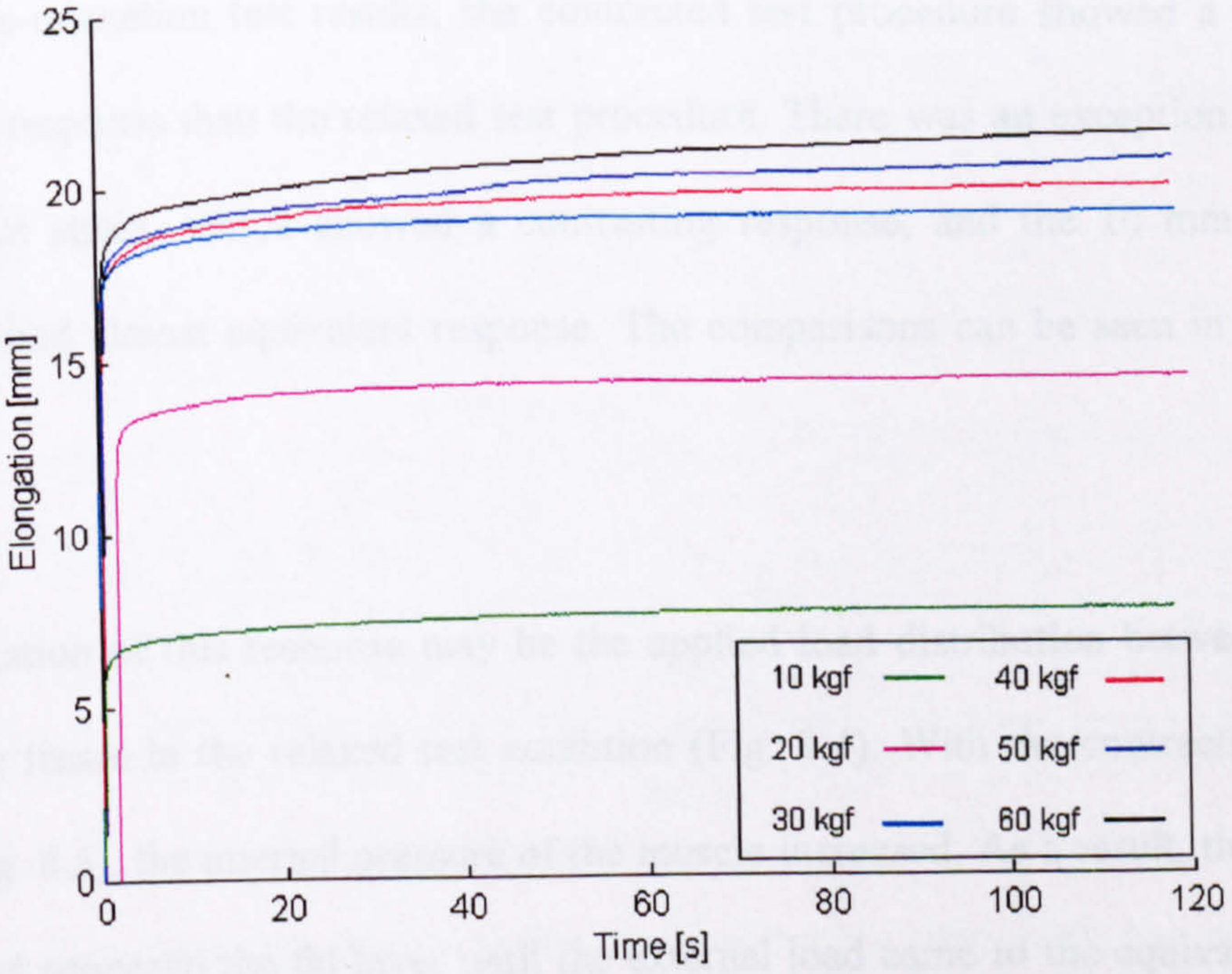

Figure 8.6. Experiment result of the creep test with the relaxed test procedure.

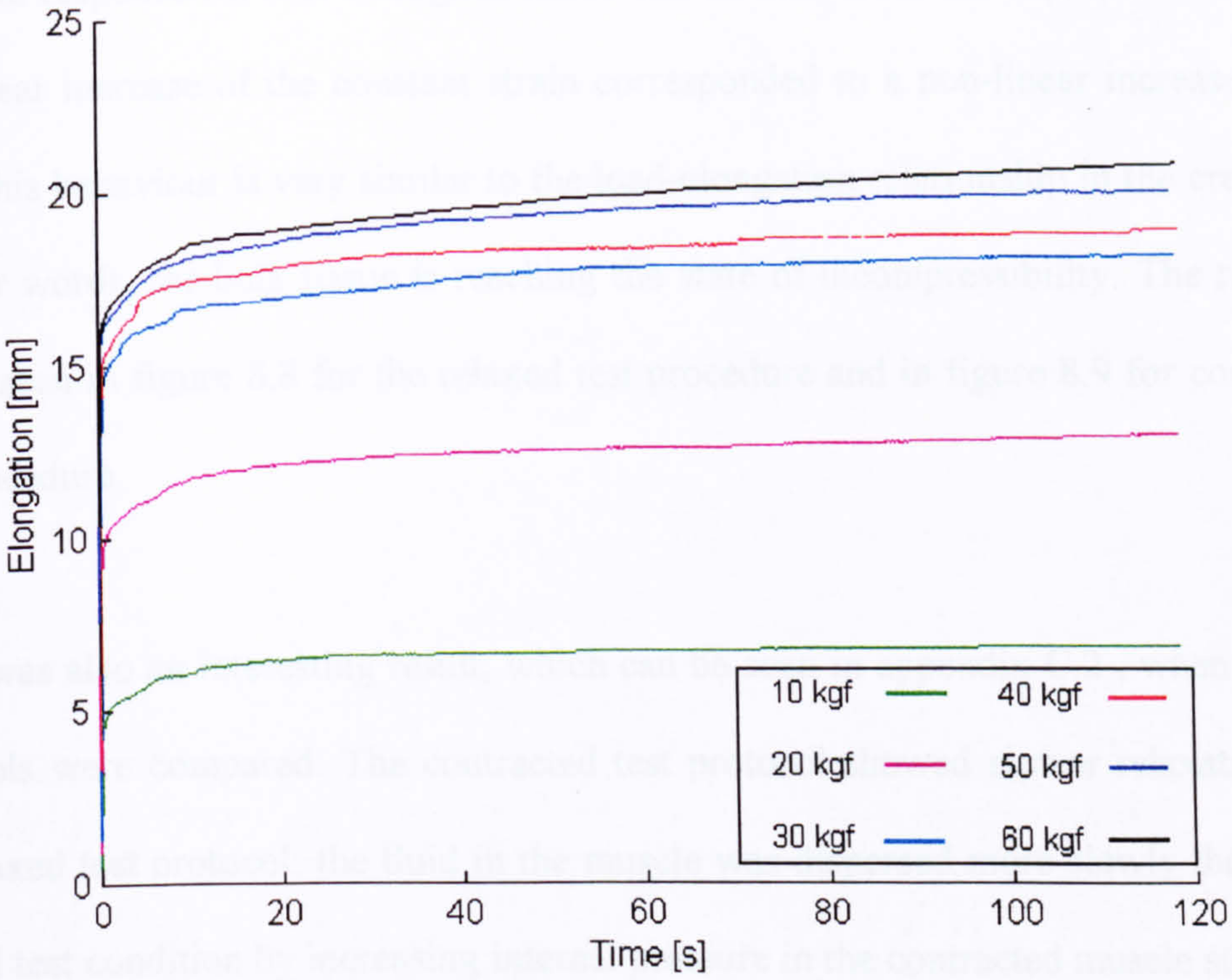

Figure 8.7. Experiment result of the creep test with the contracted test procedure.

8.1.3.2.2. Stress-relaxation Test

In the stress-relaxation test results, the contracted test procedure showed a generally higher load response than the relaxed test procedure. There was an exception for the 5 mm constant strain, which showed a contrasting response, and the 10 mm constant strain exhibited almost equivalent response. The comparisons can be seen in appendix C.2.

The explanation of this response may be the applied load distribution between the fat and muscle tissue in the relaxed test condition (Fig. 8.4). With the contraction of the muscle (Fig. 8.5), the internal pressure of the muscle increased. As a result, the external applied load squeezed the fat layer until the external load came to the equivalent value of the internal pressure of the muscle, then the external load scattered between the muscle and subcutaneous tissue.

A typical response for soft biological tissue can be seen from the experimental results. The linear increase of the constant strain corresponded to a non-linear increase of the load. This behaviour is very similar to the load-elongation relationship in the creep test; in other words, the bulk tissue is reaching the state of incompressibility. The response can be seen in figure 8.8 for the relaxed test procedure and in figure 8.9 for contracted test procedure.

There was also an interesting result, which can be seen in appendix C.2., when the two protocols were compared. The contracted test protocol showed slower relaxation than the relaxed test protocol: the fluid in the muscle was dispersed more slowly than in the relaxed test condition by increasing internal pressure in the contracted muscle structure.

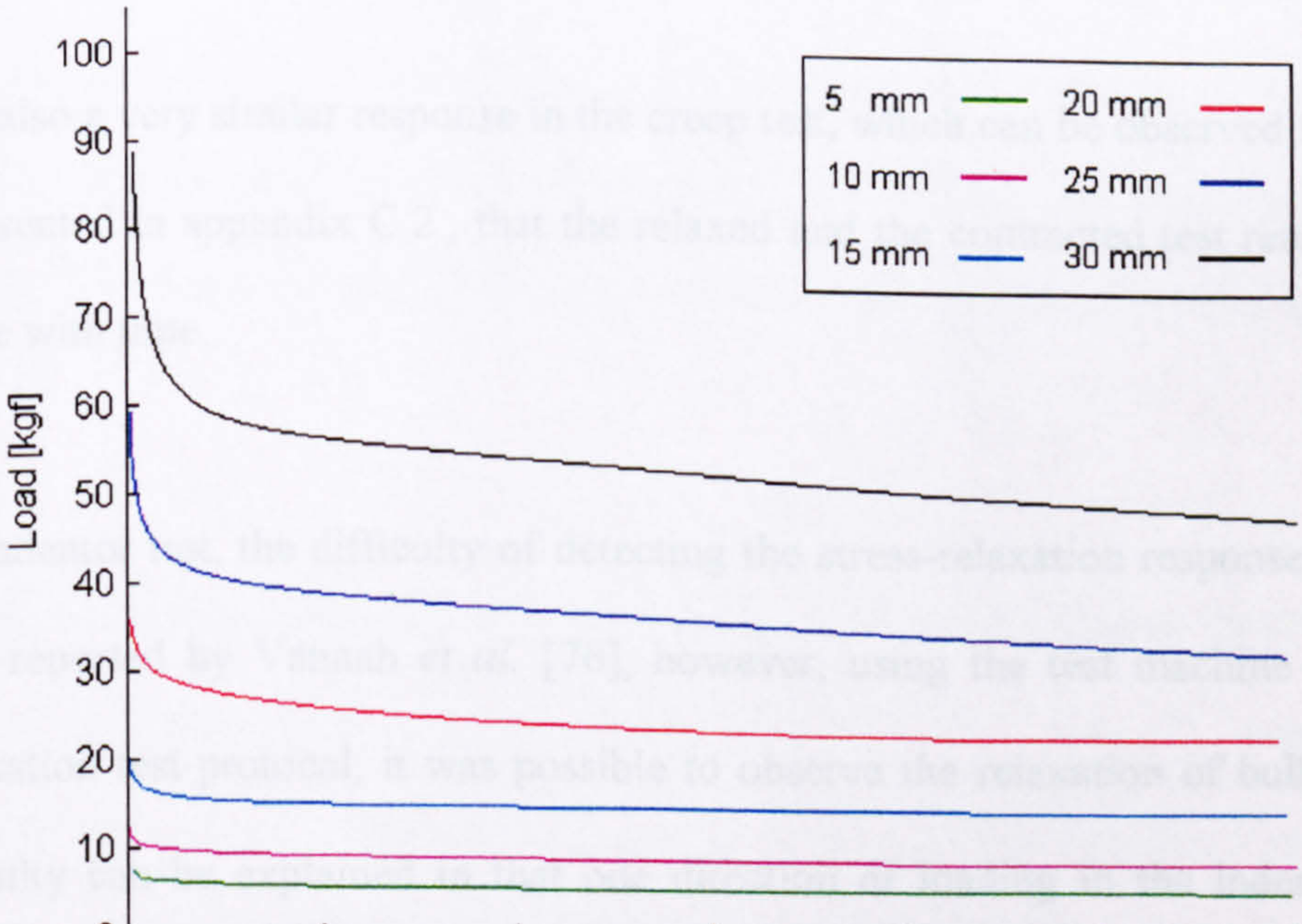

Figure 8.8. Experimental result of the stress-relaxation test with the relaxed test procedure.

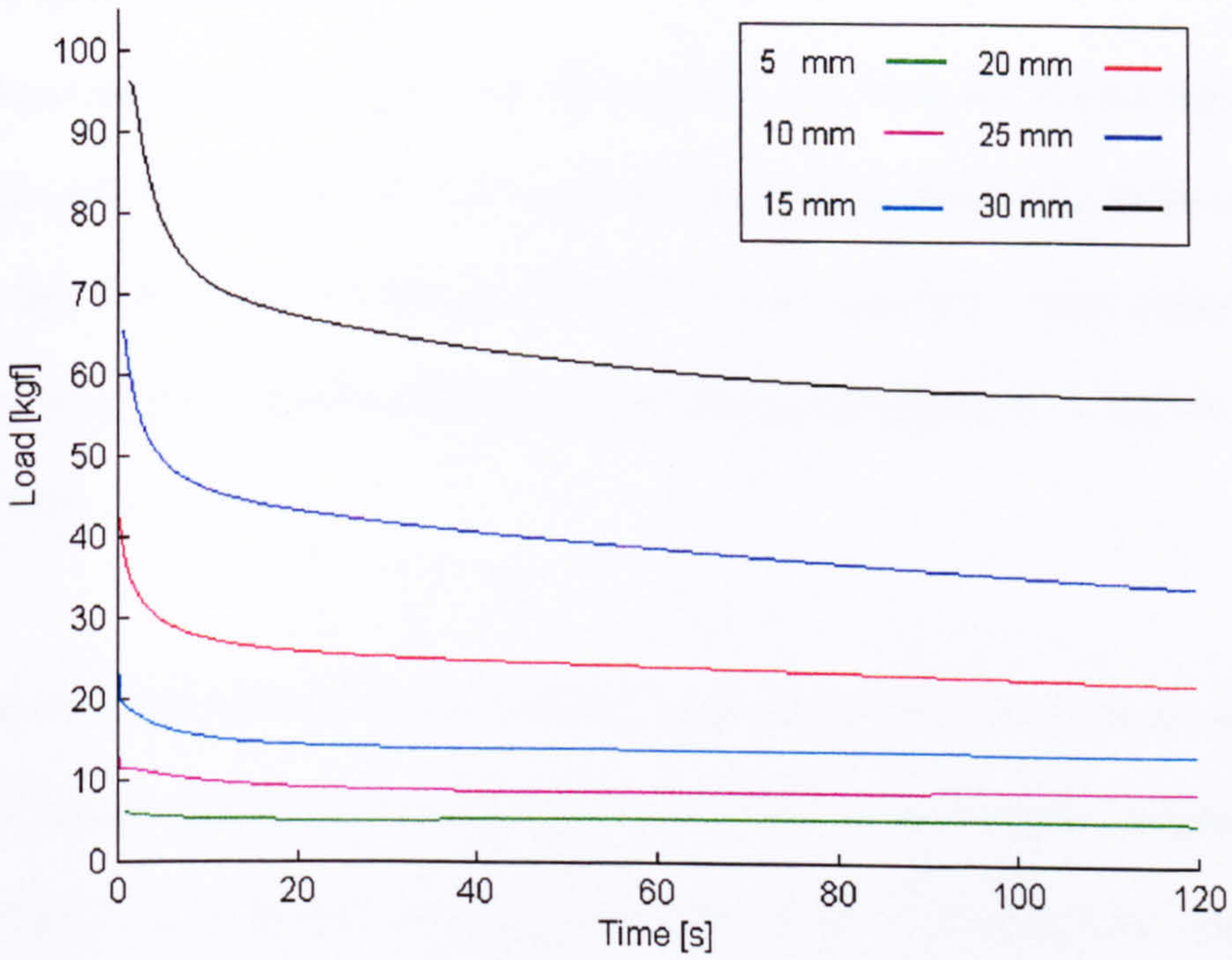

Figure 8.9. Experimental result of the stress-relaxation test with the contracted test procedure.

There was also a very similar response in the creep test, which can be observed from the figures presented in appendix C.2., that the relaxed and the contracted test results tend to converge with time.

Using an indentor test, the difficulty of detecting the stress-relaxation response of bulk tissue was reported by Vannah *et al.* [76], however, using the test machine and the stress-relaxation test protocol, it was possible to observe the relaxation of bulk tissue. This difficulty can be explained in that one direction of loading in the indentor test causes dissipation of fluid in other directions, which makes it very difficult to detect the relaxing response of the bulk tissue.

8.1.3.2.3. Stress-strain Test

In the stress-strain test, generally, a stiffer response was observed for the increase of the strain rate with the two types of test protocols. In the slow strain rate, there was enough time for the fluid to move through the bulk tissue structure. These experiments are plotted in figure 8.10 for the relaxed test condition and figure 8.11 for the contracted test condition.

When these two test protocols are compared, (see appendix D.2), it can be seen that, in the lower strain region, the relaxed test condition showed higher resistance to the applied external load than the contracted test procedure. This behaviour was similar to the behaviour of the stress-relaxation test for the low strains. This response can be explained by the fat tissue between the contracted muscle and external load (as in Fig. 8.4 and Fig. 8.5) being squeezed before the muscle tissue. On the contrary, the muscle tissue does not change its internal pressure in the relaxed test procedure, as a result, the fat and the muscle tissue compressed together. This observation also supports the explanation that was put forward earlier for the stress-relaxation test and creep test results.

In the higher region of strain, the relaxed and contracted test procedures displayed very similar load responses in the slow strain rate tests (0.5 and 1 $mm.s^{-1}$), with gradual changes with an increase of the strain rate. The contracted test procedure exhibited a stiffer response with an increase of the strain rate in the higher strain region. It is clear from the experiments that the stress-strain data obtained at a single strain-rate are not very informative, because of the large variations of the properties of viscoelastic materials with time. Thus, in practice, four different strain-rates (in the range of the

speed of the linear stepping motor) tests were used. The experiment showed that a wide range of stress-strain tests must be conducted.

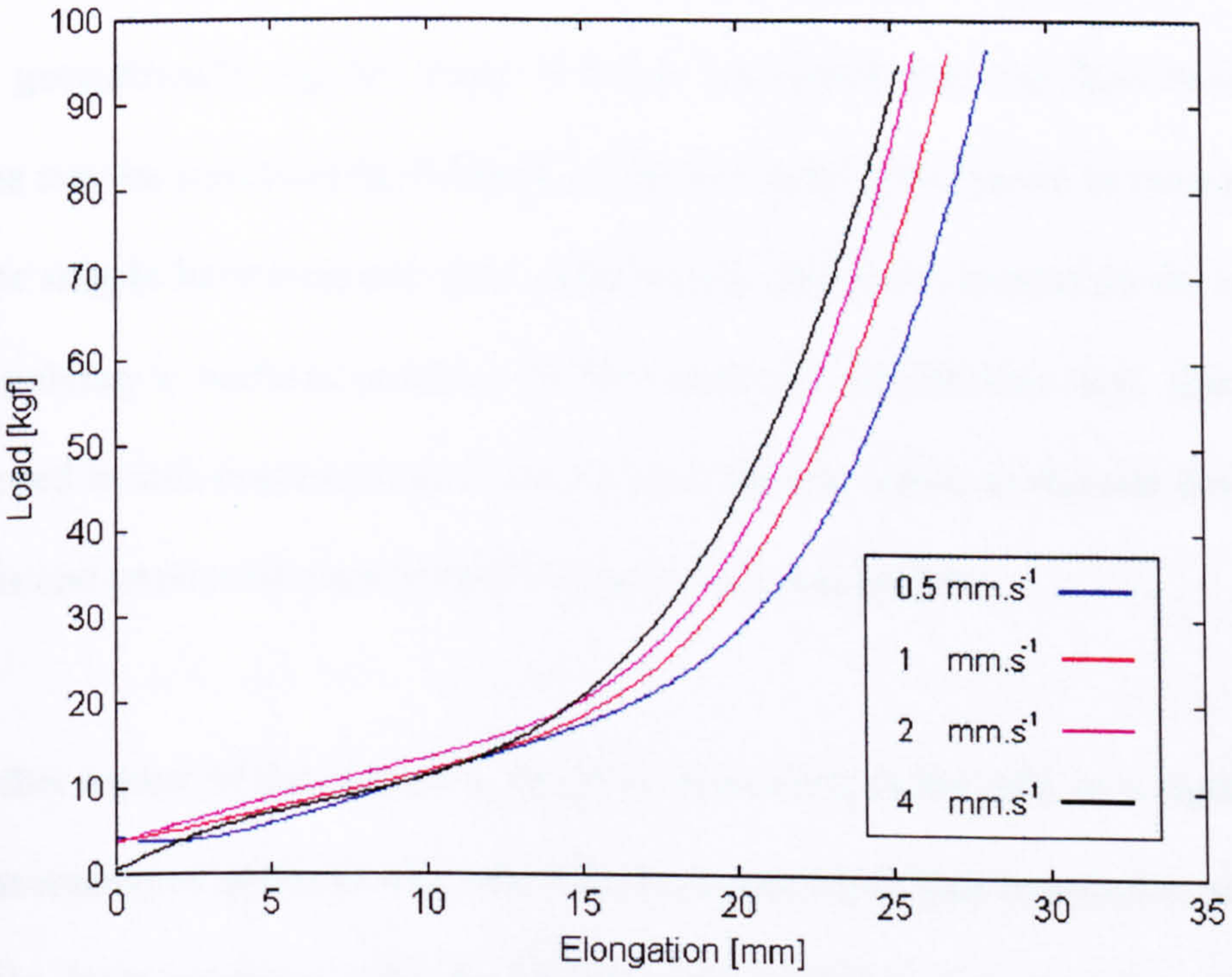

Figure 8.10. Experimental result of the stress-strain test with the relaxed test procedure.

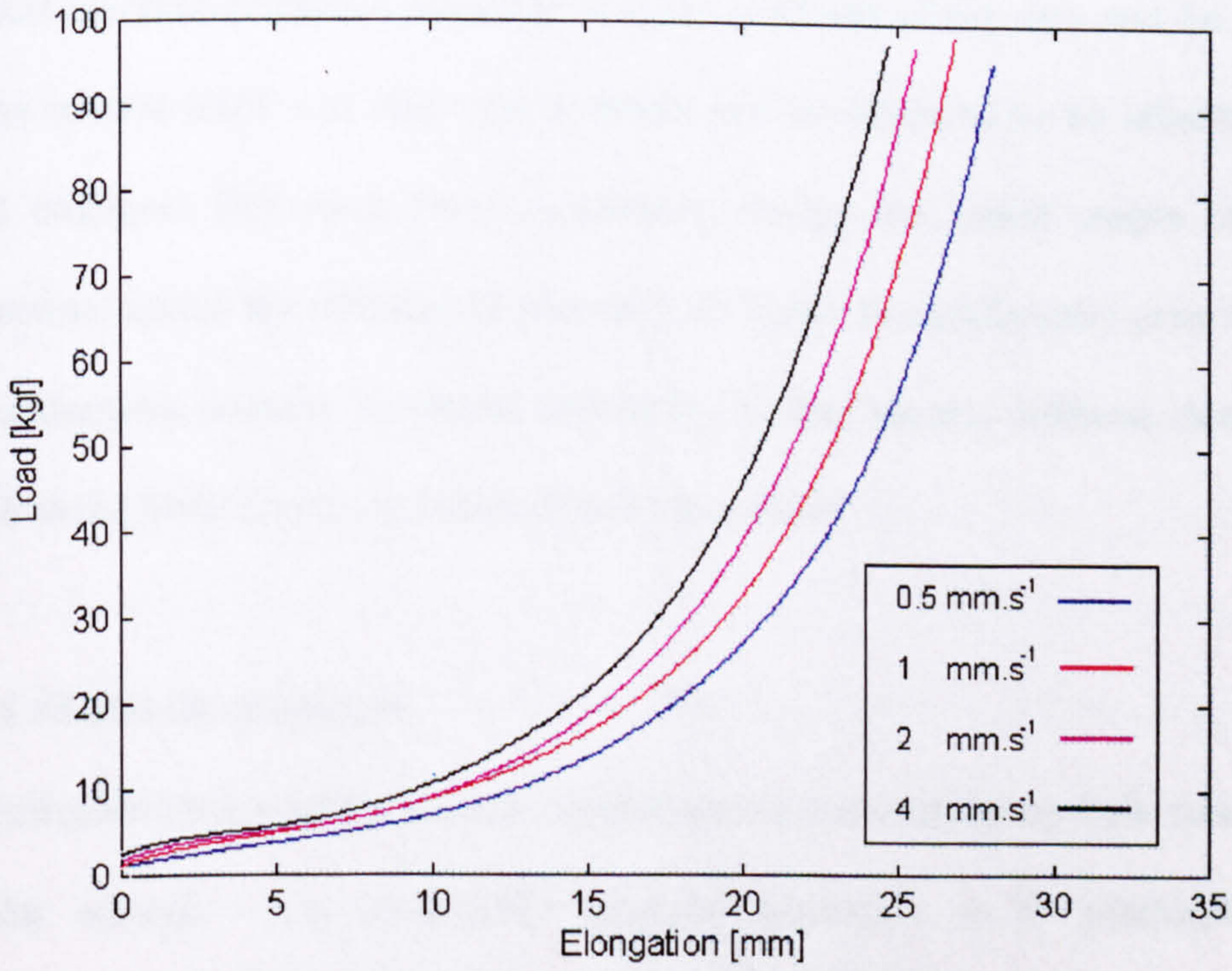

Figure 8.11. Experimental result of the stress-strain test with the contracted test procedure.

Some speculations can be made to explain why the response of the muscle belly is different from other research. This experimental procedure was *in vivo*. Most soft tissue mechanical studies use *in vitro* test methods in which tissue samples have been trimmed to a geometrically regular shape. It seems reasonable that the fluid movement in the tissue may be significantly different in the two cases, since in the *in vitro* case the edges of the sample have been cut open. Additionally, the strain exerted on the tissue, because of applying a uniform pressure in this study, is significantly less than that usually imposed in soft tissue testing. It can be said that the results of the test developed in this thesis and previously used indentor tests are not comparable.

Another aspect of the response, which is interesting, is the lack of a significant change in the measured stiffness when the muscle is activated. This is peculiar, since it appears simply from palpation with the thumb and forefinger that an activated muscle does change its stiffness. One possible explanation is that, since uniform pressure is applied, the test machine primarily measures only the stiffness of the skin and fat layers on top of the muscle itself – in this case it would not be expected to be affected by activity level changes. This must occur, especially during the initial stages of the applied deflection, unless the stiffness of skin and fat layers is significantly greater than that of the underlying muscle. A second possibility is that muscle stiffness does not change much at the limited activity levels of this experiment

8.1.4. Model Development

The microstructures of the various constituent tissues making up bulk tissue are neither regular enough - nor predictably irregular enough - to be practically modelled. Therefore, an empirical approach was used. The essential element of this mathematical model is the material property specification, or constitutive relationship, used for the

bulk tissue. At this phase of the model design, soft tissues – predominantly skeletal muscle but also other tissues such as skin and fat layers, fascia and loose connective tissue - are considered one homogeneous "bulk tissue" [42].

8.1.4.1. Mechanical Model Development

Most of the uniaxial structural viscoelastic models have been based on the discrete element combination approach. It can be observed that the Voigt model sufficiently represents the creep behaviour but does not display stress-relaxation behaviour, the Maxell model shows a reverse of these responses. If one viscoelastic model, which exhibits both creep and stress-relaxation behaviour is required, the Maxell and Voigt models can be combined. The combination model is called 'the standard linear solid model', that is explained in detail in chapter 6.

First, the creep experiment was modelled with a series of four Voigt elements. Using the fitting-by-eye method, the instantaneous elastic modulus of the soft tissue was estimated from the model fitting. The time constants of four Voigt elements were also predicted from the fitting. The calculated instantaneous elastic modulus results are very similar to reported literature. In terms of methodology, there was only one comparable investigation, which had been done by Ursino *et al.* [75]. Their results varied from 90 to 115 kPa for instantaneous elastic modulus. In the model fitting, the elastic modulus varied in the range of 43 to 96 kPa, with respect to the applied load and testing condition (relaxed or contracted). In the experiment, the instantaneous elastic modulus would increase with an increase of applied load.

A similar modelling approach was accomplished for the stress-relaxation test with a series of four Maxell elements. Because of the continuous elongation change in the seat

belt, only the average elastic modulus could be calculated. Time constants of the model were also determined from the model fitting.

Secondly, to simulate creep and stress-relaxation behaviour from one mechanical model, the standard linear solid (SLS) model was created by using the parameters which were determined from the Maxell and Voigt models. Initially, the SLS model showed a stiffer response than the Voigt and Maxell models. The stress-strain behaviour of the SLS model was simulated by changing the elastic modulus distribution in the SLS model.

The result of model fitting of creep and stress-relaxation experiments can be improved by using numerical optimisation methods. Then the calculated parameters can be used for stress-strain tests. The result of the stress-strain test was effected by 12 parameters which can be reduced by optimisation methods.

Considering the various approaches which have been followed towards soft tissue modelling, as well as the specific nature and conditions of the experiments, it is not possible to present one model as more reliable for any case than the others. However, due to its contractile properties, muscle requires a specific analysis, to characterise the active behaviour seperately from the passive response. Therefore, in the experiment design two different type of tests were carried out and modelled. The output of the modelling can be used for as input data for resolution methods, such as a finite element model. Using finite element modelling, the one-dimensional mechanical model can transform to the three-dimensional realistic simulation.

8.1.4.2. Finite Element Model Development

Resolution methods are necessary to obtain temporal descriptions of the state variables as required for the simulation. The assumption of complete linearity is a great advantage because it allows the solution of the complete dynamic problem, and leads to the exact response of the system. However, for a physical simulation, all the non-linearities of a material deformation must be taken into account. In this case, solutions can only be approximated using incremental-iterative procedures after spatial and temporal discretizations [42]. The common approach for this purpose is to combine a finite element discretization of the geometry together with a finite difference discretization of time and an updated Lagrangian iterative scheme based on the Newton-Raphson method [1]. These methods are presented in chapter 7 to provide an understanding of how complex non-linear deformation process and material constituative relations may be applied to soft tissue simulation.

Linear analysis usually leads to one exact solution, whereas non-linear ones lead to slightly different approximate solutions depending on the incremental methods applied [59, 81]. Various numerical methods have been developed for solving non-linear algebraic systems. The finite element method was applied for geometric discretization, while the finite difference and linear integration methods can be invoked for temporal integration. Various incremental or iterative algorithms may then be applied to solve the linearized incremental systems. Iterations can be applied within the increment steps to reduce the errors induced by the finite approximations. There is not a unique solution method, rather a set of possible approaches, whose efficiency depends on the problem to be solved [59, 81].

In chapter 7, a simple simulation of the creep test was analysed as a test problem; this showed that finite element analysis may help to separate the mechanical properties of bulk tissue into, predominantly, skeletal muscle, fat and the skin layer. The objective of finite element simulation was to develop a computational framework to apply the finite element method to anisotropic, viscoelastic soft tissues. To allow efficient and easy computational implementations, a Prony series approximation was developed for the elastic modulus relaxation. This approximation provided a graphic means to fit experimental data with an exponential series. A test problem was analysed to assess the performance of the Prony series approximation and the accuracy of the finite element implementation. Results indicate that the formulation can reproduce time-dependent material behaviour observed in soft tissues.

8.2. Further Directions

The design and suggested methodology could lead to further study in various areas. The difference of the mechanical properties of bulk tissue between the sexes can be easily investigated by simply applying the same test protocol for the two different sexes. It is also clear that different type of longitudinal research can be used to see the long time effect of puberty for the development of muscle tissue in children or, in an opposite way, for the ageing of muscle tissue in elderly people.

The methods developed could also be used to evaluate some illnesses, which affect muscle tissue. The response of patients to various treatments could be quantified by regular testing. A similar approach could be used for sportsman to detect the effect of training on the development of force and, consequently, the change of the mechanical properties. In muscle physiology, by the change of the contraction level, the change of

the internal muscle pressure can be studied, which is a neglected topic in the physiology of muscle.

Prediction and measurement of residuum shape change inside the prosthesis under various loading conditions is important for prosthesis design and evaluation. Surface measurement and the cross-section of the residual limb can be obtained by using MRI mesh generator software. The calculated mechanical properties from the test protocols could also be used for designing prostheses and their fittings to the limbs. Mathematical models based on finite element methods could be developed to predict the mechanical behaviour of the residuum with and without the prosthesis in place.

The result of the suggested methodology can also be used in computer graphics. Various approaches have been followed for soft tissue modelling in computer graphics. Most of them rely on the assumptions of geometrical and physical linearity of the material [17, 70, 71]. However, applying biomechanical constitutive relations is likely to produce simulations that are more realistic. Given their emprical nature, these relations may not fit exactly with the general theoretical relations and resolution methods. This leads, therefore, to various individual approaches for adjusting the models to the technical requirements of the software planned for the simulation.

8.3. Conclusions

1. A new methodology was developed to observe the mechanical response of bulk tissue under different type of loading. The response of the bulk tissue has very important information to characterise its mechanical properties as well as these of muscle and fat.

2. A new algorithm and software has been developed for creating a physically realistic finite element mesh. The software is an open system that can be extended into other areas with minor modifications.

3. A new testing machine and control software were designed to investigate the response of the bulk tissue under compression. The design is a complete system (top down) of hardware and software design. The testing machine is capable of running three different tests with minor changes.

4. The elastic moduli (E) of the bulk tissue was estimated by using the specific models -Voigt model for creep behaviour or Maxell model for stress-relaxation- which were developed for different types of experiments. Both the general and the stress-strain behaviour of the bulk tissue were presented by using the standard linear solid model.

5. A three-dimensional finite element model was created with realistic internal geometry of the human upper arm. A new computational framework was developed to apply the finite element method to anisotropic, viscoelastic soft tissue. Results showed that the formulation could represent anisotropy and time dependent behaviour of soft biological tissue.

8.4. Limitations of the Study

Like all research, this study also has limitations in terms of the design concept, instrumentation of the test rig and modelling of the soft tissue. As a design limitation, it is impossible to observe Poisson ratio by just applying uniform pressure around the human upper arm. In the design of the squeezing chamber, to avoid pinching the

subject's upper arm, a metal cover was placed on top of the two spacers where the seat-belt loop merges. This modification restricted the distribution of the applied pressure on the upper arm.

There are also some limitations from the design of the test rig. First, it might dangerous for the subject and the instrument to apply more than 60 kgf load. That is why the elastic modulus could not be observed for higher loads. Secondly, in the stress-relaxation test, the non-linear behaviour of the seat belt did not allow the application of a real constant strain. Thirdly, in the stress-strain test, the strain-rate was limited by the maximum speed of the stepper motor.

In the modelling section, however, mechanical models showed very close representations, but can only work in one dimension. To be modelled in three-dimension, finite element modelling was the solution, which is highly depending on the CPU and memory requirements of the computer.

8.5. Recommendations for Further Research

1. Further development can be made on the design of the testing system, if the system was built such that the movement of the system would be the same direction as gravity, which helps increasing the loading in the creep test and might evoke a quicker response from the stress-relaxation test.

2. The developed software for finite element mesh generation can be modified to process different types of tissue such as skin, skull and brain as well as the skin, fat and muscle tissues.

3. To be able to separate the mechanical properties of bulk tissue into the muscle and fat mechanical properties, three distinct type of subjects, who are obese, normal and lean, might be tested to observe the differences between them, which can give very important evidences for the behaviour of the fat and muscle tissues.

4. It has been observed that, in the model fitting stage of the study, the predicted and the measured characteristics of bulk tissue do not correlate very well for the lower strain region. The accuracy might be further improved by applying a numerical optimisation procedure to obtain better model parameters.

5. Further research is proposed for the finite element analysis of the bulk tissue having different material properties, to increase the finite element mesh resolution to give a better convergence between the experiment and the finite element model.

6. Another topic of interest is to test different parts of the body to observe the change of the mechanical properties of the bulk tissue with the change of the body locations.

7. Another topic yet to be explored in this field is the study of the variation of the mechanical properties of bulk tissue with change of body temperature. The effect of temperature changes on collagen fibres, which are the main building blocks of the tissues, could then be observed.

References

1. ABAQUS Theory Manual. 1992. HKS(UK) Ltd.

2. ABAQUS Users Manual. 1992. HKS(UK) Ltd.

3. Ackerman, E., Ellis, L.B. and Williams, L.E., Biophysical Science. 1979. 2nd Ed. Prentice-Hall Inc, New Jersey.

4. Aklonis, J.J. and MacKnight, W.J., Introduction to Polymer Viscoelasticity. 1983. 2nd Ed. John Wiley& Sons.

5. Armstrong, C.G., Bahrani, A.S. and Gardner, D.L., Changes in the deformational behaviour of human hip cartilage with age. Journal of Biomechanical Engineering, 1980, 102, 214-220.

6. Bagshaw, C. R. Muscle Contraction. 1993. Chapman & Hall, London.

7. Beaupre, G. S. and Carter, D. R., Finite Element Analysis in biomechanics, in Biomechanics - Structures and Systems: A Practical Approach, (ed. Biewener, A.). 1992. Oxford University Press, New York.

8. Bogen, D.K., Strain energy descriptions of biological swelling, I & II: single and multiple fluid compartment models. Journal of Biomechanical Engineering, 1987, 109, 252- 262.

9. Bolton, W., Instrumentation & Measurement. Pocket Book. 1996. 2nd Ed. Newnes, Oxford.

10. Bradley, D.A., Dawson, D., Burd, N.C. and Loader, A.J., Mechatronics: Electronics in products and processes. 1993. Chapman & Hall, London.

11. Bronzino, J.D.,. The Biomedical Engineering Handbook. 1995. CRC Press, Florida.

12. Castleman, K.R., Digital Image Processing. 1996. Prentice-Hall, Englewood Cliffs, New Jersey.

13. Chow, W.W. and Odell, E.I., Deformations and stresses in soft body tissues of a sitting person. Journal of Biomechanical Engineering, 1978, 100, 79-87.

14. Crowe, A., A mechanical model of muscle and its application to the intrafusal fibers of the mammalian muscle spindle. Journal of Biomechanics, 1970, 3, 583-592.

15. Davies, A. and Fennessy, P., Electronic Imaging for Photographers. 1996. 2nd Ed. Focal Press, Oxford, 1996.

16. Dettmann, T. and Wyatt, A.L., DOS Programmers Reference. 1993. 4th Ed. Que Corporation, Indiana.

17. Foley, J.D., Van Dam, A., Feiner, S. and Hughes, J.F., Computer Graphics: Principles and Practice. 1997. 2nd Ed. in C. Addison Wesley, Reading Massachusetts.

18. Fung, Y.C. Biomechanics Mechanical Properties of Living Tissues. 1981. Springer-Verlag, New York.

19. Gonzalez, R. C. and Woods, R. E., Digital Image Processing. 1993. Addison Wesley, Reading, Massachusetts.

20. Haddad, Y.M., Viscoelasticity of Engineering Materials. 1995. Chapman & Hall, London.

21. Hamming, R. W., Numerical Methods for Scientists and Engineers. 1973. 2nd Ed. McGraw-Hill Co., New York.

22. Hatze, H., Myocybernetic control models of skeletal muscle. Characteristics and applications. 1980 (University of South Africa, Pretoria).

23. Hayes, W.C. and Mackros, L.F., Viscoelastic properties of human articular cartilage. Journal of Applied Physiology. 1971, 3, 562 - 8.

24. Hayes, W.C., Keer, L.M., Herrmann, G. and Mackros, L.F., A mathematical analysis for indentation tests of articular cartilage. Journal of Biomechanics, 1972, 5, 541-551.

25. Hill, A.V. First and Last Experiments in Muscle Mechanics. 1970. Cambridge University Press, London.

26. Hill, T.L, Theoretical formalism for the sliding filament model of contraction of striated muscle, part I. Progress in Biophysics and Molecular Biology, 1974, 28, 267-340.

27. Hori, R.Y. and Mockros, L.F., Indentation test of human articular cartilage. Journal of Biomechanics, 1976, 9, 679-685.

28. Horowitz, A., Sheinman, I. and Lanir, Y., Non-linear incompressible finite element for simulated loading of cardiac tissue-part II: 3D formulation for thick ventricular wall segments. Journal of Biomechanical Engineering, 1988, 110, 62-68.

29. Horowittz, P. and Hill, W., The Art of Electronics. 1989. 2nd Ed. Cambridge University Press, Cambridge.

30. Humphery, J.D. and Yin, F.C.P., On constitutive relations and finite deformations of passive cardiac tissue: I. Pseudostrain-energy function. Journal of Biomechanical Engineering, 1987, 109, 298-304.

31. Hunter, P.J., McCulloch, A.D., Nielsen, P.M.F. and Smaill, B.H., A finite element model of passive ventricular mechanics. 1988 (In: Spilker, R.L., Simon, B.R. eds. Computational Methods in Bioengineering, ASME, 493-503, New York)

32. Huxley, A.F., Muscle structure and theories of contraction. Progress in Biophysics and Molecular Biology, 1957, 7, 257-318.

33. Iding, R. H., Pister, K. S. and Taylor, R. L., Identification of nonlinear elastis solids by a finite element method. Computer methods in applied mechanics and engineering. 1974, 4, 121- 142.

34. Jennings, D., Flint, A., Turton, B.C.H. and Nokes, L.D.M., Introduction to Medical Electronics Applications. 1995. Edward Arnold, London.

35. Kay, D. C. and Levine, J. R., Graphics File Formats. 1994. 2nd Ed. Windcrest/McGraw-Hill, Blue Ridge Summit, PA.

36. Kernighan, B. W. and Ritchie, D. M., The C Programming Language. 1998. 2nd Ed. Prentice-Hall, Englewood Cliffs, New Jersey.

37. Knuth, D. E., The Art of Computer Programming, Volume 3 - Sorting and Searching. 1973. Addison Wesley, Reading, Massachusetts.

38. Krouskop, T.A., Dougherty, D.R. and Winson, F.S., A pulsed doppler ultrasonic system for making non-invasive measurement of the mechanical properties of soft tissue. Journal of Rehabilitation Research and Development, 1987, 24, 1-8.

39. Levinson, S.F., Ultrasound propagation in anisotropic soft tissues: the application of linear elastic theory. Journal of Biomechanics, 1987, 20, 251-260.

40. Levinson, S.F., Masahiko, S. and Takuso, S. Sonoelastic determination of human skeletal muscle elasticity. Journal of Biomechanics, 1995, 28, 1145-1154.

41. Mak, A.F.T., Liu, G.H.W. and Lee, S.Y., Biomechanical assessment of below-knee residual limb tissue. Journal of Rehabilitation Research and Development, 1994, 31, 188-98.

42. Maurel, W., Wu, Y., Thalmann, N.M. and Thalmann, D., Biomechanical models for soft tissue simulation. 1998. Springer, Berlin.

43. McMahon, T.A., Muscle mechanics. 1987 In: Skalak, R. and Chein, S., eds. Handbook of Bioengineering,7, 1-26, McGraw-Hill, New York.

44. Messmer, H.P., The Indispensable PC Hardware Book. 1997. 3rd Ed. Addison Wesley Longman, Essex.

45. Mow, V.C., Gibbs, M.C., Lai, W.M., Zhu, W.B. and Athanasiou, K.A., Biphasic indentation of articular cartilage. Part II: a numerical algorithm and an experimental study. Journal of Biomechanics. 1989, 22, 853-861.

46. Nakamura, S., Crowninshield, R.D. and Cooper, R.R., An analysis of soft tissue loading in the foot: A preliminary report. Bull prosthetic and Research, 1981, 18, 27-34.

47. Nielsen, L.E., Mechanical Properties of Polymers and Composites. 1974. Marcel Dekker Inc., New Jersey.

48. Nigg, M.B., Herzog, W. Biomechanics of the Muscle-Skeletal System. 1994. John Wiley & Sons Ltd. West Sussex.

49. Oomens, C.W.J., Van Campen, D.H., Grootenboer, H.J. and DeBoer, L.J., Experimental and theoretical compression studies on porcine skin. 1985. Perren S.M. and Schneider, E. eds. Biomechanics: current interdisciplinary research, 221-226, Dordrecht, Netherlands.

50. Oomens, C.W.J., Van Campen, D.H. and Grootenboer, H.J., A mixture approach to the mechanics of skin. Journal of Biomechanics, 1987, 20, 877-886.

51. Oomens, C.W.J., Van Campen, D.H. and Grootenboer, H.J., In vitro compression of a soft tissue layer on a rigid foundation. Journal of Biomechanics, 1987, 20, 923-935.

52. Oomens, C. W., Ratingen, M. R. V., Janssen, J. D., Kok, J. J. and Hendricks, M. A. N. A numerical experiment method for a mechanical characterization of biological materials. Journal of Biomechanics. 1993, 26, 617 - 621.

53. Ozkaya, N. and Nordin, M. Fundamentals of Biomechanics: Equilibrium, motion and deformation. 1991. Van Nostrand Reinhold, New York.

54. Pappas, C. H. and Murray, W. H., Borland C++ Handbook. 1994. 4th Ed. Osborne/ McGraw-Hill, Berkeley, California.

55. Prendergast, P. J., Finite element models in tissue mechanics and orthopaedic implant design. Clinical Biomechanics. 1997, 12, 343 - 366.

56. Press, W. H., Teukolsky, S. A., Vetterling, W. T. and Flannery B. P., Numerical Recipies in C, The Art of Scientific Computing. 1994. 2nd Ed. Cambridge University Press, Cambridge.

57. Reynolds, D. Shape design and interface load analysis for below-knee prosthetic sockets. 1988 (Ph.D. Thesis, University of London, London).

58. Robb, R. A., Hanson, D. P., Karwoski, R. A., Larson, A. G., Workman, E. L. and Stacy, M. C., Analyze: A Comprehensive, operator-interactive software package for multidimensional medical image display and analysis. Computerized Medical Imaging and Graphics, 1989: 13 (6):433-454.

59. Rockey, K.C., Evans, H.R., Griffiths, D.W. and Nethercot, D.A., The Finite Method. 1975. Crosby Lockwood Staples, London.

60. Rumbaugh, J., Blaha, M., Premerlani, W., Eddy, F. and Lorensen, W. Object-Oriented Modelling and Design. 1991. Prentice-Hall, New Jersey.

61. Sacks, A.H., O'Neill, H. and Perkash, I., Skin blood flow changes and tissue deformations caused by cylindrical indentors. Journal of Rehabilitation Research and Development, 1987, 22, 1-6.

62. Sakamoto, M., Li, G., Hara, T. and Chao, E.Y.S., A new method for theoretical analysis of static indentation test. Journal of Biomechanics, 1996, 29(5), 679-685.

63. Schalkoff, R. J., Digital Image Processing and Computer Vision. 1989. John Wiley & Sons, New York.

64. Schildt, H., C: The Complete Reference. 1990. 2nd Ed. Osborne McGraw-Hill, Berkeley, California.

65. Schock, R.B., Brunski, J.B. and Cochran, G.V.B., *In vivo* experiments on pressure sore on biomechanics: stresses and strains in indented tissues. 1982. In: Advances in Bioengineering, ASME, 88-91, New York.

66. Steege, J.W., Schnur, D.S. and Childress, D.S., Finite element prediction of pressure at the below-knee socket interface. 1987. In: Biomechanics of normal and prosthetic gait, ASME, BED-4: 39-44, New York.

67. Steege, J.W. and Childress, D.S., Finite element modelling of the below-knee socket and limb: Phase II. 1988 In: Modelling and control issues in biomechanical systems, ASME, BED-4: 121-9, New York.

68. Tanenbaum, A.S. (1990). Structured Computer Organisation. 1990. 3rd Ed. Prentice-Hall, New Jersey.

69. Taylor, M. E., Tanner, K. E., Freeman, M. A. R. and Yettram, A. L., Stress and strain distribution within the intact femur: compression or bending?. Medical Engineering and Physics, 1996, 18(2), 122-131.

70. Terzopoulos, D., Platt, J., Barr, A., Fleischer, K., Elastically deformable models, Proceeding Siggraph '87, Computer Graphics, 1987, 21, 205-214.

71. Terzopoulos, D., Fleischer, K., Modelling inelastic deformation: viscoelasticty, plasticity, fracture. Proceeding Siggraph '88, Computer Graphics, 1987, 22, 269-278.

72. Tischer, M., PC Intern, System Programming. 1994. 5th Ed. Abacus, Michagan.

73. Tooley, M., PC-based Instrumentation and Control. 1995. 2nd Ed. Newnes, Oxford.

74. Tu, H. K., Matheny, A., Goldgof, D. B. and Bunke, H., Left ventricular boundry detection from spatio-temporal volumetric computed tomography images. Computerized Medical Imaging and Graphics, 1995: 19 (1):27-46.

75. Ursino, M. and Cristalli, C., Mathematical modelling of noninvasive blood pressure estimation techniques - Part I: Pressure transmission across the arm tissue. Journal of Biomechanical Engineering, 1995, 117, 107-116.

76. Vannah, W.M. and Childress, D.S., Indentor tests and finite element modelling of bulk muscular tissue in vivo. Journal of Rehabilitation Research and Development, 1996, 33, 239-252.

77. Wineman, A., Wilson, D. and Melvin, J. W. Material identification of soft tissue using membrane inflation. Journal of Biomechanics. 1979, 12, 841-850.

78. Winters, J. M. and Savio, L-Y. W. Multiple Muscle System Biomechanics and Movement Organization. 1990. Springer-Verlag, New York.

79. Wyatt, A.L., Using Assembly Language. 1992. 3rd Ed. Que Corporation, Indiana.

80. Zhang, M., Turner-Smith, A.R. and Roberts, V.C., The reaction of skin and soft tissue to shear forces applied externally to the skin surface. Proceedings Institute Mechanical Engineering, 1994, 208, 217-222.

81. Zienkiewicz, O, C., Taylor, R.L., The Finite Element Method. 1977. McGraw-Hill, New York.

Appendix A

Technical Drawings

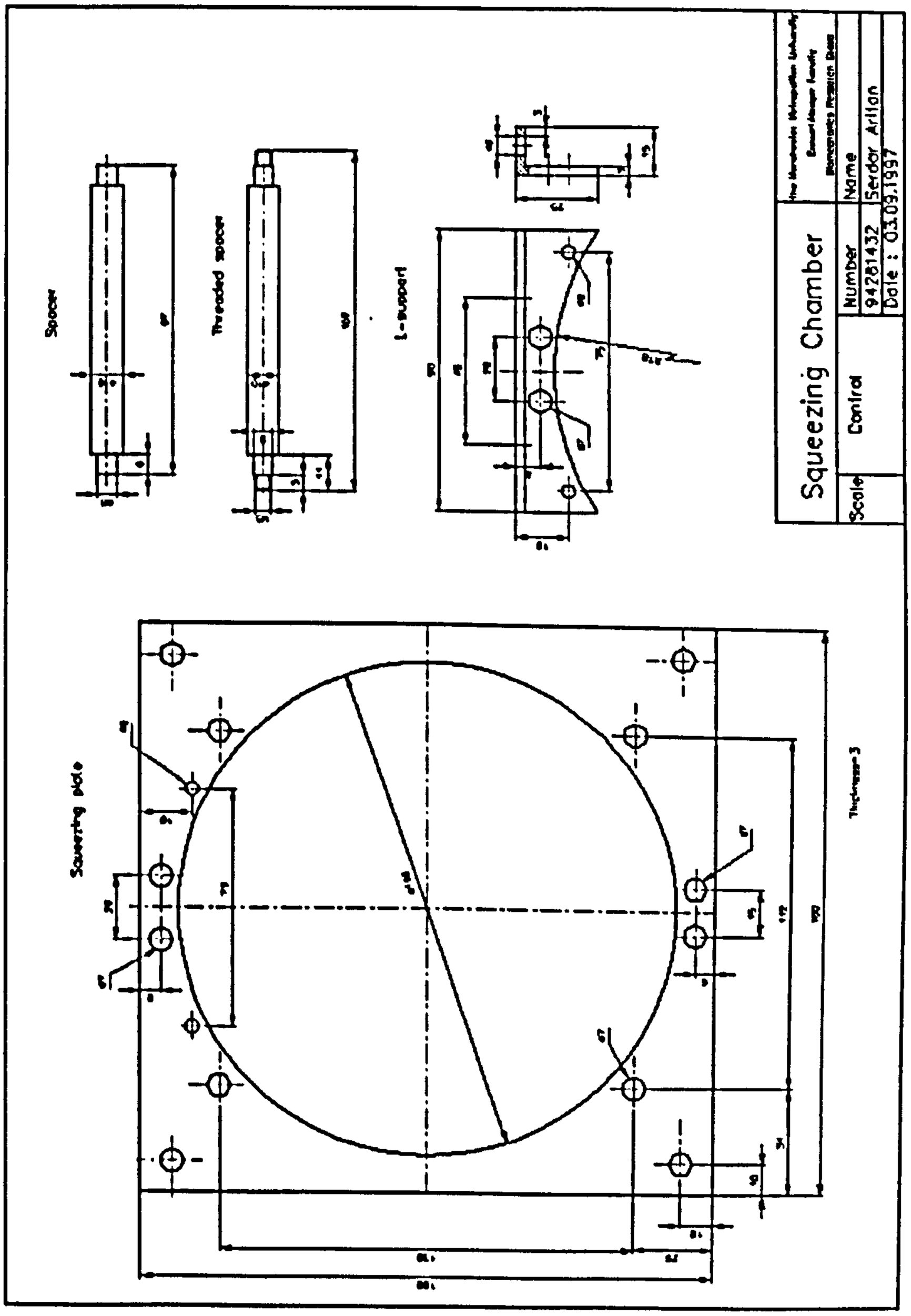

Figure A.1. Dimensions of the squeezing chamber.

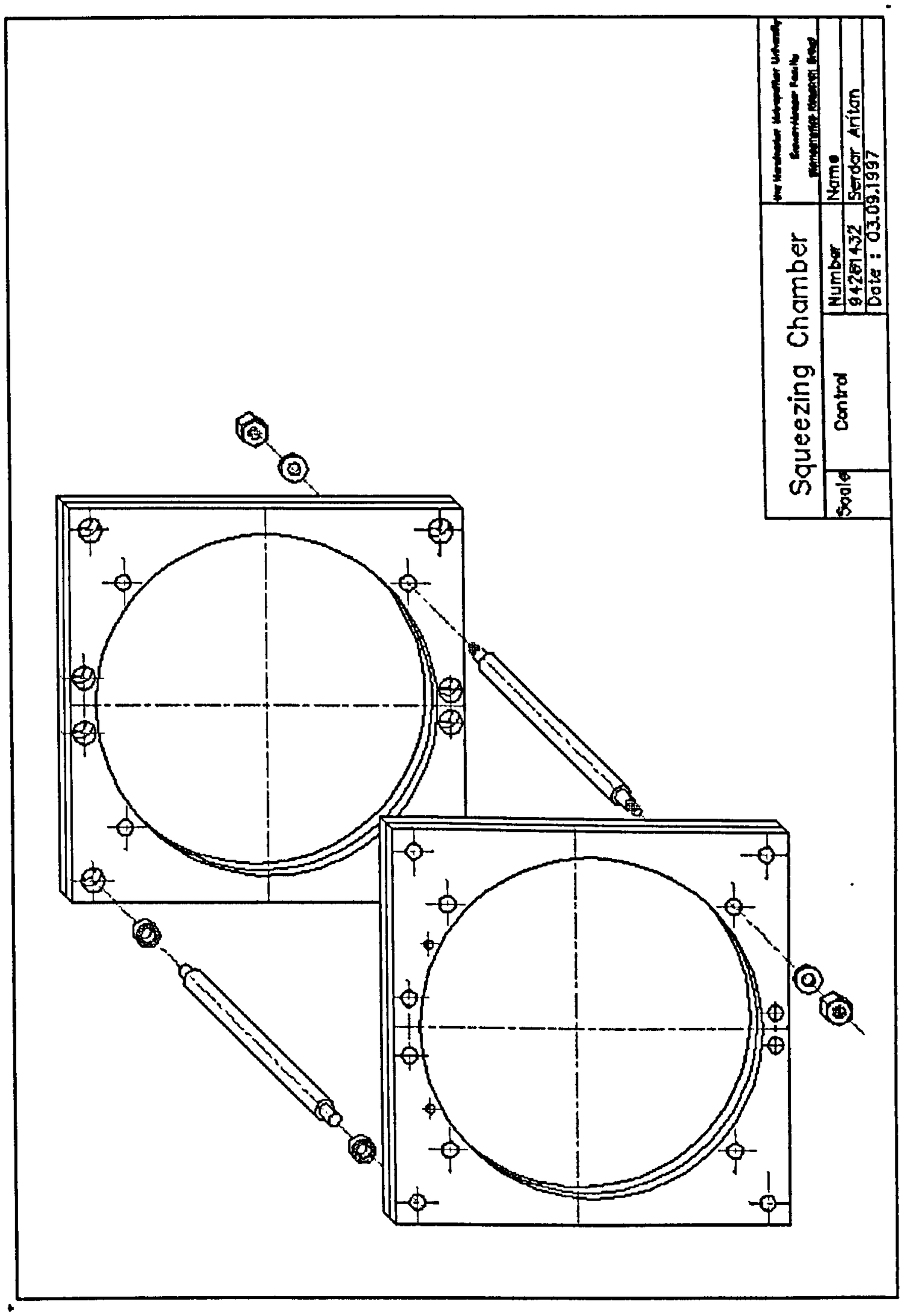

Figure A.2. Assembly of the squeezing chamber with two spacers.

Appendix A

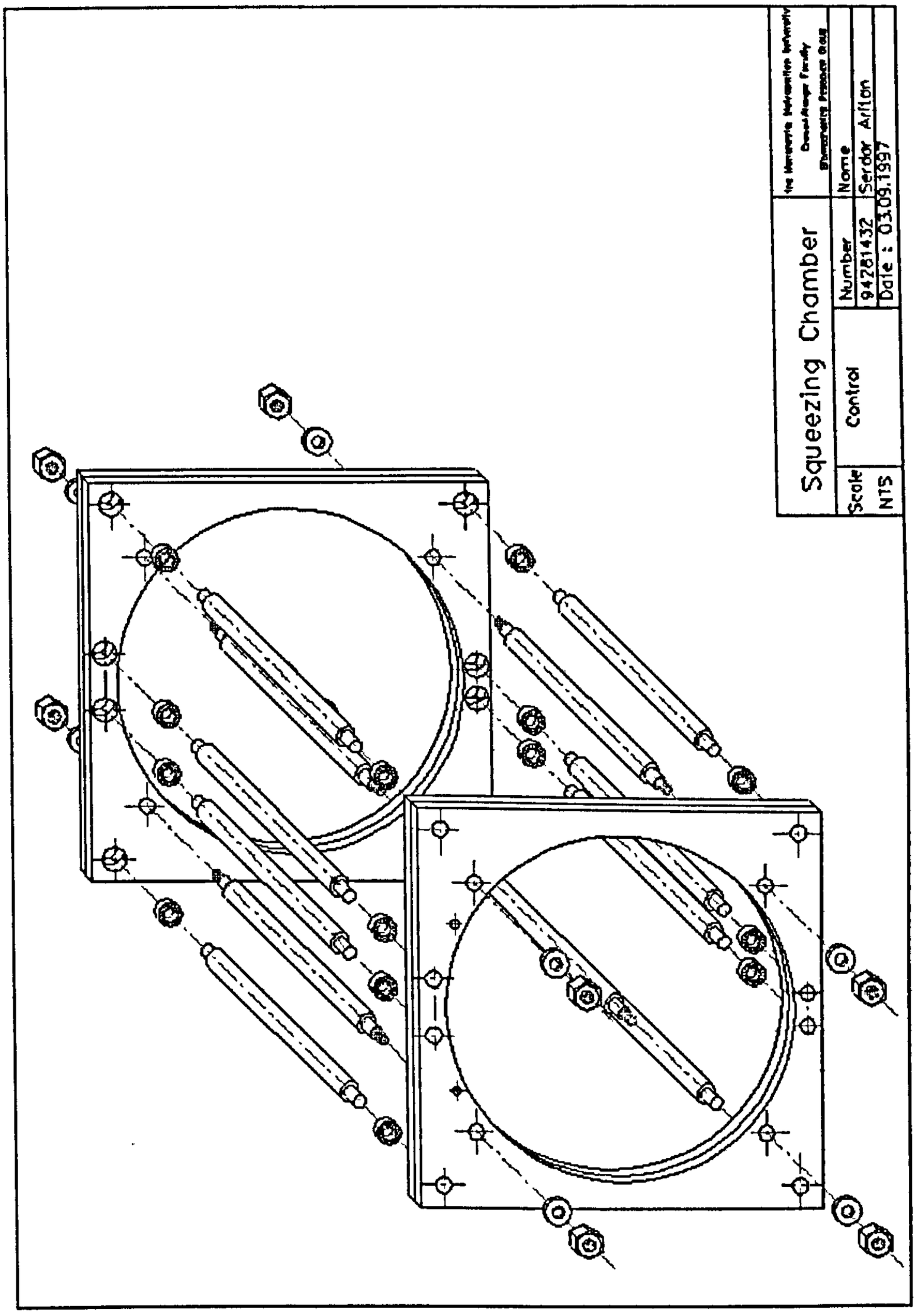

Figure A.3. Assembly of the squeezing chamber with the all spacers.

Appendix A

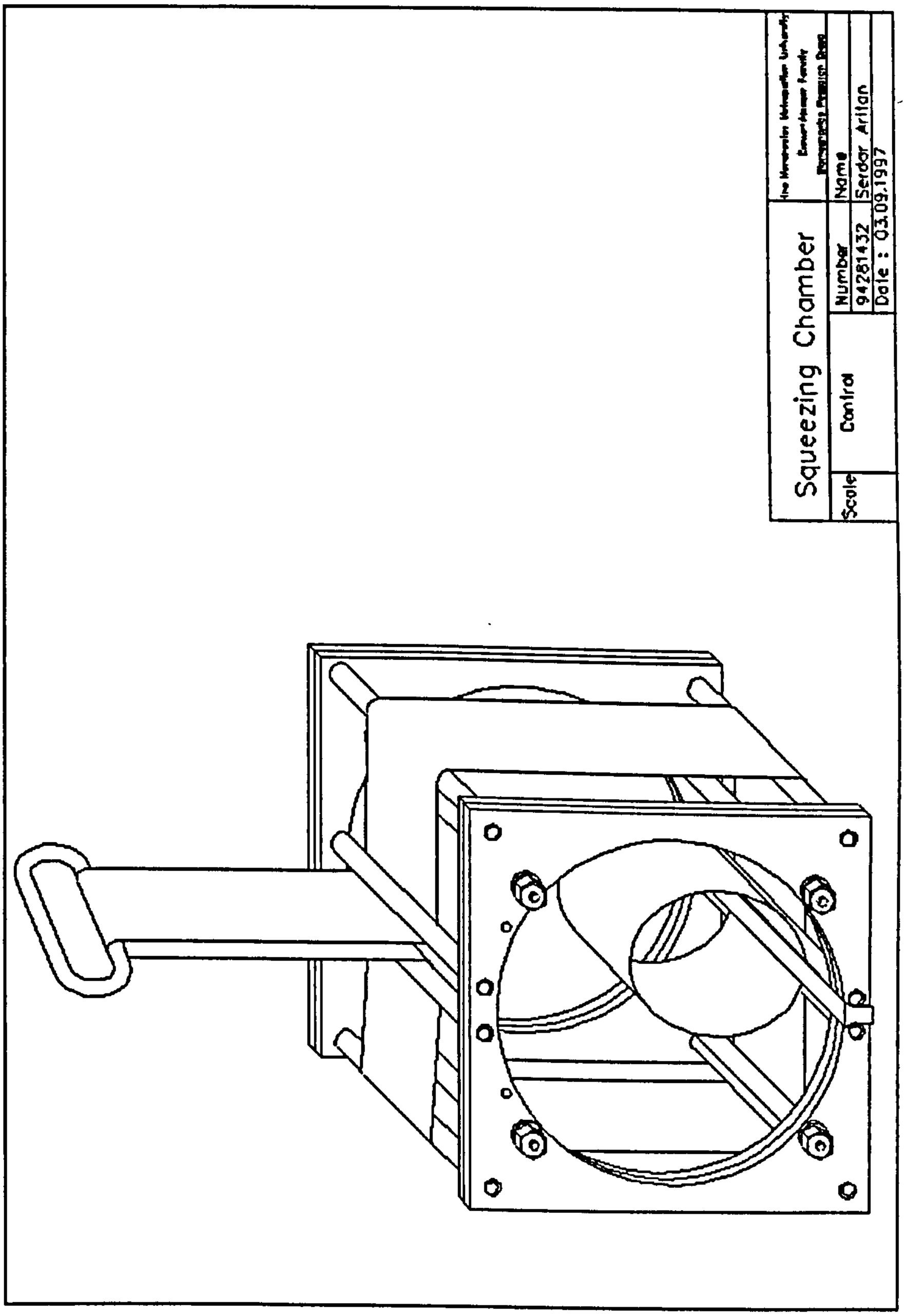

Figure A.4. Squeezing chamber with the seat belt.

Appendix A

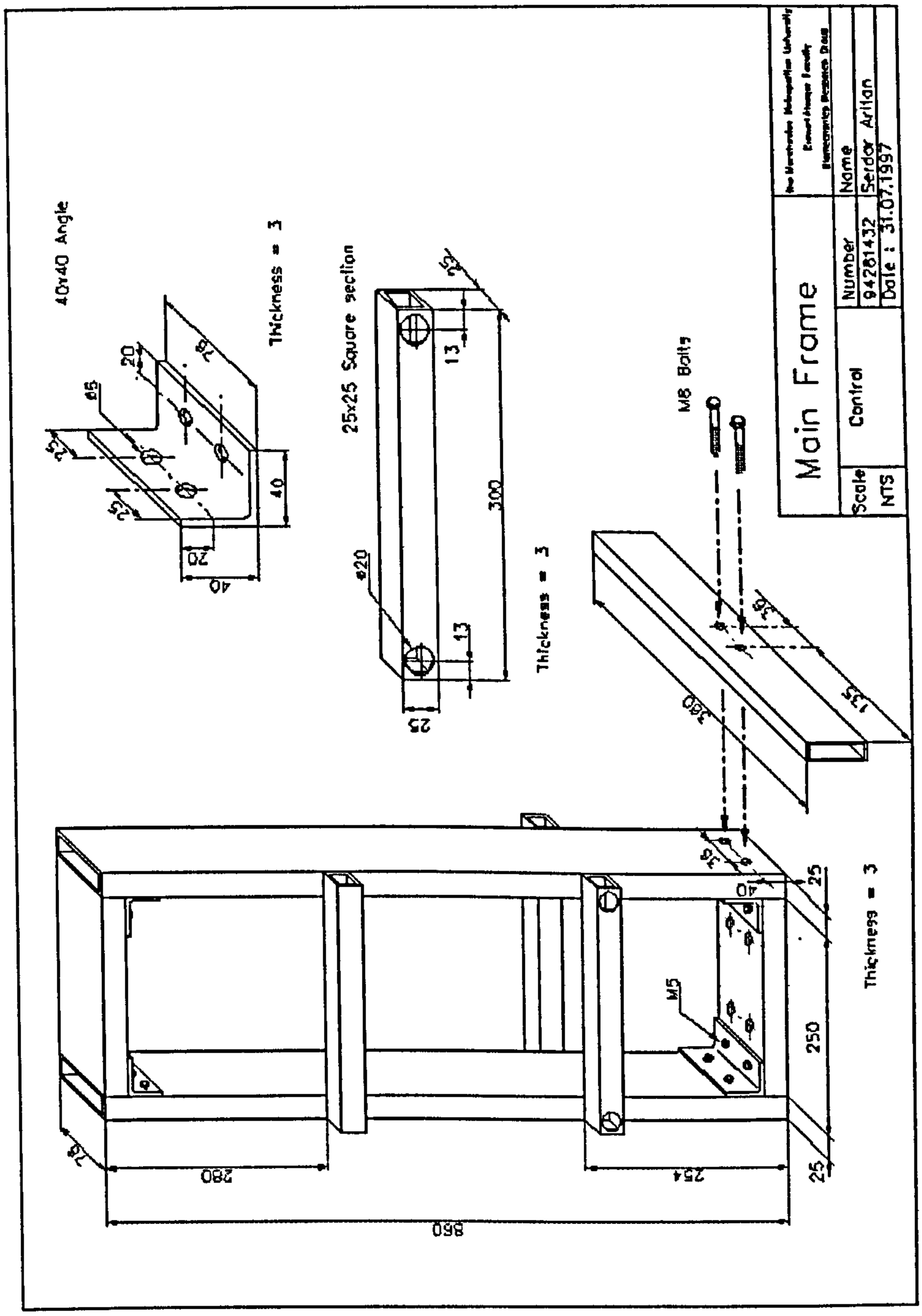

Figure A.5. Dimensions of the main frame.

Appendix A

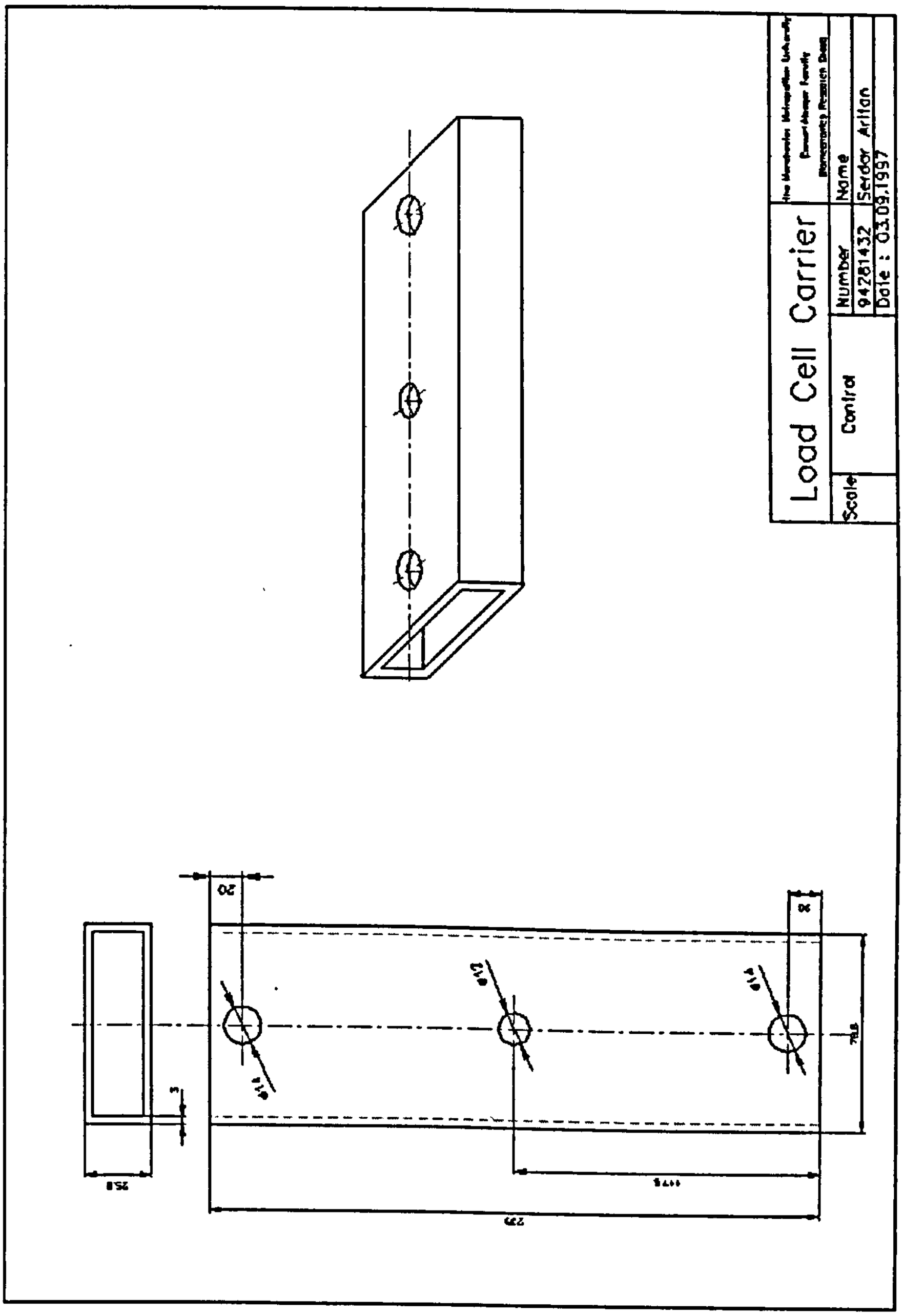

Figure A.6. Dimensions of the load cell carrier.

Appendix A

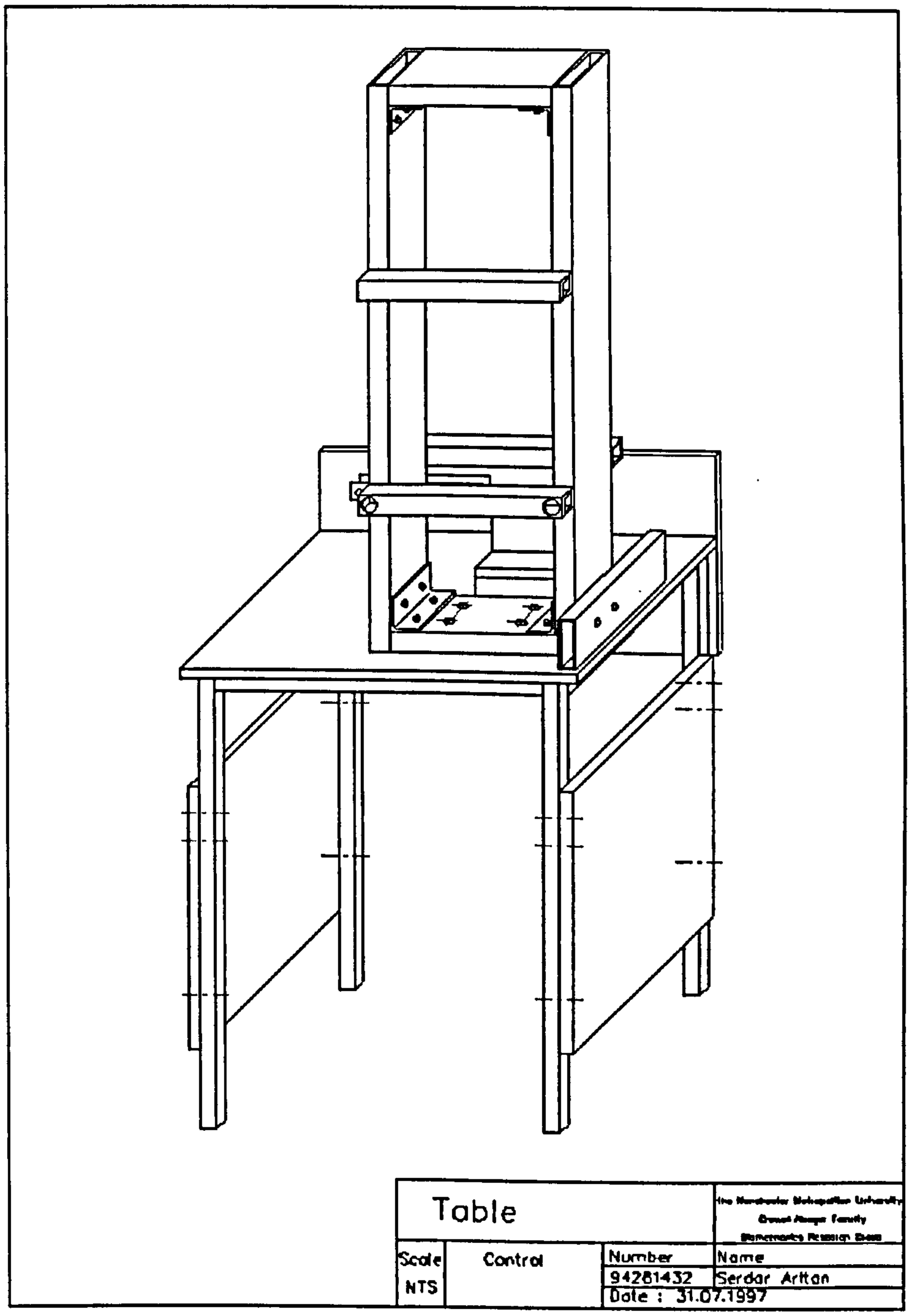

Figure A.7. Assembly of the main frame on the table.

Appendix A

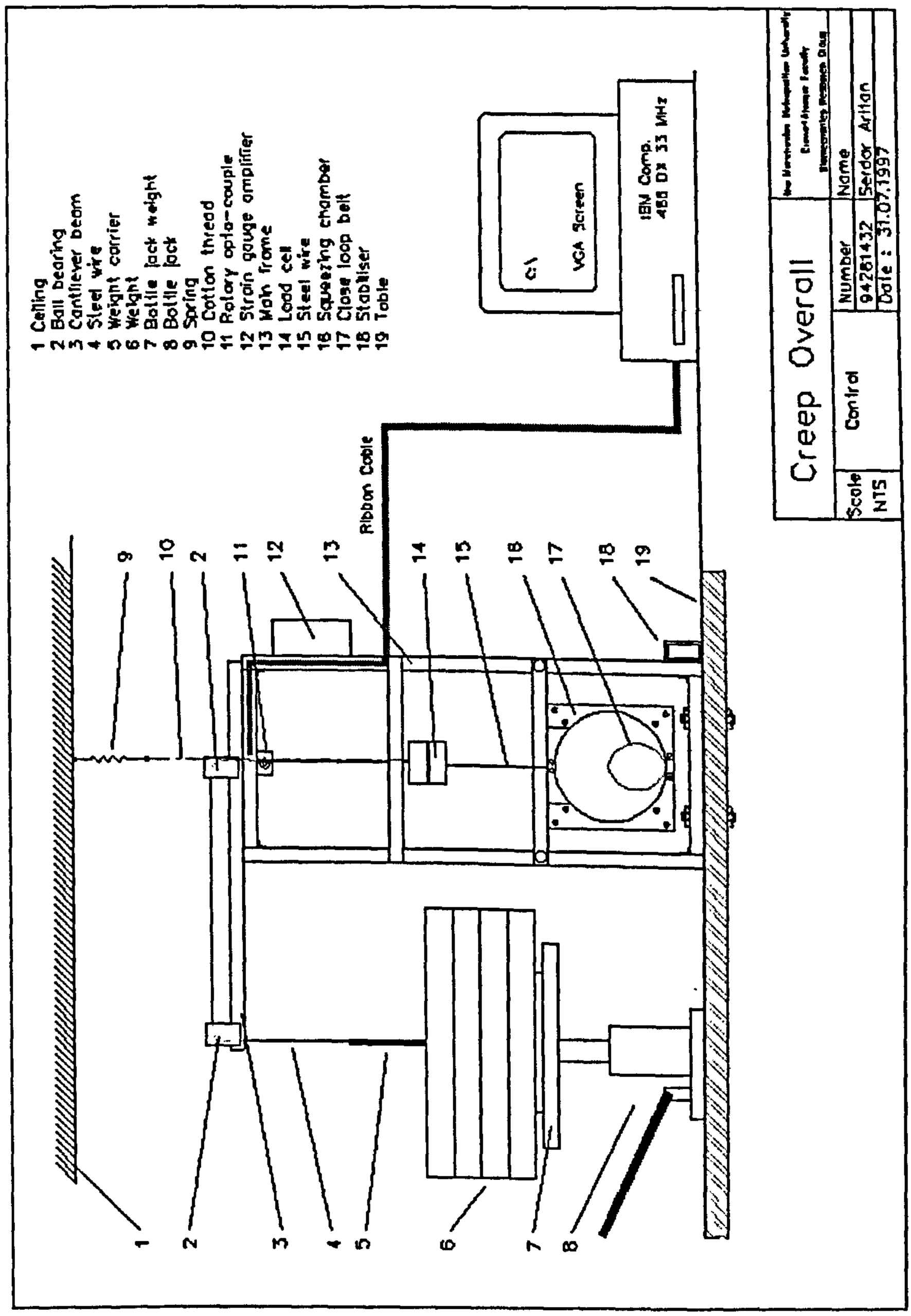

Figure A.8. Layout of the creep test design.

Appendix A

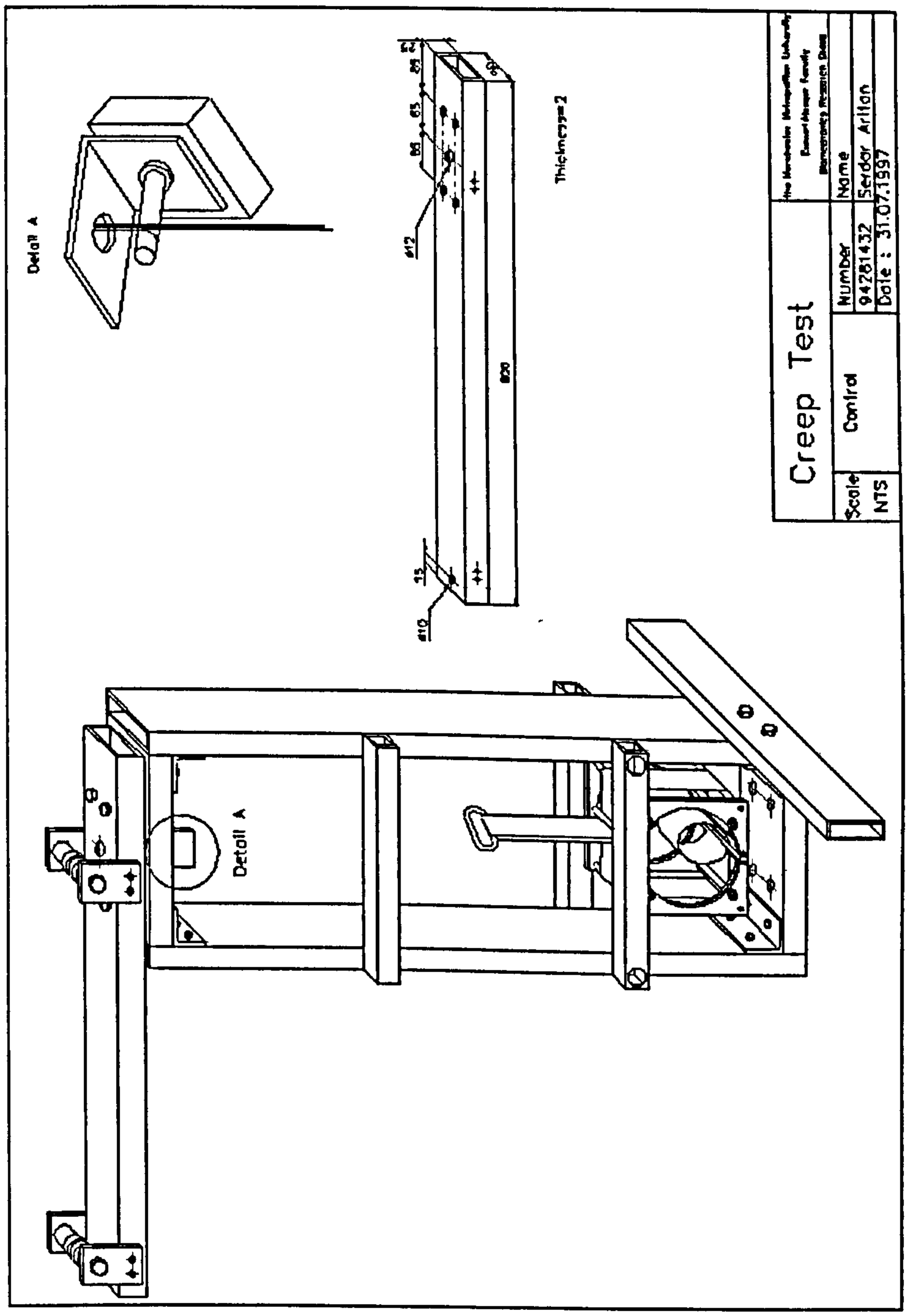

Figure A.9. Dimensions of the lever in the creep test.

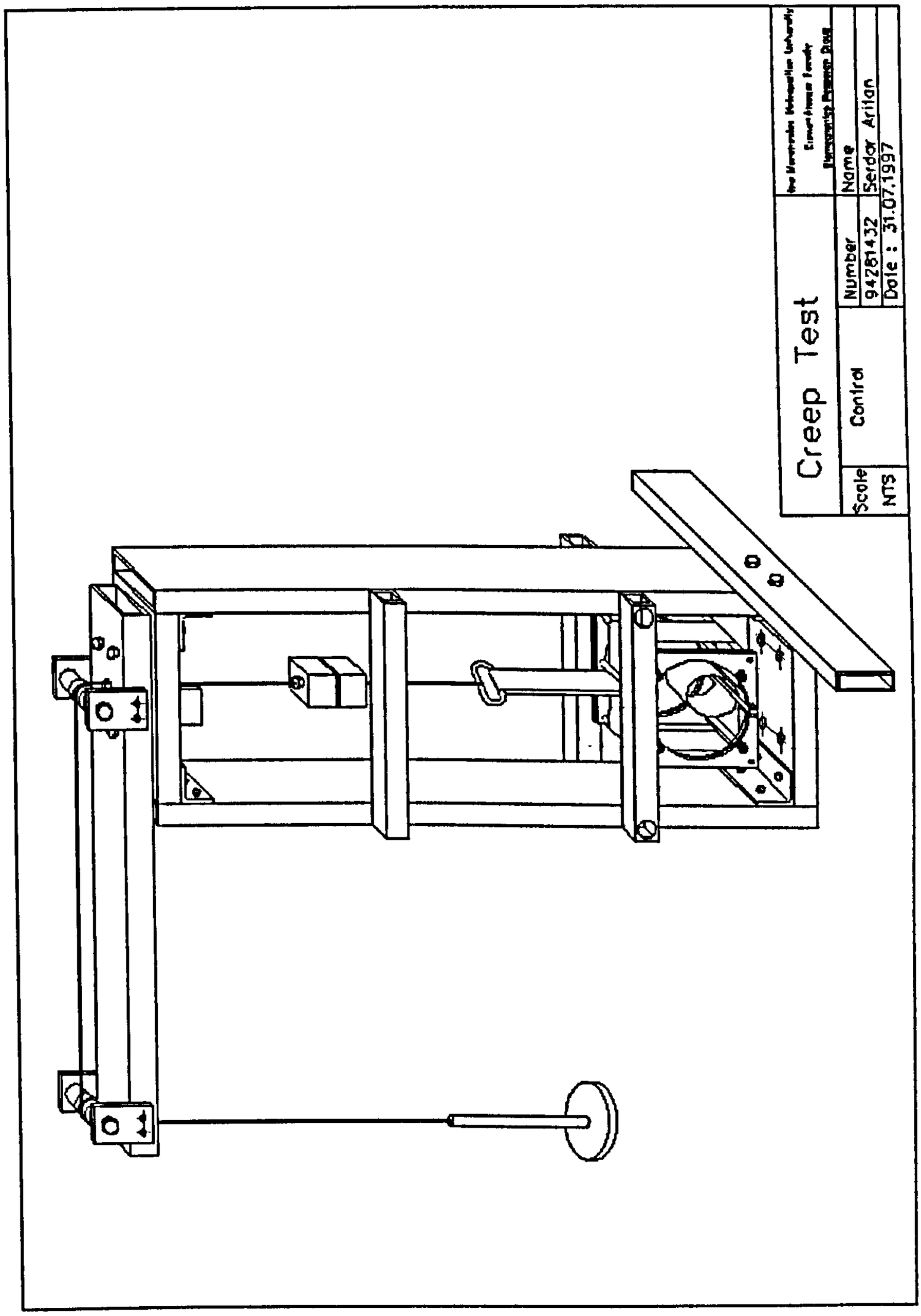

Figure A.10. Experiment design of creep test.

Appendix A

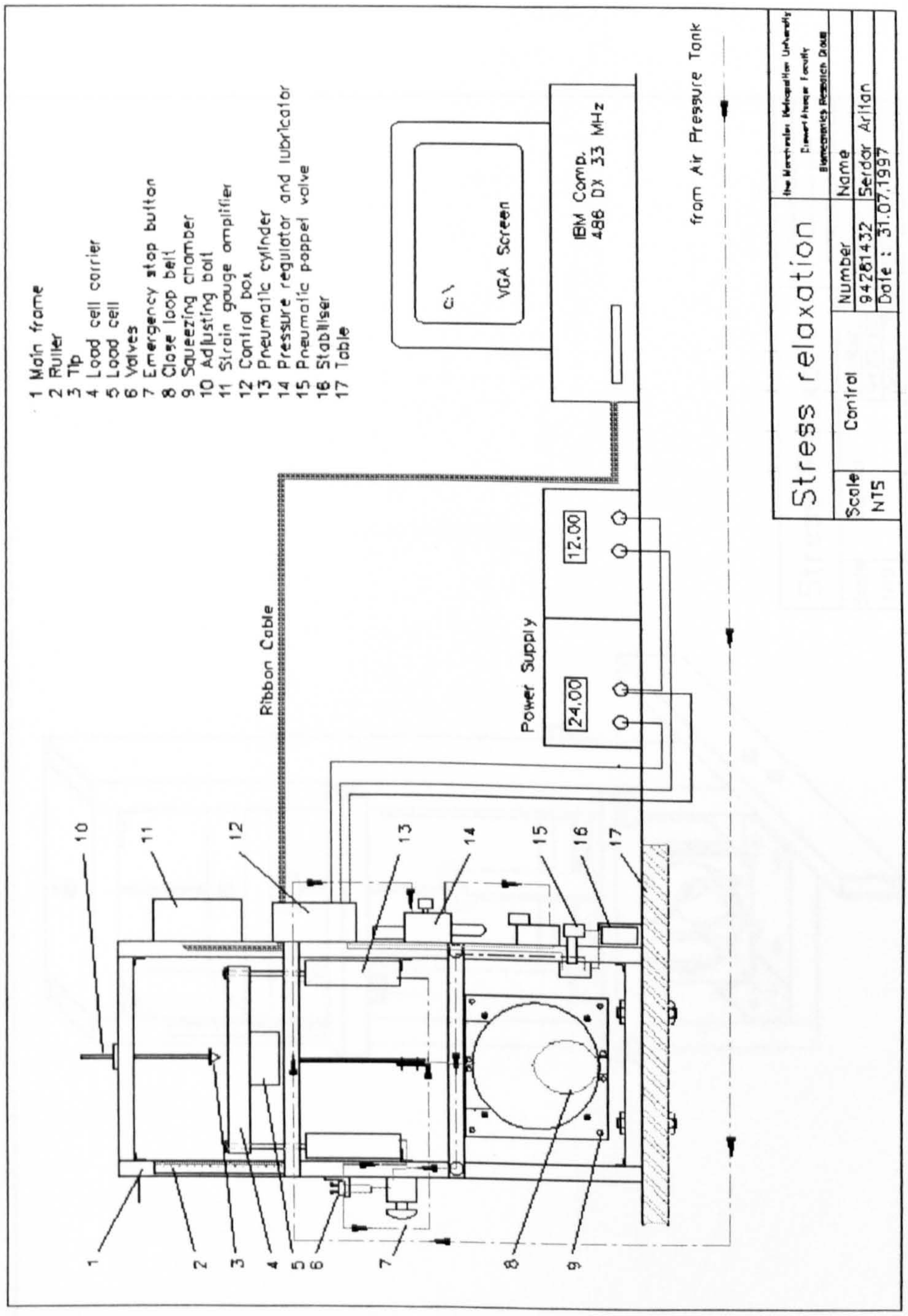

Figure A.11. Layout of the stress-relaxation test design.

Appendix A

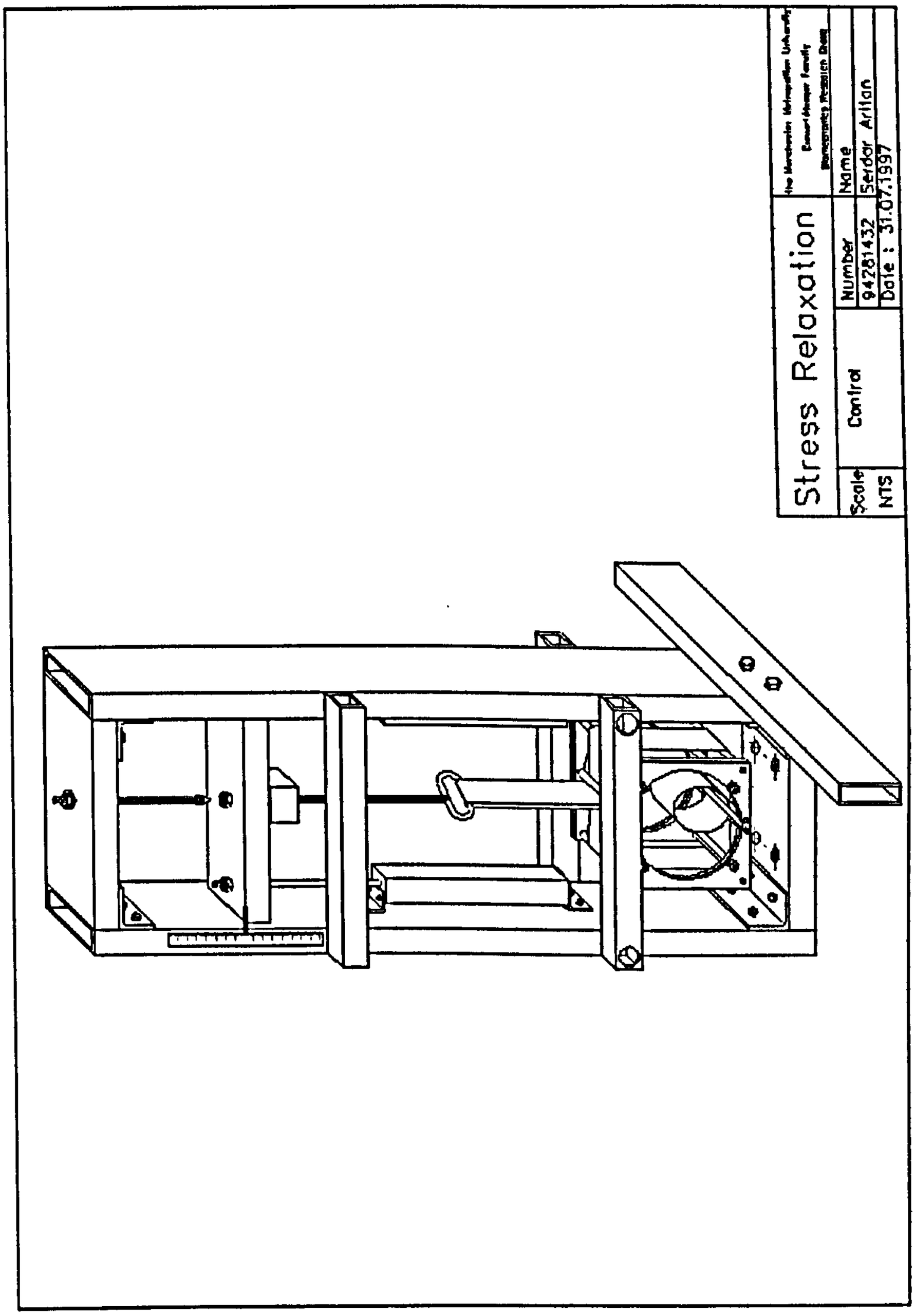

Figure A.12. Experiment design of stress-relaxation test.

Appendix A

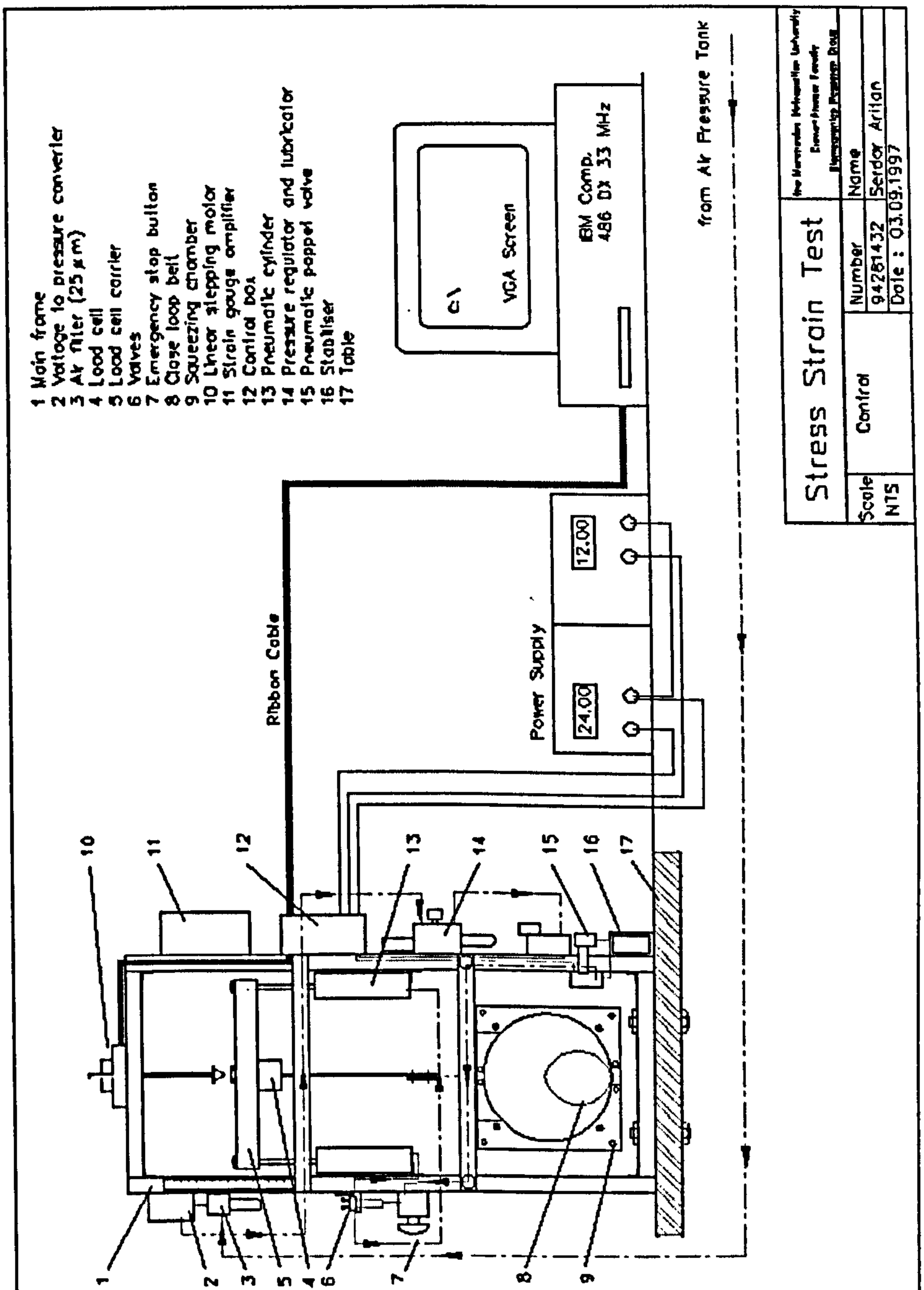

Figure A.13. Layout of the stress-strain test design.

Appendix A

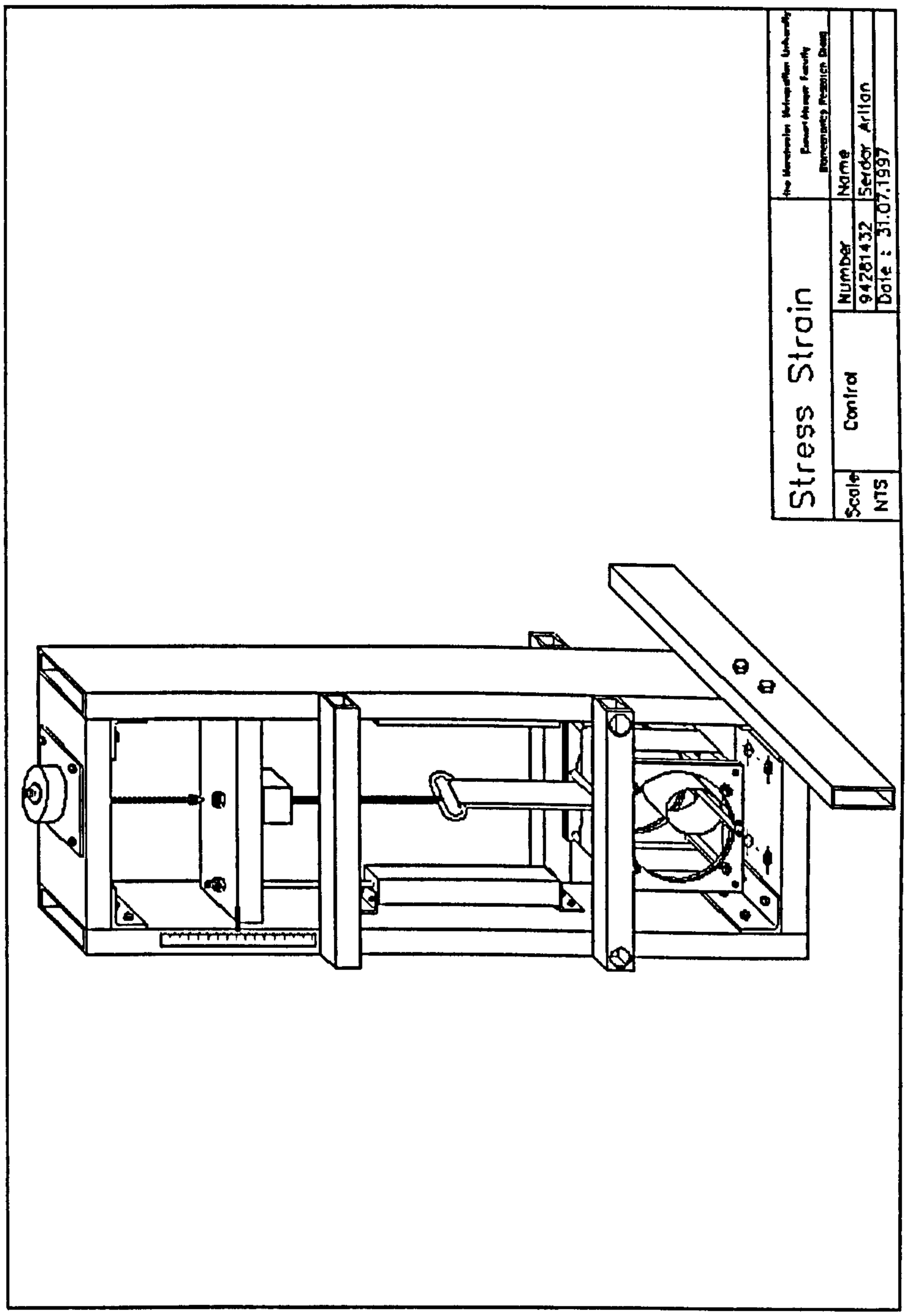

Figure A.2. Experiment design of stress-strain test.

Appendix B

Appendix B.1. Curve Fitting for Creep Test Data

Appendix B.2. Comparison of Test Protocols in Creep Test Data

Appendix B.3. Model Fitting for Creep Test Data

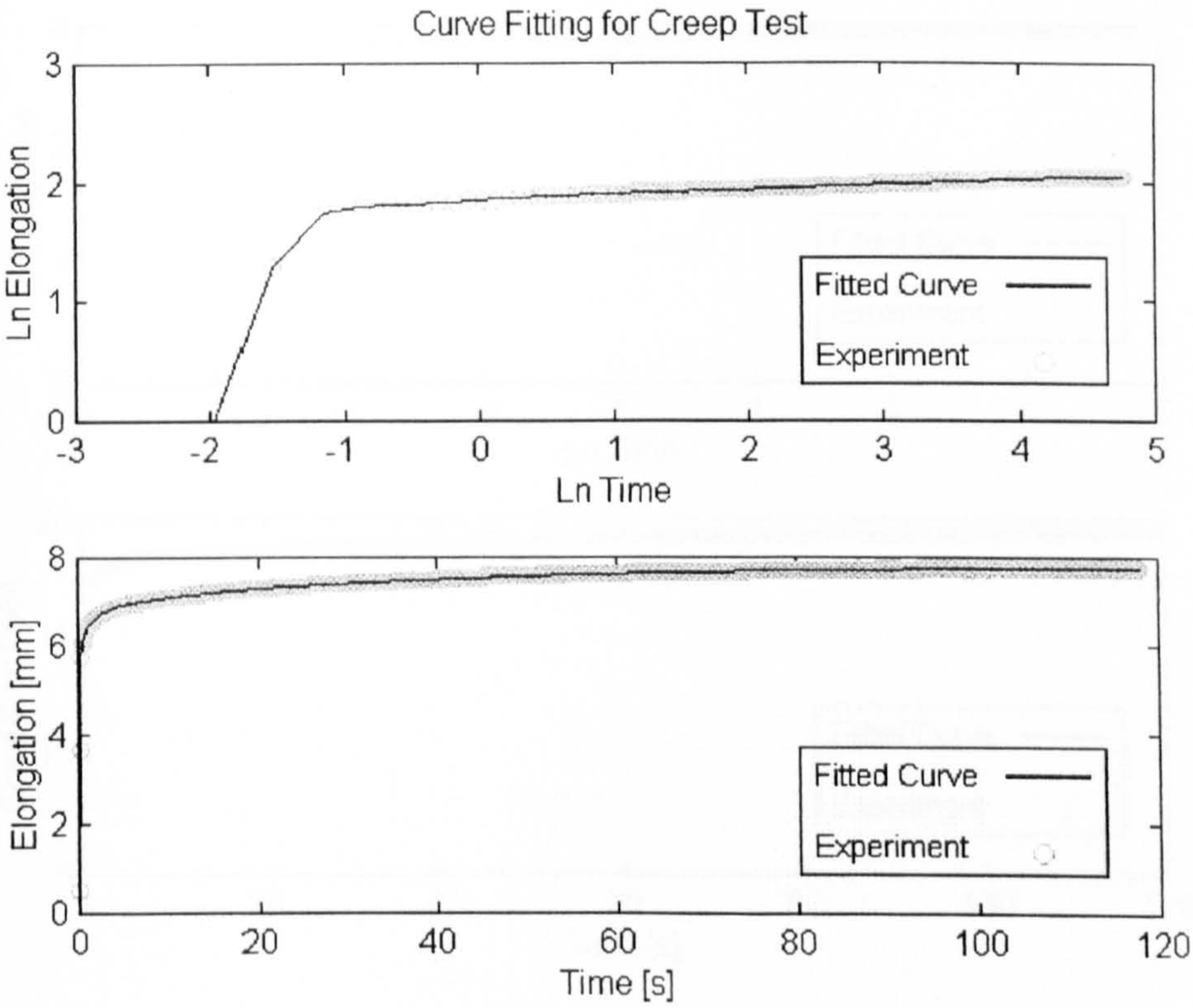

Figure B.1 Curve fitting of the creep test data for 10 kgf constant load in the relaxed procedure.

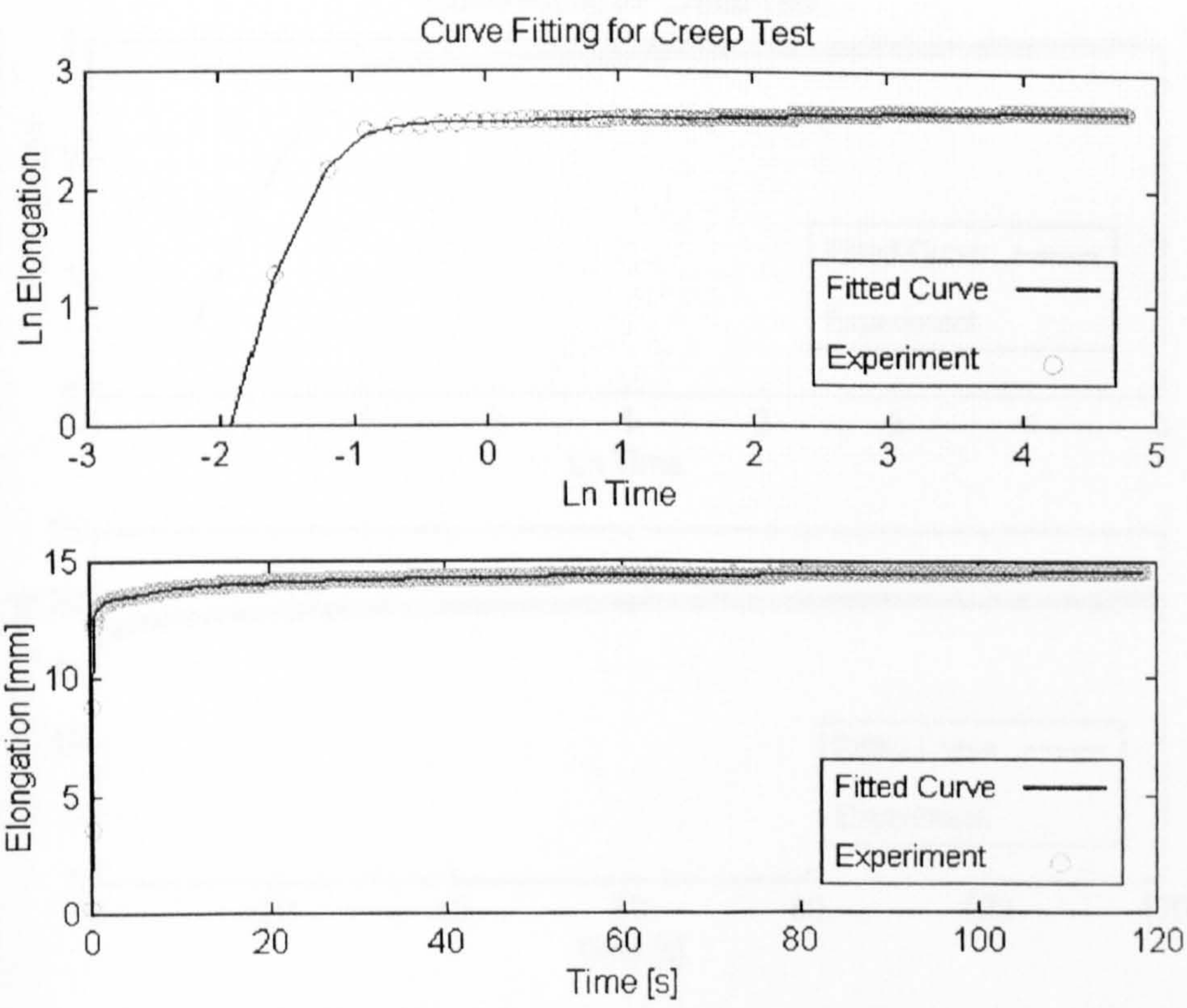

Figure B.2 Curve fitting of the creep test data for 20 kgf constant load in the relaxed procedure.

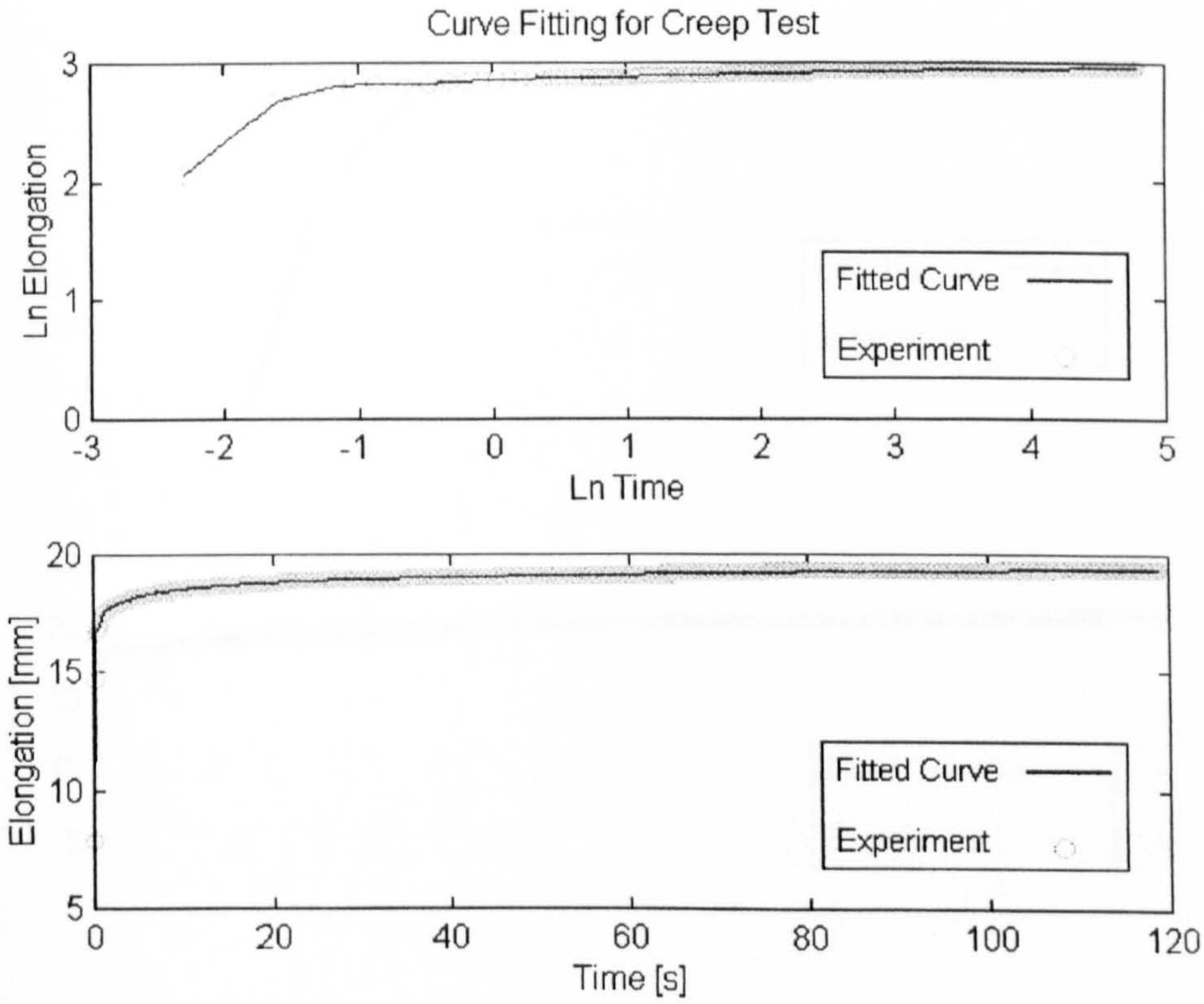

Figure B.3 Curve fitting of the creep test data for 30 kgf constant load in the relaxed procedure.

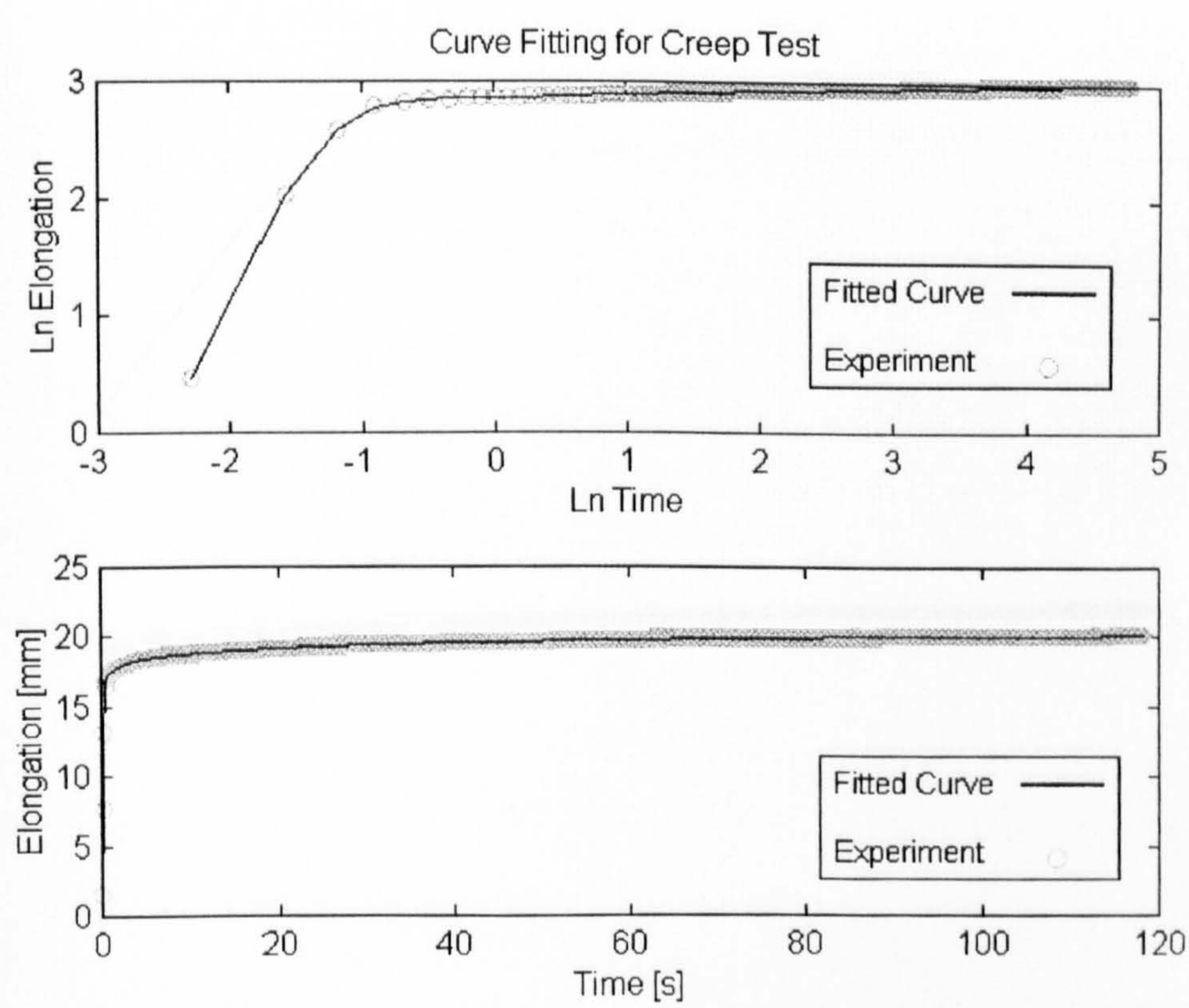

Figure B.4 Curve fitting of the creep test data for 40 kgf constant load in the relaxed procedure.

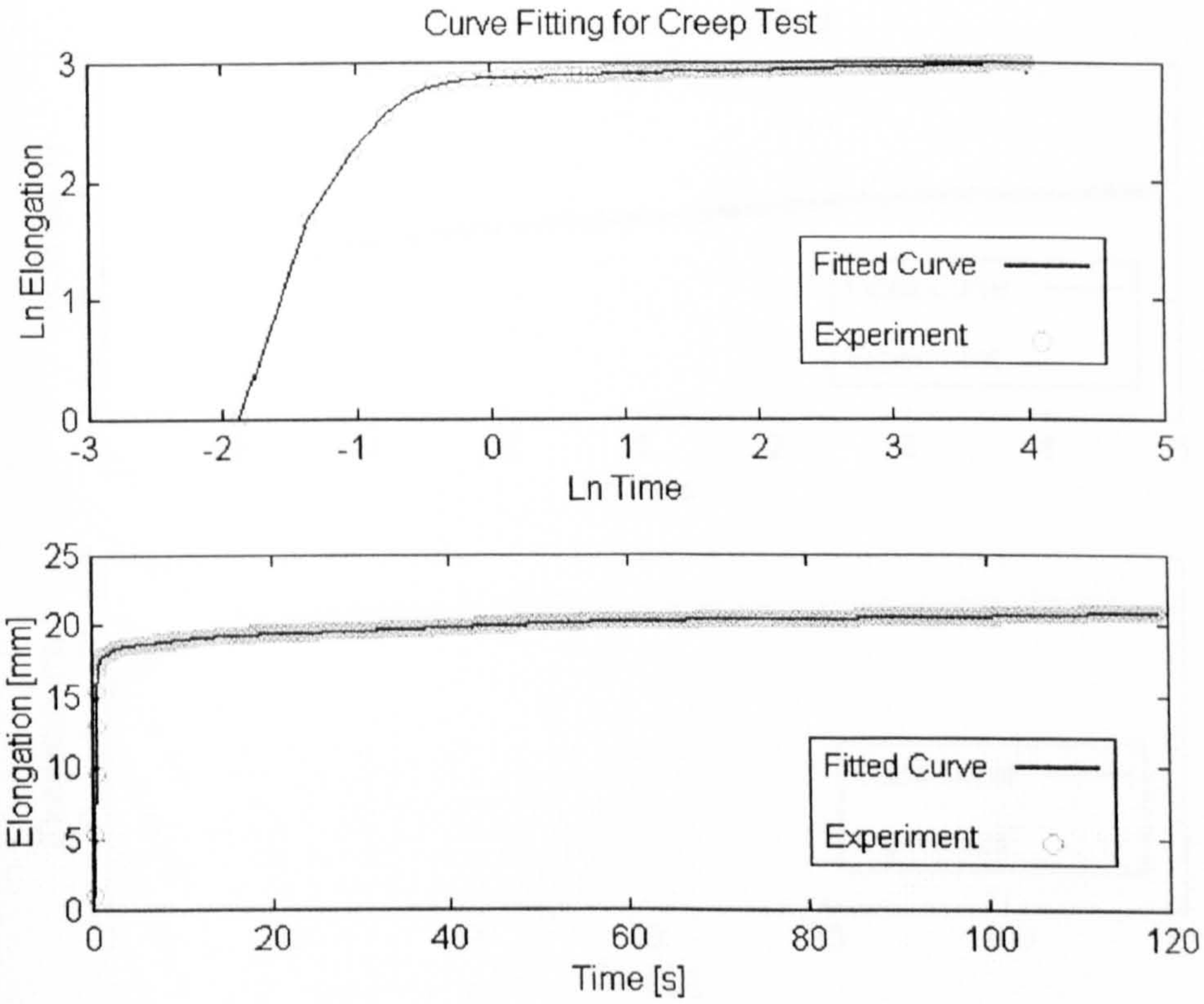

Figure B.5. Curve fitting of the creep test data for 50 kgf constant load in the relaxed procedure.

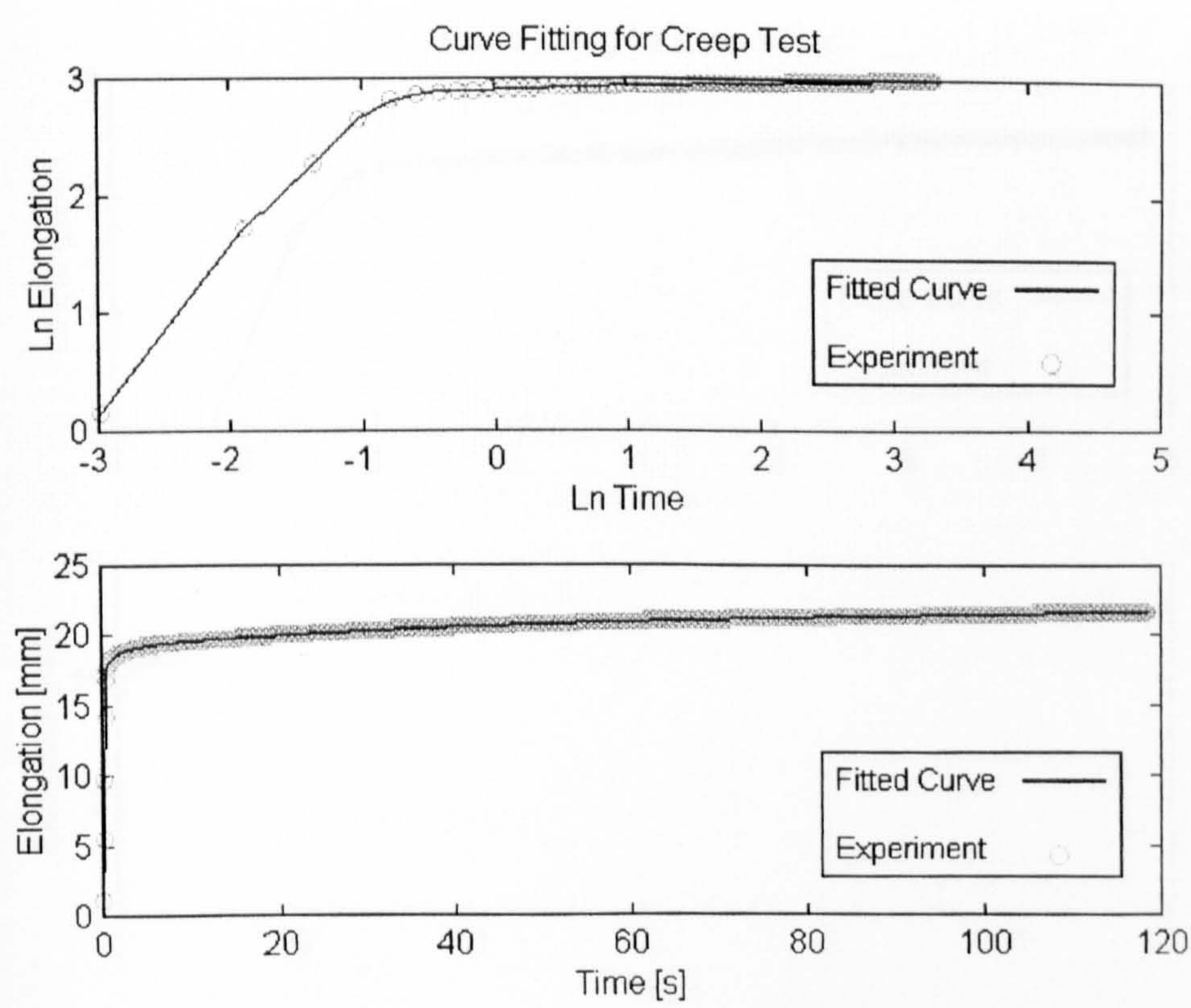

Figure B.6. Curve fitting of the creep test data for 60 kgf constant load in the relaxed procedure.

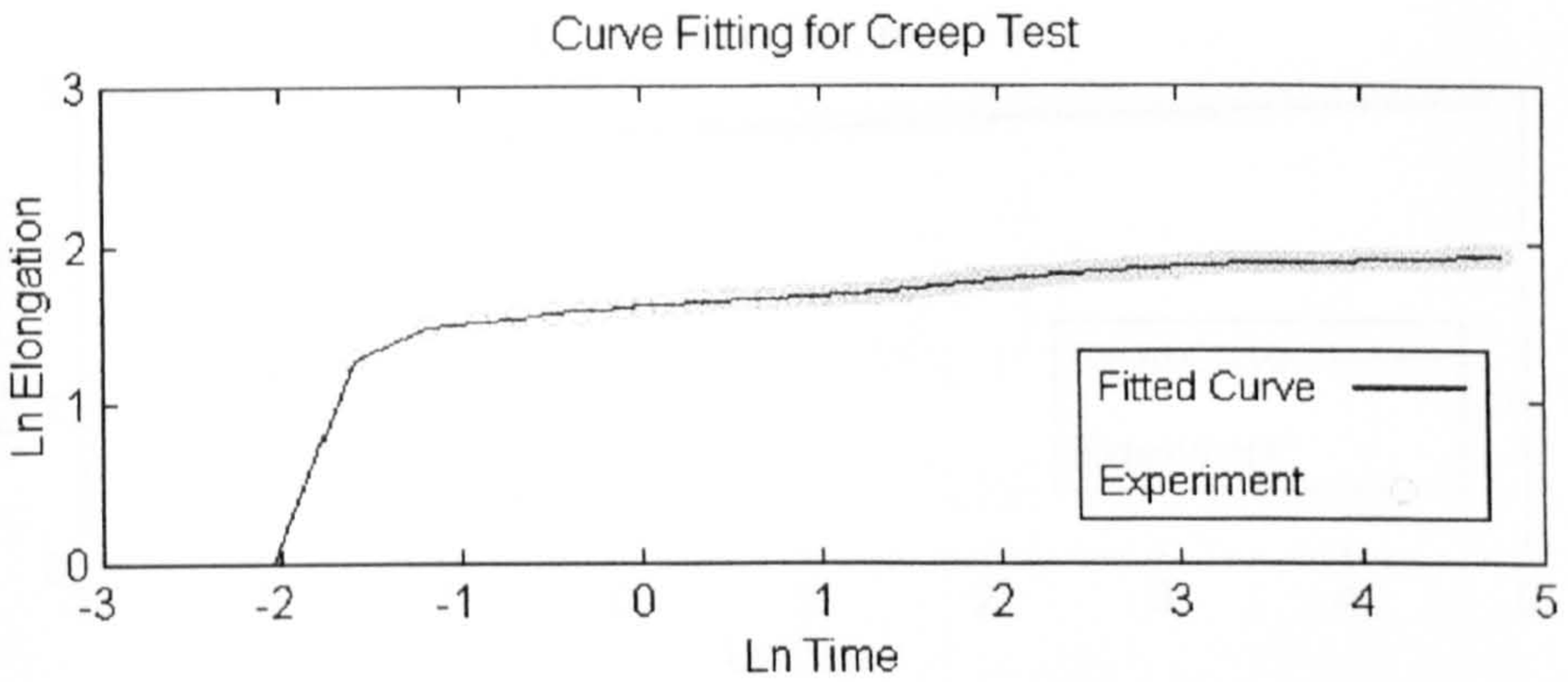

Figure B.7. Curve fitting of the creep test data for 10 kgf constant load in the contracted procedure.

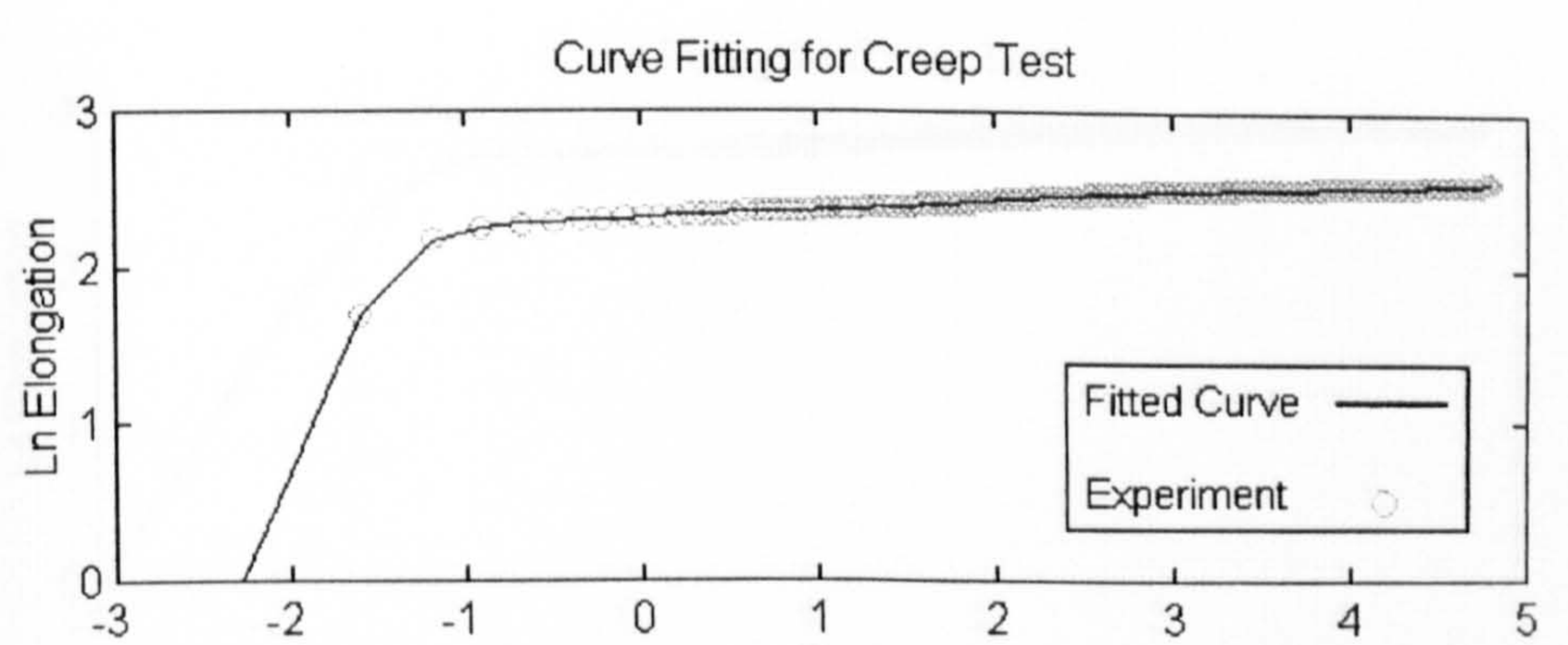

Figure B.8. Curve fitting of the creep test data for 20 kgf constant load in the contracted procedure.

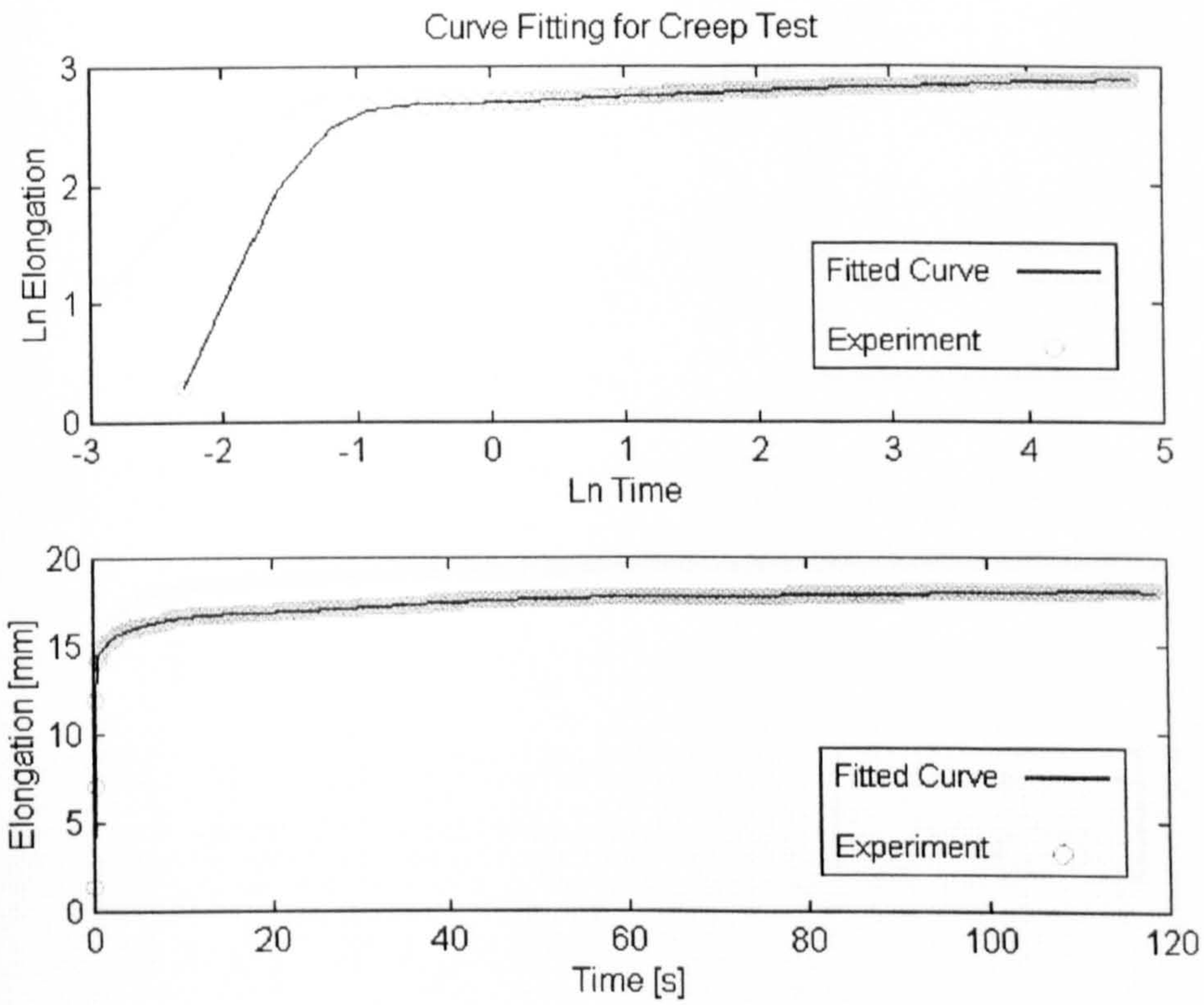

Figure B.9. Curve fitting of the creep test data for 30 kgf constant load in the contracted procedure.

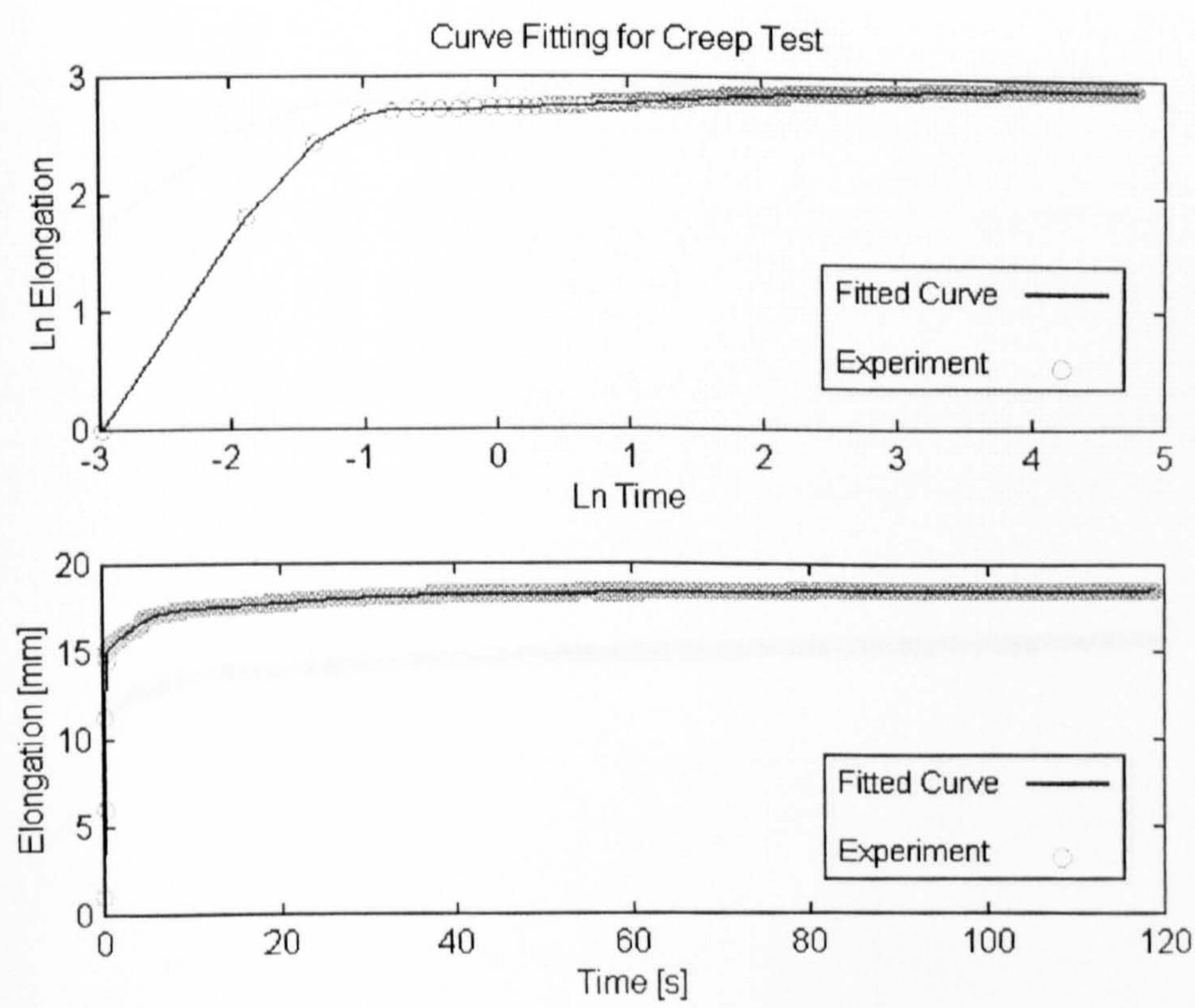

Figure B.10. Curve fitting of the creep test data for 40 kgf constant load in the contracted procedure.

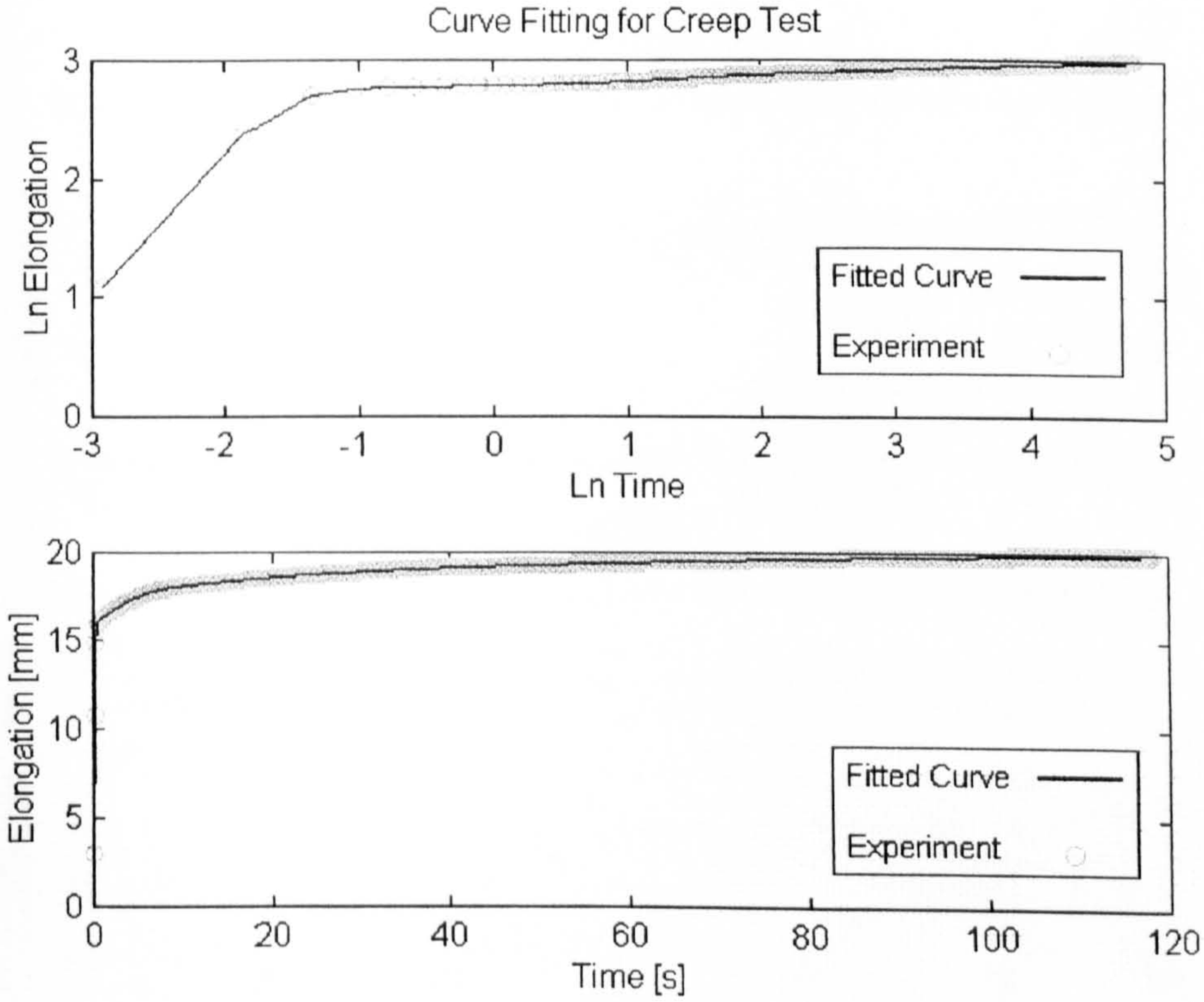

Figure B.11. Curve fitting of the creep test data for 50 kgf constant load in the contracted procedure.

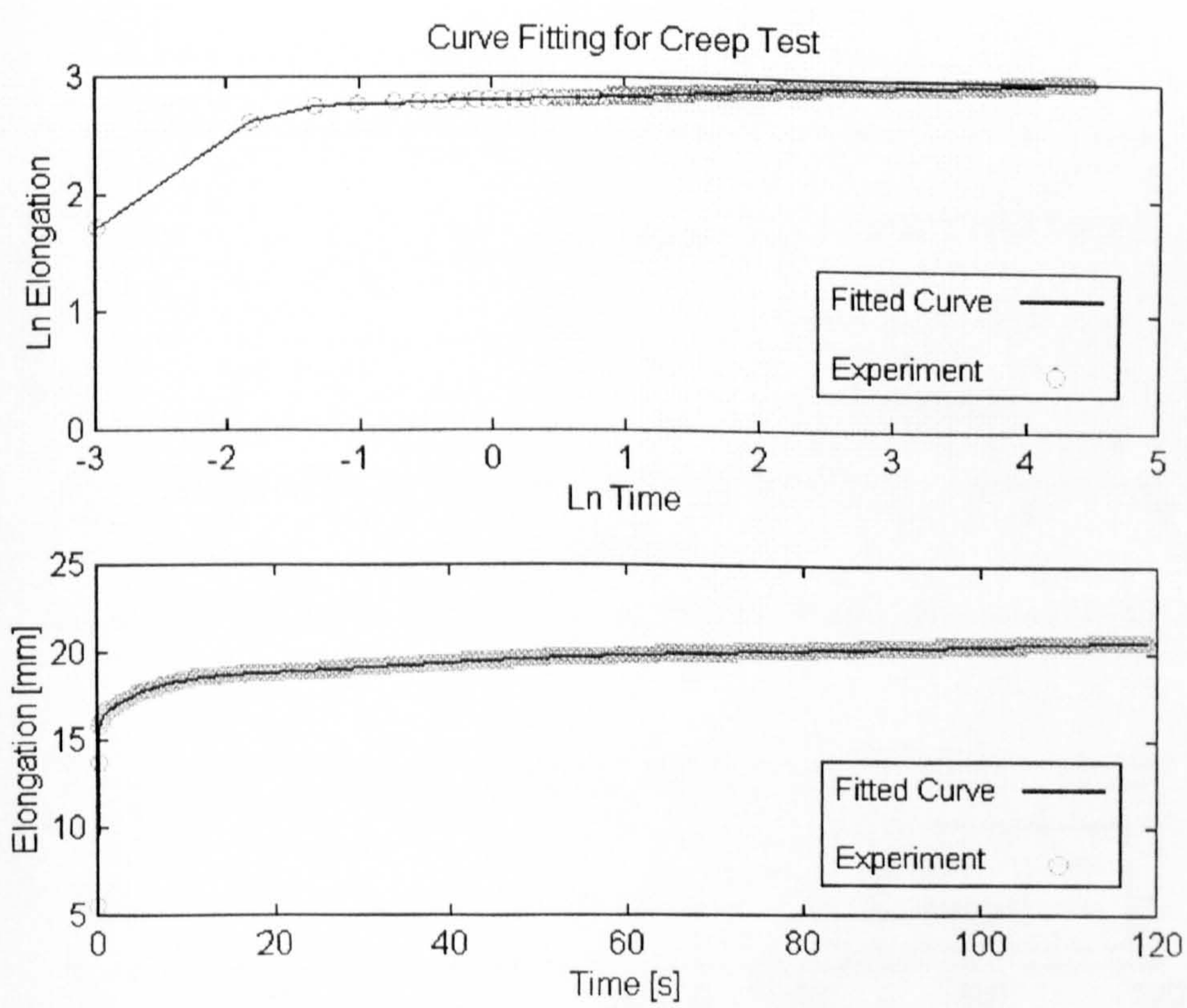

Figure B.12. Curve fitting of the creep test data for 60 kgf constant load in the contracted procedure.

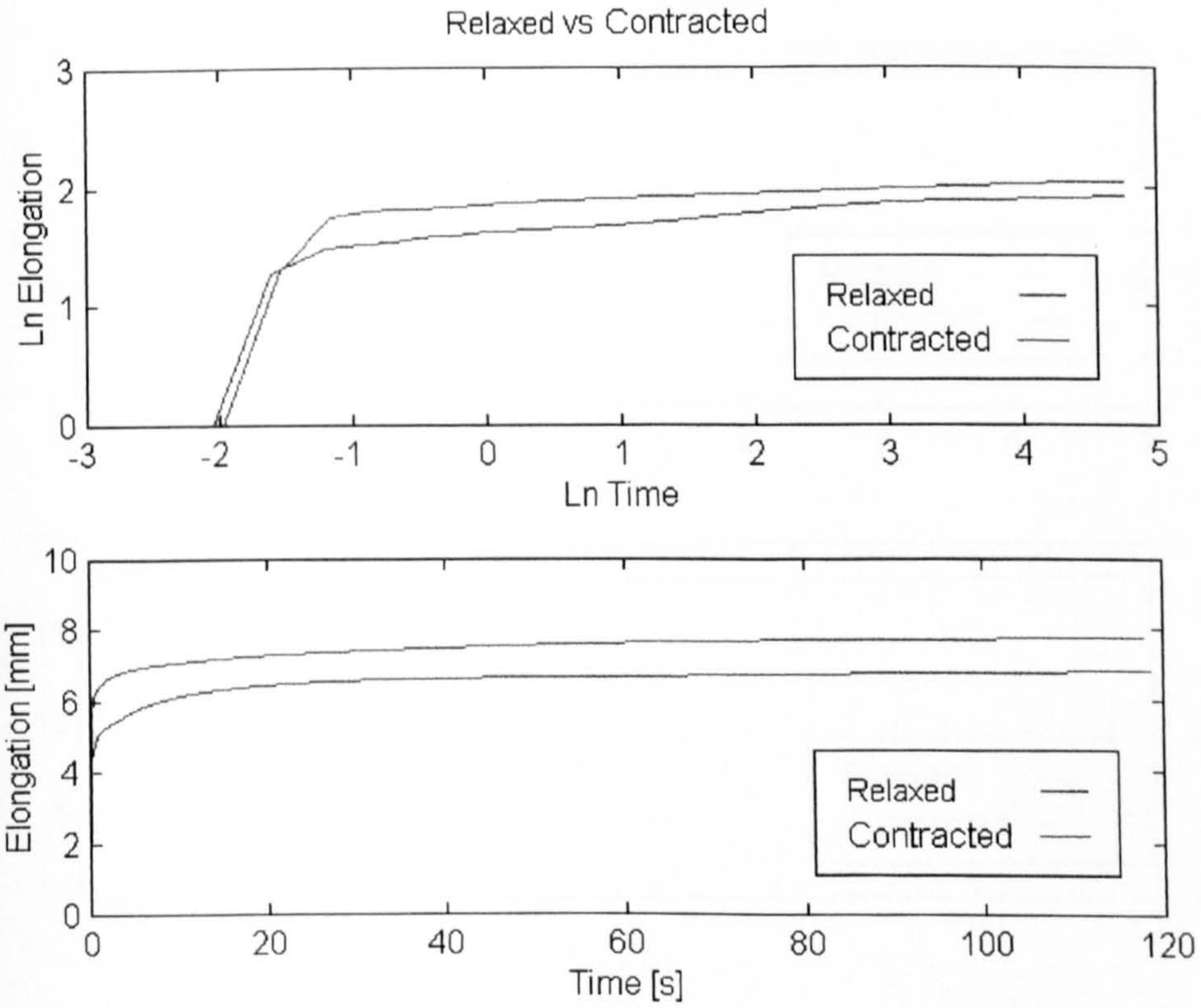

Figure B.13. Comparison of test protocols in the creep test for 10 kgf constant load.

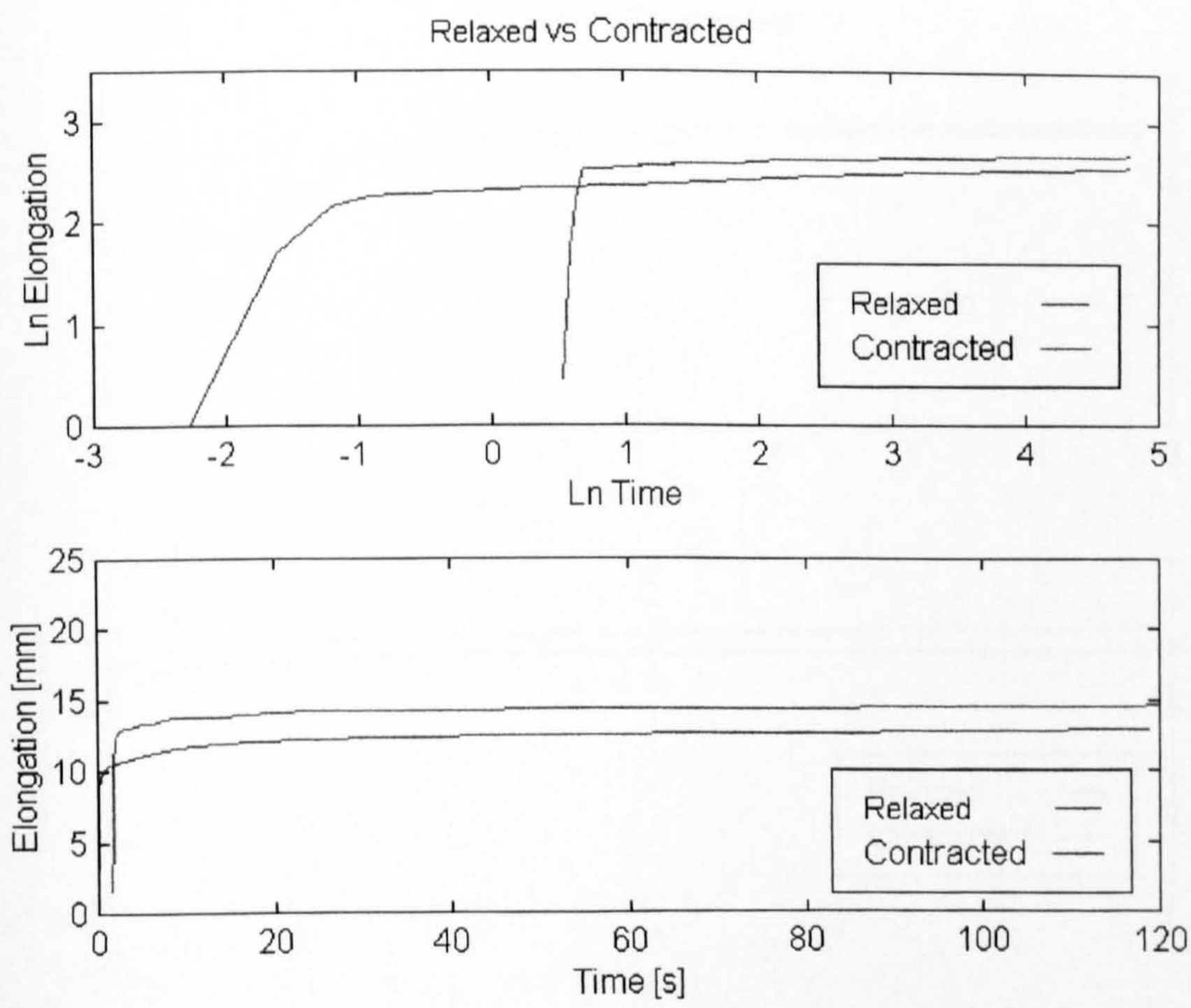

Figure B.14. Comparison of test protocols in the creep test for 20 kgf constant load.

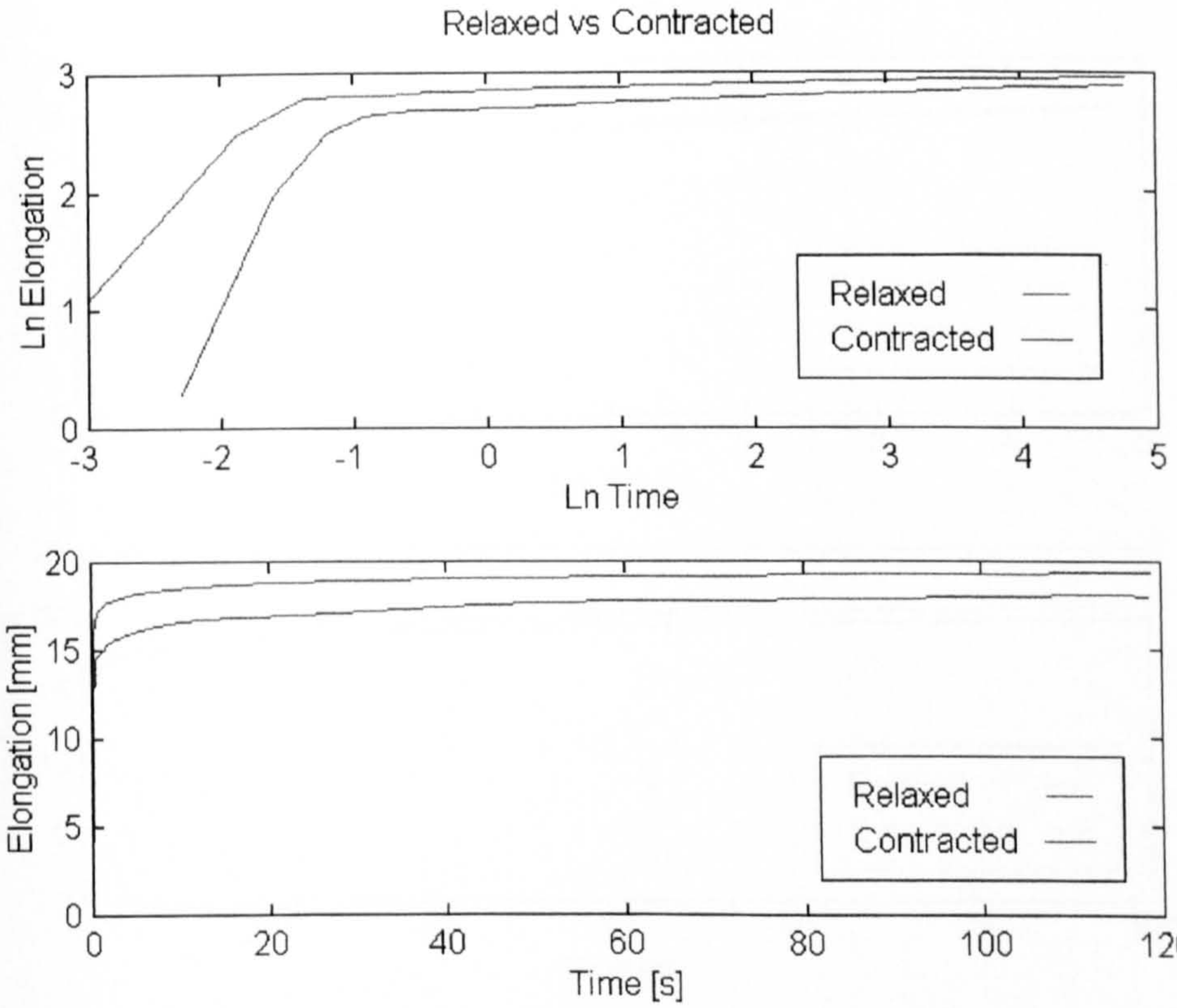

Figure B.15. Comparison of test protocols in the creep test for 30 kgf constant load.

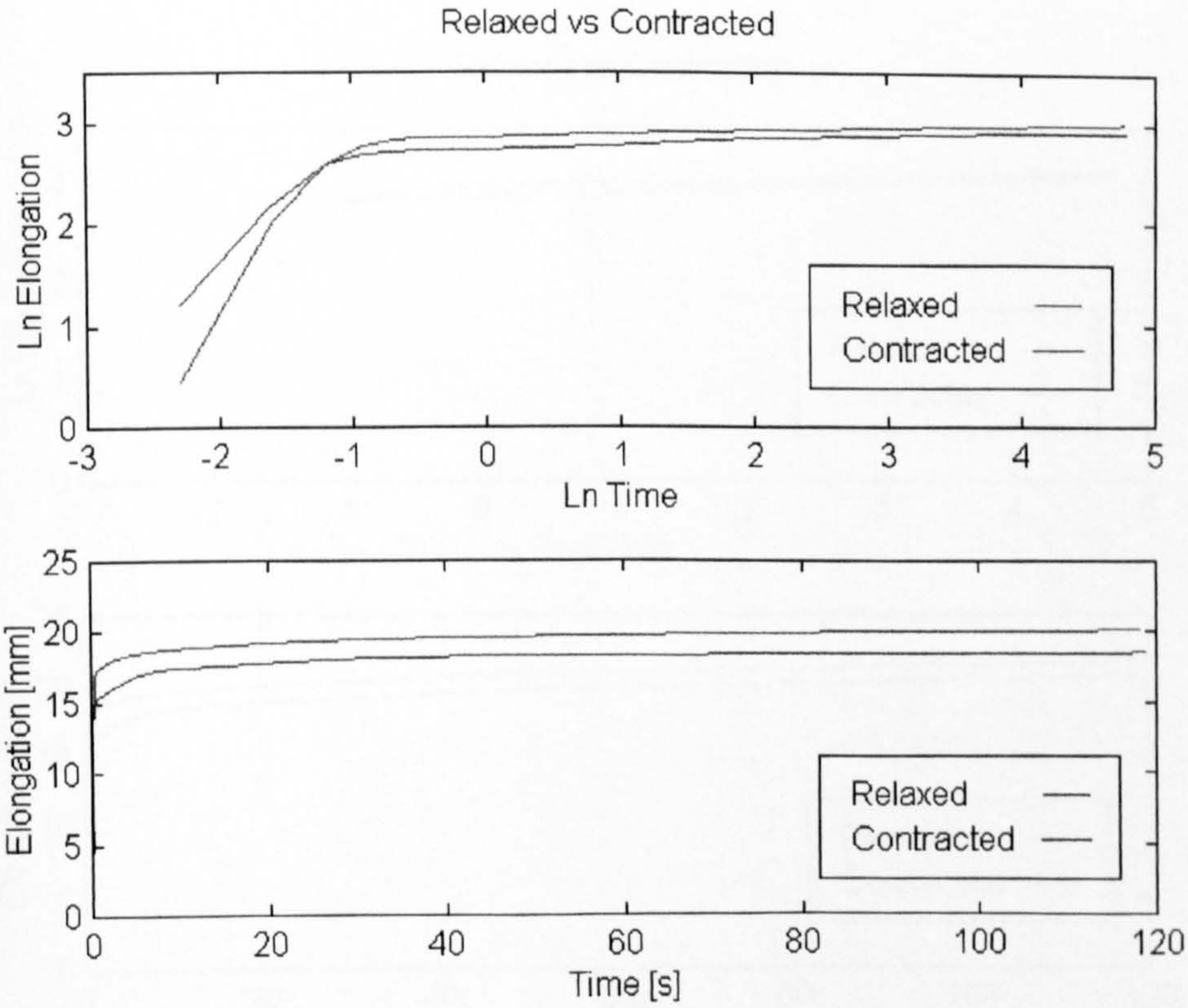

Figure B.16. Comparison of test protocols in the creep test for 40 kgf constant load.

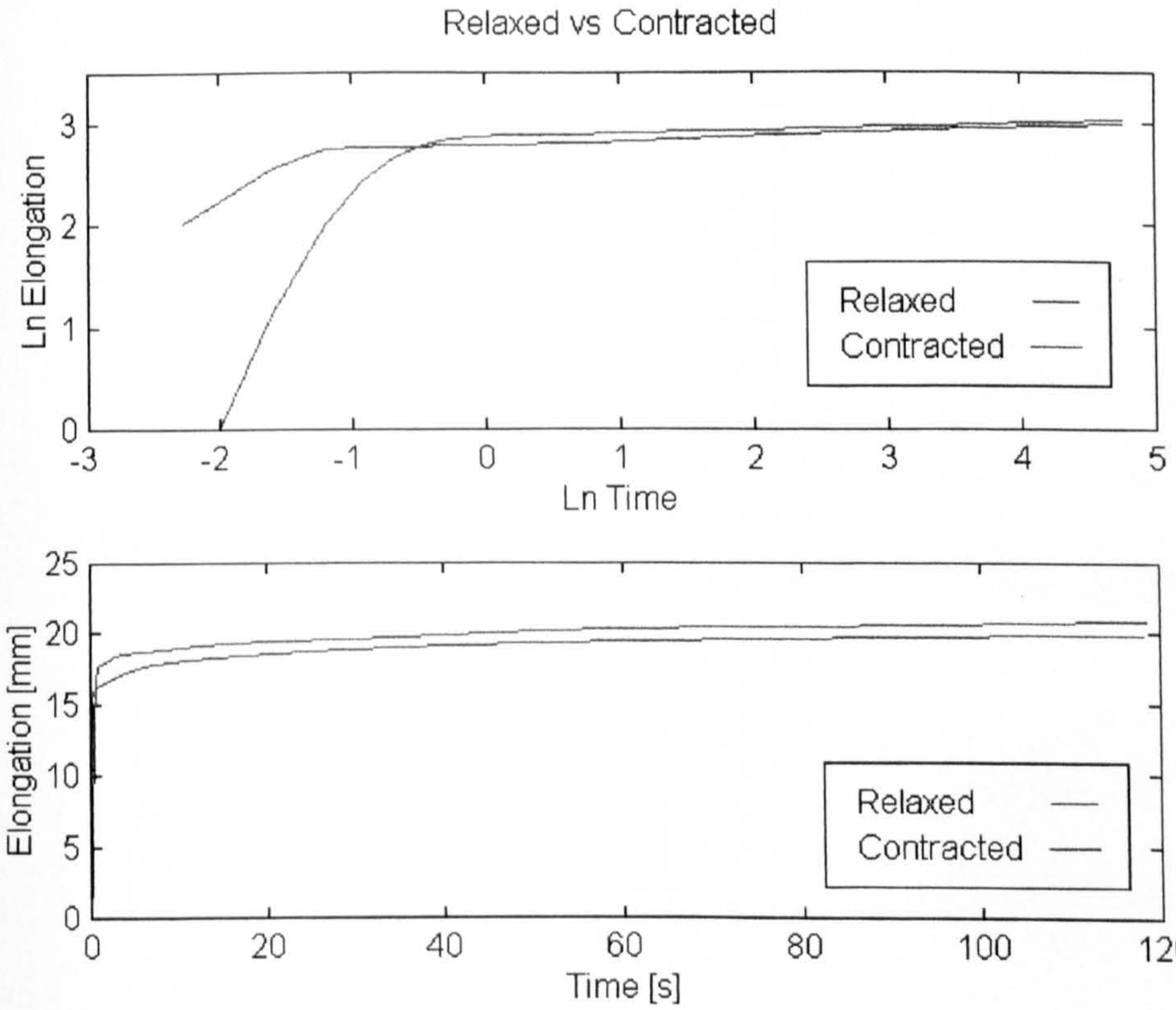

Figure B.17. Comparison of test protocols in the creep test for 50 kgf constant load.

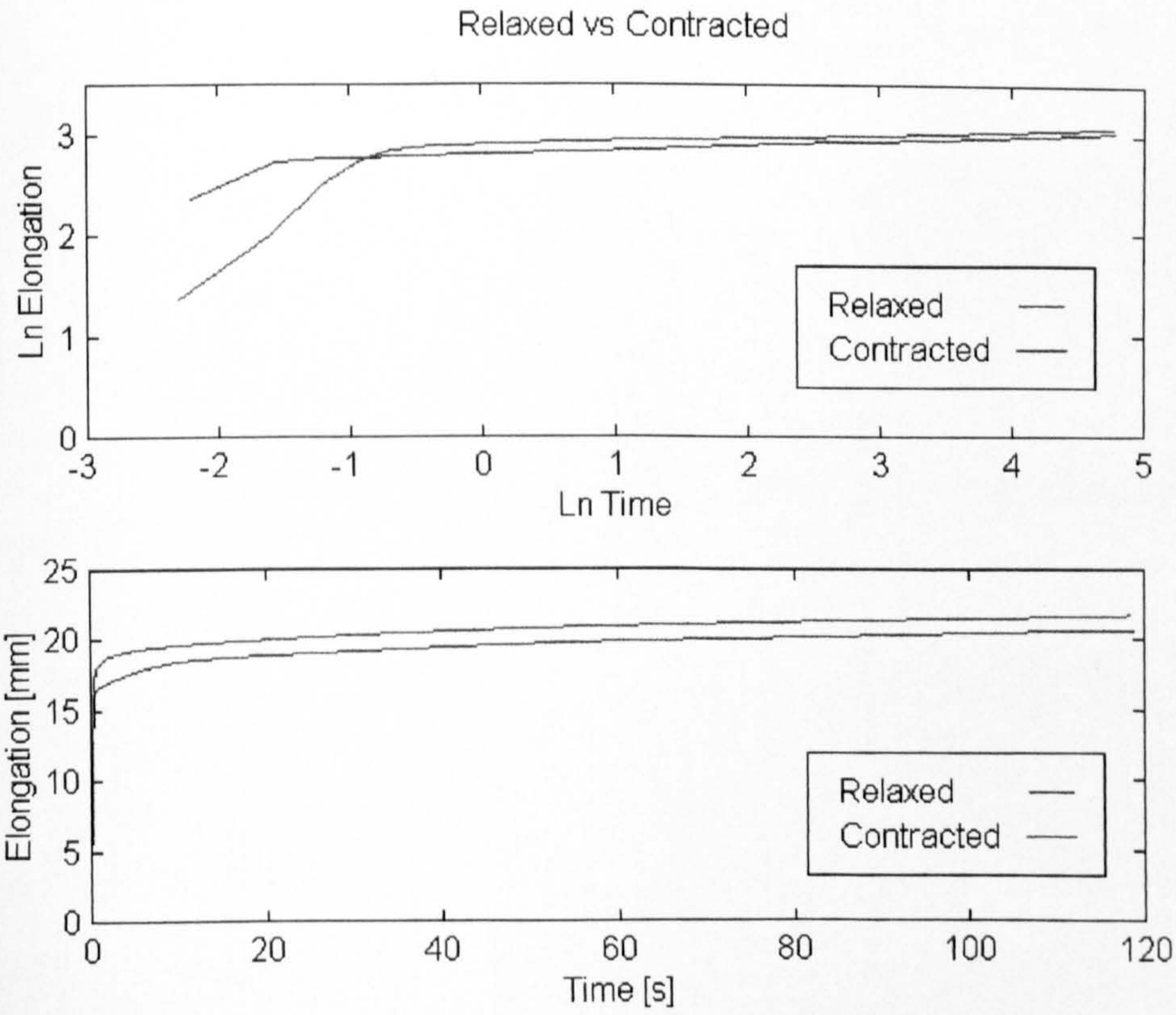

Figure B.18. Comparison of test protocols in the creep test for 60 kgf constant load.

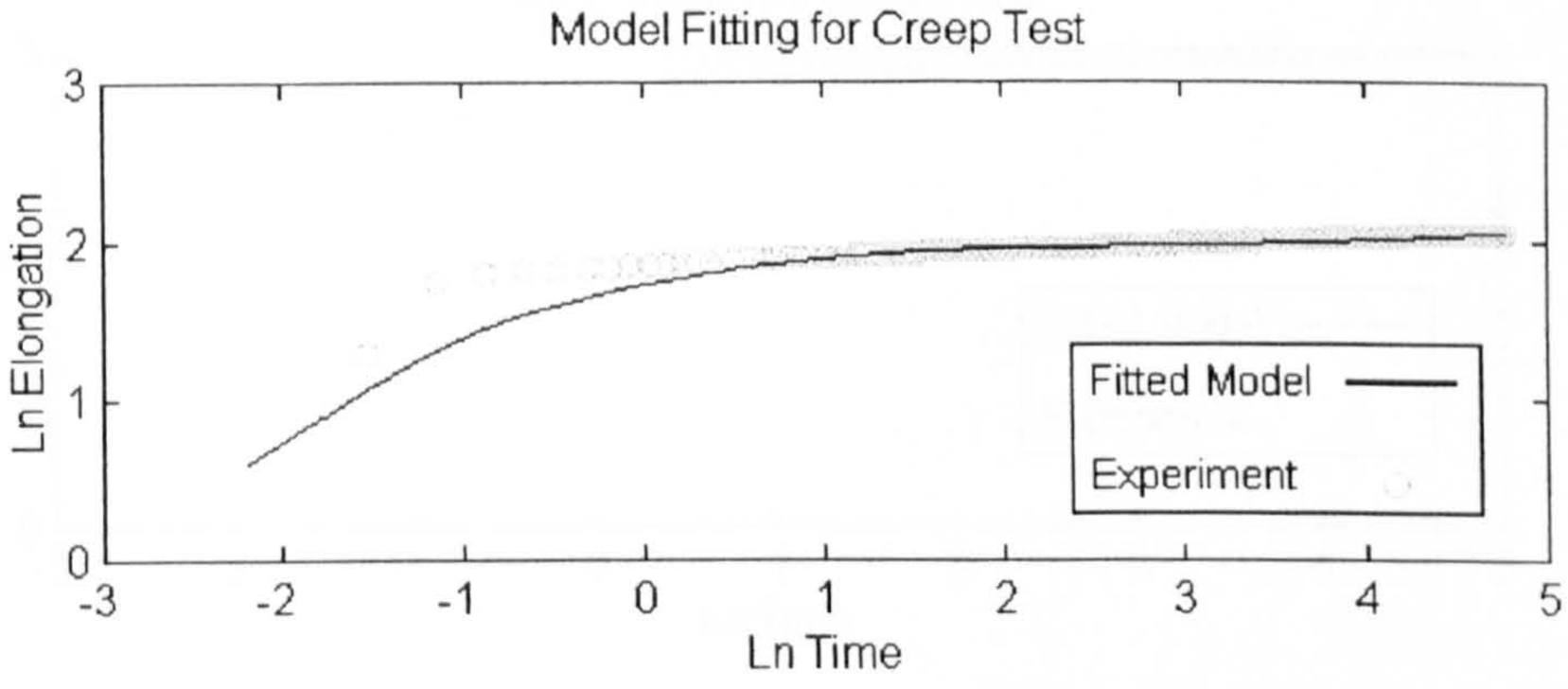

Figure . Model fitting of the creep test data for 10 kgf constant load in the relax procedure.

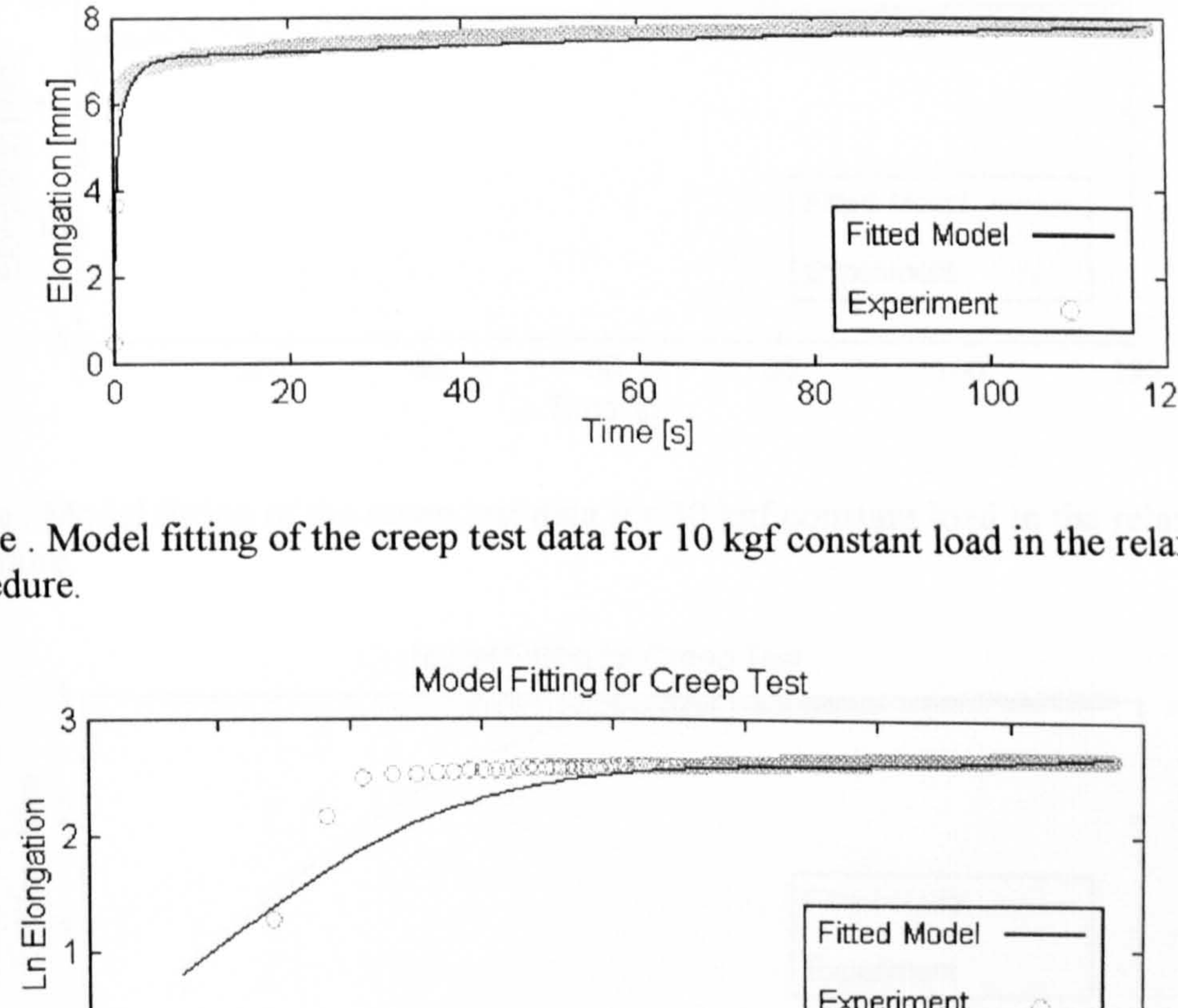

Figure . Model fitting of the creep test data for 20 kgf constant load in the relax procedure.

Appendix B

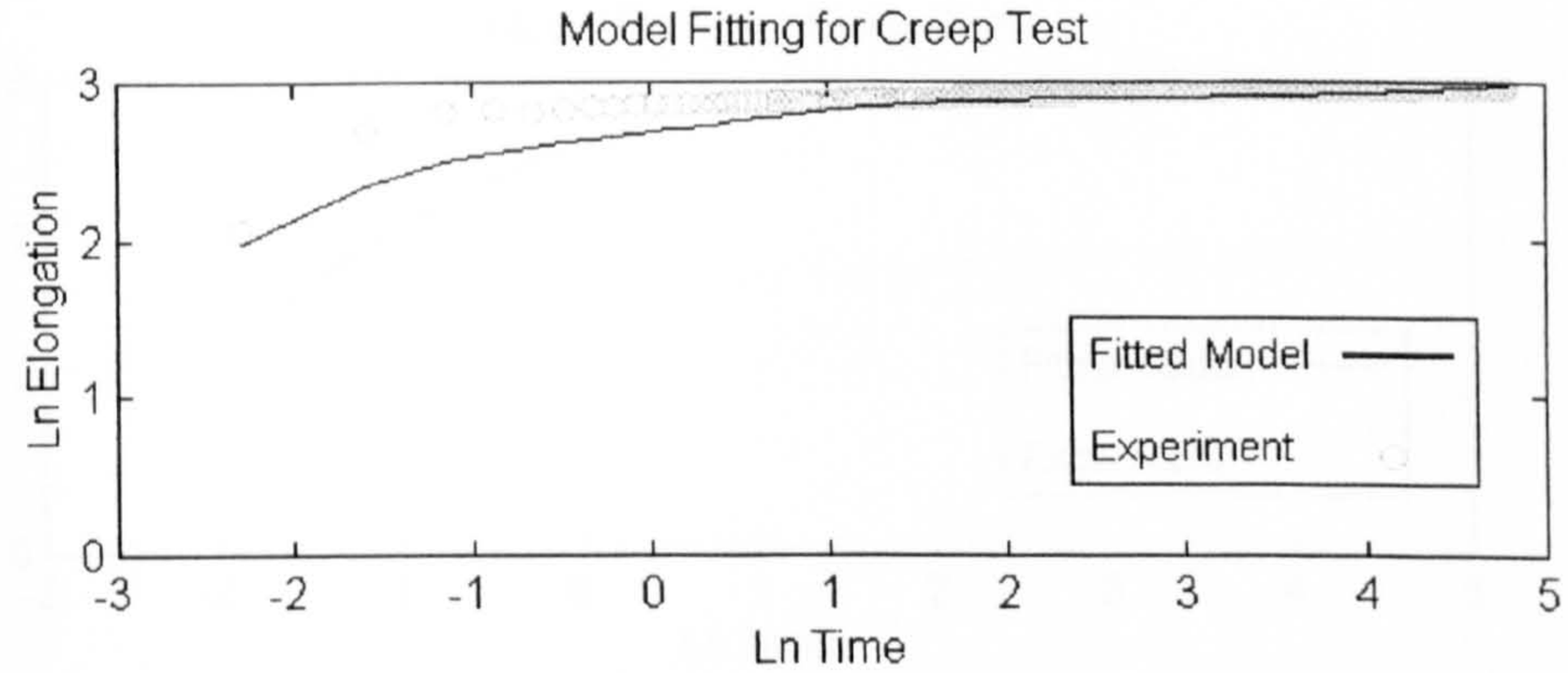

Figure . Model fitting of the creep test data for 30 kgf constant load in the relax procedure.

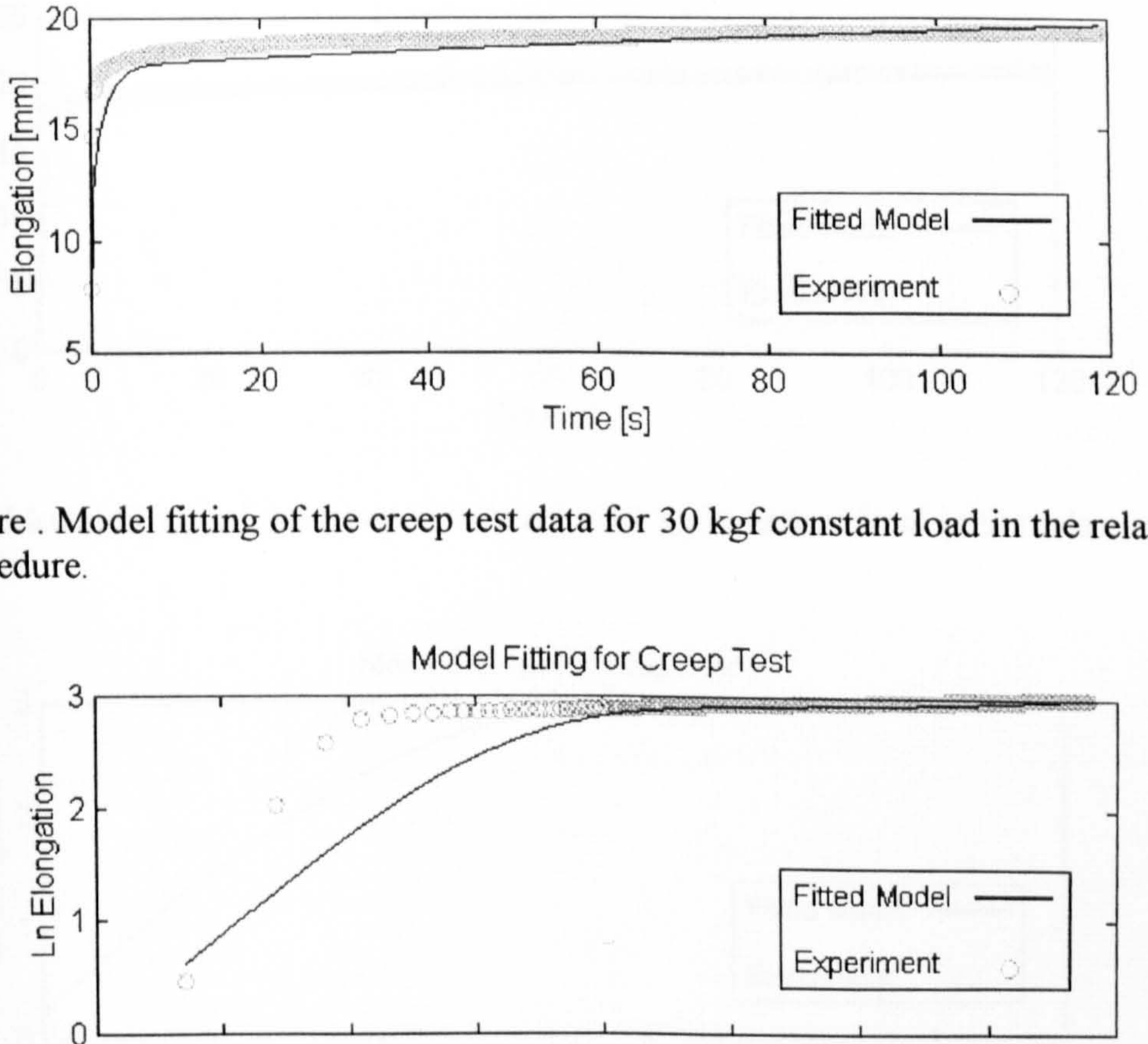

Figure . Model fitting of the creep test data for 40 kgf constant load in the relax procedure.

Appendix B

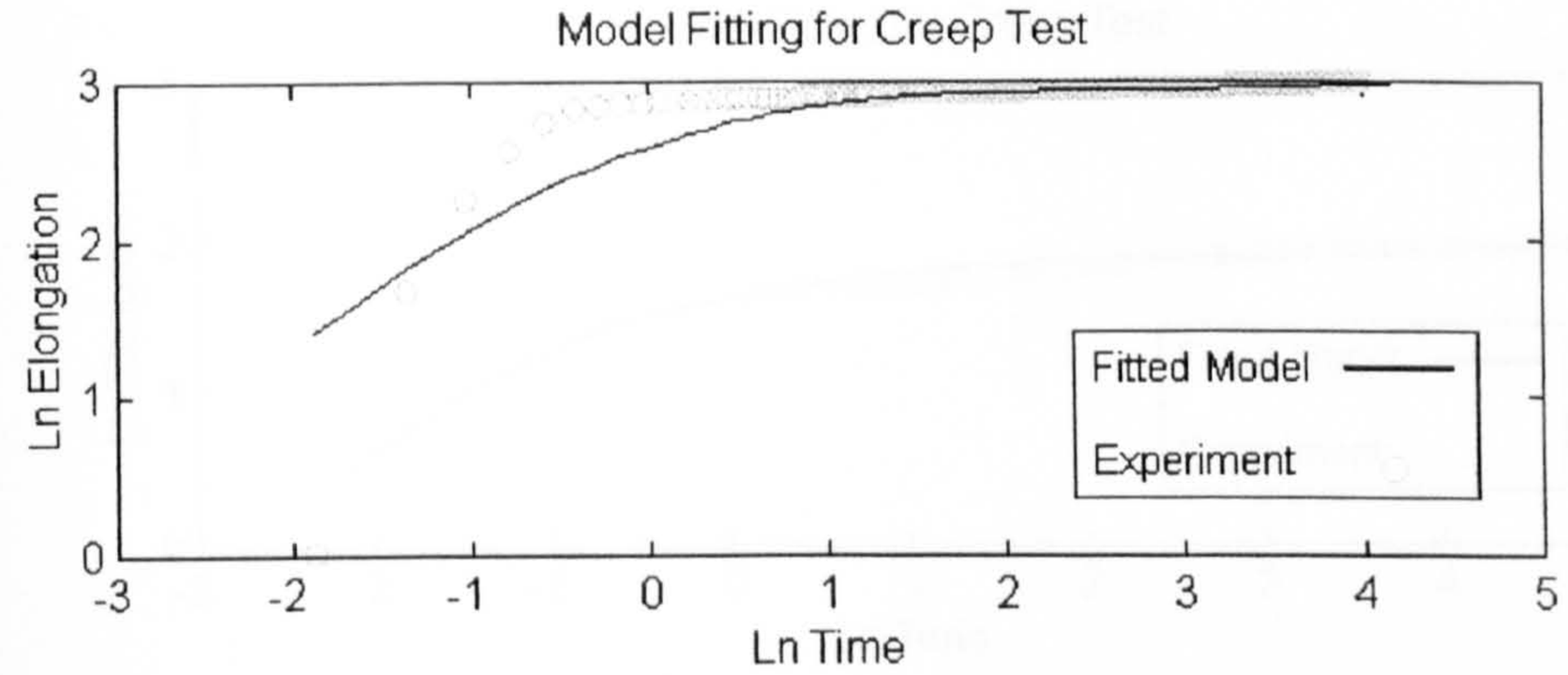

Figure . Model fitting of the creep test data for 50 kgf constant load in the relax procedure.

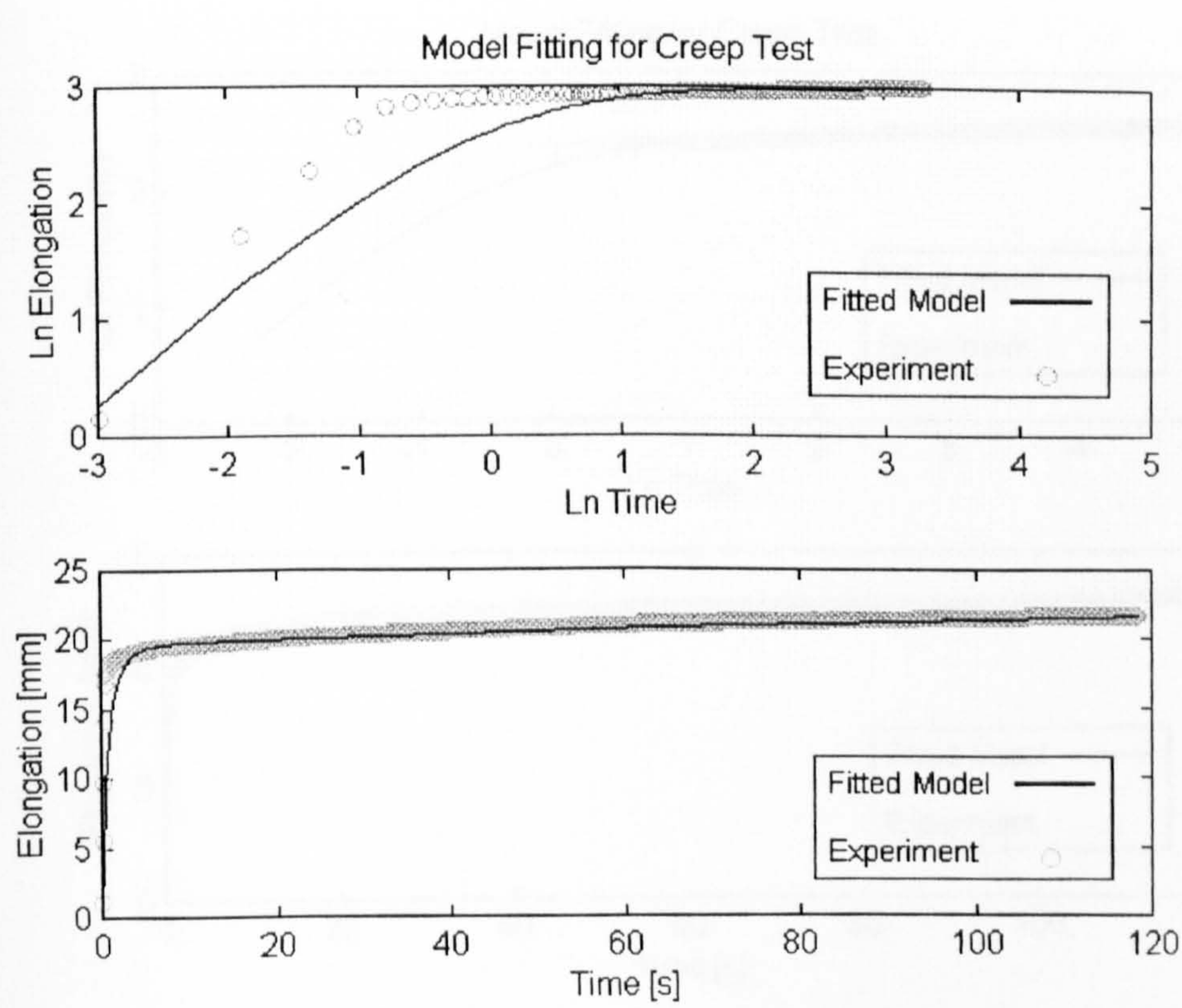

Figure . Model fitting of the creep test data for 60 kgf constant load in the relax procedure.

Appendix B

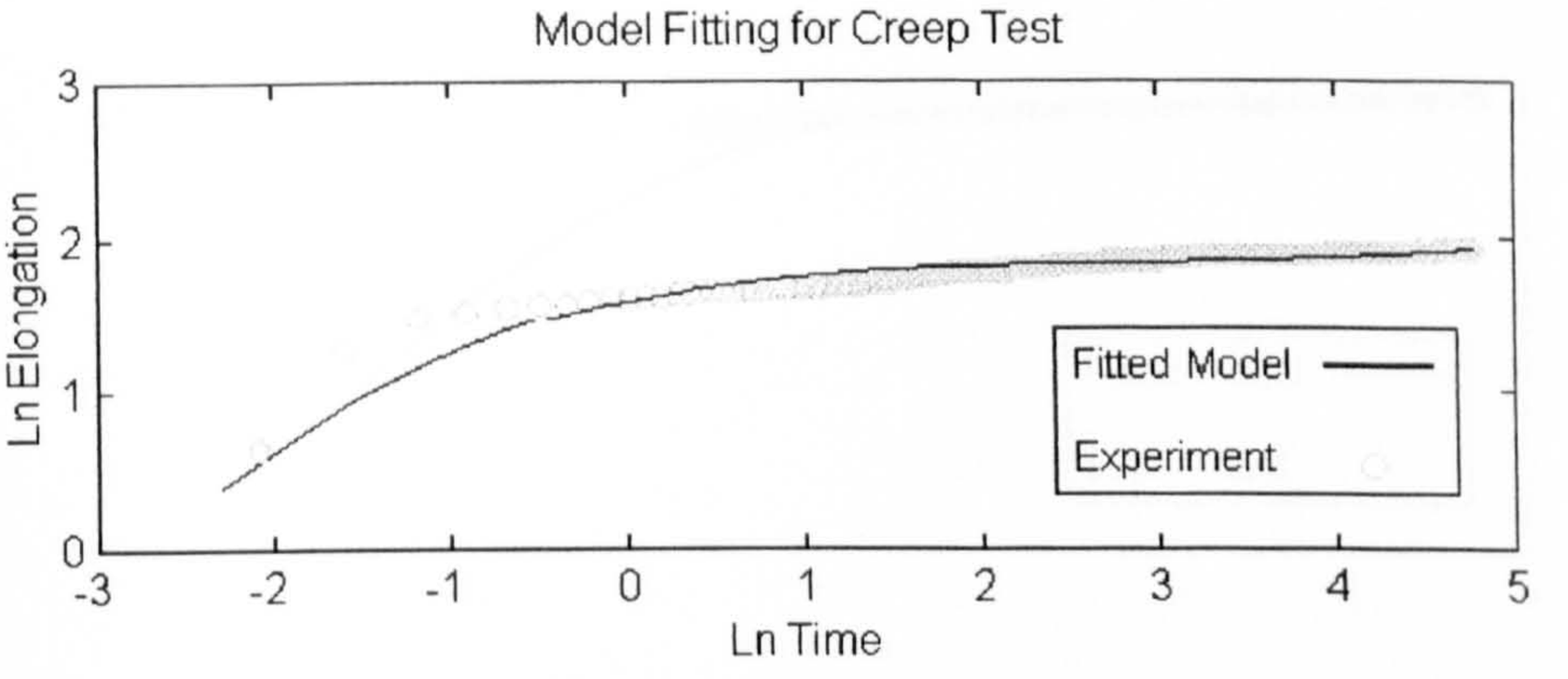

Figure . Model fitting of the creep test data for 10 kgf constant load in the contracted procedure.

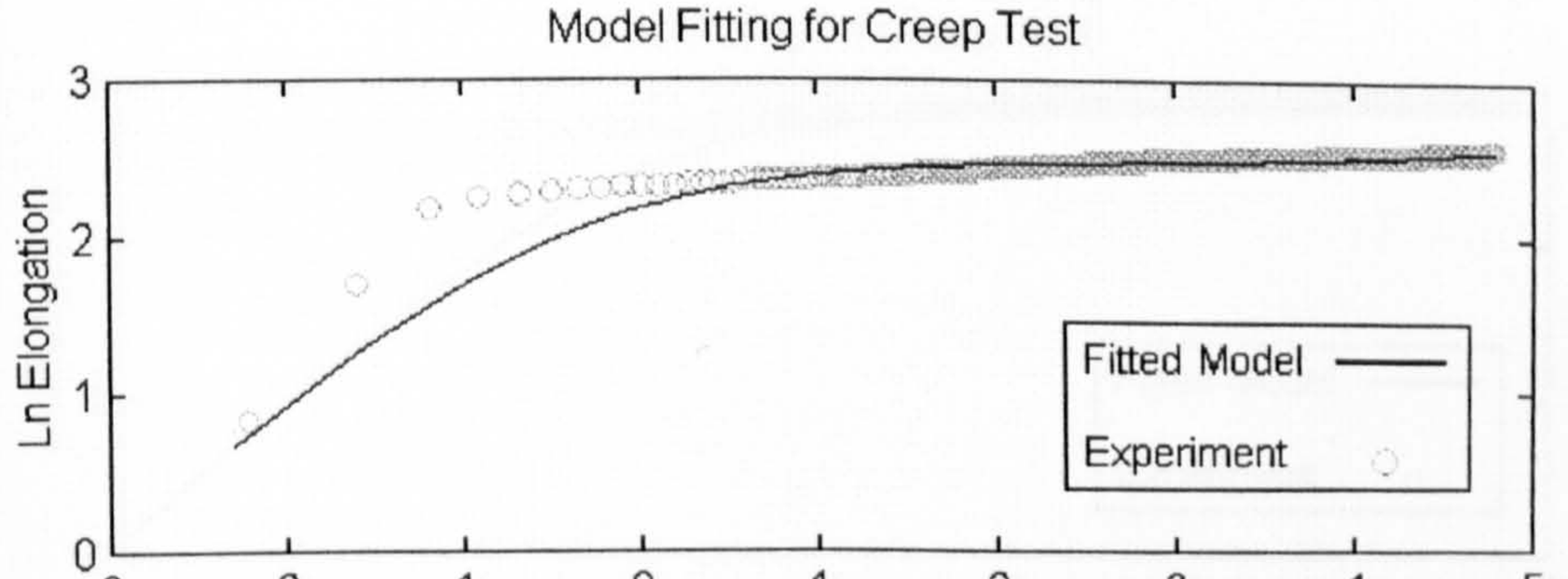

Figure . Model fitting of the creep test data for 20 kgf constant load in the contracted procedure.

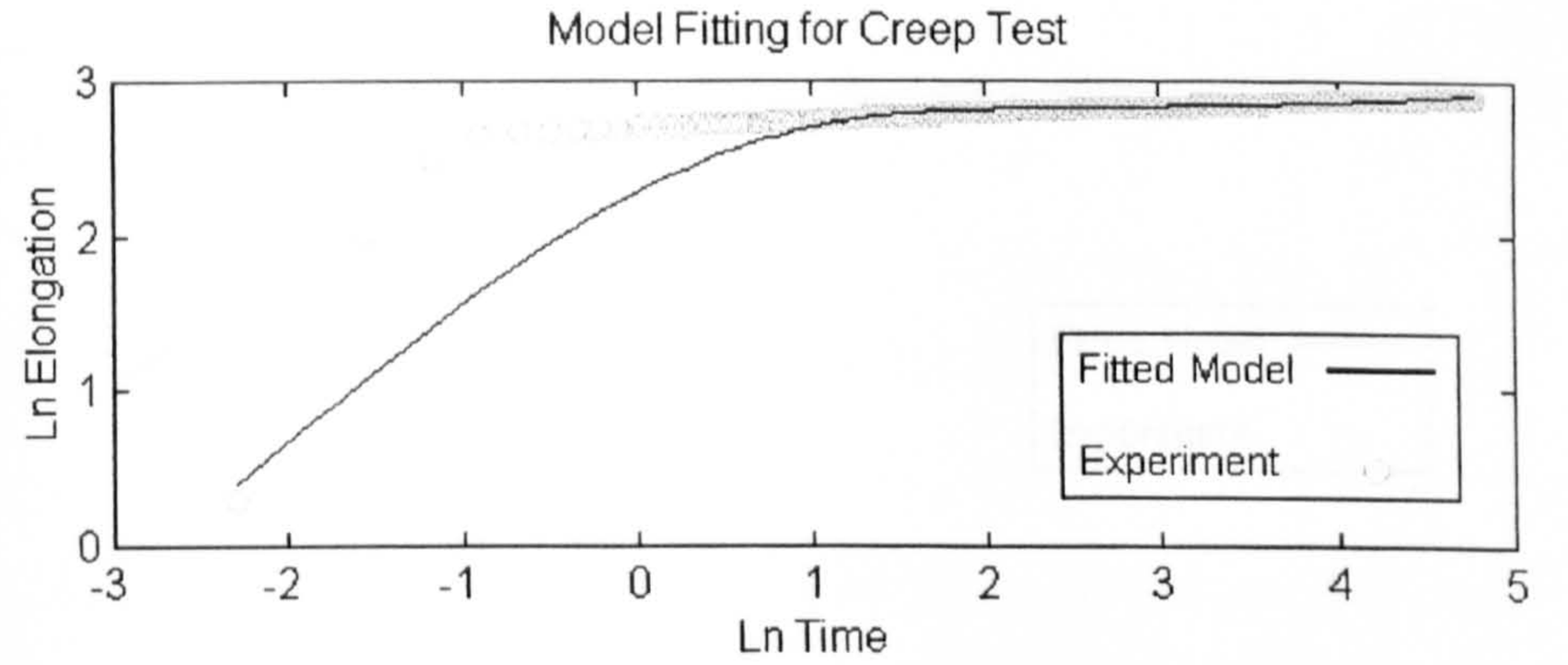

Figure . Model fitting of the creep test data for 30 kgf constant load in the contracted procedure.

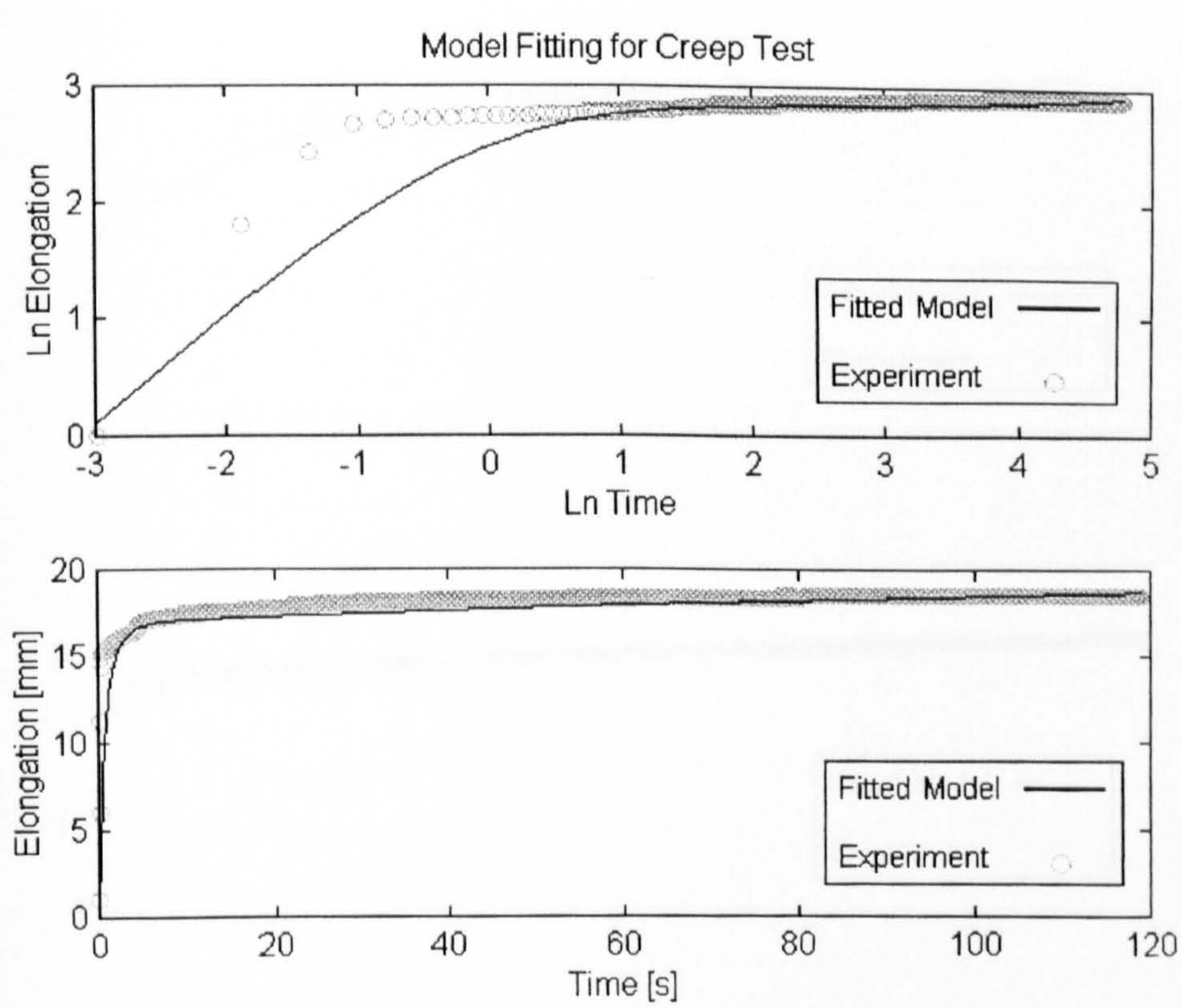

Figure . Model fitting of the creep test data for 40 kgf constant load in the contracted procedure.

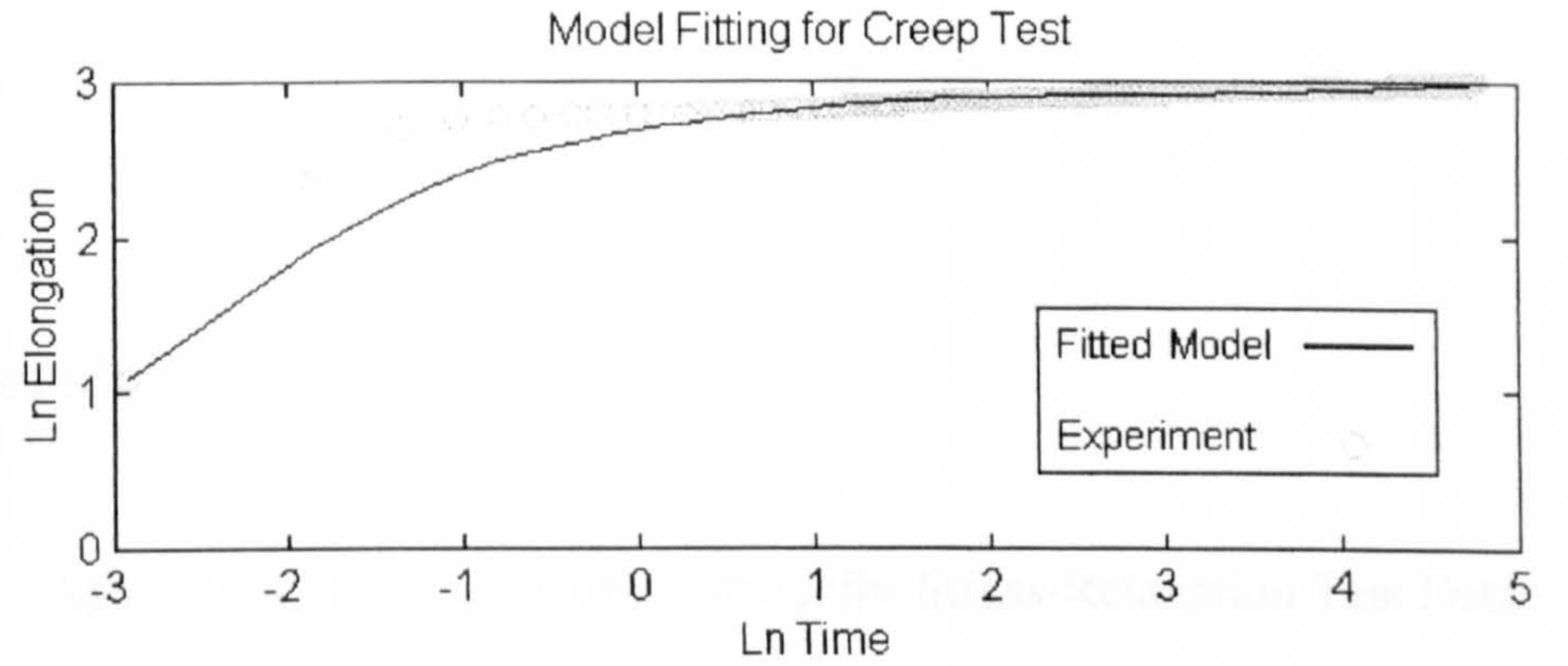

Figure . Model fitting of the creep test data for 50 kgf constant load in the contracted procedure.

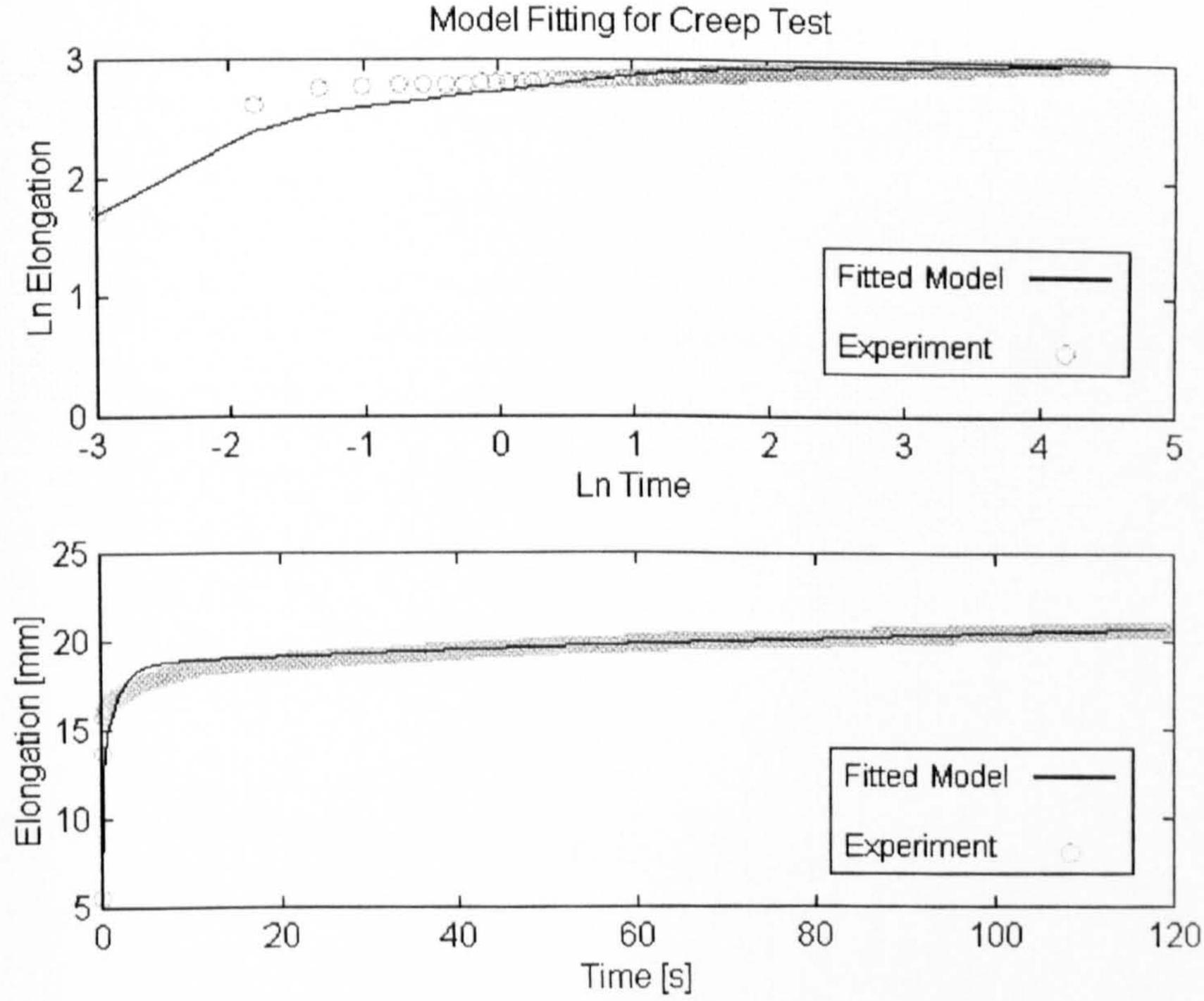

Figure . Model fitting of the creep test data for 60 kgf constant load in the contracted procedure.

Appendix C

Appendix C.1. Curve Fitting for Stress-Relaxation Test Data

Appendix C.2. Comparison of Test Protocols in Stress-Relaxation Test Data

Appendix C.3. Model Fitting for Stress-Relaxation Test Data

Appendix C

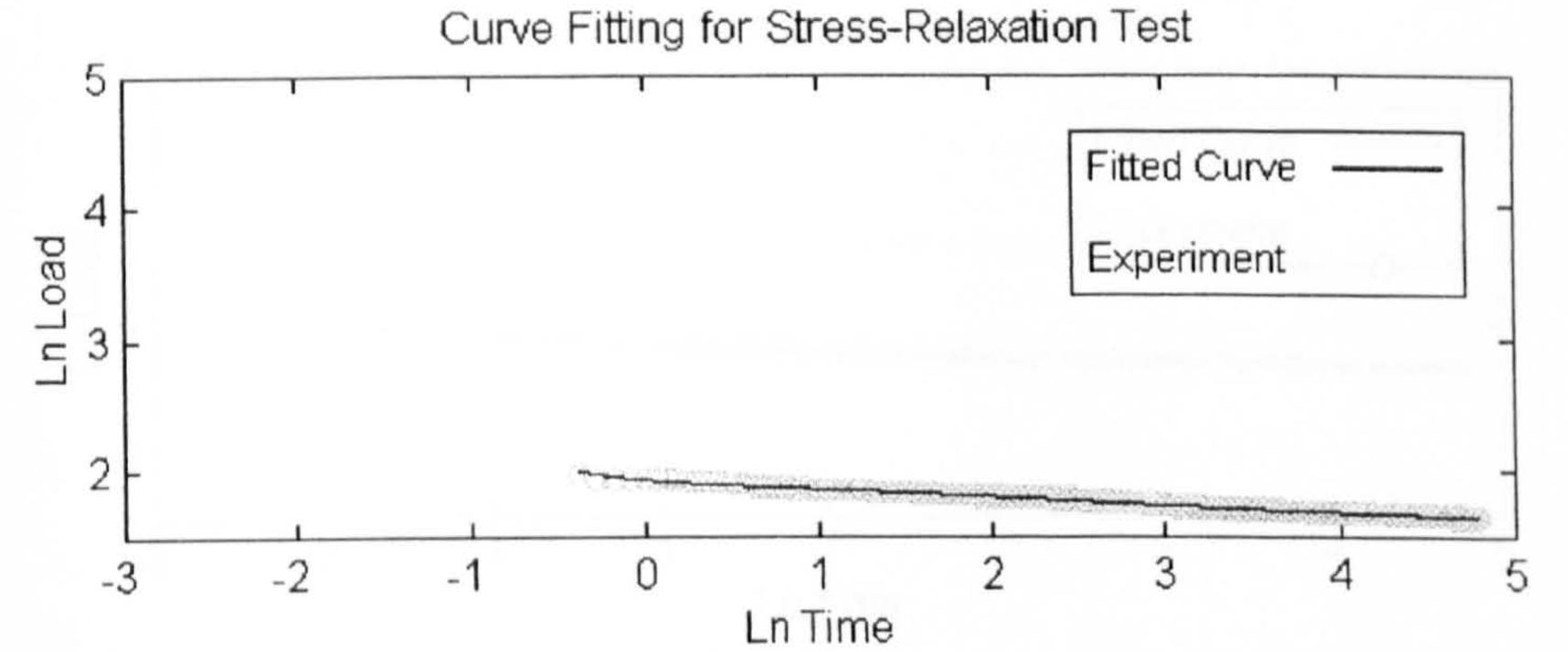

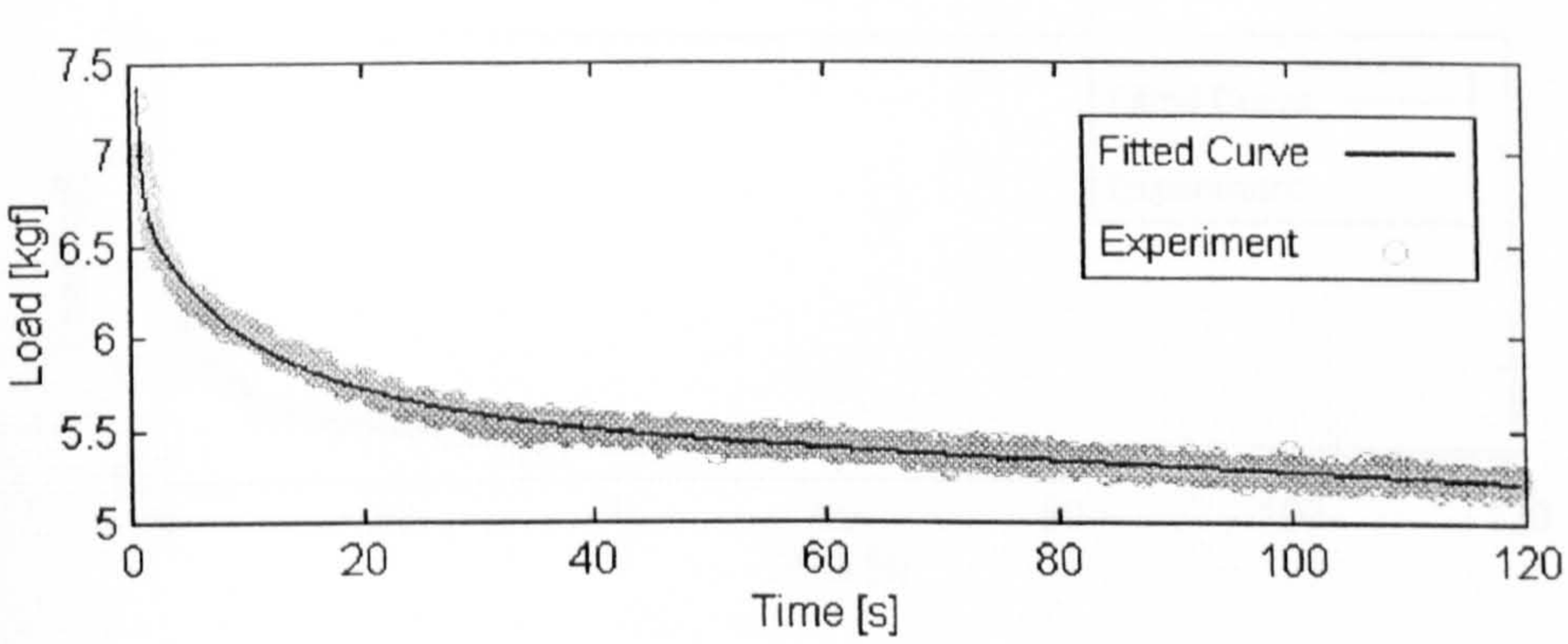

Figure C.1. Curve fitting of the stress-relaxation test data for 5 mm constant strain in the relaxed procedure.

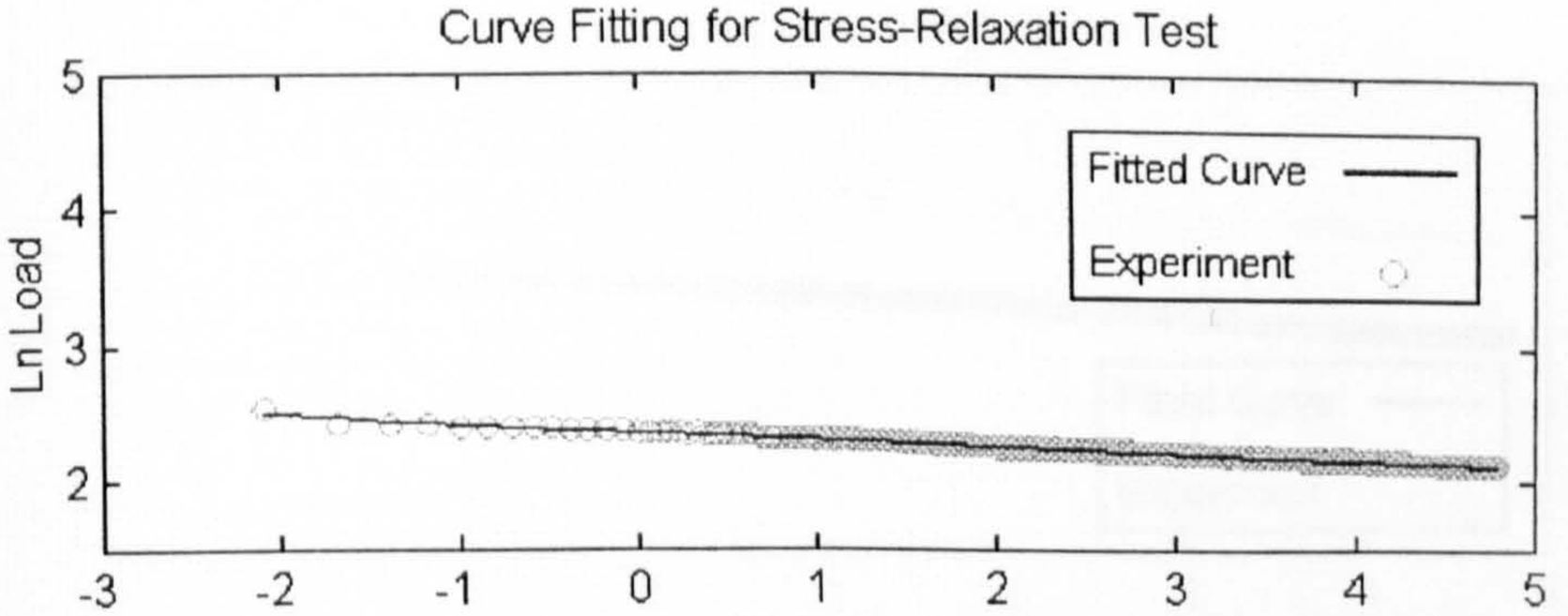

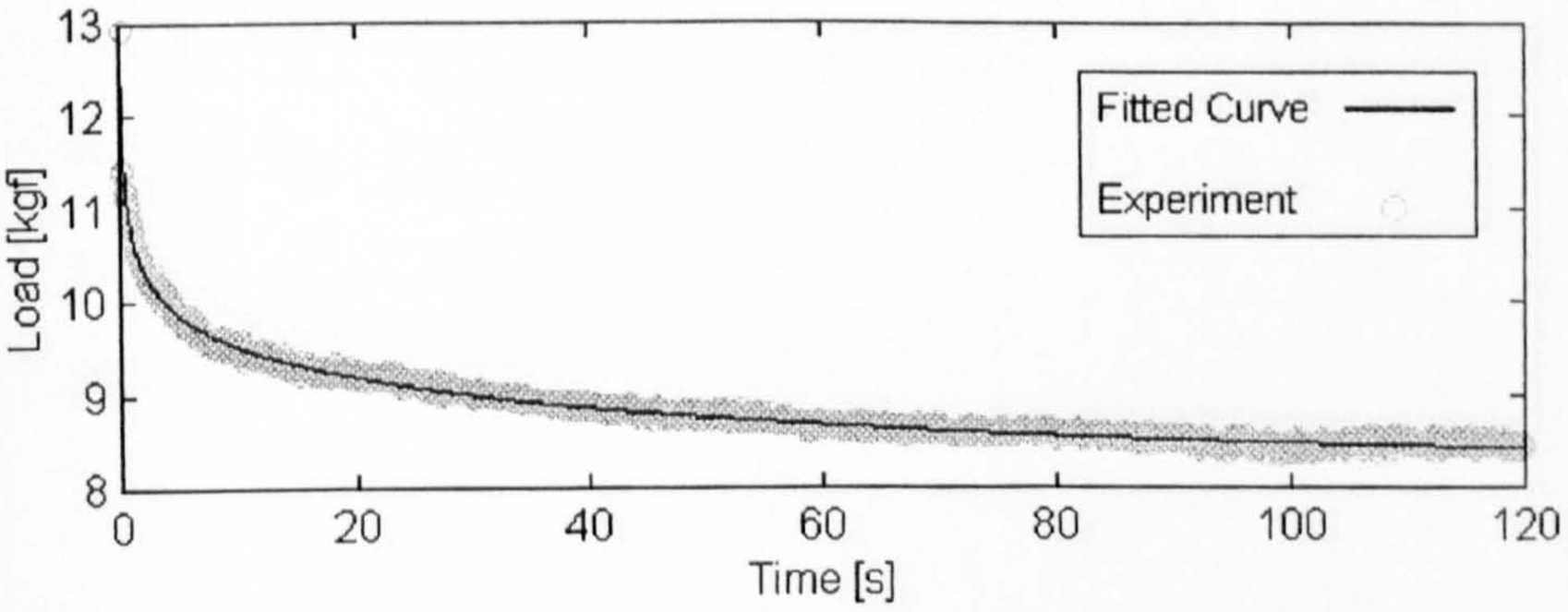

Figure C.2. Curve fitting of the stress-relaxation test data for 10 mm constant strain in the relaxed procedure.

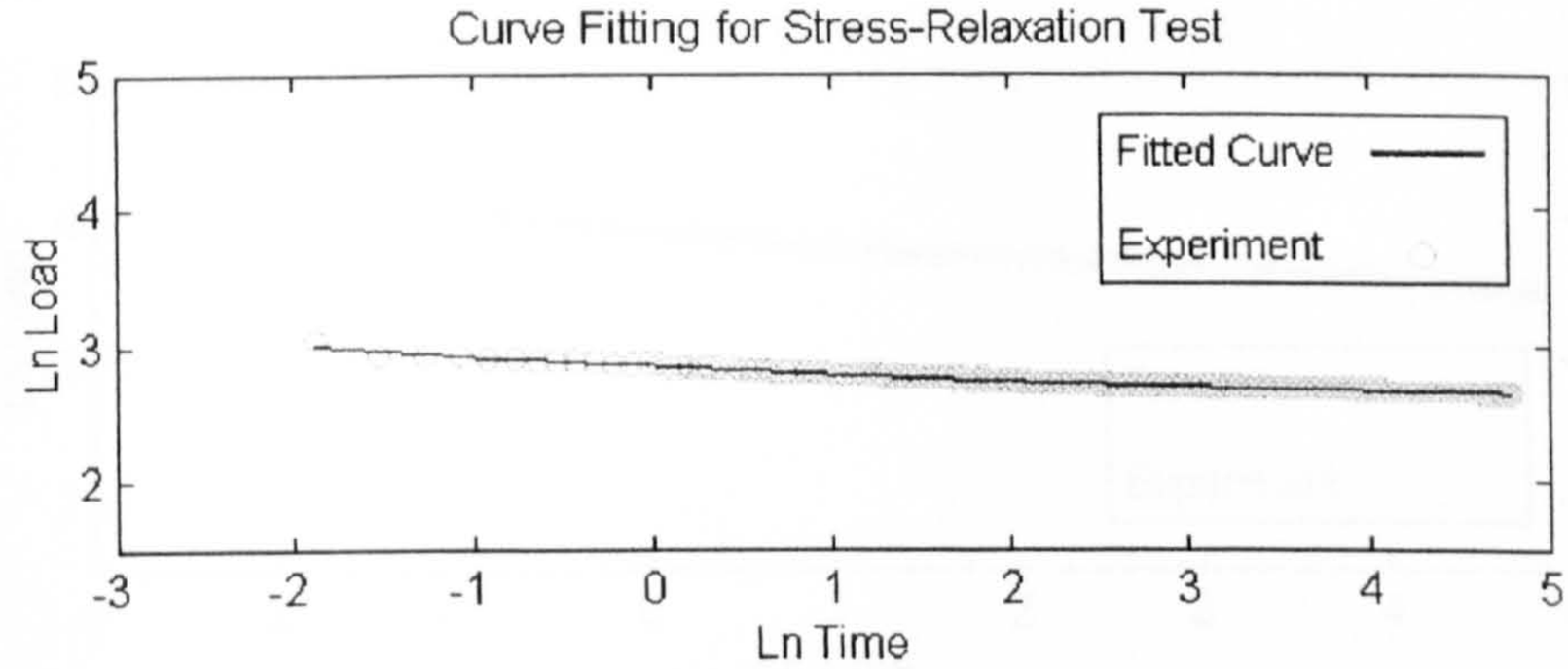

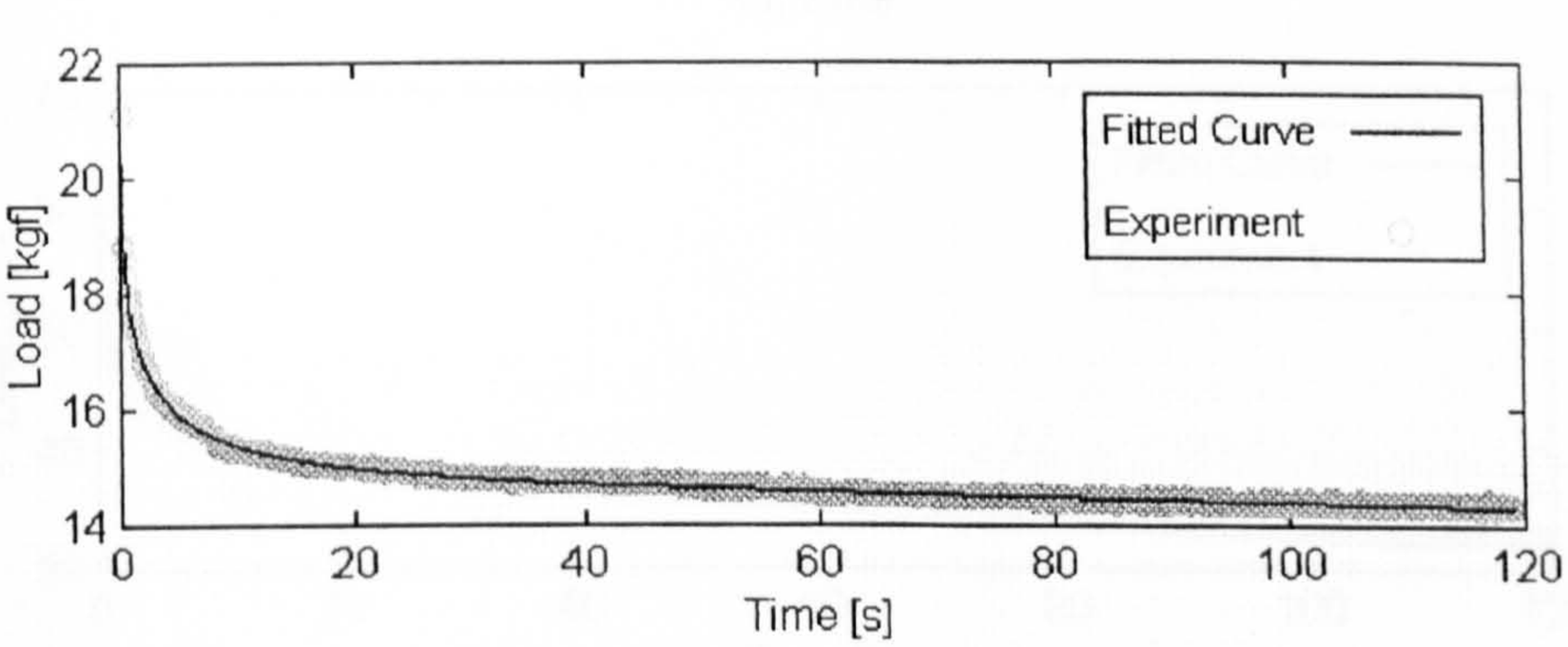

Figure C.3. Curve fitting of the stress-relaxation test data for 15 mm constant strain in the relaxed procedure.

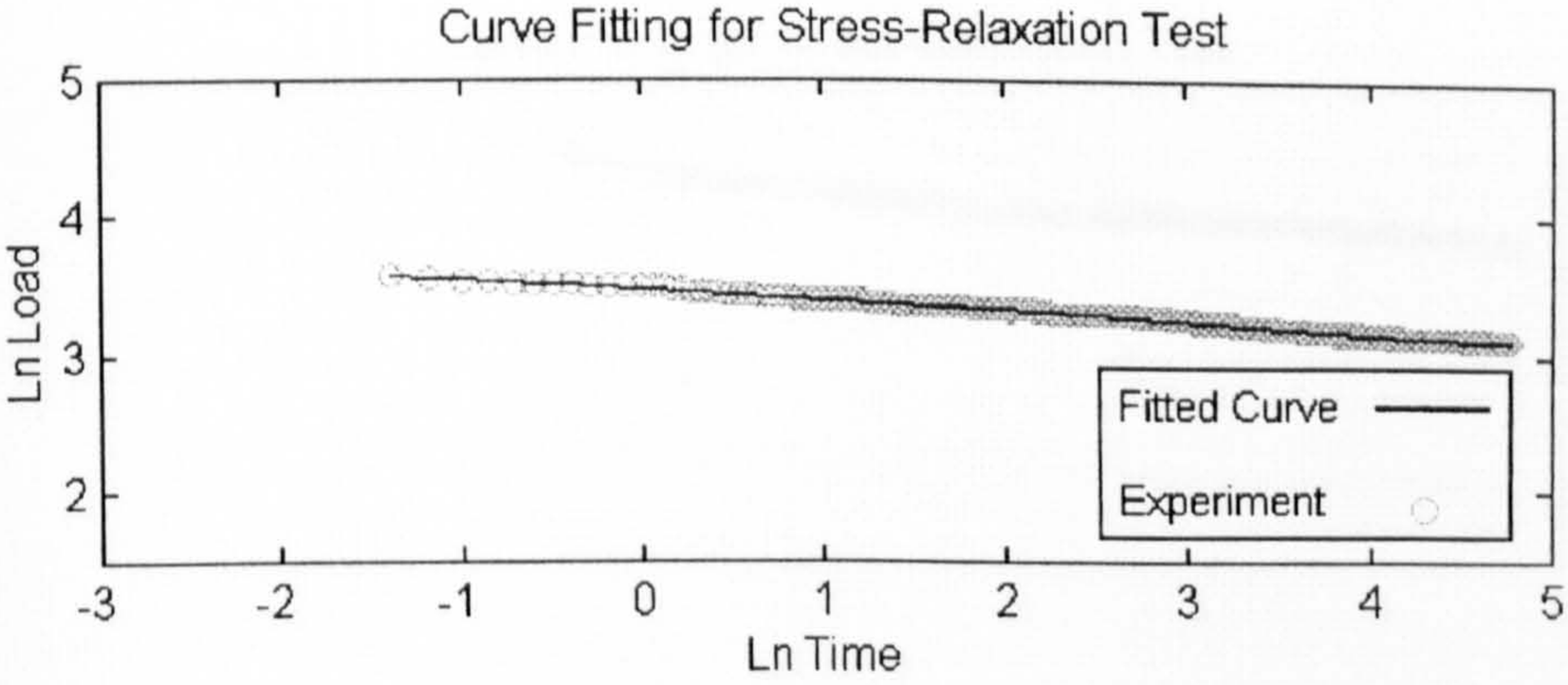

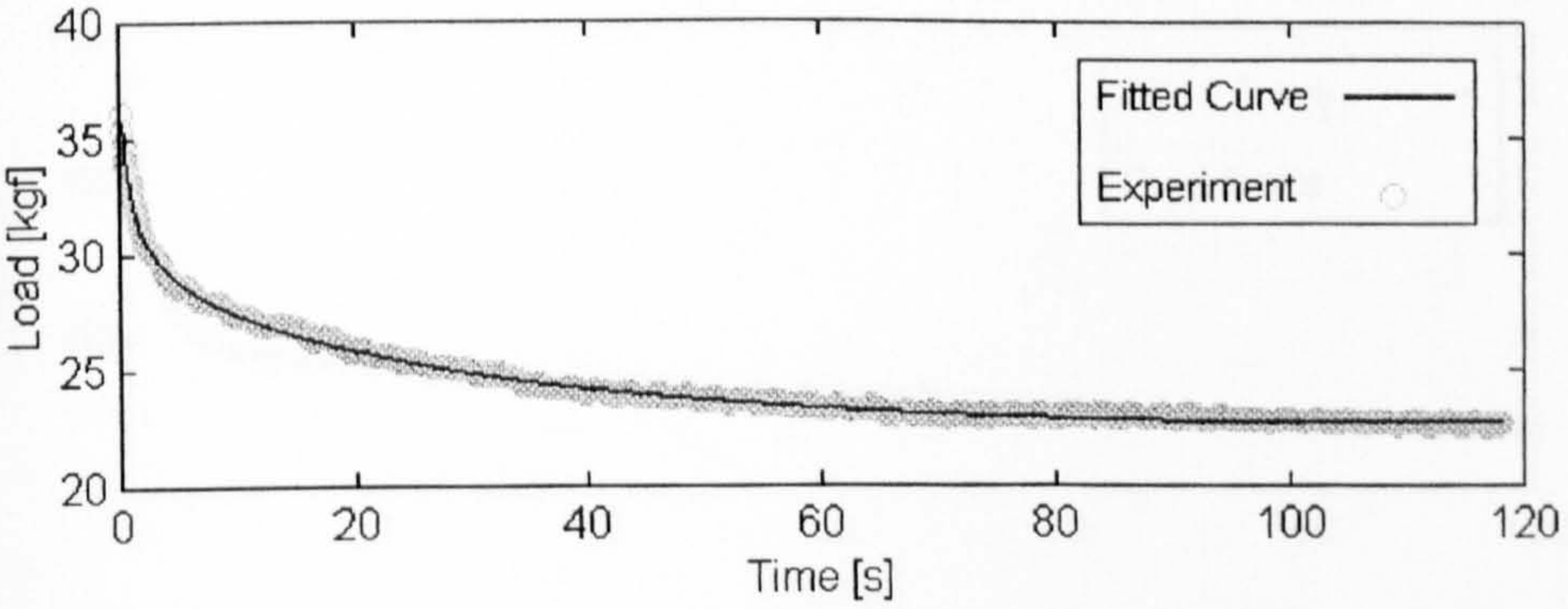

Figure C.4. Curve fitting of the stress-relaxation test data for 20 mm constant strain in the relaxed procedure.

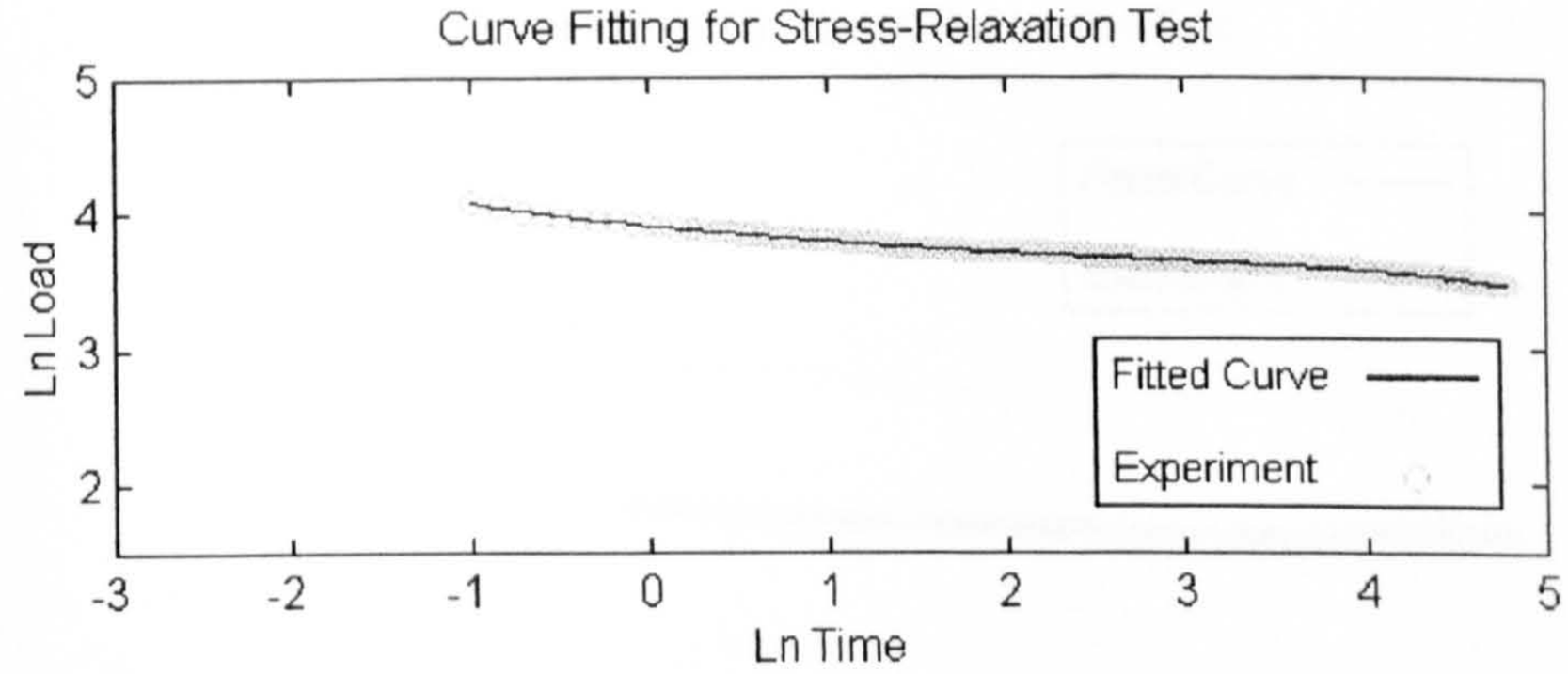

Figure C.5. Curve fitting of the stress-relaxation test data for 25 mm constant strain in the relaxed procedure.

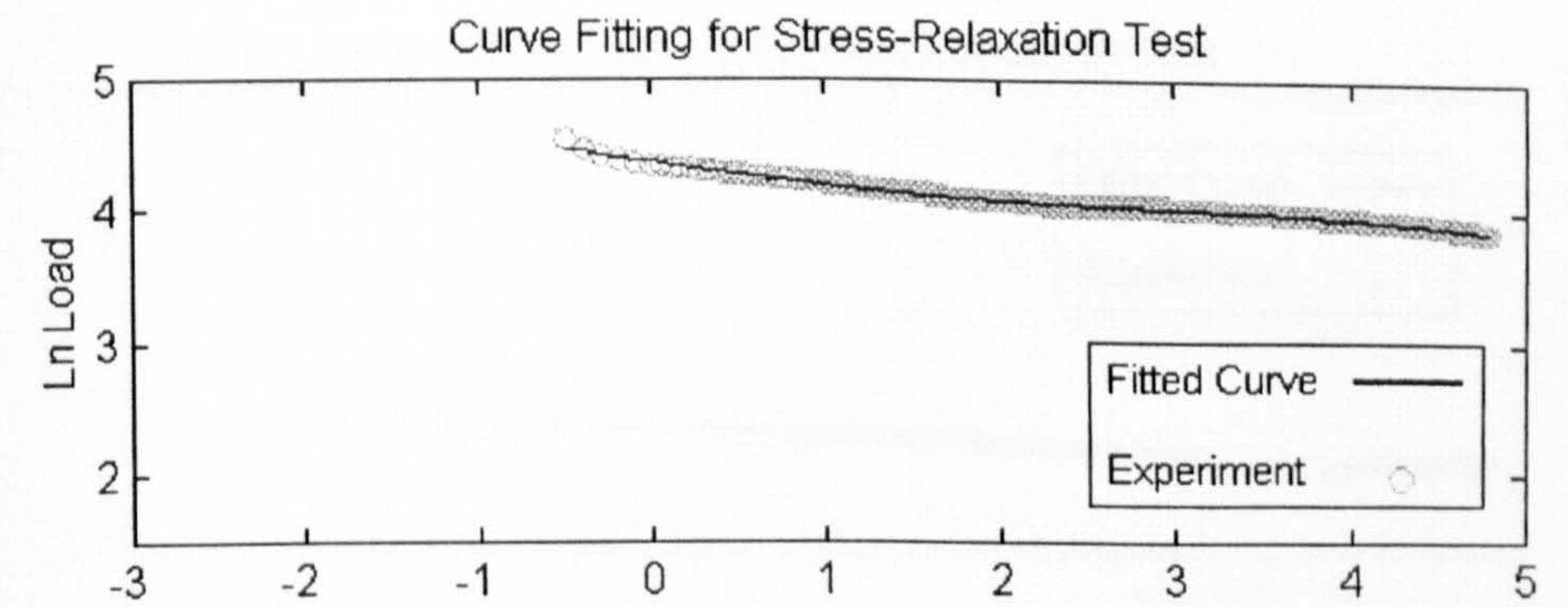

Figure C.6. Curve fitting of the stress-relaxation test data for 30 mm constant strain in the relaxed procedure.

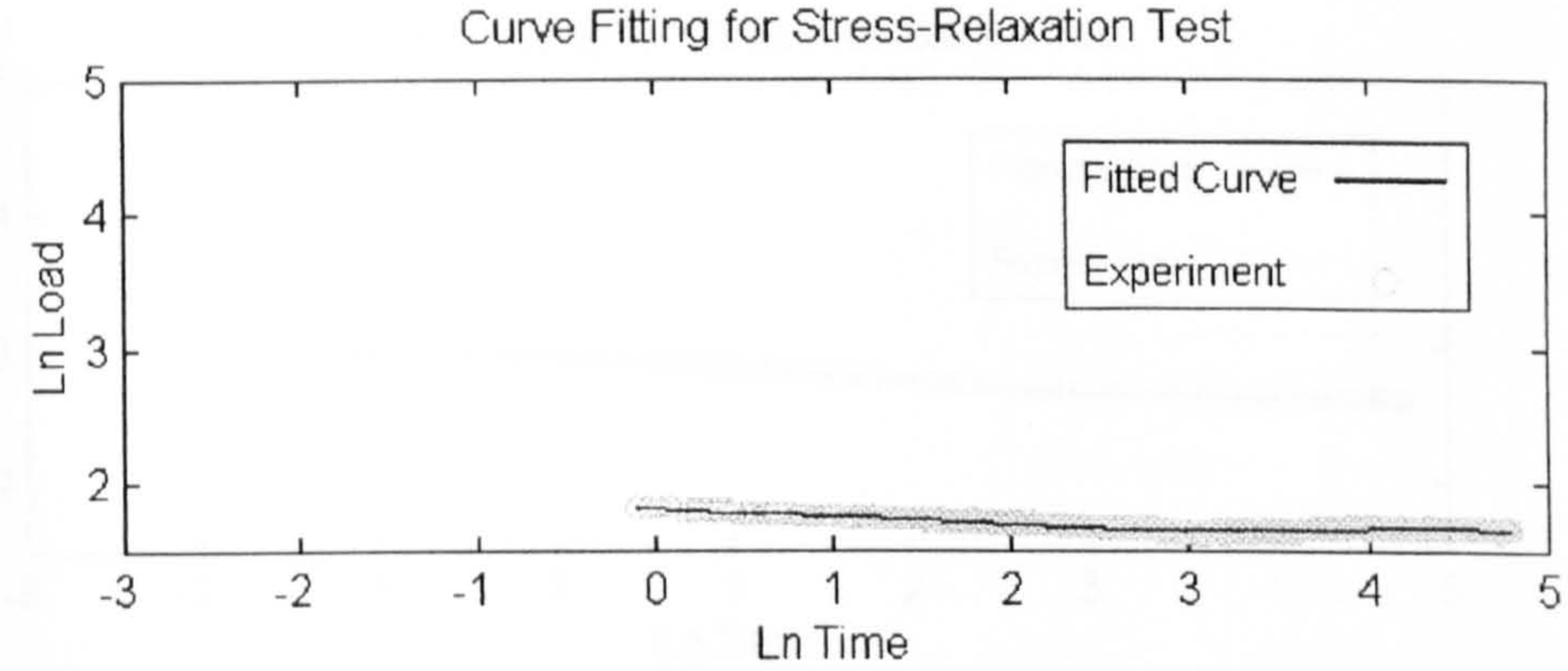

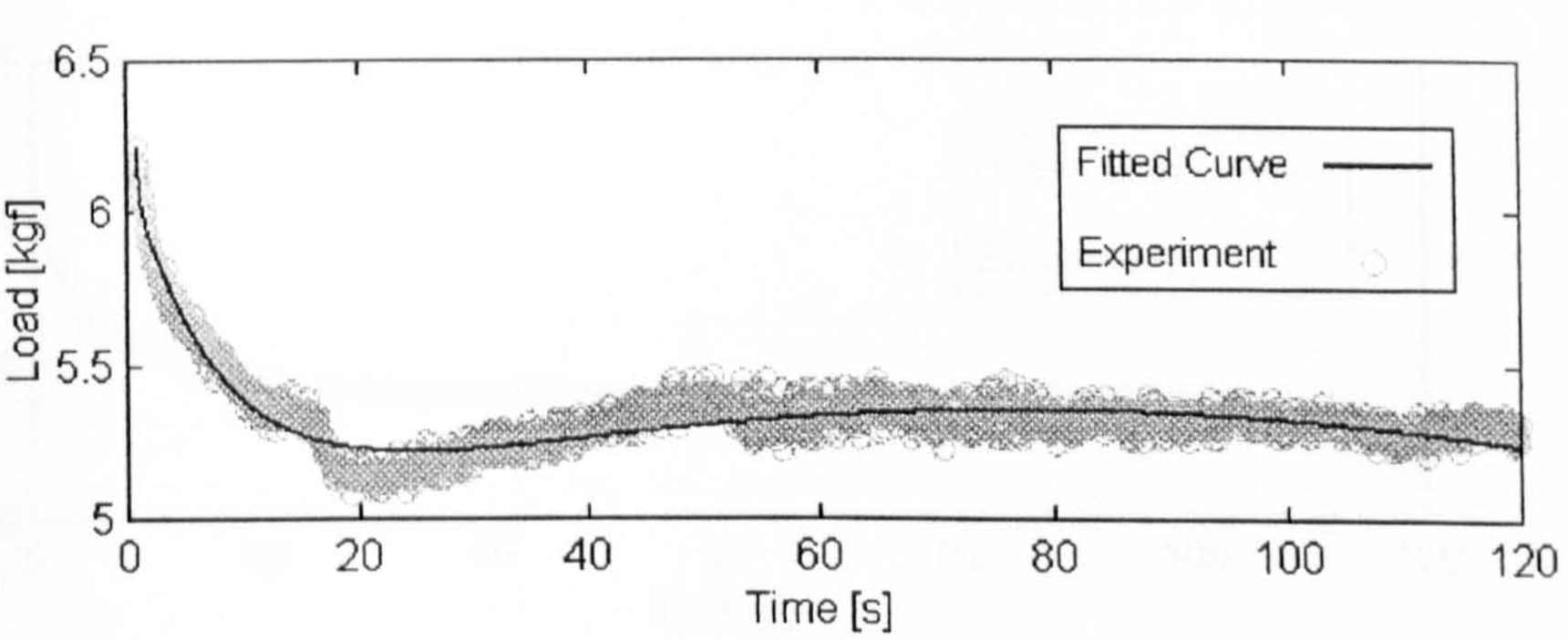

Figure C.7. Curve fitting of the stress-relaxation test data for 5 mm constant strain in the contracted procedure.

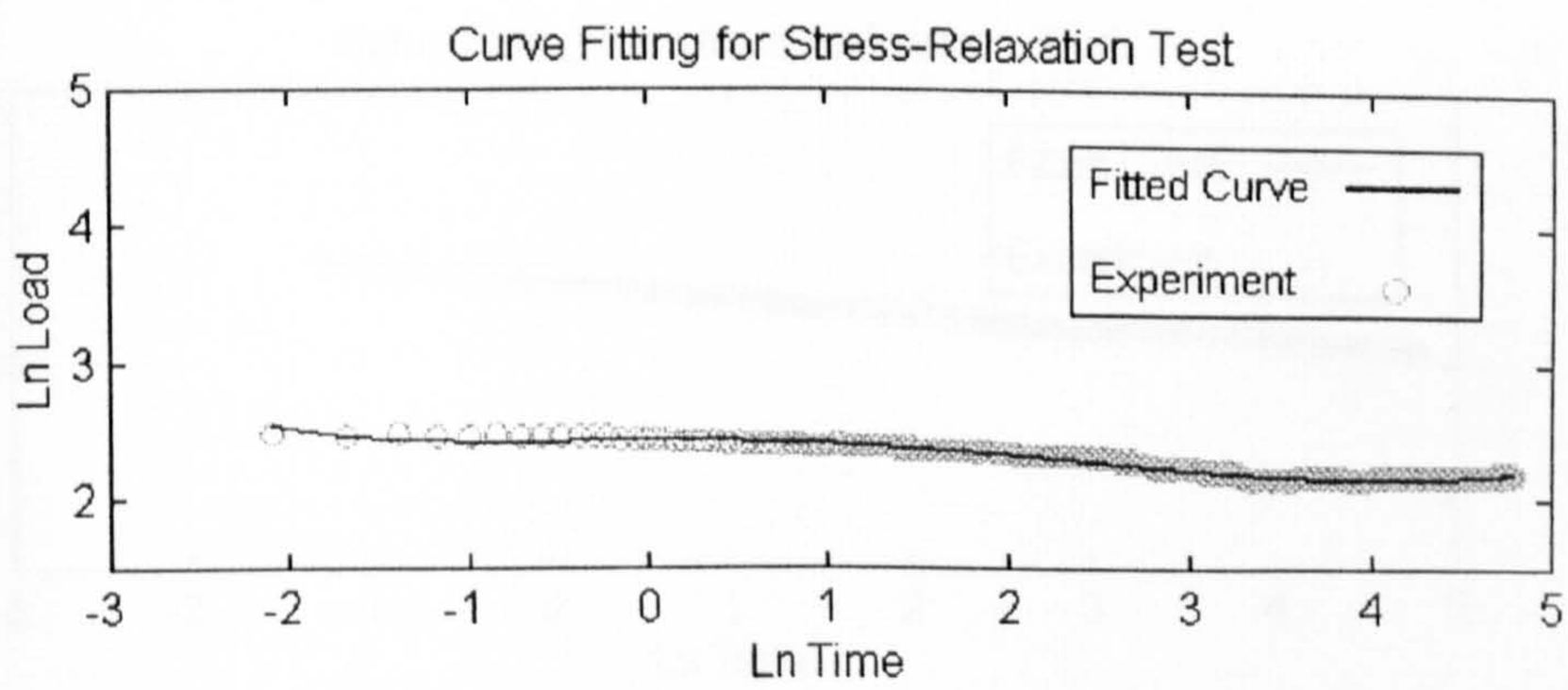

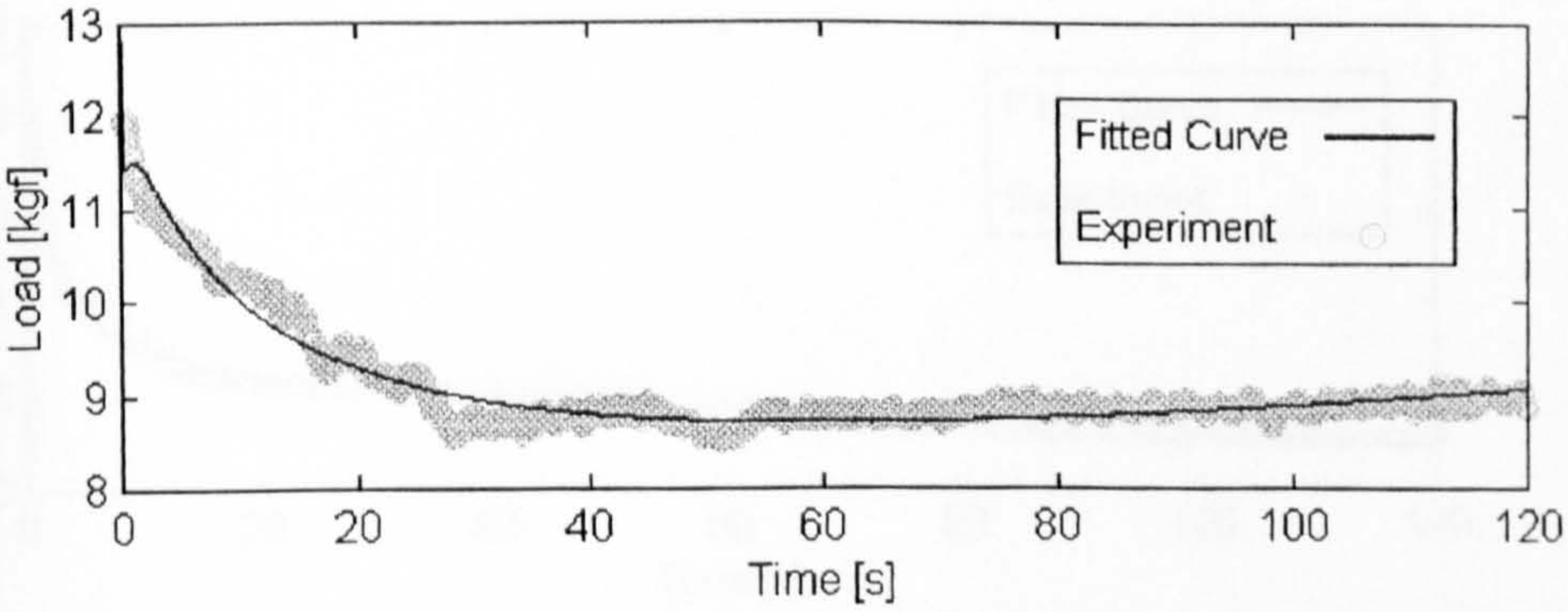

Figure C.8. Curve fitting of the stress-relaxation test data for 10 mm constant strain in the contracted procedure.

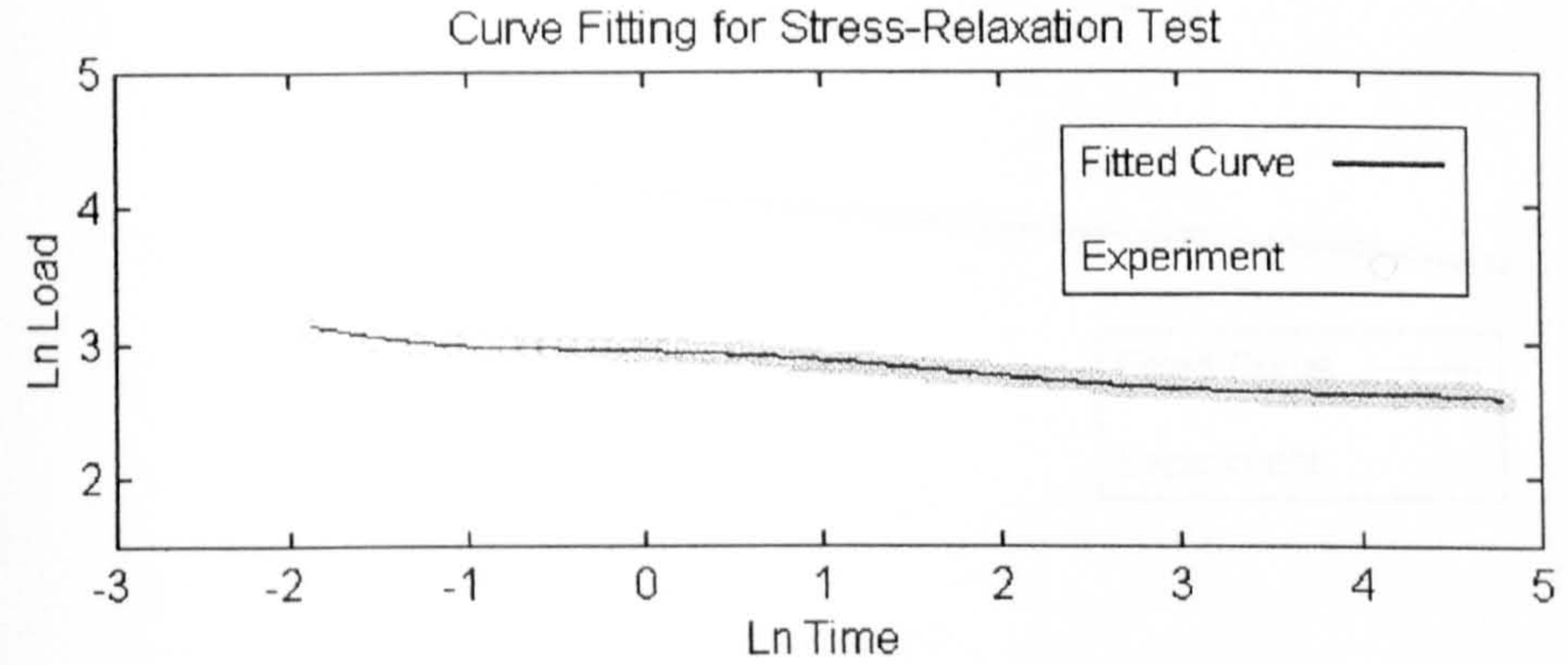

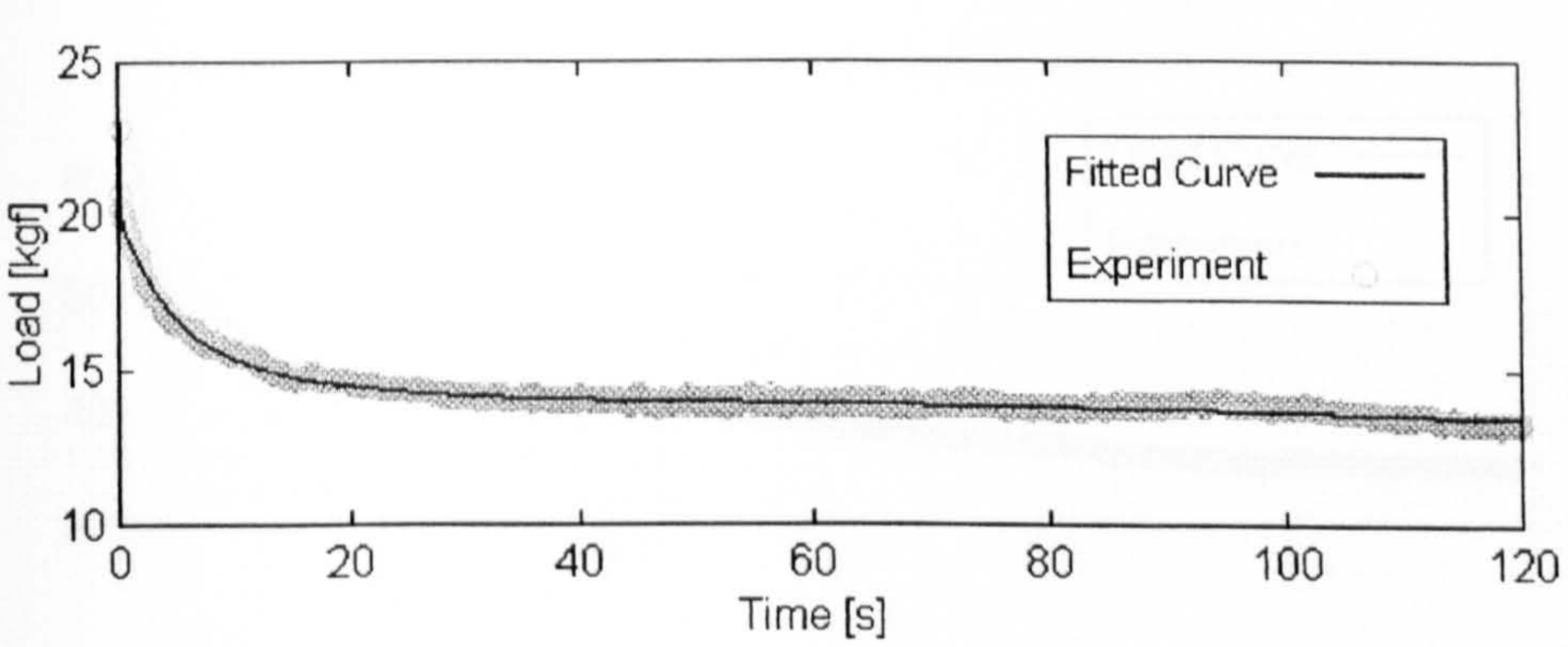

Figure C.9. Curve fitting of the stress-relaxation test data for 15 mm constant strain in the contracted procedure.

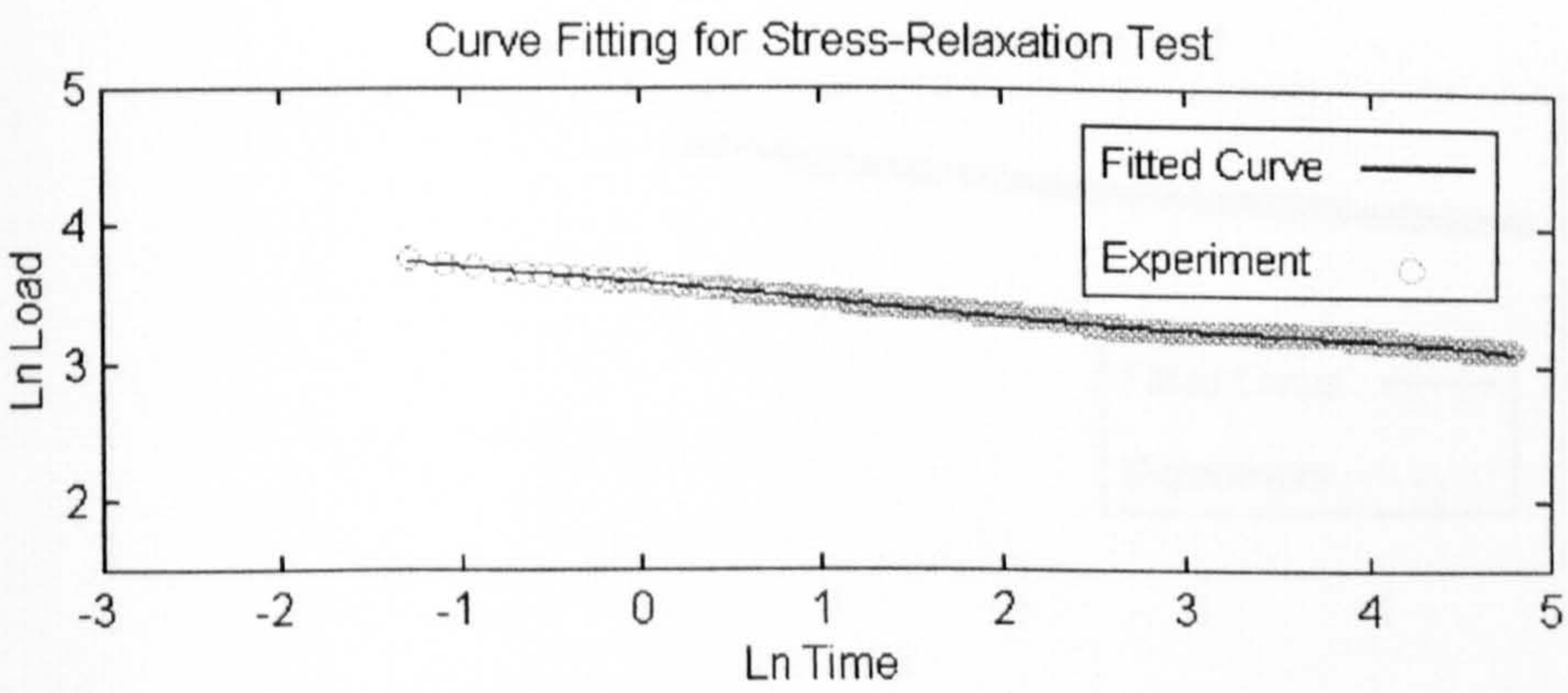

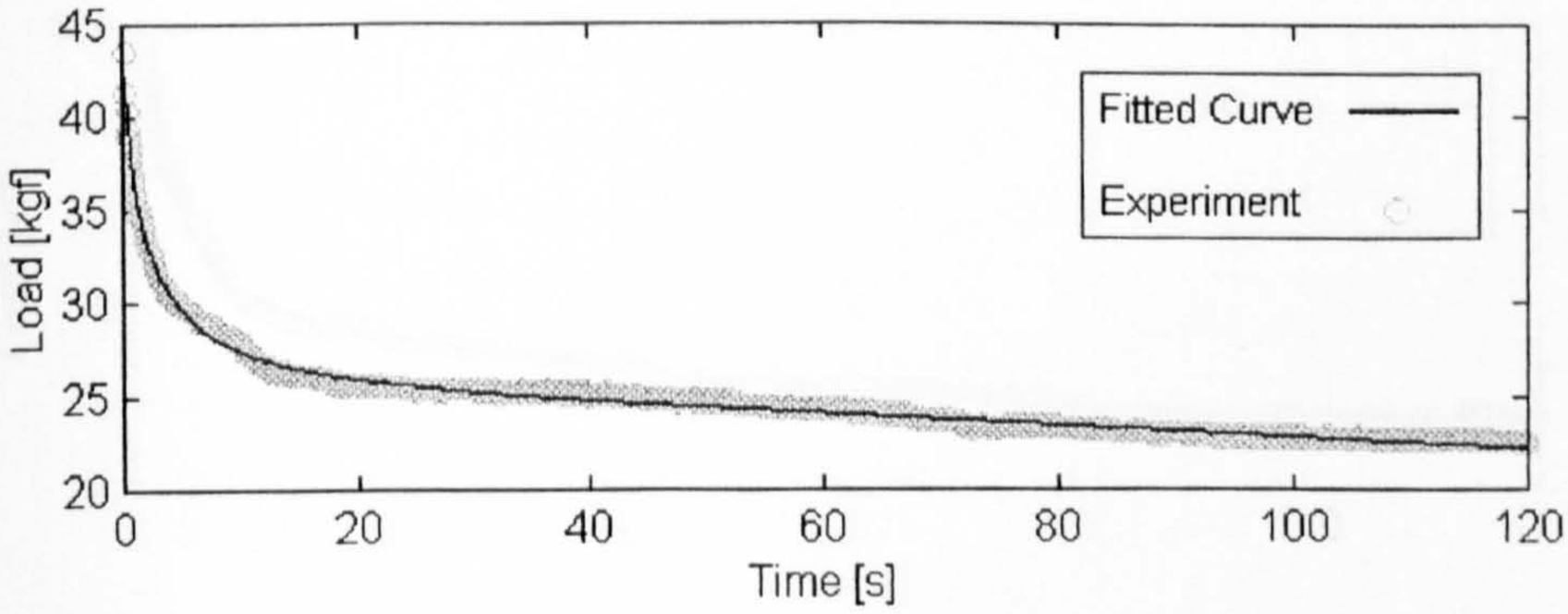

Figure C.10. Curve fitting of the stress-relaxation test data for 20 mm constant strain in the contracted procedure.

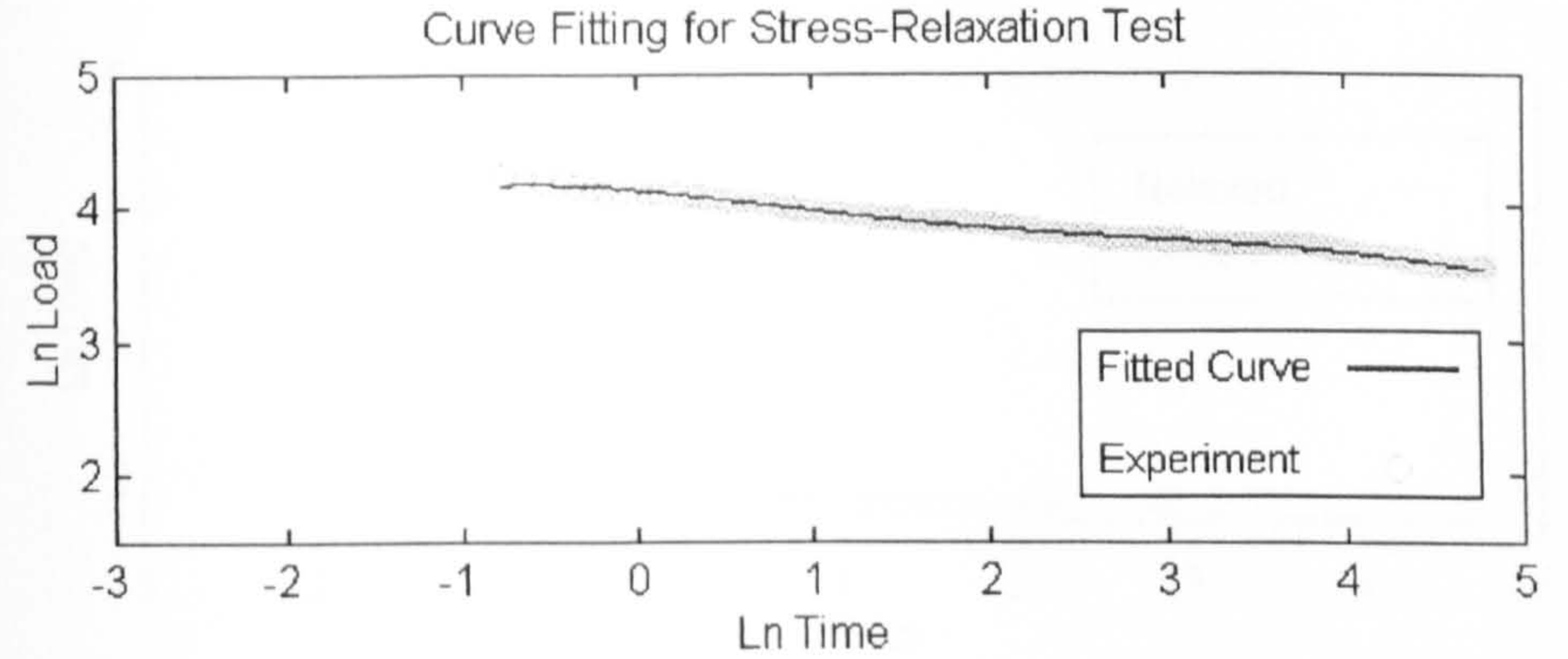

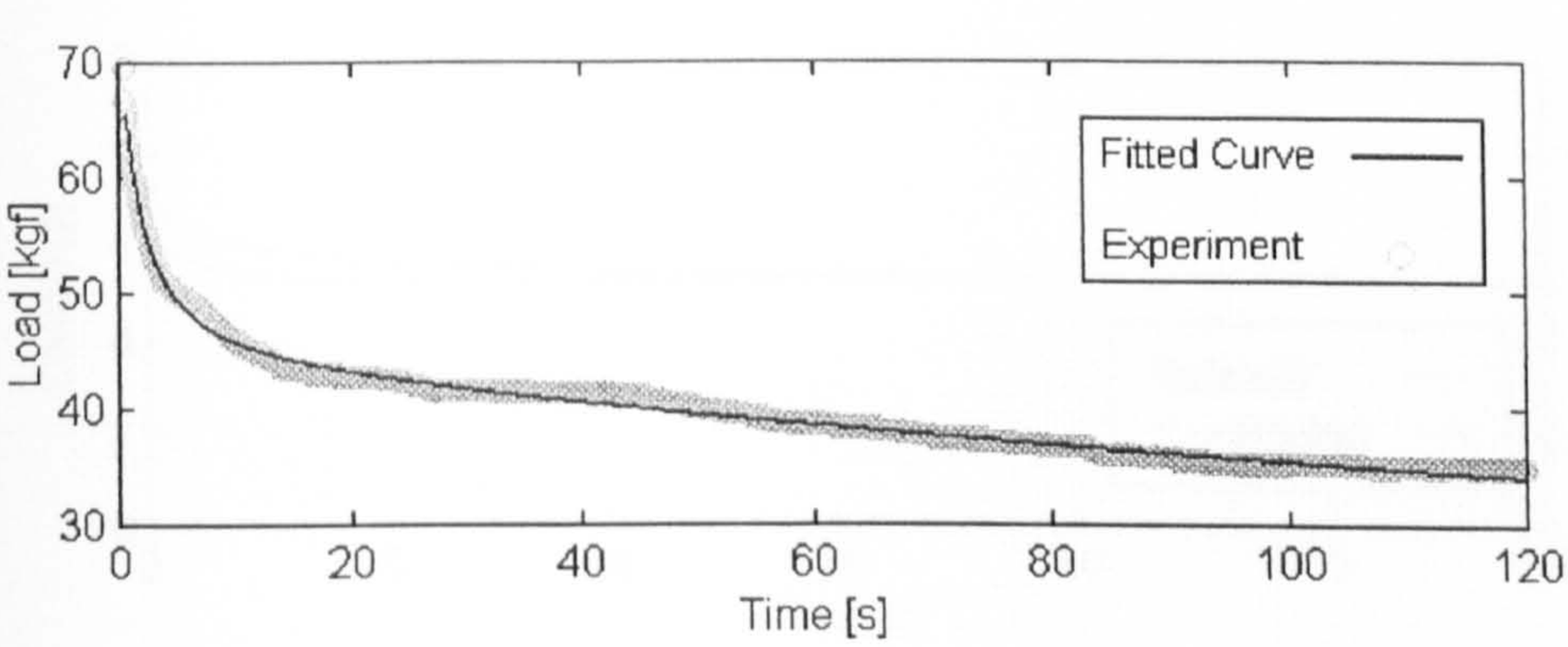

Figure C.11. Curve fitting of the stress-relaxation test data for 25 mm constant strain in the contracted procedure.

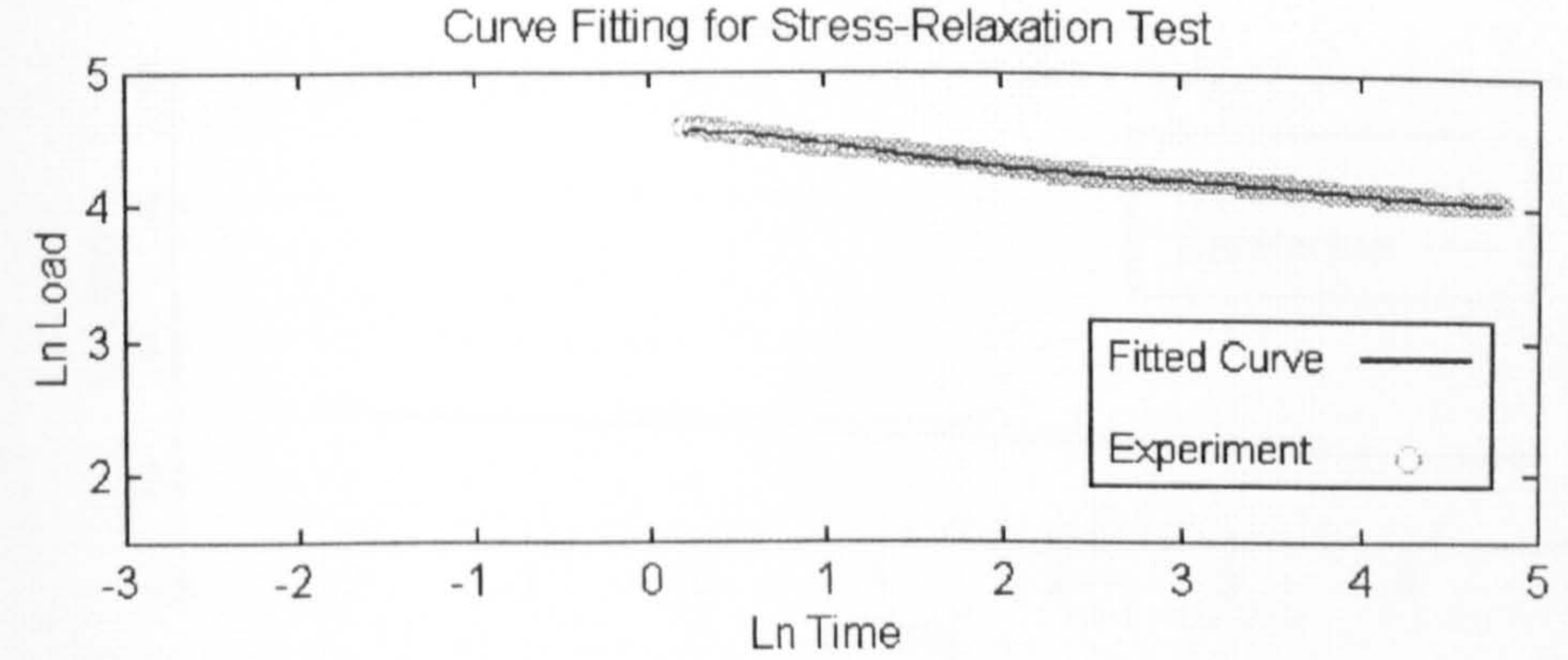

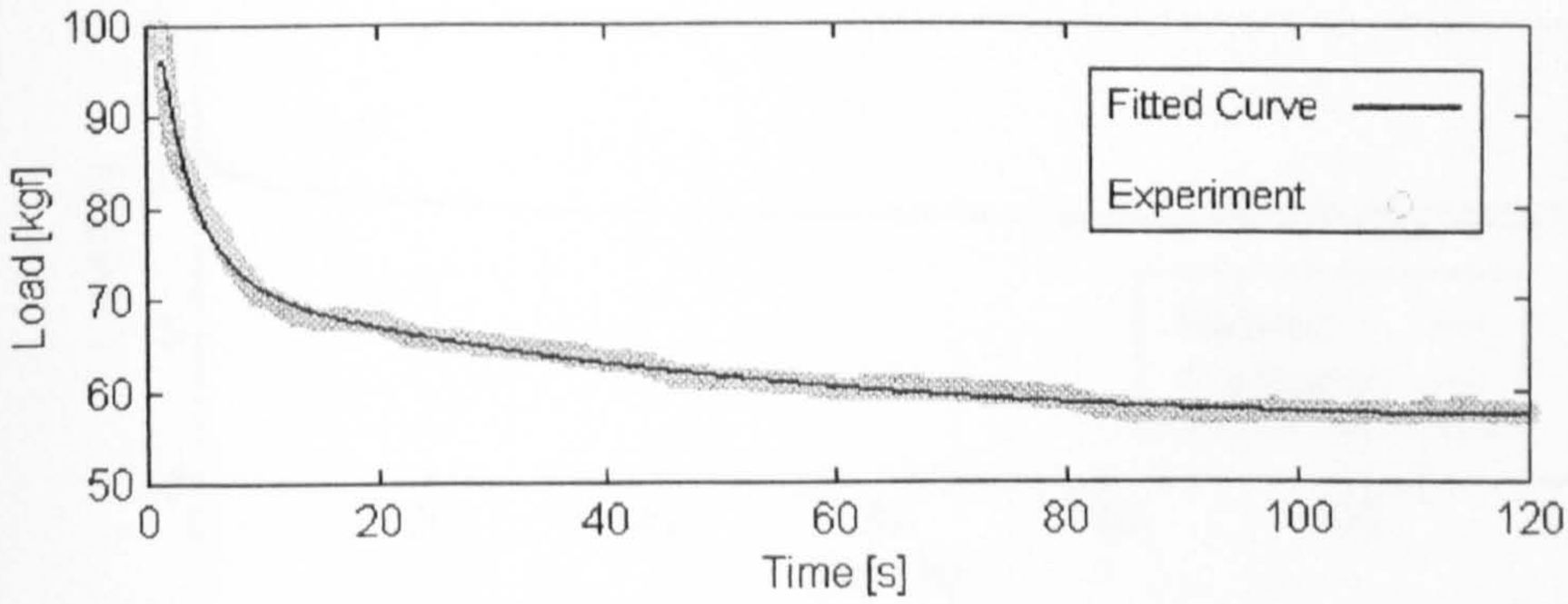

Figure C.12. Curve fitting of the stress-relaxation test data for 30 mm constant strain in the contracted procedure.

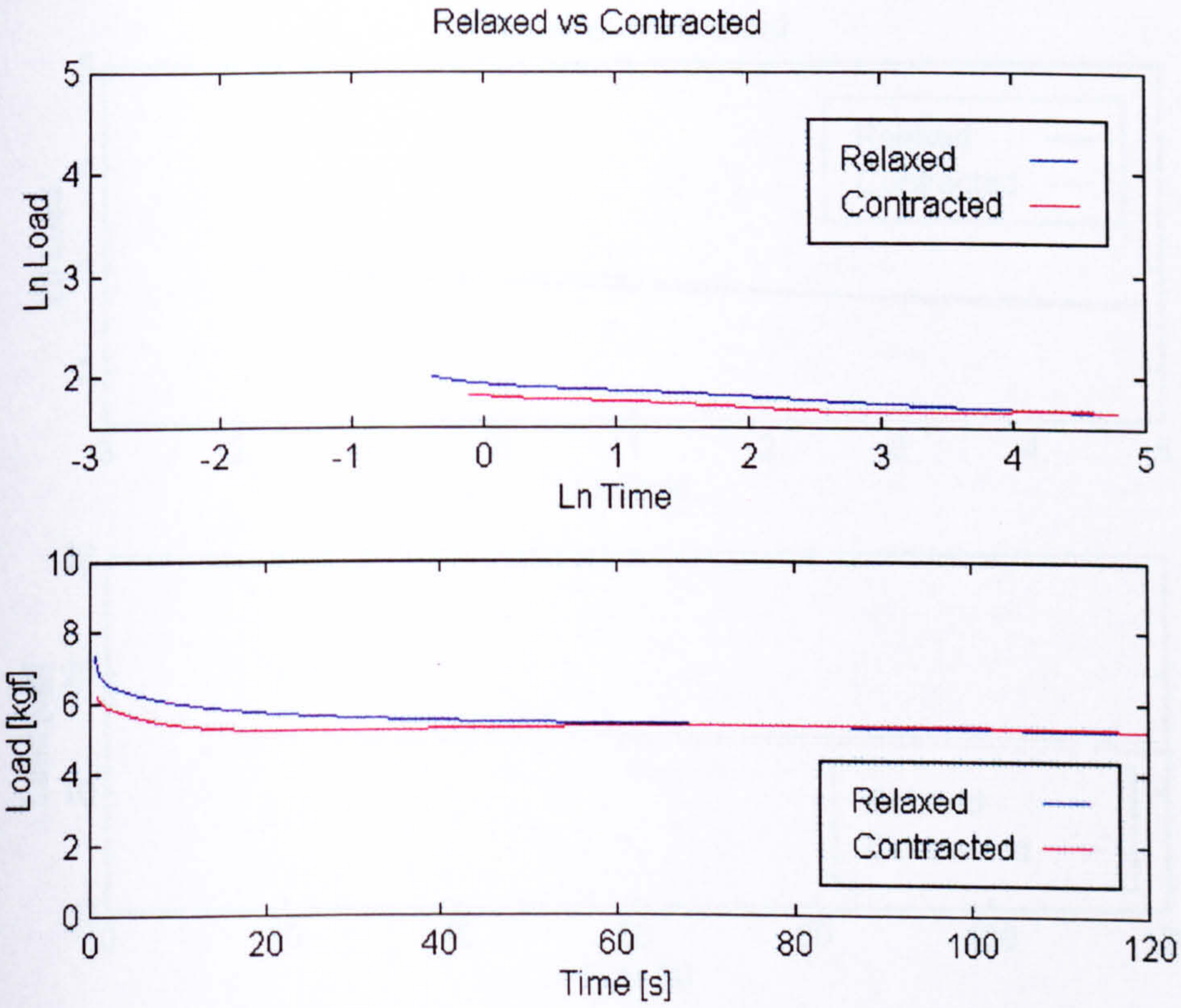

Figure C.13. Comparison of test protocols in the stress-relaxation test for 5 mm constant strain.

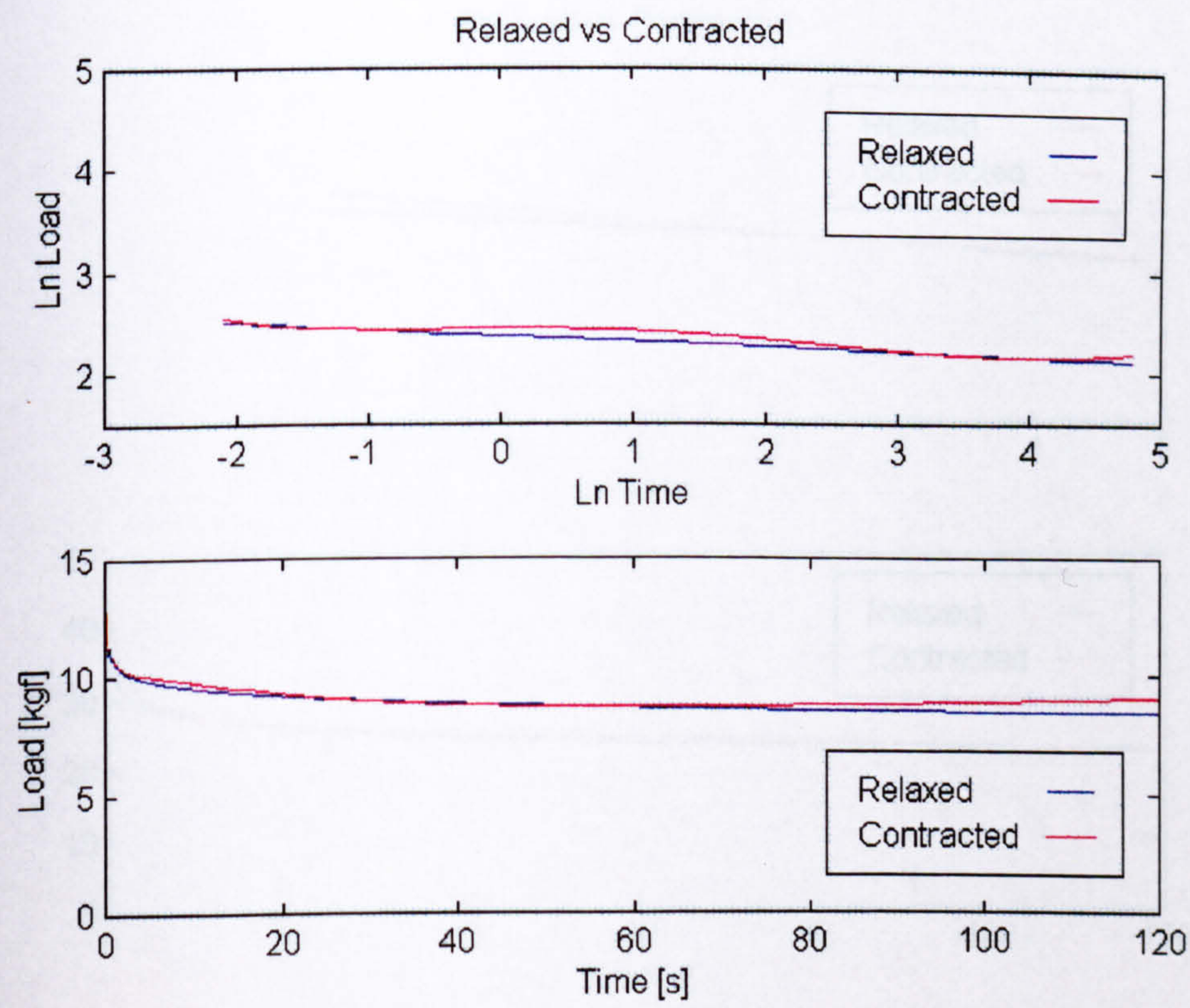

Figure C.14. Comparison of test protocols in the stress-relaxation test for 10 mm constant strain.

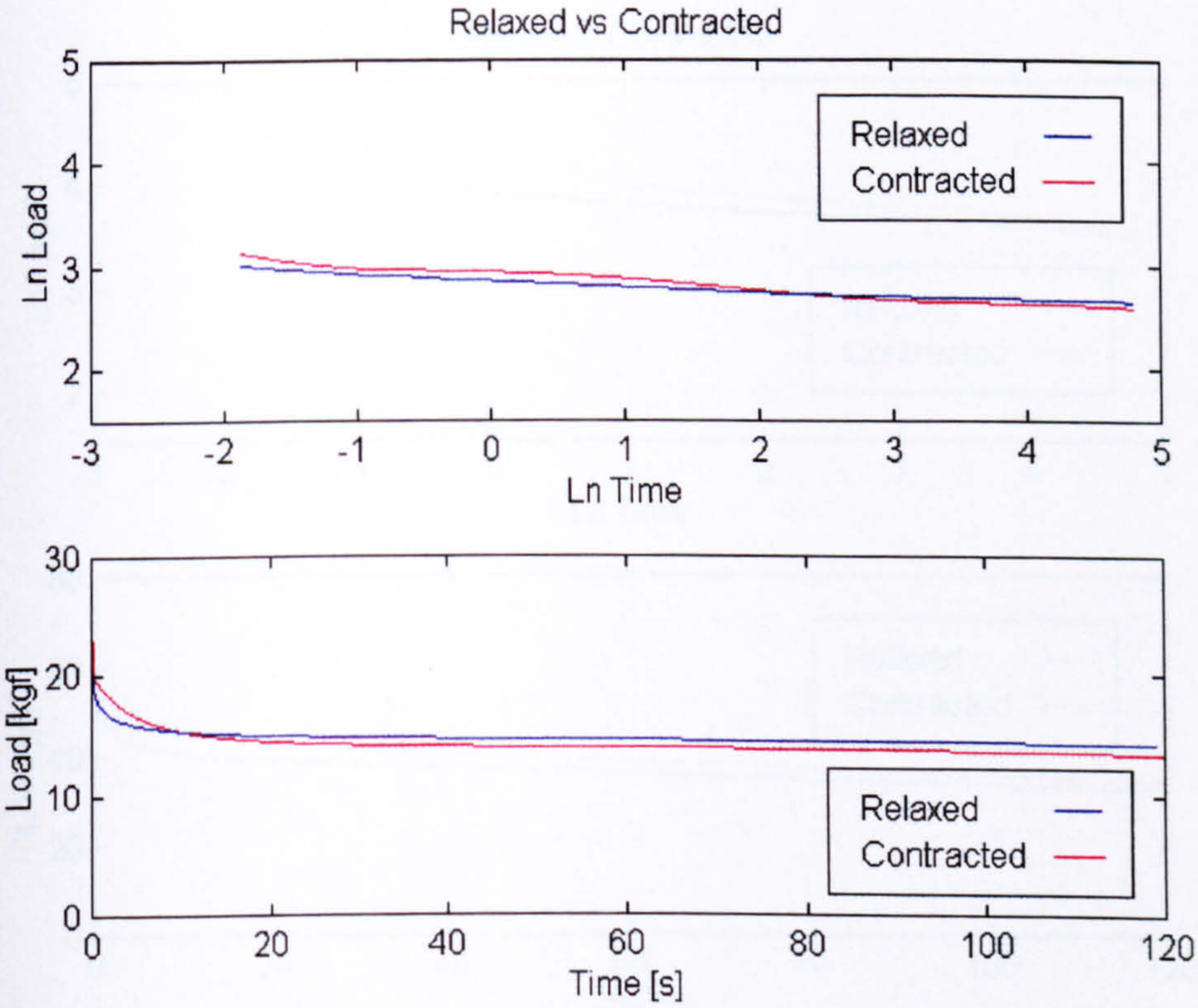

Figure C.15. Comparison of test protocols in the stress-relaxation test for 15 mm constant strain.

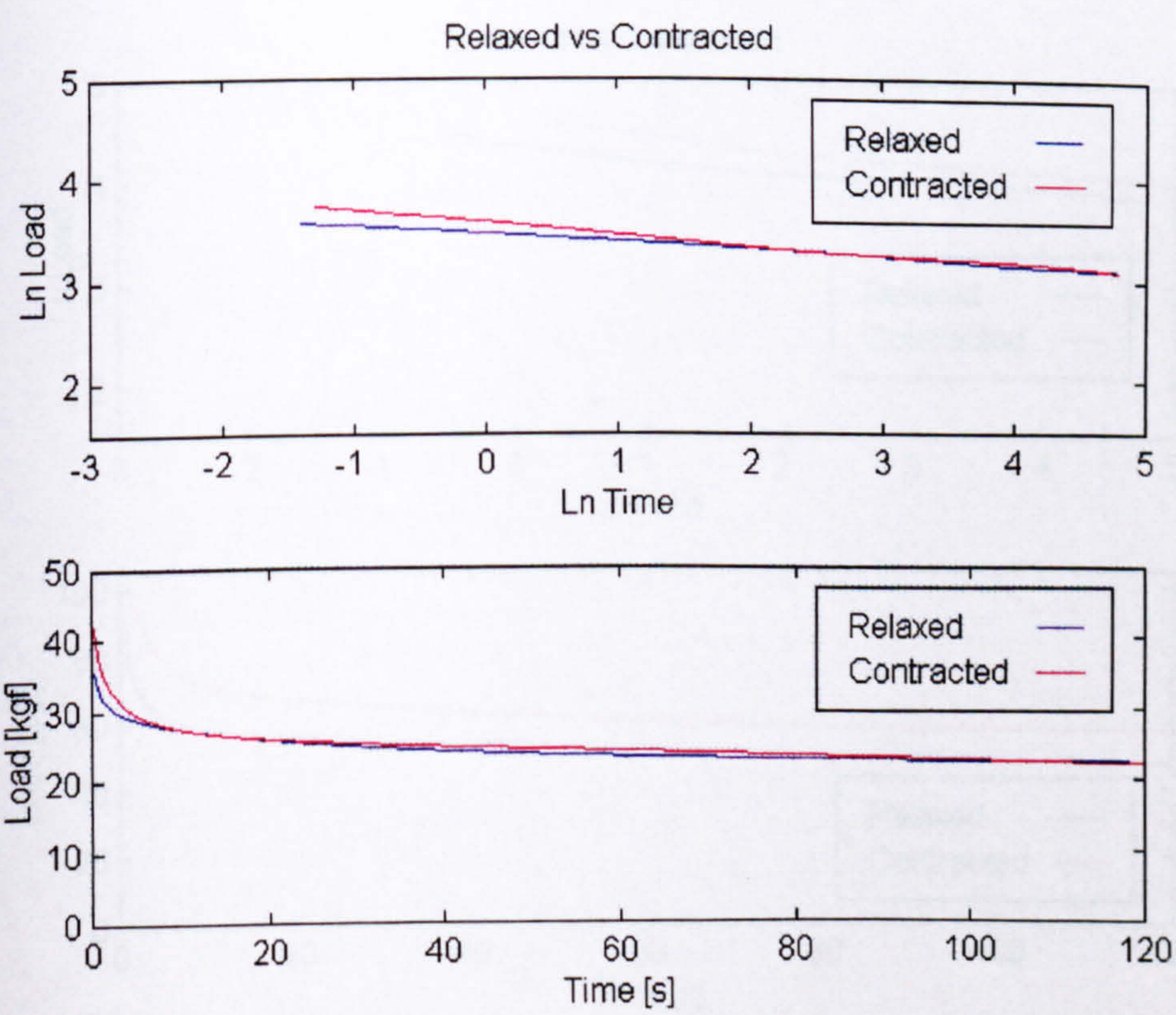

Figure C.16. Comparison of test protocols in the stress-relaxation test for 20 mm constant strain.

Appendix C

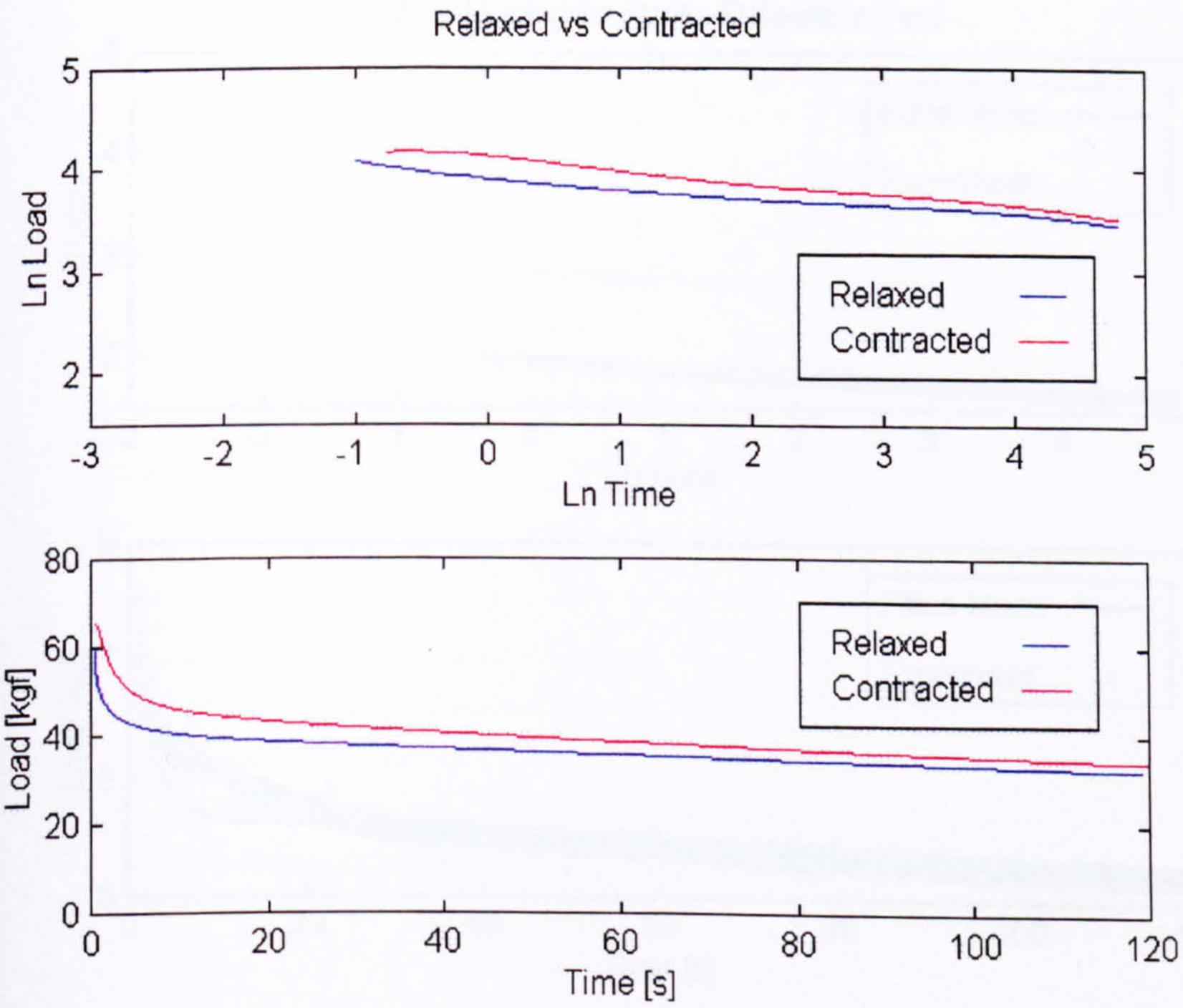

Figure C.17. Comparison of test protocols in the stress-relaxation test for 25 mm constant strain.

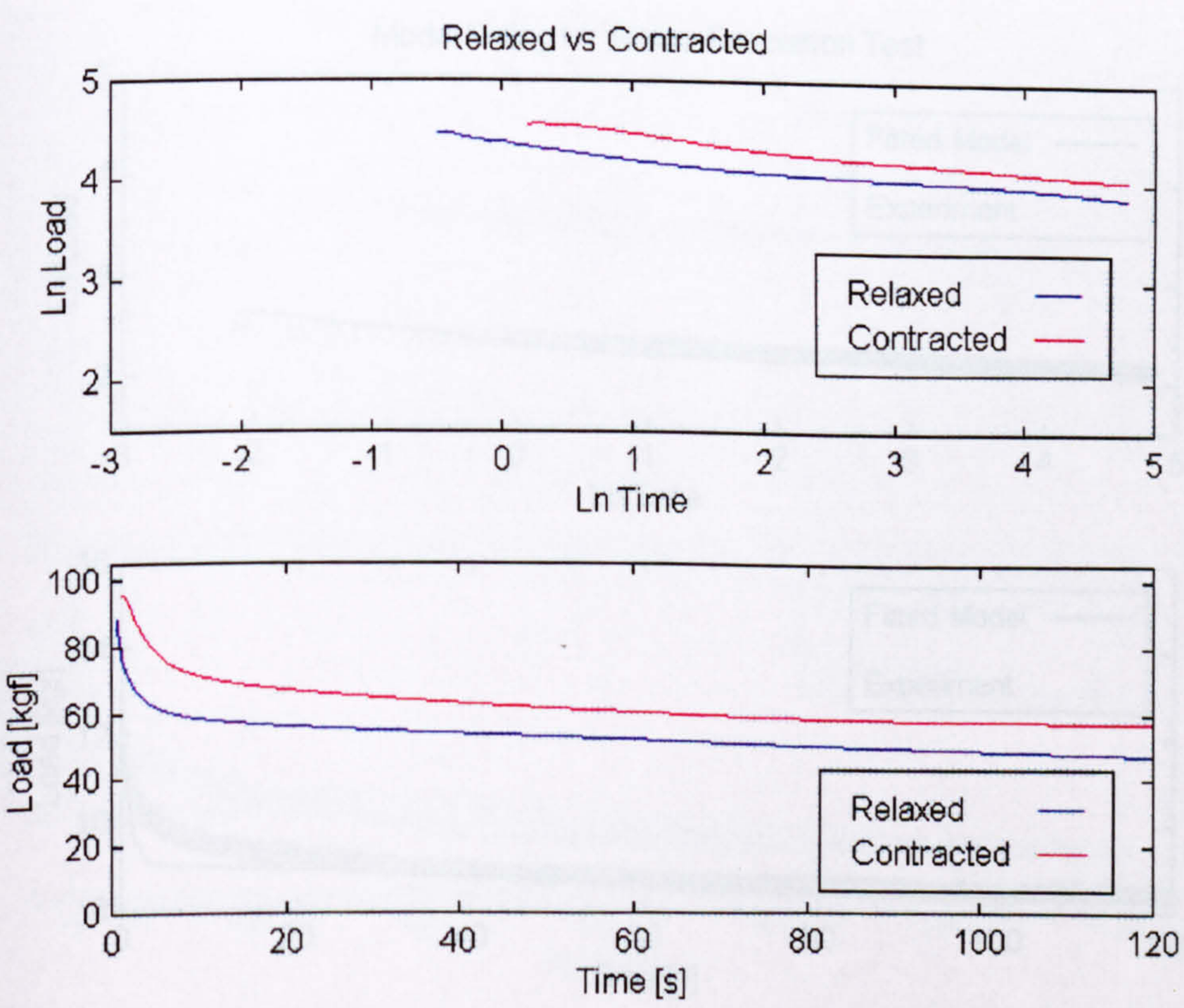

Figure C.18. Comparison of test protocols in the stress-relaxation test for 30 mm constant strain.

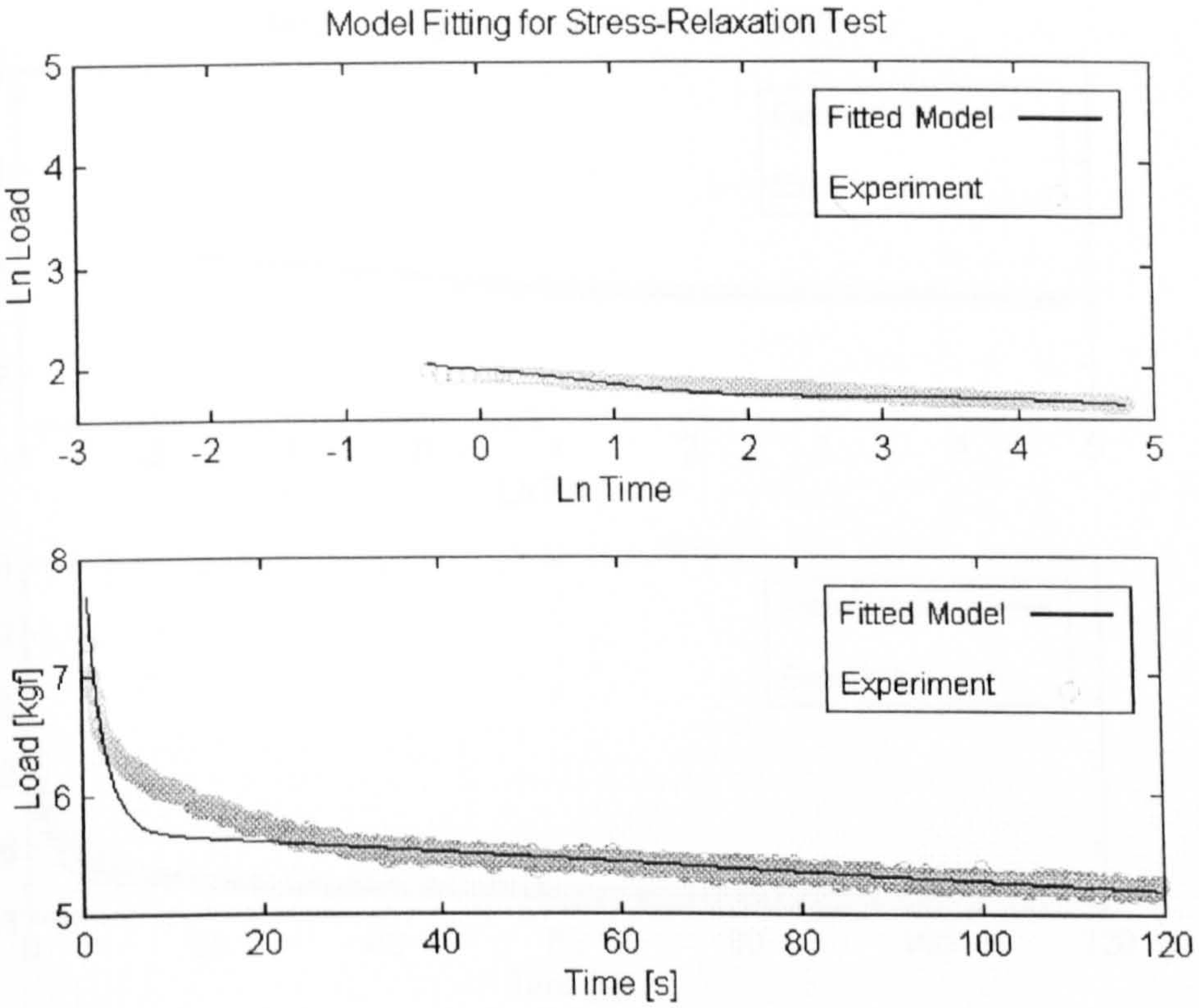

Figure C.19. Model fitting of the stress-relaxation test data for 5 mm constant strain in the relaxed procedure.

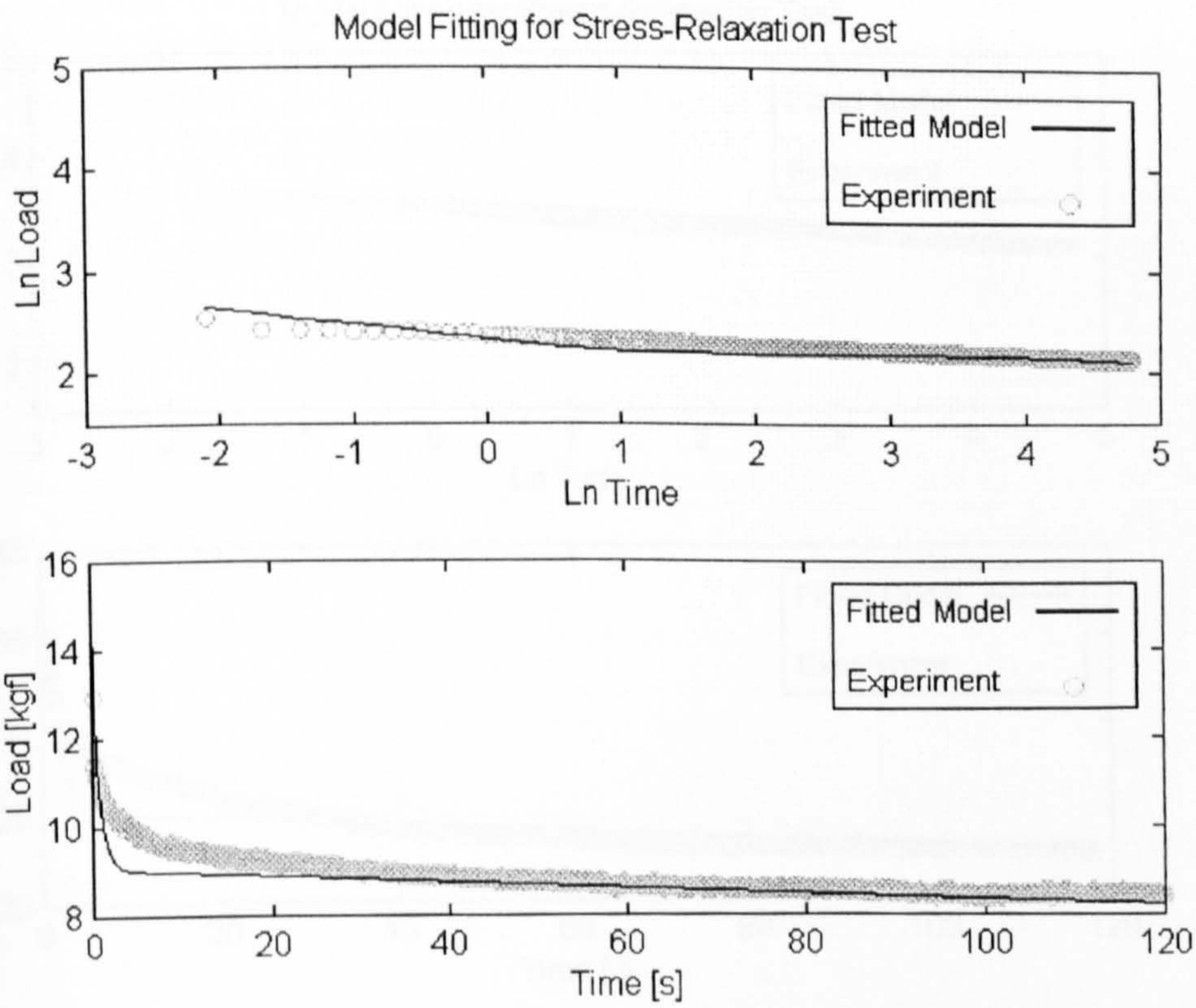

Figure C.20. Model fitting of the stress-relaxation test data for 10 mm constant strain in the relaxed procedure.

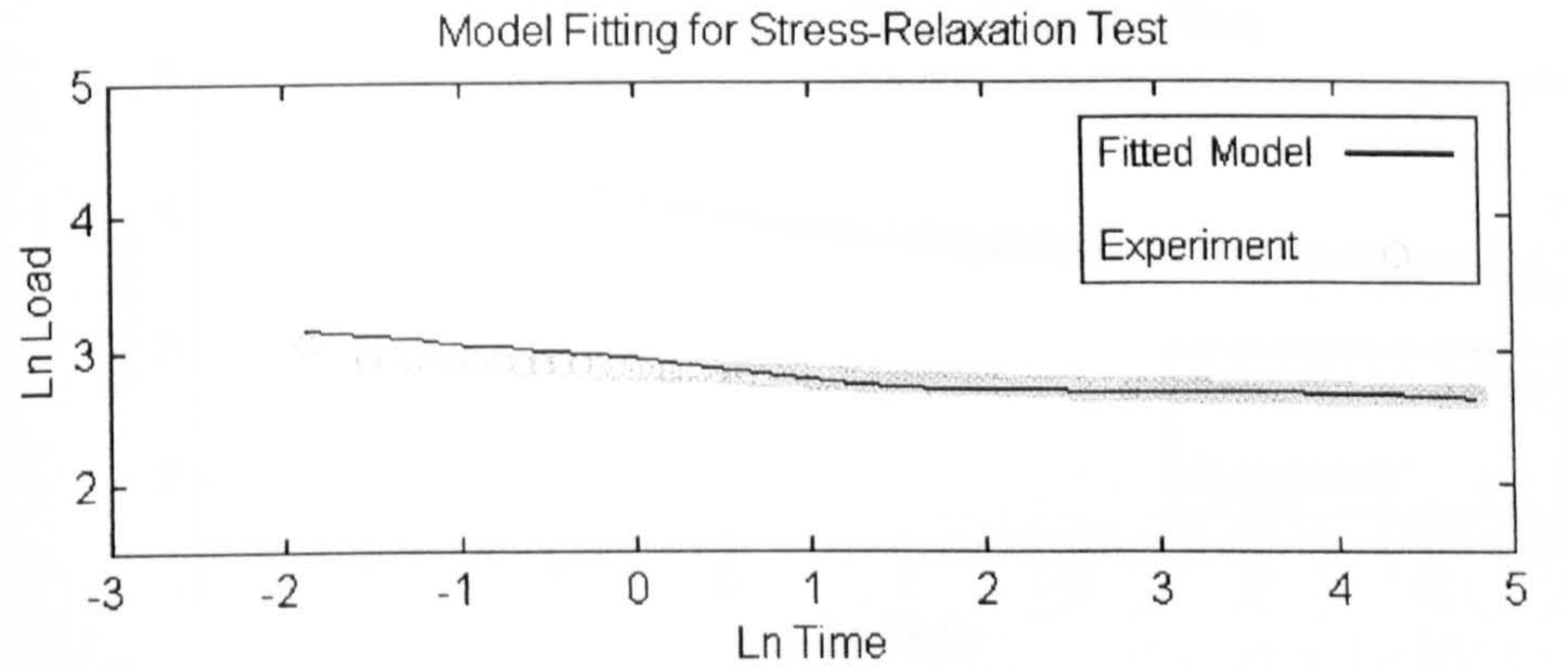

Figure C.21. Model fitting of the stress-relaxation test data for 15 mm constant strain in the relaxed procedure.

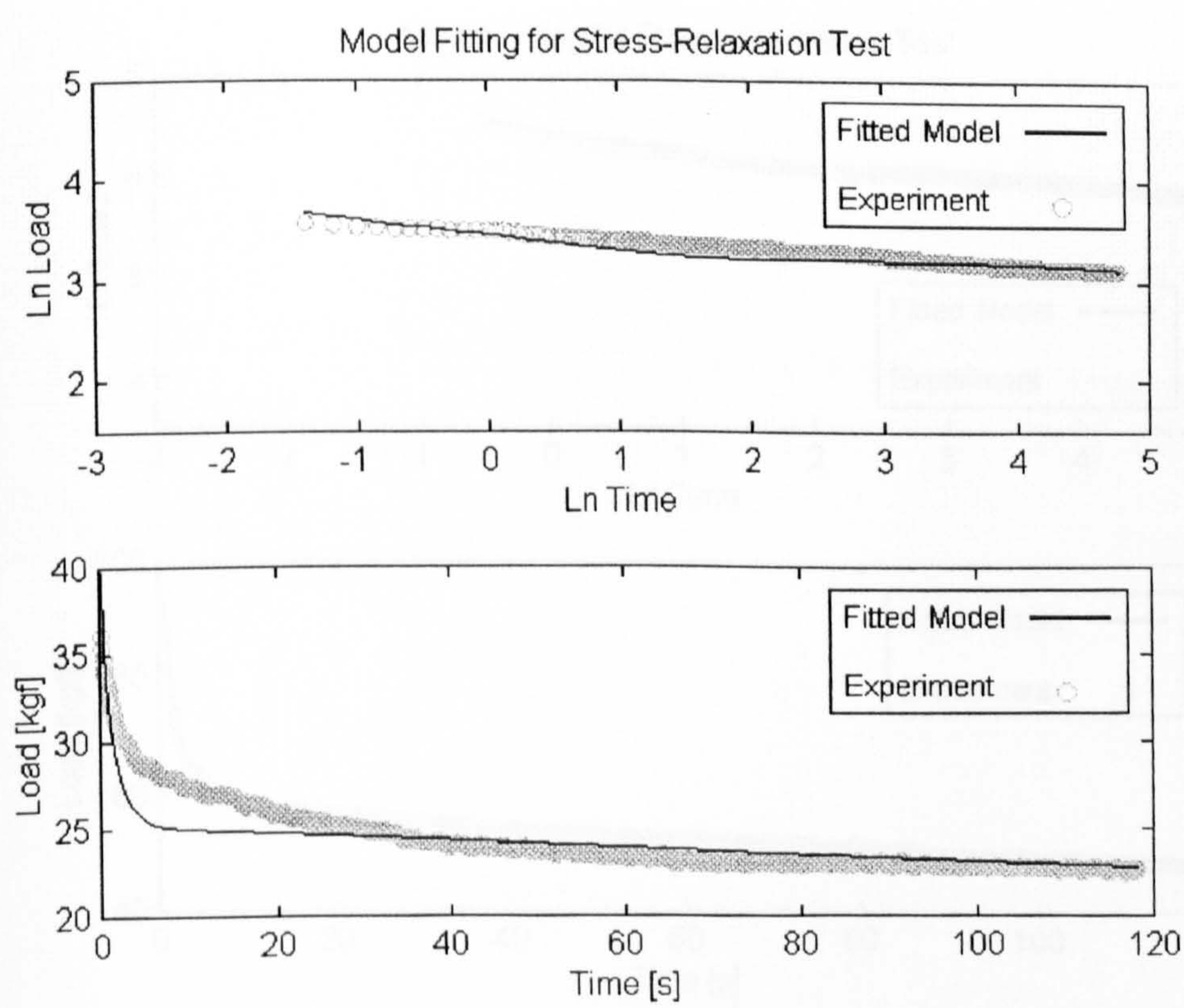

Figure C.22. Model fitting of the stress-relaxation test data for 20 mm constant strain in the relaxed procedure.

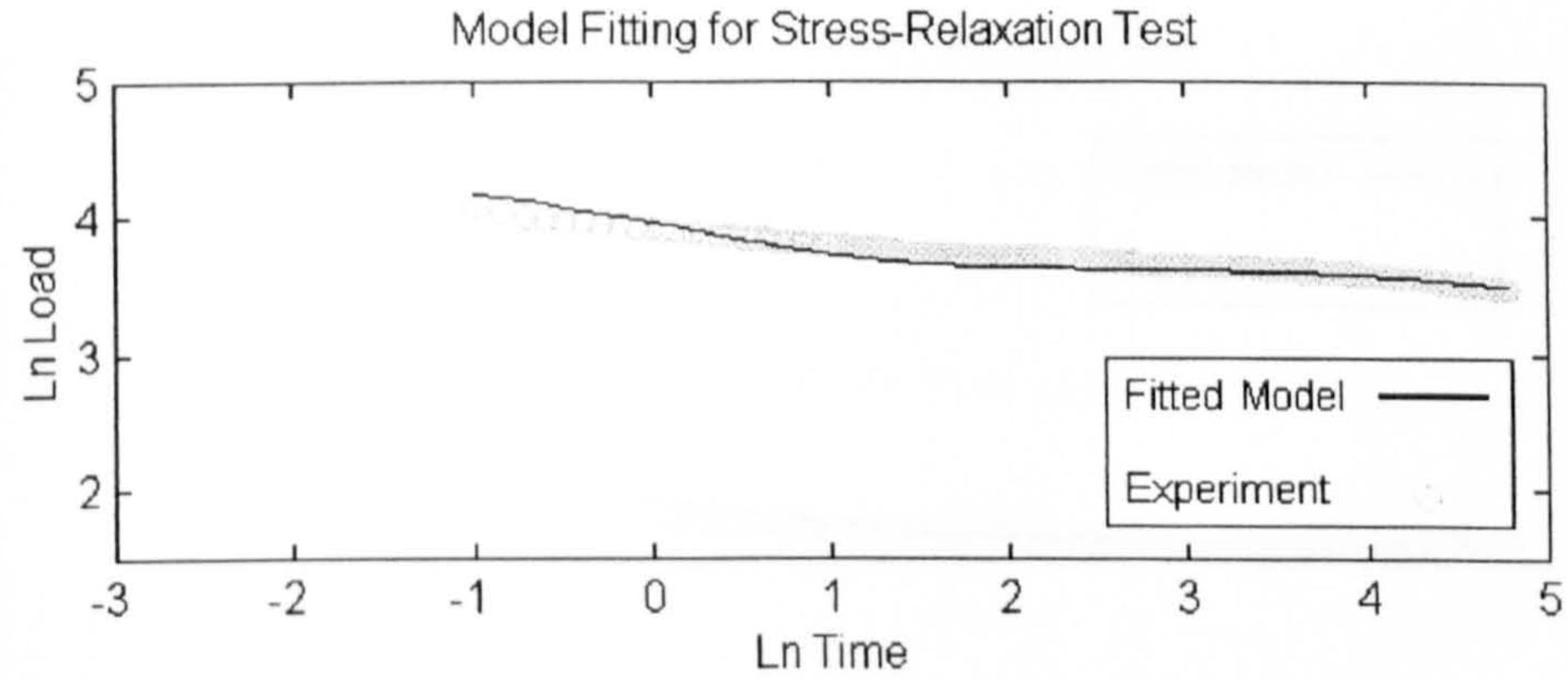

Figure C.23. Model fitting of the stress-relaxation test data for 25 mm constant strain in the relaxed procedure.

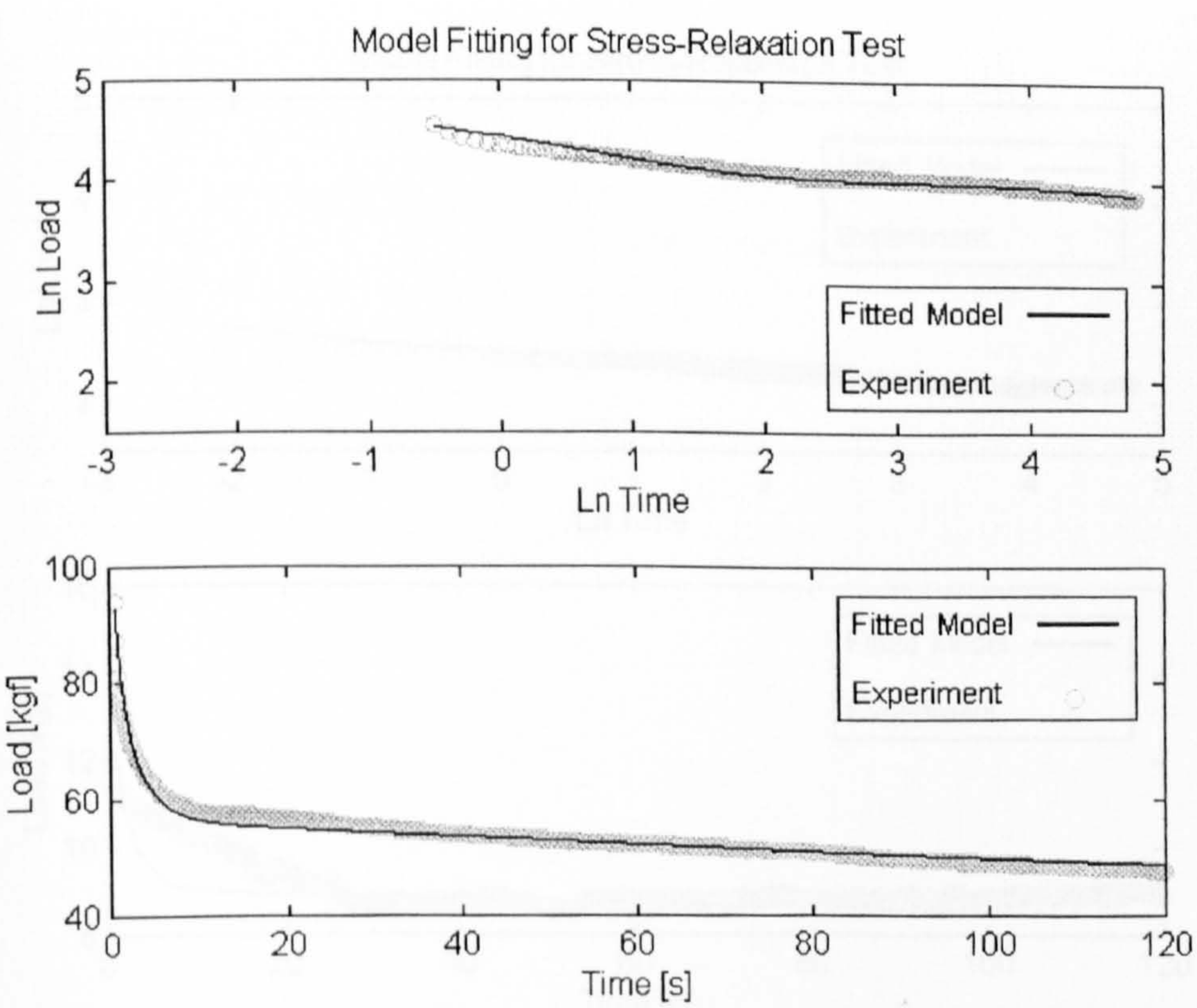

Figure C.24. Model fitting of the stress-relaxation test data for 30 mm constant strain in the relaxed procedure.

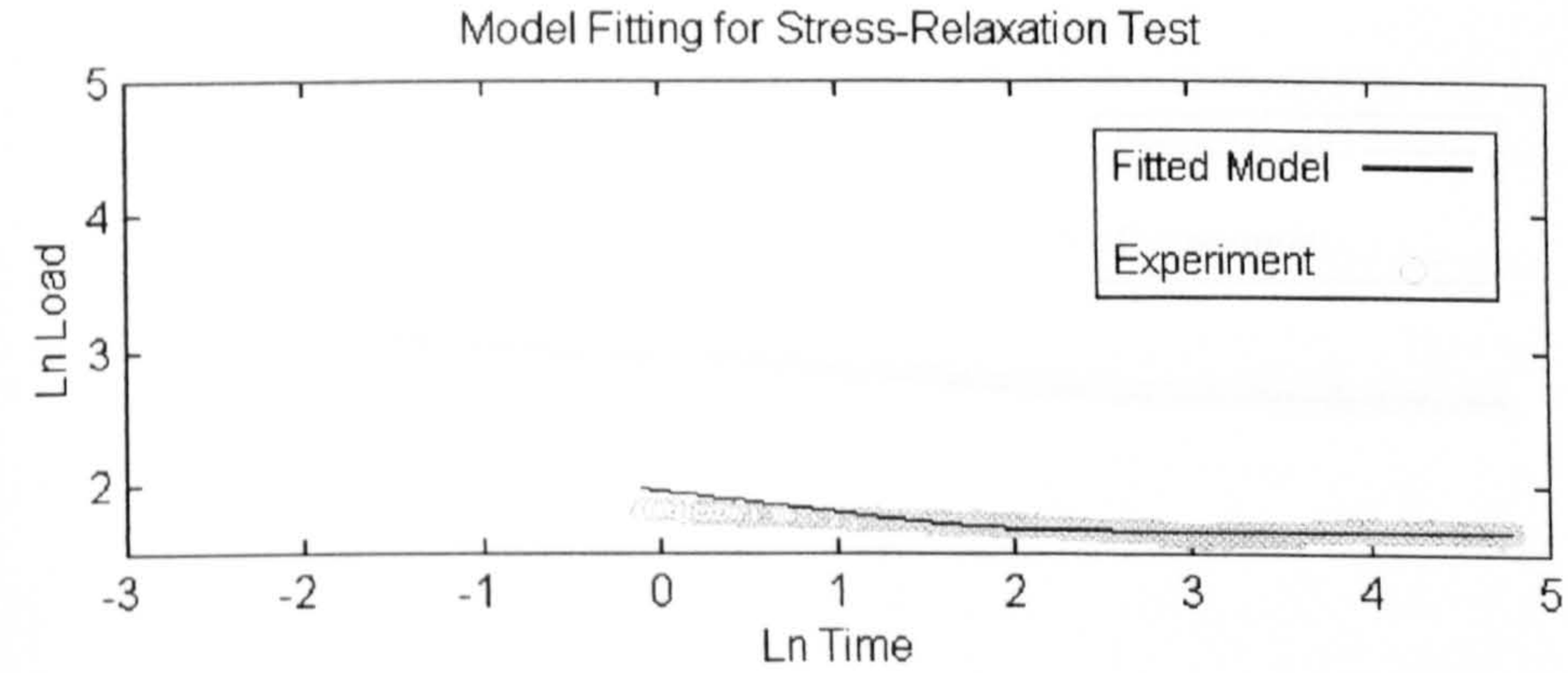

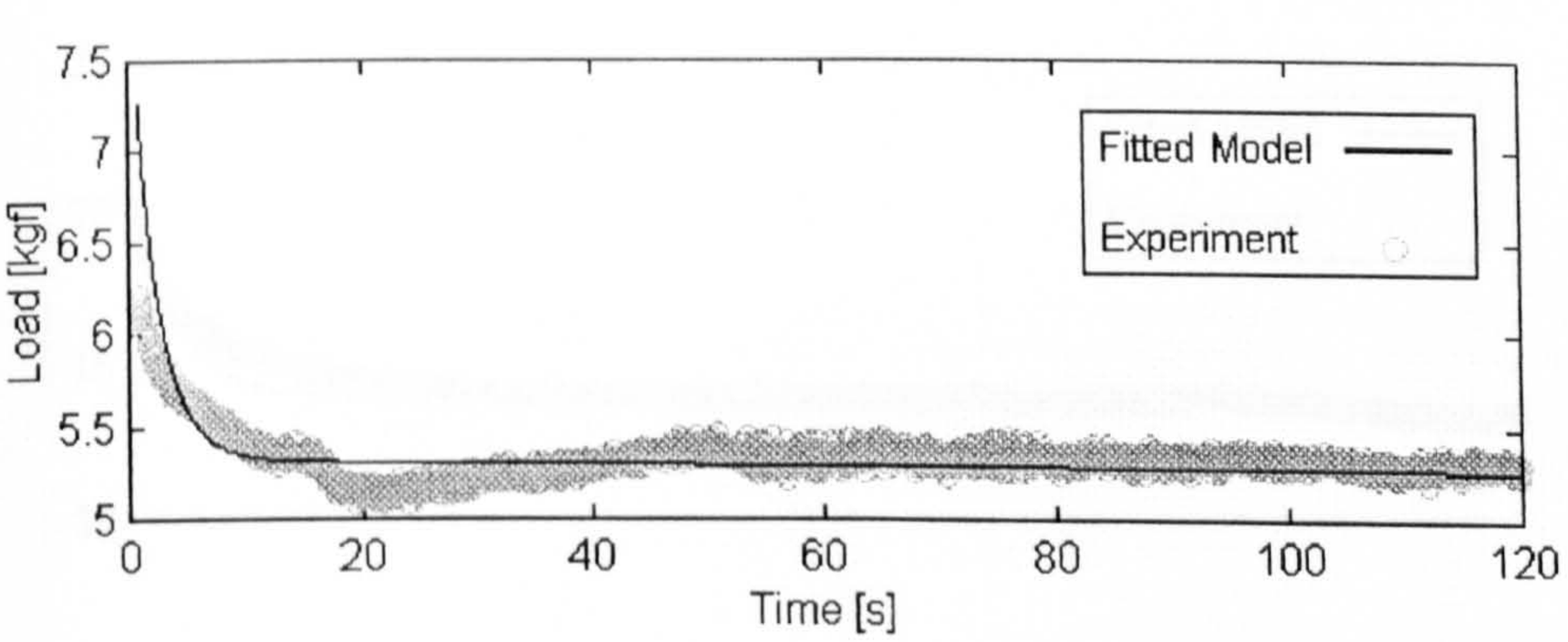

Figure C.25. Model fitting of the stress-relaxation test data for 5 mm constant strain in the contracted procedure.

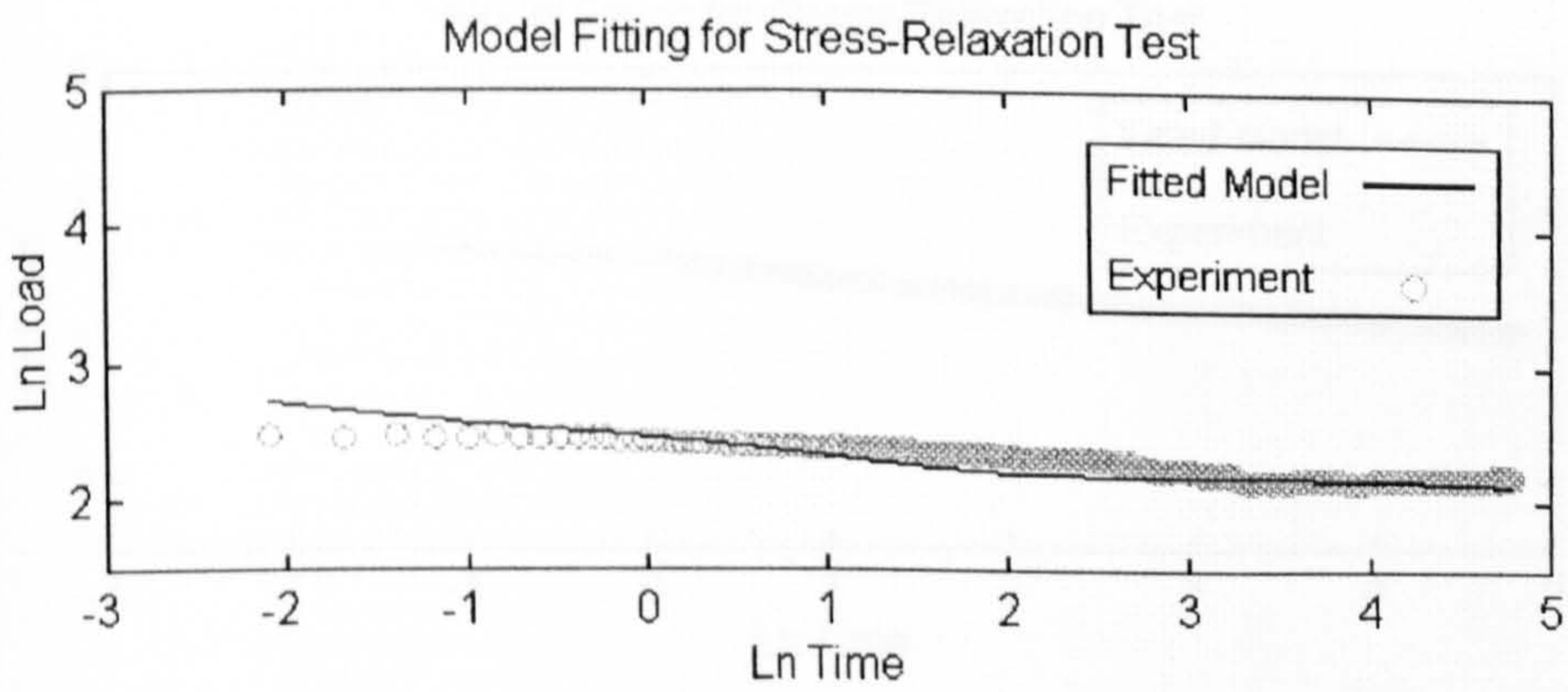

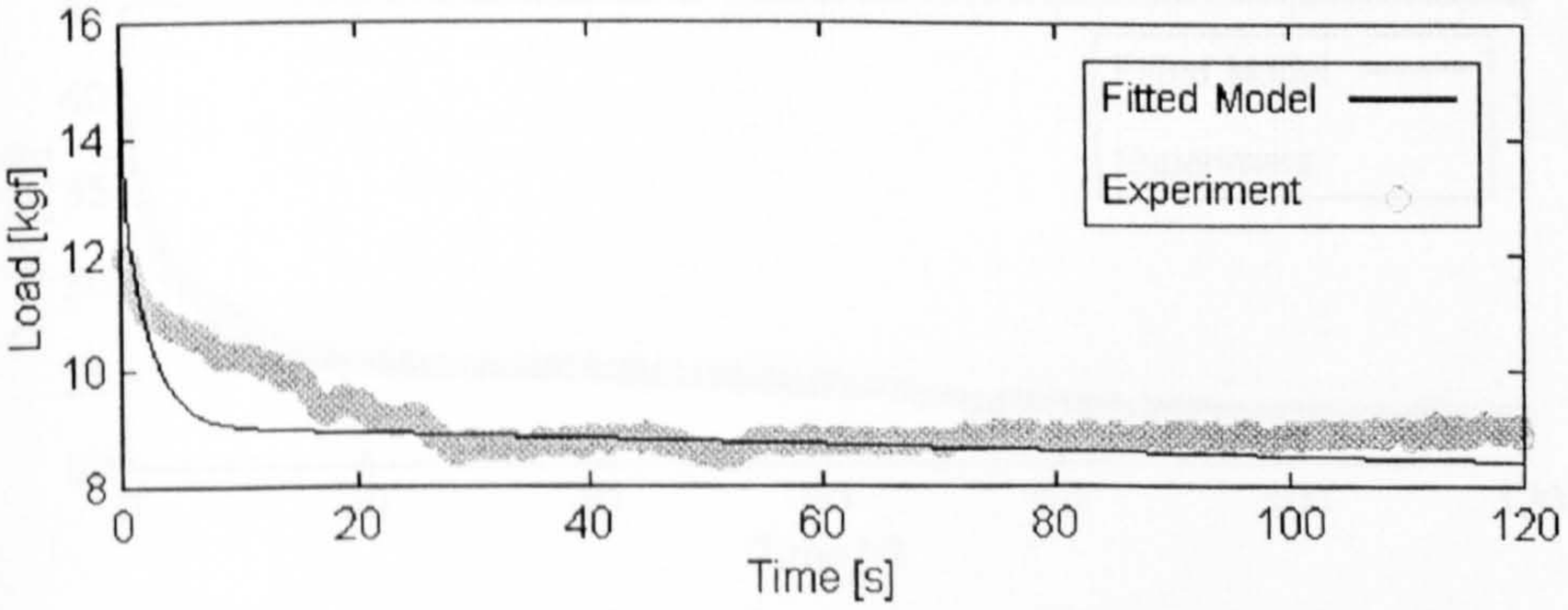

Figure C.26. Model fitting of the stress-relaxation test data for 10 mm constant strain in the contracted procedure.

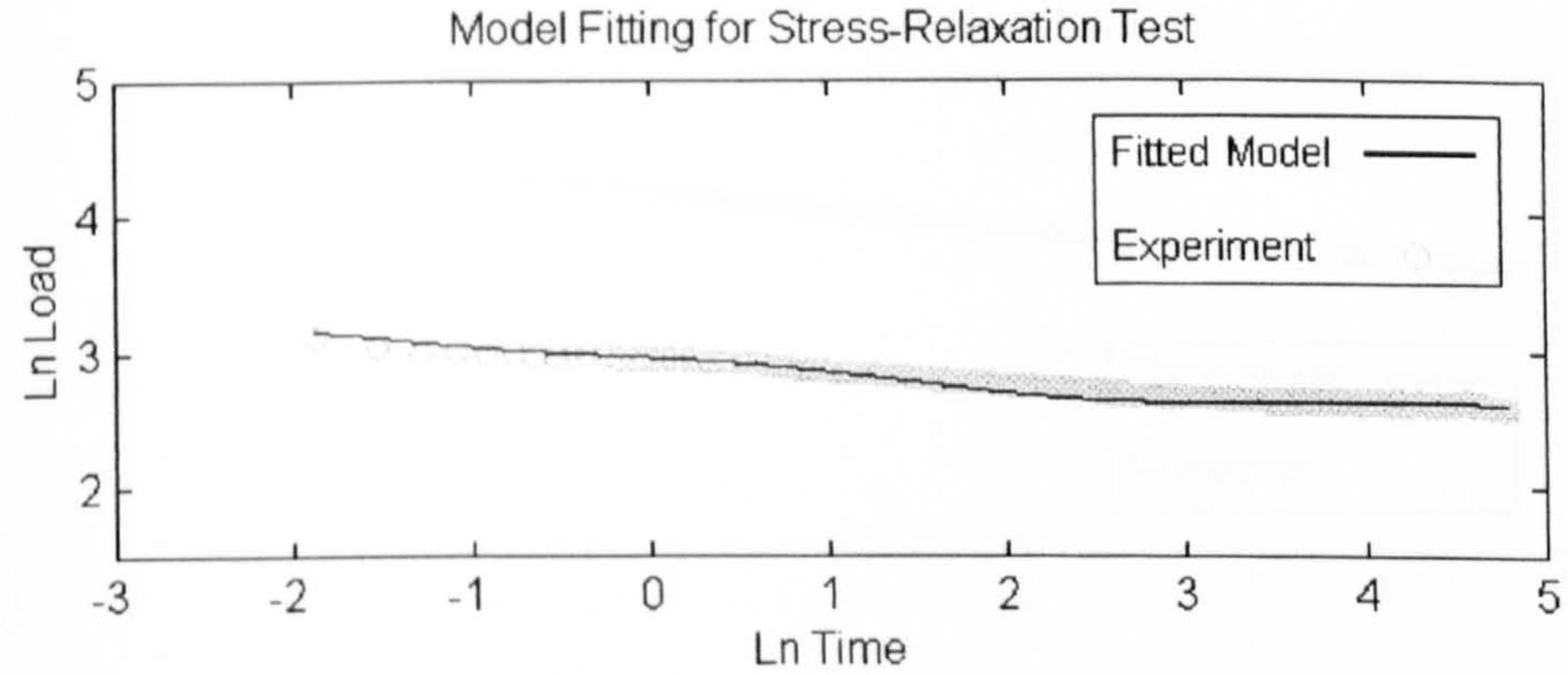

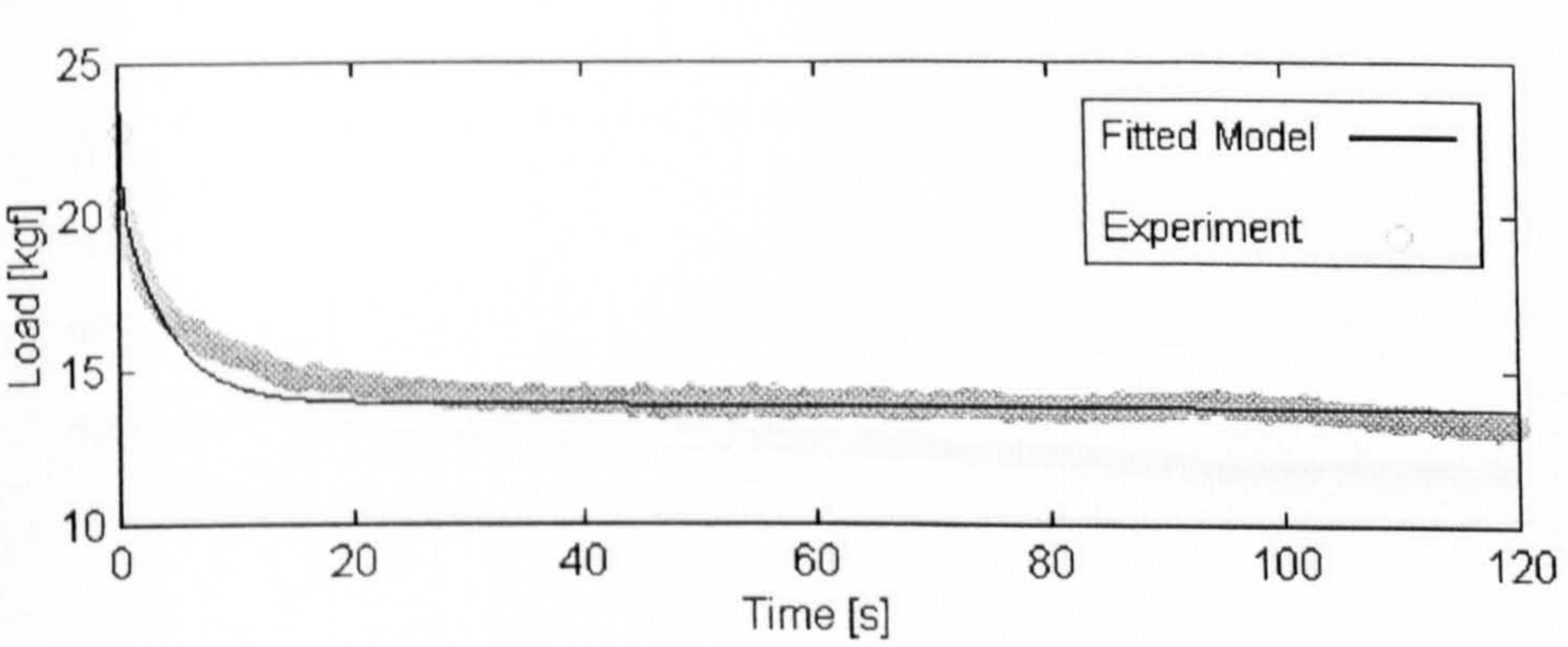

Figure C.27. Model fitting of the stress-relaxation test data for 15 mm constant strain in the contracted procedure.

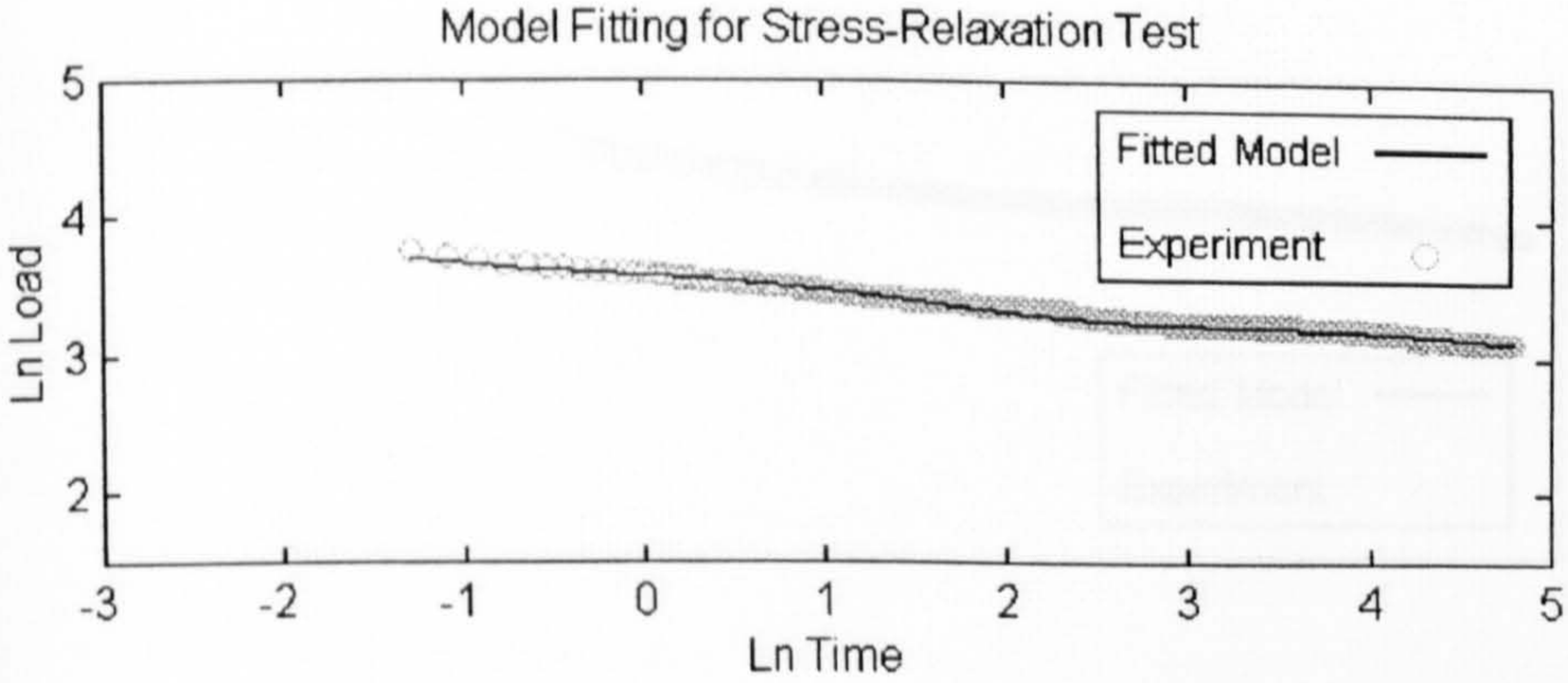

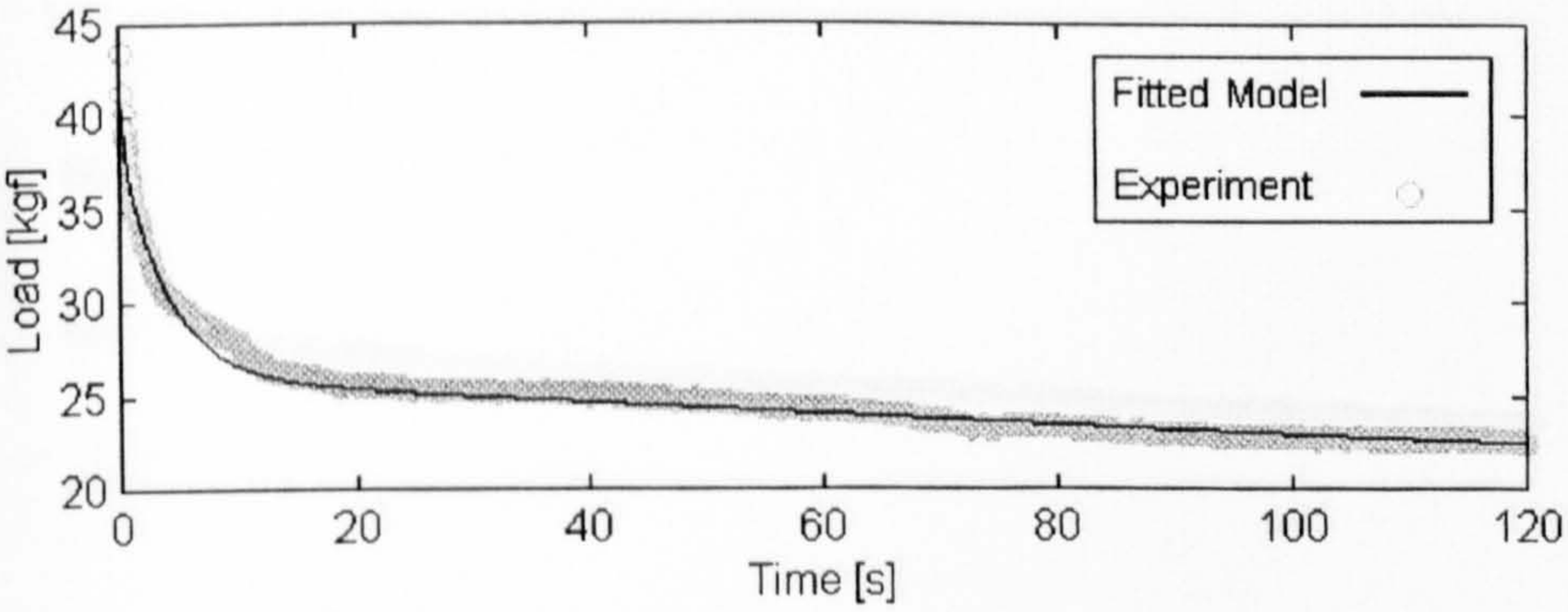

Figure C.28. Model fitting of the stress-relaxation test data for 20 mm constant strain in the contracted procedure.

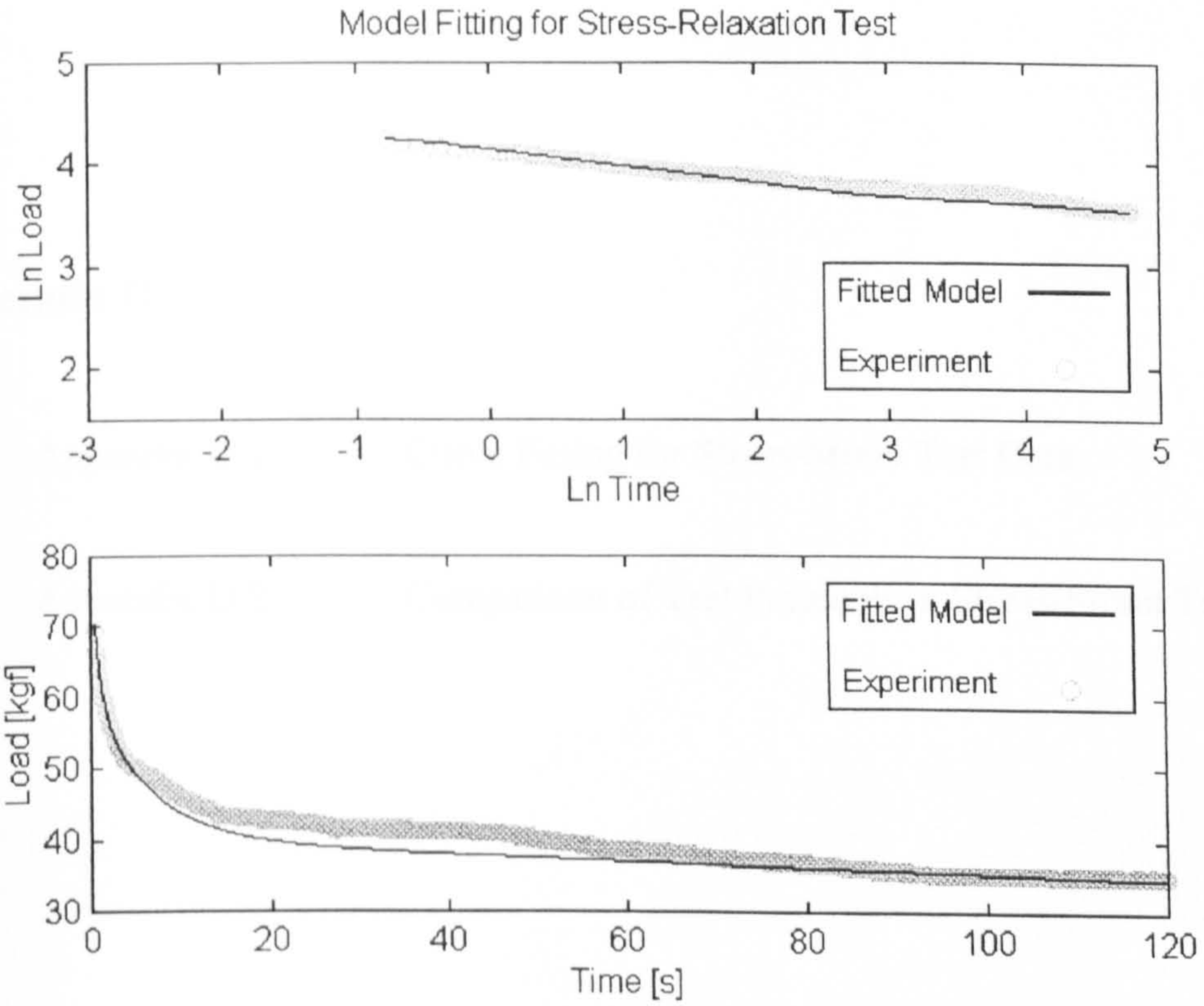

Figure C.29. Model fitting of the stress-relaxation test data for 25 mm constant strain in the contracted procedure.

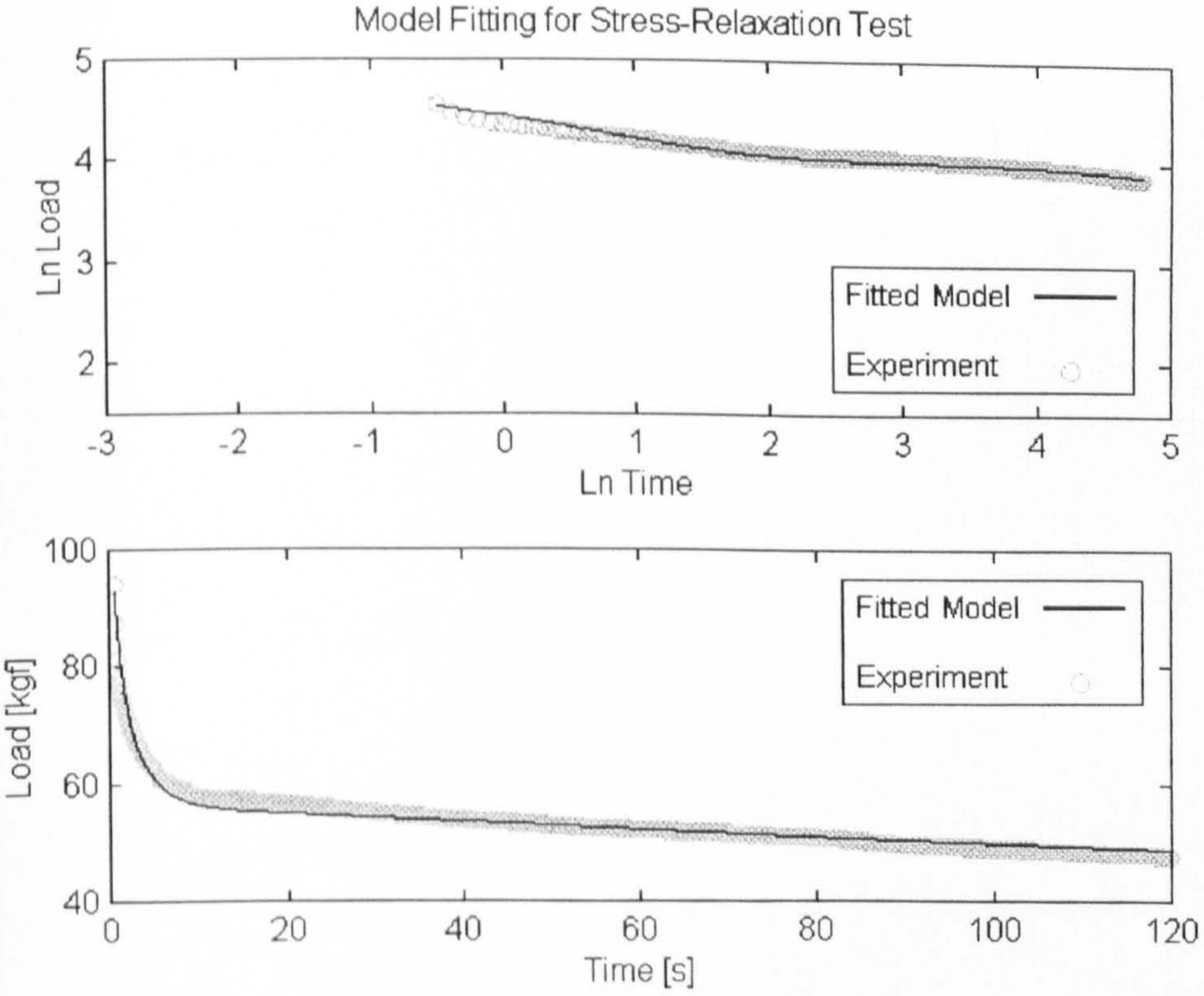

Figure C.30. Model fitting of the stress-relaxation test data for 30 mm constant strain in the contracted procedure.

Appendix D

Appendix D

Appendix D.1. Curve Fitting for Stress-Strain Test Data

Appendix D.2. Comparison of Test Protocols in Stress-Strain Test Data

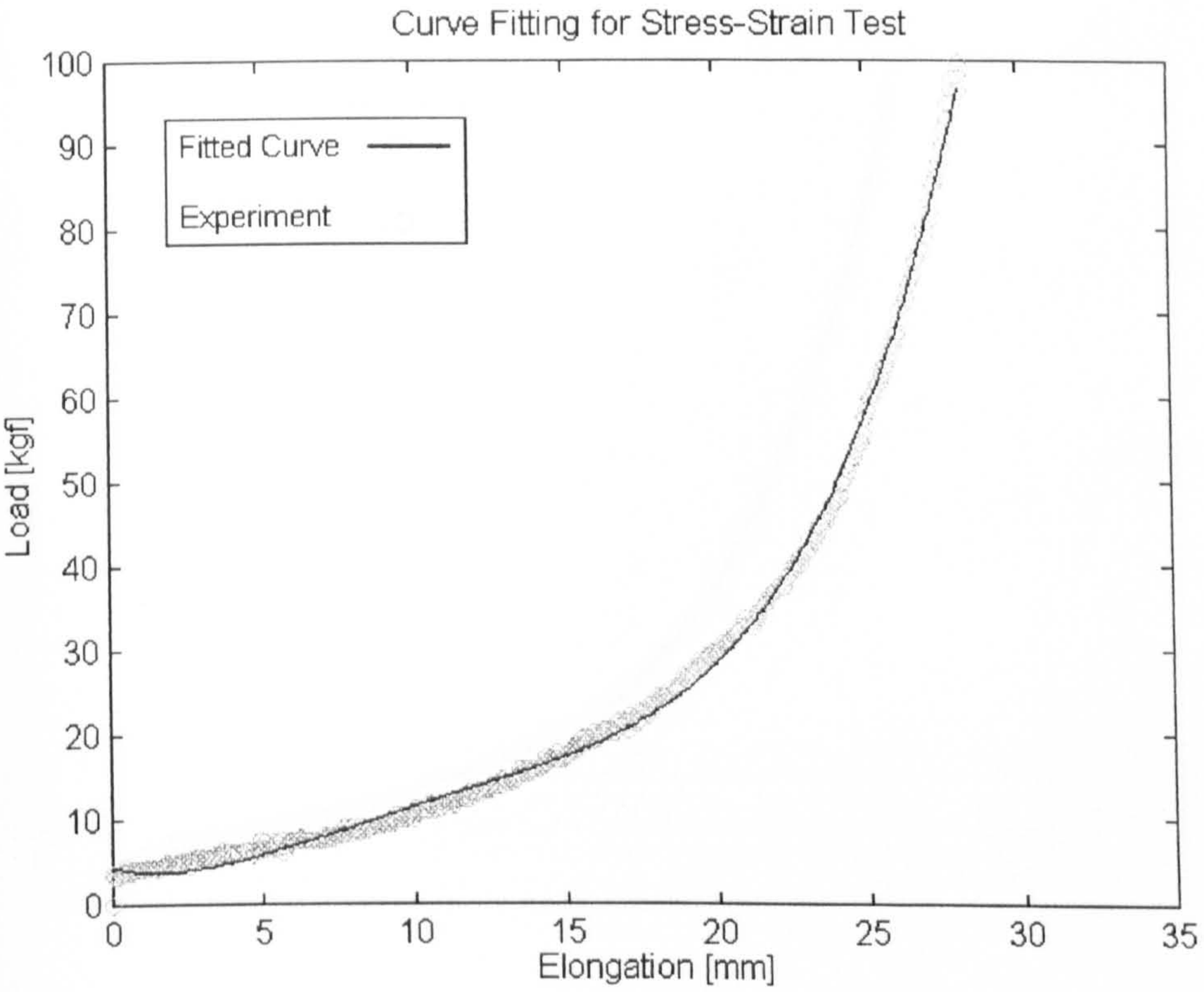

Figure D.1. Curve fitting of the stress-strain test data for 0.5 $mm.s^{-1}$ constant strain rate in the relaxed procedure.

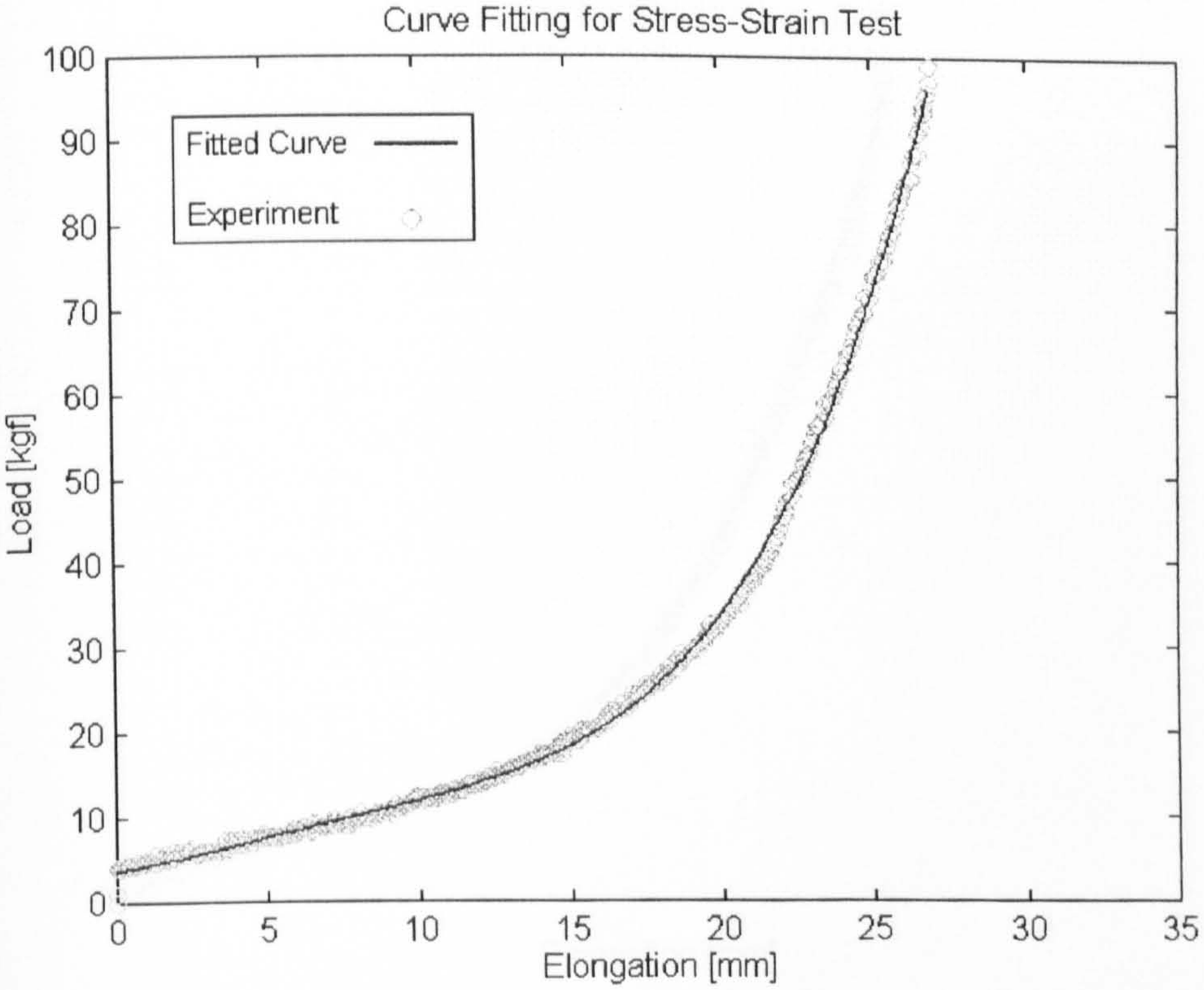

Figure D.2. Curve fitting of the stress-strain test data for 1 $mm.s^{-1}$ constant strain rate in the relaxed procedure.

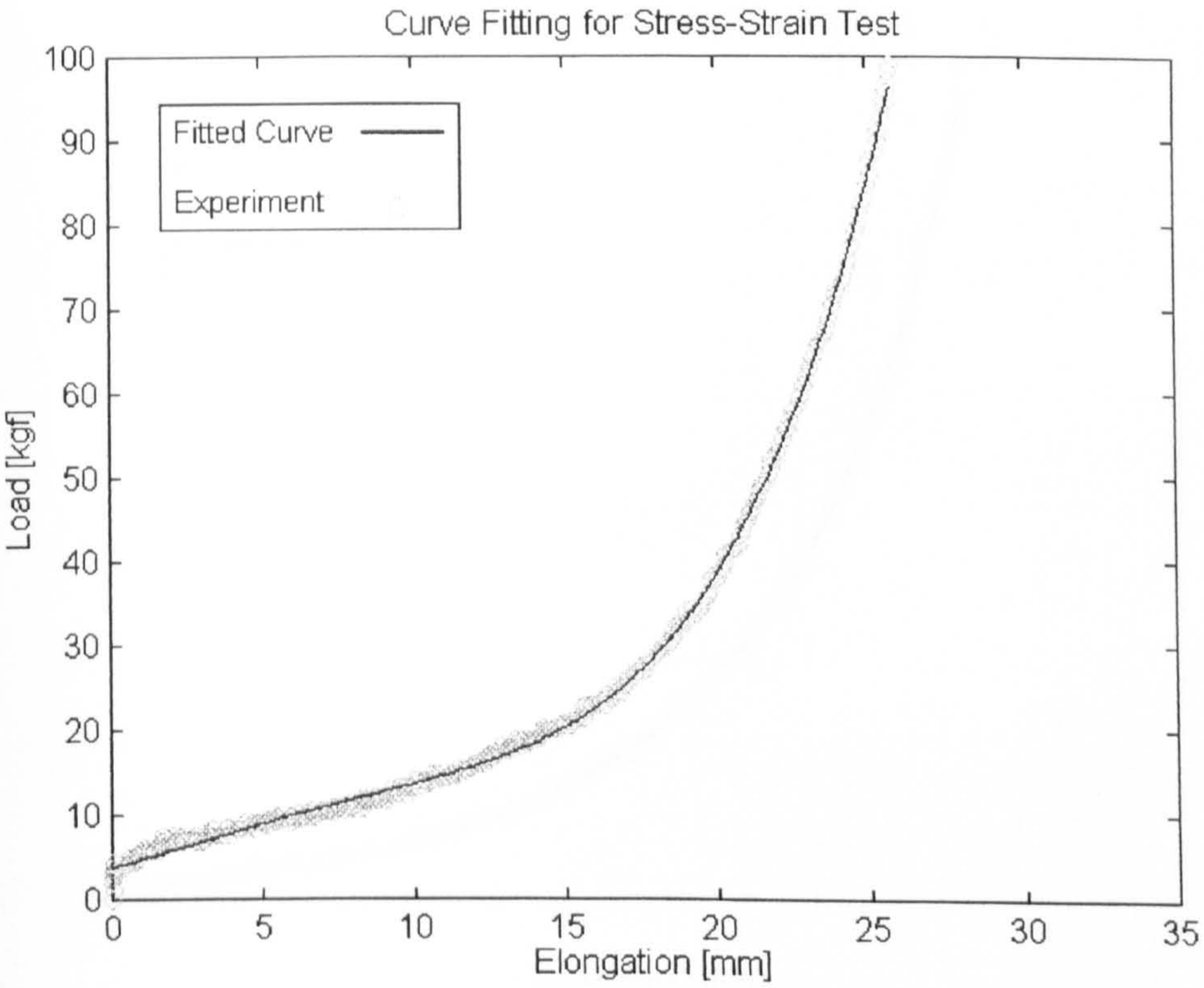

Figure D.3. Curve fitting of the stress-strain test data for 2 $mm.s^{-1}$ constant strain rate in the relaxed procedure.

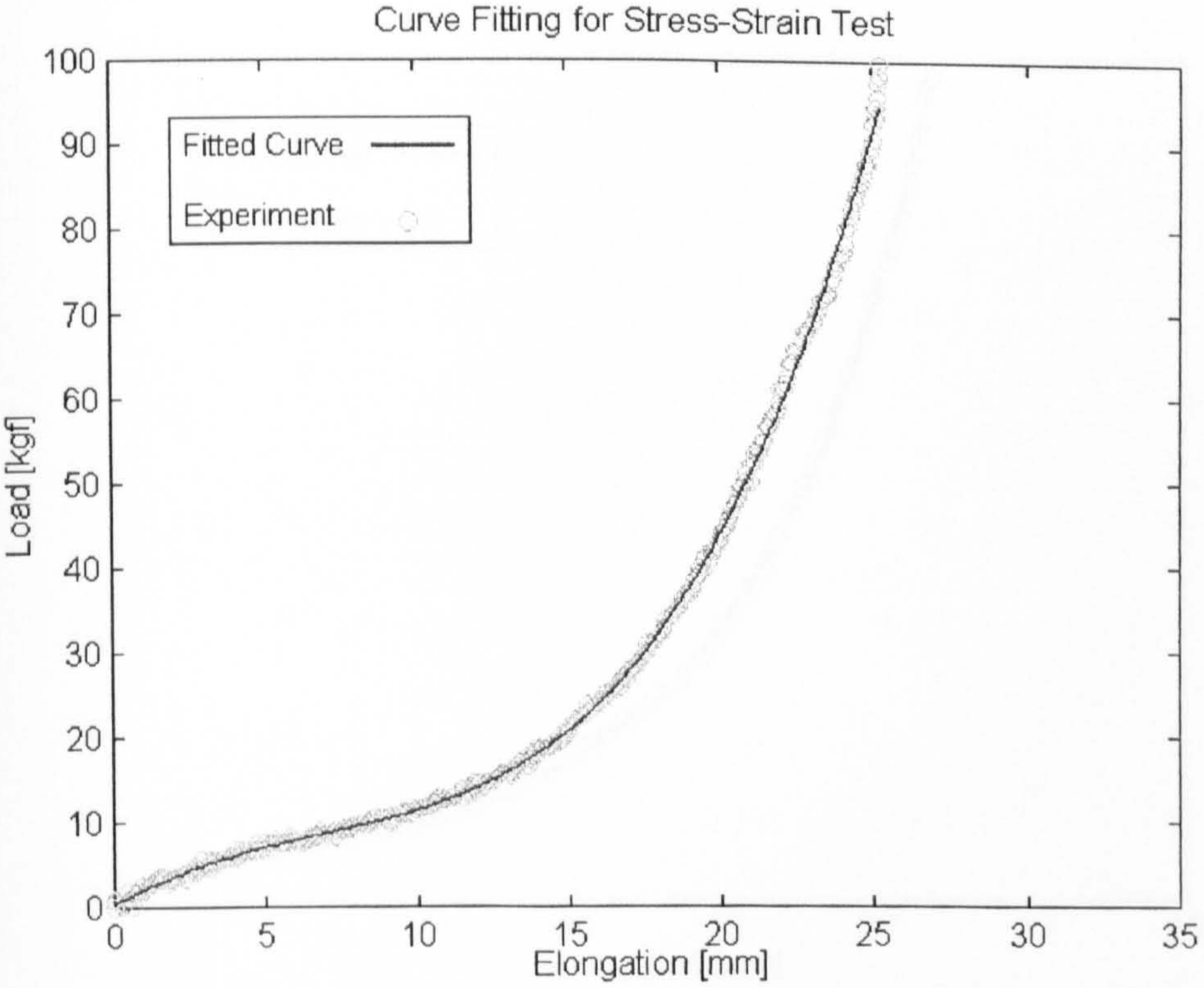

Figure D.4. Curve fitting of the stress-strain test data for 4 $mm.s^{-1}$ constant strain rate in the relaxed procedure.

Appendix D

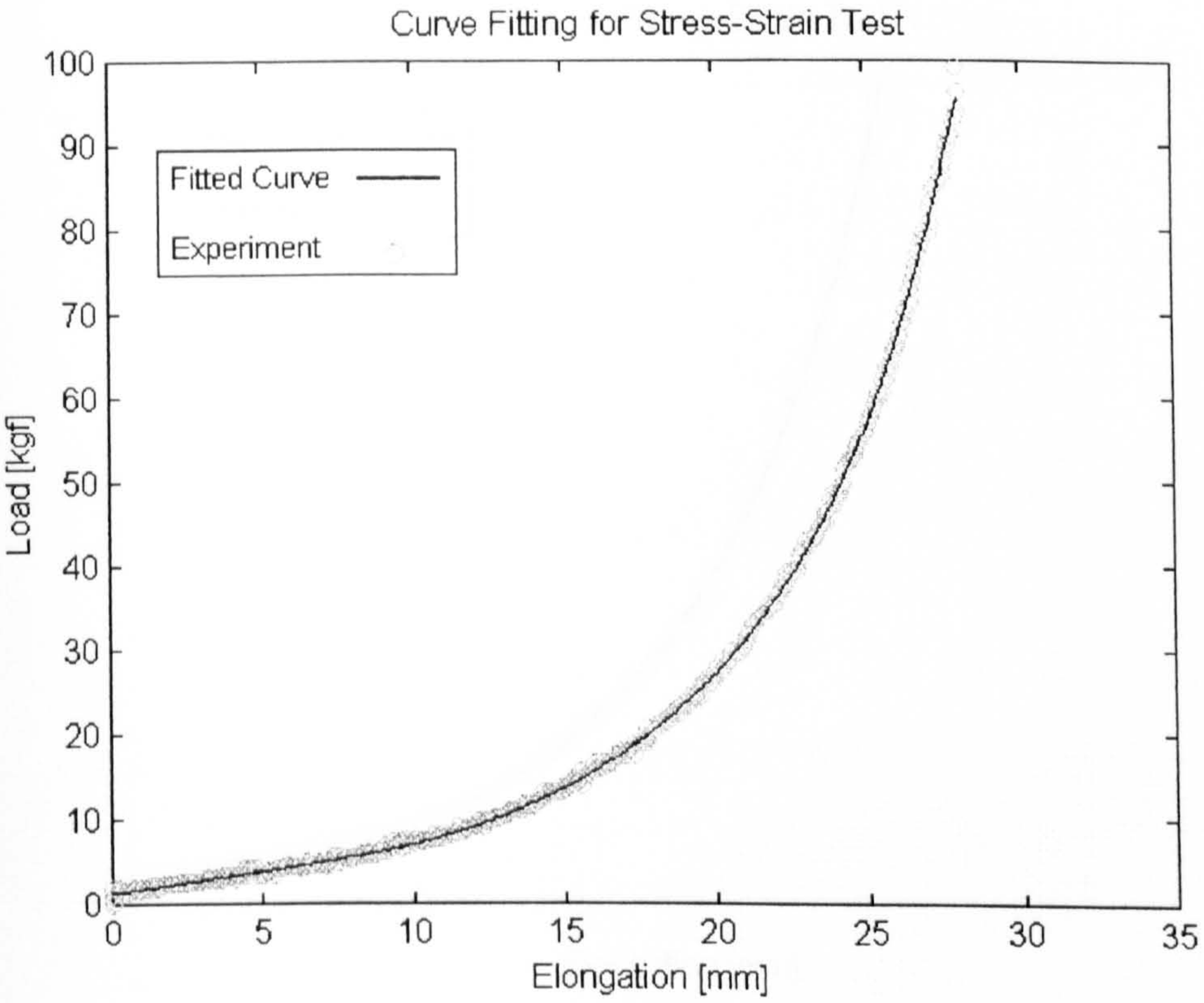

Figure D.5. Curve fitting of the stress-strain test data for 0.5 $mm.s^{-1}$ constant strain rate in the contracted procedure.

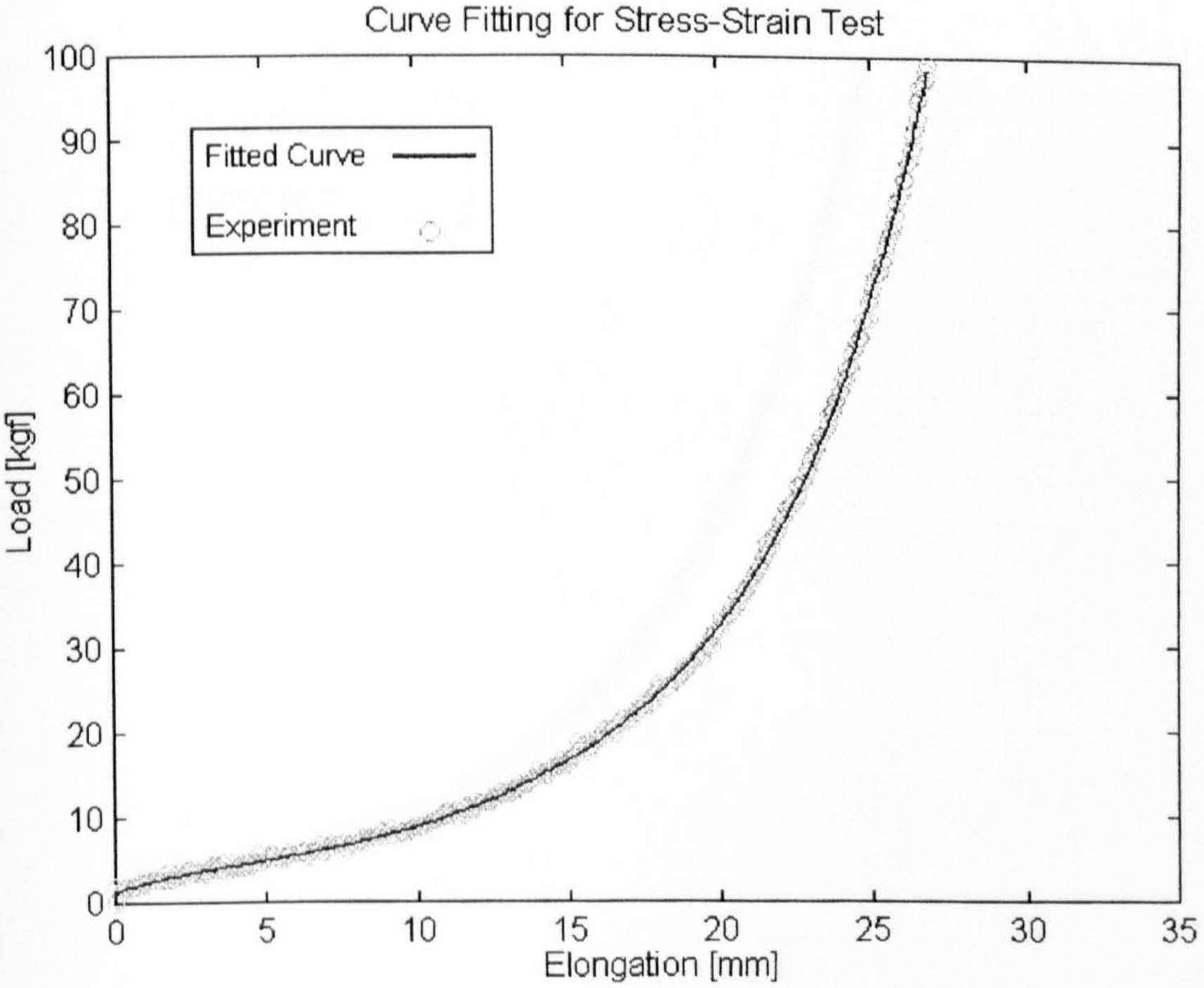

Figure D.6. Curve fitting of the stress-strain test data for 1 $mm.s^{-1}$ constant strain rate in the contracted procedure.

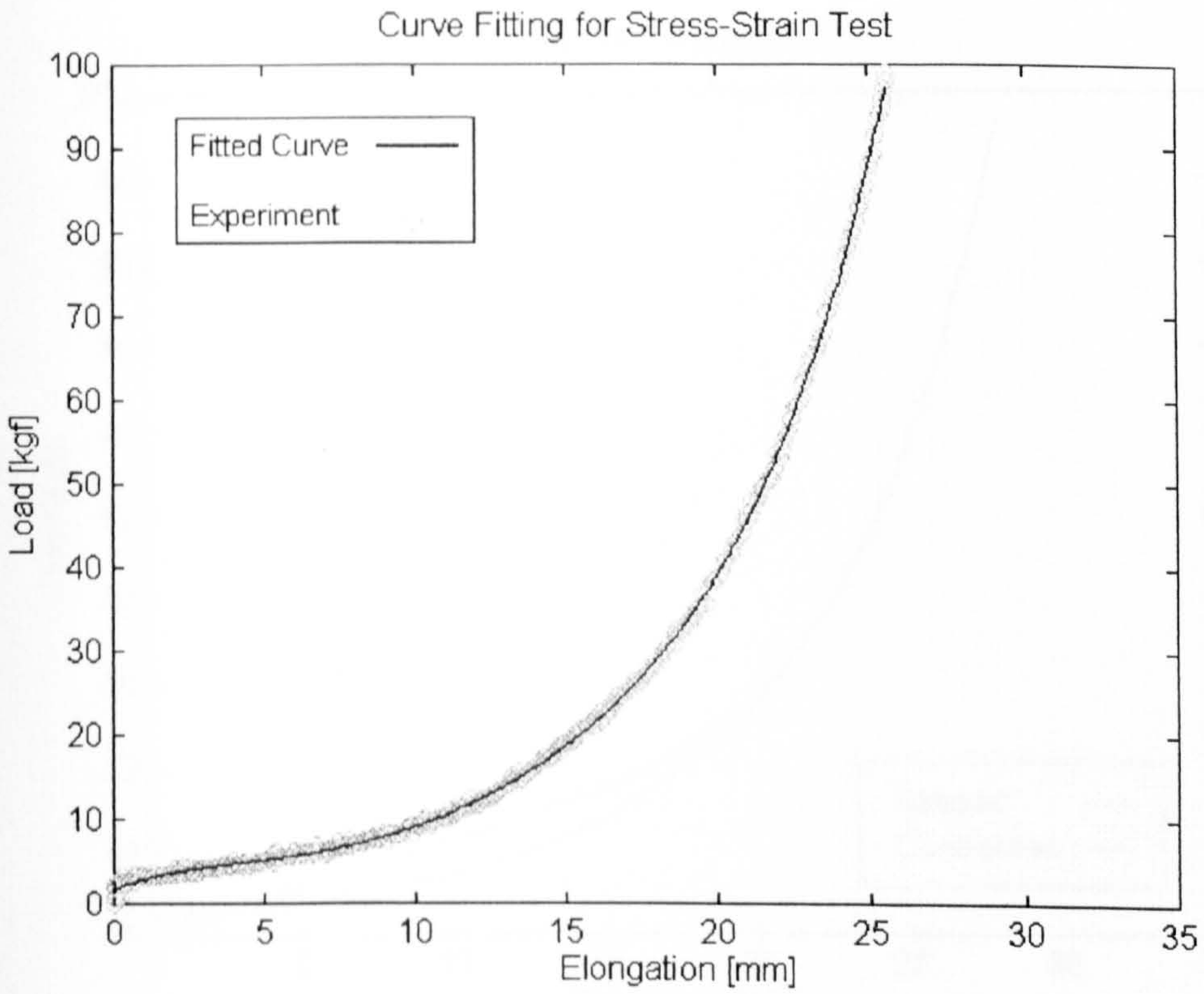

Figure D.7. Curve fitting of the stress-strain test data for 2 $mm.s^{-1}$ constant strain rate in the contracted procedure.

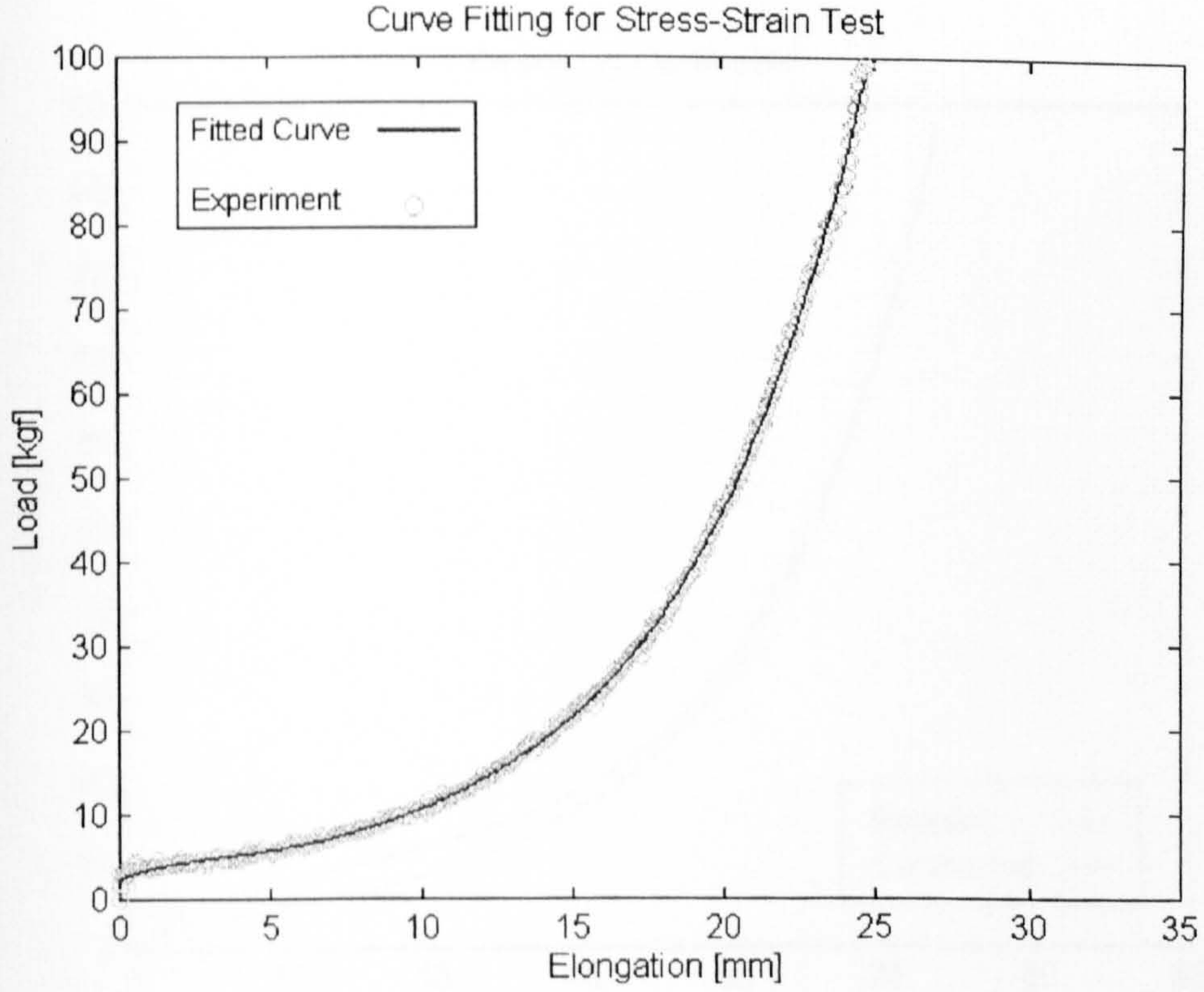

Figure D.8. Curve fitting of the stress-strain test data for 0.5 $mm.s^{-1}$ constant strain rate in the contracted procedure.

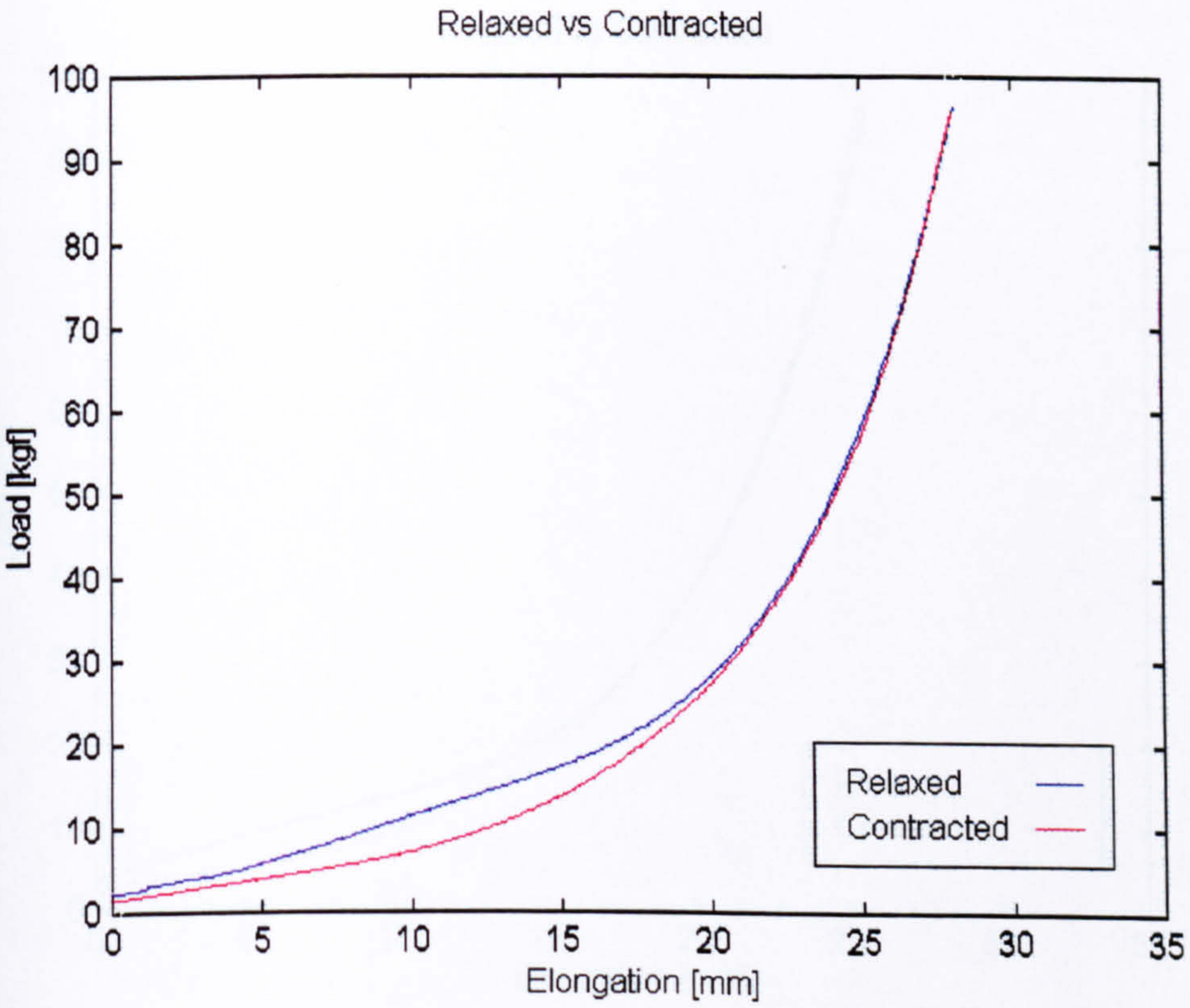

Figure D.9. Comparison of test protocols in the stress-strain test for 0.5 $mm.s^{-1}$ constant strain rate.

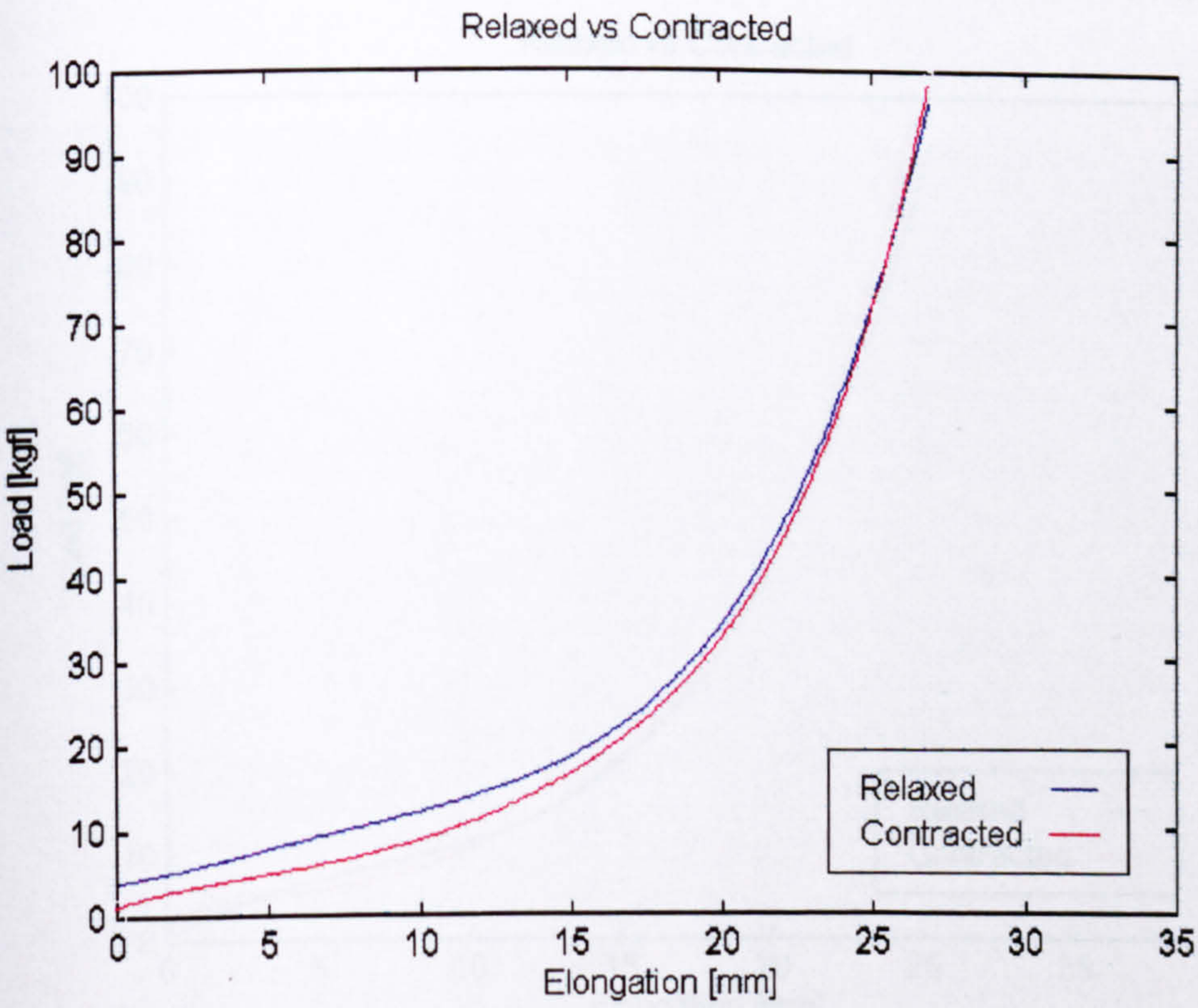

Figure D.10. Comparison of test protocols in the stress-strain test for 1 $mm.s^{-1}$ constant strain rate.

Appendix D

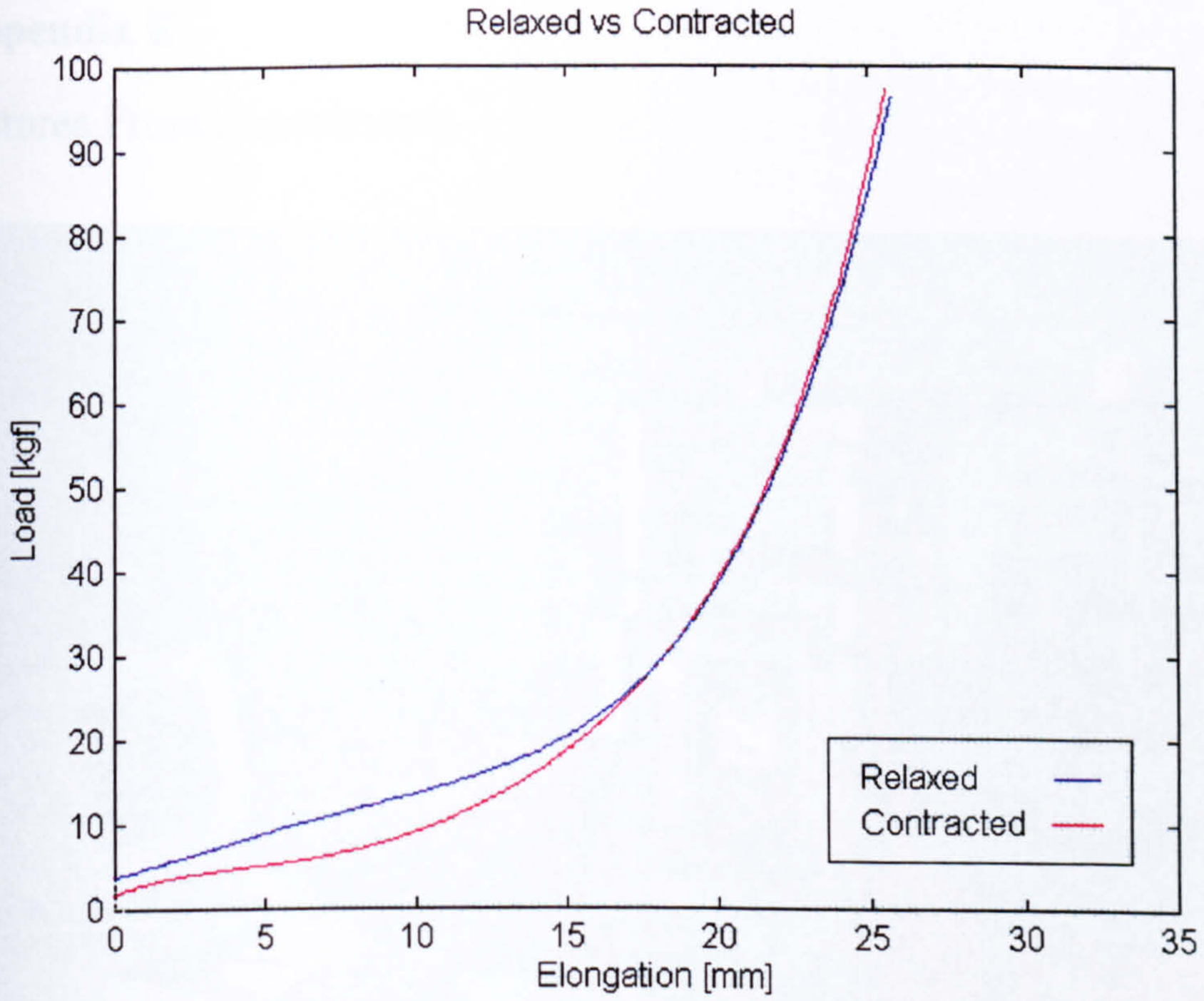

Figure D.11. Comparison of test protocols in the stress-strain test for 2 $mm.s^{-1}$ constant strain rate.

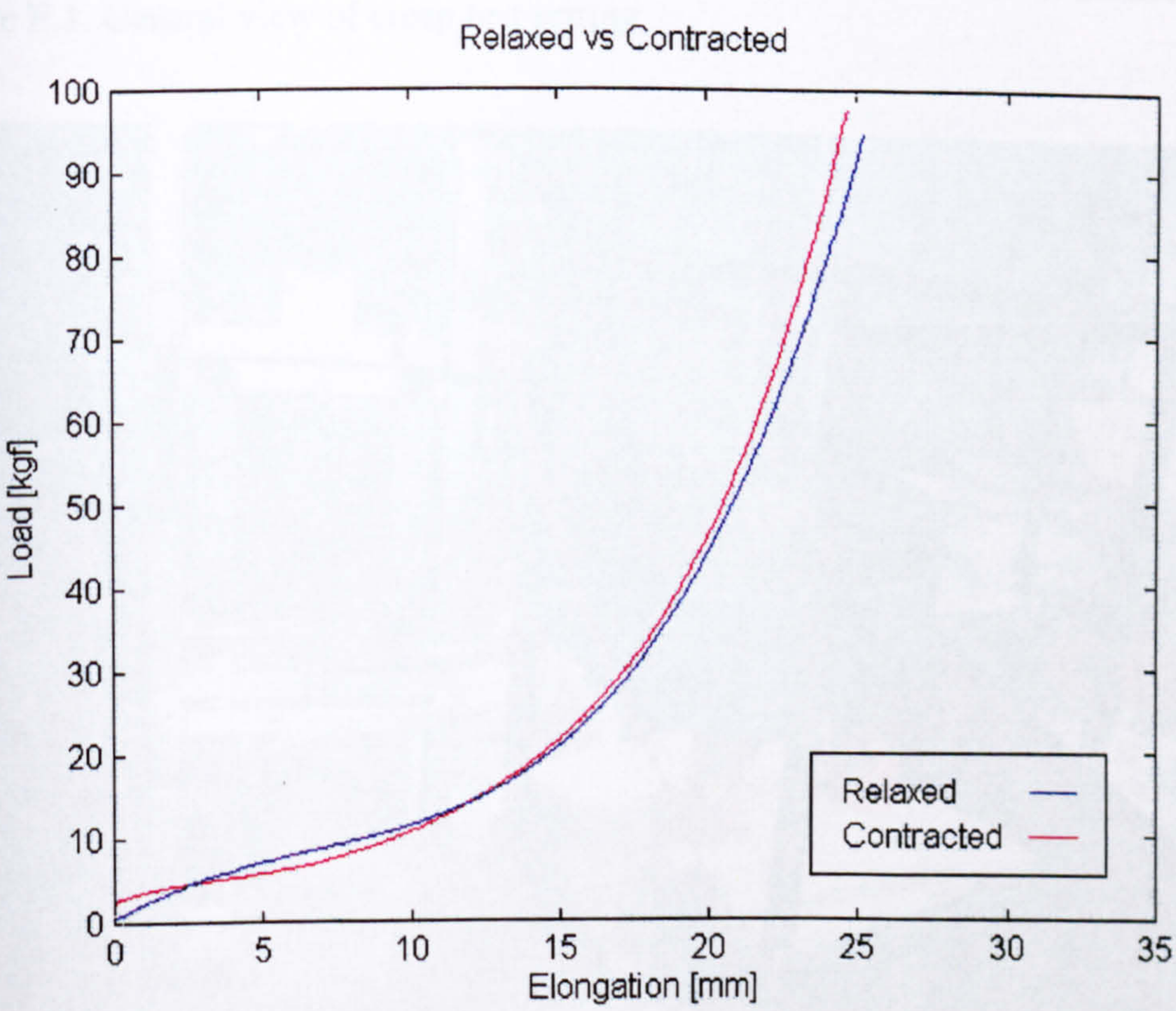

Figure D.12. Comparison of test protocols in the stress-strain test for 4 $mm.s^{-1}$ constant strain rate.

Appendix E

Pictures From Experiments

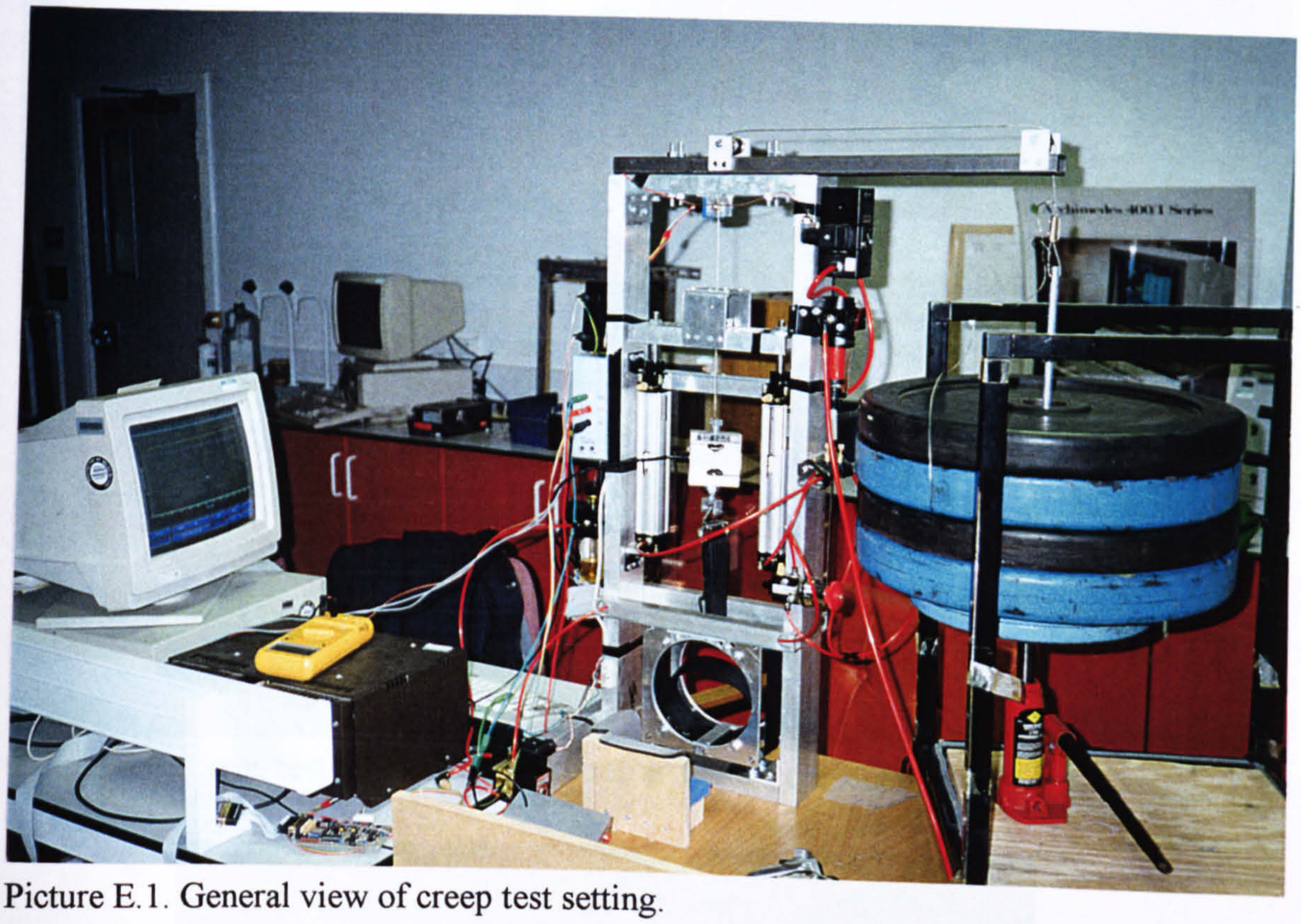

Picture E.1. General view of creep test setting.

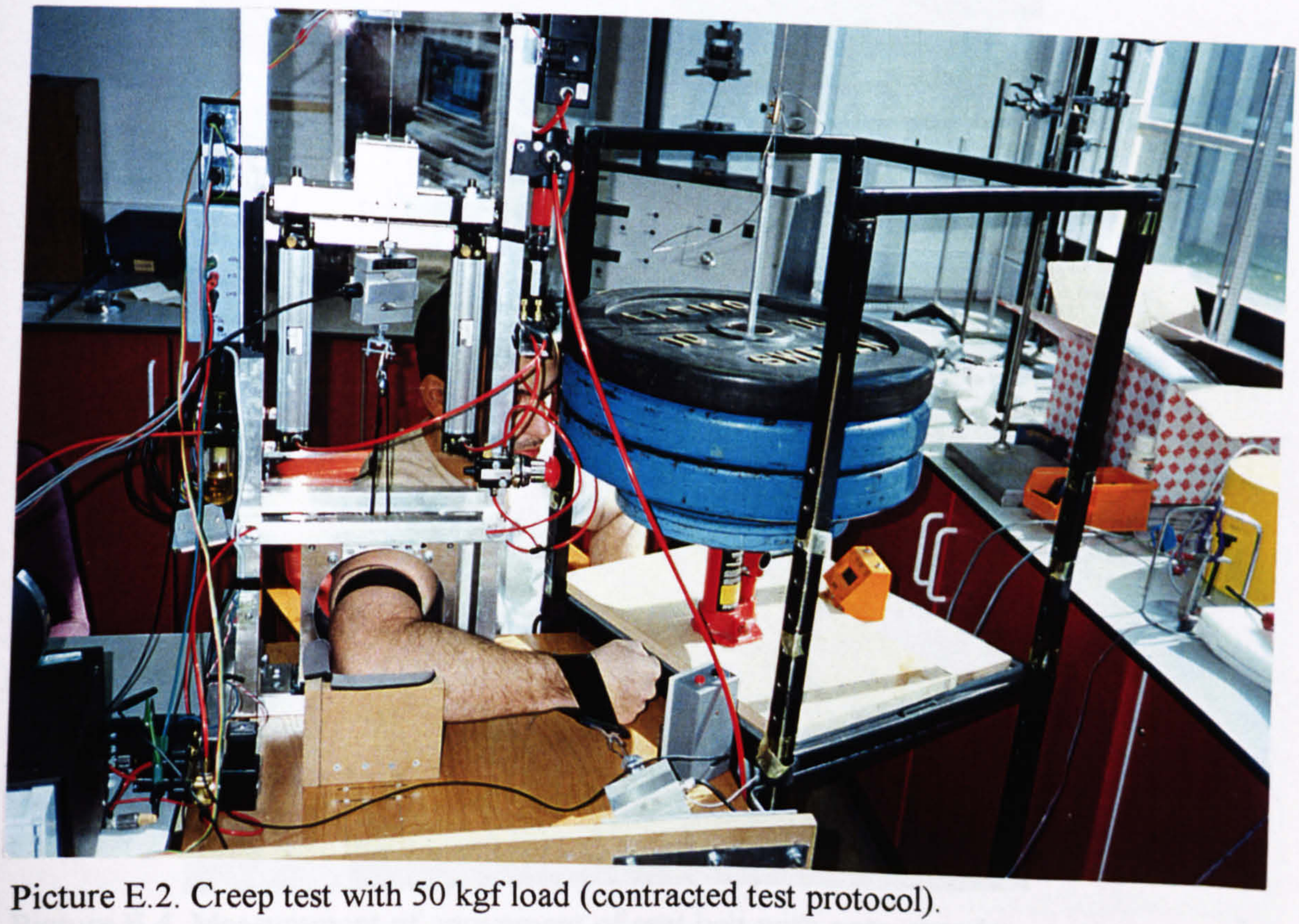

Picture E.2. Creep test with 50 kgf load (contracted test protocol).

Appendix E

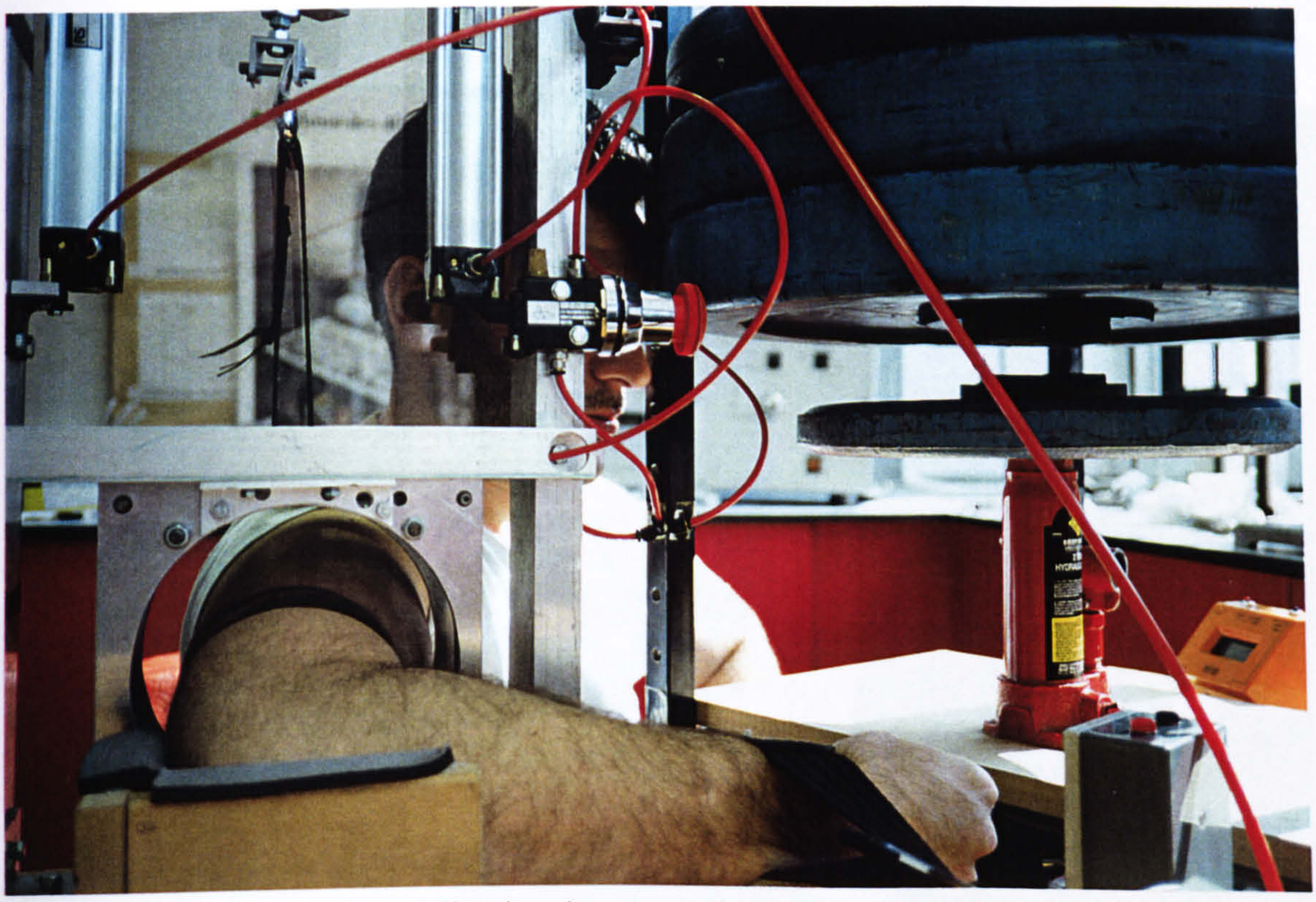

Picture E.3. Creep test data collection (contracted test protocol).

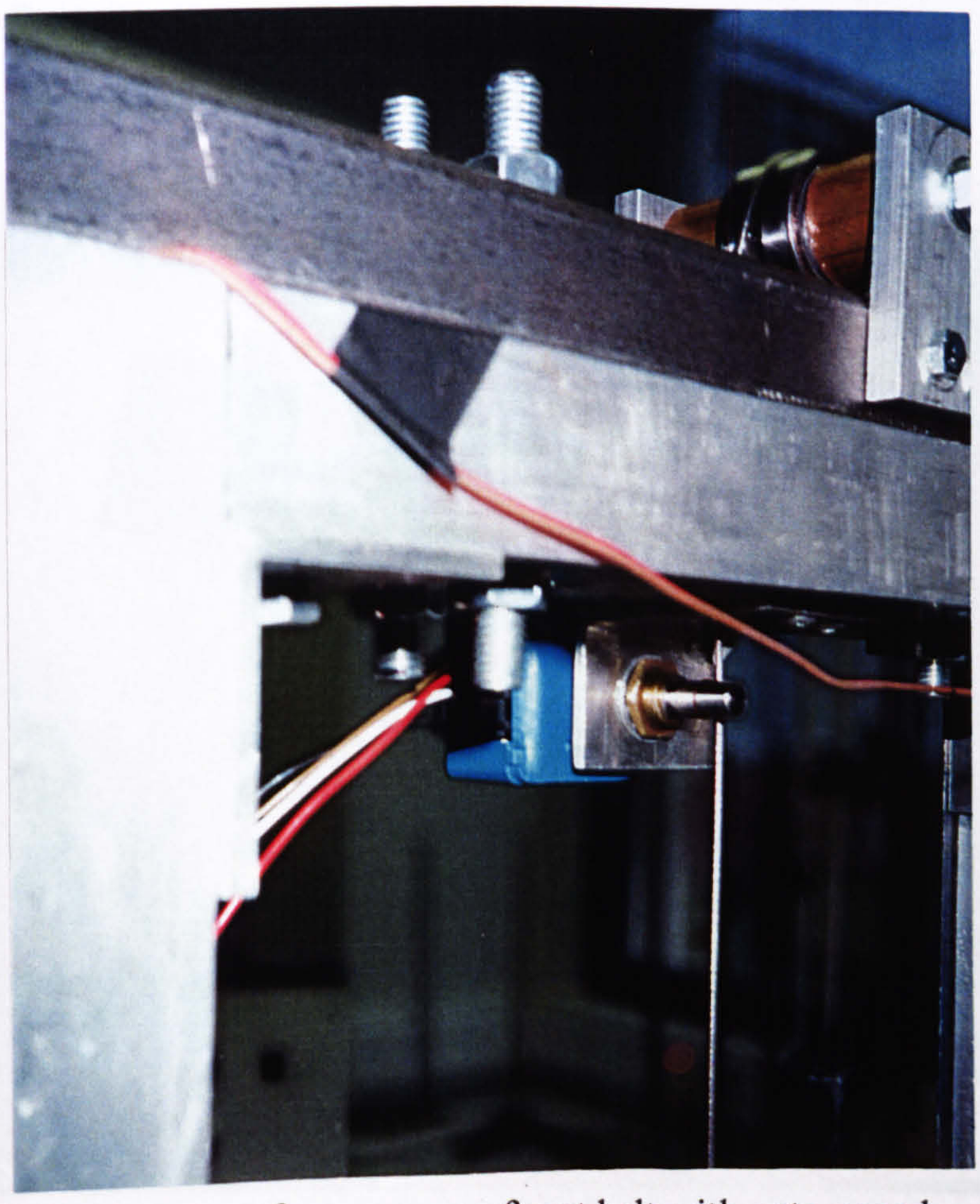

Picture E.4. Measurement of movement of seat belt with opto-encoder.

Appendix E

Picture E.5. Real time creep test output on the computer screen.

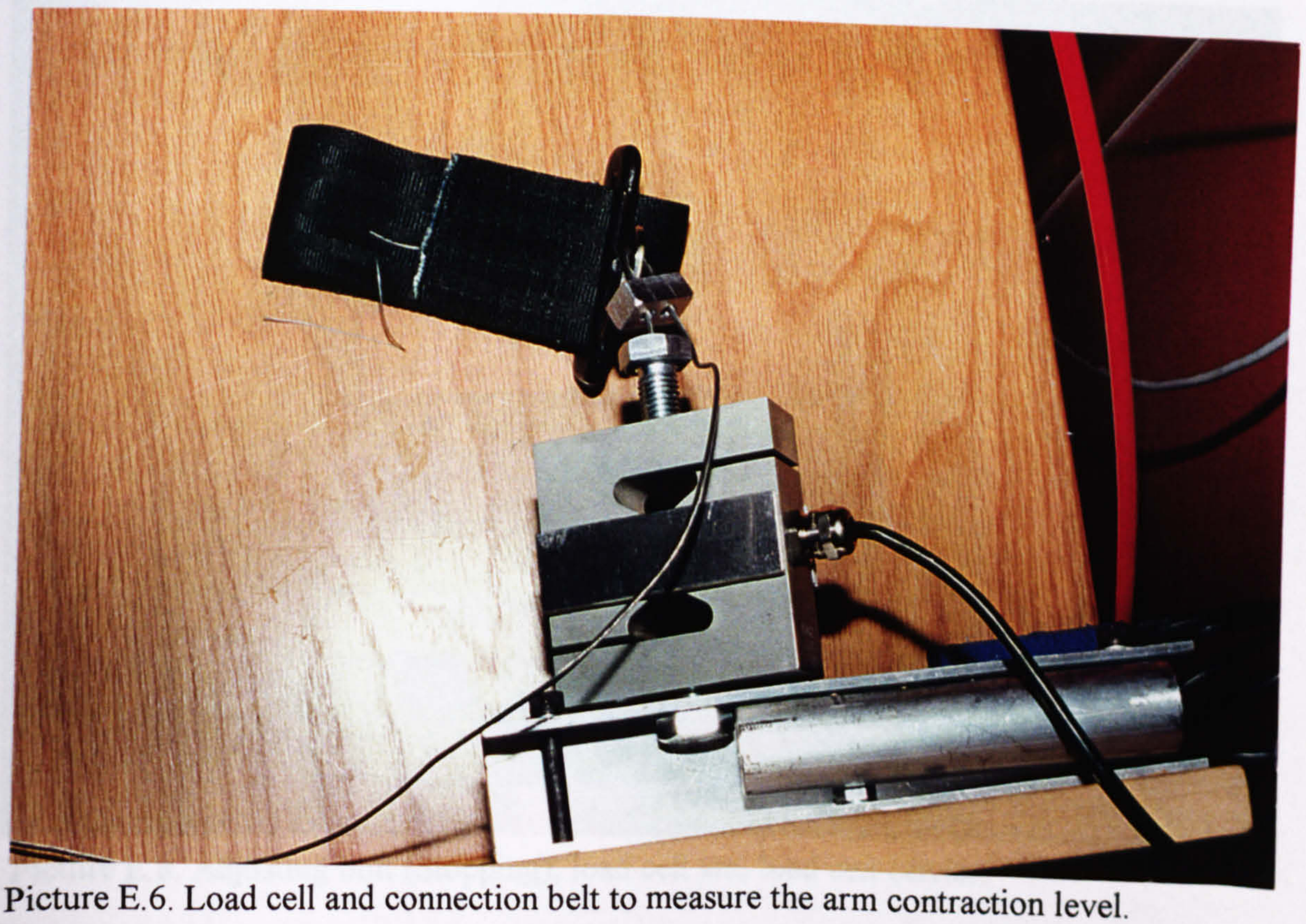

Picture E.6. Load cell and connection belt to measure the arm contraction level.

Appendix E

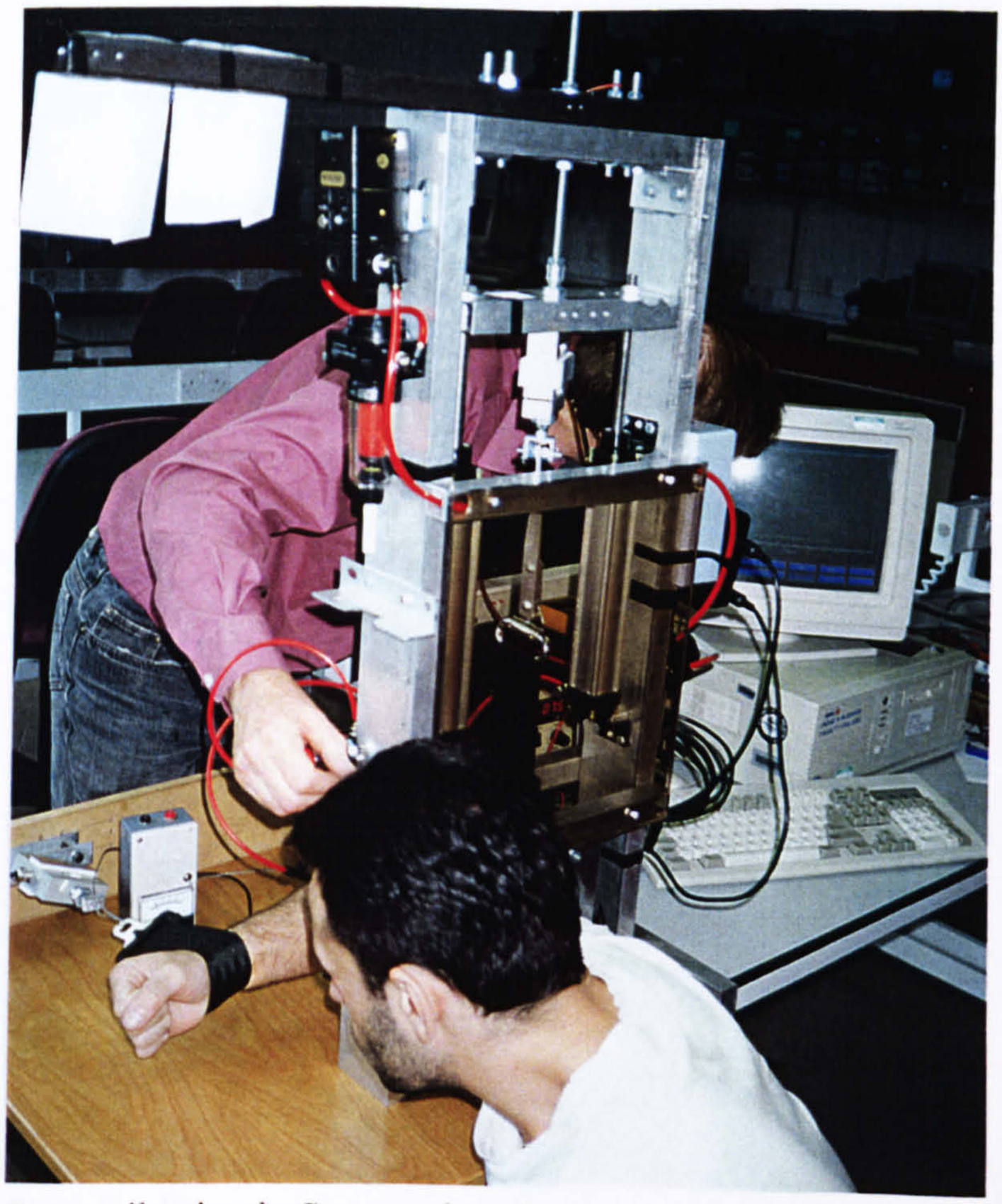

Picture E.7. Data collection in Stress-relaxation test.

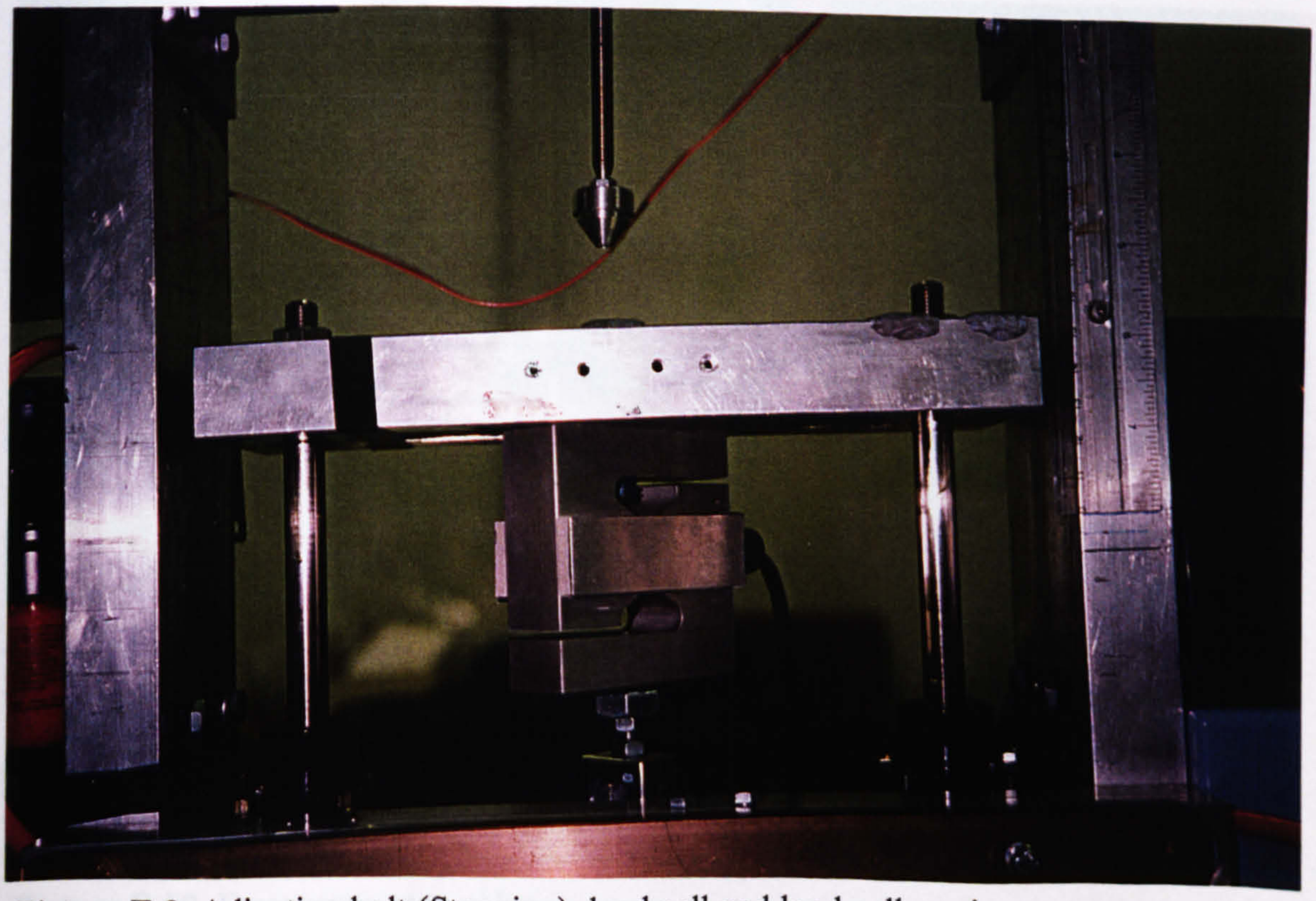

Picture E.8. Adjusting bolt (Stopping), load cell and load cell carrier.

Appendix E

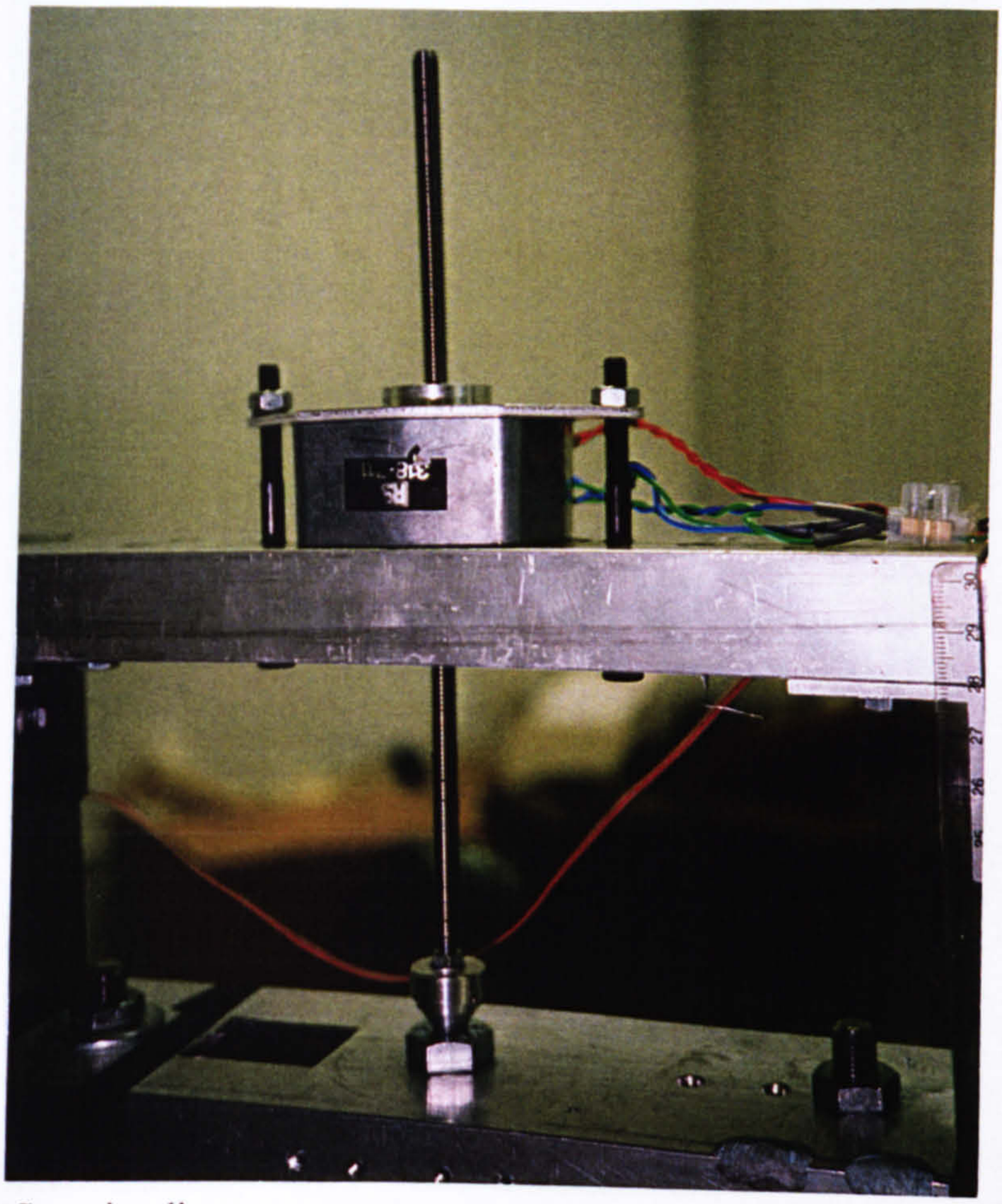

Picture E.9. Stepping linear actuator.

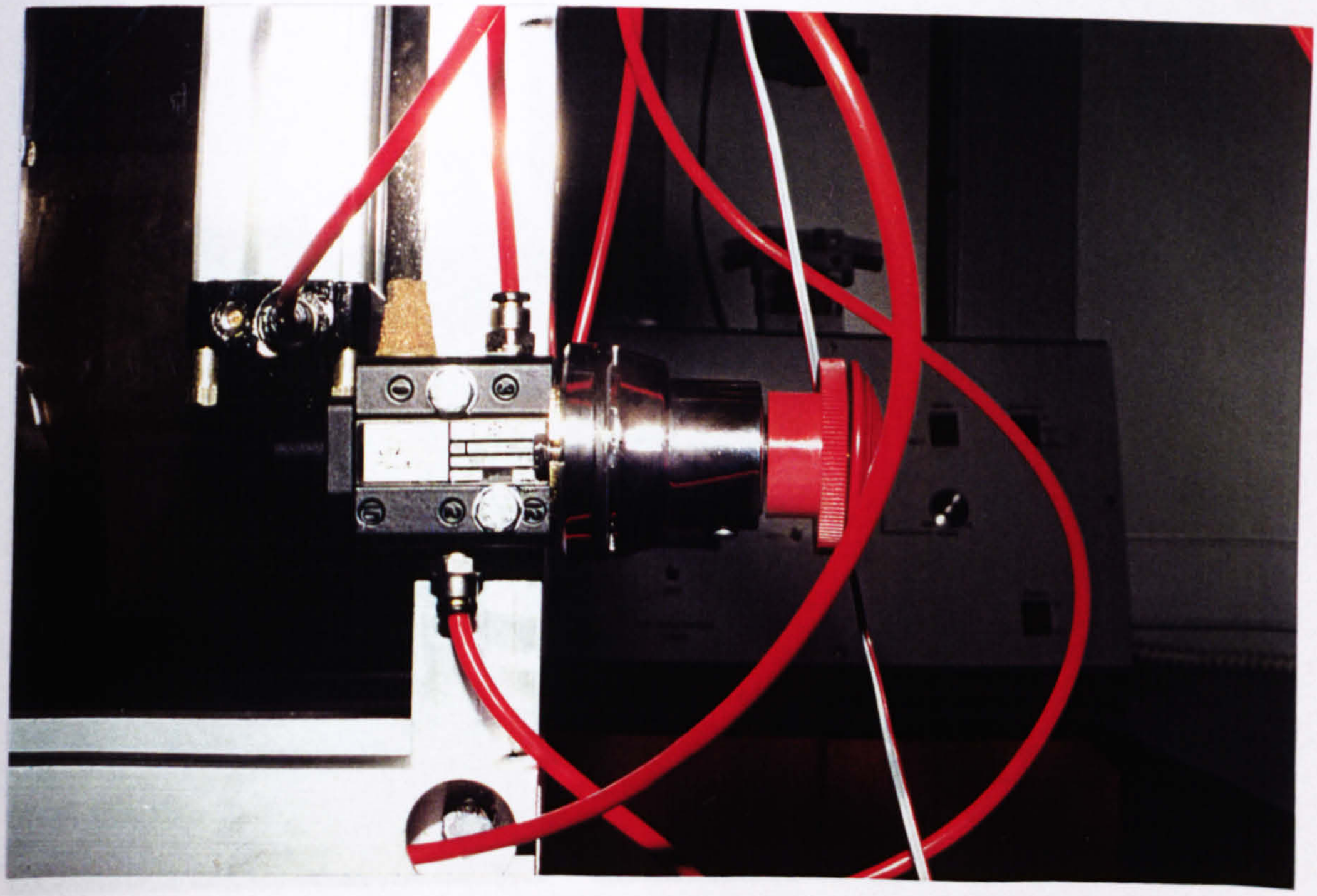

Picture E.10. Emergency stop valve.

Appendix E

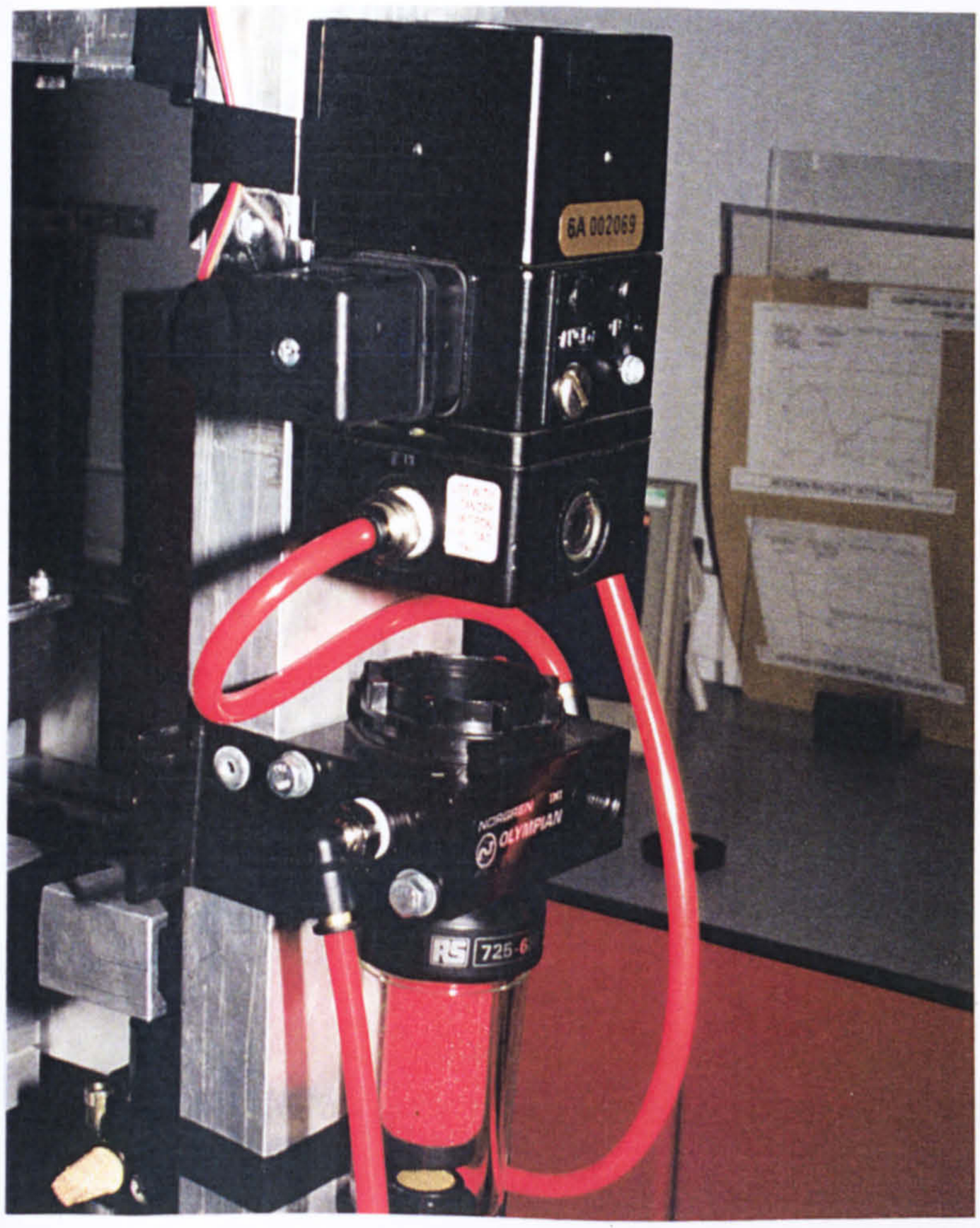

Picture E.11. Voltage-to-pressure converter and air filter.

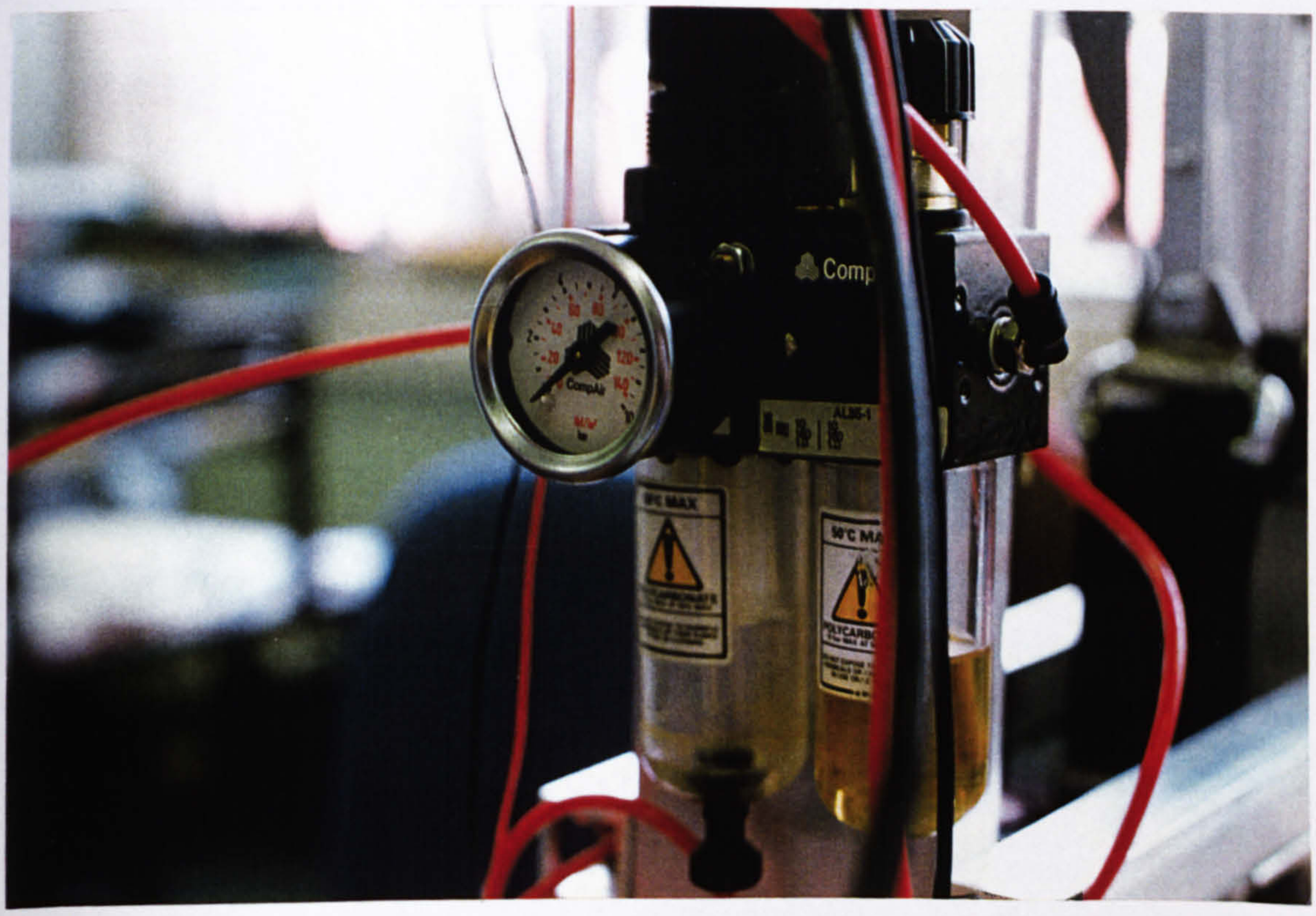

Picture E.12. Filter/Regulator and Lubricator.

Appendix F

Publications

Aritan, S., Dabnichki, P. and Bartlett, R., Program for generation of three-dimensional finite element mesh from magnetic resonance imaging scans of human limbs. Medical Engineering and Physics, 1997, 8(19), 681-689.

ELSEVIER

PII: S1350-4533(97)00039-8

Med. Eng. Phys. Vol. 19, No. 8, pp. 681–689, 1997
© 1997 IPEM Published by Elsevier Science Ltd
Printed in Great Britain
1350–4533/98 $19.00 + 0.00

Program for generation of three-dimensional finite element mesh from magnetic resonance imaging scans of human limbs

Serdar Aritan, Peter Dabnichki and Roger Bartlett

The Manchester Metropolitan University, Biomechanics Research Group, Hassall Road, Alsager ST7 2HL, UK

Received 17 March 1997, accepted 20 August 1997

ABSTRACT

A PC–AT based program for conversion of magnetic resonance imaging (MRI) scans into coordinate input for finite element mesh generation is presented. The program is written in Borland C + +3.1 and is compatible with every general-use personal computer, permitting the use of MS-DOS 3.0 or higher with a Microsoft mouse. The program is menu driven and does not demand specialised knowledge from the user. The system and memory requirements are minimal — 640 kB RAM — and it runs as a stand-alone program. A second program allows the construction of a three-dimensional representation of the limb sub-structure and generation of the FE mesh from the converted cross-sectional scans. The capabilities of the program are demonstrated using cross-sectional scans of the upper arm; the fat, muscle and bone contours were obtained to a very high level of precision (0.4 mm). © 1997 *IPEM Published by Elsevier Science Ltd*

Keywords: Image processing, finite element modelling, limb

Med. Eng. Phys., 1997, Vol. 19, 681–689, December

1. INTRODUCTION

The finite element method (FEM) is currently one of the best established numerical tools in the field of biomedical engineering and has been gaining in popularity in the computational analysis of complex biological structures. Despite the increasing amount of high quality work, a common weakness has become apparent, with the possible exception of some bone-related studies[1]. Practically all the models of bulky soft tissue areas and volumes have been based on approximate analytical representations and their geometrical accuracy has not been discussed[2–5]. This approach has been commonly adopted, for example, to reduce the computational cost or memory requirements; however, the principal reason remains the lack of accurate geometrical data in the literature. Nevertheless, the effect of geometrical accuracy has not been considered in sufficient detail.

A notable exception is an experimental simulation of the effect of the ischial tuberosity's geometry on the shear and compressive stress in buttock tissue[6]; this showed that the influence of the geometry on the stress magnitude could be very significant. In a numerical simulation of this experimental work, a possible variation of more than 60 percent was found in the shear stress. Prosthetic design and analysis, for example, require a correct description of the limb geometry and some recent studies have incorporated a highly accurate reproduction of the lower limb exterior[7–9]. However, only the surface shape was obtained using non-invasive methods, which are confined to measuring the outer contour and cannot establish the internal boundaries of the bones and tissue layers. The bone geometry is normally scanned and digitised, introducing subjective error and error of the bone's stipulation in the model. This impedes the introduction of highly accurate non-homogeneous models with a multi-layered structure. Commean *et al.*[9] proposed an innovative optical system for obtaining the outer contour of the limbs, which is highly sophisticated and accurate. However, this system cannot obtain the inter-layer boundaries.

The major reason for the current status of computational models of bulky soft tissue, as already mentioned, is the lack of reliable geometrical data in the literature which can serve the requirements of finite element analysis (FEA). Magnetic resonance imaging (MRI) and computer tomography (CT) scans seem ideal for this purpose, but to use their data is not a straightforward task and demands the implementation of image processing

Correspondence to: Mr S. Aritan.

and other numerical techniques. Currently, cost makes it infeasible for researchers to produce scans for every single subject and every different project. There is a large amount of data stored in hospitals and MRI centres all over the world to which researchers could obtain access, but not in an appropriate format for computational purposes and requiring conversion into relevant coordinate input. It should be noted that mesh generation, the first step in FE modelling, is a lengthy procedure, especially for three-dimensional problems. Ideally, a mesh should allow modifications such as density change and simulation of minor geometrical alterations, usually by changing some predefined parameters, and should be based on directly obtained anatomical data. Therefore it is important to possess an appropriate numerical tool to use the MRI data and to provide geometrical input for the generation or modification of finite element models. Most of the well established FE packages provide special facilities for parametric modification of an existing mesh. These facilities help the user to reduce the time and to increase the accuracy and reliability of model modifications.

The aim of this study was to devise a computational tool for obtaining accurate coordinate input for FE models of areas and volumes of biological structures, the emphasis being on human limbs. The program is used for transformation of MRI and CT scans into input data for FE models or other biomedical applications.

2. METHODS

The transformation of the pixel values of MRI scans into nodal coordinates in an appropriate coordinate system demands the use of image processing techniques. If an image contains a single uniformly grey object on a contrasting background, the contour line is defined by the grey level[10]. To establish the contours, one needs to analyse the field of view and to detect every change in the grey level. In the general case, when complicated contours are involved, the required algorithms are significantly more complex. Additional complications come from data processing errors, occurring as image defects. Another important issue is the required accuracy of the structure reproduction; in certain cases the researcher could neglect some relatively large inclusions such as thin layers of connective tissue in the stress analysis of human limbs.

The purpose of the program (*Figure 2*) is to automatically obtain the boundaries of the different structural layers in human limbs. The capabilities of the program were tested on cross-sectional scans of the upper arm, creating a three-dimensional reconstruction of a section of the upper arm (*Figure 7*a).

Eighteen cross-sectional scans of the right upper arm were obtained using a Siemens Magnetom Impact 1 Tesla MRI scanner. MRI scans were obtained with configuration of T1 Spin Echo and 8 mm slice thickness and 180° field of view. The subject was supine with his arm fully abducted. The scans were printed in MRI format. They were subsequently photographed on Ilford FP4 Plus negative film and printed onto matt photographic printing paper. All pictures were scanned by a Hewlett Packard Scanjet IIcx in 256 grey scale and saved as bit-map formatted files. The images were resized according to VGA high resolution (640 × 480 pixels, 16 colours) standards and saved in 16 grey scale palette in BMP format. The aspect ratio was 1.0003, which was considered in the subsequent calculations as 1.000.

3. PROGRAM STRUCTURE

The program presented consists of two modules organised in a sequential structure as illustrated in the block diagram (*Figure 1*). The program uses 36 computational functions, 10 graphics fuctions and 17 mouse functions. Severel Borland graphics functions are also used.

Each of the modules is explained in detail in the following sections. Technical programming details have been omitted for the sake of brevity and clarity. The program is menu driven and the menu is presented in *Figure 2*.

The circled numbers represent various functions; most of which are self evident and where: 1 = colour value legend; 2 = histogram: the per-

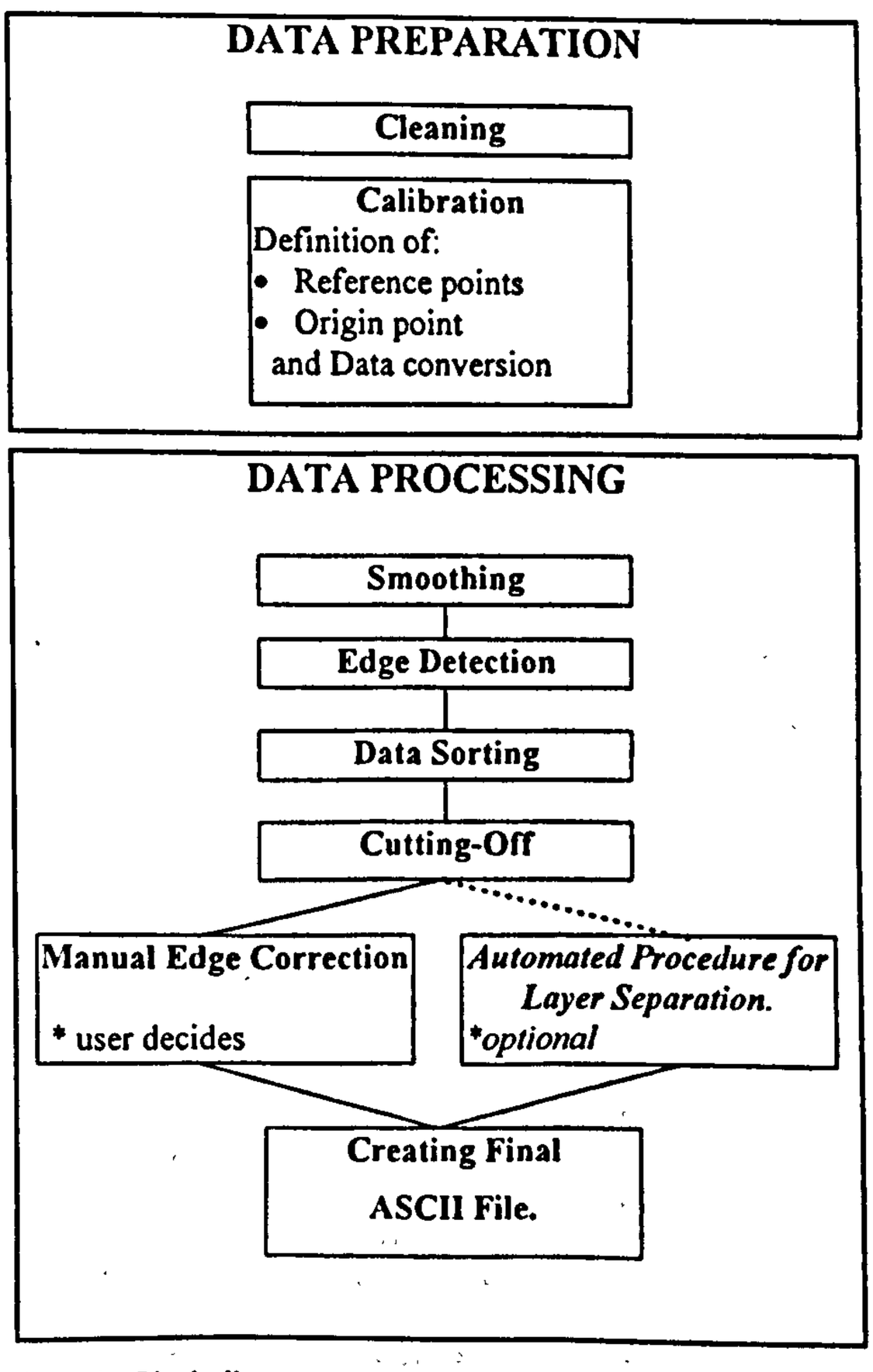

Figure 1 Block diagram.

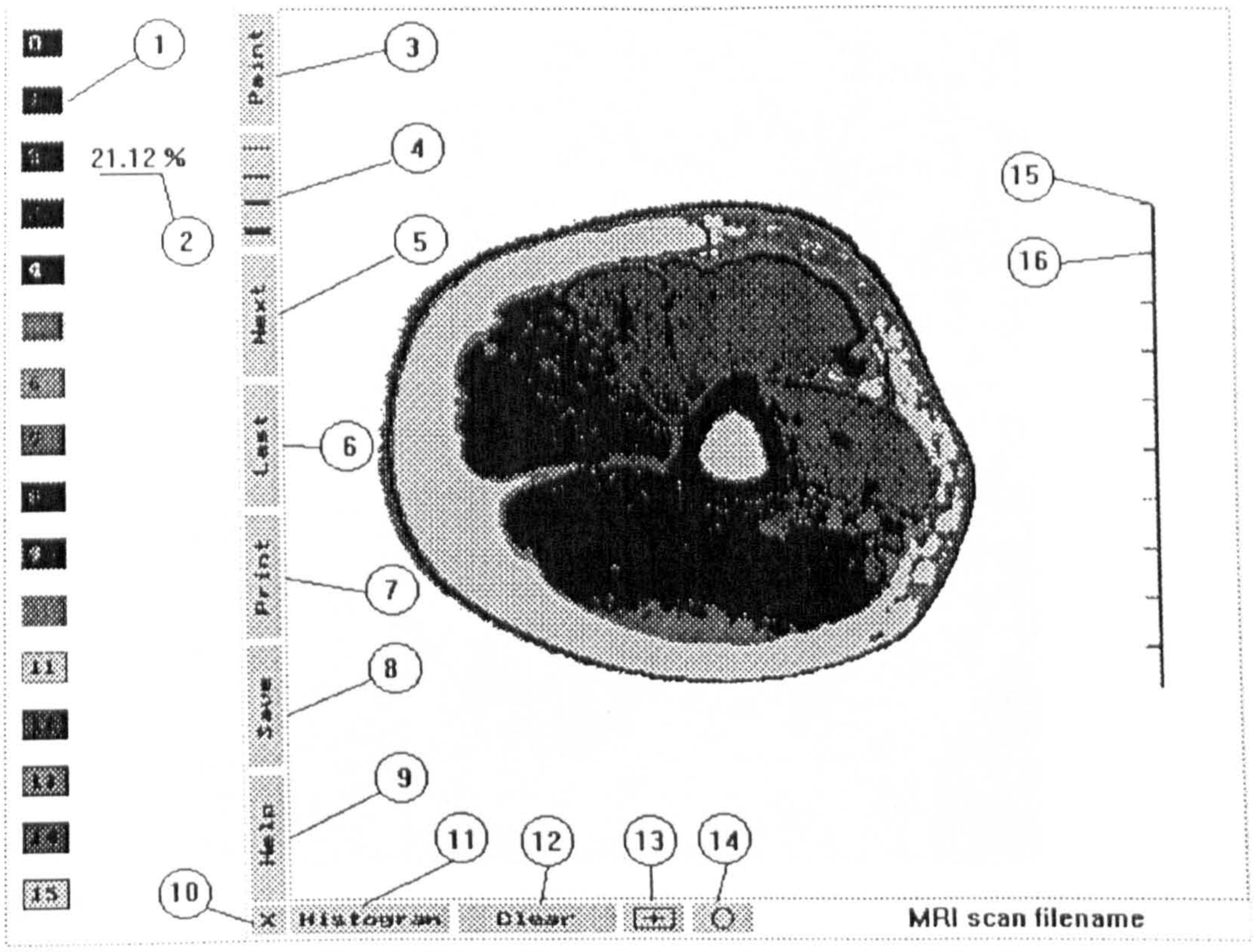

Figure 2 Menu layout.

centage of the respective colour in a selected area; 10 = exit (return to DOS); 11 calls the histogram function for a selected area; 12 = clear the selected area and relevant histogram values; 13 = calibration; 14 = scanning; 15 = reference point: (0, 0) coordinate in the global coordinate system for global orientation; 16, 15 are calibration points.

The program, as can be seen from *Figure 1*, is structured into two major phases — data preparation and data processing.

3.1. Data preparation

The first phase of the program, the data preparation, consists of two main procedures: (i) cleaning and (ii) calibration and data conversion.

3.1.1. Cleaning. Cleaning allows the user to manually replace 'unwanted' colour values of the defects occurring during data processing with the dominant colour of the surrounding area. This procedure is optionally called to 'paint' some artificially created spots (defects) which occur during the process of conversion of the MRI scans into bit-mapped files. These impurities would normally be detected by the edge-detecting algorithm and marked as possible edges; such erroneous information leads to complications in the internal contour definition. The difference between the original scan and the cleaned one can be seen by comparing *Figure 3*, the original, with *Figure 4*. Comparison of the original MRI films and derived scans can avoid erasing or altering useful information. It is apparent that the implementation of this procedure leads to homogenisation of the existing layers or areas in the image according to the researcher's perception and modelling needs. This approach was used to avoid long-running and complicated algorithms and with the clear understanding that researchers should be given the opportunity to finally assess and approve the obtained result.

3.1.2. Calibration. The MRI scans do not possess the necessary coordinate information. The data structure up to this step of the program run is saved in a binary file with the pixel domain value and colour value. In the calibration procedure, the pixel domain data is initially transformed into Cartesian coordinates. The points used to define finite elements are called nodes and their density depends on the structural, material and geometrical features of the model as well as the desired accuracy of the computational results. The origin of the radial scan lines can be selected by the user (*Figure 4*), with the frequency of the scan lines being varied until satisfactory results are achieved. This approach is similar to centre-based detection[11]. In *Figure 4*, a slice of the upper arm divided into 40 equal sectors is presented (9° angular increment). The calibration routine has an automatic and a manual option. The automatic one is adjusted to the scan format of the MRI scanner in use and the unit length (the distance between points 15 and 16 in *Figure 2*) is 10 mm. The first of them is considered as a reference point, i.e. it has the same x- and y-coordinates for all the scans.

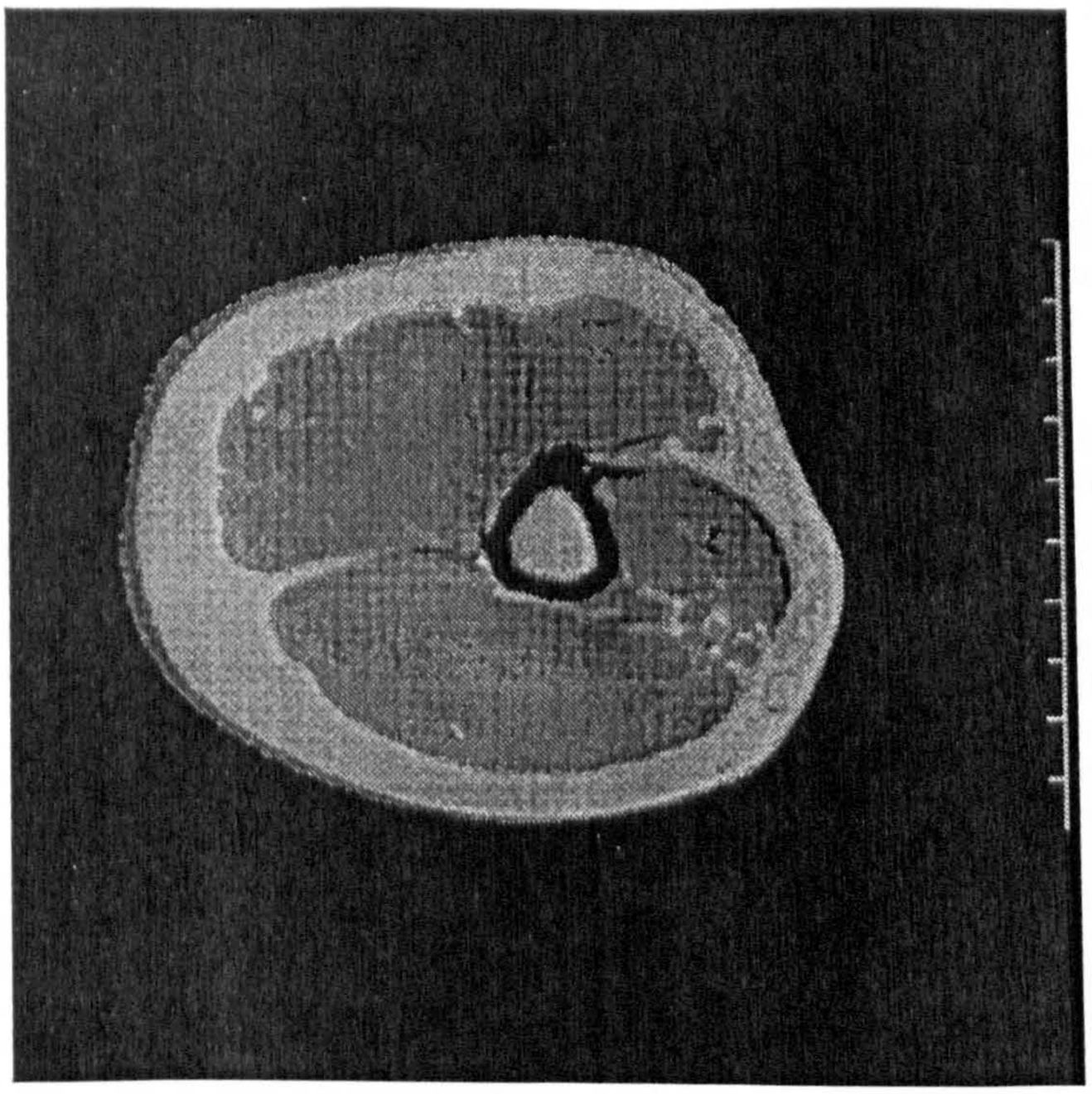

Figure 3 Original MRI scan.

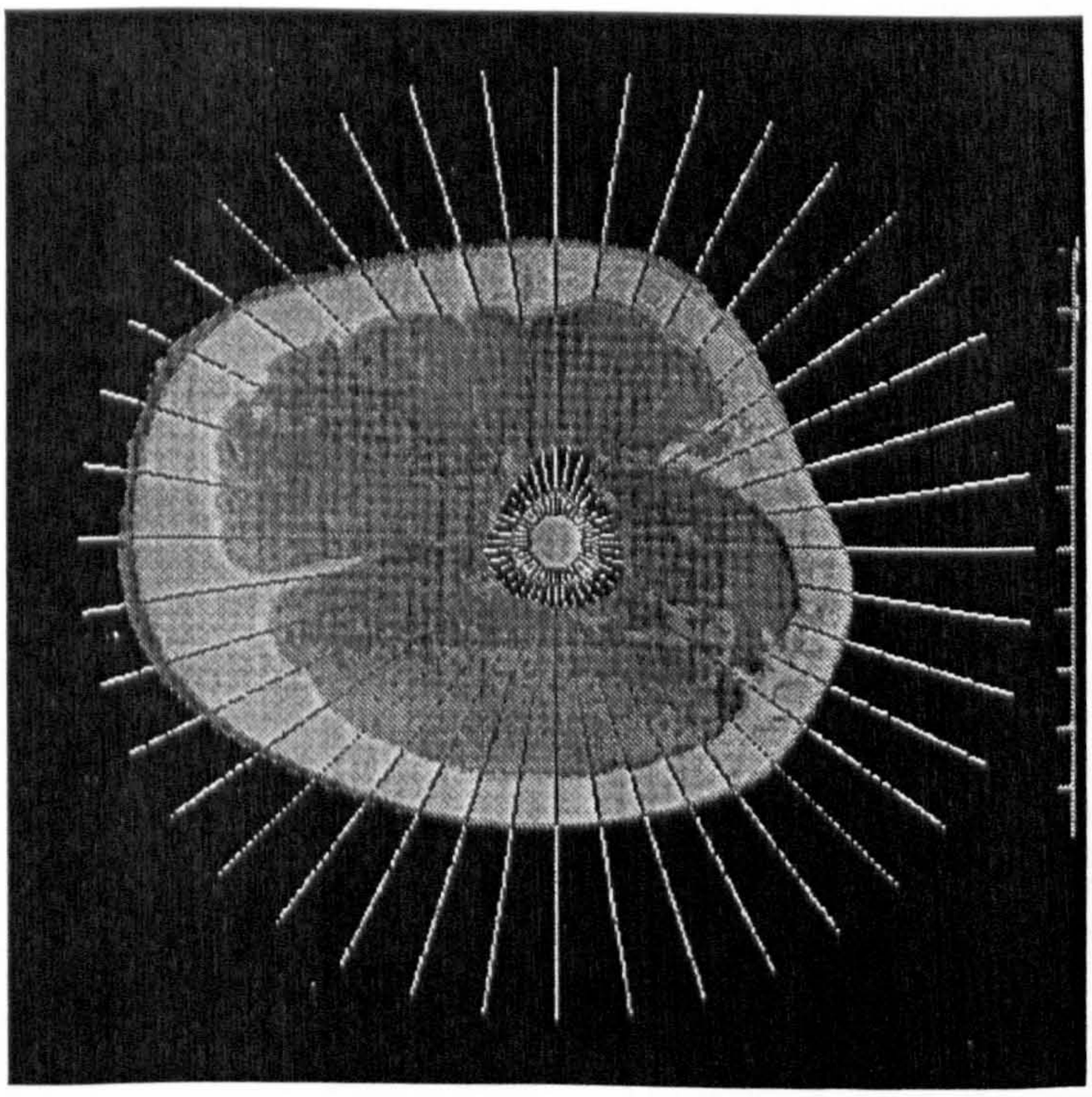

Figure 4 Model discretisation (radial lines on the cleaned picture).

This is important if the scans are to be linked into a three-dimensional structure to obtain their exact mutual position in space.

To convert the pixel values into standard coordinates using the manual procedure, the user is required to define a unit length, i.e. at least two points with a known distance between them; some externally fixed frame with attached calibration points could be used. This distance is to be defined as a program parameter. In addition to the scale factor definition, one needs to choose a fixed reference point to interrelate the coordinates in the different cross-sections. As already mentioned, the upper edge of the scale ruler (denoted as 15 in *Figure 2*) was selected in all MRI scans and recorded into the calibration file as the origin for the global coordinate system; again, some external markers could be used. At the end

of the calibration, data conversion of the scan lines takes place.

The procedures described above can be called independently by the user clicking the relevant menu button as shown in *Figure 2*. Only the cleaning procedure could be skipped, as it is optional. The other procedures are essential for the program to generate the appropriate output.

3.2. Data processing

The algorithms used in the data processing routine are sequential. Detailed description of the sub-procedures is given below.

3.2.1. Smoothing. The 'original' scanned image contains image defects that are abrupt colour changes in normally homogeneous areas. These image defects would normally trigger the edge detection algorithm to record possible edges. To reduce the number of such superficial edges, numerical smoothing of the colour values of the individual pixels along the selected radial scan lines was applied. The method applied uses moving averages, as can be seen in Equation (2). The colour value of each pixel represents a discrete function of two variables (the x- and y-coordinates of the pixel):

$$f(x_n, y_m) = C \quad (n = 0, 1, \ldots, 639;\ m = 0, 1, \ldots, 479) \tag{1}$$

$C = 0, 1, \ldots, 15$, and is originally an integer parameter representing the bit-map colour value. As the radial scan lines allow unidirectional sorting based on the radial length, both variables can have the same superscript. Therefore the new colour value attached to the pixel could be presented as:

$$f(x_i, y_i) = (f(x_i + 1, y_i + 1) + f(x_i, y_i))/2 \quad (i = 0, 1, 2, \ldots, N_l - 1) \tag{2}$$

where N_l is the number of pixels in a given radial scan line. It should be noted that after this step the colour value may not be an integer. The length definition was the standard two-dimensional norm based on the Cartesian coordinates of the pixels:

$$|n_i| = \sqrt{(x_i - x_{co})^2 + (y_i - y_{co})^2} \tag{3}$$

where x_{co}, y_{co} are the Cartesian coordinates of the selected origin of the cylindrical coordinate system.

By this procedure, sharp and abrupt colour changes are smoothed and single pixels with erroneous colour values are 'homogenised' to the dominant colour of the surrounding area.

3.2.2. Edge detection. This procedure is based on the finite difference calculus[12]. If the colour difference between two consecutive pixel values is greater than 1.0 a possible edge is indicated and recorded. This condition can be expressed mathematically as follows:

$$\Delta f(x_i, y_i) = |f(x_i + 1, y_i + 1) - f(x_i, y_i)| \tag{4}$$

$$\text{iff } \Delta f(x_i, y_i) > k \Longrightarrow \text{mark as possible edge} \tag{5}$$

$$0 < k < 15$$

A check of this condition along the defined radial lines allows detection and recording of all possible edges into a new binary file. If the smoothing procedure is performed, then the upper limit of k is 7.5. However, the smoothing routine is not used for automatic edge detection (presented later).

As explained in section 3.1.2, the pixel values have already been transformed into Cartesian coordinates. However, in the case of the scans of the upper arm, a cylindrical coordinate system is the natural choice as all the contours are closed, almost smooth and piecewise convex curves contained within a circle. The centre of the cylindrical coordinate system is defined by the user by clicking the mouse on the desired location (the centre of the bone in the current example) as the program calculates the orientation vector from the reference point (15 in *Figure 2*), and the x-axis is parallel to the Cartesian x-axis. The Cartesian coordinate values are then converted into cylindrical coordinates of the defined coordinate system. It should be noted that the Cartesian coordinate system represents the global coordinate system for all the scans and that the cylindrical coordinate system is a local system for each scan. The orientation vector allows linkage of these systems and the construction of the three-dimensional mesh.

3.2.3. Data sorting. The data obtained need to be ordered appropriately for quick and easy access and for further numerical manipulations. The Quick Sort Algorithm of Hoare[13,14] was used to order the nodes by ascending angles (key) anticlockwise and then by descending length (sub-key), using the cylindrical coordinates recorded in the file. This algorithm is the fastest existing general purpose sorting algorithm[13,14]. The data are sorted and recorded within the pre-existing binary file.

3.2.4. Cutting off. As a result of sorting, the possible edges are grouped along the radial lines and ordered by decreasing distance (length of the radius vector of the point) from the origin of the cylindrical coordinate system. An initial assumption for this procedure is that the detected edge with the longest length in a given radial line represents the outer edge. The initial cut-off value is a default real number, which can be adjusted by the user in the beginning of a particular program run but cannot be changed from scan to scan, to preserve a uniform criterion within the structure. Until the desired edge number is reached, the cut-off value is automatically adjusted with a preset increment of 0.4 mm (in the current example, equal to one pixel size in VGA resolution). This value can vary, depending on the size of the image and the scaling factor. This pass effectively stratifies the skin and fat, muscle, bone and marrow, defining each of them as a homogeneous layer. The cut-off value has a natural upper limit equal to the thickness of the thinnest layer in the structure analysed.

$$|\text{edge}_i| = n_i \quad (6)$$

where n_i is defined in Equation (3).

$$\text{outer—edge} = \sup_{f(x_i, y_i)} (n_i) \quad 0 \leq i \leq N_{ME} \quad (7)$$

where N_{ME} is the number of marked edges along a radial line.

$$\Delta l(i) = \text{length}_i - \text{length}_{i-1} \quad (8)$$

$$\text{iff } \Delta l(i) > C_{off} \Rightarrow \text{edge}_i = f(x_i, y_i) \quad (9)$$

$$\text{else} \Rightarrow \varnothing \text{ (nil return)}$$

$$\text{iff } i > N_E \Rightarrow C_{off} = C_{off} + \text{increment}$$

where C_{off} ($0.4 \leq C_{off} \leq \inf(\min t_i)$) is a threshold value representing length, t_i being the minimum thickness of a given layer or inclusion. N_E is a parameter representing a preset number of edges along a radial scan line.

However, this approach does not always allow the expected (existing) number of edges to be reached. A major drawback is that the cut-off value has a natural upper limit. If the thickness of the individual layers is significantly different, then the algorithm cannot reach the exact edge number.

3.3. Manual edge correction

This procedure is evoked if the number of detected edges in one radial scan line is greater than N_E, or when this parameter is not specified. Excessive edges are over-exposed on the original MRI scan, consecutively line-by-line helping the user to determine the unwanted edges. These redundant edges are usually caused by the existence of non-homogeneous inclusions in the tissue. The procedure allows deselection of all unwanted edges, using keyboard.

3.4. Cleaning the marked edges

At this stage all marked edges are deleted and the final binary file is created. As a feedback to the user, all consecutive edges are linked, creating a broken-line representation of the contours obtained (*Figure 5*). Consecutively this file is converted into an ASCII file to ensure compatibility with virtually all software products, as can be seen from *Figure 6*.

3.5. Automated procedure for layer separation (optional)

This part of the program is optional and is designed to automatically obtain the correct number of edges in a given structure and, therefore, to completely avoid user intervention. An inconvenience of this option is that the user is required to possess a very good pre-estimation for thickness tolerances and a very clear idea of what must be discarded or detected in a particular model. This requirement is a prerequisite for a proper choice of parameters and weight factors. A major difficulty in these definitions originates from the existence of two mutually contradictory requirements — to achieve a high level of accuracy in the edge detection and to neglect relatively big inclusions as 'non-significant'. The algorithm is designed to detect only simply connected areas, and best results are achieved on piecewise convex and smooth external boundaries. This module is not an integral part of the program and only a brief description is provided. The user is not expected to define the number of edges since the main purpose of the algorithm is to detect internal inclusions in the tissue or bone structure, which inevitably leads to a variable number of edges in different parts of the structure. The algorithm is based on the consideration of the colour function as a generalised function distribution[15]. This means that the colour values are defined as a function with a bounded compact support and an infinite number of derivatives. As the generalised functions naturally include the measure of the support set, the algorithm allows simultaneous averaging of the colour values and detection of the inclusions' boundaries. It works in two dimensions and is significantly slower with larger memory requirements. The procedure effectively performs two simultaneous tasks: homogenisation and separation. The homogenisation is based on the fundamental idea in the mechanics of continua[16], whereby the properties of a given material are represented by volume-averaged ones.

3.6. Finite element mesh generation and three-dimensional image construction

Finite element mesh generation and the three-dimensional representation of the images is a stand-alone program that uses the final binary output file created (*Figure 7*a). It has limited capabilities and is intended to be used solely for mesh generation and visualisation purposes. The visualisation is created as the nodes are ordered layer-by-layer and the corresponding nodes are linked by straight lines. For mesh generation, the user can set the desired divide (*Figure 7*b, dashed line) between the boundaries (*Figure 7*b, solid line) and the program generates the mesh coordinates as an ASCII file. The routine has some helpful features such as zoom-in, zoom-out, rotations and auto-scaling, as can be seen from *Figure 7*a. These features help the user to visually assess the results and to obtain a reasonably good idea for the finite element model.

4. RESULTS AND DISCUSSION

The capabilities of the program were illustrated on a sequence of scans of the upper arm. A three-dimensional discrete representation of a cylindrical section of the upper arm was created with an angular step increment of 9° and a 0.4 mm accuracy of node positions (*Figure 7*a).

The formatted images were processed to define the contours of skin and fat (these two layers can be split if required), muscle, bone and marrow (*Figure 7*b). The algorithm developed, similar to

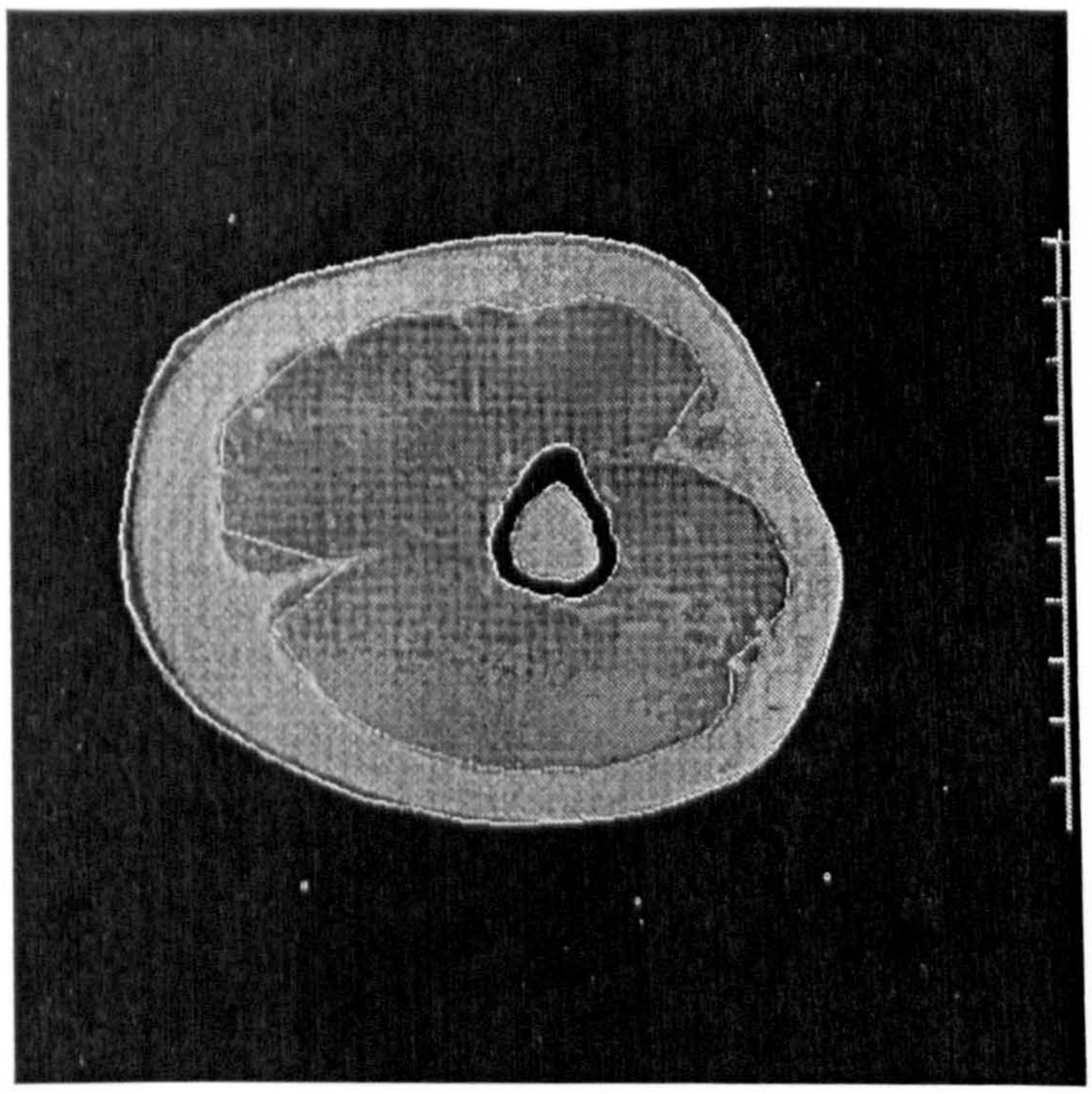

Figure 5 Image with superimposed contours.

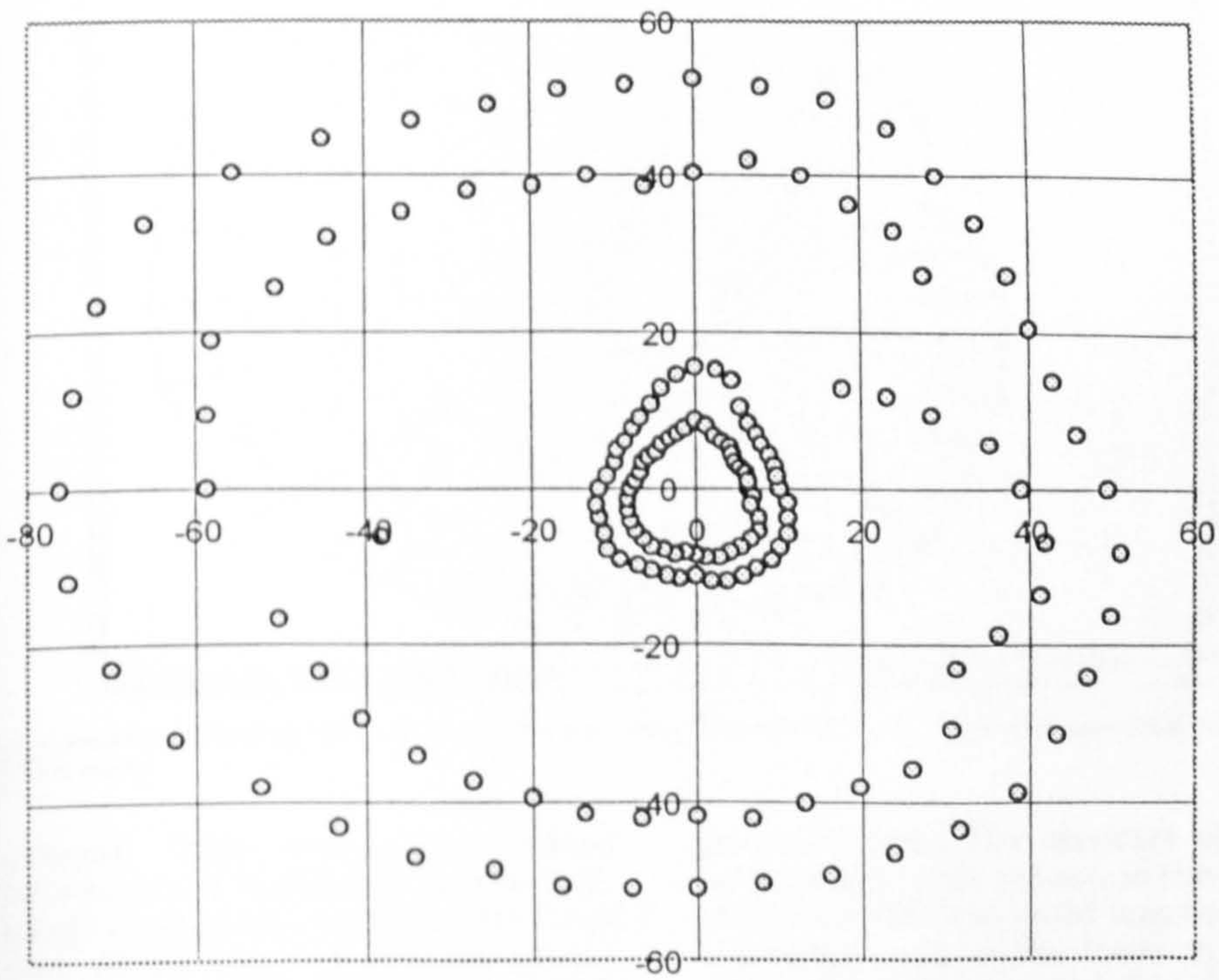

Figure 6 Cartesian coordinates of the inter-layer boundaries.

the moving average method, proved its ability to *detect* inter-layer boundaries when applied to *unidirectional* reading of pixels. The determination of the edges was based on a comparison of the finite difference value with a threshold value. A circular mask was drawn and overlaid on the cross-sectional scans of the upper arm, allowing for uniform discretisation of its contours (*Figure 4*). This circular mask was used to define the coordinates of the upper arm cross-sections in a natural local cylindrical coordinate system. Finally, the coordinates from the two-dimensional images were linked to create a three-dimensional wire frame representation of the layers.

The program developed provides a numerical tool for transforming MRI scans into nodal coordinates for input into FEA. It will also be used to study the relative deformation of the limbs in

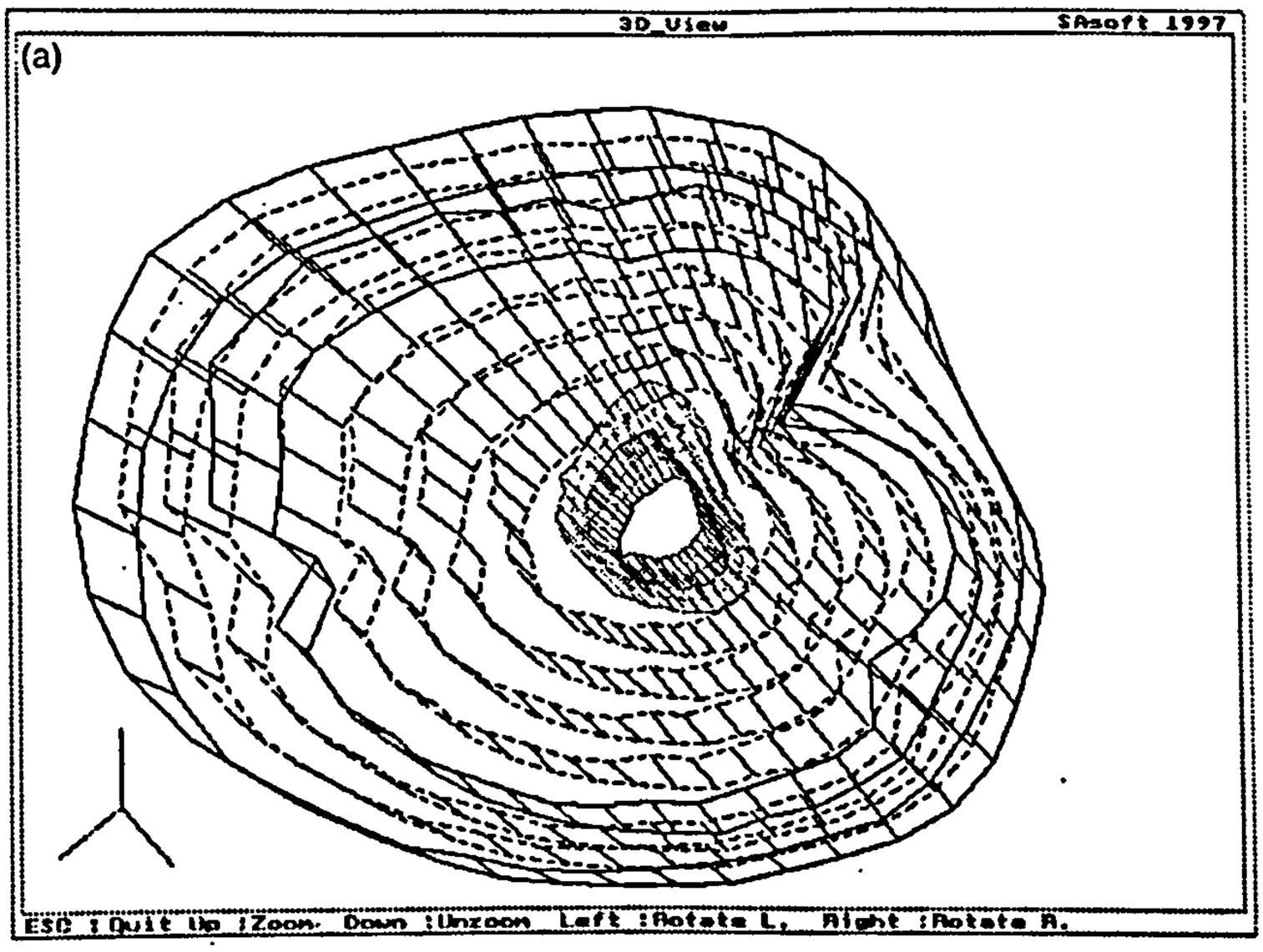

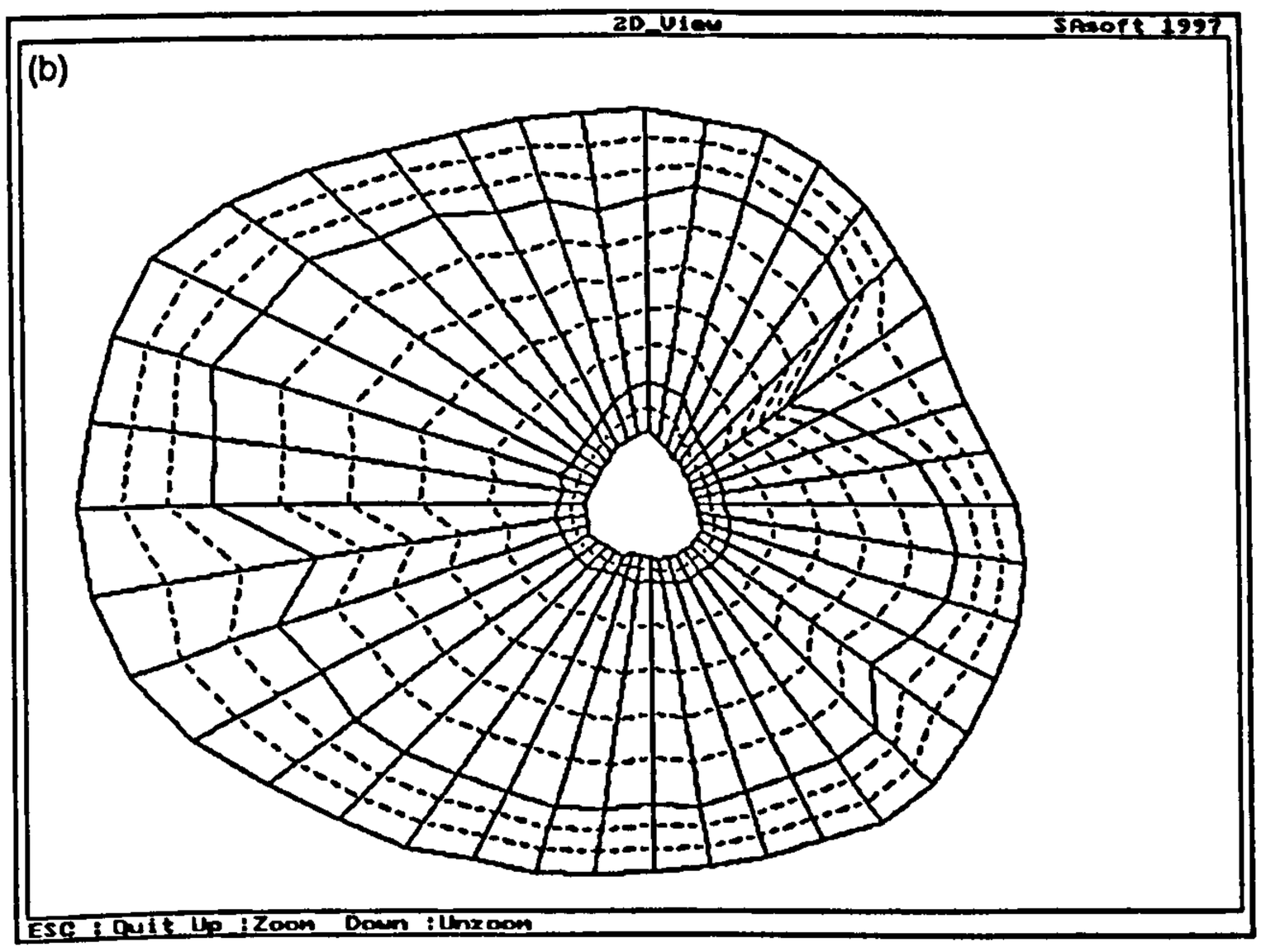

Figure 7 (a) Three-dimensional representation of the MRI scans and generated FE mesh. (b) Two-dimensional represantation of the MRI scan and generated FE mesh.

different positions. The averaging method adopted in the numerical realisation is very close to the continuum mechanics approach for homogenisation and allows clear separation of the skin, fat and muscle layers. The level of precision can be set by the user and parametric interpolation of the discrete contours is available. The output from the program can be used as digital input for manufacturing prosthetics or limb models.

Furthermore, the localised fat content can be estimated with a high level of accuracy. This application suggests that there is scope for some physiological applications such as finding muscle cross-sections or volumes. The accuracy can be improved significantly by increasing the density of the radial scan lines and using higher resolution graphics cards. The accuracy of reconstruction is obviously directly related to the ratio between one pixel and the real world length. For multiconnected areas, such as the forearm or the lower part of the leg, it is expected that the user will define the scan lines manually, using an external pointing device; the algorithm used in the example presented can then be implemented.

Finally, the cumbersome procedure used for transformation of the MRI scans into bit-map files could be avoided completely if the MRI manufacturer provided the format of the graphics file. Then either the image could be directly transformed into a bit-map file or the program could be modified to process different graphics files.

It should be noted that, in a number of studies, the bone shape was manually digitised. This man-

ual method usually adds an error that is largely stochastic and subjective. The current program can obtain the shape fully automatically and with a higher level of accuracy. The output data from the program could be utilised for prosthetic design or as input for graphics software packages.

Some further developments are deemed appropriate:

- to add facilities for conversion of different format graphics files into bit-mapped files;
- the output to be modified in order to provide input data in an appropriate format for the most popular FE products such as NASTRAN, ABAQUS, etc.;
- to develop an algorithm for more than one bone — i.e. for lower limbs; this will be added after some necessary tests.

5. CONCLUSION

A program was developed to convert MRI images to nodal coordinate input for FEA. The program is written in the C programming language and uses assembly language to access the system resources directly, thereby increasing the computational speed. The total running time for creating the full model with 18 cross-sectional scans was less than 10 min, including user intervention and three-dimensional graphics representation. This time can vary depending on the computer specifications and the quality of the MRI scans. The software was designed to be used specifically on limbs, but a potential user can find it applicable to other parts of the human body.

ACKNOWLEDGEMENTS

We would like to express our gratitude to the staff of the MRI centre at North Staffordshire Hospital and personally to the Chief Radiologist, Mr McNinch. This work has been supported by Hacettepe University, in Ankara, from where Mr Aritan is on sabbatical.

REFERENCES

1. Taylor, M. E., Tanner, K. E., Freeman, M. A. R. and Yettram, A. L., Stress and strain distribution within the intact femur: compression or bending?. *Med. Eng. Phys.*, 1996, 18(2), 122–131.
2. Dabnichki, P. A., Crocombe, A. D. and Hughes, S. C., Deformation and stress analysis of supported buttock contact. *Proc. Inst. Mech. Eng., Part H: J. Eng. in Med.*, 1994, 208, 9–17.
3. Todd, B. A. and Thacker, J. G., Three-dimensional computer model of the human buttocks *in vivo*. *J. Rehab. Res. and Dev.*, 1994, 31(2), 111–119.
4. Vannah, W. H. and Childress, D. S., Modelling the mechanics of narrowly contained soft tissues: the effect of specification of Poisson's ratio. *J. Rehab. Res. and Dev.*, 1993, 30(2), 205–209.
5. Chow, W. W. and Odell, E. I., Deformation and stresses of soft body tissue of a sitting person. *J. Biomech. Eng.*, 1974, 100, 79–87.
6. Candadai, R. S. and Reddy, N. P., Stress distribution in a physical buttock model: effect of simulated bone geometry. *J. Biomech.*, 1992, 15, 493–504.
7. Zhang, M., Lord, M., Turner, A. R. and Roberts, V. C., Development of non-linear finite element modelling of the below-knee prosthetic socket interface. *Med. Eng. Phys.*, 1995, 17(8), 59–66.
8. Silver-Thorn, M. B. and Childress, D. S., Parametric analysis using the finite element method to investigate prosthetic interface stresses for persons with trans-tibial amputation. *J. Rehab. Res. and Dev.*, 1996, 33(3), 227–238.
9. Commean, P. K., Smith, K. E. and Vanier, M., Design of a 3-D surface scanner for lower limbs prosthetics. *J. Rehab. Res. and Dev.*, 1996, 33(3), 267–278.
10. Castleman, K. R., *Digital Image Processing*. Prentice-Hall, New Jersey, 1979.
11. Tu, H. K., Matheny, A., Goldgof, D. B. and Bunke, H., Left ventricular boundry detection from spatio-temporal volumetric computed tomography images. *Comput. Med. Imag. Graph.*, 1995, 19(1), 27–46.
12. Hamming, R. W., *Numerical Methods for Scientists and Engineers*. McGraw-Hill, Tokyo, 1962.
13. Knuth, D. E., *The Art of Computer Programming, Vol. 3: Sorting and Searching*. Addison-Wesley, Reading, MA, 1973.
14. Kernighan, B. W. and Ritchie, D. M., *The C Programming Language*. Prentice Hall, New Jersey, 1988.
15. Boccara, N., *Functional Analysis: An Introduction for Physicists*. Academic Press, San Diego, CA, 1990.
16. Ciarlet, Ph., *Mathematical Elasticity, Volume 1: Three Dimensional Elasticity*. North Holland, Amsterdam, 1988.

CONTAINS DISKETTE

UNABLE TO COPY

CONTACT UNIVERSITY

IF YOU WISH TO SEE

THIS MATERIAL